Structural and Electrochemical studies of NaxMn1-yFeyO2 and NaNiO2 materials as positive electrode for Na-ion batteries

Benoit Mortemard de Boisse

université de BORDEAUX

THÈSE PRÉSENTÉE

POUR OBTENIR LE GRADE DE

DOCTEUR DE

L'UNIVERSITÉ DE BORDEAUX

ÉCOLE DOCTORALE DES SCIENCES CHIMIQUES

SPÉCIALITÉ : PHYSICO-CHIMIE DE LA MATIERE CONDENSEE

Par Benoît MORTEMARD de BOISSE

Structural and electrochemical studies of $Na_xMn_{1-y}Fe_yO_2$ and $NaNiO_2$ materials used as positive electrode materials for Na-ion batteries

Sous la direction de : Claude DELMAS
Co-directeurs : Dany CARLIER-LARREGARAY
Marie GUIGNARD

Soutenue le 1er décembre 2014

Membres du jury :

M. MAGLIONE Mario	Directeur de recherche, CNRS/ICMCB	Président
M. BOUCHER, Florent	Directeur de recherche, CNRS/IMN	Rapporteur
M. MASQUELIER, Christian	Professeur, LRCS	Rapporteur
M. HWANG, Bing-Joe	Professeur, NTUST	Examinateur
Mme. CARLIER Dany	Maître de conférences, CNRS/ICMCB	Directeur de thèse
M. DELMAS Claude	Directeur de recherche émérite, CNRS/ICMCB	Directeur de thèse
Mme. GUIGNARD, Marie	Chargée de recherche, CNRS/ICMCB	Directeur de thèse
M. WATTIAUX, Alain	Ingénieur de recherche, CNRS/ICMCB	Membre invité

Titre : Etudes structurales et électrochimiques des matériaux $Na_xMn_{1-y}Fe_yO_2$ et $NaNiO_2$ en tant qu'électrode positive de batteries Na-ion

Résumé :

Ce travail présente les études électrochimiques et structurales menées sur deux systèmes : P2/O3-$Na_xMn_{1-y}Fe_yO_2$ et O'3-Na_xNiO_2 utilisés en tant que matériaux d'électrode positive pour batteries Na-ion. Concernant le système P2/O3-$Na_xMn_{1-y}Fe_yO_2$, l'étude par diffraction des rayons X menée *in situ* pendant la charge de batteries a montré de nombreuses transitions structurales. Que leur structure soit de type P2 ou O3, les matériaux présentent une phase distordue pour les taux d'intercalation (x) les plus élevés et une phase très peu ordonnée pour les taux d'intercalation les moins élevés. Entre ces deux états d'intercalation, les phases de type P2 présentent moins de transitions que les phases de type O3. Cela entraine de meilleures propriétés électrochimiques pour les phases de type P2 (meilleure capacité en décharge, meilleure rétention de capacité…). Les spectroscopies d'absorption des rayons X et Mössbauer du ^{57}Fe ont montré que les couples redox Mn^{4+}/Mn^{3+} et Fe^{4+}/Fe^{3+} sont impliqués lors du cyclage, à bas et haut potentiel, respectivement.

Concernant O'3-$NaNiO_2$, la diffraction des rayons-X menée *in situ* pendant la charge de batteries O'3-$NaNiO_2$//Na a montré de nombreuses transitions structurales O'3 ↔ P'3 résultant du glissement des feuillets MO_2. Ces transitions s'accompagnent de mises en ordre Na^+ - lacunes dans le matériau. La taille des grains a montré avoir un intérêt majeur puisqu'elle influe sur le nombre de phases présentes simultanément dans le matériau. Lorsque la batterie est déchargée, la phase limitante $Na_{\approx 0.8}NiO_2$ est observée et empêche le retour à O'3-$NaNiO_2$

Mots clés : Batteries Na, matériaux d'électrode positive, oxydes lamellaires de sodium, mécanismes d'intercalation / désintercalation électrochimiques.

Title: Structural and electrochemical studies of $Na_xMn_{1-y}Fe_yO_2$ and $NaNiO_2$ materials used as positive electrode materials for Na-ion batteries

Abstract:

This work concerns the electrochemical and structural studies carried out on two systems used as positive electrode materials for Na-ion batteries: P2/O3-$Na_xMn_{1-y}Fe_yO_2$ and O'3-Na_xNiO_2. Concerning the P2/O3-$Na_xMn_{1-y}Fe_yO_2$ systems, *in situ* X-ray diffraction carried out during the charge of the batteries showed that both materials undergo several structural transitions. Both the P2 and O3 phases show a distorted phase for the higher intercalation rates (x) and a poorly ordered phase for the lower ones. Between these two states, P2-based materials exhibit less structural transitions than the O3-based ones. This is correlated to the better electrochemical properties the P2-based materials exhibit (better discharge capacity, better capacity retention…). X-ray absorption and ^{57}Fe Mössbauer spectroscopies showed that the Mn^{4+}/Mn^{3+} and Fe^{4+}/Fe^{3+} redox couples are active upon cycling, respectively at low and high voltage.

Concerning O'3-$NaNiO_2$, *in situ* X-ray diffraction carried out during the charge of O'3-$NaNiO_2$//Na batteries showed several structural transition between O'3 and P'3 structures, resulting from slab glidings. These transitions are accompanied by Na^+ - vacancies ordering within the "NaO_6" slabs. Upon discharge, the material does not come back to its initial state and, instead, the $Na_{\approx 0.8}NiO_2$ phase represents the maximum intercalated state. The occurrence of this limiting phase prevents O'3-$NaNiO_2$ to be considered as an interesting material for real Na-ion applications.

Keywords: Na batteries, positive electrode materials, sodium layered oxides, electrochemical intercalation / deintercalation mechanisms

Institut de Chimie de la Matière Condensée de Bordeaux

ICMCB/CNRS - UPR 9048

87, avenue du Docteur Schweitzer, 33608 Pessac Cedex

Acknowledgments

First, I would like to express my sincere gratitude to my supervisors: Dany CARLIER, Marie GUIGNARD and Claude DELMAS. They showed me great confidence and were of fantastic counselling during these three years. Their warm welcome made of the ICMCB a second home.

I would also like to thank Mario MAGLIONE for welcoming me at the ICMCB which was a highly stimulating environment to work in.

I am deeply thankful to the members of the jury: Florent BOUCHER and Christian MASQUELIER as rapporteurs, Bing-Joe HWANG as reviewer and Mario MAGLIONE as President.

This work would not have been possible without the financial support from the following institutions: *Région Aquitaine*, *Centre National de la Recherche Scientifique* and *Agence Nationale pour la Recherche* (Blanc Inter II, SIMI 8) n° 2011-IS08-01.

I would like to express my sincere thanks to everyone who contributed on this work at the ICMCB: Laurence CROGUENNEC (supervisor of *Groupe 2 : Matériaux et batteries*, for her advices and her help), Mélissa ARNAULT (experimental help), Sylvie BORDERE (Mössbauer spectroscopy), Philippe DAGAULT (TGA / DSC), Jacques DARRIET (XRD data interpretation), Cathy DENAGE (from experimental help to day-to-day in the laboratory help), Dominique DENUX (TGA / DSC), Graziella GOGLIO (auto-combustion type synthesis related discussions), Eric LEBRAUD (XRD experimental setups), Olivier NGUYEN (SQUID measurements), Stanislav PECHEV (XRD experimental setups), Sandrine QUILLATEAU (welcome desk), Stéphane TOULIN (Library) and François WEILL (TEM).

I distinctively wish to acknowledge and thank Alain WATTIAUX for introducing me to Mössbauer spectroscopy through our experiments, the GFSM congresses and numerous discussions.

A significant part of this work was carried out outside the ICMCB and I express my sincere gratitude to the following persons: Lydie BOURGEOIS (ISM, Raman spectroscopy), Christina DRATHEN (ESRF, synchrotron diffraction), Dmitry FILIMONOV (Lomonosov Moscow University, Mössbauer *in situ* cell design and discussion), Bing-Joe HWANG and his research team (NTUST / NSRRC, X-ray absorption spectroscopy experiments), Emmanuelle SUARD (ILL, neutron diffraction), Radostina STOYANOVA (Bulgarian Academy of Science, EPR experiments), Matthew SUCHOMEL (APS, synchrotron diffraction) and Thanya PHRAEWPHIPHAT (experiments on the $NaNiO_2$ system, Tokyo Institute of Technology).

Finally I would like to thank the members of *Groupe 2*, my friends and my family. They will find better acknowledgments in French in the following.

Remerciements

Je tiens tout d'abord à remercier mes encadrants de thèse, Dany CARLIER, Marie GUIGNARD et Claude DELMAS qui m'ont témoigné une grande confiance et laissé une grande autonomie au cours de ces trois années. Je suis notamment très reconnaissant de leurs nombreux et pertinents conseils. Leur accueil chaleureux a fait de l'ICMCB un second foyer.

Je voudrais également remercier Mario MAGLIONE pour m'avoir accueilli au sein de l'ICMCB, qui fut un environnement stimulant et riche en échanges.

Je tiens également à exprimer ma plus sincère gratitude aux personnes ayant accepté d'être membres du jury : Florent BOUCHER et Christian MASQUELIER, en tant que rapporteurs de ce travail et Bing-Joe HWANG en tant qu'examinateur. Je tiens une nouvelle fois à remercier Mario MAGLIONE pour en avoir assuré la présidence.

Je suis très reconnaissant envers la Région Aquitaine, le Centre National de la Recherche Scientifique ainsi qu'envers l'Agence Nationale pour la Recherche (Blanc Inter II, SIMI 8) n° 2011-IS08-01 qui ont financé ces travaux.

L'ensemble des travaux menés au cours de ces trois années sont le fruit des efforts et de la collaboration de plusieurs personnes. Je voudrais donc remercier plusieurs personnes de l'ICMCB : Laurence CROGUENNEC, responsable du groupe 2 : Energie : Matériaux et Batteries pour ses conseils et son humanisme, Mélissa ARNAULT (aide pour les expériences), Sylvie BORDERE (service Mössbauer), Philippe DAGAULT (mesures thermiques), Jacques DARRIET (traitement des données de diffraction des rayons-X), Cathy DENAGE (pour tout. Des séances MEB à sa connaissance quasi-encyclopédique du laboratoire et du groupe 2), Dominique DENUX (mesures thermiques), Graziella GOGLIO (synthèses par combustion), Eric LEBRAUD (pour sa précieuse aide sur la mise en place des expériences de DRX), Olivier NGUYEN (SQUID), Stanislav PECHEV (DRX), Sandrine QUILLATEAU (accueil) Stéphane TOULIN (pour son aide, sa disponibilité et son efficacité dans les recherches bibliographiques)) ainsi que François WEILL (MET, désolé pour $NaNiO_2$…).

Je souhaite particulièrement remercier Alain WATTIAUX pour m'avoir initié à la spectroscopie Mössbauer au gré des expériences, des congrès et de nos discussions multiples et variées, mais toujours passionnantes et passionnées.

Il m'est impensable de ne pas remercier ces personnes extérieures à l'ICMCB pour leur aide : Lydie BOURGEOIS (ISM, Spectroscopie Raman), Christina DRATHEN (ESRF, diffraction synchrotron), Dmitry FILIMONOV (Lomonosov Moscow University, design de la cellule *in situ* Mössbauer et discussions), Bing-Joe HWANG et son équipe de recherche (NTUST / NSRRC, spectroscopie d'absorption des rayons-X), Emmanuelle SUARD (ILL, diffraction des neutrons), Radostina STOYANOVA (EPR, Bulgarian Academy of Science), Matthew SUCHOMEL (APS, diffraction synchrotron) and Thanya PHRAEWPHIPHAT (Premières expériences sur le système $NaNiO_2$, Tokyo Institute of Technology).

En plus d'être un environnement scientifique de haute qualité, le groupe 2 et l'ICMCB représentent un environnement humain chaleureux exceptionnel. Pour leur gentillesse et leur amitié je souhaite remercier tous ceux qui ne figurent pas encore dans cette partie : Alexis (ALT + F4), Antoine, Arnaud (« tu veux un câlin ? »), Aurore, Brigitte, Cédric (ce fut un vrai plaisir de partager ce bureau), Céline (la place est chaude), Christophe (vive les chocobons), Delphine, Elodie (je ne peux écrire que quelques mots…), Elena, Estelle (« kikou », « oh non », « c'est sale ! »), Florian (tu materas ces VMP !), Frédéric, Gérôme, Hideyuki (see you soon in Japan), Jean-Marcel, Jun (sensei), Kais (mais… je ne peux pas écrire ça ici, voyons !), Laura (la femme chocolat), Laurent C. / J.P. (¿ Hola, qué tal?), Laurent P. (Le Mexique c'est chic), Lionel (« tu sors ! »), Liliane, Manu (Hey Manu !), Mathieu (Enfin !), Mattéo (désolé de ne pas être là pour ta soutenance !), Mélissa (b***** !), Michel M., Michel U (le seul et unique), Mickael, Nicolas (mais juste un doigt alors), Olivier (dat flash *bis*), Paola, Philippe Ve (tu l'as écouté ?), Philippe Vi., Vincent D., Vincent P. (assures-toi que les vannes restes ouvertes), Sabine, Ségolène (tu vas cartonner !), Shashi (now you have the longest name), Shawn (tu es l'un des nôtres), Stéphane (« comme le canard sur l'eau »), Sylvain (me suivras-tu cette fois ?) et Ylias. Ainsi que quelques autres hors laboratoire : Amélia (allons-y !), Pinou (chef) et Stéphane H. (s'il y a une rue à ton nom, c'est bien pour une raison !).

Je n'aurais jamais pu faire ce travail sans que tant de personnes m'aient transmis une partie de leurs connaissances. Je remercie donc sincèrement mes anciens enseignants et professeurs, et en particulier Virginie VIALLET pour m'avoir transmis sa passion de la recherche au cours d'un stage de master inoubliable.

Enfin, je souhaite remercier mes parents et ma famille sans lesquels je n'aurais jamais pu m'embarquer dans cette aventure. Merci de m'avoir laissé « dessiner en dehors des lignes » et d'avoir toléré mes premières expériences « scientifiques ».

Table of Contents

General Introduction

Mastering energy production was the requirement to build our modern society. Since electricity is delivered to houses and public facilities, it improved our way of life: we live longer, in better health and have an instant access to information and people. Nowadays, our more and more nomadic lifestyle requires to be accompanied by our communication devices. This was possible by miniaturizing the electronic components of our devices whose portability could only be achieved by their association to a mobile power source: the secondary battery technology (Nickel-Cadmium, Nickel-Metal Hydride batteries). However, as the power requirements of the mobile technologies (smartphones, laptops…) increased, it was necessary to find a new technology capable of delivering higher energy densities and the Li-ion battery technology was developed.

A_xMO_2 layered oxides (with A = Li or Na, M = transition metal and $x \leq 1$) were already known since the 1950s [1-9] and were mostly studied for their physical properties. Most of the known systems were reinvestigated in the 1980s for their reversible intercalation/deintercalation properties of the alkali ion (A^+). Among these studies, Goodenough's team discovered the electrochemical properties of $LiCoO_2$ as positive electrode in Li-ion batteries in 1980 [10]. This discovery lead to the commercialization of the first Li-ion battery by Sony© in 1991. Following this discovery almost all researches were focused on Li-ion battery materials as the sodium homologous suffers from the comparison for mobile applications. Indeed, Na element is more than 3 times heavier (22.99 $g.mol^{-1}$ vs 6.941 $g.mol^{-1}$) and is larger than the Li one (their ionic radii are respectively equal to 1.02 Å and 0.76 Å) which implicates worse volumetric and weight energy densities for the Na-ion batteries. Moreover, the Na^+/Na couple redox potential is 0.3 V higher that the Li^+/Li one ($E°_{(Na+/Na)}$ = -2.71 V *vs.* SHE[1] and $E°_{(Li+/Li)}$ = -3.01 V *vs.* SHE[1] [11]), leading to a lower energy. From the 1990s, $LiMO_2$ positive electrode materials became safer and lighter as they became more complex. Nowadays, $Li(Ni, Co, Al)O_2$ [12-15] and $Li(Ni, Mn, Co)O_2$ [16, 17] materials are preferred to $LiCoO_2$ to equip new electric vehicles. Other materials such as spinel $LiMn_2O_4$ and olivine $LiFePO_4$ are also considered [18-21]. It must be noted that, in addition of possessing interesting electrochemical properties, $LiMn_2O_4$ and $LiFePO_4$ materials represent a non-toxic alternative to cobalt-based materials.

Today, the world still faces energetic problems and disparities. If the developed countries have an easy access to energy, it is not the same for the emerging ones. This situation could lead to important ecological issues if they decide to adopt polluting energy sources such as coal. A solution to this problem would be to encourage the transition towards greener energy sources, such as solar and wind farms. However, this remains a utopia as the associated energy production is still unforeseeable and intermittent.

[1] SHE: Standard Hydrogen Electrode

The use of Li-ion batteries once seemed appealing to regulate the energy production but the price of the raw materials and the energetic price of manufacturing the batteries were so high, it would wipe out any benefit represented by the green energy sources.

In this context, the Na-ion battery technology, that was for a long time set aside, was revisited in the 2000s. Indeed, as the regulation of the energy production from renewable sources requires stationary batteries, the lower mass and volume energy densities of the Na-ion technology do not represent a problem anymore. New criteria are thus established for these applications, which are the price, abundance and eco-compatibility of the materials [22]. As a consequence, the number of studies on Na_xMO_2 materials involving non-toxic or less-toxic transition metals elements (M = Mn, Fe, Ni…) increased significantly in the 2000s [22-25]. In the present work, we focused on two systems were studied among Na_xMO_2 materials:

Investigations in the $Na_xMn_{1-y}Fe_yO_2$ system. This topic represents the first part of this manuscript. Among Na_xMO_2 systems involving several transition metals, the $Na_xMn_{1-y}Fe_yO_2$ one was never studied for its electrochemical properties in 2011 – starting date of this thesis – despite representing a low-cost and environmental friendly candidate with an interesting theoretical discharge capacity of ≈ 240 $mAh.g^{-1}$. Following Yabuuchi's et al. work of $Na_xMn_{1/2}Fe_{1/2}O_2$ materials in 2012 [26], several studies were released concerning the electrochemical and structural properties of various $Na_xMn_{1-y}Fe_yO_2$ materials [27-33].

The first chapter of our study of $Na_xMn_{1-y}Fe_yO_2$ materials focuses on the preparation and characterization of the pristine materials with y = 1/3, 1/2 and 2/3 with P2 and/or O3 structures (**Chapter A-I**). These materials were prepared by a self-combustion type synthesis I approached during my Master's degree internship in LRCS, Amiens, FRANCE with Dr. V. Viallet. Most extensive studies are then presented and focus mainly on the limitations of the different materials and on their behavior while cycling in Na batteries (**Chapters A-II** and **A-III**). These studies include electrochemical tests in various conditions, *in situ* X-ray powder diffraction during Na^+ deintercalation, structural resolutions and following of the redox properties upon Na^+ deintercalation. These last studies were part of the Franco-Taiwanese LaNaMox ANR project[2] and were the opportunity for me to go to Taiwan and to the Synchrotron facility[3]. The evolution of the electrochemical and structural properties along with the Mn / Fe ratio is discussed in **Chapter A-IV**.

[2] Blanc Inter II, SIMI 8 n° 2011-IS08-01, in partnership with NTUST, Taiwan, R.O.C.
[3] National Synchrotron Radiation Resource Center, Taiwan, R.O.C.

Investigation of the O'3-$NaNiO_2$ phase diagram. While Na_xMO_2 materials were not studied for Na-ion batteries applications for nearly two decades, numerous studies focused on the correlation between their structure and physical properties, especially concerning Na_xCoO_2. Following a similar approach, the second part of this work concerns the preparation and characterizations of Na_xNiO_2 phases (**Chapter B-I**). The evolution of the Na_xNiO_2 phase diagram upon cycling was also investigated by *in situ* X-ray powder diffraction during the full charge of a Na_xNiO_2//Na cell. Our choice of the Na_xNiO_2 phase diagram followed the study of Vassilliaras et al. who reported in 2012 the long-term electrochemical properties of O'3-$NaNiO_2$ along with an insight of the structural changes the material undergoes upon cycling [34].

Chapter I: The Na_xMO_2 layered oxides and the Na-ion battery technology

Table of Contents

The purpose of this first chapter is to give the keys required to understand the state of art of sodium layered oxides (Na_xMO_2). First the different structures of sodium layered oxides are described. Then, the principle of Na and Na-ion batteries are presented with the main electrochemical quantities employed to compare the different materials. The last part of this chapter is a bibliographic study on Na_xMO_2 materials.

I.1. Structure of the Na_xMO_2 layered oxides

I.1.a. The α-$NaFeO_2$ structure

The first described A_xMO_2 layered oxide (A = alkali element and M = transition metal(s)) was the α-$NaFeO_2$ one, using the NaCl rock salt structure type [1]. In this representation, the O^{2-} ions occupy the Cl^- position, creating a face-centered cubic network. The Na^+ and Fe^{3+} cations occupy the octahedral NaO_6 and FeO_6 sites created by the oxygen anions, respectively (the former Na^+ octahedral sites in NaCl). The difference in the ionic radii of the two ions (r_{Na^+} = 1.02 Å and $r_{Fe^{3+}}$ = 0.645 Å) imposes an altering of the Na^+ and Fe^+ ions along the [111] direction, as shown in **Figure I.1**, which leads to the rhombohedral distortion of the cubic cell (**Figure I.1b**).

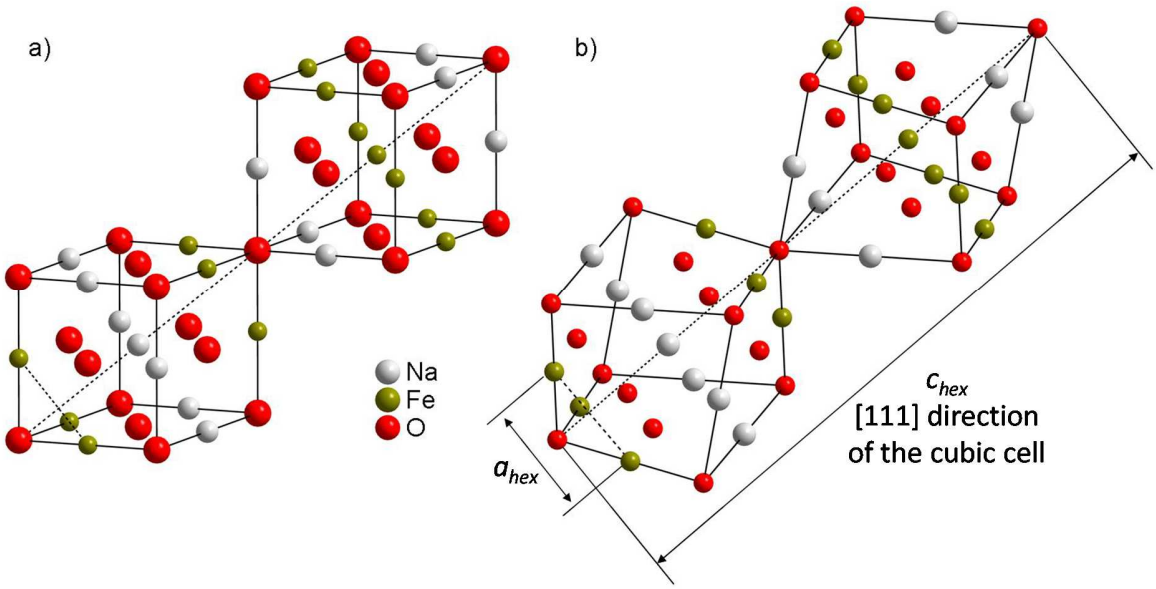

Figure I.1: Representations of (a) the α-$NaFeO_2$ structure in the NaCl rock salt-type structure and (b) the distortion of the cell due to the Na^+ / Fe^{3+} altering. Cell and atomic parameters from [35].

Nowadays, most of the layered oxides are described using a hexagonal cell instead of the rhombohedral one. In this representation the c_{hex} axis is parallel to the previous $(111)_{cubic}$ direction highlighting the cationic ordering along the c_{hex} axis: the edge-sharing FeO_6 octahedra create the $(FeO_2)_n$ layers while Na^+ ions occupy the interlayer space, as shown in **Figure I.2**.

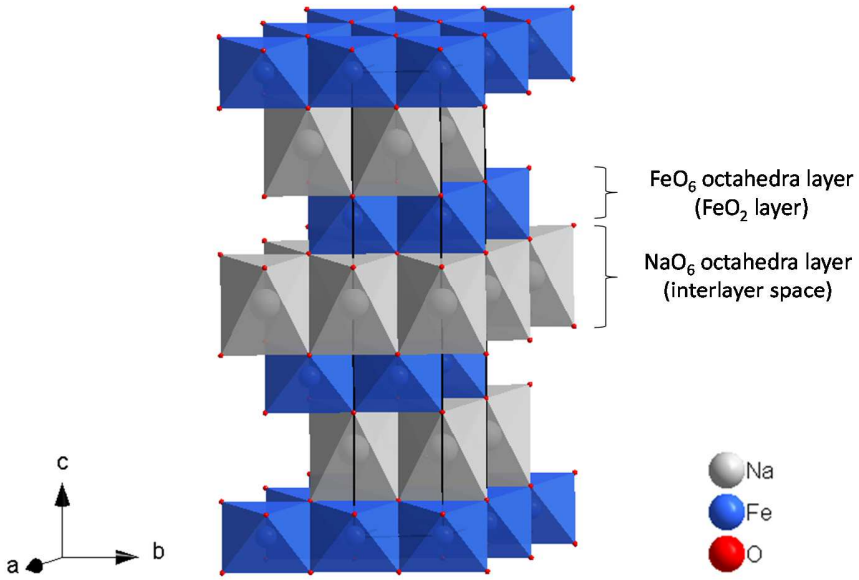

Figure I.2: Representation of the α-$NaFeO_2$ structure in the hexagonal symmetry (the unit cell is shown by black lines) highlighting the altering of the FeO_6 and NaO_6 octahedra layers along the c_{hex} axis. Cell and atomic parameters from [35].

I.1.b. Other Na_xMO_2 structures

Due to its large ionic radius, Na^+ ion can also accommodate trigonal prismatic sites between the MO_2 layers and different polytypes for sodium layered oxides Na_xMO_2 are possible, depending on the Na/M ratio, the synthesis temperature and the nature of the transition metal(s). These polytypes show different oxygen layers stacking sequences, and are easily described using a denomination specific to layered oxides [36]. It consists in a letter corresponding to the alkali geometric site (Octahedral of Prismatic) followed by the number of MO_2 layers needed to describe the structure in the hexagonal cell. A representation of the three possible structure types (O3, P3 and P2) is given in **Figure I.3**.

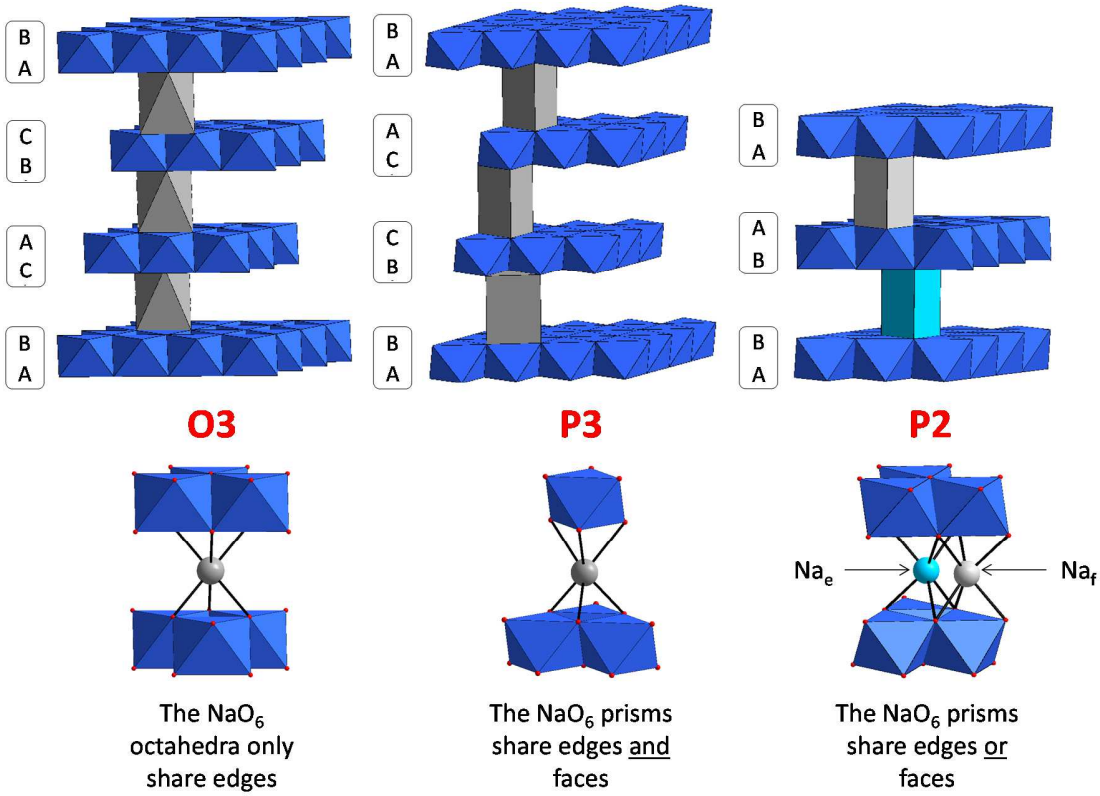

Figure I.3: Representation of the O3, P3 and P3 structure types. The Na^+ environment in the different structure types is also represented.

In the O3 structure type, the oxygen layers stack along the $\vec{c}$ direction following an ABCA… sequence. This is the structure type of α-$NaFeO_2$. Na^+ ions are located into octahedral NaO_6 sites which only share edges with the surrounding MO_6 octahedra. Materials with an O3 structure type are commonly obtained for a Na/M ratio equal or close to one [36], independently of the transition metal: M= Ti, V, Cr, Mn, Fe, Co… [1, 4, 5, 37-39]. The low repulsions between the NaO_6 octahedral sites allow filling up the sodium sites completely. This structure type is also the only one possible for $LiMO_2$ materials prepared by solid state chemistry synthesis, because of the small ionic radii of the Li^+ ion (0.76 Å).

In the P3 structure type, the oxygen layers stack following an ABBCCA… sequence and the Na^+ ions occupy prismatic sites sharing faces and edges with the surrounding MO_6 octahedra. P3 phases are usually obtained at moderate temperature (≈ 500 °C) and for lower Na/M ratios (≈ 0.5) [36].

The P2 structure type shows an ABBA… stacking sequence of the oxygen layers and the Na^+ ions also occupy prismatic sites. However these sites are different from the P3 structure as the NaO_6 polyhedra share either edges (Na_e site) or faces (Na_f site) with the surrounding MO_6 octahedra. Due to higher electrostatic repulsions between the Na_f^+ and M^{n+} ions, the Na_f site is less favorised and the observed Na_f : Na_e ratio is usually close to 1 : 2 for x ≈ 0.7. Note that adjacent Na_e and Na_f sites cannot be occupied

simultaneously. These materials are commonly obtained by solid state chemistry synthesis for a Na/M ratio inferior to 1 (usually ≈ 0.7) [36].

The space groups and atomic positions used to describe the O3, P3 and P2 structures are given in **Table I.1**. The table also shows that only the atomic positions of the oxygen and sodium ions differ between the O3 and P3 structure types. Moreover, for P3 and P2, the crystallographic sites for Na^+ ions cannot be fully occupied because the distance between two nearest sites is too short and is incompatible with the Na^+ size.

Structure type	Space Group (number)	Atomic positions				
		Na_e	Na_f	Na	M	O
O3	R-3m (# 166)			3b (0 0 1/2)	3a (0 0 0)	6c (0 0 z_{O3}) $z_{O3} \approx 0.27$
P3				6c (0 0 z_{P3}) $z_{P3} \approx 5/6$	3a (0 0 0)	6c (0 0 z_{P3}) $z_{P3} \approx 0.40$
P2	$P6_3/mmc$ (# 194)	2b (2/3 1/3 1/4)	2d (0 0 1/4)		2a (0 0 0)	4f (1/3 2/3 z_{P2}) $z_{P2} \approx 0.09$

Table I.1: Usual space groups and atomic positions for the O3, P3 and P2 structure types.

I.1.c. Distorted structures and the cooperative Jahn-Teller Effect

Presentation of the Jahn-Teller effect

In 1937, H.A. Jahn and E. Teller proved the theorem stating that "any nonlinear molecular system in an electronic state with orbital degeneracy will be unstable and will undergo a distortion to lower its symmetry in order to lift the degeneracy and lower the energy" [40]. A simplified interpretation is that for some electronic configurations of transition metal ions (M^{n+}), the associated ML_6 octahedra (L = Ligand) will be distorted. However, the Jahn-Teller theorem predicts only that a distortion must occurs to lift the degeneracy but does not predict the geometrical nature of the distortion, which will commonly consist in either the elongation or shortening of the M-L bonds along the z axis of the octahedron.

In transition metal solid state chemistry, strongest Jahn-Teller effects are expected for the electronic configurations with unevenly occupied e_g orbitals such as [41, 42]:

- High-spin (HS) d^4 (t_{2g}^3 e_g^1): HS Cr^{2+}, Mn^{3+}, Fe^{4+} …
- Low-spin (LS) d^7 (t_{2g}^6 e_g^1): LS Ni^{3+}, Co^{2+}…
- LS d^9 ($t_{2g}^6 e_g^3$): LS Cu^{2+}, Ag^{2+} …

The electronic configurations and lifts of degeneracy concerning the HS d^4 and LS d^7 electronic configurations we encountered during this work are represented in **Figure I.4** and clearly show the lowering of the energy accompanying the lift of degeneracy. The ML_6 octahedra are represented with oxygen atoms as ligands.

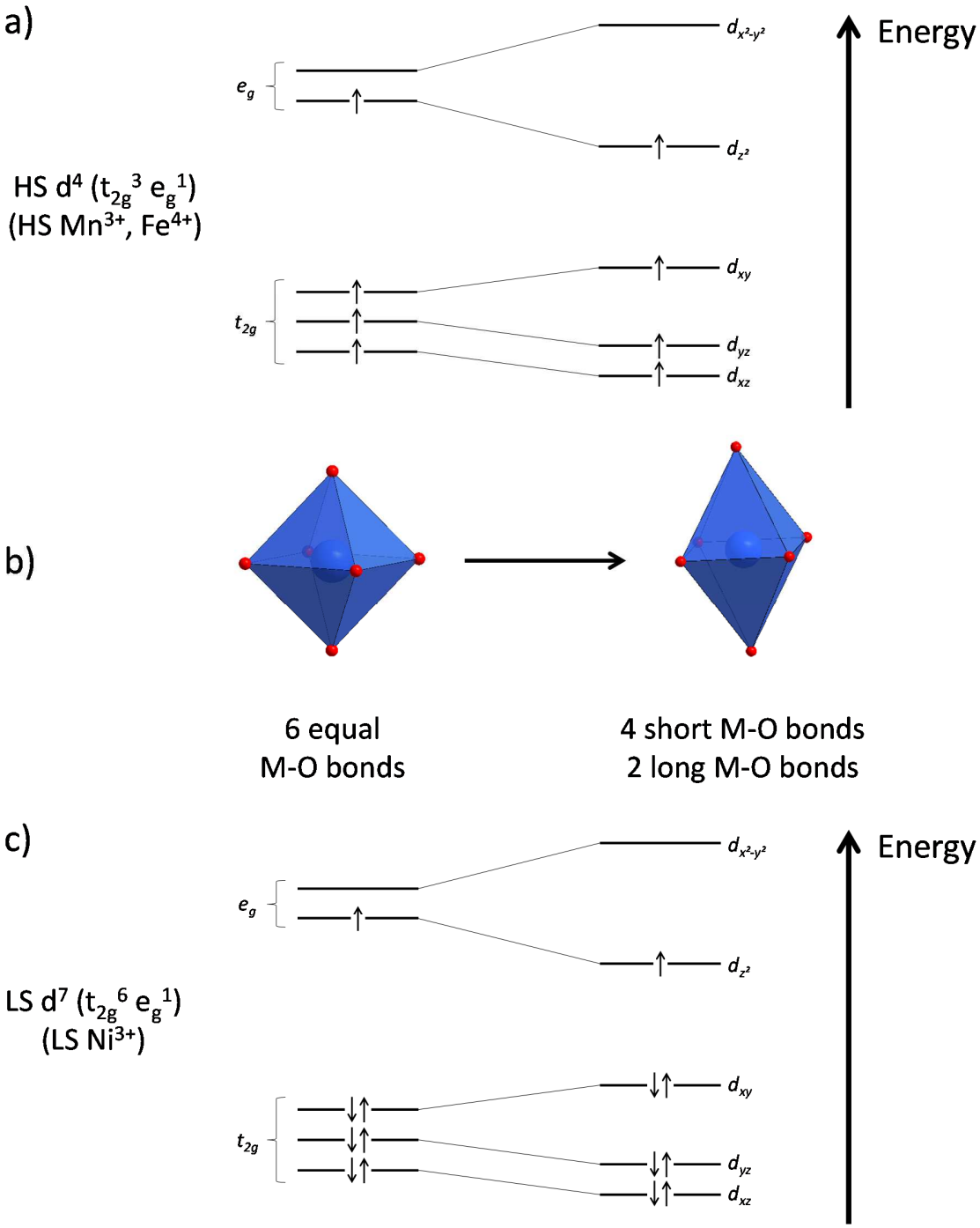

Figure I.4: Representation of the ground electronic states and lift of degeneracy of 3d orbitals for the (a) HS $3d^4$ and (c) LS $3d^7$ configuration states. A schematic representation of the corresponding MO_6 octahedra is also given (b).

In the A_xMO_2 materials, each MO_6 octahedron is connected to 6 MO_6 octahedra by sharing edges. Therefore, if the fraction of $M_{(Jahn\text{-}Teller)}O_6$ distorted octahedra is high enough, the distortion can affect the surrounding $M_{(non\ Jahn\text{-}Teller)}O_6$ octahedra and a *cooperative Jahn-Teller effect* is observed. In Na_xMO_2 materials, the cooperative Jahn-Teller effect leads to the macroscopic distortion of the hexagonal symmetry. A prim symbol is added to the nomenclature to differentiate the corresponding distorted materials: P'2, P'3 or O'3. A projected representation of the distorted structures is given in **Figure I.5** below. Note that the prim symbol is also used to describe distorted materials whose distortion does not result from a cooperative Jahn-Teller effect.

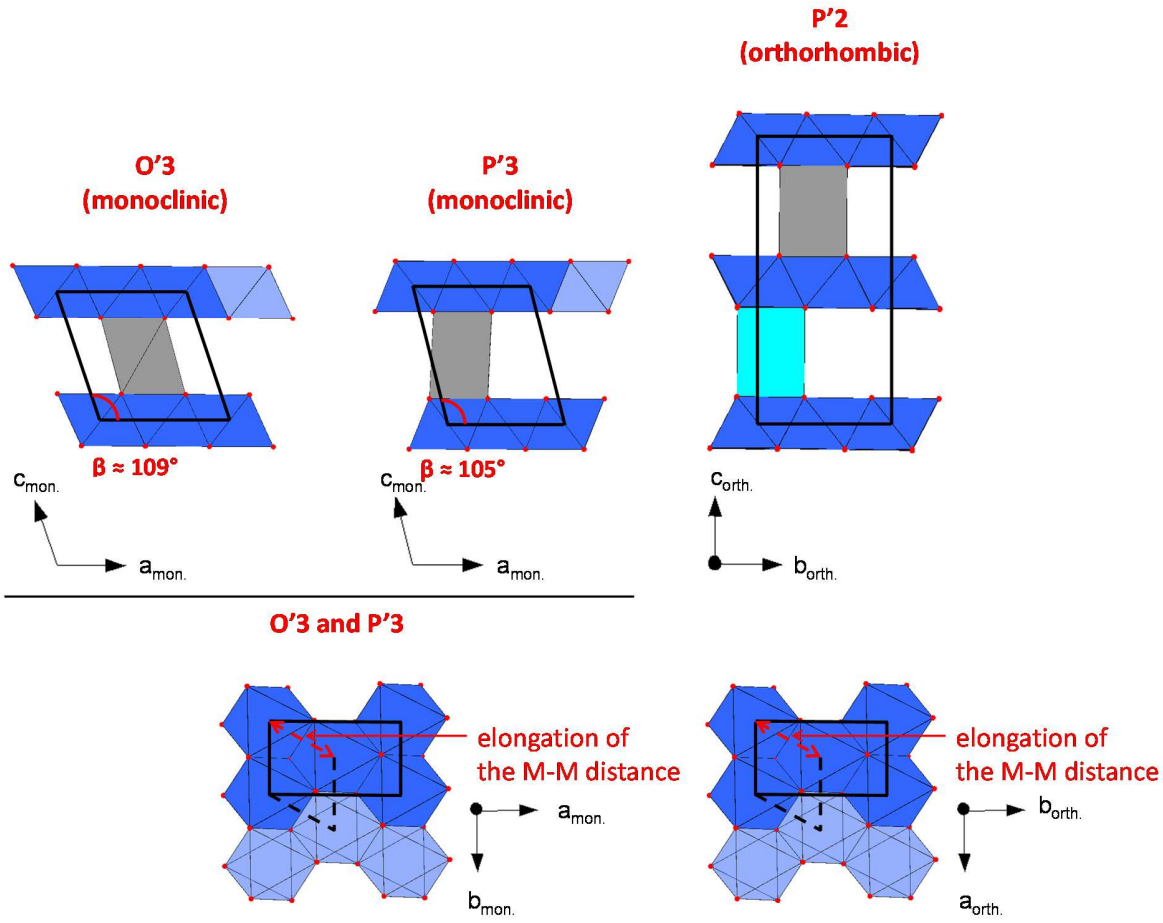

Figure I.5: Projections of the distorted structures in the ($a_{mon.}$,$c_{mon.}$) and ($a_{mon.}$,$b_{mon.}$) planes (O'3, P'3) or in the ($b_{orth.}$,$c_{orth.}$) and ($a_{orth.}$,$b_{orth.}$) ones (P'2).

P'2 structure types exhibit orthorhombic crystal symmetry whereas the O'3 and P'3 structure types exhibit a monoclinic one. The only differences between the O'3 and P'3 structures are the atomic positions of the oxygen and sodium atoms. The space groups and atomic positions used to describe the P'2, P'3 and O'3 structures are given in **Table I.2**.

Structure type	Space Group (number)	Atomic positions				
		Na_e	Na_f	Na	M	O
O'3	C2/m (# 166)			2c (0 0 1/2)	2a (0 1/2 0)	4i (x_O 0 z_O)
P'3				4i (x_{Na} 0 z_{Na})	2a (0 1/2 0)	4i (x'_O 0 z'_O)
P'2	Cmcm (# 63)	4c (0 y_{Nae} 1/4)	4c (0 y_{Naf} 1/4)		4a (0 0 0)	8f (0 y_O z_O)

Table I.2: Usual space groups and atomic positions for the P'2, P'3 and O'3 distorted structure types.

Relations between the hexagonal cells and the orthorhombic and monoclinic cells

It is possible to describe the undistorted hexagonal structures into the orthorhombic or monoclinic cells. The relations between the hexagonal symmetries and the lower ones for an undistorted example are given in **Table I.3**.

Transformation Hexagonal cell → orthorhombic or monoclinic cell	Relations
P2 (hex.) → P'2 (orth.)	$\overrightarrow{a_{orth.}} = \overrightarrow{a_{hex.}}$ $\overrightarrow{b_{orth.}} = \overrightarrow{a_{hex.}} + 2\,\overrightarrow{b_{hex.}}$ $\overrightarrow{c_{orth.}} = \overrightarrow{c_{hex.}}$
P3 (hex.) → P'3 (mon.) O3 (hex.) → O'3 (mon.) (choice # 1)	$\overrightarrow{a_{mon.}} = 2\,\overrightarrow{a_{hex.}} + \overrightarrow{b_{hex.}}$ $\overrightarrow{b_{mon.}} = \overrightarrow{b_{hex.}}$ $\overrightarrow{c_{mon.}} = -\frac{4}{3}\overrightarrow{a_{hex.}} - \frac{2}{3}\overrightarrow{b_{hex.}} + \frac{1}{3}\overrightarrow{c_{hex.}}$ $\beta_{mon.} \approx 122°$
P3 (hex.) → P'3 (mon.) O3 (hex.) → O'3 (mon.) (choice # 2)	$\overrightarrow{a_{mon.}} = 2\,\overrightarrow{a_{hex.}} + \overrightarrow{b_{hex.}}$ $\overrightarrow{b_{mon.}} = -\overrightarrow{b_{hex.}}$ $\overrightarrow{c_{mon.}} = -\frac{2}{3}\overrightarrow{a_{hex.}} - \frac{1}{3}\overrightarrow{b_{hex.}} - \frac{1}{3}\overrightarrow{c_{hex.}}$ $\beta_{mon.} \approx 107°$

Table I.3: Relations between the hexagonal cell parameters and the orthorhombic (P2 / P'2 structures) or monoclinic (O3 / O'3 and P3 / P'3) ones for a non-distorted example.

As shown in **Table I.3**, two choices are possible to describe the O'3 and P'3 structures. They are differentiated by the atomic positions, the $c_{mon.}$ cell parameter and the $\beta_{mon.}$ angle. These relations between the hexagonal P3 and O3 structures and the monoclinic ones are represented in **Figure I.6**.

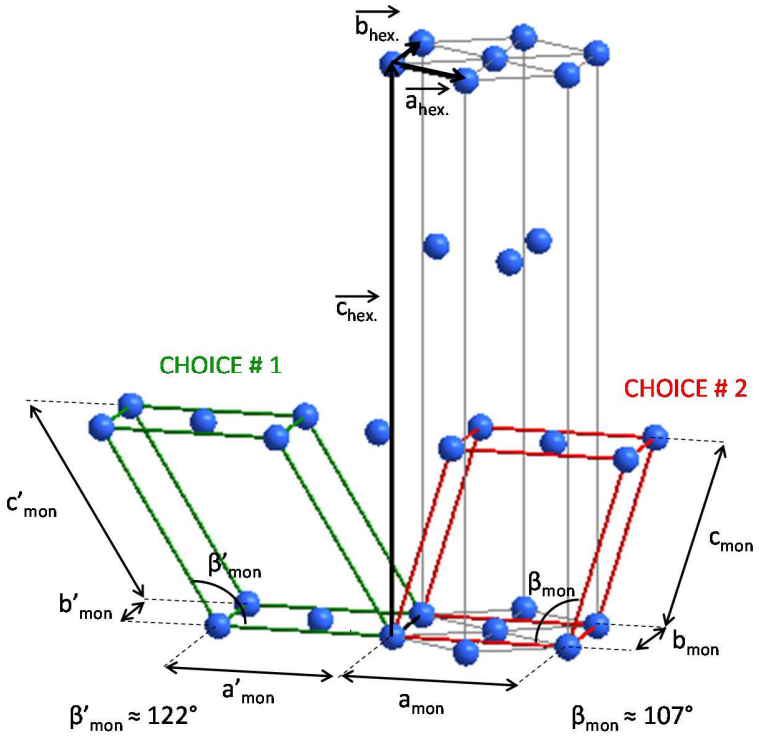

Figure I.6: Representation of the relations between the hexagonal cell and the two possible monoclinic ones. For more clarity the monoclinic cells have been shifted and only the transition metal atoms are represented.

For phases with undistorted structure, the $b_{orth.}$ or $a_{mon.}$ cell parameter is equal to $\sqrt{3}$ $b_{hex.}$. Therefore the comparison between the undistorted and distorted cells will give precious information on the origin of the distortion in the P'2, P'3 or O'3 structures, through the $b_{orth.}/a_{orth.}$ or $a_{mon.}/b_{mon.}$ ratio:

- If the $b_{orth.}/a_{orth.}$ or $a_{mon.}/b_{mon.}$ ratio is close to $\sqrt{3}$ (≈1.73), the Jahn-Teller distortion is negligible.
- If the $b_{orth.}/a_{orth.}$ or $a_{mon.}/b_{mon.}$ ratio is significantly higher than $\sqrt{3}$, the distortion is considered as being induced by a cooperative Jahn-Teller effect.

The correlation between the $b_{orth.}/a_{orth.}$ or $a_{mon.}/b_{mon.}$ ratio and the cooperative Jahn-Teller effect was first reported by Parant et al. in 1971 in Na_xMnO_2 materials [5].

I.1.d. Determination of the distances in the hexagonal and distorted structures

From the cell parameters it is possible to obtain an estimation of the *interslab distance* between two layers of transition elements and the *in plane* transition metal distances. A representation of the interslab and the in plane M-M distances in the orthorhombic and monoclinic cells is given in **Figure I.7**. The relations between the crystal structure and the interslab and in plane distances are given in **Table I.4**.

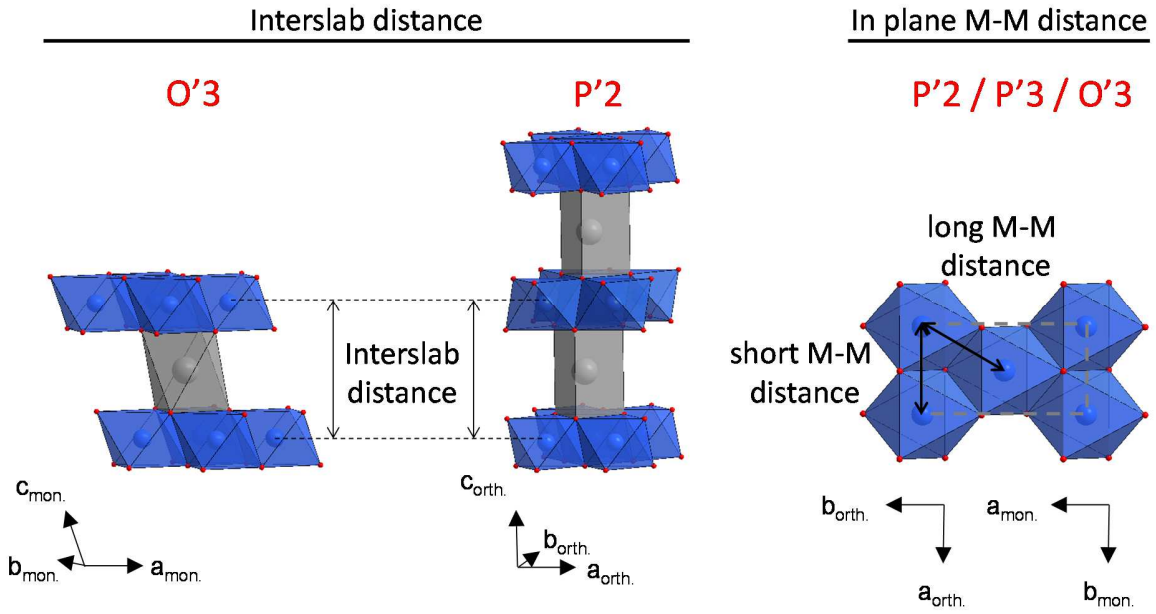

Figure I.7: Representation of the interslab distance (left) and in plane M-M distances (right) into the orthorhombic and monoclinic structures.

Structure-type	Interslab distance	In plane M-M distance estimation
P2 (hexagonal)	$c_{hex.}$ / 2	$a_{hex.}$
P'2 (orthorhombic)	$c_{orth.}$ / 2	$a_{orth.}$ (short M-M distance) $\frac{\sqrt{a_{orth.}^2 + b_{orth.}^2}}{2}$ (long M-M distance)
P3 / O3 (hexagonal)	$c_{hex.}$ / 3	$a_{hex.}$
P'3 / O'3 (monoclinic)	$c_{mon.}$ x sin ($\beta_{mon.}$)	$b_{mon.}$ (short M-M distance) $\frac{\sqrt{a_{mon.}^2 + b_{mon.}^2}}{2}$ (long M-M distance)

Table I.4: Relations between the cell parameters of the different structures and the interslab and in plane M-M distances.

Examples of the cooperative Jahn-Teller effect in O'3-$NaNiO_2$ and O'3-$NaMnO_2$

An example of the importance of the cooperative Jahn-Teller effect in O'3-$NaNiO_2$ and O'3-$NaMnO_2$ is given in **Table I.5**. In these materials, 100 % of the involved transition metal ions present a Jahn-

Teller effect (LS $3d^7$ for Ni^{3+} and HS $3d^4$ for Mn^{3+}). The $a_{mon.}/b_{mon.}$ ratio highlights a stronger cooperative Jahn-Teller effect in O'3-$NaMnO_2$ than in O'3-$NaNiO_2$ in agreement with the difference in M-O distances.

	O'3-$NaNiO_2$	**O'3-$NaMnO_2$**
Cell parameters (S.G.: C2/m)		
a =	5.311(1) Å	5.673(1) Å
b =	2.840(1) Å	2.856(1) Å
c =	5.568(1) Å	5.807(1) Å
β =	110.44(1) °	113.29(1) °
$a_{mon.}/b_{mon.}$ ratio	1.87	1.99
$M^{3+}O_6$ octahedron		
short M-O distances:	4 * 1.91(1) Å	4 * 1.94(1) Å
long M-O distances:	2 * 2.14(1) Å	2 * 2.39(1) Å

Table I.5: Cell parameters, $a_{mon.}/b_{mon.}$ ratios and M-O distances in O'3-$NaNiO_2$ and O'3-$NaMnO_2$. O'3-$NaNiO_2$: data from [43], O'3-$NaMnO_2$: data from [44].

I.2. Na_xMO_2 layered oxides as positive electrode materials in Na and Na-ion batteries

I.2.a. Principle of Na and Na-ion batteries

The Na-ion battery technology involves materials able to exchange sodium ions between two electrodes. Depending on the chemical potential of these electrodes are associated the terms of *positive electrode* (higher potential) and *negative electrode* (lower potential), in order to avoid the *cathode* and *anode* terms which can be confusing as they depend if the battery is charged or discharged. The two electrodes are separated by an electrolyte, which usually consists in a sodium salt dissolved into a non-aqueous solvent. For a Na cell, the assembled battery is represented in its initial state in **Figure I.8a**.

During the electrochemical charge of the battery, a current is applied to oxidize the transition element(s) constituting the positive electrode and to reduce the Na^+ ions at the negative one. To balance the charge neutrality of the material, Na^+ ions are deintercalated from the structure at the positive electrode and go into the electrolyte, as illustrated in **Figure I.8b**. Meanwhile, on the negative electrode, the Na^+ ions are reduced using the extra electrons (e^-) provided by the external circuit. The opposite phenomenon happens during the discharge of the battery, as illustrated in **Figure I.8c**: once the electrical circuit is closed, the transition metals elements at the positive electrode are reduced and the Na^+ ions are reintercalated. The oxidation of the metallic Na^0 from the negative electrode provides electrons to the electrical circuit.

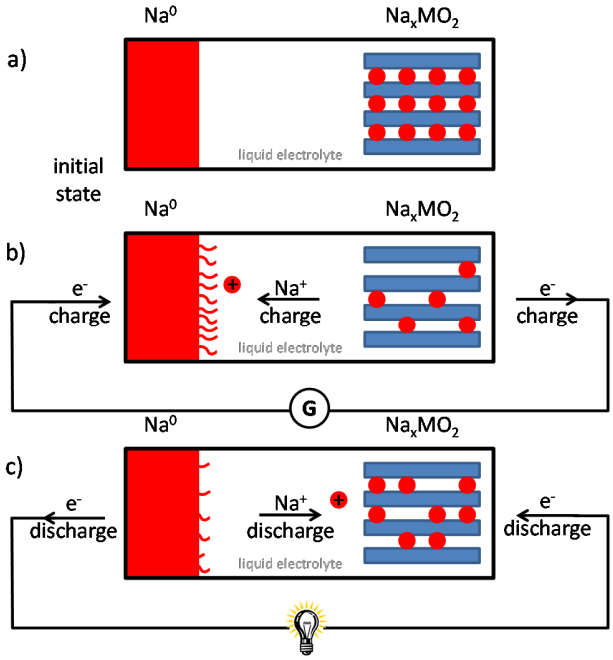

Figure I.8: Representation of a Na battery in (a) its initial state and during (b) the charge and (c) the discharge of the cell.

The nature of the negative electrode gives the denomination of the technology. If the negative electrode consists in sodium metal, the battery will be referred to as a *Na battery*. On the other hand, if the negative electrode is an insertion / alloy / conversion compound which doesn't involve the reduction of Na^+ ions in Na metal, the battery will be referred to as a *Na-ion battery* by analogy to the Li-ion technology. The use of an alkali metal foil (Li or Na) leads to the formation of *dendrites* during the charge (visible in **Figure I.8b**), which grow as the cycle number increases, the result being the degradation of the battery by short circuit. Therefore, the Na battery technology is limited to the study of the materials at the laboratory scale and is unsuitable for real applications. A lot of researches are ongoing to find materials which can insert Na^+ at low voltage. Among them hard carbon is one of the best materials so far [45-47].

I.2.b. Electrochemical variables

Several variables are used to compare and evaluate the performances of batteries. Three of them –the sodium content, the discharge capacity and the charge/discharge rate– were mostly used in this work and are described in the following.

Sodium content

The sodium content, noted x, expresses the concentration of Na^+ ions intercalated in the material at a given moment. For Na_xMO_2 materials, it corresponds to the Na/M ratio. The number of (de)inserted ions Δx can be deduced from the capacity (Q) knowing the value of applied current and time of application of the current, as follows:

$$Q = It = \frac{F\,\Delta x\,n}{3600} \qquad \textbf{(I.1)}$$

With:

Q: Capacity (A.h)

I: Current value (A)

t: duration of the (dis)charge (h)

F: Faraday's constant = 96485 $C.mol^{-1}$

Δx: number of (de)inserted ions

n: number of moles of Na_xMO_2 (mol) in the battery

Discharge capacity

The discharge capacity represents the amount of electrical charges given by the electrochemical system. For comparison purposes, it is expressed as per mass of active material. The theoretical discharge capacity is given by the following formula:

$$Q_m^{th} = \frac{\Delta x . F}{3600 . Mw}$$

With:

Q_m^{th}: theoretical capacity per mass of active material (A.h.g^{-1})

Δx: number of inserted e$^-$ (or Na$^+$)

F: Faraday's constant = 96485 C.mol^{-1}

Mw: Molar weight of Na_xMO_2 at x_0 (g.mol^{-1})

x_0: initial intercalation amount in the material

(I.2)

Experimentally, only a fraction of the Na$^+$ ions can be (de)inserted during the cycling of the battery and the experimental discharge capacity never reaches the theoretical one.

Charge / discharge rate

The rate corresponds to the current value applied in order to reach the theoretical charge / discharge capacity in t hours. It is given by the following formula:

$$It = Q_m^{th}$$

With:

I: current value (A)

t: expected duration of the (dis)charge (hours)

Q_m^{th}: theoretical capacity per mass of active material (A.h.g^{-1})

(I.3)

The rate is noted C/t. This notation implies that the requested time (hours) to reach the theoretical charge or discharge capacity is equal to t. For example a C/20 rate means that the battery would be fully charged or discharged in 20 hours. Because of thermodynamics and kinetic effects, the rate will impact the amount of Na$^+$ ions accessible in the material within a given voltage window: a high rate value will usually lower the number of extracted / inserted Na$^+$ ions.

I.2.c. The galvanostatic curves

The variations of the voltage of the battery (E) as a function of the sodium content (x) or *galvanostatic curve* give precious information concerning the structural changes the materials undergo upon cycling. Three kinds of behaviors can be observed on the E = f(x) curves, as represented in **Figure I.9**:

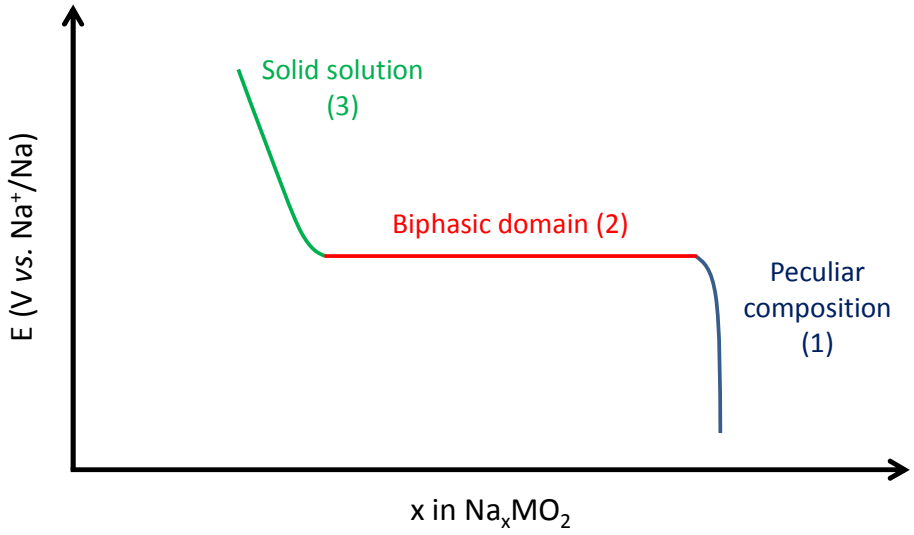

Figure I.9: Schematic representation of the possible behaviors observed in a galvanostatic cycling.

(1) The voltage suddenly increases or decreases and marks a "jump" on the E = f(x) curve. This is characteristic of a *peculiar composition* and highlights the existence of a single phase with a well-defined structure. Very often it is a stoichiometric phase or a *supercell* with ordered cation distribution [48]. The composition domain for the existence of such phases is very narrow.

(2) The voltage does not evolve with the Na content and creates a *plateau*. This behavior is characteristic of a *biphasic domain e.g.* there is equilibrium between two phases of different compositions and structures. Only the ratio between these two phases evolves along the plateau.

(3) The voltage evolves continuously as a function of x. This is the signature of a *solid solution*. The structure remains the same, only the sodium amount varies constantly during the sodium (de)intercalation.

All the voltages mentioned in the present manuscript will be expressed *vs*. the Na^+/Na redox couple.

I.2.d. Na_xMO_2 layered oxides in the literature

The study of the electrochemical properties of the Na_xMO_2 layered oxides is marked by two main periods of an important number of publications. The first one happened in the 1980s and corresponds to the exploration of several Na_xMO_2 materials along with $LiMO_2$. Na_xMO_2 materials involving only one transition metal were mostly studied.

The second period started in the 2000s and is still ongoing in 2014. The advanced electrochemical properties of some Na_xMO_2 involving one transition metal were revisited and new Na_xMO_2 materials of mixed composition on the M site were synthesized and characterized.

Na_xMO_2 materials involving one transition metal

Na_xMO_2 materials involving one transition metal were the first to be studied, long before the search for positive electrode materials. The first Na_xMO_2 materials with M = Fe [1], Co [3, 4, 49, 50], V [9, 39], Cr [9] or Ni [2] were synthesized to study their physical and / or structural properties. Then the search for positive electrode materials lead to the investigation of their electrochemical properties, starting with the P'3-$Na_{0.6}CoO_2$, P2-$Na_{0.7}CoO_2$, O'3-$Na_{0.77}CoO_2$ and O3-$NaCoO_2$ materials by Delmas et al. in 1981 [51]. The electrochemical activity of these materials *i.e.* their ability to reversibly (de)intercalate the Na^+ ion was demonstrated. Following the same reasoning, other Na_xMO_2 were reinvestigated to confirm their electrochemical activity such as O'3-$NaNiO_2$ [38], O3-$NaCrO_2$ [38], P2-Na_xMnO_2 [52], O'3-$NaMnO_2$ [52] and O3-$NaTiO_2$ [53]. In the early 2010s, more advanced studies of the electrochemical properties were performed on these different materials along with new ones (P2-$Na_{0.7}VO_2$ and O3-$NaVO_2$ [54-56]). The results are summed up in **Table I.6**.

Na_xMO_2 material	Structure type	Studied E range	Discharged capacity (C-rate)	Capacity retention	References
Na_xVO_2	P2	1.2 – 2.5 V 1.4 – 2.5 V	≈ 120 mAh.g^{-1} (C/20) 110 mAh.g^{-1} (C/100)	constant (11 cycles) constant (10 cycles)	[54, 56]
	O3	1.2 – 2.5 V 1.4 – 2.5 V	≈ 120 mAh.g^{-1} (C/20) ≈ 126 mAh.g^{-1} (C/100)	constant (15 cycles) /	[54, 55]
$NaCrO_2$	O3	2.2 – 3.8 V 2.0 – 3.6 V 2.0 – 3.6 V 2.6 – 3.4 V	104 mAh.g^{-1} (C/50) ≈ 120 mAh.g^{-1} (1C) ≈ 100 mAh.g^{-1} (C/10) ≈ 115 mAh.g^{-1} (C/50)	96 % (10 cycles) 67 % (50 cycles) 85 % (8 cycles) 96% (40 cycles)	[57-60]
Na_xMnO_2	P2	2.0 – 3.8 V	≈ 150 mAh.g^{-1} (C/2)	33 % (10 cycles)	[61]
	O'3	2.0 – 3.8 V	185 mAh.g^{-1}(C/10)	71 % (20 cycles)	[44]
$NaFeO_2$	O3	2.5 – 3.4 V 2.5 – 3.5 V 2.5 – 4.0 V	75 mAh.g^{-1} (C/20) ≈ 100 mAh.g-^{1}(C/20) 70 mAh.g^{-1} (C/20)	80 % (30 cycles) 50 % (30 cycles) 0 % (30 cycles)	[62]
Na_xCoO_2	P2	2.0 – 3.8 V 2.0 – 3.5 V	≈ 150 mAh.g^{-1} (C/100) ≈ 75 mAh.g^{-1} (C/12)	/ 93 % (90 cycles)	[48] [63]
$NaNiO_2$	O'3	1.25 – 3.75 V	≈ 150 mAh.g^{-1} (C/10)	80 % (20 cycles)	[34]

Table I.6: Electrochemical properties of different Na_xMO_2 materials. All voltages ranges are expressed *versus* the Na^+/Na redox couple.

The galvanostatic curves of most of these materials exhibit several voltage jumps due to the existence of Na / vacancy orderings [34, 38, 44, 48, 51, 53-61, 64]. On a structural point of view, the Na / vacancy orderings create a *superstructure* which is often indexed based on the *substructure* lattice parameters. In some of these materials, the peculiar compositions are separated by biphasic domains indicated by voltage plateaus [34, 38, 44, 48, 51, 53-61, 64].

It is noteworthy that $NaFeO_2$ and $NaTiO_2$ are the only $NaMO_2$ materials with one transition element that do not show intermediate peculiar phases [53, 62]. It is suggested that the instability of the Fe^{4+} and Ti^{4+} cations leads to their migration to the interlayer space [35, 37].

The structural transitions resulting from MO_2 slabs glidings [36] can represent an important problem concerning battery applications if they lead to the degradation of the positive electrode material, as for O3-$NaFeO_2$. On the other hand, the huge voltage jumps can be hard to predict and represent a problem for monitoring the battery behavior. Materials showing a continuous variation of the voltage along with the Na content are usually preferred.

Na_xMO_2 materials with mixed occupation of the M site

The substitution or partial replacement of the transition metal is an interesting way to improve the electrochemical properties of the Na_xMO_2 materials by impacting the following criteria:

- It sometimes stabilizes the materials on a wider sodium composition domain by preventing structural transitions. For example, several studies focused on the replacement of Fe into O3-$NaFeO_2$ by Mn [26-33, 65, 66], Ni [67], Ni + Co [68] or Ni + Mn [46, 69], resulting in better electrochemical properties. Recently, Kim et al. and Xu et al. studied the impact of Li substitutions in $Na_x[Li_yNi_zMn_{1-y-z}]O_2$ [70, 71]. The *in situ* X-ray powder diffraction (XRPD) characterization of P2-$Na_x(Li_{0.12}Ni_{0.22}Mn_{0.66})O_2$ showed no P2 → O2 transition upon charge, as it was evidenced for P2-$Na_xNi_{1-y}Mn_yO_2$ [72].
- The substitutions are a way to stabilize new structural types that cannot be obtained with only one transition element. For example, the only structure types accessible for Ni and Fe based sodium layered oxides are the O'3-$NaNiO_2$ and O3-$NaFeO_2$ ones. Thanks to the partial replacement of the Ni and Fe transition metals, different studies report the synthesis of various P2 materials in the P2-$Na_xFe_{1-y}Mn_yO_2$ [26, 28-33, 66] and P2-$Na_xNi_{1-y}Mn_yO_2$ [72-78] phase diagrams.
- Moreover, the substitutions reduce or suppress the important voltage jumps associated to the Na/vacancy orderings previously discussed. For instance, the Mn substitution in the P2-Na_xCoO_2 material suppress almost every voltage jump except for the x = 1/2 one [79].

Following these reasonings, several new P2 and O3 materials were synthesized and characterized. Their electrochemical properties are summarized in **Table I.7**.

Table I.7 only sums up the advanced electrochemical studies carried out on the displayed materials. Several preliminary studies reported the synthesis of the materials or the possibility to reversibly intercalate and deintercalate Na^+ ions. Hence, Xia et al. and Paulsen et al., studied the structure of several $Na_xMn_{1-y}Ni_yO_2$ materials [74, 80]. Lu and Dahn published an *in situ* XRPD study of the P2-$Na_{2/3}Mn_{2/3}Ni_{1/3}O_2$ phase diagram and suggested the P2 → O2 phase transition for $x_{Na} < 1/3$ in 2001 [72]. The preliminary works of Parant in the 1970s showed the feasibility of the Mn substitution in O3-$NaFeO_2$ and highlighted two structural domains (P2 and O3) depending on the Na content [81]. The studies of Sharma et al. [82] and Paulsen et al. [74] on $Na_xMn_{1-y}Co_yO_2$ materials were completed in 2011 by Carlier et al, showing that P2-$Na_{2/3}Mn_{1/3}Co_{2/3}O_2$ was electrochemically active in a Na cell [79]. It must be noted that no long-term electrochemical study was yet carried out on the O3-$NaNi_{0.6}Co_{0.4}O_2$ material synthesized by Saadoune et al. in 1996 [83]. The first study of the $Na_xNi_{1-y-z}Mn_yCo_zO_2$ system, which represents one of the most promising positive electrode materials for Na-ion batteries, is attributed to Lu et al. who studied

the intercalation of water in several $A_xNi_{1-y-z}Mn_yCo_zO_2$ (A = Li, Na) materials prepared from P2-$Na_{2/3}Ni_{1/3-x}Mn_{2/3}Co_xO_2$ materials [84].

Na_xMO_2 material	Studied E range	Discharged capacity (C-rate)	Capacity retention[4]	References
$Na_xMn_{1-y}Ni_yO_2$				
P2-$Na_{2/3}Mn_{2/3}Ni_{1/3}O_2$	2.3 – 4.1 V	82 mAh.g^{-1} (C/5)	92 % (50 cycles)	[76]
O3-$NaMn_{1/2}Ni_{1/2}O_2$	2.2 – 3.8 V	125 mAh.g^{-1} (C/50)	> 95 % (10 cycles)	[57, 78]
	2.2 – 3.8 V	105 mAh.g^{-1} (1C)	75 % (50 cycles)	[78]
	2.0 – 4.0 V	77 mAh.g^{-1} (1C)	91 % (100 cycles)	[85]
	2.0 – 4.5 V	140 mAh.g^{-1} (C/10)	29 % (100 cycles)	[85]
$Na_xMn_{1-y}Fe_yO_2$				
P2-$Na_{2/3}Mn_{2/3}Fe_{1/3}O_2$	2.0 – 3.8 V	≈ 155 mAh.g^{-1} (C/20)	93 % (10 cycles)	[66]
	2.0 – 4.5 V	≈ 150 mAh.g^{-1} (C/10)	93 % (20 cycles)	[30]
	1.5 – 4.3 V	≈ 204 mAh.g^{-1} (C/20)	75 % (40 cycles)	[32]
P2-$Na_{2/3}Mn_{0.65}Fe_{0.35}O_2$	1.5 – 4.3 V	≈ 208 mAh.g^{-1} (C/20)	67 % (30 cycles)	[86]
P2-$Na_xMn_{1/2}Fe_{1/2}O_2$	1.5 – 4.2 V	190 mAh.g^{-1} (C/20)	74 % (30 cycles)	[26, 28]
	1.5 – 4.3 V	160 mAh.g^{-1} (C/10)	56 % (40 cycles)	[33]
O3-$NaMn_{1/2}Fe_{1/2}O_2$	1.5 – 4.2 V	≈ 110 mAh.g^{-1} (C/20)	68 % (30 cycles)	[26]
O3-$NaMn_{1/3}Fe_{2/3}O_2$	2.0 – 3.8 V	≈ 100 mAh.g^{-1} (C/20)	93 % (10 cycles)	[66]
$Na_xMn_{1-y}Co_yO_2$				
P2-$Na_{0.7}Mn_{0.89}Co_{0.11}O_2$	1.5 – 3.8 V	138 mAh.g^{-1} (C/3)	67 % (20 cycles)	[87]
P2-$Na_{2/3}Mn_{1/2}Co_{1/2}O_2$	1.5 – 4.0 V	123 mAh.g^{-1} (C/8)	69 % (30 cycles)	[88]
P2-$Na_{0.79}Mn_{0.3}Co_{0.7}O_2$	2.0 – 3.8 V	60 mAh.g^{-1} (C/2)	87 % (60 cycles)	[89]

Table I.7a: Electrochemical performances of different Na_xMO_2 with mixed compositions on the M site. All voltages ranges are expressed *versus* the Na^+/Na redox couple.

[4] Due to the sodium content of the starting P2 materials, the capacity retention is compared to the 2nd cycle.

Na_xMO_2 material	Studied E range	Discharged capacity (C-rate)	Capacity retention[5]	References
$Na_xFe_{1-y}Ni_yO_2$				
O3-$NaFe_{1/2}Ni_{1/2}O_2$	2.0 – 3.8 V	112 mAh.g^{-1} (C/8)	55 % (30 cycles)	[67]
O3-$NaFe_{0.3}Ni_{0.7}O_2$	2.0 – 3.8 V	135 mAh.g^{-1} (C/8)	74 % (30 cycles)	[67]
$Na_xNi_{1-y-z}Co_yFe_zO_2$				
O3-$NaNi_{1/3}Co_{1/3}Fe_{1/3}O_2$	2.0 – 4.2 V	165 mAh.g^{-1} (C/20)	91 % (20 cycles)	[68]
$Na_xNi_{1-y-z}Mn_yFe_zO_2$				
O3-$NaNi_{1/3}Mn_{1/3}Fe_{1/3}O_2$	1.5 – 4.0 V	≈ 130 mAh.g^{-1} (C/2)	77% (150 cycles)	[46]
O3-$NaNi_{0.3}Mn_{0.3}Fe_{0.4}O_2$	2.0 – 3.8 V	≈ 135 mAh.g^{-1} (C/20)	80 % (50 cycles)	[69]
O3-$NaNi_{0.2}Mn_{0.2}Fe_{0.6}O_2$	2.0 – 3.8 V	≈ 135 mAh.g^{-1} (C/20)	60 % (50 cycles)	[69]
P2-$Na_{0.67}Ni_{0.15}Mn_{0.65}Fe_{0.2}O_2$	1.5 – 4.3 V	208 mAh.g^{-1} (C/20)	71 % (50 cycles)	[86]
$Na_xNi_{1-y-z}Mn_yCo_zO_2$				
P2-$Na_{0.7}Ni_{0.3}Mn_{0.6}Co_{0.1}O_2$	1.7 – 4.0 V 1.5 – 4.0 V 1.7 – 4.3 V	≈ 125 mAh.g^{-1} (C/20) ≈ 160 mAh.g^{-1} (C/20) ≈ 190 mAh.g^{-1} (C/20)	94 % (20 cycles) 82 % (20 cycles) 54 % (10 cycles)	[90]
P2-$Na_{0.45}Ni_{0.22}Mn_{0.66}Co_{0.11}O_2$	2.1 – 4.2 V	≈ 140 mAh.g^{-1} (C/10)	72 % (275 cycles)	[91, 92]
P2-$Na_{2/3}Ni_{0.15}Mn_{0.65}Co_{0.2}O_2$	2.0 – 4.4 V	≈ 140 mAh.g^{-1} (C/12)	90 % (50 cycles)	[93]
P2-$Na_{0.7}Ni_{1/9}Mn_{2/9}Co_{2/3}O_2$	2.0 – 4.2 V 2.0 – 4.5 V	≈ 110 mAh.g^{-1} (C/20) ≈ 140 mAh.g^{-1} (C/20)	89 % (90 cycles) 86 % (10 cycles)	[94]
O3-$NaNi_{1/3}Mn_{1/3}Co_{1/3}O_2$	2.0 – 3.75 V	120 mAh.g^{-1} (1C)	75 % (50 cycles)	[95]
$Na_xNi_{1-y-z-w}Mn_yCo_zAl_wO_2$				
P2-$Na_{2/3}Ni_{0.15}Mn_{0.65}Co_{0.15}Al_{0.05}O_2$	2.0 – 4.4 V	≈ 130 mAh.g^{-1} (C/12)	95.4 % (50 cycles)	[93]
$Na_xNi_{1-y-z}Mn_yLi_zO_2$				
P2-$Na_{0.80}Ni_{0.22}Mn_{0.66}Li_{0.12}O_2$	2.0 – 4.4 V	133 mAh.g^{-1} (C/10)	91 % (50 cycles)	[70]

Table I.7b: Electrochemical performances of different Na_xMO_2 with mixed compositions on the M site. All voltages ranges are expressed *versus* the Na^+/Na redox couple.

[5] Due to the sodium content of the starting P2 materials, the capacity retention is compared to the 2nd cycle.

Table I.7 highlights some interesting tendencies:

(1) Materials with P2 structure type allow reaching higher capacity than those with O3 one.

(2) Some of the materials exhibit a capacity retention superior to 90 % after at least 10 cycles for C-rates comprised between C/20 and 1C: P2 and O3-$Na_xMn_{1-y}Ni_yO_2$ [57, 76, 78, 85], P2-$Na_xMn_{1-y}Fe_yO_2$ [30, 66],O3-$NaNi_{1/3}Co_{1/3}Fe_{1/3}O_2$ [68], P2-$Na_xNi_{1-y-z}Mn_yCo_zO_2$ [90, 93], P2-$Na_xNi_{1-y-z-w}Mn_yCo_zAl_wO_2$ [93] and P2-$Na_xNi_{1-y-z}Mn_yLi_zO_2$ [70].

However, due to the very different experimental conditions, it is impossible to conclude on the best positive electrode material: the voltage ranges have a huge impact on the cyclability as a too high upper voltage can lead to the material degradation. For example, the O3-$NaMn_{1/2}Ni_{1/2}O_2$ exhibits an interesting capacity retention of 91 % after 100 cycles when cycled between 2.0 and 4.0 V [85] but this capacity retention drops to 29 % if the upper voltage limitation is increased to 4.5 V [85]. Therefore, one must be precautious when comparing one system to another.

Towards high voltage batteries: improving the electrolyte

Around the world, people working on Na-ion batteries have to face another important problem which is the electrolyte degradation. The organic solvent-based electrolyte tends to decompose at the low and / or high voltage. To overcome this issue, several sodium salts ($NaClO_4$, $NaPF_6$ or $NaCF_3SO_3$ [96]) and organic solvents (Propylene Carbonate (PC), DiEthyl Carbonate (DEC), DiMethy Carbonate (DMC), Ethylene Carbonate (EC)…) were studied with or without adding an additive (FluoroEthylene Carbonate (FEC)) to reduce the decomposition issue [97]. If the use of Vinylene carbonate (VC) in Li-ion batteries electrolyte was already shown to efficiently reduce the electrolyte decomposition issue [98], no study is reported yet on its impact on Na-ion batteries electrolyte. The $NaPF_6$ in PC and $NaClO_4$ in PC electrolytes usually decompose for E > 3.5 V *vs.* Na^+/Na [48]. The $NaPF_6$ in EC/DEC electrolyte exhibits better stability [96], as for the $NaPF_6$ in PC + 2wt % FEC one [99]. The search for a stable electrolyte assuring maximum stability demands a rigorous and fastidious work that Bhide et al. started in 2014 [100] by comparing electrolytes made of the different sodium salts ($NaClO_4$, $NaPF_6$ and $NaCF_3SO_3$) dissolved into an EC + DMC mixture under different cycling conditions (salt concentration, voltage ranges, electrode materials…). In this thesis, only a few different electrolytes were tested and will be presented later.

Chapter II: Experimental techniques

Table of contents

This chapter represents the experimental section of this manuscript. Its purpose is to explain the sample preparation for the electrochemical and structural characterizations of the Na_xMO_2 phases studied in this thesis. Some explanations are also given concerning the electrochemical cycling curves. Experimental devices used for structural characterizations are also presented. The synthesis method used to obtain the Na_xMO_2 phases studied in this thesis is described at the beginning of each part dedicated to a system.

II.1. Electrochemical characterizations

II.1.a. Electrode preparations

For most of the characterizations, the positive electrode consists in a mixture of Active Material (Na_xMO_2 phase), Carbon Black and PolyTetraFluoroEthylene (AM, CB and PTFE, respectively) mixed in a 77/17/6 weight ratio. CB is a mixture of carbon soot and graphite and is used to enhance the electrical conductivity of the positive electrode. The use of PTFE (Teflon®) is requested to give the electrode its plastic properties by creating a matrix maintaining all electrode components together. After the 3 components are weighted and ground in a mortar under argon atmosphere, 10 mm diameter electrodes of approximately 22 mg are cut from the paste.

PTFE cannot be used in electrodes prepared to study the structure of the materials as it requires dispersed powder. Therefore, the electrodes consist in a mixture of active material and carbon black in a 80 : 20 weight ratio (total mass ≈ 80mg). Once ground, the mixture is pressed into a pellet (∅ 10 mm, 4 tons pressure) to facilitate the handling of the electrode and increase its electrical conductivity.

II.1.b. Assembly of a Na battery

The characterization of the positive electrode materials studied in this manuscript requested the assembly of Na batteries under argon atmosphere in a glovebox. At the laboratory scale, two systems referred as *Swagelok™-type* and *coin cell* are commonly used. After assembling they are plugged to a Biologic VMP3 potentiostat in order to perform the electrochemical characterizations.

The Swagelok™-type cell

The Swagelok™-type cells are named after the Swagelok™ Company, specialized in the manufacturing of tube, valves … for gas and fluid systems. As the materials involved in the battery are very air sensitive, their products were used as battery containers. Nevertheless, the first electrochemical cells following a similar blueprint were used before the apparition of this name and are still in use in our laboratory. A representation and picture of the Swagelok™-type system is given in **Figure II.1**. The positive and negative electrodes are reposing on stainless steel current collectors. Three layers of Whatman™ glass fiber separators provide a support for the liquid electrolyte absorption and prevent any short circuit due to the dendritic growth from the Na foil. Once assembled, the battery is plugged into a glass container into an Ar filled glovebox to avoid moisture and oxygen contamination outside of the glovebox (visible in **Figure II.1b**).

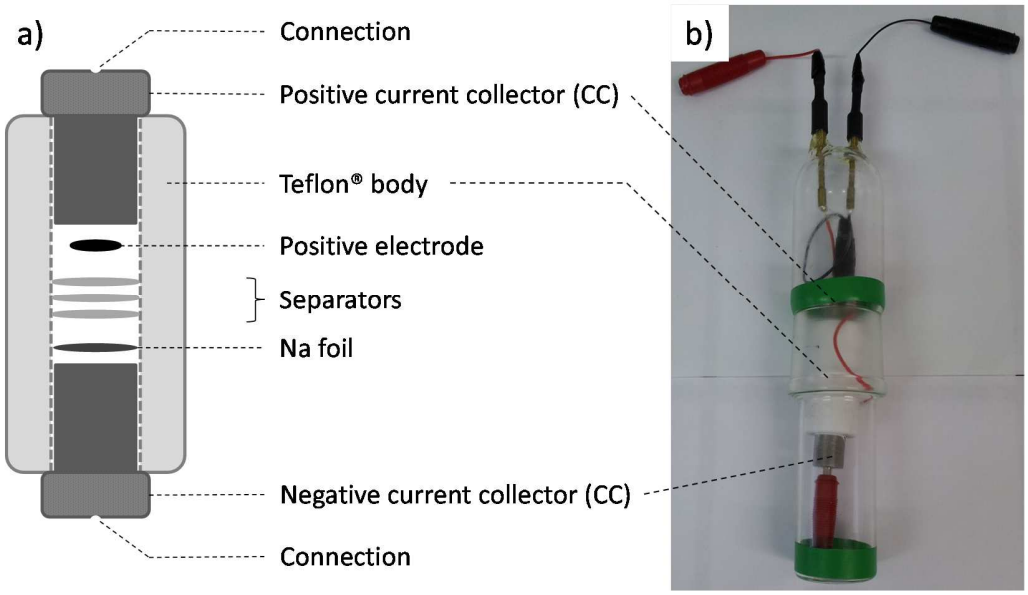

Figure II.1: (a) Schematic representation of the Swagelok™-type cell and (b) picture of a Swagelok™-type battery.

Concerning this work, the Swagelok-type cells were mostly used for the preparation of materials through a *Potentiostatic route* or for short electrochemical characterizations.

The 2032 coin cell

The coin cell batteries are similar to the ones available commercially. The assembly of a Na battery in these containers is similar to the one previously described. As shown in **Figure II.2**, the positive electrode is in contact with the current collector and separated from the negative electrode by 3 layers of separator. However, the Na foil is now deposited on a stainless support and separated by a stainless steel spring from the negative current collector in order to maintain the pressure while assuring the electrical contact. A joint prevents the apparition of short circuits resulting from the contact between the two current collectors and ensure the airtightness of the cell once sealed using a manual press inside the glovebox. Pictures of an assembled cell are given in **Figure II.2c**.

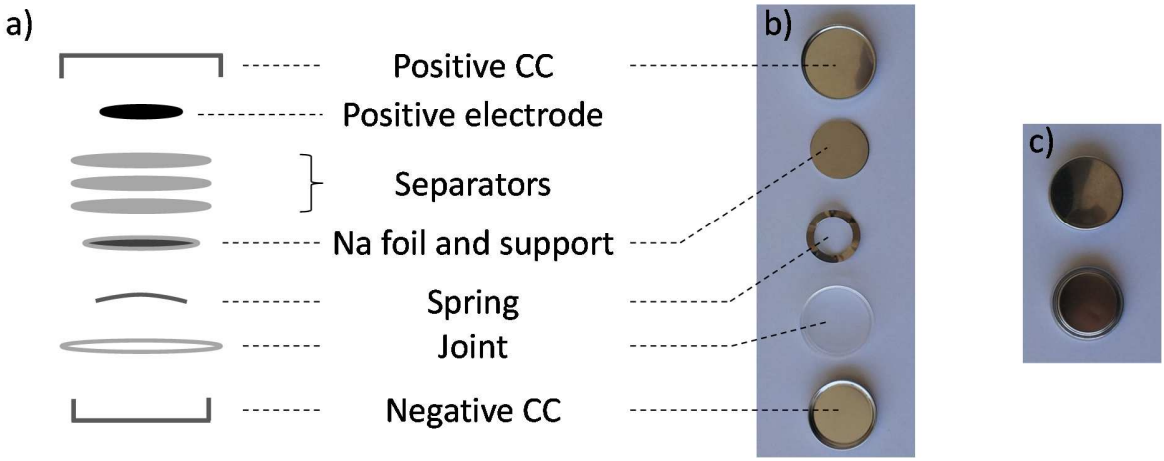

Figure II.2: (a) Schematic description of a coin cell, (b) picture of the corresponding parts and (c) top and bottom view of a sealed coin cell.

These cells were used for long or precise electrochemical characterizations as they offer more reproducible conditions than the Swagelok™-type cells. Moreover, there is no rotation movement during the assembling which avoids any damage to the positive electrode. The major drawback is that these cells are not recoverable entirely and only the spring and stainless support can be used again after cleaning.

II.1.c. Galvanostatic cycling

As implied by the designation, these characterizations are performed under a constant current indicated by the rate. The evolution of the voltage is plotted as a function of time or sodium content. In this work, the rates mostly used were C/100, C/50 and C/20 *i.e.* 1 mol of Na^+ ions per Na_xMO_2 formula unit was theoretically desinserted/inserted in 100, 50 or 20 hours, respectively. By convention, the positive and negative values of the current consist in the charge and discharge states of the battery, respectively.

The voltage of the battery can be expressed as a function of the difference in the chemical potential of sodium between the positive and negative electrodes. In this thesis, all the batteries were assembled with metal sodium as the negative electrode. Therefore the state and chemical potential of the

negative electrode do not evolve during electrochemical cycling. The measured variations of the voltage are then only correlated to the variations of the chemical potential of the positive electrode. The measured cell voltage is expressed versus the Na^+/Na redox couple (*vs.* Na^+/Na) and is plotted as a function of the sodium content (x in Na_xMO_2, cf. **Chapter I**) or time.

II.1.d. Galvanostatic Intermittent Titration Technique: GITT

If galvanostatic cycling is the best way to characterize a battery under given utilization conditions, the material is never characterized in a relaxed state. Indeed, the shape of the E = f(t) or E = f(x) curves can be impacted by the rate and if the current value is too high, several information can be misevaluated or missed. The GITT cycling mode consists in altering galvanostatic charge or discharge and relaxation periods in order to measure the voltage of the material corresponding to precise sodium contents. A typical representation of a GITT cycling experiment is given in **Figure II.3** and shows the succession of the galvanostatic charge and relaxation steps.

To highlight the differences between a galvanostatic (C/50) and a GITT cycling, the curves of a $Na_xMn_{1/3}Fe_{2/3}O_2/NaPF_6$ in PC (1M) + 2wt% FEC/Na^0 battery are shown in **Figure II.4**. As one can see, the value of the voltage is different in galvanostatic charge and discharge on the red curve, compared to the voltage after relaxation on the black GITT curve. This is related to the contribution of two phenomenons. The first one corresponds to the sudden voltage drop observed at the beginning of the relaxation (**Figure II.3**) and corresponds to the *polarization*, induced by the various resistances within the battery. The effect of the *polarization* on the cycling curves is explained by Ohm's law: V = R * I (V: voltage (V), R: resistance (Ohm) and I: current (A)). The second phenomenon is visible through the slope decrease following the polarization (**Figure II.3**). When a current is applied to the battery, a *composition gradient* occurs between the core of the electrode material (Na^+-rich) and its borders (Na^+-poor). The slope decrease observed on the E = f(t) curve corresponds to the Na^+ *diffusion* within the material (homogenization). Once the material is homogeneous, its E = f(t) curve do not show any evolution of the voltage and we consider it reached *equilibrium*.

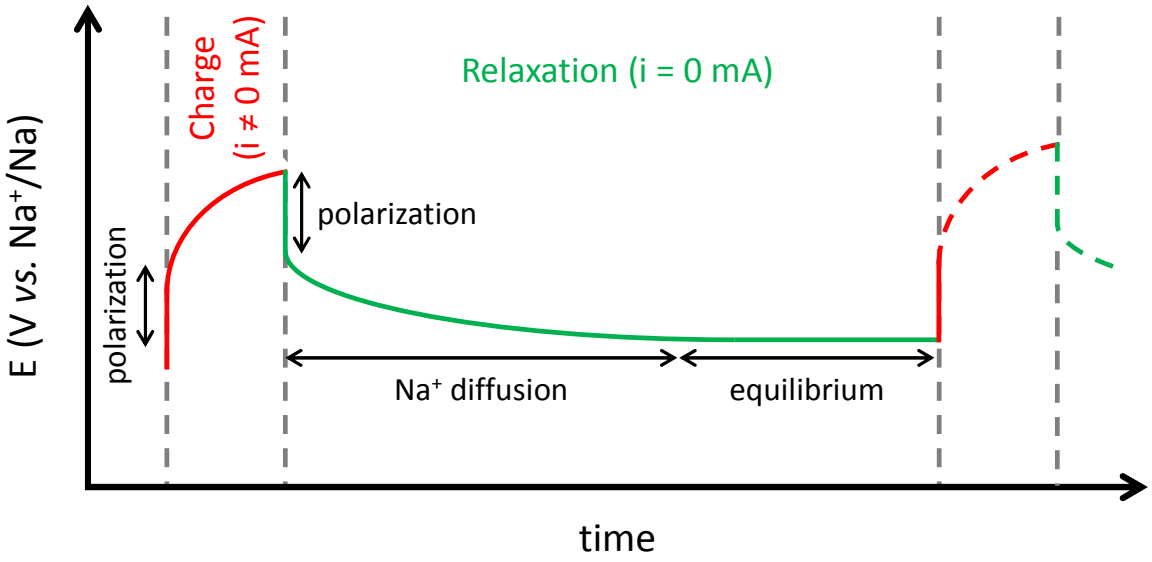

Figure II.3: Schematic representation of the GITT mode: evolution of the voltage of a Na battery as a function of time.

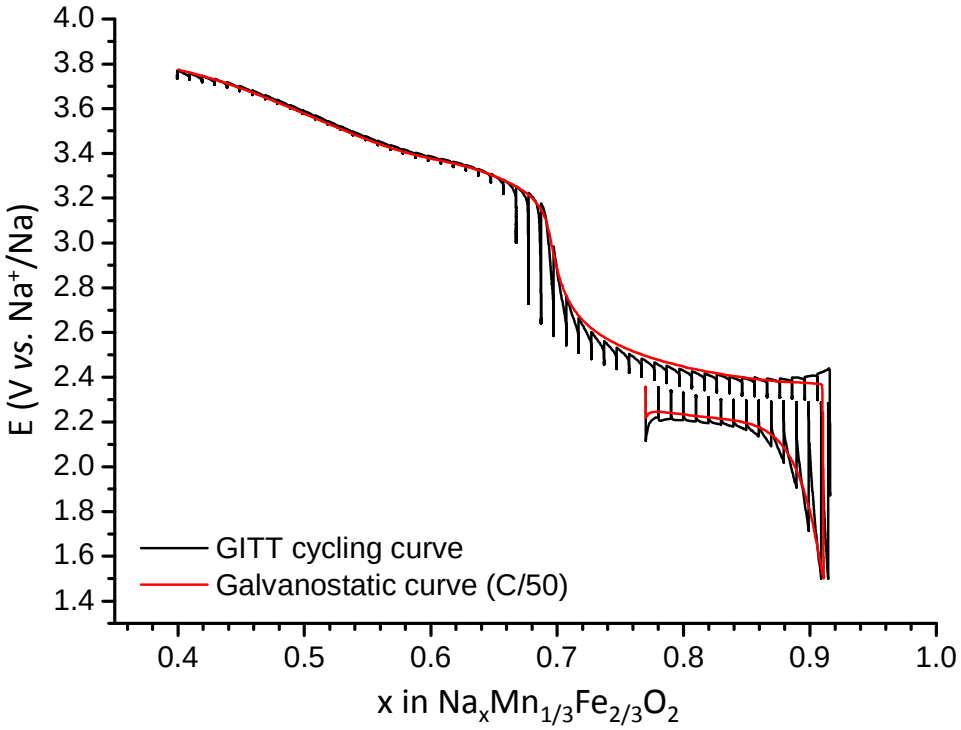

Figure II.4: Comparison between the GITT and the galvanostatic curves for two batteries involving the same positive electrode material.

II.1.e. Potentiostatic synthesis

The purpose of this technique is to prepare a Na_xMO_2 material by controlling precisely their sodium content. The batteries are (dis)charged galvanostatically at C/100 (sintered pellets) or C/50 (composite pellets with CB) until they reach the targeted voltage. This voltage is then maintained until the current is negligible. A schematic explanation is given in **Figure II.5** below. The experiments are then manually stopped and the batteries are entered into the glovebox to be washed 3 to 5 times with DiMethyl Carbonate (DMC) to remove the electrolyte.

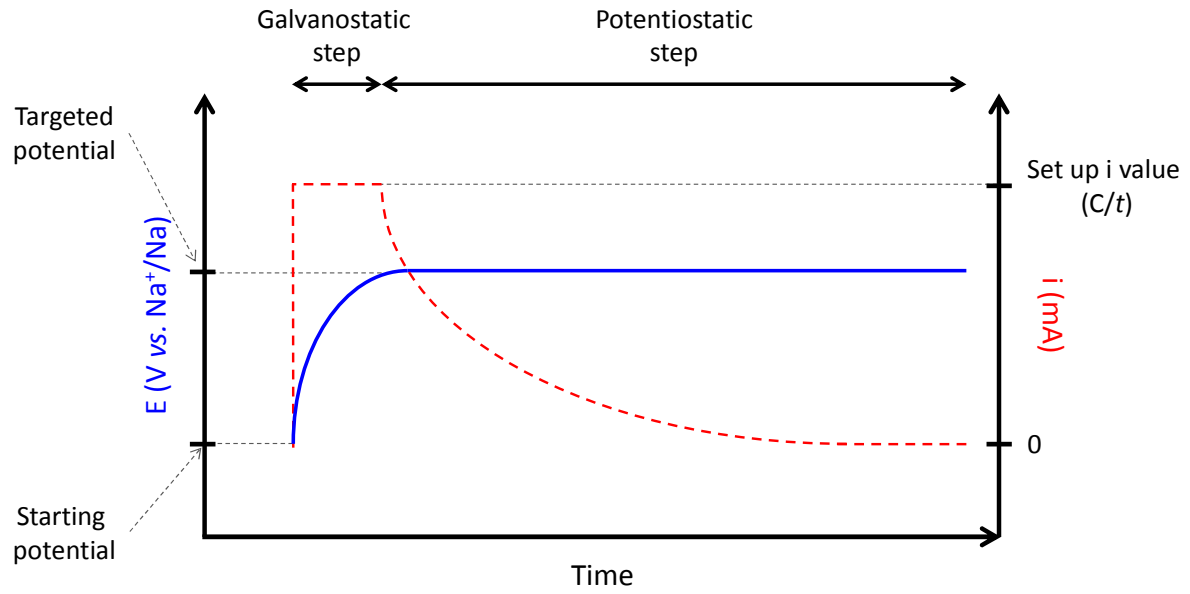

Figure II.5: Schematic representation of the potentiostatic synthesis route.

II.2. Structural characterizations

II.2.a. Laboratory and synchrotron X-Ray powder diffraction (XRPD)

As for most of their Na_xMO_2 homologues, the $Na_x(Mn,Fe)O_2$ and Na_xNiO_2 materials are very sensitive to air and moisture. Therefore, it is necessary to manipulate the samples in Argon filled glove boxes and to confine them into airtight systems in order to characterize them. It is possible thanks to specifically designed cells (laboratory XRPD) and capillaries (laboratory and synchrotron XRPD).

Every refinement of the structures from the diffraction patterns (X-Rays, Neutron or synchrotron) was realized using the Jana2006 software [101]. The absorption correction factor was systematically used for the Bragg Bentano geometry or for the Debye Sherrer ones [102]. The variances were corrected using the Berar's factor associated to the refinement [103].

Ex situ XRPD in airtight sample holders

For these measurements, the powders are first sifted through a 40 µm sieve to ensure a homogeneous distribution of the particle sizes. The sifted powder is then deposited on the diffraction plane of the airtight sample holder using a razor blade, in order to prevent preferred orientation of the Na_xMO_2 particles due to their plate-like shape. The airtightness is maintained through the use of a polyimide window which is transparent to X-rays for $2\theta > 10°$. To ensure that the sample is not exposed to air during long measurements (12h), a small piece of metallic sodium acting as a getter is added in the cell, outside of the diffraction beam path: due to the higher sensitivity the sodium has to oxygen and water, if a small quantity of air was to enter the cell, it would react with the sodium instead of the powder. This technique allowed us to get good quality XRPD patterns using the Cu $k\alpha_{1,2}$ radiation (collaboration with E. Lebraud, Engineer at ICMCB). A graphite (002) monochromator was used to suppress the fluorescent signal due to the iron specie in the $Na_xMn_{1-y}Fe_yO_2$ samples. The measurements were carried out in the 10 – 120 ° range and the Lebail or Rietveld refinements were performed in the same ranges. The 2θ ranges presented in this manuscript may differ for clarity purposes.

Ex situ XRPD and Synchrotron XRPD in glass and polyimide capillaries

As for the previously described measurements, the powders are sifted to ensure that the size of the agglomerates is lower than 40 µm. The powders are then loaded into capillaries whose nature and diameter will depend on the analyzed material and the diffraction technique apparatus, as presented in the following table:

	XRPD		**S-XRPD ESRF**	**S-XRPD APS**
	$Na_x(Mn,Fe)O_2$	Na_xNiO_2		
Nature	glass	glass	glass	polyimide
Inner diameter	0.1 mm	0.3 mm	1.0 mm	1.0 mm
Sealing	flame	flame	glue (epoxy)	glue (epoxy)
λ	Cu $k\alpha_{1,2}$		0.399845 Å	0.413913 Å
2θ range	10 – 120°		3-44°	1-60°

Table II.1: Experimental conditions concerning the XRPD and Synchrotron XRPD experiments carried out in this work.

- Concerning XRPD, the glass capillaries diameter was impacted by the analyzed material. A 0.3 mm capillary is an optimum for the Na_xNiO_2 material as it offers the possibility to use more powder and to get a better signal/noise ratio. On the contrary, the presence of iron in the $Na_x(Mn,Fe)O_2$ material lead to a fluorescence problem, as the diffractometer is not equipped with a monochromator. Therefore, a minor powder quantity coupled to a higher counting time was required to get a better XRPD pattern. At the laboratory scale, the capillary system offers the advantages of using a small quantity of powder and to conserve the samples as the capillaries were filled under Ar and sealed using a flame. It was the technique chosen to confirm the materials purity before running a Synchrotron XRPD pattern.

- Concerning SXRPD, the capillaries were filled under argon and sealed in the glovebox using epoxy glue, whatever their nature. Glass capillaries were used at former ID 31 beamline at the European Synchrotron Research Facility (ESRF, Grenoble, France) in collaboration with Dr. C. Drathen and polyimide capillaries were used at 11-BM beamline at the Advanced Photon Source (APS, Argonne National Laboratory, Argonne, IL, USA) in collaboration with Dr. M. Suchomel. The advantage of the polyimide capillaries is their flexibility that facilitates their handling within the glovebox.

For the refinements associated to the capillary setup, we considered a 50% packing of the powder into the capillaries to evaluate the absorption correction factor.

In situ XRPD during electrochemical cycling

In situ XRPD coupled to electrochemical cycling of a specifically designed cell is a powerful tool to investigate a phase diagram as it was already shown for other Na_xMO_2 material [48, 54-56, 70, 72]. The positive electrode current collector consists in a beryllium window, which is transparent to X-Rays and only shows two main diffraction peaks for $2\theta > 45°$. The cell is simultaneously placed in the diffractometer and plugged to a potentiostat to control and record the electrochemical part of the experiment (galvanostatic cycling, measure of the electrochemical variable…). The positive electrode was made from an Active Material / Carbon black / PTFE as described in the *Electrode preparation* section. Two types of experiments were carried out:

- ***In situ* XRPD at the equilibrium.** This method is the most commonly used for *in situ* XRPD. The battery follows a GITT cycling protocol, altering (dis)charge and relaxation steps. At the end of the relaxation period an XRPD pattern is recorded when the voltage shows no important variation.
  This technique characterizes the material in its relaxed state and the obtained XRPD pattern corresponds to a precise Na content in the material. It is therefore the best choice to observe Na/vacancies orderings and other peculiar compositions. To better separate close diffraction

peaks, we carried out these experiments using a diffractometer equipped with a germanium (111) monochromator in order to only use the Cu kα_1 incident radiation (λ = 1.54056 Å).

- ***Operando in situ* XRPD.** This method is commonly used at user facilities such as synchrotron and neutron facilities in which the available time is limited. The battery is continuously (dis)charged and the XRPD measurement is carried out in the same time. Therefore, there is a difference in the sodium content between the beginning and the end of each XRPD pattern. It requires optimizing the conditions to get a good data quality corresponding to a small x range. This technique is the best choice to characterize a battery in real cycling conditions and a quick option to characterize materials with no peculiar compositions.

Two different cells were used depending on the diffractometer manufacturer and are represented in **Figure II.6**.

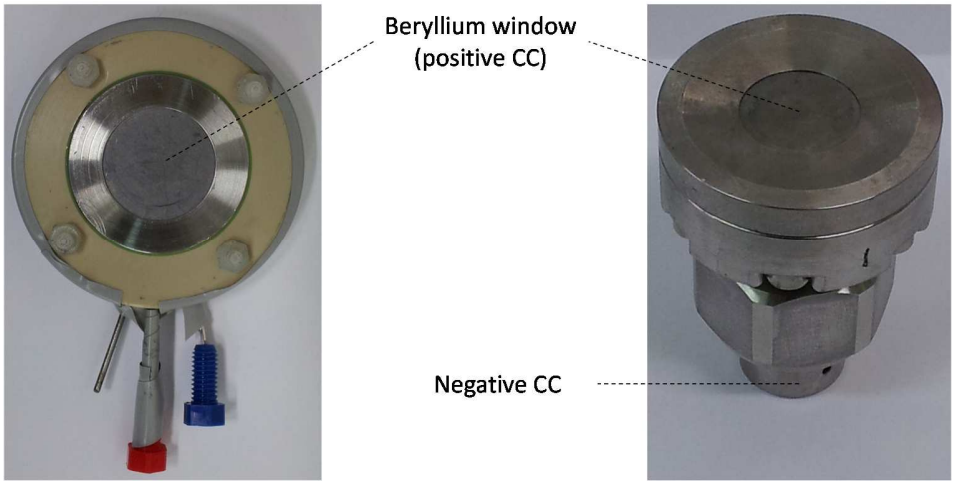

Figure II.6: Cells used for (left) Panalytical and (right) Bruker diffractometers.

The assembly of the Panalytical cell is similar to the one of the coin cell-type battery. On the contrary, the assembly of the Bruker cell is similar to the one of the Swagelok™-type cell. This model was developed in LRCS (Amiens, France) [104].

II.2.b. ^{57}Fe Mössbauer spectroscopy

Mössbauer spectroscopy is a technique commonly used to characterize iron and tin based solid state materials. It is complementary to XRPD as it gives information about the oxidation state and the local environment that XRPD cannot provide. It is based on a physical phenomenon observed in solid state matter evidenced by R. L. Mössbauer: the Mössbauer effect [105, 106]: a *Mössbauer source*, constituted of an excited element, emits a gamma photon accompanying the nuclear transition from the excited state to the fundamental one (**Figure II.7a**).

The gamma photon has then to be absorbed (rezoning absorption) by a stable nucleus of similar nature (*absorber*) which will get excited (**Figure II.7b**). As the absorption and emission of gamma photons are very energetic phenomenon, both the Mössbauer source and absorber have to be bounded in the solid state of their respective matrixes/amorphous lattices/crystal lattices, in order to avoid any energy loss due to recoil. As for every spectroscopy technique, it is necessary to scan a sufficient energy range. As the Mössbauer source emits a monochromatic radiation, varying the energy is achieved using the Doppler effect, moving the Mössbauer source while keeping the absorber still. The detector records the transmitted beam as a function of the velocity. This results in a Mössbauer spectrum, represented in **Figure II.8**.

All measurements in the present work were performed at room temperature with a constant acceleration Halder – type spectrometer using a ^{57}Co source (Rh matrix) in transmission geometry.

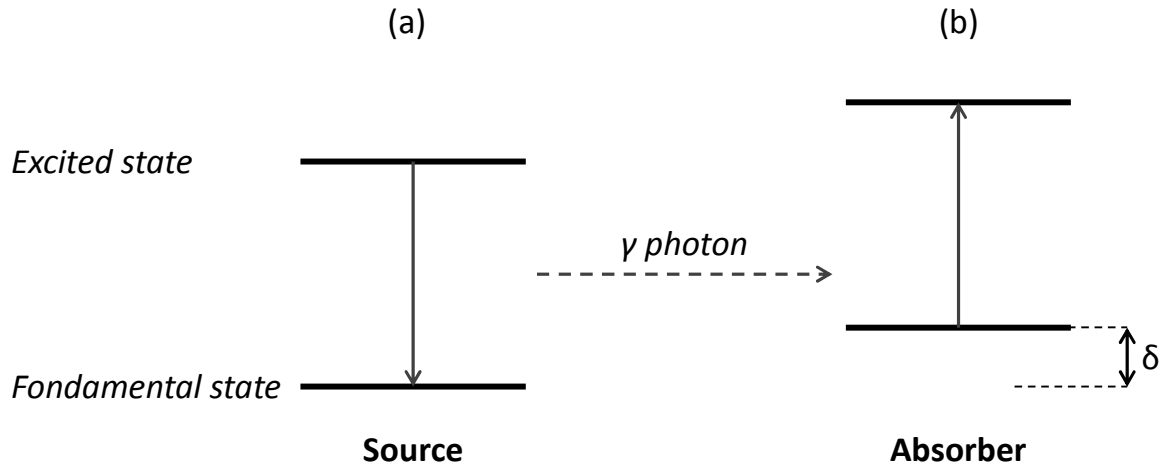

Figure II.7: Rezoning (a) emission and (b) absorption of a γ photon.

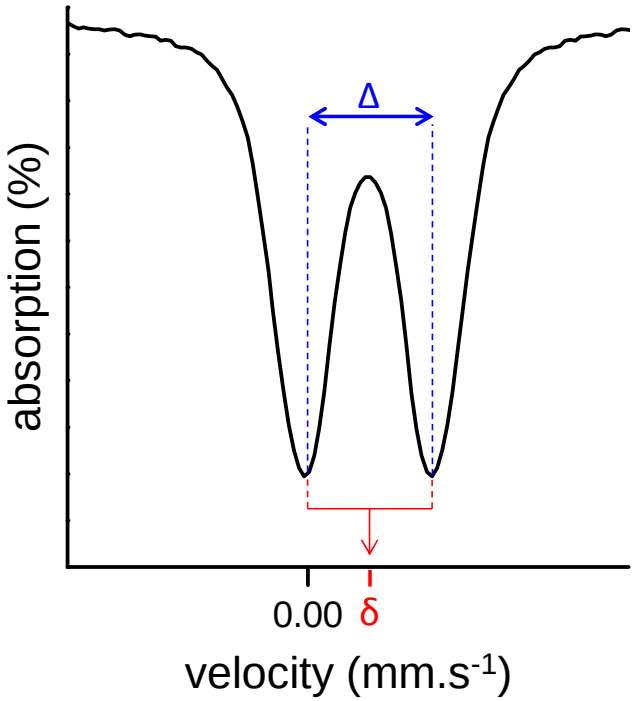

Figure II.8: Graphical representation of the isomer shift δ and the quadrupole splitting Δ for a doublet observed in a Mössbauer spectrum.

A Mössbauer spectrum is described by several variables, represented in **Figure II.8** and described here after:

The chemical shift: δ

The *chemical shift* **δ** is expressed in $mm.s^{-1}$ and corresponds to the shift of the absorption maxima to the origin (0 $mm.s^{-1}$) given by a reference (usually Fe α). It is a consequence of the resonance energy of the nucleus which is impacted by the transition of the electrons on its s orbital. Depending on the s electron charge density, the spectrum can be shifted in a positive or in a negative direction. For a multiplet, the chemical shift is given by the position of the barycenter of the different peaks, as shown in **Figure II.8**. The chemical shift gives precious information on the oxidation and spin states and the surrounding environment of the Mössbauer probe (Fe or Sn).

The quadrupole splitting: Δ

The *quadrupole splitting* **Δ** is expressed in $mm.s^{-1}$. It is only observed for multiplets and corresponds to the gap between the Mössbauer peaks, as shown in **Figure II.8**. The quadrupole splitting is observed only when two conditions are fulfilled:

(1) The nucleus must have an angular momentum I > 1/2. The charge distribution in the nucleus is therefore non-spherical and the nucleus possesses an *electric quadrupole moment*.

(2) The electronic repartition of the charges around the nucleus must be non-spherical, creating an *electric field gradient*. The electric field gradient is impacted by (i) the ions surrounding the probed atom or (ii) the valence electrons of the probed atom, the latter being the most important. In the case of the HS-Fe^{3+} ion ($3d^5$) in an octahedral coordination, the valence electrons are evenly distributed and thus only the surrounding ions will impact the electric field gradient.

The interaction between the electric quadrupole moment and the electric field gradient(s) will then lift the degeneracy of the nuclear states, as represented in **Figure II.9** for an excited ^{57}Fe atom: the 3/2 → 1/2 transition is divided into two sub-states: $m_I = \pm 1/2$ and $m_I = \pm 3/2$, creating as many peaks on the spectrum, which will correspond to a *doublet*.

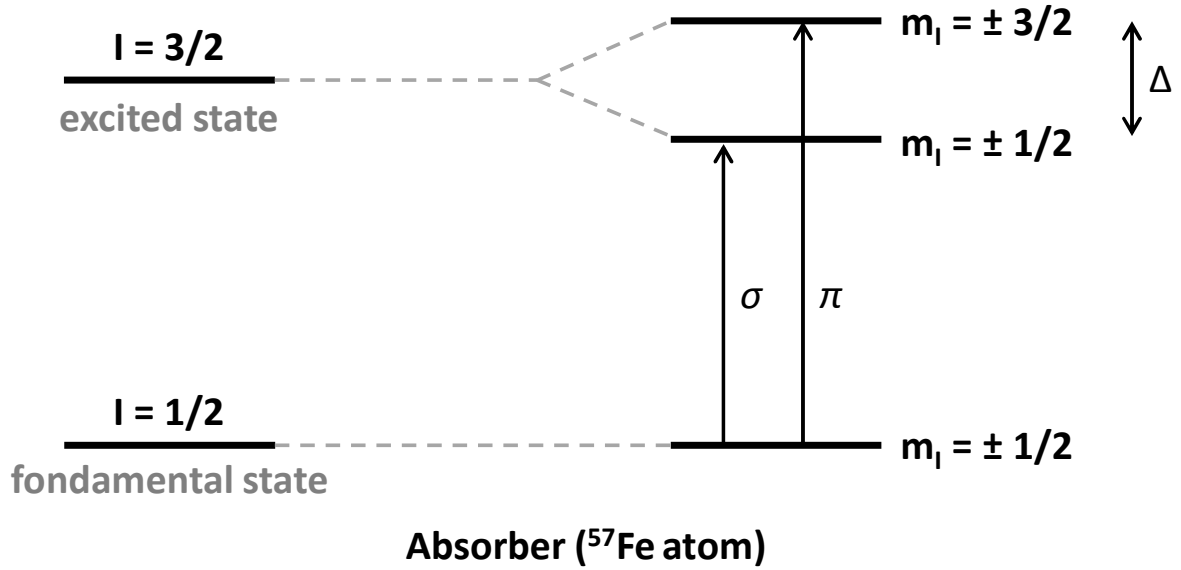

Figure II.9: Quadrupole splitting diagram of the $I_e = 3/2$ level of an excited ^{57}Fe nucleus.

Concerning the Fe^{3+} and Fe^{4+} ions, the quadrupole splitting gives precious information on the deformation of the site and on the cationic distribution around it.

The magnetic splitting (also hyperfine splitting or Zeeman effect)

The magnetic splitting is the result of the interactions between the nuclei and any surrounding magnetic field. As for the quadrupole splitting, the resulting spectrum will consist in a multiplet, generally a sextet. The exploitation of the spectrum gives precious information on the magnetic interactions. In this work no measurement was performed on magnetically ordered materials.

The populations: P

When several Mössbauer sites are involved, *populations* **P** are attributed to each site. They can correspond to different materials (phase mixtures), different oxidation states sharing the same (or different) crystallographic sites or to the same oxidation states sharing different crystallographic sites.

Data interpretation: fit of the spectrum

Every spectrum is first described by one or several Lorentzian Mössbauer peak(s) in a *Lorentzian fit*. This step allows refining the chemical shift, the quadrupole splitting and the Full Width at Half Maximum (FWHM) parameters. If the spectrum is too broad, it is possible to fit the spectrum using a *distribution fit*, which will describe the Mössbauer peaks based on distributions of quadrupole splitting. This calculation requires fixing a reasonable value for the FWHM (typically between 0.20 and 0.30 $mm.s^{-1}$). An average value of the quadrupole splitting (Δ*) is refined along with the populations associated to the various Mössbauer sites.

Experimental: in situ ^{57}Fe Mössbauer spectroscopy

Due to the severe regulations concerning the use of radioactive materials, all the measurements have to be done by habilitated people. At ICMCB, measurements were performed by A. Wattiaux, Research Engineer and S. Bordère, Researcher. The Mössbauer spectra were recorded at RT with a constant acceleration Halder – type spectrometer using a ^{57}Co source (Rh matrix) in the transmission geometry. The velocity was calibrated using pure iron metal as the standard material, which also corresponds to the reference of the spectra.

To follow the evolution of the Mössbauer spectra during the cycling of a Na battery, we adapted an *in situ* cell previously used in our laboratory [107] in collaboration with D. Filimonov[6], Invited Professor. The main challenge consisted in the selection of the materials constituting the cell which must not contain iron traces or absorb the signal if in the beam path. Therefore, aluminum, copper and stainless steel were banned. By analogy to *in situ* XRPD cells, a beryllium window is used as the positive current collector. The negative current collector consisted in a pierced stainless steel piece surrounding a polymer window. To assure the electrical conductivity and the pressure inside the cell, a stainless steel spring terminated by two hollow stainless steel disks was used. The schematic and photographic representations of the cell are given in **Figure II.10**. The positive electrode consisted in a diameter 13 mm pellet of AM and CB in a 80 : 20 ratio, with a total mass of ≈ 100 mg (*i.e.* ≈ 3 mg Fe per cm^2 for the $Na_xMn_{1/3}Fe_{2/3}O_2$ system). Due to the long measurement time (48 h) requested for each spectrum, we followed a similar protocol to the one described in the *potentiostatic synthesis* section: the battery was first discharged and the voltage was

[6] Lomonosov Moscow State University, Russia

maintained for several days to ensure a stable current response. After a preliminary measurement, the cell was charged at C/100 until the next targeted voltage which was maintained for two days. The spectrum was then recorded during the following 48 hours under constant voltage of the cell. These two steps were repeated for all the targeted voltages/sodium contents.

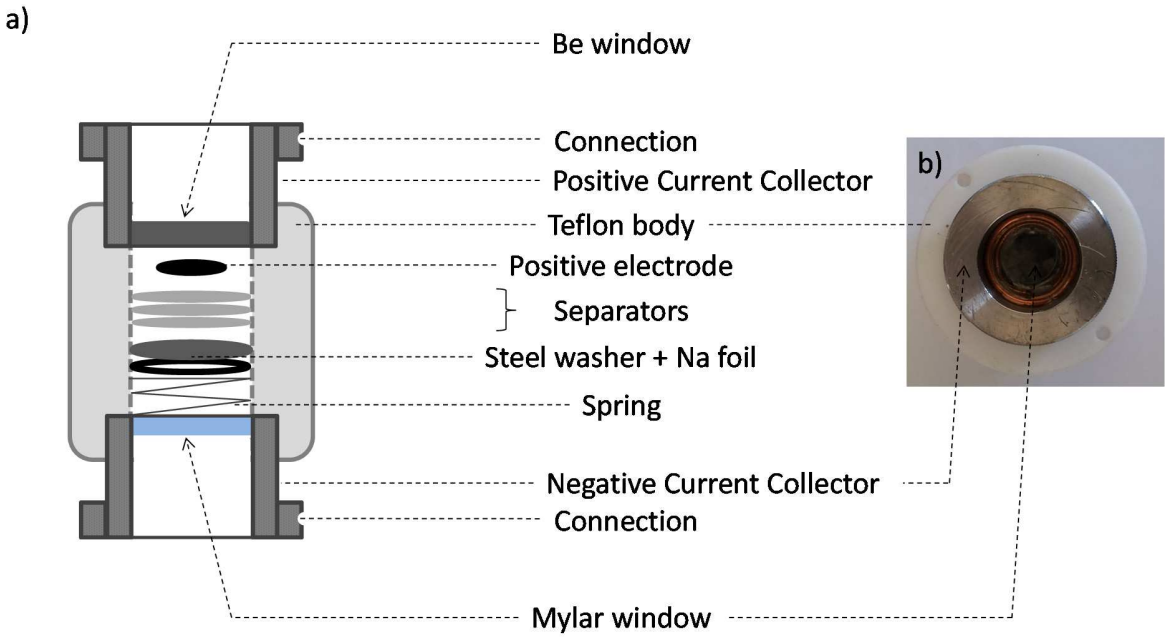

Figure II.10: (a) Schematic representation and (b) photography of the Mössbauer *in situ* cell.

Experimental: ex situ ^{57}Fe Mössbauer spectroscopy

Because *in situ* ^{57}Fe Mössbauer spectroscopy experiments are very time consuming and necessitate using a Mössbauer spectrometer during 4 weeks for only 2 weeks of measurements, we carried out several other experiments *ex situ*. The targeted materials are prepared through the Potentiostatic route described previously on an Active Material + Carbon Black pellet. After cycling, the material is washed and a Mössbauer *ex situ* airtight cell is assembled. The sample is maintained between two Mylar™ windows and placed in a brass support. The airtightness of the cell is assured by an o-ring joint.

II.2.c. X-ray absorption spectroscopy

X-ray absorption spectroscopy or XAS is a commonly used technique at user facilities which allows the determination of local structures and oxidation state. It is based on the excitation of the core-level electrons of an atom (K, L or M shells) when it is exposed to X-rays of specific energy (edge) equal to the energy difference between the excited and fundamental electronic states. This phenomenon is the basis of photoelectric absorption. The absorption **A** of the X-ray beam through a slab is proportional to the ratio between the intensities of the incident and transmitted X-ray beams. It is also calculated from the absorption coefficient of the cross-section μ_a, as represented in **Figure II.11** and detailed in equation **(II.1)**:

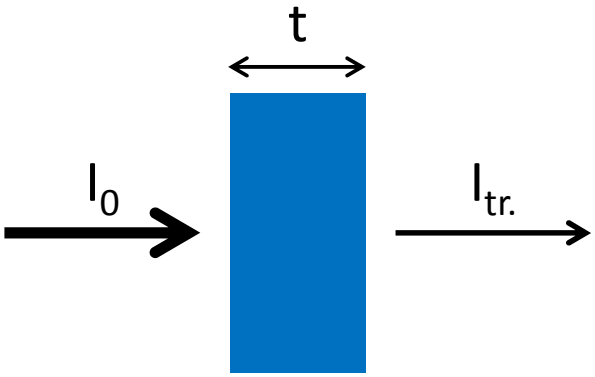

Figure II.11: Transmission of an X-ray beam through a slab of thickness t.

$$A = 1 - \frac{I_{tr.}}{I_0} = 1 - e^{-n\mu_a t} \quad \textbf{(II.1)}$$

With:

$I_{tr.}$: Intensity of the transmitted beam

I_0: Intensity of the incident beam

n: number of atoms per volume unit in the slab

μ_a: photoabsorption of the cross section

t: thickness of the slab

The linear experimental setup allowing the measure of the transmission is shown in **Figure II.12**.

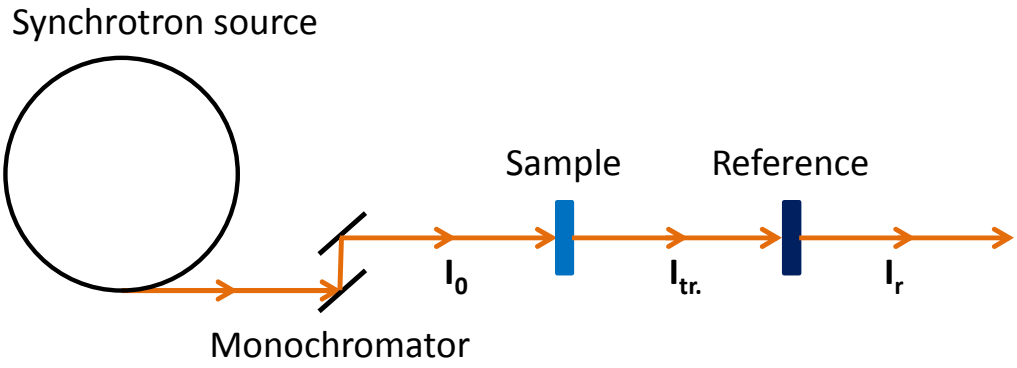

Figure II.12: Schematic representation of the measurement setup line of a XAS experiment.

The X-ray beam exits the synchrotron ring and its energy is controlled by a monochromator. Its intensity I_0 is measured through a first ion chamber before crossing the sample. After crossing the sample, its intensity $I_{tr.}$ is measured again. This step is reproduced with a reference (I_r), usually consisting in a foil of the pure element, if possible (Fe, Mn, Ni, Co…). The interest of measuring the reference is to obtain a comparison point for the determination of oxidation state of the absorbing atom.

The calculated absorption is then plotted as a function of the incident beam energy to give the X-ray absorption spectroscopy spectrum, as shown in **Figure II.13**.

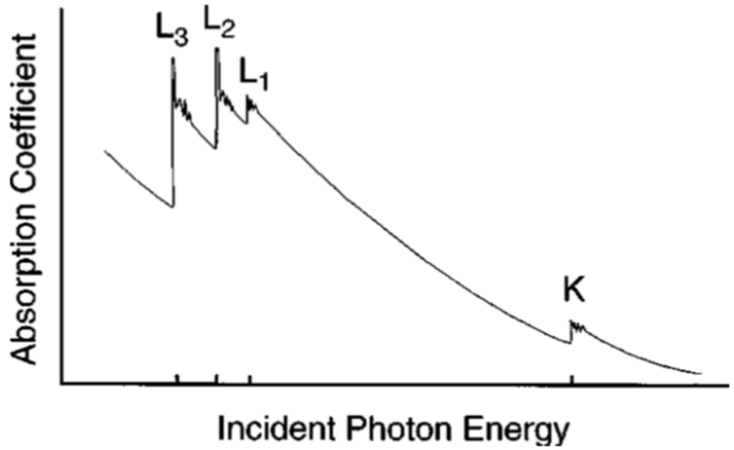

Figure II.13: Variation of the absorption through the absorption coefficient as a function of the incident photon energy.

Four edges labeled, as K, L_1, L_2 and L_3, are visible in **Figure II.13**. The same features can be observed before, at and after every edge: (1) the X-ray absorption decreases with the increase of the incident photon energy, (2) a sharp rises appear, corresponding to the edge and (3) the absorption decreases when the incident photon energy increase following a series of oscillations. These phenomenons result from the interactions between the electron wave and the nearby atoms. Usually, the user only focuses on one edge per element. A typical XAS spectrum is shown in **Figure II.14**.

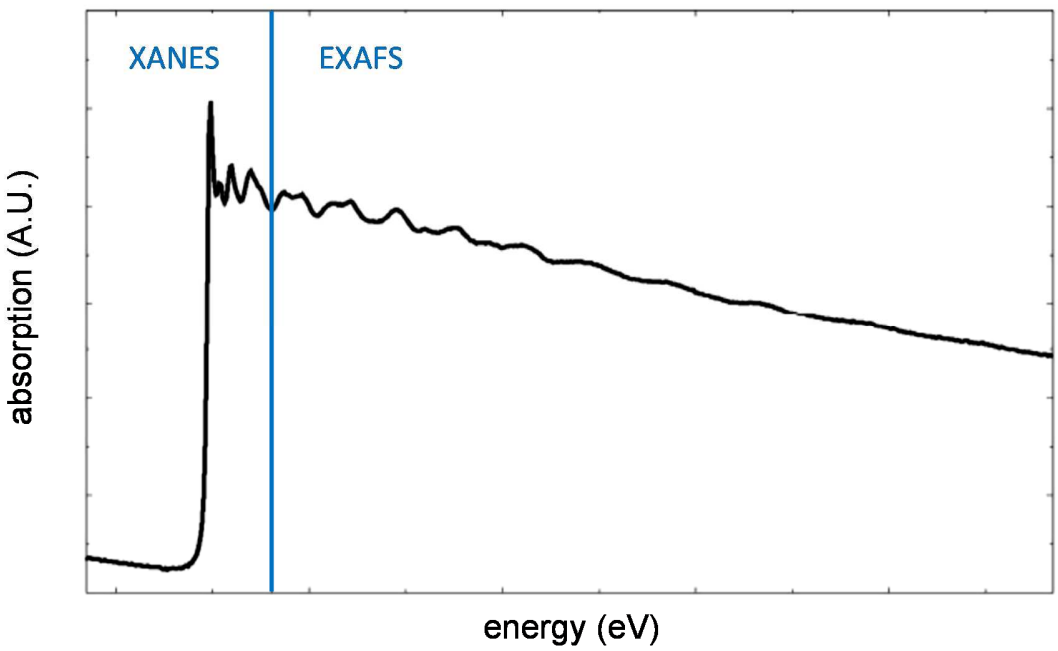

Figure II.14: Example of a XAS spectrum and its division into the XANES and EXAFS subparts.

As represented in **Figure II.14**, the measured XAS spectrum can be divided into two areas that give various information on the material:

X-ray Absorption Near Edge Structure: XANES

The X-ray absorption near edge spectroscopy or XANES part of the spectrum contains information on the oxidation state and coordination environment of the absorbing atom. In our materials, XANES was only used to confirm the oxidation state of the absorbing atoms and required the analysis of several reference compounds ($Mn^{III}_2O_3$ and $Li_2Mn^{IV}O_3$ for the Mn K-edge for example).

Extended X-ray Absorption Fine Structure: EXAFS

The extended X-ray absorption fine structure or EXAFS part of the spectrum contains information on the surrounding neighbors of the absorbing atom. Its fit necessitates known reference materials and a good description of the structure. Once all parameters are known, it is possible to use Fourier transformation on the EXAFS spectra to determine the distances between the absorbing atom and the nearest neighbors [108].

Experimental: Operando in situ XAS

All the measurements were carried out on the 17C beam line at National Synchrotron Radiation Research Center (NSRRC) in Taiwan, R.O.C. in collaboration with the group of Pr. Bing Joe Hwang of National Taiwan University of Science and Technology (NTUST). These measurements were part of the ANR project LaNaMox between ICMCB and NTUST.

The cell consisted in a coin cell battery similar to the one presented at the beginning of this chapter. The positive and negative current collectors were drilled in the center and recovered with polyimide tape. In order to maintain the electronic conductivity, a thin aluminum foil transparent to X-ray was used. The second difference to the previously discussed coin cells comes from the liquid electrolyte which is obtained by dissolving $NaPF_6$ into a mixture of EC and DEC (1 : 1 volume ratio, final concentration of 1 $mol.l^{-1}$).

All data refinements were carried out at NTUST by Cheng Ju-Hsiang as they required an important knowledge of X-ray Absorption Spectroscopy and of the corresponding softwares.

II.2.d. Chemical analysis

The Na / M and the Mn / Fe ratios of the various materials were verified by chemical analysis using an optical emission spectrometer equipped with an Inductively Coupled Plasma (ICP) source. The ionization of an argon flux creates a hot plasma (6000 K – 10000 K) that will vaporize the dissolved sample into unbound atoms and excited ions. While coming back to their fundamental state, these atoms and ions will emit ultraviolet and visible photons. A photomultiplier counts the photons and the comparison to a series of reference samples will allow the quantification. In our materials, only the Ni, Fe, Mn and Na cations could be quantified. The samples were prepared by dissolving 10 mg of powder into boiling aqua regalia (HCl : HNO_3 mixture in a 1 : 2 ratio). Three measures were realized for each sample on a Varian 720ES apparatus by L. Etienne, Engineer at ICMCB.

Part A

Study of the $Na_xMn_{1-y}Fe_yO_2$ phase diagram(s) with y = 1/3, 1/2 and 2/3

Chapter A-I: Synthesis and first characterizations of the pristine materials

Table of contents

The first part of the present work focuses on the $Na_xMn_{1-y}Fe_yO_2$ materials (y = 1/3, 1/2 and 2/3). In this first chapter, an extended bibliographic study is presented along with the motivations that drove us to study this particular system among Na_xMO_2 layered oxides. The synthesis of the pristine materials is first described before we present their structural and morphological characterizations. Last, we present the first electrochemical characterizations of the different materials.

A-I.1. The $Na_xMn_{1-y}Fe_yO_2$ layered oxides in the literature

The first study on the $Na_x(Fe,Mn)O_2$ system was realized during Parant's Ph.D. thesis defended in 1970 in Bordeaux [81]. His aim was to study the phase diagram in the MnO_2 – $NaFeO_2$ system: The $Na_xFe_xMn_{1-x}O_2$ phase diagram. Depending on the x value, several structural domains were isolated, including a pure O3 domain for $0.7 \leq x \leq 1.0$ and a pure P2 domain for $0.45 \leq x \leq 0.55$. As these materials did not show any interesting physical properties, no other study was reported before 2003 when Matsumura et al. reported the synthesis of P2-$Na_{2/3}Mn_{1/3}Fe_{2/3}O_2$ (+ Fe_2O_3 impurity) as an intermediate for the preparation of new Li-ion positive electrode materials after a $Na^+ \leftrightarrow Li^+$ ionic exchange [65].

The reinvestigation of the P2 systems started at ICMCB by Dr. D. Carlier and Dr. C. Delmas in 2010 in collaboration with Pr. R. Stoyanova[7]. This work was the starting point of my Ph.D. Simultaneously to this Ph.D., several papers were published. The use of $Na_xFe_{1-y}Mn_yO_2$ materials as positive electrode materials in Na batteries was first mentioned in 2011 by Yabuuchi et al. [66]. They reported the solid state synthesis and the charge/discharge profiles of the P2-$Na_{2/3}Mn_{2/3}Fe_{1/3}O_2$ and O3-$Na_1Mn_{1/3}Fe_{2/3}O_2$ phases. The huge leap in the publication number concerning this system started in April 2012 when the same authors reported the structural and electrochemical properties of the P2-$Na_{2/3}Mn_{1/2}Fe_{1/2}O_2$ and O3-$Na_1Mn_{1/2}Fe_{1/2}O_2$ phases in Nature Materials [26]. These materials showed second cycle discharge capacities of 190 $mAh.g^{-1}$ and ≈ 110 $mAh.g^{-1}$ for the P2 and O3 phases respectively when cycled between 1.5 and 4.3 V at C/20. In the following months, Yoncheva et al. reported the synthesis of P'3-$Na_{2/3}Mn_{1-y}Fe_yO_2$ phases (y = 0; 1/3; 2/3) in collaboration with ICMCB [27]. The $Na_xMn_{1-x}Fe_xO_2$ phase diagram ($0.5 \leq x \leq 1.0$) and its electrochemical properties were reinvestigated by Thorne et al. in 2013 who obtained similar results on the P2-$Na_{0.5}Mn_{1/2}Fe_{1/2}O_2$ phase than those from Yabuuchi et al. [28]. In 2014, Zhao et al. published the first study focusing on the P2-$Na_{2/3}Mn_{2/3}Fe_{1/3}O_2$ phase and investigated the electrochemical and thermal properties of this material [32]. They obtained an interesting second discharge capacity of 193 $mAh.g^{-1}$ while cycling the corresponding Na cell into the 1.5 – 4.3 V range at C/20.

[7] Bulgarian Academy of Sciences, Institute of general and Inorganic Chemistry, Bulgaria.

Despite the interesting discharge capacities of the P2-$Na_xMn_{1-y}Fe_yO_2$ materials, an important drawback is that the starting material represents an intermediate state of intercalation. This is a problem for Na-ion batteries as it requires an over-sodiated negative electrode. To overcome this issue, Singh et al. suggested adding 5 % of NaN_3 into the electrode preparation [29]. This Na source decomposes during the cycling to compensate the lack of Na into the starting material. However it releases gaseous N_2 into the battery increasing the pressure of the system which can lead to safety issues.

In all the studies reported in the literature, P2 and O3-$Na_xMn_{1-y}Fe_yO_2$ materials are prepared by a solid state chemistry synthesis, involving a Na precursor (Na_2CO_3 [28, 29, 65] or Na_2O/Na_2O_2 [26, 28, 33] mixed with Fe (Fe_2O_3 [26, 29, 32, 33] or Fe_3O_4 [28, 65]) and Mn (Mn_2O_3 [26, 29, 32, 65] or MnO_2 [28, 33]) oxides. The mixture is then heated under air or O_2 for 12 – 36 hours with [28, 33] or without [26, 27, 29, 32, 65] a previous ball milling step.

A-I.2. Synthesis of the pristine materials

A-I.2.a. The aqueous self-combustion type synthesis

When we started the study of the $Na_xMn_{1-y}Fe_yO_2$ phase diagram, only Parant's thesis and Matsumura et al.'s work on the P2-$Na_{2/3}Mn_{1/3}Fe_{2/3}O_2$ phase were published [65, 81]. At ICMCB, the P2-$Na_{2/3}Mn_{2/3}Fe_{1/3}O_2$ phase was studied by Dr. M. Yoncheva (Invited researcher) in 2010 and by Dr. T Okamura (Invited Post-doctorant) in 2011. Their materials were prepared by co-precipitation and classic solid state synthesis routes, respectively.

The first goal of this thesis was to synthesize other $Na_xMn_{1-y}Fe_yO_2$ materials. Mn / Fe ratios of 1 / 1 ($Na_xMn_{1/2}Fe_{1/2}O_2$) and 1 / 2 ($Na_xMn_{1/3}Fe_{2/3}O_2$) were targeted. Unfortunately, our attempts to synthesize materials with new Mn / Fe ratios based on the existing protocols were not successful. Therefore, we tried the self-combustion synthesis route (or smoldering combustion synthesis). This synthesis route consists in a redox reaction between an oxidizer and a fuel. The oxidizer (oxidizing agent) usually consists in transition metal and/or alkali nitrates ($LiNO_3$, $NaNO_3$, $M^{3+}(NO3\text{-})_3$, $M^{2+}(NO3\text{-})_2$…). The fuel represents the reducing and chelating agent of the reaction. Glycine ($H_2N\text{-}CH_2\text{-}COOH$) represents one of the most used fuels for self-combustion type syntheses [109]. When the solution is heated, the reaction occurs following two steps:

1) Glycine undergoes polycondensation according to **(A-I.1)**:

$$^{+}H_3N\text{-}CH_2\text{-}COO^{-} + {}^{+}H_3N\text{-}CH_2\text{-}COO^{-} \rightarrow {}^{+}H_3N\text{-}CH_2\text{-}CO\text{-}NH\text{-}CH_2\text{-}COO^{-} + H_2O \quad \textbf{(A-1.1)}$$

2) The redox reaction occurs according to **(A-I.2)**:

$$2\ M(NO_3)_3 + \alpha\ NH_2CH_2COOH + (2.25\ \alpha - 7.5)\ O_2 \rightarrow M_2O_3 + 2\ \alpha\ CO_2 + 2.5\ \alpha\ H_2O + (3+0.5\ \alpha)\ N_2 \quad \textbf{(A-I.2)}$$

As one can see depending on the oxidizer / fuel ratio (α in **(A-I.2)**) the reaction will necessitate an external source of oxygen (air). This oxidizer / fuel ratio is a key parameter of the reaction as it also influences the flame temperature reached during the reaction (typically above 1000°C [109, 110]). Self-combustion syntheses result in the obtention of a homogeneous, small-sized precursor or poorly crystallized phase [111]. Using self-combustion type synthesis, our idea was to prepare a precursor with a good distribution between Fe and Mn.

A-I.2.b. Synthesis of the pristine materials

Following a self-combustion synthesis protocol, the $Na_xMn_{1-y}Fe_yO_2$ materials are synthesized by dissolving manganese, iron and sodium nitrates (Alfa Aesar $Mn(NO_3)_2.4H_2O$ (97% purity), $Fe(NO_3)_3.9H_2O$ (98%) and $NaNO_3$ (99%) respectively) into water. The final concentration of the Mn and Fe solutions is 1 $mol.l^{-1}$. A 10 wt % excess of $NaNO_3$ is added to take into account the high volatility of sodium oxide. After total dissolution, glycine (Sigma-Aldrich, ≥ 99%) is added. After a few attempts, we chose the molar NO^{3-} / glycine ratio (oxidizer / fuel) equal to 8 / 1 in order to lower the temperature and violence of the reaction. A dark brown coloration occurs in the solution, resulting from the complexation between the Fe^{3+} ions and glycine [112]. The complexation is also expected to affect the Mn^{2+} ions. The solution is then poured into a ceramic bowl and placed into a sand bath heated at 480°C on a hot plate for several hours. Once the combustion is complete, a fine black powder is obtained after grinding, as shown in **Figure A-I.1** along its Scanning Electron Microscopy (SEM) micrograph.

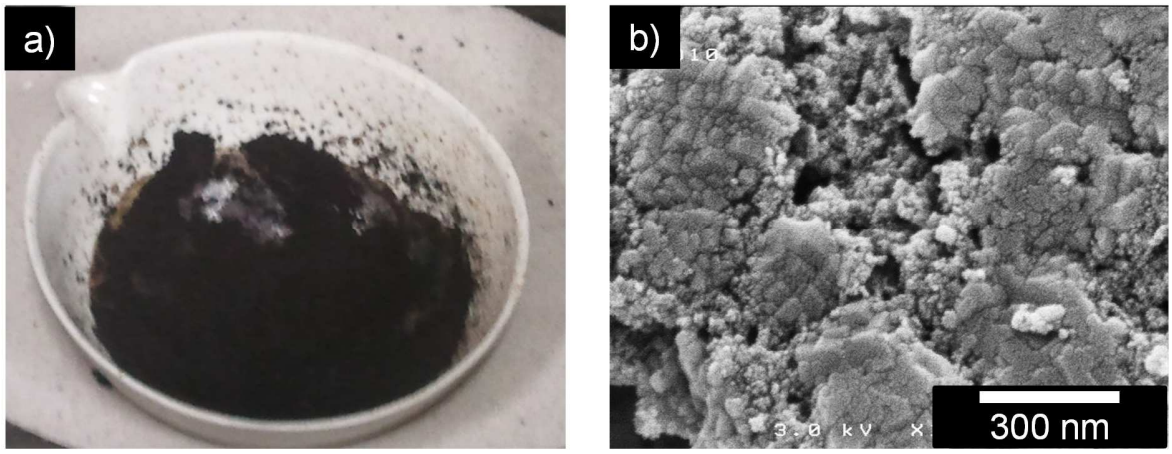

Figure A-I.1: (a) photography and (b) Scanning Electron Microscopy micrograph of the product of the self-combustion synthesis of a $Na_xMn_{1-y}Fe_yO_2$ material after grinding.

The SEM micrograph highlight a very heterogeneous powder containing particles with sizes comprised between ≈ 50 nm and 150 nm which tend to agglomerate into bigger grains of various sizes and up to 1 µm.

The XRPD pattern of the product of the combustion product is given in **Figure A-I.2**, along with the phase identification. Only the 20° ≤ 2θ ≤ 60° angular region is shown as it exhibits the most intense and numerous diffraction peaks.

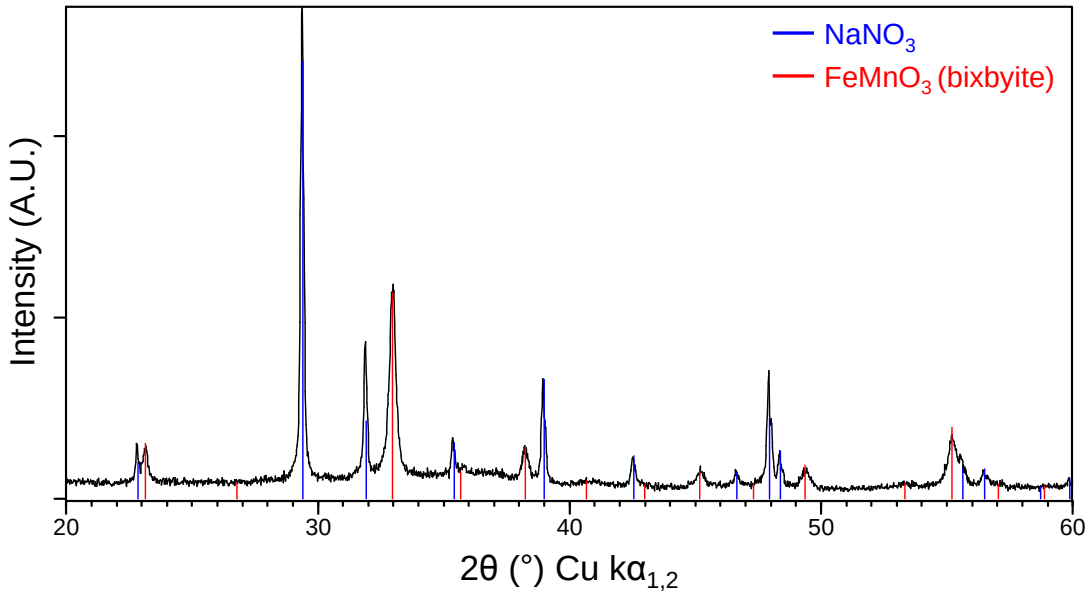

Figure A-I.2: XRPD pattern and phase identification of the product recovered after the self-combustion synthesis step of the P2-$Na_xMn_{2/3}Fe_{1/3}O_2$ phase and before heat treatment.

The XRPD patterns recorded after the self-combustion synthesis of every materials exhibit sharp diffraction peaks allowing the identification of two inorganic compounds: a mixed Mn and Fe oxide similar to $Fe^{III}Mn^{III}O_3$ (indicated by the blue vertical lines in **Figure A-I.2**) along with unreacted $NaNO_3$ (red vertical lines). It is noteworthy that no traces of hematite (Fe_2O_3) were observed.

The combustion product is then heated in a gold boat in a tubular furnace, first at 700 °C for 20 h under air to allow the chemical reaction between $NaNO_3$ and the $Mn_{1-y}Fe_yO_3$ precursor. A second heat treatment performed at 1000 °C for 5 h under O_2 is then applied to better crystallize the material. The heating ramps are equal to +5°C.min^{-1}. A graphical representation of the heat treatment step is given in **Figure A-I.3**.

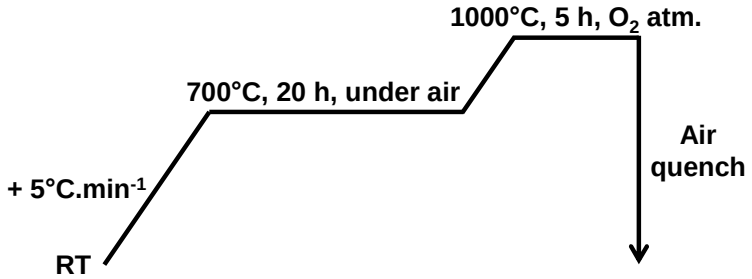

Figure A-I.3: Schematic representation of the heat treatment step of the $Na_xMn_{1-y}Fe_yO_2$ materials.

After the heat treatment, the samples are quenched down to room temperature and stored into an Ar filled glovebox to avoid reaction with moisture. The targeted mass of final product is 5 g.

A-I.2.c. Investigation of the $Na_xMn_{1-y}Fe_yO_2$ phase diagrams by self-combustion synthesis

All materials show the same tendency when increasing the Na / (Mn + Fe) ratio while keeping the Mn / Fe one constant: for the lowest sodium ratios ($x_{Na} \approx 0.6$) a **P2 + Fe_2O_3** phase domain is observed, followed by several others upon increase of the sodium content: **P2**, **P2 + O3**, **O3** and finally **O3 + O'3**. Depending on the Mn / Fe ratio the limits of pure phase domains vary. We therefore studied the $Na_xMn_{2/3}Fe_{1/3}O_2$, $Na_xMn_{1/2}Fe_{1/2}O_2$ and $Na_xMn_{1/3}Fe_{2/3}O_2$ phase diagrams for $0.6 \leq x \leq 1.0$, with a theoretical sodium variation of 0.025 Na^+ per formula unit. The synthesis protocol is similar to the first one we described; however we targeted 2 g of final product for each sample. The XRPD measurements were carried out in the selected 15.5° – 16.5° and 31° – 40° 2θ ranges (Cu $k\alpha_{1,2}$) in 0.1 mm diameter capillaries in order to highlight the present phases (Fe_2O_3, P2, O3 and O'3). The determined phase diagrams are represented in **Figure A-I.4**.

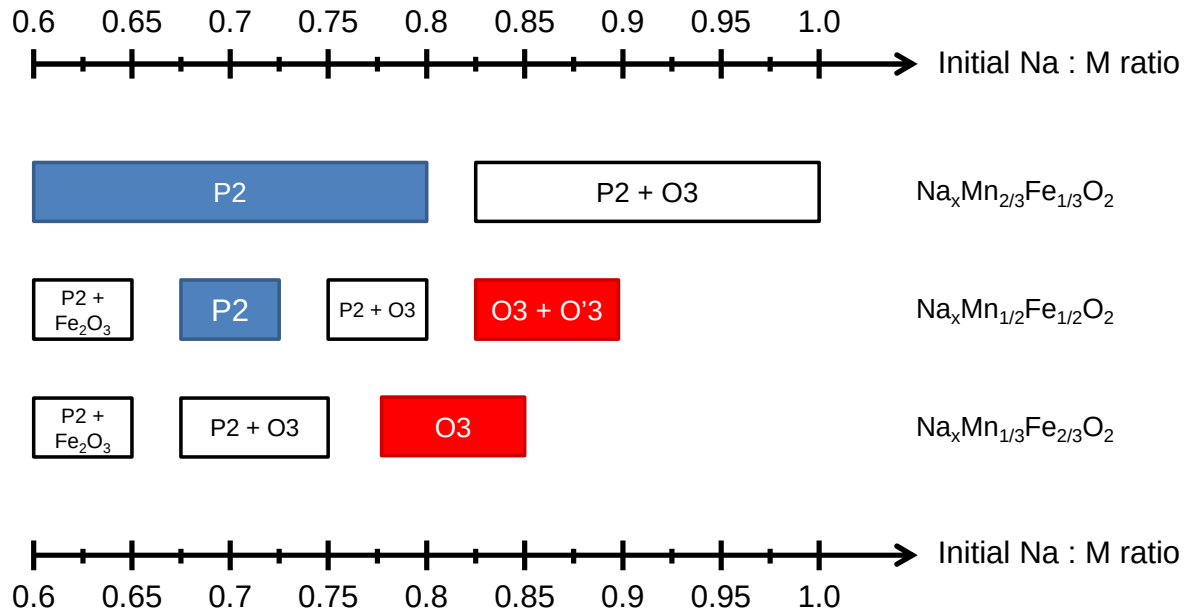

Figure A-I.4: Phase diagrams as a function of the sodium content for the $Na_xMn_{2/3}Fe_{1/3}O_2$, $Na_xMn_{1/2}Fe_{1/2}O_2$ and $Na_xMn_{1/3}Fe_{2/3}O_2$ systems.

From **Figure A-I.4**, we can observe two tendencies between the different $Na_xMn_{1-y}Fe_yO_2$ compositions:

(1) High Mn contents stabilize P2-type structures. Indeed, a pure P2 phase domain is observed for $0.6 \leq x \leq 0.8$ for the $Na_xMn_{2/3}Fe_{1/3}O_2$ system, while it is observed between $0.675 \leq x \leq 0.775$ for the $Na_xMn_{1/2}Fe_{1/2}O_2$ one. No pure P2 phase was obtained for the $Na_xMn_{1/3}Fe_{2/3}O_2$ phase system, in agreement with Matsumura et al. [65].

(2) On the contrary, high Fe contents stabilize O3-type structures and pure O3 phases were obtained starting x = 0.775 (theoretical Na : M ratio) in the $Na_xMn_{1/3}Fe_{2/3}O_2$ system. Only an O3 + O'3 phase domain was obtained in the $Na_xMn_{1/2}Fe_{1/2}O_2$ system and no pure O3 phase domain was evidenced in the $Na_xMn_{2/3}Fe_{1/3}O_2$ system. However, several studies report the existence of pure O'3-$NaMnO_2$ phase [5, 44] suggesting that a Fe substitution in this material would be possible. Our failure in obtaining a pure O'3 or O3-$Na_xMn_{2/3}Fe_{1/3}O_2$ phases could be induced by our synthesis route. Following the same reasoning, it must be noted that almost-pure O3-$NaMn_{1/2}Fe_{1/2}O_2$ was obtained by Yabuuchi et al. by direct solid state synthesis, but shows traces of P2-$Na_xMn_{1/2}Fe_{1/2}O_2$ and Na_3MnO_4 [26].

According to (1) and (2), increasing the Mn (Fe) contents will stabilize the P2 (O3) phases on a wider Na range.

We then targeted the structure types by controlling the sodium content: the P2-$Na_{0.77}Mn_{2/3}Fe_{1/3}O_2$, the P2-$Na_{0.67}Mn_{1/2}Fe_{1/2}O_2$, the (O3+O'3)-$Na_{0.82}Mn_{1/2}Fe_{1/2}O_2$ and the O3-$Na_{0.82}Mn_{1/3}Fe_{2/3}O_2$ phases.

A-I.3. Characterization of the pristine materials

A-I.3.a. X-ray powder diffraction analysis

The XRPD patterns corresponding to the targeted materials are shown in **Figure A-I.5**. They exhibit pure P2 and O3 phases except for the $Na_{0.82}Mn_{1/2}Fe_{1/2}O_2$ composition, as predicted (O3+O'3 mixture). The cell parameters and interslab distances of the different materials are reported in **Table A-I.1**. The structure of each material will be further discussed in their corresponding sections (**Chapters A-II** and **A-III**).

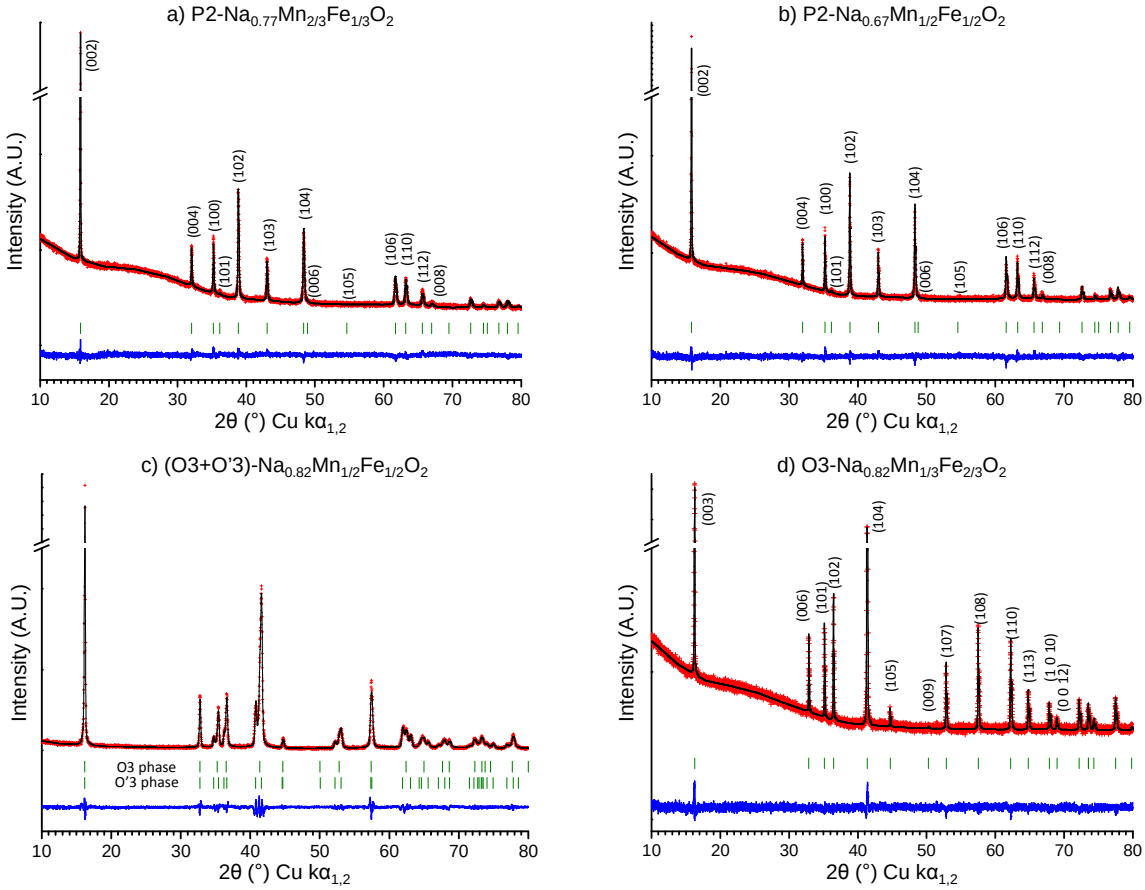

Figure A-I.5: Observed and calculated XRPD patterns for (a) the P2-$Na_{0.77}Mn_{2/3}Fe_{1/3}O_2$, (b) the P2-$Na_{0.67}Mn_{1/2}Fe_{1/2}O_2$, (c) the (O3+O'3)$Na_{0.82}Mn_{1/2}Fe_{1/2}O_2$ and (d) the O3-$Na_{0.82}Mn_{1/3}Fe_{2/3}O_2$ phases. Red crosses: observed, black line: calculated, blue line: difference plot and green bars: Bragg reflections. (a, b, d): Rietveld refinement and (c): LeBail profile.

	P2-$Na_{0.77}Mn_{2/3}Fe_{1/3}O_2$	**P2-$Na_{0.67}Mn_{1/2}Fe_{1/2}O_2$**	**(O3+O'3)$Na_{0.82}Mn_{1/2}Fe_{1/2}O_2$**		**O3-$Na_{0.82}Mn_{1/3}Fe_{2/3}O_2$**
Space group	$P6_3/mmc$	$P6_3/mmc$	R-3m (O3)	C2/m (O'3)	R-3m
a (Å)	2.9392(1)	2.9386(1)	2.9730(3)	5.2170(7)	2.9805(1)
b (Å)	/	/	/	2.9462(3)	/
c (Å)	11.1648(6)	11.1884(4)	16.396(4)	5.7515(8)	16.3264(5)
β (°)	/	/	/	108.24(1)	/
Interslab distance (Å)	5.5824(6)	5.5942(4)	5.465(4)	5.463(3)	5.4421(5)

Table A-I.1: Cell parameters and Interslab distances of the P2-$Na_{0.77}Mn_{2/3}Fe_{1/3}O_2$, P2-$Na_{0.67}Mn_{1/2}Fe_{1/2}O_2$, (O3+O'3)$Na_{0.82}Mn_{1/2}Fe_{1/2}O_2$ and O3-$Na_{0.82}Mn_{1/3}Fe_{2/3}O_2$ phases.

The P2 and O3 phases crystallize in the hexagonal ($P6_3/mmc$) and the rhombohedral (R-3m) systems, respectively. The cell parameters of the different materials are very close to those reported in the literature for the same Mn / Fe ratios [26-29, 32]. As expected from the various stacking, a larger interslab distance is observed in P2-type structures than in O3-type ones, in agreement with the larger size of the prismatic sites compared to the octahedral ones.

We attribute the existence of the O'3 phase in the (O3+O'3)-$Na_{0.82}Mn_{1/2}Fe_{1/2}O_2$ mixture to the cooperative Jahn Teller effect of the Mn^{3+} ions as suggest the $a_{mon.}/b_{mon.}$ = 1.77 ratio. We then expect the O'3 phase to have higher Mn^{3+} content -*i.e.* higher sodium content- than the O3 one if the Mn / Fe ratio is constant. It also possible that two materials with slightly different Mn / Fe ratios coexist in the (O3+O'3)-$Na_{0.82}Mn_{1/2}Fe_{1/2}O_2$ mixture.

For every batch of material, the ICP-AES analysis confirms the Mn / Fe and Na / (Mn + Fe) ratios. The theoretical and experimental ratios are compared to the one determined by the Rietveld refinement on the structures from the synchrotron XRPD patterns in **Table A-I.2**. The Rietveld refinements of the structures of the different materials will be detailed in **Chapters A-II** and **A-III**.

Targeted $Na_xMn_{1-y}Fe_yO_2$ material	**Na: (Mn + Fe) ratio (ICP-AES)**	**Mn: (Mn + Fe) ratio (ICP-AES)**	**Fe: (Mn + Fe) ratio (ICP-AES)**	**Na:(Mn + Fe) ratio (Rietveld)**
P2-$Na_{0.77}Mn_{2/3}Fe_{1/3}O_2$	0.77(2)	0.64(2)	0.36(2)	0.66(2)
P2-$Na_{0.67}Mn_{1/2}Fe_{1/2}O_2$	0.66(2)	0.47(2)	0.53(2)	0.62(1)
O3-$Na_{0.82}Mn_{1/2}Fe_{1/2}O_2$	0.81(2)	0.47(2)	0.53(2)	Undetermined
O3-$Na_{0.82}Mn_{1/3}Fe_{2/3}O_2$	0.83(2)	0.31(2)	0.69(2)	0.77(1)

Table A-I.2: ICP-AES results for the pristine materials synthesized by self-combustion synthesis.

Table A-I.2 shows that the targeted sodium compositions and transition metal contents are confirmed by ICP-AES analysis in the range of experimental errors, confirming that the 10 wt% of excess Na vaporized during the synthesis and/or the heat treatment step. However, the Na contents deduced from the Rietveld refinement of the different materials conducted to lower Na contents. We suppose that a significant part of the Na^+ ions were vaporized from the material, probably during the air quenching step, creating Na_2CO_3 and NaOH at the surface of the material. The sodium contents determined by the Rietveld refinements would therefore give a better estimation of the amount of the intercalated Na^+ ions and will be considered.

A-I.3.b. Morphology

The different P2 and O3 phases were analyzed by Scanning Electron Microscopy to determine their morphology. **Figure A-I.6** shows the Scanning Electron Microscopy micrographs corresponding to the P2-$Na_{0.62}Mn_{1/2}Fe_{1/2}O_2$ and O3-$Na_{0.77}Mn_{1/3}Fe_{2/3}O_2$ materials, which are representative of the P2 and O3-$Na_xMn_{1-y}Fe_yO_2$ materials, respectively.

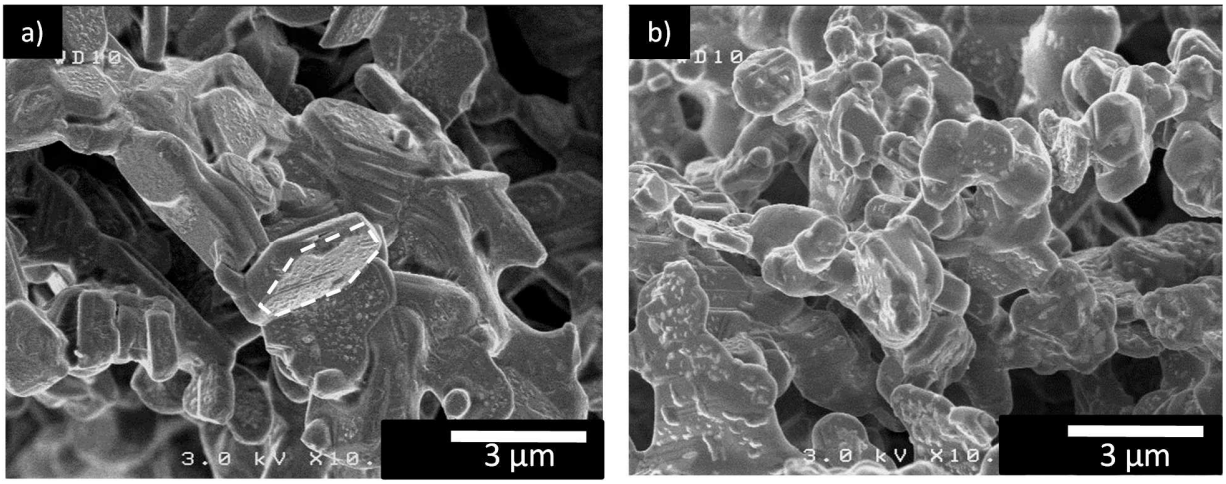

Figure A-I.6: Scanning Electron Microscopy micrographs for (a) the P2-$Na_{0.67}Mn_{1/2}Fe_{1/2}O_2$ and (b) the O3-$Na_{0.82}Mn_{1/3}Fe_{2/3}O_2$ phases.

It appears that the material with the P2-type structure exhibits well-shaped particles of 3.4 µm average diameter and 200 nm thicknesses. The hexagonal plate-shaped particle morphology is similar to other P2-type phases [61, 88, 91]. The O3-type phases show round-shaped particles of 3 µm average size. The small imperfections on the surface of both materials are due to air exposition during the sample handling prior to the gold sputtering. The impurity amount increased both in number and size with the air exposure time. We believe it corresponds to NaOH /Na_2CO_3 impurities which are formed on the surface as sodium leaves the material, allowing the average Mn oxidation state to increase. All phases present agglomerated particles with larger sizes than the ones reported by Yabuuchi et al. (500 nm mean size) [26]. This is certainly related to the higher synthesis temperature of our materials (1000°C *vs.* 700-900°C [26]).

A-I.3.c.Electrochemistry

To confirm the electrochemical activity of the various materials, we prepared Na-cells involving the $Na_xMn_{1-y}Fe_yO_2$ phases as active materials.

Optimization of the liquid electrolyte

First, we investigated the influence of electrolyte additives in order to optimize the cycling properties, using an upper cutoff voltage of 3.8 V. The role of fluoroethylene carbonate (FEC) on the prevention of the electrolyte was recently studied by Komaba et al. [99] while vinyldiene carbonate (VC) is a well-known additive used for Li-ion batteries electrolytes [98]. **Figure A-I.7** shows the first four cycles obtained from the O3-$Na_{0.77}Mn_{1/3}Fe_{2/3}O_2$ phase (starting by a discharge) using the pure $NaPF_6$ in PC (1M) electrolyte (**Figure A-I.7a**), the $NaPF_6$ in PC (1M) + 2 wt% VC one (**Figure A-I.7b**) or the $NaPF_6$ in PC (1M) + 2 wt% FEC one (**Figure A-I.7c**). The first cycle is highlighted in red for all experiments. The corresponding capacity retentions upon cycling are given in **Figure A-I.7d**.

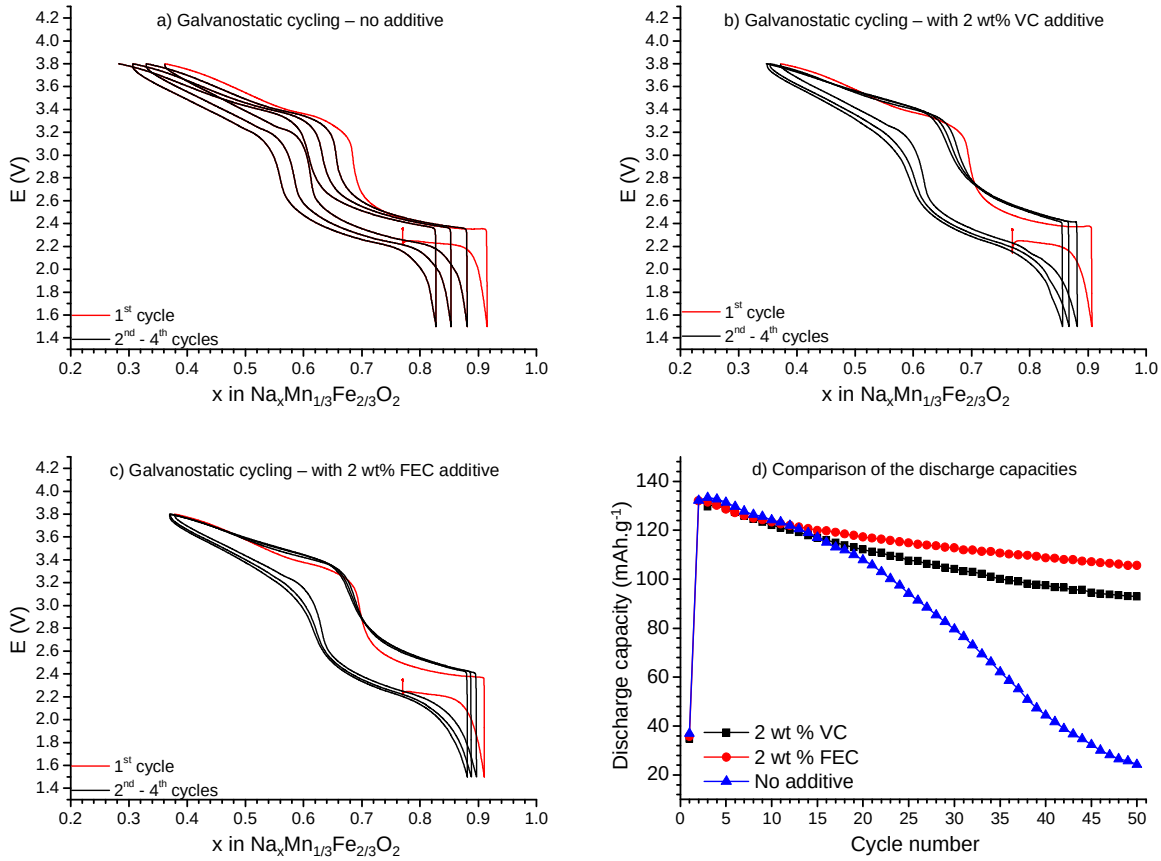

Figure A-I.7: Galvanostatic cycling curves involving the O3-$Na_{0.77}Mn_{1/3}Fe_{2/3}O_2$ material at the positive electrode recorded between 1.5 and 3.8 V at C/50: (a) without any additive, (b) with the VC electrolyte additive and (c) with the FEC electrolyte additive. The associated discharge capacities are also represented (d).

As one can see, the use of 2 wt% of VC or FEC additives in the electrolyte clearly prevents the electrolyte decomposition in the 1.5 – 3.8 V voltage window, leading to a better overlap of the cycling curves and to better capacity retention. A discharge capacity of ≈ 132 mAh.g^{-1} is reached on the second cycle in this voltage range and the capacity retention is equal to 92 % at the 12th cycle. After further cycling, the behavior strongly depends on the electrolyte used: without additive (in blue) a sudden decrease of the capacity is observed. Thanks to the use of additives, the capacity fading is reduced. Among the two additives considered, FEC leads to slightly better results than VC and was then further used for our studies. In the literature, the FEC additive was also shown to play a key role in preventing the electrolyte decomposition: without any additive the propylene carbonate solvent reacts with the Na foil constituting the negative electrode, the resulting reductive decomposition forming sodium propyl carbonate [99].

Galvanostatic cycling between 1.5 and 3.8 V

All the $Na_xMn_{1-y}Fe_yO_2$ phases were then tested as positive electrode materials in Na batteries involving the $NaPF_6$ in PC (1 M) + 2 wt% FEC electrolyte. **Figure A-I.8** shows the evolution of the voltage of the cells as a function of the Na content when cycled between 1.5 and 3.8 V.

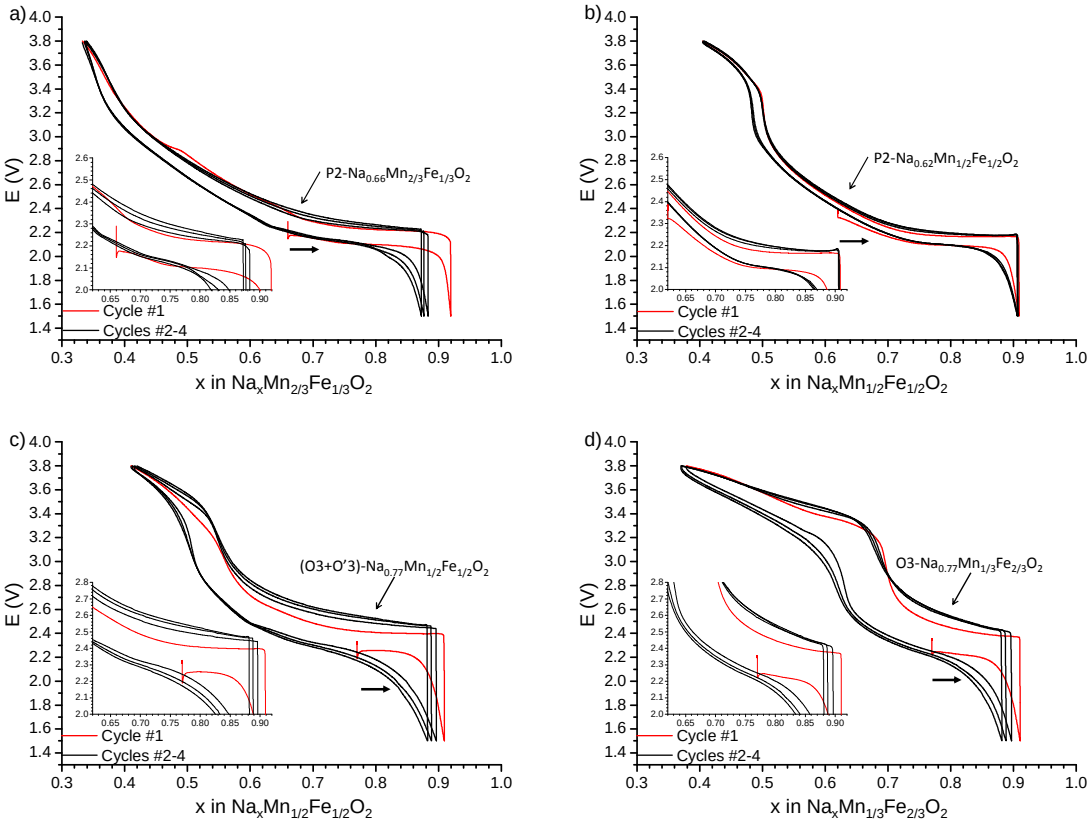

Figure A-I.8: Galvanostatic cycling curves of the Na/ $NaPF_6$ in PC (1 M) + 2 wt% FEC /$Na_xMn_{1-y}Fe_yO_2$ cells obtained at a C/50 rate starting by a discharge between 1.5 and 3.8 V. (a) P2-$Na_xMn_{0.66}Mn_{1/3}Fe_{2/3}O_2$, (b) P2-$Na_{0.62}Mn_{1/2}Fe_{1/2}O_2$, (c) (O3+O'3)-$Na_{0.77}Mn_{1/2}Fe_{1/2}O_2$ and (d) O3-$Na_{0.77}Mn_{1/3}Fe_{2/3}O_2$. A magnification of each curve around the starting point is shown in the insets.

Identical behaviors were observed starting by a charge or by a discharge (only the curves starting by a discharge are shown here). For every single phase, the charge and discharge curves look quite similar, indicating a good reversibility of the Na intercalation/deintercalation process. No shift of the curves is observed with the cycle number, indicating that no noticeable electrolyte decomposition occurs. All electrochemical curves exhibit the same features: starting by a discharge, sodium intercalation leads to a plateau, signature of a biphasic domain, until we reach the maximum intercalated composition. As shown in **Table A-I.3**, the plateau is slightly higher in voltage for the O3 phases than for the P2 ones (≈ 0.2 V). This indicates that a higher energy is required to (de)insert the Na^+ ions from the inter-layer space in the O3 stacking. The lower polarization of the P2-type structures suggests an easier diffusion path than for the O3-type structures, as evidenced in the P2 and O3-Na_xVO_2 phases [113]. Concerning the (O3+O'3)-$Na_{0.77}Mn_{1/2}Fe_{1/2}O_2$ phase, one can see that the starting point (inset of **Figure A-I.8c**) is located on the voltage plateau. We assume that this plateau is characterized by equilibrium between the O3 and O'3 stacking types and that the intercalated state of the O3 materials corresponds to an O'3 structure. By analogy, different structures derived from the P2-type are also expected for the intercalated P2 phases.

Formula of the starting material	**Voltage of the voltage plateau (V)**	
	1st discharge	**1st charge**
P2-$Na_{0.66}Mn_{2/3}Fe_{1/3}O_2$	2.08 V	2.21 V
P2-$Na_{0.62}Mn_{1/2}Fe_{1/2}O_2$	2.08 V	2.17 V
(O3+O'3)-$Na_{0.77}Mn_{1/2}Fe_{1/2}O_2$	2.25 V	2.40 V
O3-$Na_{0.77}Mn_{1/3}Fe_{2/3}O_2$	2.25 V	2.40 V

Table A-I.3: Values of the voltage plateaus associated to the first discharge and first charge for the different $Na_xMn_{1-y}Fe_yO_2$ materials.

Upon further deintercalation, the E = f(x) curves exhibit a solid solution behavior and undergo a sudden voltage jump at $x \approx y_{Fe}$ for the materials with Mn / Fe ratios equal to 1 / 1 and 1 / 2. These voltage jumps may correspond to a change of redox process from $Mn^{3+} \rightarrow Mn^{4+}$ to $Fe^{3+} \rightarrow Fe^{4+}$ as already shown in the literature by X-Ray Absorption Spectroscopy and Mössbauer Spectroscopy [26, 28]. If for the P2 phases the first discharge is similar to the others, one can notice an important increase of the polarization for the E = f(x) curves associated to the O3 materials in the Mn^{4+}/Mn^{3+} redox couple activity range while the polarization decreases in the Fe^{4+}/Fe^{3+} one. **Figure A-I.9** compares the evolution of the discharge capacities of the batteries assembled with the various $Na_xMn_{1-y}Fe_yO_2$ materials. The theoretical discharge capacity of the P2 and O3 materials is approximatively equal to 240 $mAh.g^{-1}$ (considering 1 Na^+ intercalated per formula unit).

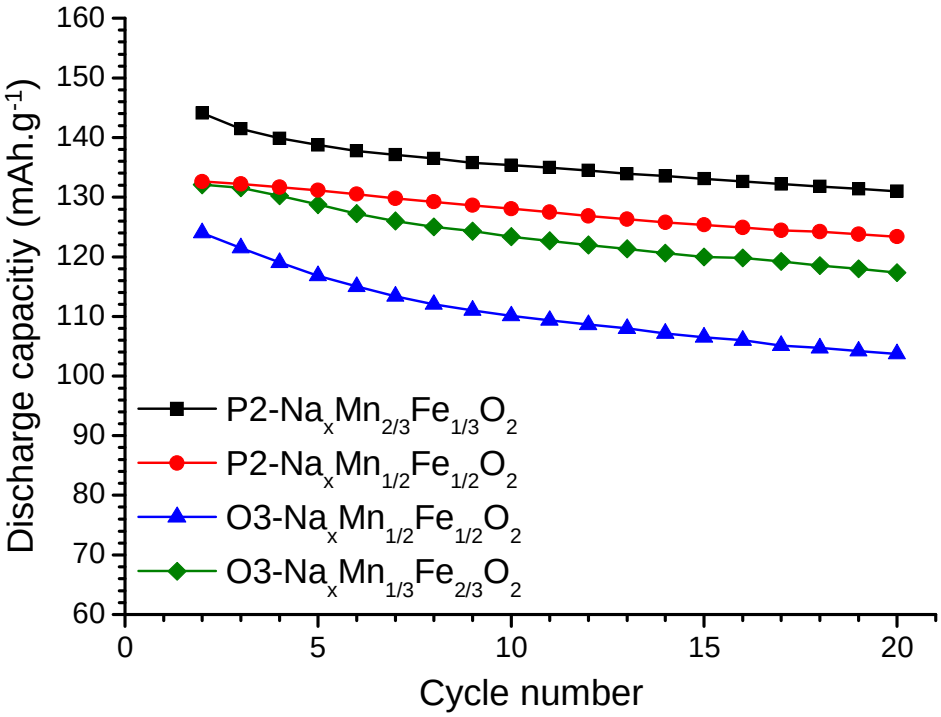

Figure A-I.9: Discharge capacities corresponding to the Na//$Na_xMn_{1-y}Fe_yO_2$ cells cycled between 1.5 and 3.8 V and assembled from the P2-$Na_{0.66}Mn_{2/3}Fe_{1/3}O_3$ (black), P2-$Na_{0.62}Mn_{1/2}Fe_{1/2}O_2$ (blue), (O3+O'3)-$Na_{0.77}Mn_{1/2}Fe_{1/2}O_2$ (red) and O3-$Na_{0.77}Mn_{1/3}Fe_{2/3}O_2$ (green) materials.

Comparing the second discharge capacities, one can see that the battery assembled from P2-$Na_{0.66}Mn_{2/3}Fe_{1/3}O_2$ reach the highest value (144 mAh.g^{-1}). Decreasing the Mn content in the P2 structures lowers this capacity to 133 mAh.g^{-1} for the $Na_xMn_{1/2}Fe_{1/2}O_2$ composition. On the contrary, decreasing the Mn content increases the second discharge capacity for the O3 structures and 132 mAh.g^{-1} are available for the $Na_xMn_{1/3}Fe_{2/3}O_2$ composition *vs.* 124 mAh.g^{-1} for the and $Na_xMn_{1/2}Fe_{1/2}O_2$ one. In average, the discharge capacity of the batteries prepared with P2-type materials at the positive electrode is higher, following the general trend mentioned in the introduction.

Looking at the 20th cycle discharge capacity retentions, all phases exhibit similar values: 91 % (P2-$Na_xMn_{2/3}Fe_{1/3}O_2$), 93 % (P2-$Na_xMn_{1/2}Fe_{1/2}O_2$), 91 % (O3-$Na_xMn_{1/2}Fe_{1/2}O_2$) and 89 % (O3-$Na_xMn_{1/3}Fe_{2/3}O_2$). Despite it exhibits a higher second discharge capacity; the $Na_xMn_{1/3}Fe_{2/3}O_2$ composition shows worse capacity retention than the $Na_xMn_{1/2}Fe_{1/2}O_2$ one among the O3 structures. Furthermore, comparing the two $Na_xMn_{1/2}Fe_{1/2}O_2$ materials, the P2-type one show slightly better stability.

By comparison to the literature, P2-$Na_{0.62}Mn_{1/2}Fe_{1/2}O_2$ exhibits a lower second discharge capacity than the one reported by Yabuuchi et al [26]: 133 mAh.g^{-1} *vs.* 190 mAh.g^{-1}. This difference is explained by the lower voltage limitation of our study (3.8 V *vs.* 4.3 V).

It is thus surprising that the second discharge capacities of our O3-$Na_xMn_{1/2}Fe_{1/2}O_2$ and O3-$Na_xMn_{1/3}Fe_{2/3}O_2$ phases are higher than the ones reported by Yabuuchi et al. (124 mAh.g^{-1} *vs.* ≈ 110 mAh.g^{-1} respectively for O3-$Na_xMn_{1/2}Fe_{1/2}O_2$ and ≈ 132 mAh.g^{-1} *vs.* 90 mAh.g^{-1} respectively for O3-$Na_xMn_{1/3}Fe_{2/3}O_2$). These differences could come from the different preparation conditions, as we prepared O3 phases with an initial Na amount lower than one (*vs.* one in [26, 66]) and a 1000°C final heat treatment under O_2 atmosphere (*vs.* 700°C in air in [26]). Furthermore, these systems could present transition metal vacancies in the slab thus stabilizing more Mn^{4+} ions as expected from the ideal formula. Such transition metal vacancies were already observed in P'2-Na_xMnO_2 phases [5, 52, 114]. In this hypothesis, the formula of the materials should be rewrote as $Na_{2x/(2+y)}(Mn,Fe)_{2/(2+y)}\square_{y/(2+y)}O_2$.

Chapter A-II: O3-$Na_{0.77}Mn_{1/3}Fe_{2/3}O_2$ and (O3+O'3)-$Na_{0.77}Mn_{1/2}Fe_{1/2}O_2$

Table of contents

This chapter focuses on the characterization of the O3 pristine materials and the study of their phase diagram along with the Na content. First, the structural and electrochemical properties of O3-$Na_{0.77}Mn_{1/3}Fe_{2/3}O_2$ are investigated. The same investigations are then carried out on (O3+O'3)-$Na_{0.77}Mn_{1/2}Fe_{1/2}O_2$. The last part of this chapter concerns the redox mechanisms associated to the Na deintercalation for both materials.

A-II.1. The $Na_xMn_{1/3}Fe_{2/3}O_2$ system

A-II.1.a. Synchrotron X-ray and Neutron powder diffraction studies of the pristine material

Synchrotron X-ray powder diffraction

Because of the fluorescence of the Mn and Fe species under the Co and Cu kα radiations, respectively, we carried out synchrotron X-ray powder diffraction (synchrotron XRPD) experiments[8] that achieves very good signal / noise ratio and thus allowed a better structural determination than routine XRPD. The collected synchrotron diffraction pattern of O3-$Na_{0.77}Mn_{1/3}Fe_{2/3}O_2$ and the calculated diagram resulting from the structural Rietveld refinement method are shown in **Figure A-II.1**. The corresponding cell and atomic parameters are reported in **Table A-II.1**. The 2θ scale corresponding to the Cu $kα_1$ radiation is given as a guide.

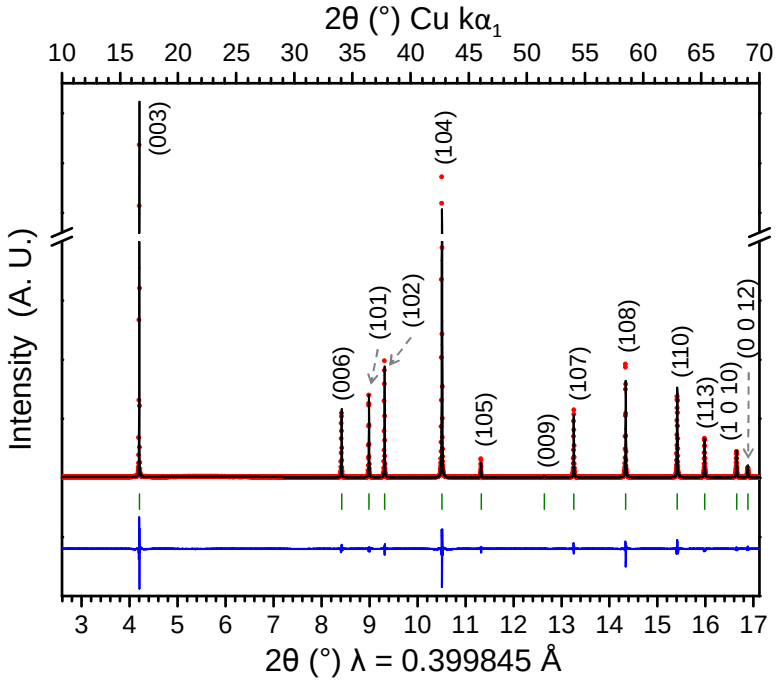

Figure A-II.1: Observed and calculated (Rietveld method) synchrotron XRPD pattern for the O3-$Na_{0.77}Mn_{1/3}Fe_{2/3}O_2$ starting phase. Red dots: experimental, black line: calculated, blue line: difference and green bars: Bragg positions.

[8] In collaboration with Dr. C. Drathen, ESRF, Grenoble, France (ID31 beamline).

Space group: **R-3m** $a_{hex.}$ = 2.9820(1) Å, $c_{hex.}$ = 16.3420(2) Å						
Atom	Wyckoff	Coordinates			Occupancy	ADP (Å²)
Na	3b	0	0	1/2	0.77(1)	1.3(1)
Mn	3a	0	0	0	1/3	0.47(2)
Fe	3a	0	0	0	2/3	
O	6c	0	0	0.2692(3)	1	0.75(8)
Rwp = 11.32%; R_B = 2.93%						

Table A-II.1: Structural parameters and reliability factors calculated from the synchrotron XRPD pattern of the O3-$Na_{0.77}Mn_{1/3}Fe_{2/3}O_2$ starting phase.

The lattice parameters of the hexagonal cell (R-3m space group): $a_{hex.}$ = 2.98195(3) Å and $c_{hex.}$ = 16.3420(2) Å are close to those of the literature on the O3-$NaMn_{1/2}Fe_{1/2}O_2$ material ($a_{hex.}$ = 2.9590(6) Å and $c_{hex.}$ = 16.522(2) Å [26]). The difference to the values of the $a_{hex.}$ and $c_{hex.}$ parameters could result from the different sodium contents between the two materials and the different Mn / Fe ratio. The excellent data quality allowed us to refine the various atomic displacement parameters (ADP), which was impossible from the laboratory XRPD patterns. The total Mn/Fe site occupancy was fixed equal to 1.0 and the ADP value for the transition metal ions refined to 0.47(2) Å². The occupancy and ADP of the Na^+ ion are equal to 0.77(1) and 1.3(1) Å² respectively. This high value of the Na^+ ion ADP can result from the high mobility of the Na^+ ion into the interslab space and is not uncommon in these materials [79, 94, 115]. The final sodium content determined by Synchrotron XRPD (x = 0.77(1)) is lower than the theoretical one (x = 0.82) and the one of the formula determined by ICP-AES analysis ($Na_{0.83}Mn_{0.31}Fe_{0.69}O_2$). This indicates that a small portion of the Na^+ ions were expelled from the material, probably during the air quenching step or by reaction with the oxygen and water in the glovebox as discussed in **Chapter A-I**. Note that the occupancy of the O site was fixed to 1.0, thus only the corresponding ADP value is refined and is equal to 0.75(8) Å². In the latter, this material will be referred to as O3-$Na_{0.77}Mn_{1/3}Fe_{2/3}O_2$.

Previous works on Mn-based alkali layered oxides showed the possibility of transition metal vacancies due to the spontaneous oxidation of Mn^{3+} according to the reaction: 4 Mn^{3+} → 3 Mn^{4+} + □ [5, 52, 114]. We considered this possibility and refined the occupancy of the transition metal sites in our material. However this did not lead to a significant improvement of the refinement as the occupation of the transition metal sites did not deviate significantly from 1.0. In the following, the O3-$Na_{0.77}Mn_{1/3}Fe_{2/3}O_2$ formula will be considered for the pristine material. If one assumes that iron is trivalent, there is 0.23 Mn^{4+} and 0.10 Mn^{3+} per formula unit.

Neutron powder diffraction

Because of the presence of $Mn^{3+/4+}$ and Fe^{3+} ions in the 1:2 ratio, we considered the possibility of an ordering within the transition metal layer even if the difference in ionic radii (Mn^{3+} (r = 0.58 Å), Mn^{4+} (r = 0.53 Å), Fe^{3+} (r = 0.63 Å)) is not very large. The material was studied by neutron diffraction on the D2B beamline at ILL[9]. Contrarily to XRPD, neutron diffraction allows distinguishing Fe from Mn thanks to the very different Fermi lengths (equal to -3.73 fm and +9.93 fm for the ^{55}Mn (100 % abundance) and ^{56}Fe (91.75 % abundance) nuclei, respectively).

The neutron powder diffraction pattern of the pristine material is shown in **Figure A-II.2**. As no superstructure peak appears on the neutron diffraction pattern, we concluded that O3-$Na_{0.77}Mn_{1/3}Fe_{2/3}O_2$ does not exhibit any long-range ordering between the transition metal ions. The structure of the material was then refined from the XRPD and neutron diffraction data using Pseudo-Voigt functions to describe each pattern as shown in **Figure A-II.2**. The corresponding cell and atomic parameters are given in **Table A-II.2**. This combined refinement leads to a structure in very good agreement with the structural model obtained from Synchrotron XRPD and gives a final content of 0.68(1) Fe and 0.32(1) Mn, in good agreement with the expected one.

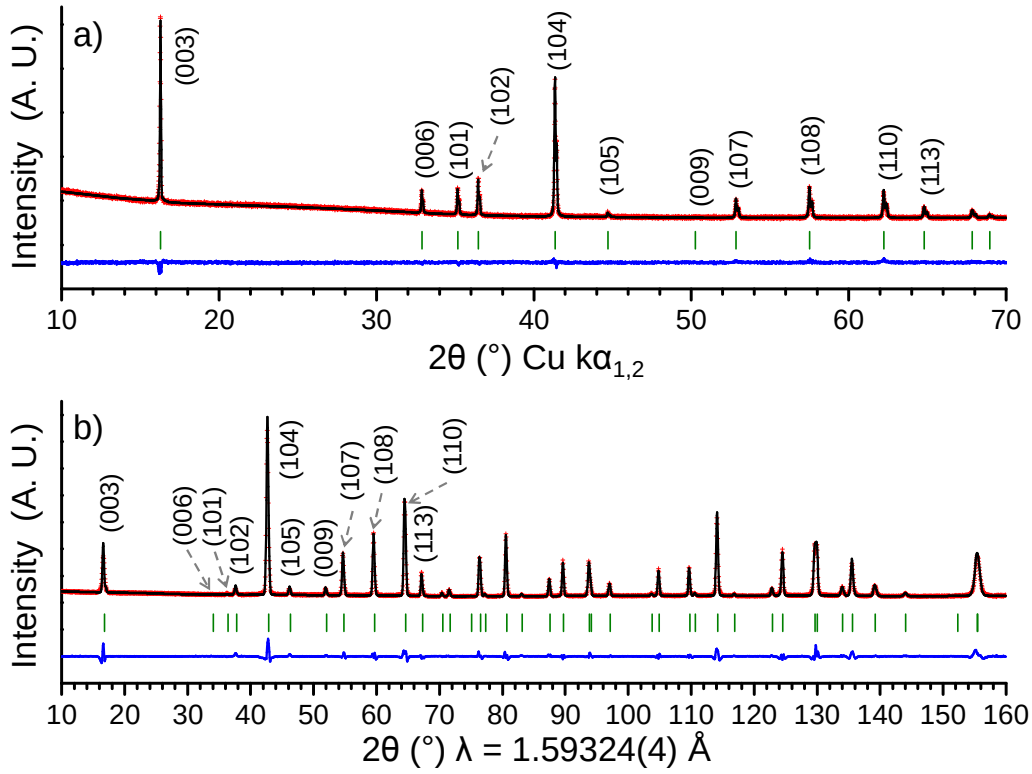

Figure A-II.2: Observed and calculated (Rietveld method) (a) XRPD and (b) neutron powder diffraction patterns for the O3-$Na_{0.77}Mn_{1/3}Fe_{2/3}O_2$ pristine material. Red crosses: experimental, black line: calculated, blue line: difference and green bars: Bragg positions.

[9] In collaboration with Dr. E. Suard, ILL, Grenoble, France.

		XRPD			Neutron diffraction	
Cell parameters (S.G.: **R-3m**)	$a_{hex.}$ (Å)	2.9804(1)				
	$c_{hex.}$ (Å)	16.3249(3)				
Wavelength (Å)		Cu k$\alpha_{1,2}$			1.59319(5)	
Atomic parameters:		x	y	z	Occ.	ADP (Å²)
	Na (3b)	0	0	1/2	0.78(1)	1.54(3)
	Mn (3a)	0	0	0	0.32(1)	0.50(2)
	Fe (3a)	0	0	0	0.68(1)	
	O (6c)	0	0	0.269(1)	1	0.87(1)
R_{wp} (%)		2.07			6.75	
Global R_{wp} (%)		3.52				

Table A-II.2: Structural parameters and reliability factors calculated from the combined refinement of the O3-$Na_{0.77}Mn_{1/3}Fe_{2/3}O_2$ pristine material based on the XRPD and neutron powder diffraction patterns.

A-II.1.b. Electrochemistry

Influence of the cut-off voltage

After confirming the electrochemical activity of the material (**Chapter A-I.3.c.**) we investigated the impact of the upper voltage cutoff on the electrochemical properties. The cycling curves obtained in the 1.5 – 3.8 V, 1.5 – 4.0 V and 1.5 – 4.3 V ranges are given in **Figures A-II.3a**, **A-II.3b** and **A-II.3c** respectively. As previously, the first four cycles are shown, starting by a discharge and the first cycle is highlighted in red. The evolution of the discharge capacity is given in **Figure A-II.3d**.

As one can see, the increase of the upper cutoff voltage above 3.8 V clearly induces an extra capacity for the second discharge (**Figure A-II.3d**), associated to a higher polarization of the cycling curve. The discharge capacities of the batteries cycled up to 4.0 and 4.3 V are comparable and follow the same decrease tendency toward the values of cell cycled up to 3.8 V, reached approximately after the 14th cycle. This large decrease of the discharge capacity is visible in **Figures A-II.3b** and **A-II.3c** through the decrease of the available Na^+ ions for (de)insertion.

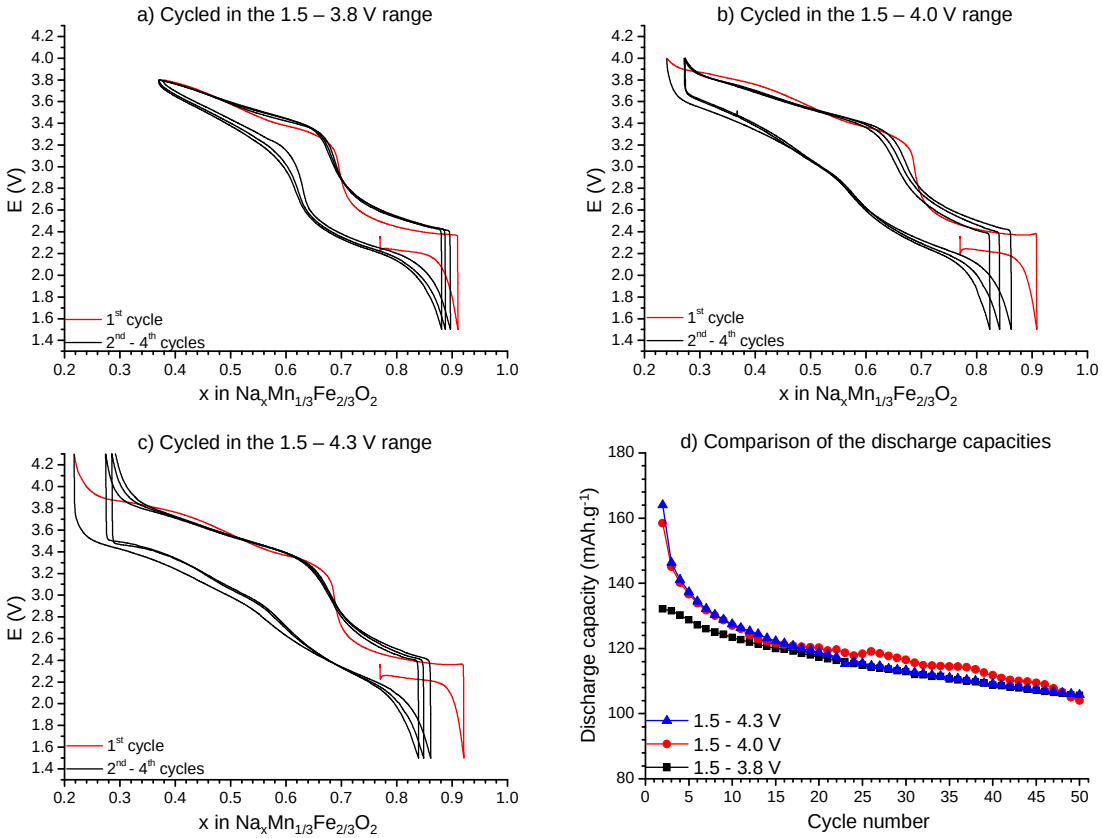

Figure A-II.3: Galvanostatic cycling curves associated to the $Na_xMn_{1/3}Fe_{2/3}O_2$ system recorded (a) between 1.5 and 3.8 V, (b) between 1.5 and 4.0 V and (c) between 1.5 and 4.3 V at C/50. (d) Associated discharge capacities. The capacities of the first cycles are not shown on (d) as they correspond to the partially intercalated state.

To better understand the impact the cut-off voltage has on the material, we realized a series of SEM micrographs on an un-cycled electrode (**Figures A-II.4a-b**) and on electrodes collected after 50 cycles between 1.5 and 3.8 V (**Figures A-II.4c-d**), between 1.5 and 4.0 V (**Figures A-II.4e-f**) and between 1.5 and 4.3 V (**Figures A-II.4g-h**).

The SEM micrographs of the un-cycled electrode are representative of the raw material with monolithic grains. On the contrary, the micrographs collected after 50 cycles up to 3.8 V, 4.0 V or 4.3 V highlight the cracking of the material. However, the capacity decay occurring after a few cycles at high voltage cannot be explained by dramatic changes of the microstructure.

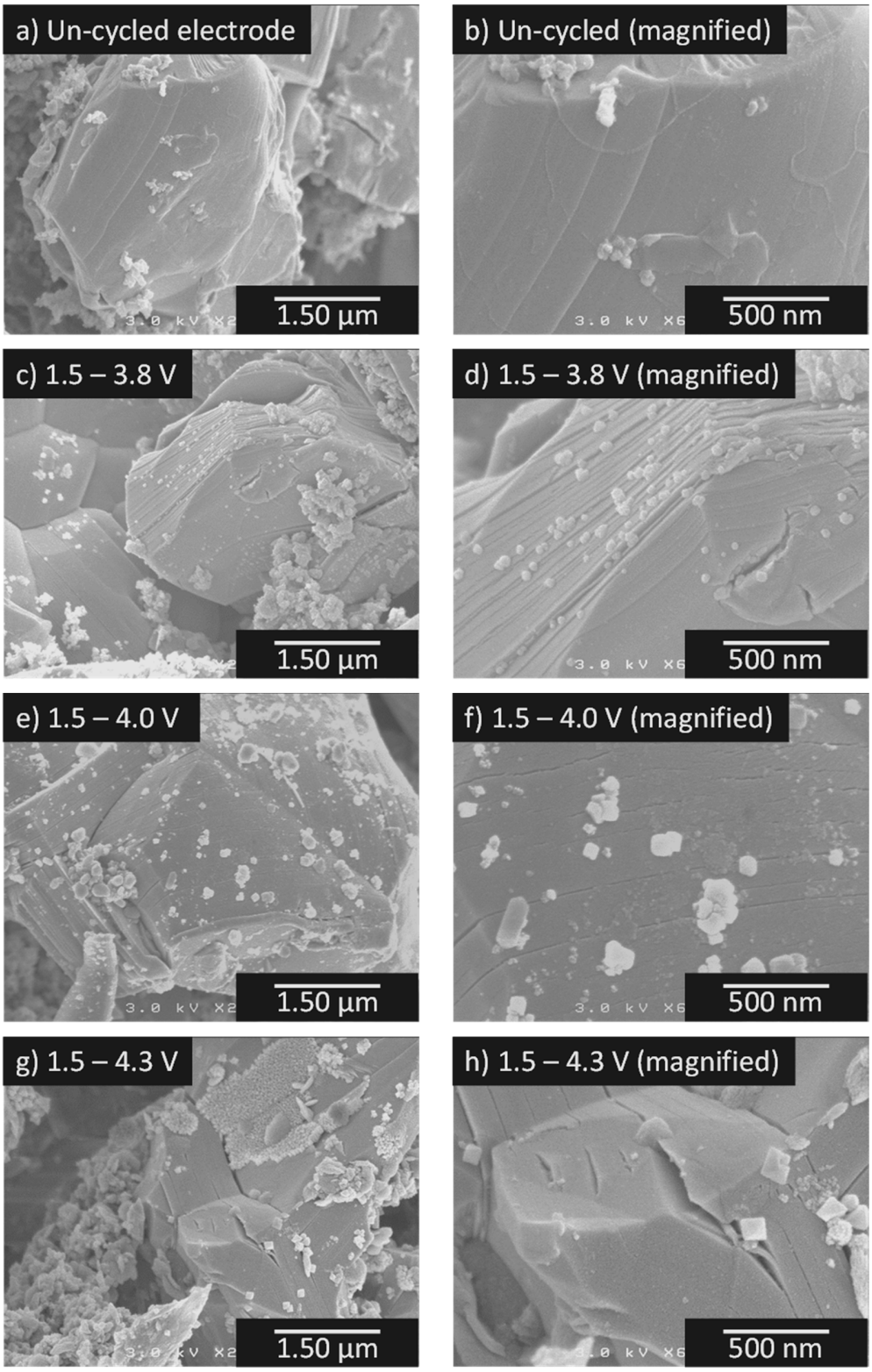

Figure A-II.4: SEM micrographs of (a,b) an un-cycled electrode involving the O3-$Na_{0.77}Mn_{1/3}Fe_{2/3}O_2$ material and similar electrodes cycled 50 times (c,d) between 1.5 and 3.8 V, (e,f) between 1.5 and 4.0 V and (g,h) between 1.5 and 4.3 V.

GITT cycling

For a better understanding of the electrochemical behavior of the $Na_xMn_{1/3}Fe_{2/3}O_2$ system, a Galvanostatic Intermittent Titration Technique (GITT) experiment was performed as shown in **Figure A-II.5** below:

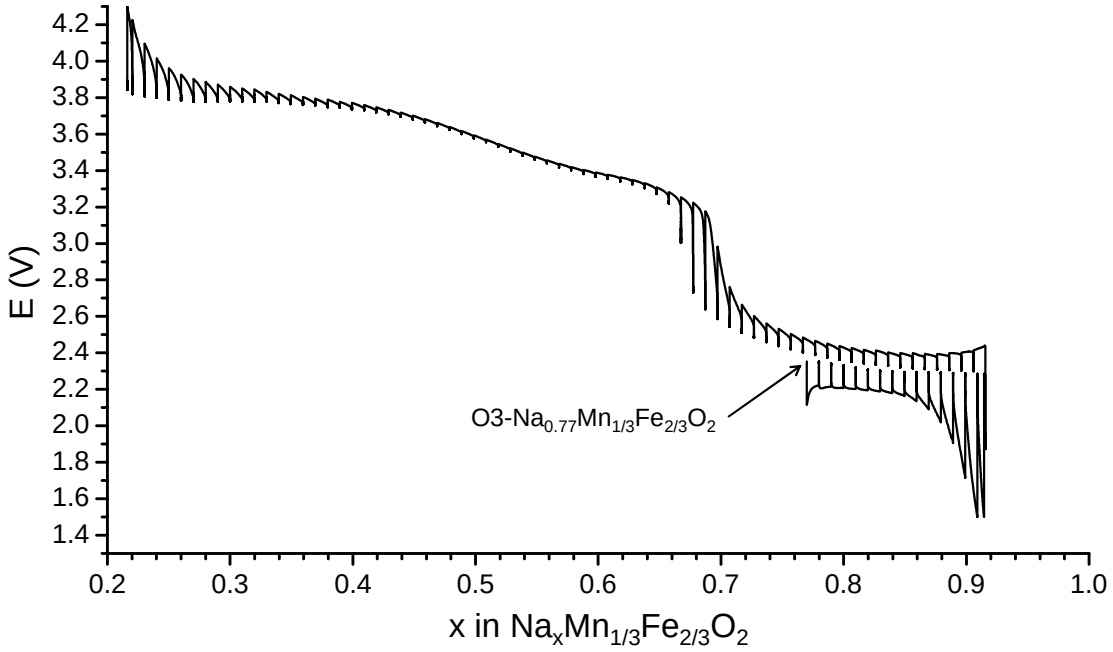

Figure A-II.5: GITT cycling of the $Na_xMn_{1/3}fe_{2/3}O_2$ system recorded with steps of ≈0.01 Na per formula unit. Relaxation condition: $\Delta V < 4$ mV.h^{-1}.

Starting with a discharge from x = 0.77, the material exhibits a reversible plateau at low voltage for $0.85 \leq x < 0.92$ corresponding to a biphasic domain. Upon charging and after the voltage plateau ($x < 0.85$), the voltage continuously increases and overcomes a sudden jump at $x \approx 0.67$. This voltage jump seems to correspond to the change in the active redox process: from $Mn^{3+} \rightarrow Mn^{4+}$ to $Fe^{3+} \rightarrow Fe^{4+}$. During further charging ($0.4 < x < 0.65$), the voltage slightly increases. One can observe a lower polarization in this range. Then, above 3.8 V ($x \approx 0.37$), the curve describes a voltage plateau followed by a graduated increase of the polarization with the upper potential. This strongly suggests that a new and unknown reaction occurs at high voltage.

A-II.1.c. *In situ* XRPD study during Na deintercalation

To follow the structural changes that the material undergoes during Na^+ deintercalation, we carried out an *operando in situ* XRPD study during the charge of a $Na_xMn_{1/3}Fe_{2/3}O_2$//Na battery. Data were collected during the first charge following a preliminary discharge of the cell that lead to the $Na_{0.96}Mn_{1/3}Fe_{2/3}O_2$ composition as the starting point. In order to be close to the fully intercalated phase, the galvanostatic discharge was followed by a potentiostatic intercalation at 1.5 V until the current was close to 0 mA. After recording the pattern of the electrode material at 1.5 V, the battery was charged at C/80. The acquisition conditions were optimized to record an XRPD pattern every 0.013 Na^+ / formula unit: the selected angular ranges were 13-20° and 30-43°, the step size 0.02° and the acquisition time ≈ 4s / step.

Selected parts of the resulting XRPD patterns are shown in **Figure A-II.6a** along with the corresponding charging curve of the battery up to 4.3 V (**Figure A-II.6b**). As the pattern superposition makes it difficult to see the changes occurring in some parts of the charge, the same experiment is presented in the inverse order in **Figure A-II.7a**.

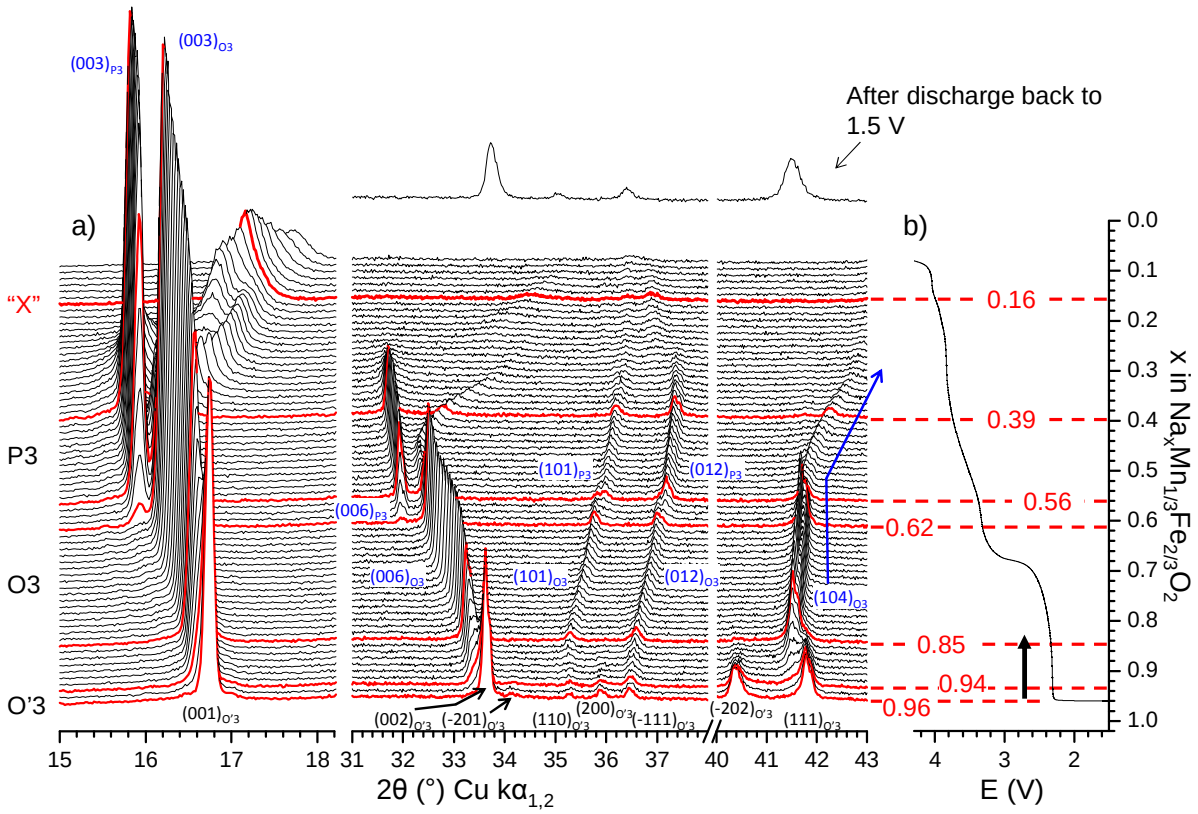

Figure A-II.6: (a) XRPD patterns recorded *in situ* (*operando* mode) during the charge of a $Na_xMn_{1/3}Fe_{2/3}O_2/NaPF_6$ in PC (1M)/Na cell along with (b) the corresponding galvanostatic curve. Blue Miller indexes: O3 and P3 phases. Black Miller indexes: O'3 phase.

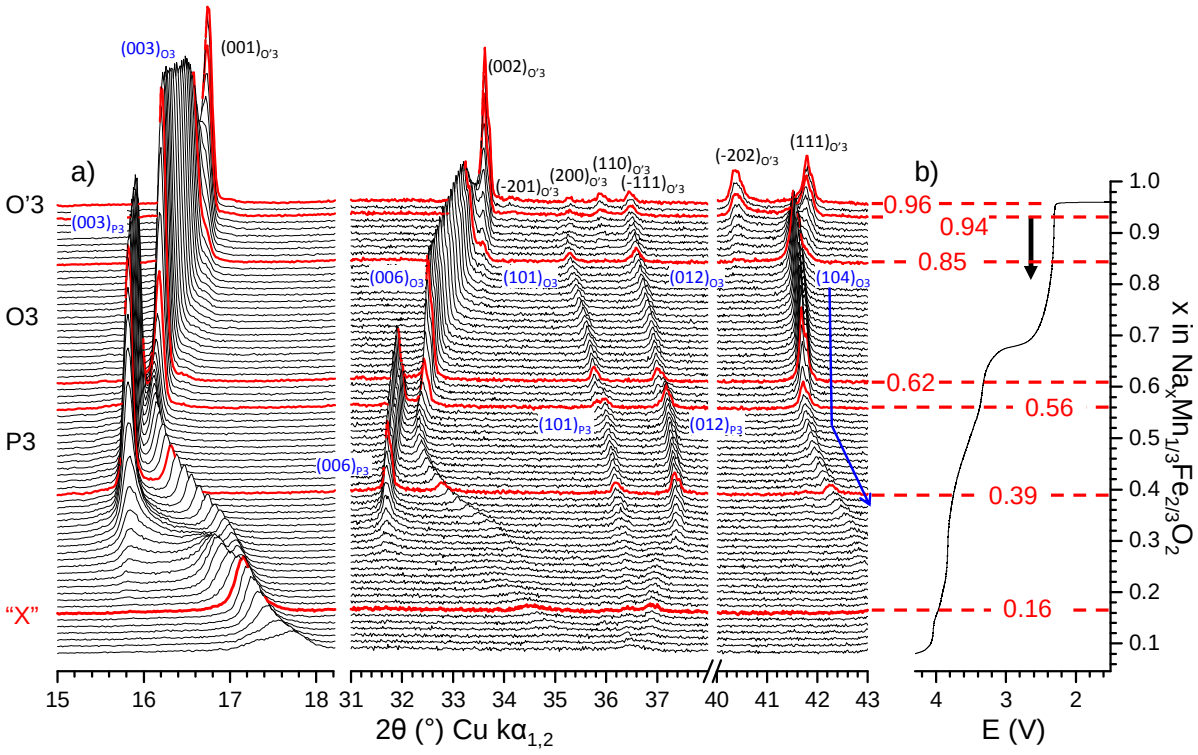

Figure A-II.7: Inverse representation of the *operando in situ* experiment carried out on the $Na_xMn_{1/3}Fe_{2/3}O_2$ system: (a) XRPD patterns and (b) corresponding galvanostatic curve. Blue Miller indexes: O3 and P3 phases. Black Miller indexes: O'3 phase.

As it is further detailed, several structural changes occur during the charge. In the almost fully intercalated state a structural distortion (O'3) is observed. The sodium deintercalation leads to the formation of the O3 phase (the pristine one) through a biphasic domain in the $0.85 \leq x < 0.94$ composition range. For $x < 0.62$ the P3 structure type appears. It exhibits a larger interslab distance due to the prismatic environment of the sodium ions as shown by the $(00l)_{P3}$ which appears at lower angles. The structural modification is clearly shown by the disappearance of the $(104)_{O3}$ diffraction peak which is always very weak on the XRPD patterns of P3 phases in comparison with the O3 ones.

Surprisingly the O3 type phase does not disappear completely upon charging (**Figure A-II.7**). Moreover, the $(00l)_{O3}$ diffraction lines shift to higher angles upon sodium deintercalation, which indicates a strong decrease of the interslab distance. This unexpected result is reproducible and reversible if the battery is discharged. In order to check if this special behavior is related to an experiment carried out of equilibrium, another *in situ* study was performed during a GITT charge, where the XRPD patterns were recorded at the end of each relaxation step ($dE/dt < 2.6$ mV.h^{-1}). The same behavior was also found and is presented in **Figure A-II.8**.

Obviously, for $x < 0.62$, there is coexistence of two systems that are deintercalated simultaneously. This point will be further discussed in details.

From the cell parameters, it is possible to estimate the interslab distances, corresponding to $c_{hex.}/3$ for the O3 and P3 phases or to $c_{mon.} \sin(\beta)$ for O'3. The evolution of the interslab distances and cell parameters are plotted in **Figures A-II.9a-b** respectively as a function of the Na content. The cycling curve is also represented in **Figure A-II.9c** as a guide.

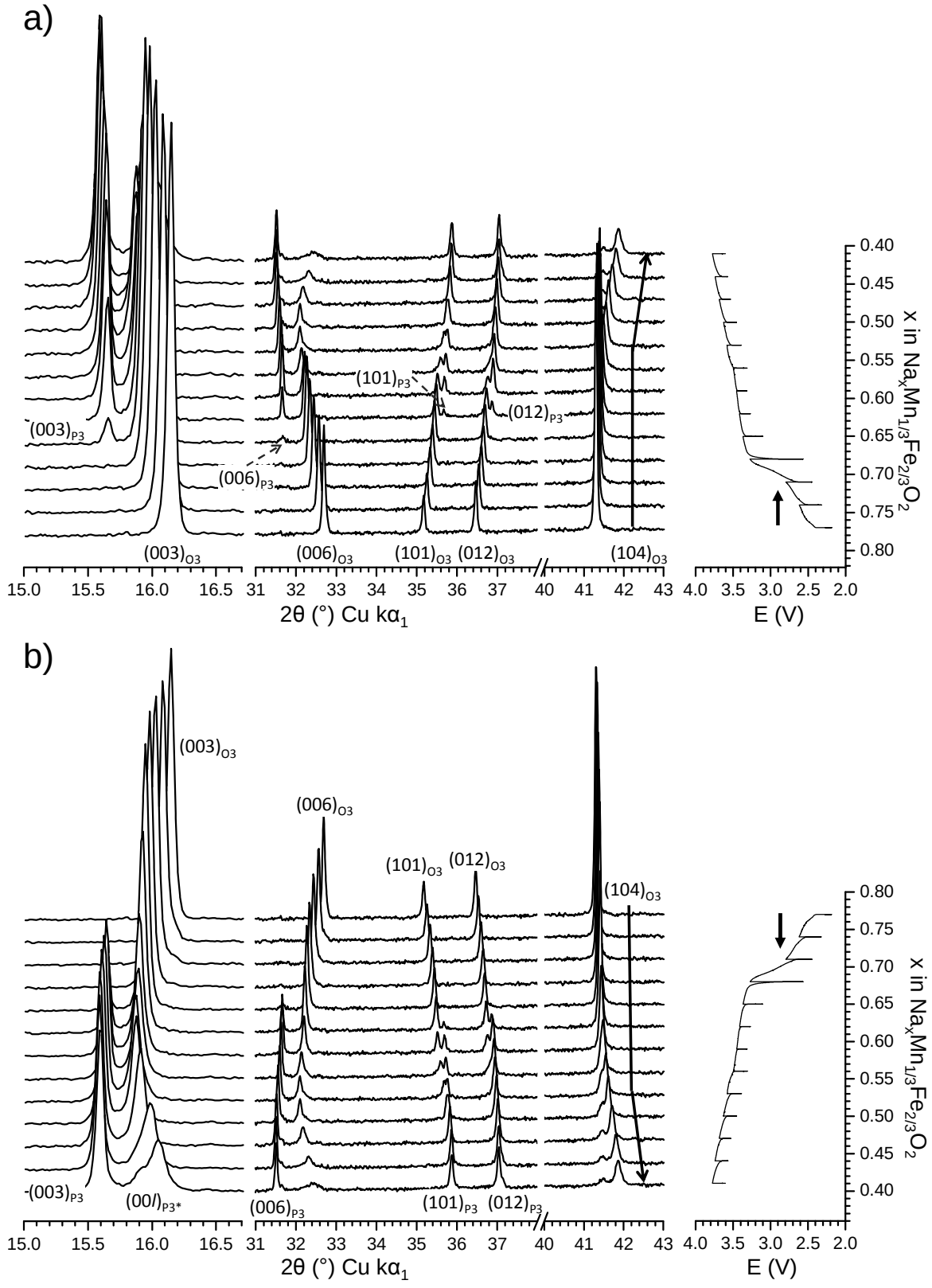

Figure A-II.8: (left) XRPD patterns recorded *in situ* during the relaxation of a $Na_xMn_{1/3}Fe_{2/3}O_2$/$NaPF_6$ in PC (1M) + 2 wt% FEC/Na cell along with (right) the corresponding galvanostatic GITT curve.

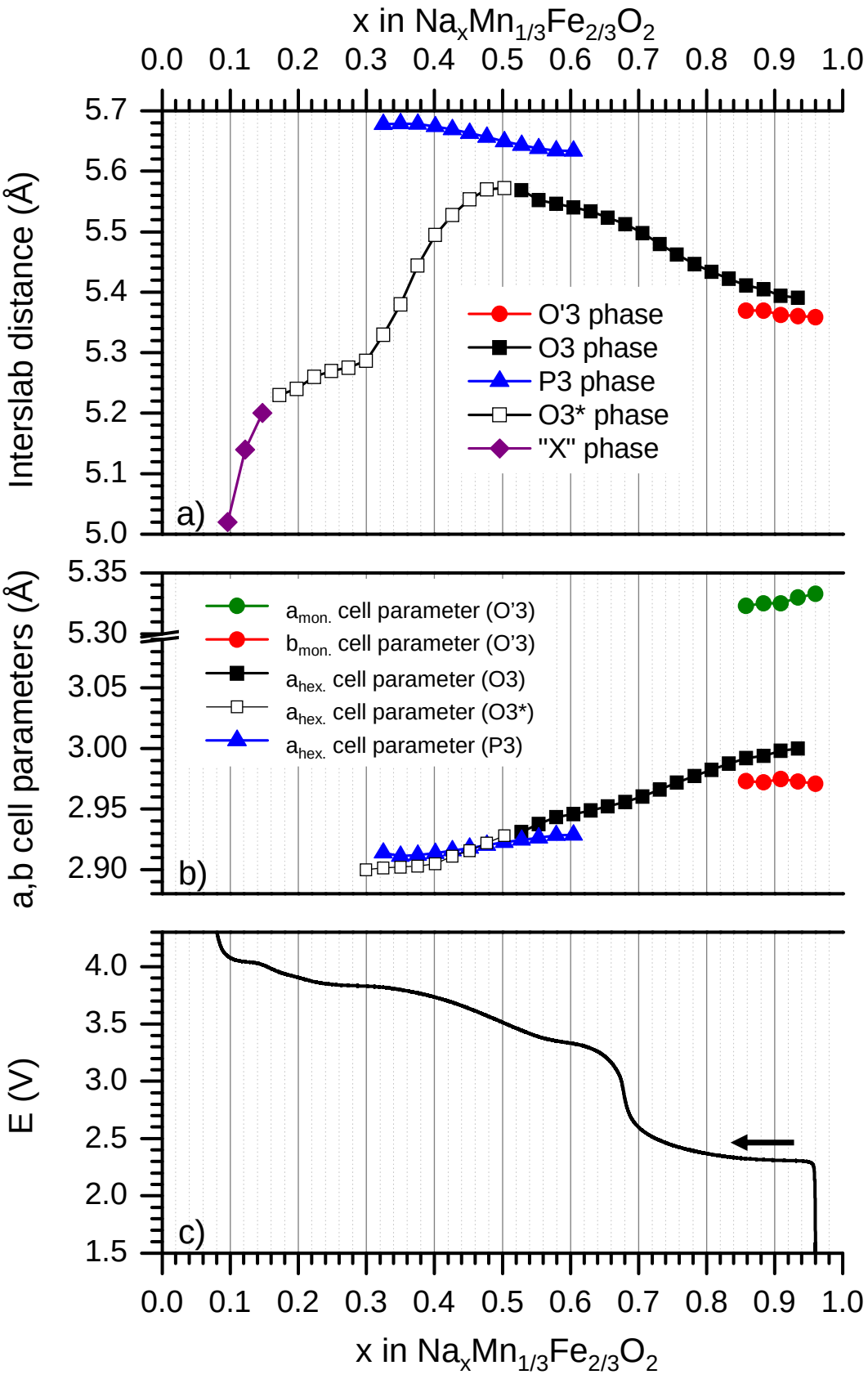

Figure A-II.9: Evolution of the (a) interslab distance and (b) a and b cell parameters of the O'3, O3 and P3-$Na_xMn_{1/3}Fe_{2/3}O_2$ phases upon sodium deintercalation. The galvanostatic curve is shown as a guide (c).

The XRPD pattern of the initial phase of the *operando in situ* XRPD experiment, $Na_{0.96}Mn_{1/3}Fe_{2/3}O_2$ (end of discharge), can be indexed in the monoclinic system (C2/m space group, O'3 structure). The monoclinic distortion of the cell is clearly emphasized by the splitting of the $(012)_{hex.}$ and $(104)_{hex.}$ diffraction lines of the O3 structure to the $(-111)_{mon.}$ + $(200)_{mon.}$ and to the $(-202)_{mon.}$ + $(111)_{mon.}$ ones respectively. During Na^+ deintercalation from $Na_{0.96}Mn_{1/3}Fe_{2/3}O_2$, a very narrow composition domain is observed for the O'3 phase ($0.94 < x < 0.96$), followed by a biphasic domain (characterized by the voltage plateau), observed for $0.85 \leq x \leq 0.94$. In this domain, the small number of diffraction peaks available to fit the profile prevents from giving a really accurate value of the cell parameters for the two phases. Nevertheless, it appears that the interslab distance is slightly higher for the O3 phase than for the O'3 one. This is induced by the lower Na content in the O3 phase, which lowers the screening effect of the Na^+ ions on the surrounding O planes.

For $0.62 < x < 0.85$ the system exhibits a solid solution with an O3 type structure as observed for the pristine material. The interslab distance increases as sodium is removed from the interlayer space, enhancing again the repulsion between the O atoms from the MO_2 planes. On the contrary, the M-M in plane distance ($a_{hex.}$ parameter) decreases as the average ionic size of the M^{n+} ions decreases upon oxidation.

Upon Na^+ deintercalation a new phase with a P3 type structure appears for $x < 0.62$, while the intensity of the O3 phase diffraction lines decreases. As previously mentioned, a significant part of the O3 type phase remains. The position of its $(003)_{O3}$ diffraction line continues to shift to lower 2θ angles down to $x = 0.50$ and then to higher 2θ angles for $x < 0.50$ (**Figure A-II.10**). The corresponding domain will be referred to as "O3*". This shift shows that the interslab distance increases upon deintercalation and then decreases at the end of the charge as it is observed for all O3 type A_xMO_2 (A = Li, Na) systems [116]. Note that in the Li_xCoO_2 and Li_xNiO_2 systems, the complete lithium deintercalation leads to the O1 type structure ("ABAB" packing) [117].

For $x \leq 0.16$ a new phase, noted "X", is observed. Its $(00l)_X$ diffraction line shift continuously to higher 2θ angles upon deintercalation, indicating a decrease of the interslab distance.

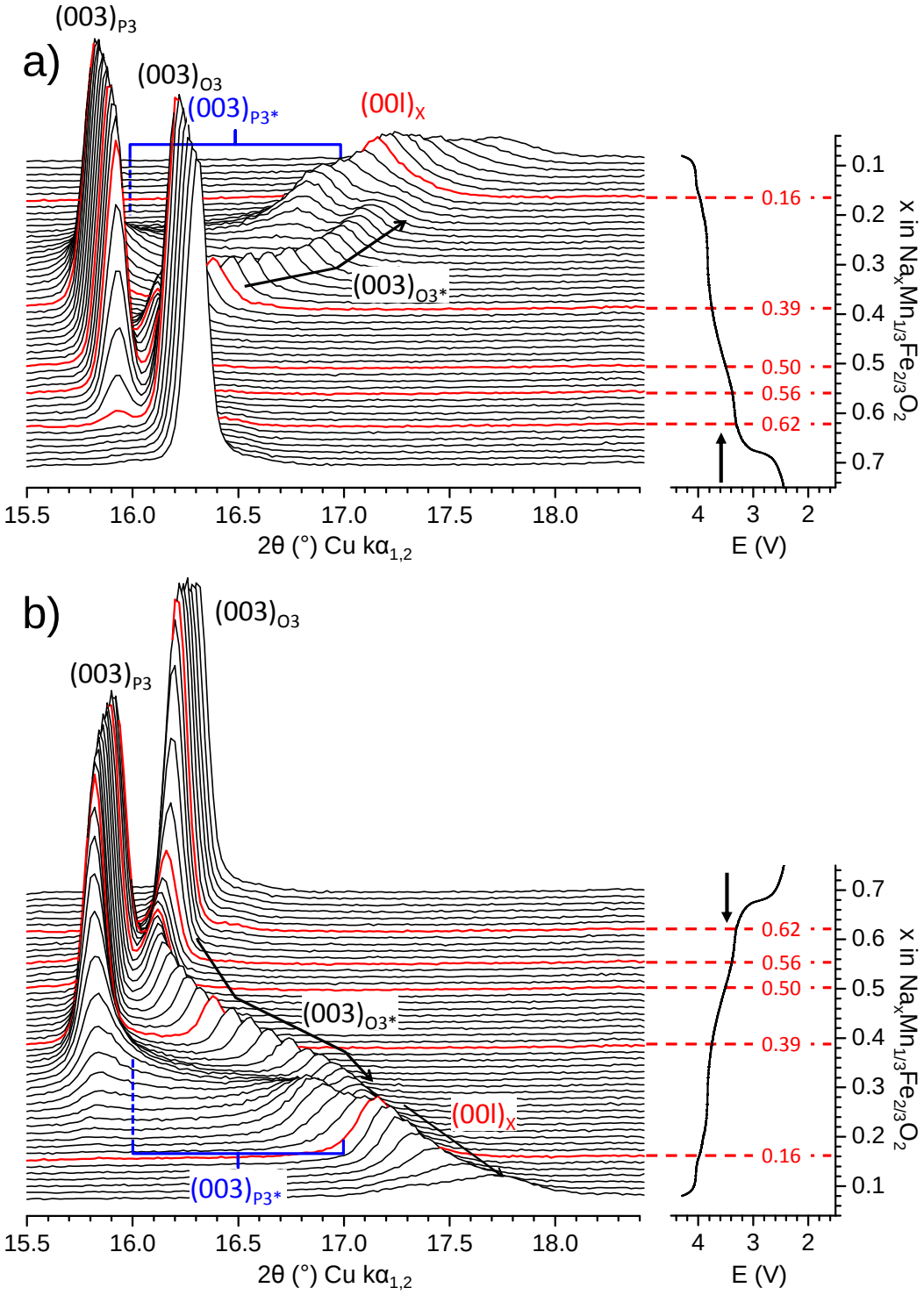

Figure A-II.10: Magnifications in the $0.3 \leq x \leq 0.7$ region of the XRPD patterns recorded during the *operando in situ* XRPD experiment carried out on the $Na_xMn_{1/3}Fe_{2/3}O_2$. The red lines highlight the limitations of the solid solutions and / or biphasic domains.

The position of the $(003)_{P3}$ line remains constant between $0.56 < x < 0.62$ as expected for a biphasic domain and then shifts to lower angles, which indicates the occurrence of a solid solution ($0.39 < x < 0.56$) also for the P3 type phase. This behavior is more clearly seen in **Figure A-II.10** that shows the variation of the (003) line of both phases during the battery charge. In the $0.39 < x < 0.50$ region, there is a two phases domain between two solid solutions (O3* and P3).

When x decreases below 0.39 the position of the $(003)_{P3}$ line remains constant while its intensity decreases. Simultaneously, a broadening appears on the high angle side, which suggests the formation of stacking faults within the P3 phase. One can make the hypothesis that when a too large number of sodium is deintercalated from P3, some MO_2 slabs glide to create an octahedral surrounding for the remaining Na^+ ions. The P3 phase with stacking faults is noted P3* in the following. The number of this type of planes continuously increases when Na^+ ions are deintercalated from the material, in agreement with the shift of the $(003)_{P3*}$ diffraction line to lower 2θ angles.

For x = 0.16, the diffraction lines of the O3* and P3* phases have merged into a new phase, noted "X". Due to the relative sharpness and symmetry of the $(00l)_X$ diffraction line, we expect no stacking faults in the "X" phase. The same hypothesis (formation of the NaO_6 octahedron environment for highly deintercalated phases) was primarily observed during *operando in situ* XRPD measurements by Lu and Dahn for the Na^+ deintercalation from P2-$Na_{2/3}Mn_{2/3}Ni_{1/3}O_2$, which leads to the O2 type structure [72]. The authors found an interslab distance equal to 4.32 Å, which is very similar to the NiO_2 one [117]. The interslab distance in our material (5.02 Å for x = 0.1) is in agreement with the presence of remaining Na^+ ions (x = 0.15). More recently, Xu et al. also concluded on the formation of NaO_6 octahedra to accompany the deintercalation of P2-$Na_{0.80}Li_{0.12}Ni_{0.22}Mn_{0.66}O_2$ by DFT calculations [70]. In the latter case, an O2 type structure was also obtained from the P2 one. For $x < 0.1$, a new diffraction line appears at $2\theta \approx 17.3°$, indicating that a new biphasic domain or new stacking faults could be expected. However we cannot rely on this information only and more experiments would be needed to confirm this feature. A schematic representation of the $Na_xMn_{1/3}Fe_{2/3}O_2$ phase diagram is given in **Figure A-II.11**.

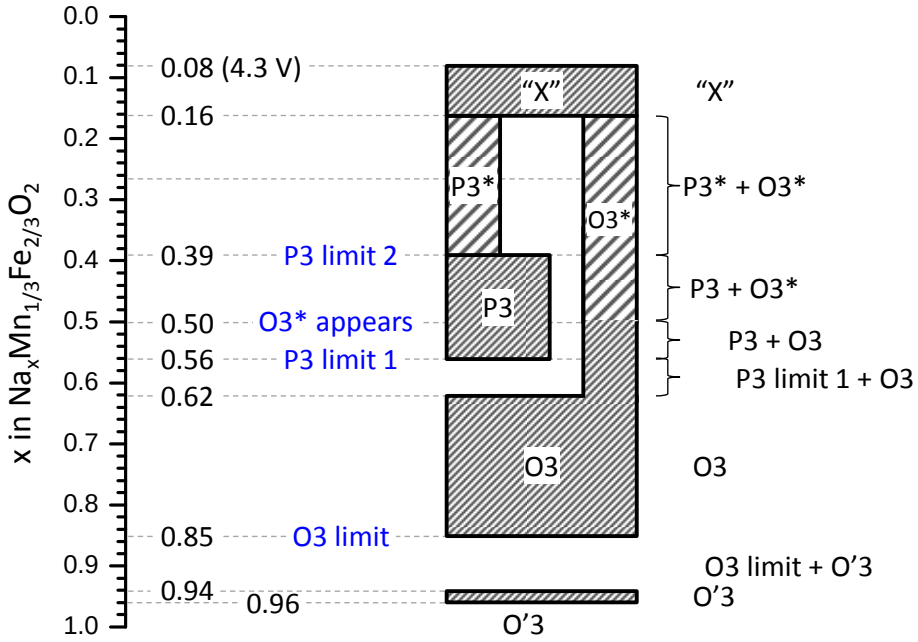

Figure A-II.11: Schematic representation of the $Na_xMn_{1/3}Fe_{2/3}O_2$ phase diagram upon Na deintercalation deduced from the *operando in situ* XRPD experiment. In the $0.16 < x < 0.62$ range, several systems (related to O3 and P3) are simultaneously observed.

The simultaneous presence of two phases with the O3 and P3 structures type involved in the deintercalation process is difficult to understand. To explain it, we can make the hypothesis of composition fluctuations that are not detected in XRPD data of the starting material: (i) the coexistence of particles with slightly different Mn / Fe ratios or (ii) the existence of particles with or without Mn vacancies. It is well known that the relative stability of the O3 and P3 packing is directly correlated to the bond covalence within the slab and to the sodium amount [36]. In this hypothesis, a part of the O3 phase is going through deintercalation following a solid solution process while the other part is transformed into the P3 phase. Further experiments are required to confirm this behavior.

To study the reversibility of the diverse structural transitions, we discharged the cell back to 1.5 V and recorded the XRPD pattern under constant voltage and with the same acquisition parameters. The XRPD patterns recorded after the first and second discharges are presented in **Figure A-II.12**. Surprisingly after the second discharge the monoclinic distortion is not observed. This is explained by the lower sodium content after the second discharge ($x \approx 0.8$). The Mn^{3+} content (≈ 13 % of the M^{n+} ions) is not enough to induce the cooperative Jahn-Teller effect. The lower sodium content intercalated implies that the material underwent an irreversible structural transition during the charge that may depend on the cycling conditions. The migration of Fe into the interlayer space can be considered, as suggested for Na_xFeO_2 [35].

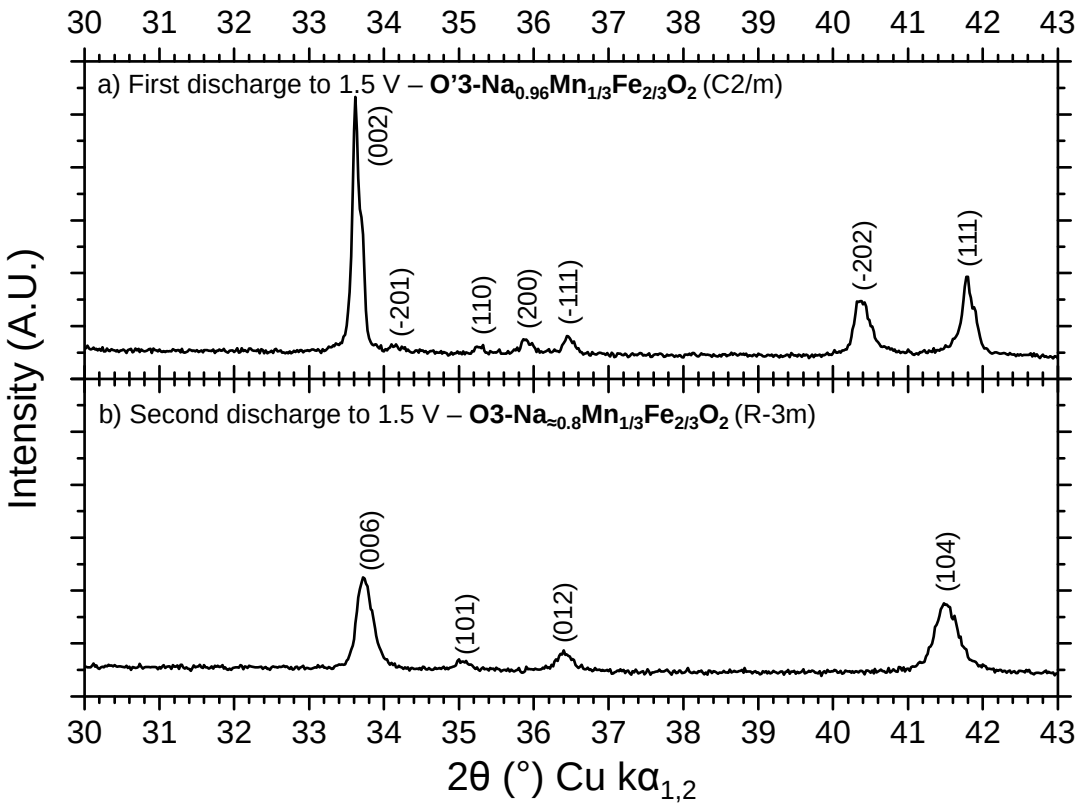

Figure A-II.12: XRPD patterns recorded *in situ* during a potentiostatic step (1.5 V) after a) the first and b) the second discharges of the *operando in situ* experiment carried out on the $Na_xMn_{1/3}Fe_{2/3}O_2$ system.

A-II.1.d. *Ex situ* Synchrotron X-ray diffraction study of the different structural domains

In order to better understand the structures of the various $Na_xMn_{1/3}Fe_{2/3}O_2$ phases, we prepared three samples (O'3, O3 and P3) by the potentiostatic route. A battery whose positive electrode consisted in a pellet of the active material and carbon black was (dis)charged to a desired voltage. Once reached, the voltage was maintained for several days in order to reach equilibrium. After washing and drying the electrode, a capillary was made to analyze the material by Synchrotron X-ray Powder Diffraction (SXRPD)[10]. Materials prepared at a significantly higher voltage showed a loss of crystallinity and were not characterized by synchrotron XRPD.

The O'3-$Na_{0.96}Mn_{1/3}Fe_{2/3}O_2$ phase

The targeted voltage for the preparation of the O'3 material was 1.5 V (end of the first discharge on the E = f(x) curve). **Figure A-II.13** shows the experimental and calculated synchrotron XRPD patterns for the O'3-type phase. The corresponding cell and atomic parameters are given in **Table A-II.3**.

In order to correctly refine the profile of the peaks, we considered an anisotropic broadening through the use of tensor parameters as implemented in the Jana 2006 Software [101]. This method was already used to accurately describe complex structures that cannot be refined using conventional Pseudo-Voigt pattern matching refinement [118]. For layered materials, the selective broadening of some peaks often highlights the presence of stacking faults [26, 72, 119]

In agreement with the *in situ* XRPD experiment, the pattern of the almost fully intercalated phase is indexed in the monoclinic system (C2/m space group). Its cell parameters are very close to those found for the x = 0.96 composition in the *in situ* study. The Rietveld refinement of the Na content lead to x = 0.96(2). The $a_{mon.}/b_{mon.}$ ratio is equal to 1.80, confirming the cooperative Jahn-Teller effect associated to HS-Mn^{3+} ions. From the atomic positions, it clearly appears that the MO_6 octahedra are distorted and show two long M-O bonds (2.14(2) Å) and 4 short ones ((2.02(1) Å) as shown in **Table A-II.3**. It is surprising that only a small amount of Mn^{3+} ions (≈ 1/3 of the transition metal ions) is enough to generate a cooperative distortion of the structure. The formation of this monoclinic phase is the origin of the biphasic domain for $0.85 \leq x_{Na} \leq 0.96$.

[10] In collaboration with Dr. C. Drathen, ESRF, Grenoble, France.

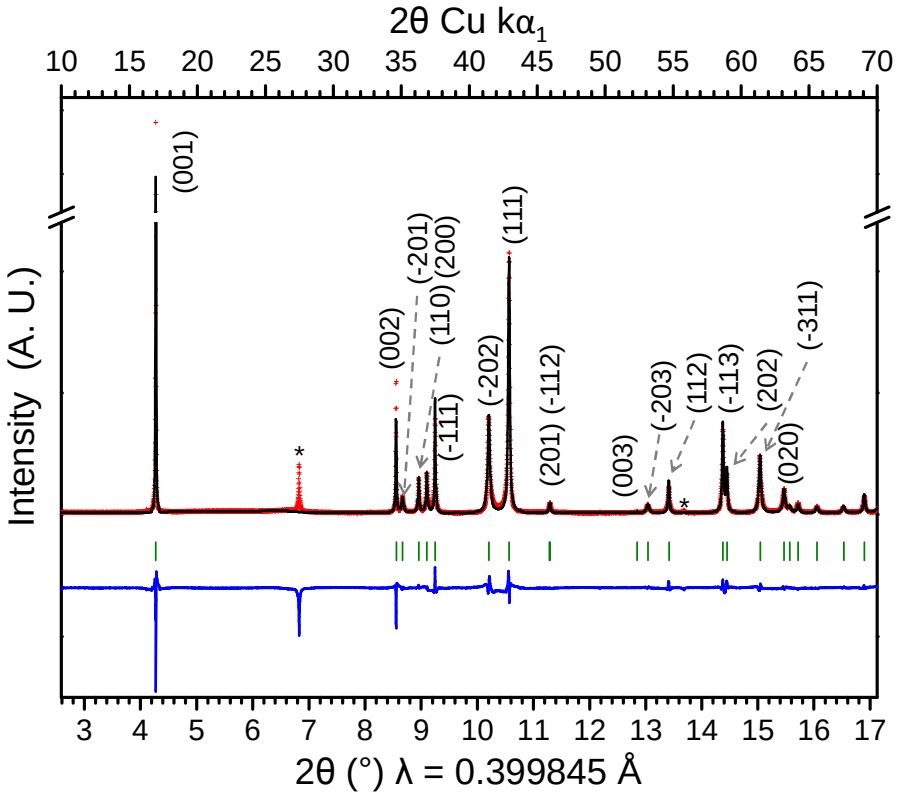

Figure A-II.13: Observed and calculated (Rietveld method) synchrotron XRPD patterns of the O'3-$Na_{0.96}Mn_{1/3}Fe_{2/3}O_2$ phase. Red crosses: experimental, black line: calculated, blue line: difference and green bars: Bragg positions. The * symbol indicates the graphite diffraction lines which were excluded for the refinement.

O'3-$Na_{0.96}Mn_{1/3}Fe_{2/3}O_2$ Space group : C2/m $a_{mon.}$ = 5.3447(5) Å, $b_{mon.}$ = 2.9717(2) Å, $c_{mon.}$ = 5.6858(5) Å, $\beta_{mon.}$ = 109.48(1)° $a_{mon.}/b_{mon.}$ = 1.80						
Atom	Wyckoff	Coordinates			Occupancy	ADP (Å²)
Na	2c	0	0	1/2	0.96(2)	0.5(3)
Mn	2b	0	1/2	0	1/3	0.3(1)
Fe	2b	0	1/2	0	2/3	
O	4i	0.227(3)	0	0.202(2)	1	0.5(3)
M-O distances		4 * 2.02(1) Å		2 * 2.14(2) Å		
Rwp = 11.41%; R_B = 2.44% (with excluded regions)						

Table A-II.3: Structural parameters and reliability factors calculated from the refinement of the structure of the O'3 phase from the synchrotron XRPD pattern.

The O3-$Na_{2/3}Mn_{1/3}Fe_{2/3}O_2$ phase

To prepare the O3-$Na_{2/3}Mn_{1/3}Fe_{2/3}O_2$ material we targeted the middle of the voltage jump on the E = f(x) curve (E_{eq} = 2.8 V, x = 0.67). According to the *in situ* XRPD study, we expect a pure O3 phase. The calculated and observed Synchrotron XRPD patterns are represented in **Figure A-II.14**. The corresponding cell and atomic parameters are given in **Table A-II.4**.

The synchrotron XRPD data shows a pure O3 phase whose structure and cell parameters are comparable to the starting one. The $c_{hex.}$ and $a_{hex.}$ cell parameters are larger (16.545(1) Å *vs.* 16.3420(2) Å) and smaller (2.9589(1) Å *vs.* 2.9820(1) Å) respectively than those of the pristine material, in agreement with the lower Na content (x = 0.67 *vs.* x = 0.77 initially). Moreover, it is noteworthy that no extra-diffraction lines resulting from sodium/vacancy ordering are observed, as it is the case for several $Na_{2/3}MO_2$ materials with only one type of transition metal [48, 55, 56].

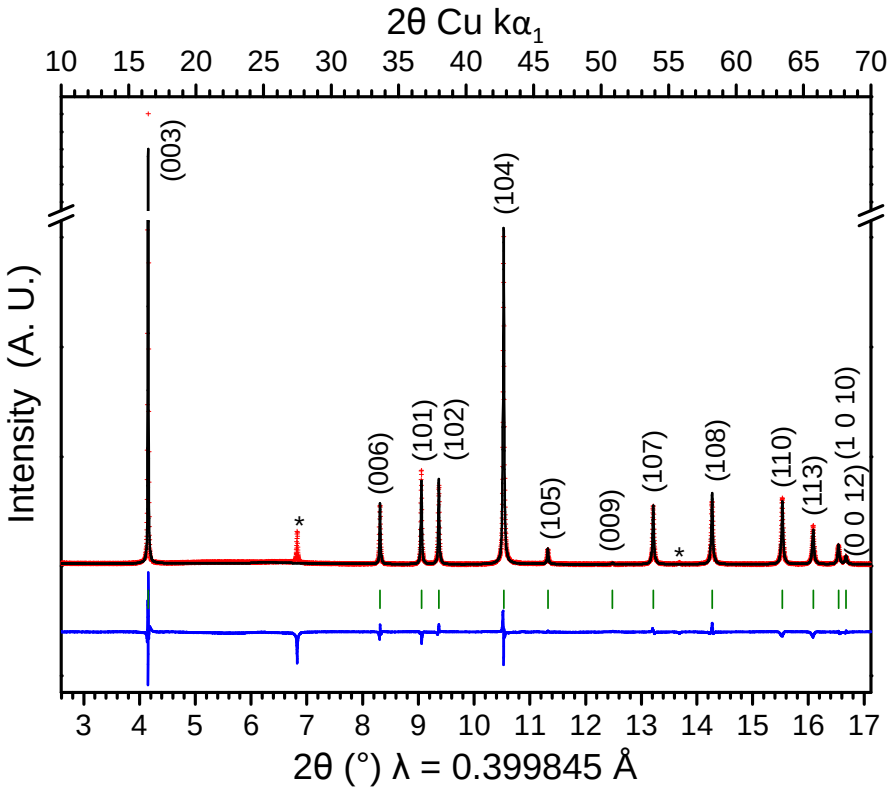

Figure A-II.14: Observed and calculated (Rietveld method) synchrotron XRPD patterns of the O3-$Na_{2/3}Mn_{1/3}Fe_{2/3}O_2$ phase. Red crosses: experimental, black line: calculated, blue line: difference and green bars: Bragg positions. The * symbol indicates the graphite diffraction lines which were excluded for the refinement.

O3-$Na_{0.67}Mn_{1/3}Fe_{2/3}O_2$ Space group: **R-3m** $a_{hex.}$ = 2.9591(1) Å, $c_{hex.}$ = 16.545(1) Å						
Atom	Wyckoff	Coordinates			Occupancy	ADP (Å²)
Na	3b	0	0	1/2	0.67(1)	2.4(2)
Mn	3a	0	0	0	1/3	0.53(3)
Fe	3a	0	0	0	2/3	
O	6c	0	0	0.2701(2)	1	0.77(8)
M-O distances		6 * 2.00(1) Å				
Rwp = 8.40%; R_B = 5.91% (with excluded regions)						

Table A-II.4: Structural parameters and reliability factors calculated from the refinement of the structure of the O3 phase from the synchrotron XRPD pattern.

The P3-$Na_{0.61}Mn_{1/3}Fe_{2/3}O_2$ phase

The sample of the P3 phase was prepared by targeting E_{eq} = 3.4 V. The Synchrotron XRPD pattern corresponding to the P3 phase is represented in **Figure A-II.15** along with the calculated one. The cell and atomic parameters corresponding to this refinement are given in **Table A-II.5**.

The synchrotron XRPD pattern of the P3-type phase is successfully fitted with a small impurity of the O3 phase. In the P3 stacking type, the sodium ion occupies a prismatic NaO_6 site which shares a face and three edges with the surrounding MO_6 octahedra. This change in coordination results from the gliding of two MO_2 planes in the structure whose corresponding O positions move from an "ABCABC" stacking to an "ABBCCA" one. The refinement of the Na content leads to the P3-$Na_{0.61(3)}Mn_{1/3}Fe_{2/3}O_2$ formula. Due to a stronger electrostatic Na^+-$M^{3+/4+}$ repulsion through the common NaO_6 / MO_6 face, the sodium ion is slightly off centered in its prismatic environment along the *c*-direction (z_{Na} = 0.168(1) instead of z = 1/6 if centered) ; separating the Na-O distances into three long (2.49(3) Å) and three short ones (2.41(3) Å). The higher Na^+ ion diffusion expected in the P3 structure explains the huge decrease of the polarization at the O3 → P3 transition that we discussed along with the GITT curve (**Figure A-II.5**).

The evolution of the M-O and Na-O distances in MO_6 and NaO_6 polyhedra of O'3-$Na_{0.96}Mn_{1/3}Fe_{2/3}O_2$, O3-$Na_{2/3}Mn_{1/3}Fe_{2/3}O_2$ and P3-$Na_{0.61}Mn_{1/3}Fe_{2/3}O_2$ phases are represented in **Figure A-II.16** along with the evolution of the MO_2 slab thicknesses. The evolution of the interlayer space was already discussed with the *operando in situ* experiment carried out during Na^+ deintercalation: due to the lowering of the screening effect of the Na^+ ions on the surrounding oxygen planes, the interslab distance increases during Na^+ deintercalation for the O'3/O3 and P3 phase domains. **Tables A-II.3**, **A-II.4** and **A-II.5** allow calculating the MO_2 slab thicknesses for the associated O'3, O3 and P3 materials. Their comparison shows that lowering the Na^+ content induces thinner MO_2 slabs (from a 2.17(1) Å thickness (x = 0.96) to 2.06(1) (x = 0.61)), due to the increasing amount of M^{4+} ions: their smaller ionic radii increase the strength of the M-O bonds, resulting in thinner MO_2 slabs.

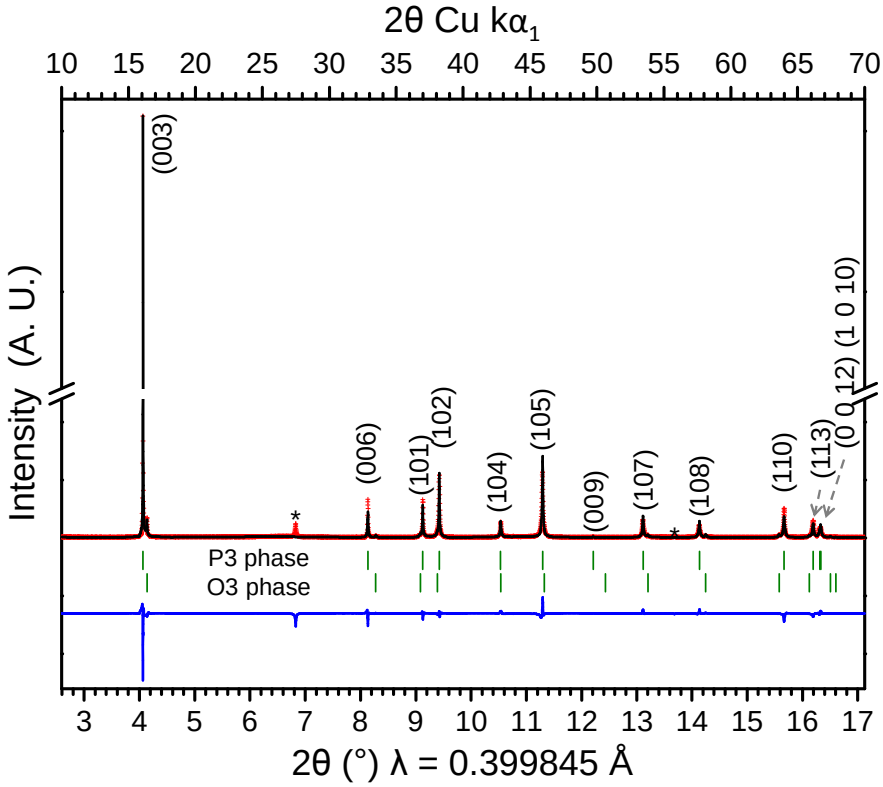

Figure A-II.15: Observed and calculated (Rietveld method) synchrotron XRPD patterns of the P3-$Na_{0.57}Mn_{1/3}Fe_{2/3}O_2$ phase. Red crosses: experimental, black line: calculated, blue line: difference and green bars: Bragg positions. The * symbol indicates the graphite diffraction lines which were excluded for the refinement.

P3-$Na_{0.61}Mn_{1/3}Fe_{2/3}O_2$ Space group: **R-3m** $a_{hex.}$ = 2.9338(1) Å, $c_{hex.}$ = 16.913(1) Å						
Atom	Wyckoff	Coordinates			Occupancy	ADP (Å²)
Na	6c	0	0	0.168(1)	0.61(3)	3.0(7)
Mn	3a	0	0	0	1/3	0.44(5)
Fe	3a	0	0	0	2/3	
O	6c	0	0	0.394(1)	1	0.7(2)
M-O distances	6 * 1.99 (1) Å					
Rwp = 11.82%; R_B = 6.35% (with excluded regions)						

Table A-II.5: Structural parameters and reliability factors calculated from the refinement of the structure of the P3 phase from the synchrotron XRPD pattern.

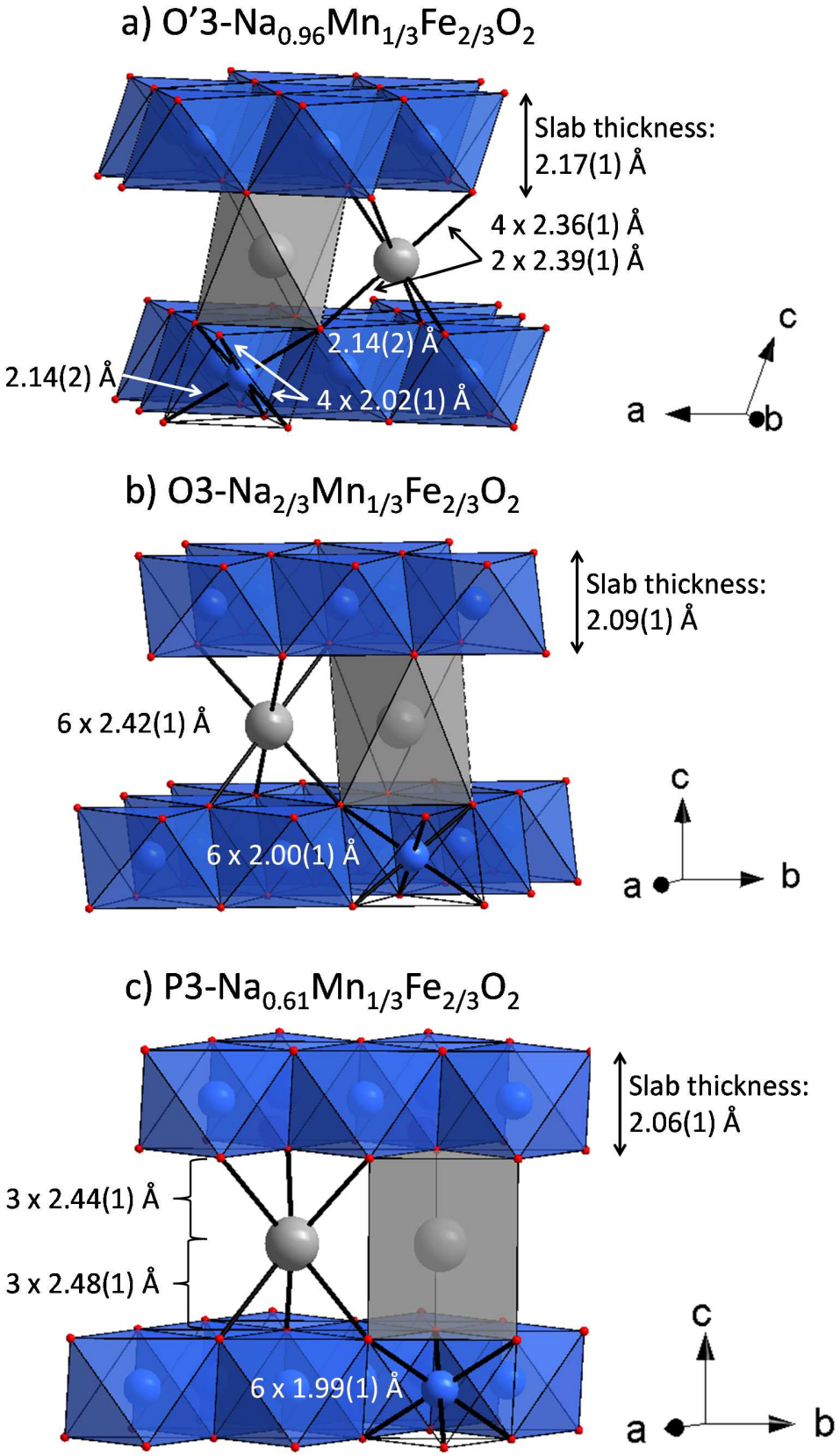

Figure A-II.16: Comparison of the distances in the MO_6 and NaO_6 polyhedra in a) O'3-$Na_{0.96}Mn_{1/3}Fe_{2/3}O_2$, b) O3-$Na_{2/3}Mn_{1/3}Fe_{2/3}O_2$ and c) P3-$Na_{0.61}Mn_{1/3}Fe_{2/3}O_2$. The MO_2 slab thicknesses are also indicated. For the O3 and P3 type phases, only a part of the stacking sequence is shown for clarity purposes.

A-II.2. The $Na_xMn_{1/2}Fe_{1/2}O_2$ system

The mixture of the O3 and O'3 phases in the "$Na_{0.77}Mn_{1/2}Fe_{1/2}O_2$" material prevented any advanced structural characterization: the O3 and O'3 phases showing very close diffraction peaks, it is impossible to perform a Rietveld refinement of the structures, as it leads to the divergence of the software or aberrant results. Therefore, only a LeBail refinement (profile matching) of the XRPD pattern was performed, as presented in **Chapter A-I** (**Figure A-I.4c**).

A-II.2.a. Electrochemistry

Influence of the cut-off voltage

However, as this material showed electrochemical activity, more advanced characterizations were carried out to study the impact of the upper cut-off voltage. The galvanostatic E = f(x) curves recorded in the 1.5 – 3.8 V, 1.5 – 4.0 V and 1.5 – 4.3 V ranges are presented in **Figure A-II.17a-c**, respectively. The first four cycles are represented with the first one is highlighted in red. The evolution of the associated discharge capacities is shown in **Figure A-II.17d**.

As expected, the increase of the upper cut-off voltage leads to a better capacity for the first cycle. For every experiment the first cycle is slightly different from the other ones which show a higher polarization and a smoother potential jump at $x \approx 0.55$. While the 2nd, 3rd and 4th cycles are similar for the $E_{cut\text{-}off}$ = 3.8 V and 4.0 V curves. The $E_{cut\text{-}off}$ = 4.3 V curve shows a decrease of the reversibly (de)intercalated sodium content between the 2nd and 4th cycles: from 0.68 Na^+ to 0.6 Na^+ per formula unit, respectively. This phenomenon is correlated to the important discharge capacity loss observed for the first 6 cycles in **Figure A-II.17d**. The capacity retentions associated to the 29th cycle for the different experiments are quite different: 80 %, 91% and 75 % for $E_{cut\text{-}off}$ = 3.8 V, 4.0 V and 4.3 V, respectively. Surprisingly the experiment carried out in the 1.5 – 4.0 V range show the best capacity retention.

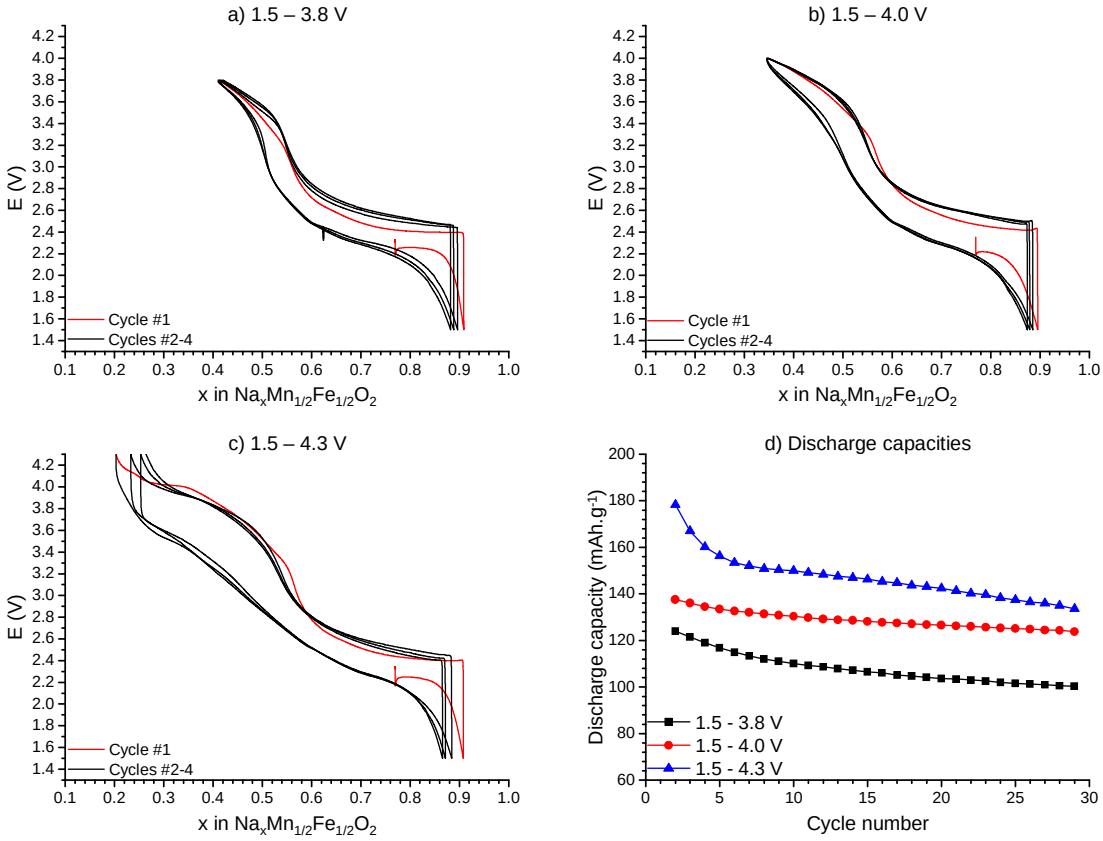

Figure A-II.17: Galvanostatic cycling curves associated to the $Na_xMn_{1/2}Fe_{1/2}O_2$ system recorded (a) between 1.5 and 3.8 V, (b) between 1.5 and 4.0 V and (c) between 1.5 and 4.3 V at C/50. (d) Associated discharge capacities. The capacities of the first cycles are not shown on (d) as they correspond to the partially intercalated state of the material.

GITT cycling

To better understand the behavior of this material, a GITT experiment was carried out as shown in **Figure A-II.18a**. For comparison purposes, the GITT curve of the $Na_xMn_{1/3}Fe_{2/3}O_2$ material is given in **Figure A-II.18b**.

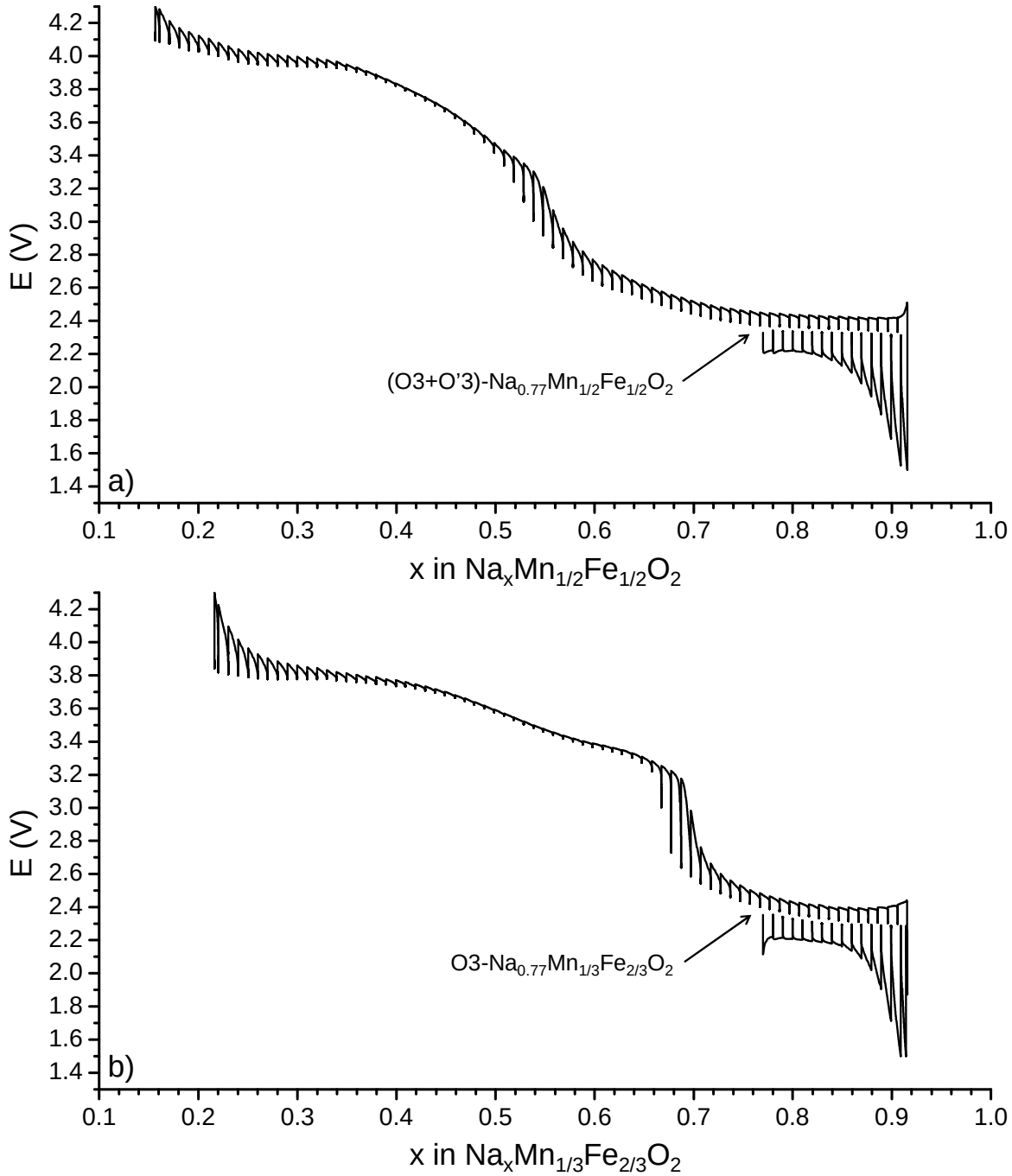

Figure A-II.18: GITT cyclings with steps of 0.01 Na per formula unit and a $\Delta V < 4$ mV.h^{-1} relaxation condition for the (a) $Na_xMn_{1/2}Fe_{1/2}O_2$ and (b) $Na_xMn_{1/3}Fe_{2/3}O_2$ compositions.

As discussed in **Chapter A-I**, the starting point of the curve (x = 0.77) is located on the voltage plateau, in agreement with the fact that two phases are present in the pristine material (O3 and O'3). This plateau is observed in the 0.77 ≤ x ≤ 0.9 Na range upon intercalation and is reversible. Upon deintercalation, a voltage overshoot is observed at x = 0.91, indicating that the intercalated phase (presumably O'3) is highly resistive. After the voltage plateau (x > 0.77), the voltage continuously increases and mark a smooth voltage jump at x ≈ 0.55, corresponding to the change of the active redox couple from Mn^{4+}/Mn^{3+} to Fe^{4+}/Fe^{3+}. Then, the polarization decreases and the voltage continuously increases up to E ≈ 3.95 V where a voltage plateau is observed for 0.25 ≤ x ≤ 0.33. After this voltage plateau, the polarization gradually increases up to 4.3 V. Comparing to the GITT cycling curve of the $Na_xMn_{1/3}Fe_{2/3}O_2$ system for which the voltage jump occurs at x ≈ 0.67 in good agreement with the change in the redox process, we observe the voltage jump at x ≈ 0.55 instead of x = 0.5 for the $Na_xMn_{1/2}Fe_{1/2}O_2$ system. Moreover, the voltage jump is quite smooth instead of marking a sudden jump as for the $Na_xMn_{1/3}Fe_{2/3}O_2$ composition. It is impossible to give any explanation on this phenomenon based on the GITT curve only.

A-II.2.b. *Operando in situ* XRPD study during Na deintercalation

To follow the structural changes that the material undergoes during Na^+ deintercalation, we carried out an *operando in situ* XRPD study during the charge of a $Na_xMn_{1/2}Fe_{1/2}O_2$//Na battery. As for the experiment carried out on the O3-based $Na_xMn_{1/3}Fe_{2/3}O_2$ system, data were collected during the first charge following a preliminary discharge of the cell that lead to the $Na_{0.95}Mn_{1/2}Fe_{1/2}O_2$ composition as the starting point. In order to be close to the fully intercalated phase the galvanostatic discharge was followed by a potentiostatic intercalation at 1.5 V until the current was close to 0 mA. The XRPD pattern was recorded. The battery was then charged at C/100 and the conditions were optimized to record the XRPD patterns in the 13 – 20° and 30 – 43° 2θ ranges in one hour. Therefore, two successive XRPD patterns should correspond to a sodium step of 0.01 Na^+ per formula unit. Unfortunately, a huge electrolyte decomposition issue occurred for this experiment as no additive was employed at that time and it is impossible to rely on the x values of the galvanostatic curve. Instead, we plotted the galvanostatic curve as a function of time as shown in **Figures A-II.19** and **A-II.20** in inverse order. Knowing the potential corresponding to every XRPD pattern, it is possible to give an estimation of the sodium contents by comparison to a galvanostatic curve recorded with the FEC additive. For clarity purpose, only the sodium contents of the structural domain limitations are given.

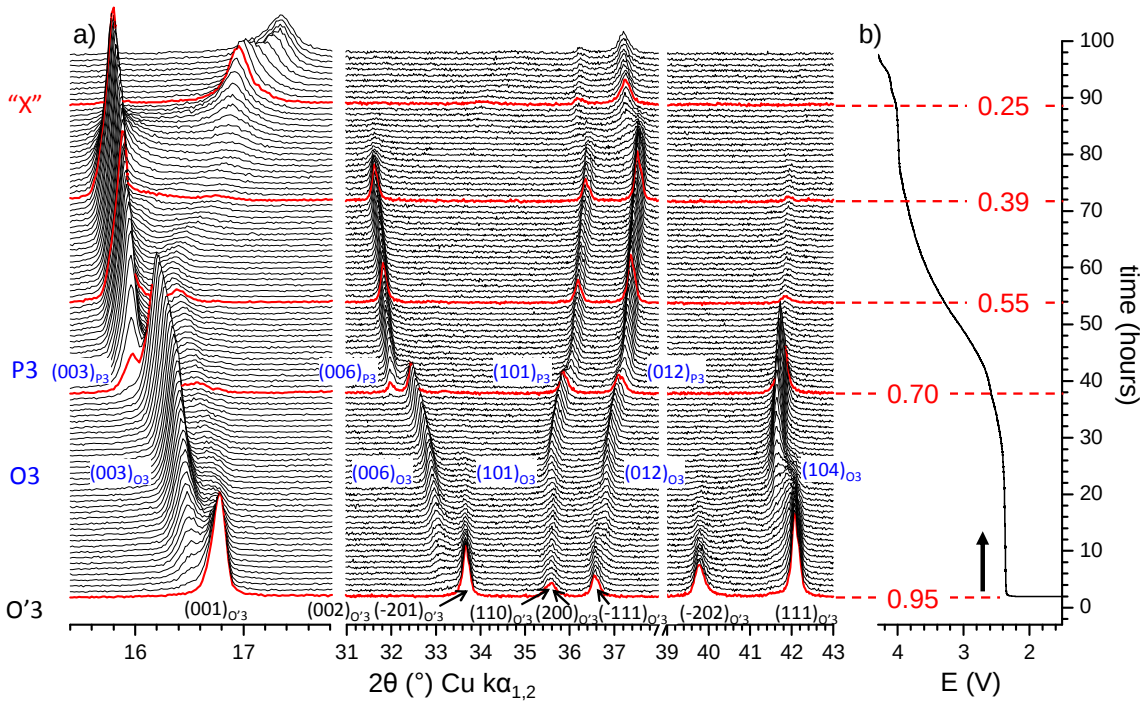

Figure A-II.19: (a) XRPD patterns recorded *in situ* (*operando* mode) during the charge of an $Na_xMn_{1/2}Fe_{1/2}O_2$/$NaPF_6$ in PC (1M)/Na cell along with (b) the corresponding galvanostatic curve. The red XRPD patterns correspond to the limitations of the different structural domains. Blue Miller indexes: O3 and P3 phases. Black Miller indexes: O'3 phase.

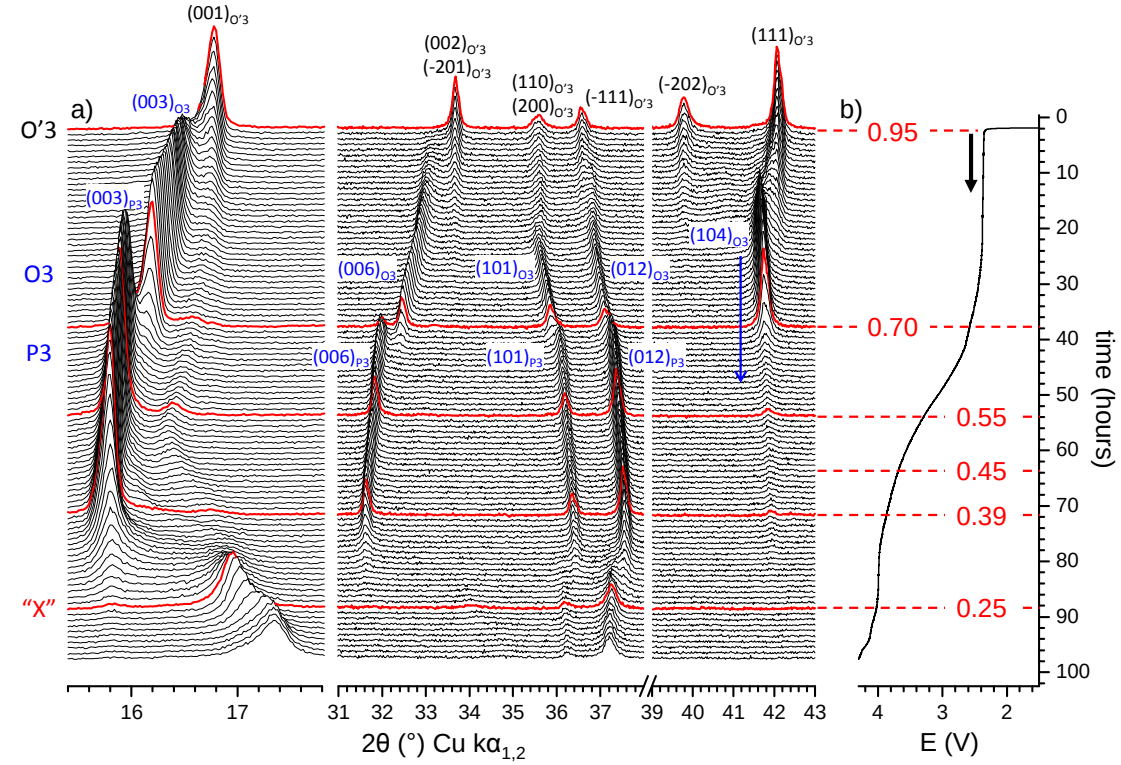

Figure A-II.20: Inverse representation of the *operando in situ* experiment carried out on the $Na_xMn_{1/2}Fe_{1/2}O_2$ system: (a) XRPD patterns and (b) corresponding galvanostatic curve. Blue Miller indexes: O3 and P3 phases. The red XRPD patterns correspond to the limitations of the different structural domains. Blue Miller indexes: O3 and P3 phases. Black Miller indexes: O'3 phase.

As it is further discussed several structural domains are observed during the charge. The almost fully intercalated state exhibits a structural distortion induced by the Mn^{3+} ions (O'3 phase). Na^+ deintercalation leads to the formation of an O3 phase through a biphasic domain (XRPD patterns recorded between the 3rd and 12th hours). At the 38th hour of the experiment ($x \approx 0.70$) the P3 phase appears through an O3 + P3 biphasic domain in the $0.55 \leq x \leq 0.70$ range. Then for $x \leq 0.25$, a new phase labeled "X" is observed.

As in the $Na_xMn_{1/3}Fe_{2/3}O_2$ system, a residual diffraction peak corresponding to the interslab distance remains at $2\theta \approx 16.6°$ and shifts to lower 2θ values upon deintercalation to $x = 0.55$. For $x < 0.55$, the position of the residual diffraction peak shifts towards higher 2θ values. One can suppose the residual diffraction peak corresponds to an O3 phase which is deintercalated without transforming into the P3 one.

From the XRPD patterns it was possible to determine the cell parameters by Full Pattern Matching or by the 2θ position of the (00*l*) and supposedly (012) diffraction lines. The estimated interslab distances and cell parameters are shown in **Figure A-II.21** along with the galvanostatic curve.

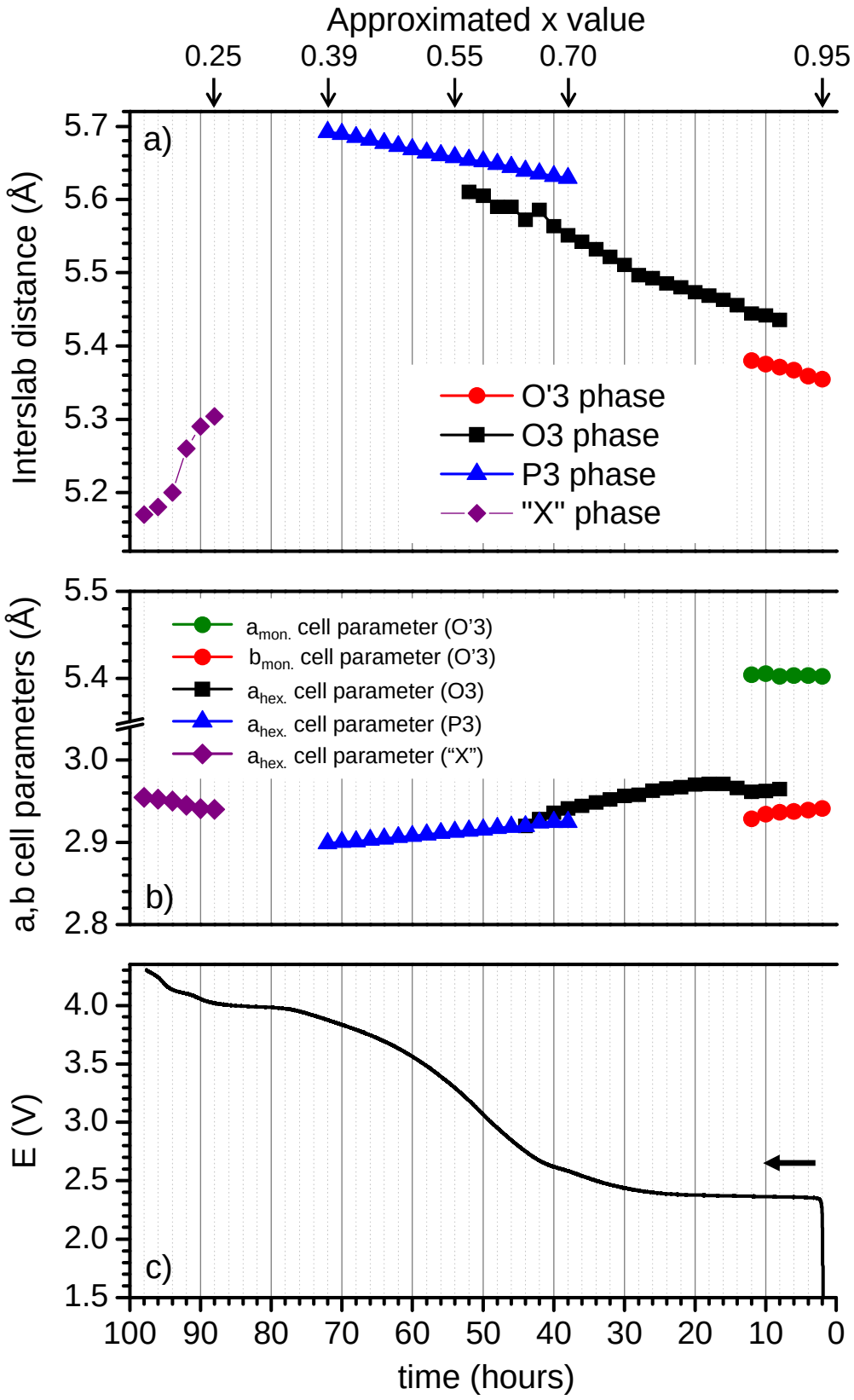

Figure A-II.21: Evolution of the (a) interslab distances and (b) cell parameters of the different phases observed in the $Na_xMn_{1/2}Fe_{1/2}O_2$ system during the *operando in situ* XRPD study. The galvanostatic curve is shown as a guide on (c).

The XRPD pattern of the almost fully intercalated phase, $Na_{0.95}Mn_{1/2}Fe_{1/2}O_2$, can be indexed in the monoclinic system (space group C2/m, O'3 structure). As for O'3-$Na_{0.96}Mn_{1/3}Fe_{2/3}O_2$, the monoclinic distortion is emphasized by the splitting of the $(012)_{hex.}$ and $(104)_{hex.}$ diffraction peaks of the O3 structure to the $(-111)_{mon.}$ + $(200)_{mon.}$ and to the $(-202)_{mon.}$ + $(111)_{mon.}$ ones, respectively (**Figures A-II.19** and **A-II.20**). The high sodium content in this phase decreases the repulsions between the surrounding O planes. This leads to a small interslab value of approximatively 5.37 Å. The O'3 phase is observed alone on a very narrow range as the O3 phase is evidenced at the 3rd hour of the experiment. The biphasic domain between the O'3 and O3 phases, observed between the 3rd and 12th hours of the experiment, corresponds to the voltage plateau observed at ≈ 2.3 V on the GITT cycling curve (**Figure A-II.18**). The interslab distance of the O3 phase is slightly higher than the O'3 one in the biphasic domain (≈ 5.44 Å *vs.* ≈ 5.37 Å, *cf.* **Figure A-II.21**). This is due to the lower Na amount in the O3 phase which lowers the screening effect on the surrounding O planes. Then, the O3 phase follows a solid solution behavior and its interslab distance continuously increases for the previously stated reason. At the 38th hour of the experiment (x ≈ 0.70) the P3 phase appears (**Figure A-II.19**). It is characterized by a larger interslab distance (5.63 Å *vs*. 5.55 Å for the O3 phase at x ≈ 0.70) induced by the formation of NaO_6 prismatic sites. For x < 0.39, the P3 phase disappears while a new (00*l*) diffraction peak appears at ≈ 17 °. Following our hypothesis previously stated on the $Na_xMn_{1/3}Fe_{2/3}O_2$ system, we believe that the observation of this new diffraction peak to be induced by the increasing amount of stacking faults into the P3-type material.

For x = 0.25 only one phase remains. This phase is labeled "X" by analogy to the experiment carried out in the O3-based $Na_xMn_{1/3}Fe_{2/3}O_2$ system. It exhibits a small interslab distance (≈ 5.3 Å) indicating an octahedral environment of the remaining Na^+ ions. Upon further deintercalation the interslab distance decreases, as observed for all O3-type A_xMO_2 (A = Li, Na) systems [116]. At the very end of the experiment the asymmetry on the low angle part of the $(00l)_{"X"}$ diffraction peak suggests the appearance of a new phase.

The O'3 → O3 → P3 → "X" structural evolution upon charge is comparable to the structural behavior observed in the $Na_xMn_{1/3}Fe_{2/3}O_2$ system. Several residual diffraction peaks are observed during the experiment, as indicated by arrows in **Figure A-II.22**. The first one (green arrow in **Figure A-II.22**) is similar to the one of the O3* phase observed in the $Na_xMn_{1/3}Fe_{2/3}O_2$ system. As for the $Na_xMn_{1/3}Fe_{2/3}O_2$ system, we suppose the origin of this intermediate phase to be (i) slight variation of Mn / Fe ratios or (ii) the coexistence of particles with or without Mn vacancies (**A-II.1.c**). The two other residual diffraction peaks (pink and blue arrows in **Figure A-II.22**) show a different behavior as they suddenly appear on the XRPD patterns. As for the P3* phase in the $Na_xMn_{1/3}Fe_{2/3}O_2$ system, we believe that these diffraction peaks show the apparition of stacking faults in the P3 phase.

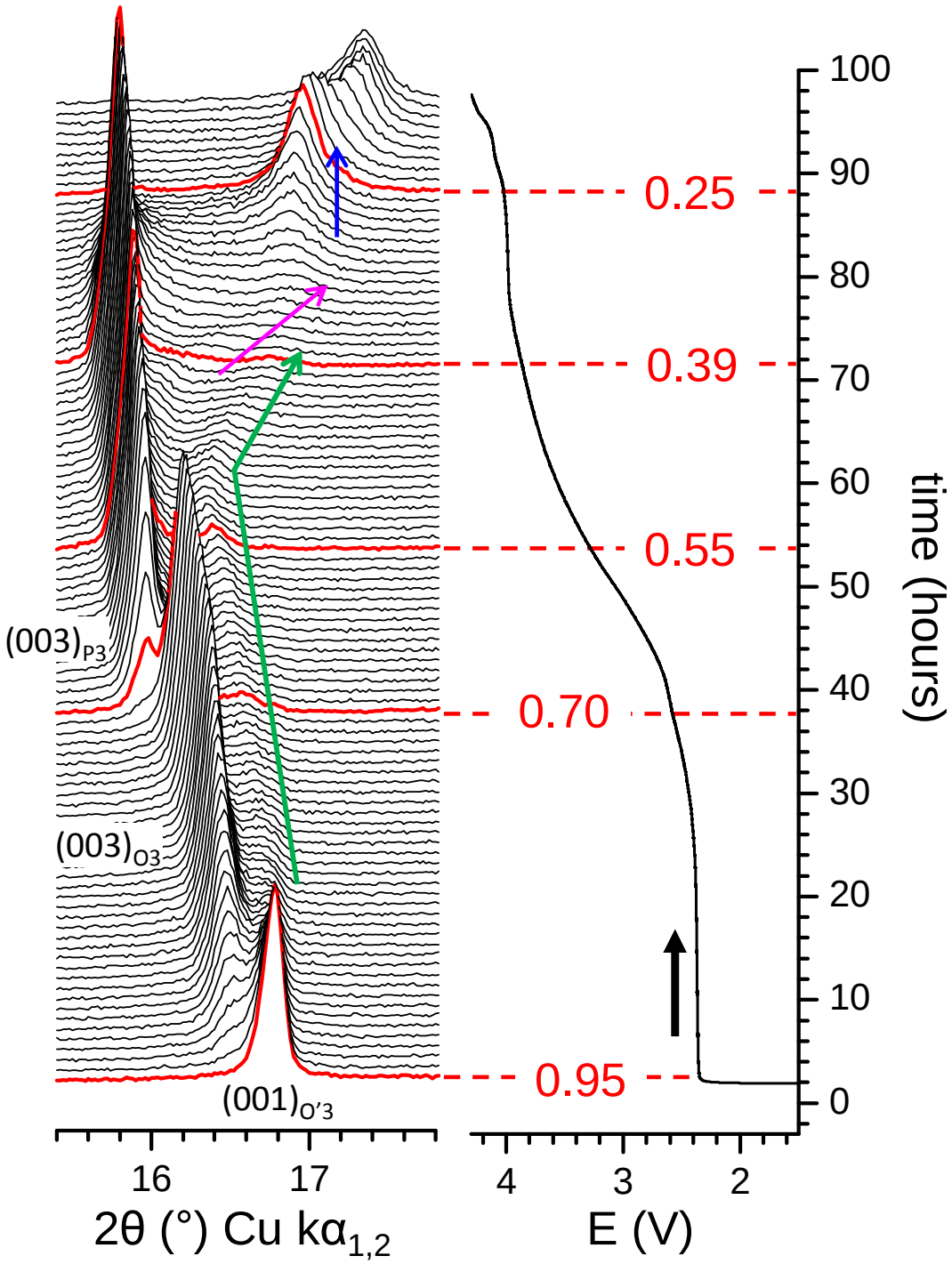

Figure A-II.22: XRPD patterns recorded *in situ* (*operando* mode) during the charge of an $Na_xMn_{1/2}Fe_{1/2}O_2/NaPF_6$ in PC (1M)/Na cell: highlighting of the intermediate phases (green, pink and blue arrow).

To study the reversibility of the diverse structural transitions, we discharged the cell back to 1.5 V and recorded the XRPD pattern under constant voltage and with the same acquisition parameters. The XRPD patterns recorded after the first and second discharges are presented in **Figure A-II.23**.

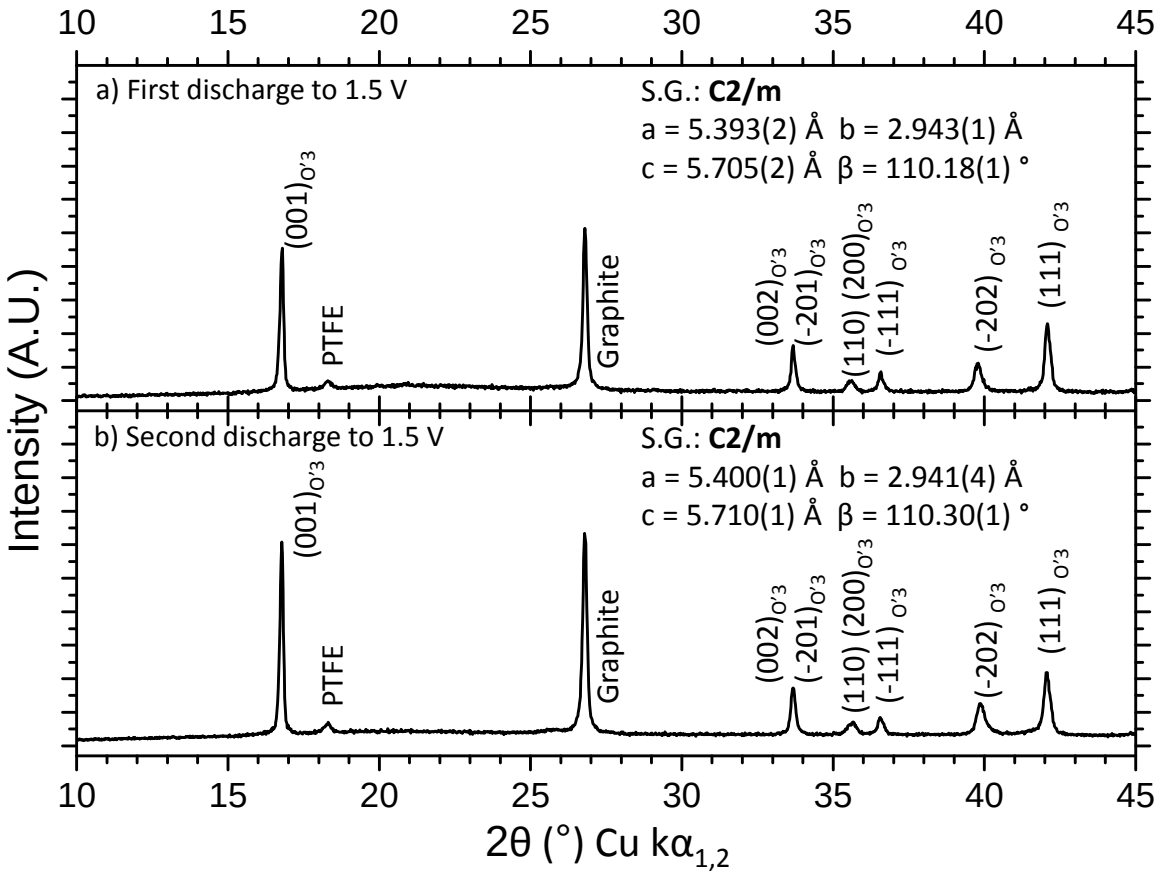

Figure A-II.23: Comparison of the XRPD patterns of the $Na_xMn_{1/2}Fe_{1/2}O_2$ system recorded under constant voltage at 1.5 V: (a) at the beginning of the *operando in situ* XRPD experiment and (b) after cycling to 4.3 V and discharge back to 1.5 V.

As one can see, the same monoclinic distortion is observed after the second discharge and the LeBail refinement of both patterns give the same cell parameters. We therefore conclude that cycling up to 4.3 V does not degrade the material after one cycle. In the $Na_xMn_{1/3}Fe_{2/3}O_2$ system, the same experiment did not lead to the monoclinic distortion of the structure of the intercalated phase. As both systems underwent the same structural transitions, it is possible that the higher Mn content in the $Na_xMn_{1/2}Fe_{1/2}O_2$ system stabilizes the material by preventing the Fe migration to the interlayer space. This could also explain the better capacity retention observed in the 1.5 – 4.0 V range for $Na_{0.77}Mn_{1/2}Fe_{1/2}O_2$ (91 % after 30 cycles) compared to $Na_{0.77}Mn_{1/3}Fe_{2/3}O_2$ (74 % after 30 cycles).

A-II.2.c. *Ex situ* Synchrotron X-ray diffraction study of O'3-$Na_{0.95}Mn_{1/2}Fe_{1/2}O_2$

In order to better understand the structure of the fully intercalated phase, we prepared a sample of the O'3 phase by the potentiostatic route (E_{eq} = 1.5 V). This sample was then washed and analyzed by synchrotron XRPD. The experimental and calculated synchrotron XRPD patterns for the intercalated phase are represented in **Figure A-II.24**. The corresponding cell and atomic parameters are reported in **Table A-II.6**.

For reasons already mentioned, the profile of the diffraction peaks was fitted using anisotropic broadening of the diffraction peaks. The pattern of the intercalated O'3-$Na_xMn_{1/2}Fe_{1/2}O_2$ phase is indexed in monoclinic system (C2/m space group) with cell parameters very close to those determined in the *in situ* experiment. The refinement of the sodium content leads to the O'3-$Na_{0.95}Mn_{1/2}Fe_{1/2}O_2$ formula.

By comparison to the O'3-$Na_{0.96}Mn_{1/3}Fe_{2/3}O_2$ material, the higher Mn content of the O'3-$Na_{0.95}Mn_{1/2}Fe_{1/2}O_2$ material induces a more important cooperative Jahn Teller effect: (1) the $a_{mon.}/b_{mon.}$ ratio is higher for the O'3-$Na_{0.95}Mn_{1/2}Fe_{1/2}O_2$ phase (1.84) than for the O'3-$Na_{0.96}Mn_{1/3}Fe_{2/3}O_2$ one (1.80) and (2) the distortion of the MO_6 octahedra is higher as they exhibit longer (2 * 2.19(1) Å) and shorter (4 * 1.99(1) Å) M-O bonds than for the O'3-$Na_{0.96}Mn_{1/3}Fe_{2/3}O_2$ material (2 * 2.14(1) Å and 4 * 2.02(2) Å, respectively). The MO_2 slab thickness is higher (2.18(1) Å) for O'3-$Na_{0.96}Mn_{1/3}Fe_{2/3}O_2$ than for O'3-$Na_{0.95}Mn_{1/2}Fe_{1/2}O_2$ (2.15(1) Å), which is coherent with the larger ionic radii of the Fe^{3+} ion (r = 0.63 Å) compared to the Mn^{3+} one (r = 0.58 Å).

The other structural domains (O3, P3) were not studied by synchrotron XRPD due to their similarity to the O3-$Na_xMn_{1/3}Fe_{2/3}O_2$ and P3-$Na_xMn_{1/3}Fe_{2/3}O_2$ ones and to time limitations.

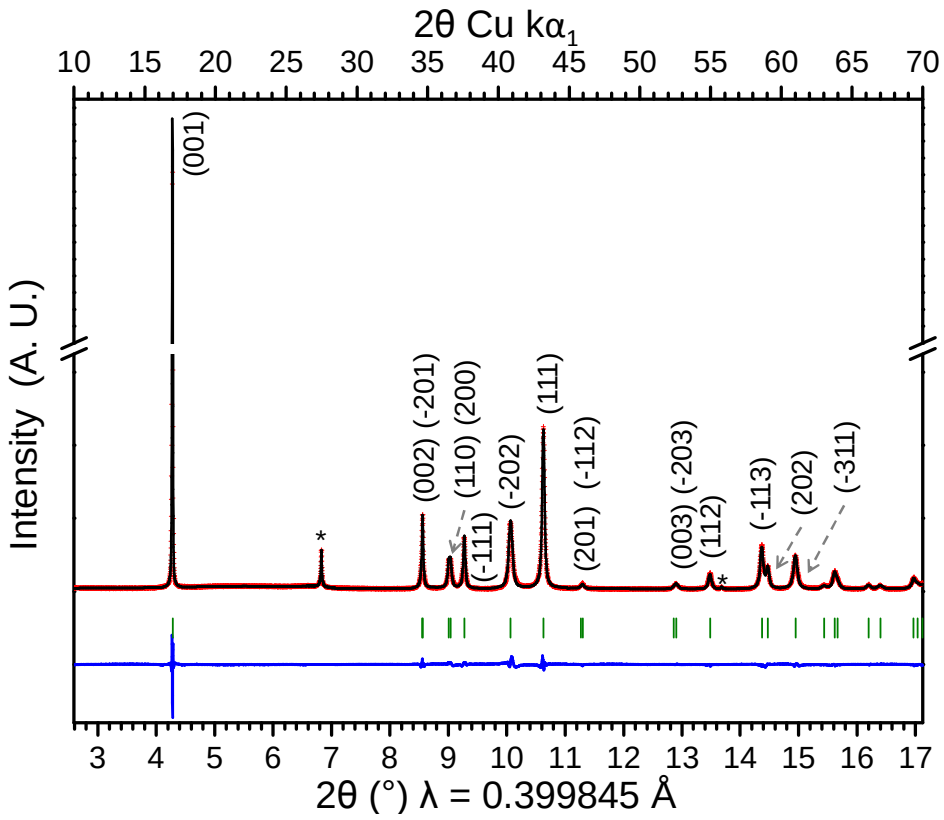

Figure A-II.24: Observed and calculated (Rietveld Method) synchrotron XRPD patterns of the O'3-$Na_{0.95}Mn_{1/2}Fe_{1/2}O_2$ phase. Red crosses: experimental, black line: calculated, blue line: difference and green bars: Bragg positions. The * symbol indicates the graphite diffraction lines which were excluded for the refinement.

O'3-$Na_{0.95}Mn_{1/2}Fe_{1/2}O_2$ Space group : C2/m $a_{mon.}$ = 5.4111(8) Å, $b_{mon.}$ = 2.9433(3) Å, $c_{mon.}$ = 5.711(1) Å, $\beta_{mon.}$ = 110.31(1)° $a_{mon.}/b_{mon.}$ = 1.84						
Atom	Wyckoff	Coordinates			Occupancy	ADP
Na	2c	0	0	1/2	0.95(3)	0.3(4)
Mn	2b	0	1/2	0	1	0.8(1)
Fe	2b	0	1/2	0		
O	4i	0.221(3)	0	0.201(2)	1	0.5(3)
M-O distances (Å)		4 * 1.99(1)		2 * 2.19(1)		
Rwp = 9.50%; R_B = 7.55% (with excluded regions)						

Table A-II.6: Structural parameters and reliability factors calculated from the refinement of the structure of the O'3-$Na_{0.95}Mn_{1/2}Fe_{1/2}O_2$ phase from the synchrotron XRPD pattern.

A-II.3. Study of the redox mechanisms during Na deintercalation for the O3-based $Na_xMn_{1/3}Fe_{2/3}O_2$ and $Na_xMn_{1/2}Fe_{1/2}O_2$ systems

We studied the redox mechanisms involved during Na^+ deintercalation for the two O3-based systems. The open current voltage charge curves extracted from the GITT cyclings shown in **Figure A-II.25** already give an insight of the activity ranges of the Fe^{4+}/Fe^{3+} and Mn^{4+}/Mn^{3+} redox couples as the voltage jumps are located at $x \approx 1/2$ (which corresponds approximatively to the iron content in the $Na_xMn_{1/2}Fe_{1/2}O_2$ system) and at $x \approx 2/3$ (which corresponds to the iron content in the $Na_xMn_{1/3}Fe_{2/3}O_2$ system). This suggests that the Mn^{4+}/Mn^{3+} redox couple is active at low voltage and that the Fe^{4+}/Fe^{3+} one is active at high voltage. To confirm these assumptions, we carried out *operando in situ* X-ray absorption spectroscopy[11] and *in situ* and *ex situ* ^{57}Fe Mössbauer spectroscopy[12] measurements.

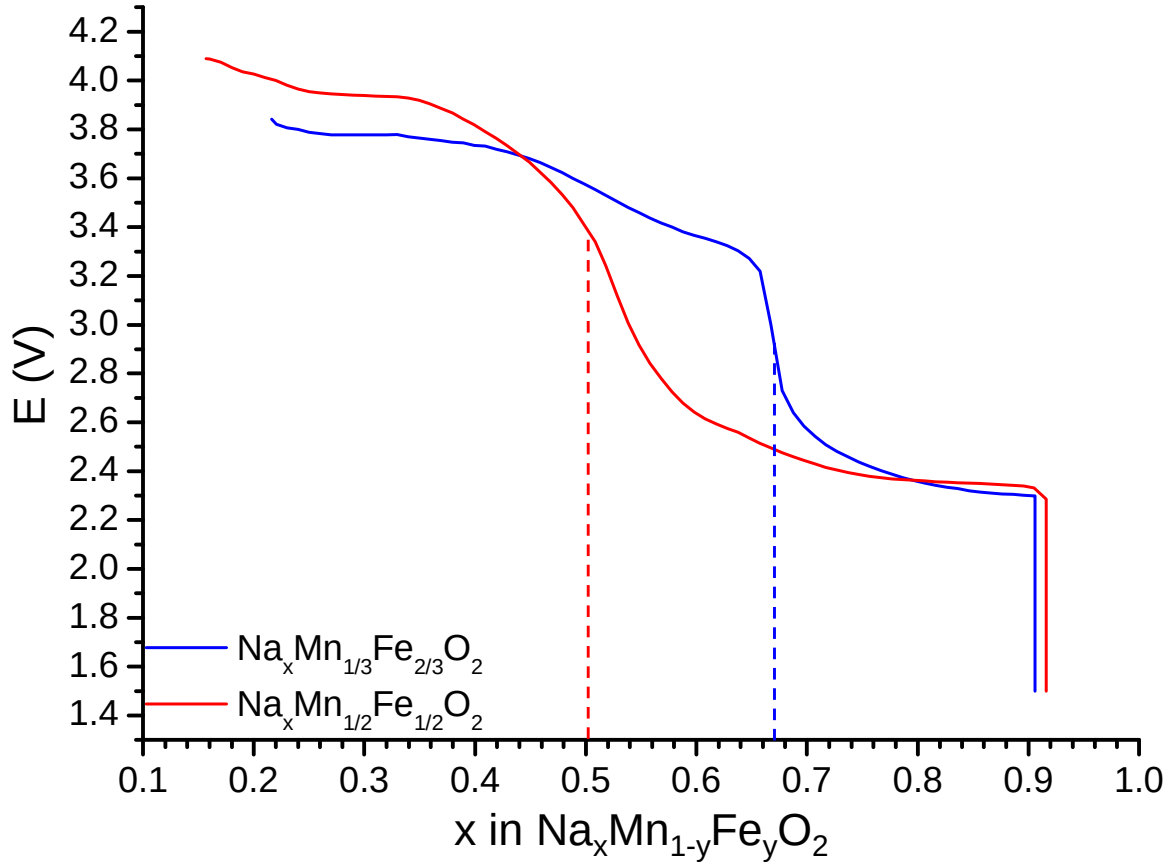

Figure A-II.25: Open current voltage charging curves extracted from the GITT cycling cones for (red) $Na_xMn_{1/2}Fe_{1/2}O_2$ and (blue) $Na_xMn_{1/3}Fe_{2/3}O_2$. The dashed lines represent the expected position of the voltage jump associated to the change of redox process during charge if the redox potentials of Fe^{4+}/Fe^{3+} and Mn^{4+}/Mn^{3+} are well separated.

[11] In collaboration with Pr. Bing-Joe Hwang, NTUST / NSRRC, Taiwan, R.O.C.

[12] In collaboration with :
Pr. D. Filimonov, Lomonosov Moscow State University, Russia (Design of the cell, result discussions).
Dr. S. Bordère, Researcher at ICMCB (Experimental tests of the cell).
Dr. A. Wattiaux, Research Engineer at ICMCB (*in situ* and *ex situ* experiments, data fittings and result discussions).

A-II.3.a. Operando in situ X-ray Absorption Near Edge Spectroscopy study

The *in situ* X-ray Absorption Spectroscopy study was performed *in operando* due to the time limitations on the synchrotron beamline[13]. The evolution of the X-ray Absorption Near Edge Spectroscopy parts of the spectrum are shown in **Figure A-II.26** for the $Na_xMn_{1/3}Fe_{2/3}O_2$ (**Figures A-II.26a** and **A-II.26b**) and $Na_xMn_{1/2}Fe_{1/2}O_2$ (**Figures A-II.26c** and **A-II.26d**) compositions. The Mn and Fe K-edges were recorded and are compared to various references, presented in **Figures A-II.26e** and **A-II.26f**, respectively.

Concerning the $Na_xMn_{1/3}Fe_{2/3}O_2$ system, one can notice an important shift of the Mn K-edge towards the higher energy values as Na^+ is deintercalated from the structure in the $2/3 \leq x < 1$ range. We associate this shift to the $Mn^{3+} \rightarrow Mn^{4+}$ redox reaction as confirmed by the selected references (**Figure A-II.26e**). In the same sodium content region, no significant shift is observed on the Fe K-edge spectra, indicating that only the Mn^{4+}/Mn^{3+} redox couple is active at low potential / high sodium contents ($x > 0.67$) as suggested. For $x < 0.67$, no significant shift is observed on the spectra corresponding to the Mn K-edge while a small one is observed for the Fe K-edge. The references for the oxidation of Fe(III) consist in O3-$NaFeO_2$ prepared by solid state chemistry and in a $Na_{0.55}FeO_2$ phase prepared by electrochemical deintercalation. Their XANES spectra are presented in **Figure A-II.26f** and only show a small shift in the spectrum position to higher energy values along with Na^+ deintercalation, which is similar to the behavior observed in our material. It is strongly suggested that the $Fe^{3+} \rightarrow Fe^{4+}$ redox process is associated to the higher voltages, confirming our assumption.

Concerning the $Na_xMn_{1/2}Fe_{1/2}O_2$ composition, a shift of the Mn K-edge is observed in the $0.5 < x < 1$ and confirms the $Mn^{3+} \rightarrow Mn^{4+}$ redox reaction as discussed previously. The spectra of the Fe K-edge show no important variation from $x = 0.91$ to $x = 0.62$. Therefore, the Fe^{4+}/Fe^{3+} redox couple does not seem active in the high Na content (low voltage) region. For $x < 0.62$, the opposite tendencies are observed: the Mn K-edge spectra do not show any evolution between $x = 0.51$ and $x = 0.46$ while the Fe K-edge spectra show an important shift towards higher energies, especially in the $0.46 \leq x \leq 0.51$ range, strongly suggesting the $Fe^{3+} \rightarrow Fe^{4+}$ redox process at high voltage. However, the XANES spectra cannot exclude the simultaneous oxidation of Mn^{3+} and Fe^{3+} on a very narrow x range as no spectra were recorded for $0.62 < x < 0.51$. Such a feature was already observed in our laboratory on the O3-$Li_xNi_{0.30}Co_{0.70}O_2$ system by a ^7Li NMR study [120] and could explain the smooth voltage jump observed at $x \approx 0.55$ for the $Na_xMn_{1/2}Fe_{1/2}O_2$ system.

[13] In collaboration with Pr. Hwang's research team, NTUST/NSRRC, Taiwan, R.O.C. Beamline (NSRRC): 17C.

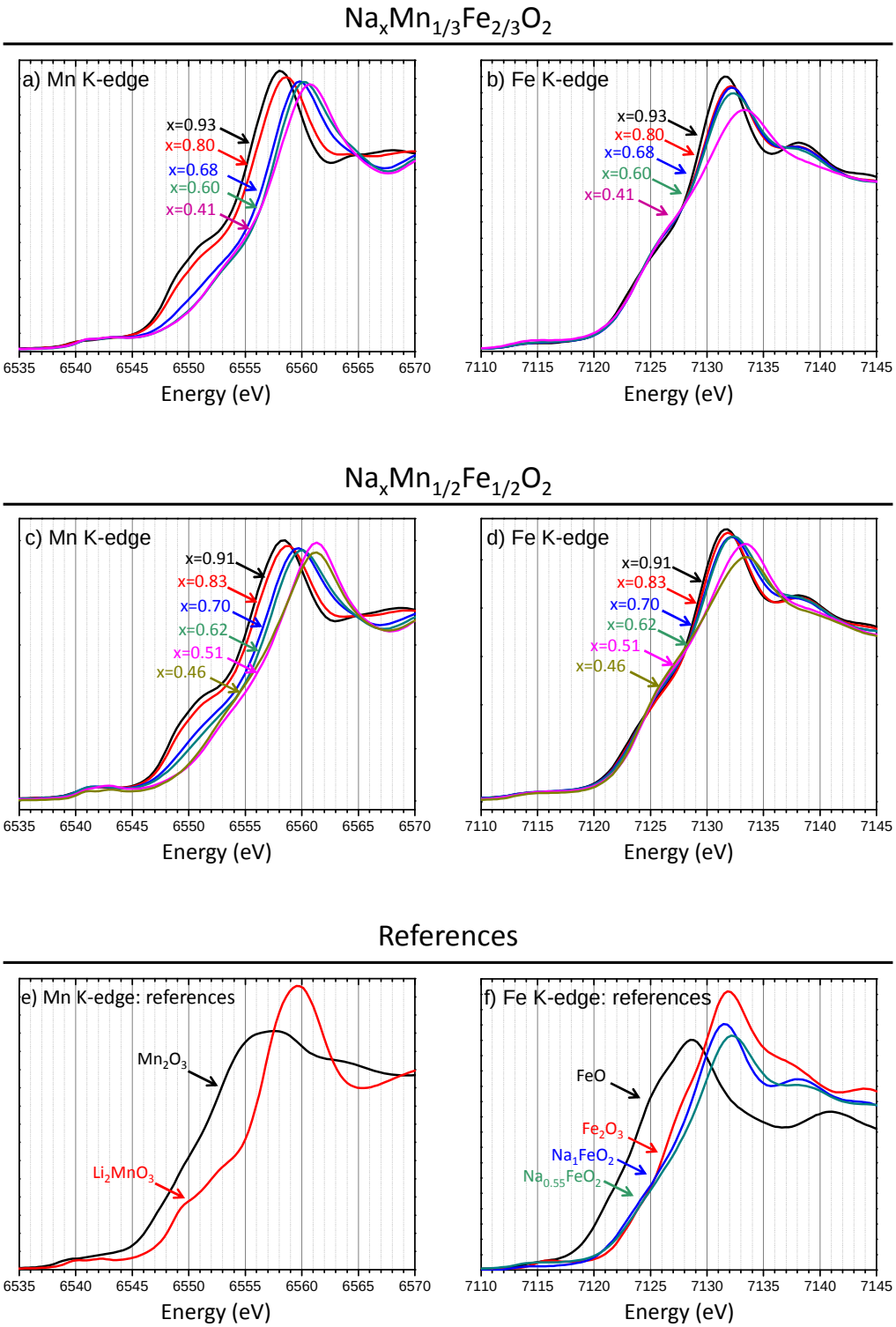

Figure A-II.26: *Operando In situ* X-ray Absorption Near Edge Spectroscopy (XANES) spectra corresponding to the Mn and Fe K-edges and recorded during the charge of the (a,b) Na//$Na_xMn_{1/3}Fe_{2/3}O_2$ and (c,d) Na//$Na_xMn_{1/2}Fe_{1/2}O_2$ cells. The Mn references for Mn^{3+} (Mn_2O_3) and Mn^{4+} (Li_2MnO_3) are given in (e). The Fe references for Fe^{2+} (FeO), Fe^{3+} (Fe_2O_3, $NaFeO_2$) and $Fe^{3.45+}$ ($Na_{0.55}FeO_2$) are given in (f).

A-II.3.b. ^{57}Fe Mössbauer spectroscopy study

To monitor the activity of the Fe^{4+}/Fe^{3+} redox couple during the electrochemical cycling, ^{57}Fe Mössbauer spectroscopy was performed on both systems. As the $Na_xMn_{1/3}Fe_{2/3}O_2$ one exhibits the higher Fe content, its Mössbauer study was performed *in situ* and constituted a reference for other experiments. Because of the important time that an *in situ* ^{57}Fe Mössbauer experiment requires (≈ 1 month) the study of the $Na_xMn_{1/2}Fe_{1/2}O_2$ system was performed *ex situ*.

In situ ^{57}Fe Mössbauer spectroscopy study of the $Na_xMn_{1/3}Fe_{2/3}O_2$ system

The Mössbauer spectrum of the O3-$Na_{0.77}Mn_{1/3}Fe_{2/3}O_2$ pristine material was first recorded as shown on top of **Figure A-II.27**. It exhibits a quadrupole doublet that can be fitted by a Lorentzian profile. The fit of the spectrum necessitates two Fe sites (**Table A-II.7**). The corresponding isomeric shifts are typical of high spin (HS) Fe^{3+} ions in octahedral sites and so the sites were labelled as Fe^{3+} (A) and Fe^{3+} (B). These two sites are represented by the blue and green lines in **Figure A-II.27**. The higher value of the quadrupole splitting for the Fe^{3+} (A) site (Δ = 0.88 mm.s^{-1}) indicates that the local environment of the FeO_6 octahedron is more impacted by the surrounding disorder than the Fe^{3+} (B) site (Δ = 0.58 mm.s^{-1}). The populations (P) give a majority of the Fe^{3+} (B) site (75%). In the literature, Yabuuchi et al. also used two Fe^{3+} sites to fit the spectrum of P2-$Na_{2/3}Mn_{1/2}Fe_{1/2}O_2$ [26]. Thorne et al. used two Fe^{3+} sites and a Fe^{4+} one to fit the spectra of P2/O3-$Na_xMn_{1-x}Fe_xO_2$ phases. However, the population of the Fe^{4+} in their Mössbauer studies is inferior to 2 % for most of the materials [28].

We then conducted the *in situ* Mössbauer study. The spectra of the $Na_xMn_{1/3}Fe_{2/3}O_2$ phases were recorded for selected sodium contents: x = 0.96, 0.85, 0.67, 0.58 and 0.38 during charge, following an initial discharge, and after a negligible residual current was observed for each composition. The recorded spectra are shown in **Figure A-II.27b**. As one can see, there is no significant variation of the peak positions for $0.96 \geq x \geq 0.67$ as highlighted in **Figure A-II.28a**. On the opposite, there is a significant shift of the peak positions to lower velocity values for $x \leq 0.58$ as highlighted in **Figure A-II.28b**. This indicates a change in the oxidation state of the Fe^{3+} ions.

As for the pristine material, all spectra exhibit a quadrupole doublet whose asymmetry and FWHM increase as sodium is removed from the structure (**Figure A-II.27b**).

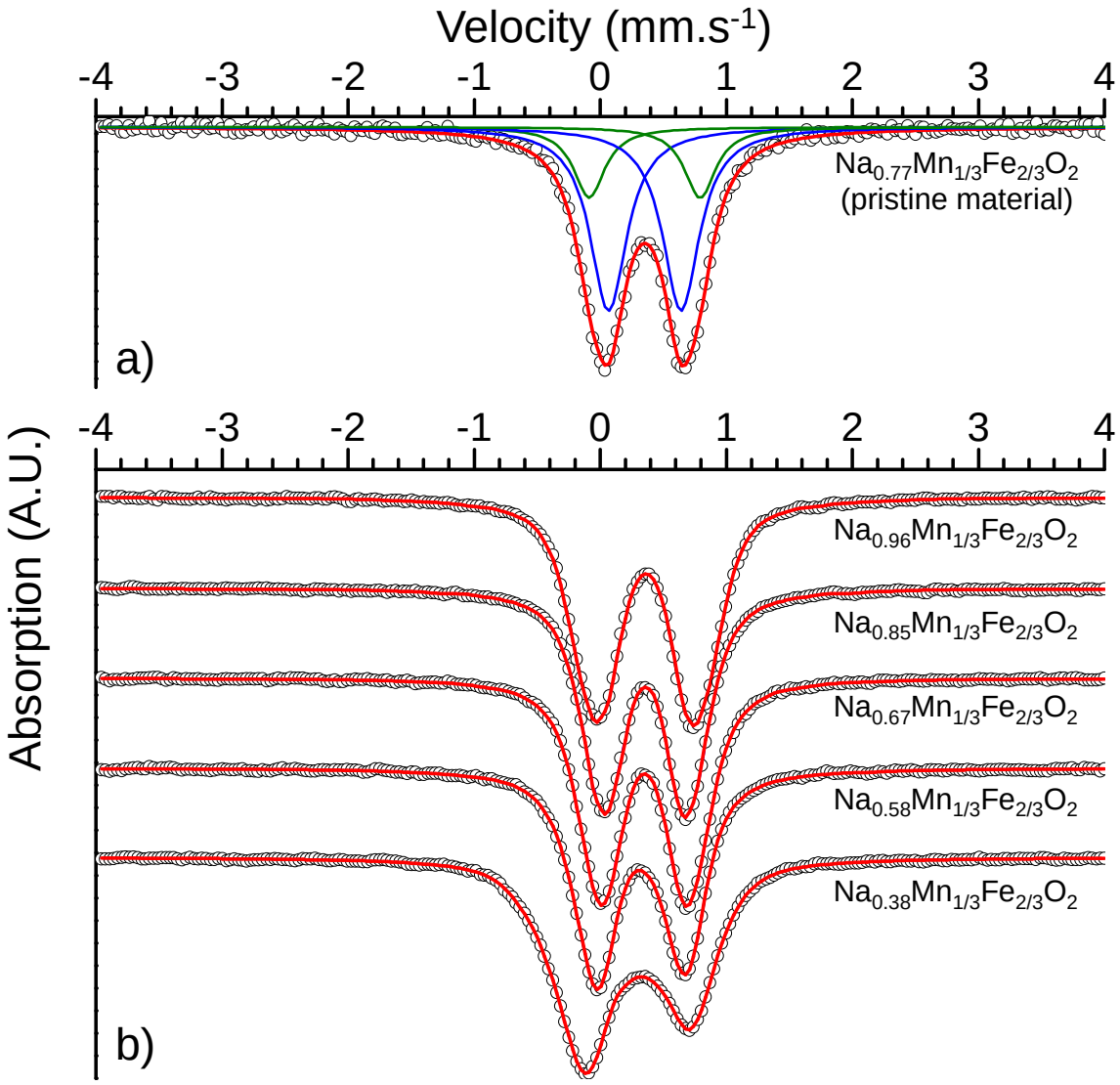

Figure A-II.27: ^{57}Fe Mössbauer spectra (a) of the pristine material and (b) recorded *in situ* during the charge of a $Na_xMn_{1/3}Fe_{2/3}O_2$ //Na battery. Black circles: experimental and red lines: calculated.

Site	δ (mm.s^{-1})	FWHM (mm.s^{-1})	Δ (mm.s^{-1})	P (%)
Fe^{3+}(A)	0.353	0.30	0.88	25
Fe^{3+}(B)	0.354	0.35	0.58	75

Table A-II.7: Mössbauer parameters corresponding to the spectrum of the O3-$Na_{0.77}Mn_{1/3}Fe_{2/3}O_2$ pristine material.

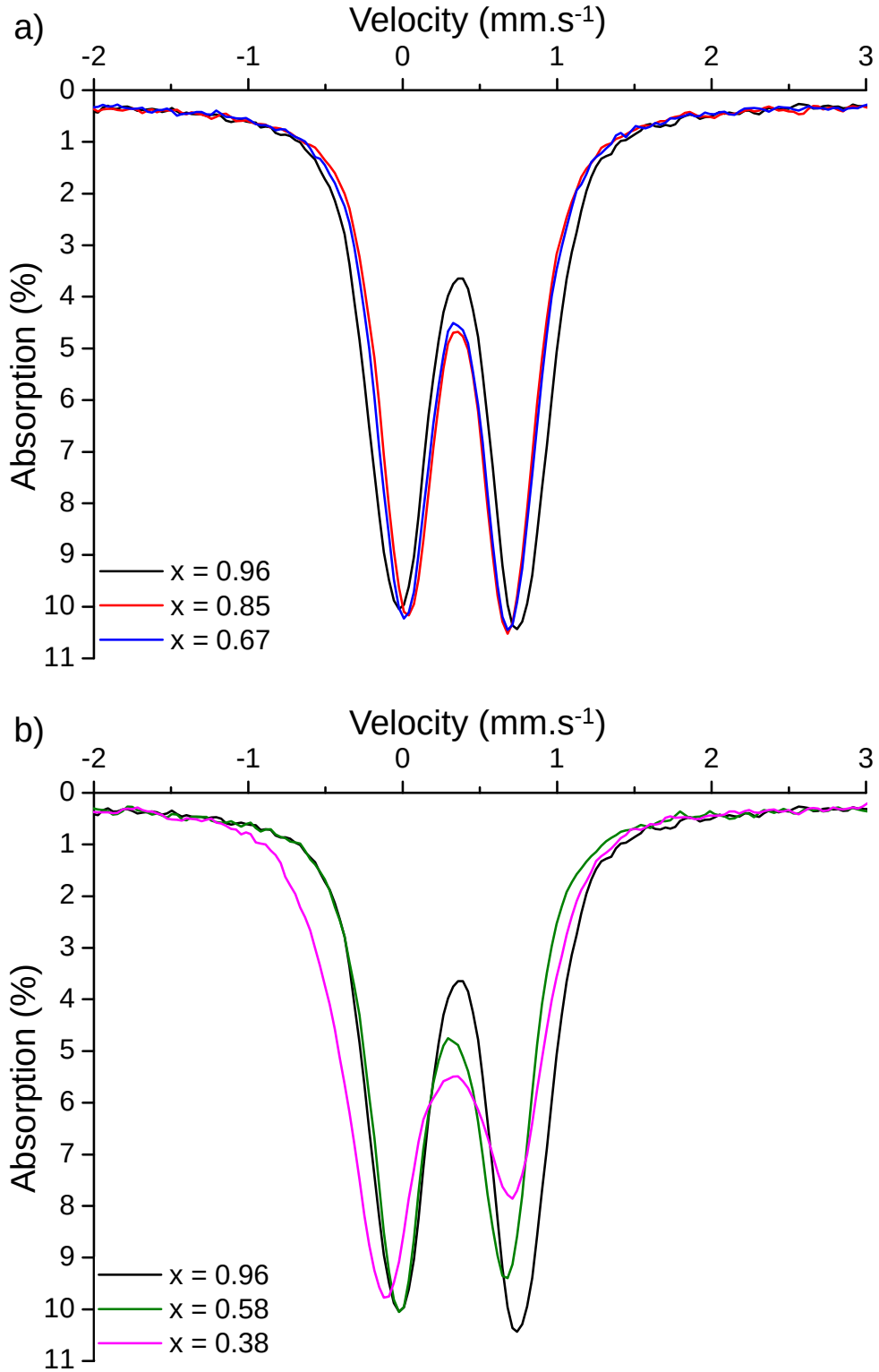

Figure A-II.28: Superposition of different Mössbauer spectra in the $Na_xMn_{1/3}Fe_{2/3}O_2$ system: (a) x = 0.96 (black line), x = 0.86 (red line) and x = 0.67 (blue line) compositions and (b) x = 0.96 (black line), x = 0.58 (green line) and x = 0.38 (pink line) compositions.

A preliminary refinement using Lorentzian profile lines gives the number of Fe^{n+} sites involved for each composition, as reported in **Table A-II.8**. For $0.67 \leq x < 1$, two Fe^{3+} sites ($\delta \approx 0.34 – 0.37$ mm.s^{-1}) are required to describe the spectra. As they do not show an important shift upon deintercalation, one can conclude that the Fe^{3+} ions are not involved in the redox process at low voltage and that only the Mn^{3+} are oxidized upon Na^+ deintercalation. For $x < 0.67$, we note the appearance of the Fe^{4+} ($\delta \approx 0$ mm.s^{-1}) and $Fe^{(3+z)+}$ ($\delta \approx 0.10 – 0.18$ mm.s^{-1}) sites, confirming that the Fe^{3+} ions are oxidized at high voltage.

We observe an important broadening of the FWHM of the spectra upon deintercalation from x = 0.96 to x = 0.38. This observation is coherent with the appearance of new Fe^{n+} sites. It also suggests an increasing disorder in the material upon Na^+ deintercalation. To take into account this phenomenon a second calculation has been realized based on fixed isomer shifts deduced from the Lorentzian profile type refinement. The FWHM values have been fixed to 0.20 for the x = 0.96 and 0.85 samples; 0.25 for the x = 0.67 sample and 0.30 for the x = 0.58 and 0.38 ones to take into account the increasing disorder in the material. From these distribution fittings, we determined the average quadrupole splitting (Δ^*) and the population of the different iron sites which are presented in **Table A-II.8** along with the developed formula and awaited Fe^{n+} populations. The quadrupole splitting of the maxima of the distribution (Δ_{max}) is also given.

Awaited results from electrochemistry			Mössbauer results												
Developed formula	%Fe^{3+}	%Fe^{4+}	Fe^{3+} (1)			Fe^{3+} (2)							Δ_{max} ($mm.s^{-1}$)	%Fe^{3+}	%Fe^{4+}
			δ ($mm.s^{-1}$)	Δ* ($mm.s^{-1}$)	P (%)	δ ($mm.s^{-1}$)	Δ* ($mm.s^{-1}$)	P (%)							
$Na_{0.96}Mn^{3+}_{0.29}Mn^{4+}_{0.04}Fe^{3+}_{0.67}Fe^{4+}_{0}O_2$	100	0	0.355	1.00	40	0.365	0.71	60					0.93	100	0
$Na_{0.85}Mn^{3+}_{0.15}Mn^{4+}_{0.18}Fe^{3+}_{0.67}Fe^{4+}_{0}O_2$	100	0	0.351	0.81	39	0.360	0.61	61					0.80	100	0
$Na_{0.67}Mn^{3+}_{0}Mn^{4+}_{0.33}Fe^{3+}_{0.67}Fe^{4+}_{0}O_2$	100	0	0.341	0.78	41	0.360	0.67	59					0.67	100	0
Developed formula	%Fe^{3+}	%Fe^{4+}	Fe^{3+}			Fe^{4+}			$Fe^{(3+z)+}$				Δ_{max} ($mm.s^{-1}$)	%Fe^{3+}	%Fe^{4+}
			δ ($mm.s^{-1}$)	Δ* ($mm.s^{-1}$)	P (%)	δ ($mm.s^{-1}$)	Δ* ($mm.s^{-1}$)	P (%)	δ ($mm.s^{-1}$)	Δ* ($mm.s^{-1}$)	P (%)	Repartition between			
												Fe^{3+} (%)	Fe^{4+} (%)		
$Na_{0.58}Mn^{3+}_{0}Mn^{4+}_{0.33}Fe^{3+}_{0.58}Fe^{4+}_{0.09}O_2$	87	13	0.336	0.70	78	0.04	0.19	3	0.175	0.68	19	9	10	0.70	87	13
$Na_{0.38}Mn^{3+}_{0}Mn^{4+}_{0.33}Fe^{3+}_{0.38}Fe^{4+}_{0.29}O_2$	57	43	0.321	0.87	57	0.048	0.55	24	0.107	0.77	19	4	15	0.87	61	39

Table A-II.8: Developed formulas, awaited Fe^{n+} populations and Mössbauer parameters corresponding to the fit of the spectra presented in **Figure A-II.27b** for the $Na_xMn_{1/3}Fe_{2/3}O_2$ system. The standard deviations on the isomer shift values are equal to 0.002 $mm.s^{-1}$. The population of the $Fe^{(3+z)+}$ is distributed into the Fe^{3+} and Fe^{4+} sites by the formula: $P(Fe^{3+}) = (\delta(Fe^{3+z})-\delta(Fe^{4+})) / (\delta(Fe^{3+})-\delta(Fe^{4+}))$.

The results can be separated in two groups, depending on the active redox process: $Mn^{3+} \rightarrow Mn^{4+}$ ($x \geq 2/3$) and $Fe^{3+} \rightarrow Fe^{4+}$ ($x < 2/3$). The spectra corresponding to the x = 0.96, 0.85 and 0.67 samples are quite similar as shown in **Figure A-II.28a** and can be fitted using two Fe^{3+} sites, as for the pristine material. These sites are labelled as Fe^{3+} (1) and Fe^{3+} (2) to avoid any confusion with the sites deduced from the Lorentzian fit. The associated signals correspond to doublets which show very close isomer shifts (δ = 0.355 $mm.s^{-1}$ and 0.365 $mm.s^{-1}$ for the x = 0.96 composition). The quadrupole splitting Δ^* values of the two Fe^{3+} sites corresponding to the O'3 phase (x = 0.96) are quite different from each other (Δ^* = 1.00 $mm.s^{-1}$ and 0.71 $mm.s^{-1}$ for the Fe^{3+} (1) and Fe^{3+} (2) sites respectively). As the Δ^* parameter is directly correlated to the deformation of the FeO_6 site, the high Δ^* value for the Fe^{3+} (1) site indicates that it is the most impacted by the cooperative Jahn-Teller effect of the surrounding Mn^{3+} ions. Moreover, when the structure evolves from O'3 to O3, the Δ^* value of the Fe^{3+} (1) site decreases continuously indicating it is also the most impacted by the $Mn^{3+} \rightarrow Mn^{4+}$ redox reaction. In the meantime, the Δ^* value of the Fe^{3+} (2) site does not show any evolution. Therefore, we can conclude that the Fe^{3+} (1) site corresponds to a local Fe environment mostly surrounded by Mn^{n+} ions (even though there is a distribution of environments) while the Fe^{3+} (2) site corresponds to a local Fe environment mostly surrounded by other Fe^{3+} ions (including also a distribution of environments). The populations of these two sites give an average Fe^{3+} (1) : Fe^{3+} (2) ratio of 40 : 60 and is maintained in the $0.96 \geq x \geq 0.67$ range. In the same Na range, the isomeric shift (δ) values decreases, upon Na^+ deintercalation (from 0.355 $mm.s^{-1}$ to 0.341 $mm.s^{-1}$ for Fe^{3+} (1) and from 0.365 $mm.s^{-1}$ to 0.360 $mm.s^{-1}$ for Fe^{3+} (2)), in agreement with the increase of the Mn average oxidation state in the nearby Fe^{3+} ion area.

For lower sodium contents ($x < 0.67$) all the Mn^{3+} ions have been oxidized to Mn^{4+} according to the XANES measurements and the active redox process is now $Fe^{3+} \rightarrow Fe^{4+}$. The Mössbauer spectra of the x = 0.58 and x = 0.38 phases can be fitted using three Fe^{n+} sites. The first one shows an isomer shift of 0.336 – 0.321 $mm.s^{-1}$ (depending on the Na content) and is attributed to the HS-Fe^{3+} ions in octahedral environments. The second one is characterized by an isomer shift close to 0 $mm.s^{-1}$, typical of the Fe^{4+} ion in octahedral environment, as also observed in other oxides, in the High Spin [121] or Low Spin [122, 123] states. The spin state in our compounds has not yet been established. The existence of the Fe^{3+} and Fe^{4+} sites was predictable, based on the charge compensation in the material and was already investigated in the Na_xFeO_2 phase diagram by Takeda [35] and in the P2-$Na_xMn_{1/2}Fe_{1/2}O_2$ phase [26, 28]. Confirming the developed formulae in **Table A-II.8**, the population of the Fe^{4+} site increases as the one of the Fe^{3+} site decreases upon Na^+ deintercalation. The third site shows an intermediate isomer shift between $Fe^{3+}$and Fe^{4+}. We associated this site to an intermediate $Fe^{(3+z)+}$ oxidation state that can result from fast electron hopping between the Fe^{3+} and Fe^{4+} ions, as already observed in the $Li_xNi_{0.70}Fe_{0.15}Co_{0.15}O_2$ system [121] and

in the $Ni_{1-y}Fe_yOOH_x$ / $Ni_{1-y}Fe_y(OH)_2$ one, both *ex* [122] and *in situ* [123]. This intermediate $Fe^{(3+z)+}$ oxidation state can be separated into the Fe^{3+} and Fe^{4+} ones considering that the sum of the populations of the involved Fe^{3+} and Fe^{4+} sites is equal to one and using the following formula: $P(Fe^{3+}) = (\delta(Fe^{3+z})-\delta(Fe^{4+})) / (\delta(Fe^{3+})-\delta(Fe^{4+}))$, where $P(Fe^{3+})$ is the population of the involved Fe^{3+} ions. The repartition of the population of the $Fe^{(3+z)+}$ site into the Fe^{3+} and Fe^{4+} ones is given in **Table A-II.8**. We observe good agreement between the material compositions deduced from the Mössbauer data ($Na_{0.58}Mn_{1/3}Fe_{2/3}O_2$ and $Na_{0.40}Mn_{1/3}Fe_{2/3}O_2$) and the ones deduced by electrochemistry ($Na_{0.58}Mn_{1/3}Fe_{2/3}O_2$ and $Na_{0.38}Mn_{1/3}Fe_{2/3}O_2$, respectively). Furthermore, the Δ* values between the two samples increase significantly as Na^+ is removed from the system, and especially for the Fe^{4+} site (Δ* = 0.19 $mm.s^{-1}$ and 0.55 $mm.s^{-1}$ for the x = 0.58 and x = 0.38 compositions respectively), indicating an increasing disorder inside the material from the x= 0.58 to the x = 0.38 compositions. This statement is in agreement with the *in situ* XRPD results which showed the coexistence of two phases: P3 (majority) and O3* (minority).

The Mössbauer results obtained on the $Na_xMn_{1/3}Fe_{2/3}O_2$ system show that the $Mn^{4+/3+}$ and $Fe^{4+/3+}$ redox couples are successively involved during the electrochemical deintercalation in agreement with the electrochemical results which show a sudden voltage increase for x = 2/3.

Ex situ ^{57}Fe Mössbauer spectroscopy study of the $Na_xMn_{1/2}Fe_{1/2}O_2$ system

No Mössbauer spectrum was recorder for the pristine material as it involves two different phases (mixture of O3 and O'3). Several compositions were prepared by the potentiostatic route on pellets consisting of Carbon Black and Active Material. The targeted compositions were x = 0.95 (E = 1.5 V, ≈ 100 % Mn^{3+}, O'3 structure), x = 0.67 (E = 2.56 V, O3 structure), x = 0.55 (middle of the voltage jump (E = 2.97 V), ≈ 100 % Mn^{4+}), x = 0.44 (E = 3.7 V) and x = 0.22 (E = 4.0 V). The spectra corresponding to these compositions are shown in **Figure A-II.29** and are compared altogether in **Figure A-II.30**. All spectra exhibit a quadrupole doublet. As for the study carried out on the $Na_xMn_{1/3}Fe_{2/3}O_2$ system, the spectra can be separated into two groups depending if Fe^{3+} ions are involved or not in the oxidation processes. The preliminary fit using a Lorentzian profile shows that Fe^{3+} ions are not involved in the redox process for 0.5 ≤ x < 1.0 (**Figures A-II.29a-c**) and are partially oxidized for x < 0.55 (**Figures A-II.29d-e**).

The spectrum of the almost fully intercalated phase (**Figure A-II.29a**) exhibits a higher FWHM than the spectra recorded for x = 0.67 and x = 0.55. This is a consequence of the reduction of the Mn^{4+} ions, which induce the cooperative Jahn-Teller effect responsible of the monoclinic distortion in O'3-$Na_{0.95}Mn_{1/2}Fe_{1/2}O_2$.

The spectra recorded for the x = 0.44 and x = 0.22 materials exhibit an increasing broadening upon deintercalation. An increasing dissymmetry is also observed on the low-velocity side of the spectra, induced by the appearance of Fe^{4+} ions. These two phenomenons indicate an increase of the disorder in the material, in agreement with the *operando in situ* XRPD experiment (increasing number of stacking faults to form the "X" phase and presence of an intermediate phase).

All spectra were fitted by a Lorentzian of distribution fit. In the Mn^{3+} → Mn^{4+} activity range, the spectra corresponding to the x = 0.95, 0.67 and 0.55 composition require two sites to be fitted. The associated isomeric shifts are comprised between 0.338 and 0.345 $mm.s^{-1}$ and therefore correspond to Fe^{3+} ions in an octahedral FeO_6 environment. These sites are labeled Fe^{3+}(A) and Fe^{3+}(B) in **Table A-II.9**. If the quadrupole splitting values associated to the two sites are quite similar from x = 0.95 to x = 0.55 ($\Delta_{Fe3+(A)}$ = 0.86 – 0.96 $mm.s^{-1}$ and $\Delta_{Fe3+(B)}$ = 0.62– 0.64 $mm.s^{-1}$), the FWHM values are higher for the x = 0.95 material ($\Gamma_{Fe3+(A)}$ = 0.37 $mm.s^{-1}$ and $\Gamma_{Fe3+(B)}$ = 0.33 $mm.s^{-1}$) than for the x = 0.67 and x = 0.55 ones ($\Gamma_{Fe3+(A)}$ ≈ 0.32 $mm.s^{-1}$ and $\Gamma_{Fe3+(B)}$ ≈ 0.28 $mm.s^{-1}$). As previously explained this broadening is the consequence of the cooperative Jahn-Teller effect induced by the important amount of Mn^{3+} ions (≈ 45 % of the total transition metal ions amount).

The spectra recorded when the Fe^{3+} → Fe^{4+} redox process is involved, for x = 0.44 and 0.22, exhibit an increasing FWHM, implying an increase of the disorder. The spectra were fitted by a Lorentzian fit (x =

0.44 composition) or by a distribution one (x = 0.22). Independently of the fitting method three Mössbauer sites are required to successfully fit the spectra (**Table A-II.9**). The first one shows an isomer shift comprised between 0.336 and 0.35 $mm.s^{-1}$ and corresponds to the remaining HS Fe^{3+} ions. The second one shows an isomer shift close to 0 $mm.s^{-1}$ and is associated to Fe^{4+} ions. The third site is characterized by an intermediate shift comprised between 0.321 $mm.s^{-1}$ and 0.20 $mm.s^{-1}$ as Na^+ is deintercalated. This site is associated to the fast electron hopping phenomenon (Fe^{3+z} site) between Fe^{3+} and Fe^{4+}, as discussed previously for the Fe rich system. The increasing Δ and Δ* values along with Na^+ deintercalation for the $Fe^{(3+z)+}$ site (Δ = 0.72 $mm.s^{-1}$ → Δ* = 0.94 $mm.s^{-1}$) and Fe^{4+} one (Δ = 0.1 $mm.s^{-1}$ → Δ* = 0.64 $mm.s^{-1}$) confirm the increasing disorder in the material upon Na^+ deintercalation, according to our *operando in situ* XRPD study.

The repartition of the population of the $Fe^{(3+z)+}$ site between the Fe^{3+} and Fe^{4+} ones gives a Fe^{3+} : Fe^{4+} ratio equal to 95 : 5 (x = 0.44) and 68 : 32 (x = 0.22) and confirm the increasing amount of Fe^{4+} in the material upon Na^+ deintercalation. The difference between the formulae determined by Mössbauer spectroscopy ($Na_{0.47}Mn_{1/2}Fe_{1/2}O_2$ and $Na_{0.32}Mn_{1/2}Fe_{1/2}O_2$, respectively) and the ones determined by electrochemistry ($Na_{0.44}Mn_{1/2}Fe_{1/2}O_2$ and $Na_{0.22}Mn_{1/2}Fe_{1/2}O_2$, respectively) may result from an underestimation of the Na content, which lead to an overestimation of the Fe^{4+} one in the formulae determined from electrochemistry.

The Mössbauer results obtained on the $Na_xMn_{1/2}Fe_{1/2}O_2$ system show that the $Mn^{4+/3+}$ and $Fe^{4+/3+}$ redox couples are successively involved during the electrochemical deintercalation, as in the $Na_xMn_{1/3}Fe_{2/3}O_2$ system. This conclusion is in agreement with the electrochemical results which show a smooth voltage increase for $x \approx 1/2$.

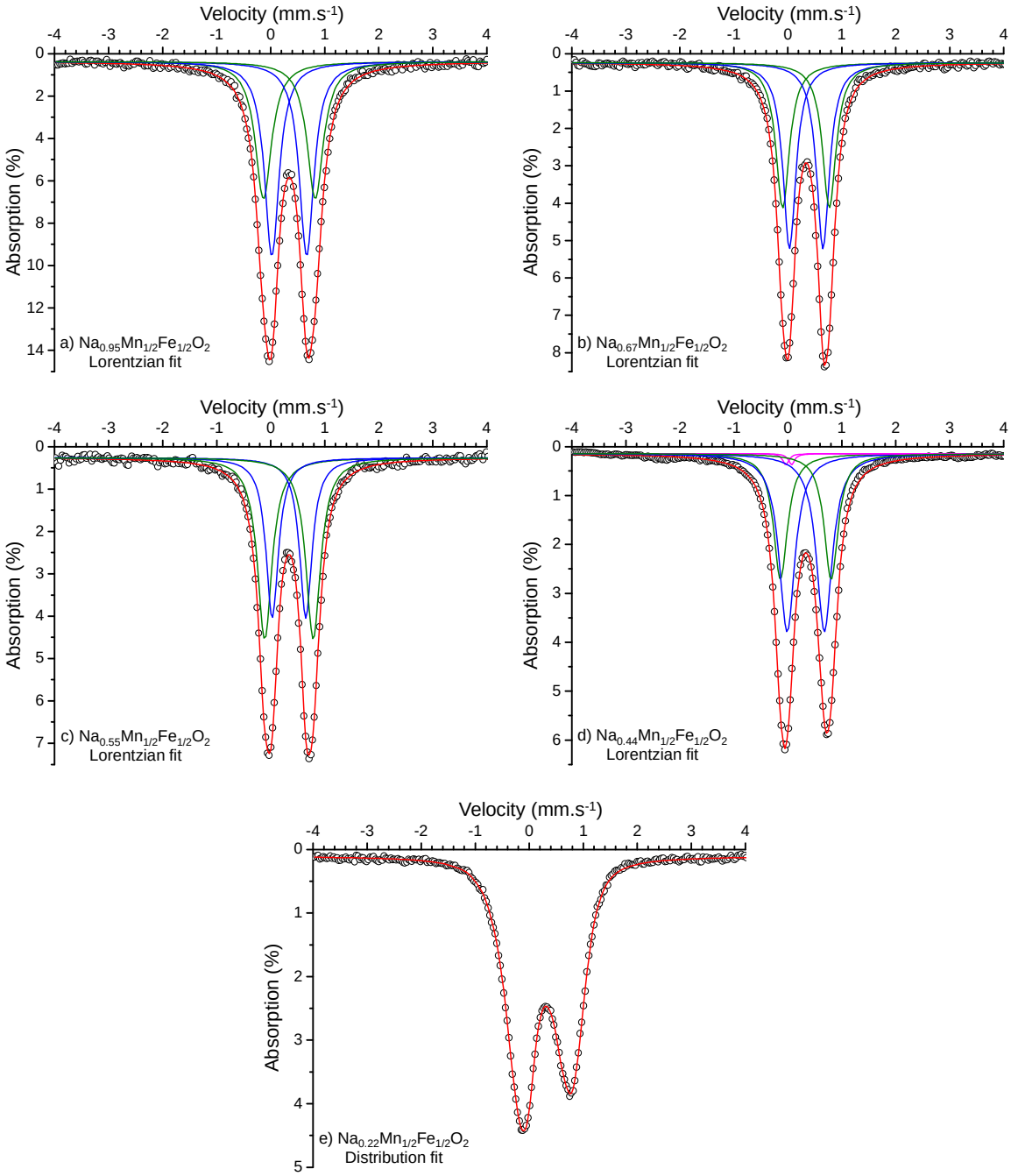

Figure A-II.29: ^{57}Fe Mössbauer spectra recorded *ex situ* for the $Na_xMn_{1/2}Fe_{1/2}O_2$ system at the (a) x = 0.95, (b) x = 0.67, (c) x = 0.55, (d) x = 0.44 and (e) x = 0.22 compositions. Black circles: experimental and red lines: calculated. The different Mössbauer sites deduced from the Lorentzian fittings are represented by the blue, pink and green lines.

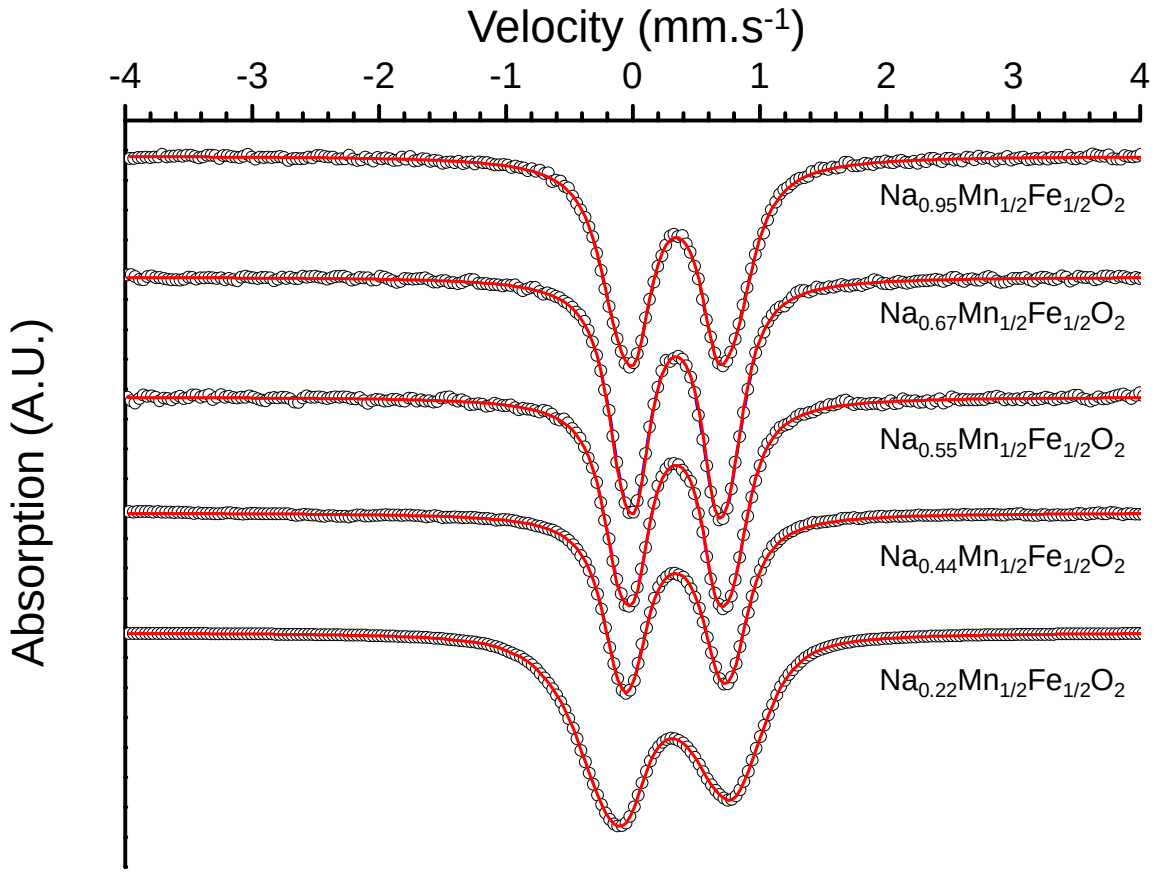

Figure A-II.30: Comparison of the Mössbauer spectra recorded for the $Na_xMn_{1/2}Fe_{1/2}O_2$ system. Black dots: experimental and red line: calculated.

Awaited results from electrochemistry			Mössbauer results (Lorentzian fit)															
Developed formula	%Fe^{3+}	%Fe^{4+}	Fe^{3+}(A)				Fe^{3+} (B)										%Fe^{3+}	%Fe^{4+}
			δ ($mm.s^{-1}$)	Δ ($mm.s^{-1}$)	Γ ($mm.s^{-1}$)	P (%)	δ ($mm.s^{-1}$)	Δ ($mm.s^{-1}$)	Γ ($mm.s^{-1}$)	P (%)								
$Na_{0.95}Mn^{3+}_{0.45}Mn^{4+}_{0.05}Fe^{3+}_{0.50}Fe^{4+}_{0}O_2$	100	0	0.345	0.96	0.37	44	0.344	0.64	0.33	56							100	0
$Na_{0.67}Mn^{3+}_{0.17}Mn^{4+}_{0.33}Fe^{3+}_{0.50}Fe^{4+}_{0}O_2$	100	0	0.338	0.86	0.31	46	0.343	0.62	0.29	54							100	0
$Na_{0.55}Mn^{3+}_{0.05}Mn^{4+}_{0.45}Fe^{3+}_{0.50}Fe^{4+}_{0}O_2$	100	0	0.339	0.90	0.33	57	0.340	0.62	0.28	43							100	0

Developed formula	%Fe^{3+}	%Fe^{4+}	Fe^{3+}				Fe^{4+}				$Fe^{(3+z)+}$						%Fe^{3+}	%Fe^{4+}
			δ ($mm.s^{-1}$)	Δ ($mm.s^{-1}$)	Γ ($mm.s^{-1}$)	P (%)	δ ($mm.s^{-1}$)	Δ ($mm.s^{-1}$)	Γ ($mm.s^{-1}$)	P (%)	δ ($mm.s^{-1}$)	Δ ($mm.s^{-1}$)	Γ ($mm.s^{-1}$)	P (%)	Repartition between			
															Fe^{3+} (%)	Fe^{4+} (%)		
$Na_{0.44}Mn^{3+}_{0}Mn^{4+}_{0.50}Fe^{3+}_{0.44}Fe^{4+}_{0.06}O_2$	88	12	0.336	0.94	0.31	37	0.03	0.1	0.24	2	0.321	0.72	0.24	61	58	3	95	5

Mössbauer results (Distribution fit)																		
Developed formula	%Fe^{3+}	%Fe^{4+}	Fe^{3+}				Fe^{4+}				$Fe^{(3+z)+}$						%Fe^{3+}	%Fe^{4+}
			δ ($mm.s^{-1}$)	Δ* ($mm.s^{-1}$)	Γ ($mm.s^{-1}$)	P (%)	δ ($mm.s^{-1}$)	Δ* ($mm.s^{-1}$)	Γ ($mm.s^{-1}$)	P (%)	δ ($mm.s^{-1}$)	Δ* ($mm.s^{-1}$)	Γ ($mm.s^{-1}$)	P (%)	Repartition between			
															Fe^{3+} (%)	Fe^{4+} (%)		
$Na_{0.22}Mn^{3+}_{0}Mn^{4+}_{0.50}Fe^{3+}_{0.22}Fe^{4+}_{0.28}O_2$	44	56	0.35	0.90	0.25	52	0.02	0.64	0.25	18	0.20	0.94	0.25	30	16	14	68	32

Table A-II.9: Developed formulas, awaited Fe^{n+} populations and Mössbauer parameters corresponding to the fit of the spectra of the $Na_xMn_{1/2}Fe_{1/2}O_2$ system presented in **Figure A-II.29**. The standard deviations on the isomer shift values are equal to 0.002 $mm.s^{-1}$. The population of the $Fe^{(3+z)+}$ is distributed into the Fe^{3+} and Fe^{4+} sites by the formula: $P(Fe^{3+}) = (\delta(Fe^{3+z})-\delta(Fe^{4+})) / (\delta(Fe^{3+})-\delta(Fe^{4+}))$.

A-II.4. Conclusion on the O3-based $Na_xMn_{1-y}Fe_yO_2$ systems

In this chapter were further investigated the electrochemical and structural properties of the O3-based $Na_xMn_{1-y}Fe_yO_2$ materials.

As mentioned in **Chapter A-I**, the O3-based systems exhibit worst electrochemical properties than the P2-based systems (poorer conductivity, inferior discharge capacity…). However, the electrochemical properties can be improved by increasing the Mn / Fe ratio from 1/2 to 1/1. This increase allows maintaining good discharge capacity in the 1.5 – 4.0 V range as 91 % of the second cycle discharge capacity are still reached for the $Na_xMn_{1/2}Fe_{1/2}O_2$ system *vs.* 74 % for the $Na_xMn_{1/3}Fe_{2/3}O_2$ one, after 29 cycles.

In situ XRPD during the charge of Na-cells showed that the O3-based materials undergo a series of structural transitions: O'3 → O3 → P3 → "X" from the fully intercalated state to the deintercalated ones (up to 4.3 V). However, several residual phases of unknown origin are observed simultaneously to the O3 and P3 domains. We suggested that these residual phases could result from (i) the coexistence of particles with slightly different Mn / Fe ratios or (ii) the existence of particles with or without Mn vacancies.

Thanks to X-ray absorption spectroscopy and Mössbauer spectroscopy, we confirmed that the Mn^{3+} → Mn^{4+} redox process is active at low voltage and that the Fe^{3+} → Fe^{4+} one is active at high voltage, upon Na^+ deintercalation.

Chapter A-III: P2-$Na_{0.62}Mn_{1/2}Fe_{1/2}O_2$ and P2-$Na_{0.66}Mn_{2/3}Fe_{1/3}O_2$

Table of contents

In this chapter, the structural and electrochemical properties of the P2-based materials are investigated, first on the $Na_xMn_{1/2}Fe_{1/2}O_2$ system and then on the $Na_xMn_{2/3}Fe_{1/3}O_2$ one. The last part of this chapter focuses on the redox mechanisms involved upon Na deintercalation for both compositions.

A-III.1. The $Na_xMn_{1/2}Fe_{1/2}O_2$ system

A-III.1.a. Synchrotron X-ray and neutron powder diffraction studies of the pristine material

Synchrotron X-ray Powder Diffraction

The synchrotron XRPD[14] pattern of the P2-$Na_{0.67}Mn_{1/2}Fe_{1/2}O_2$ pristine material is shown in **Figure A-III.1** along with the calculated diagram resulting from the Rietveld refinement of the structure. The cell and atomic parameters corresponding to the Rietveld refinement are reported in **Table A-III.1**. The 2θ scale corresponding to the Cu $k\alpha_1$ radiation is given as a guide.

The pattern is refined in the hexagonal $P6_3/mmc$ space group, as expected for a P2 type phase. The refined cell parameters ($a_{hex.}$ = 2.9405(1) Å and $c_{hex.}$ = 11.1957(2) Å) are very close to those of the literature for the x = 0.67 composition [26]. The very good signal / noise ratio allows us to refine the occupation of the different Na sites along with the different isotropic ADPs. The overall sodium content is equal to 0.62(3), which is in good agreement with the targeted composition ($Na_{0.67}Mn_{1/2}Fe_{1/2}O_2$) and the formula determined by ICP-AES analysis ($Na_{0.66}Mn_{0.47}Fe_{0.53}O_2$). In the following, this material is designed as P2-$Na_{0.62}Mn_{1/2}Fe_{1/2}O_2$. The associated ADPs are equal to 1.8(7) and 1.9(4) Å² for the two sodium sites (Na_f and Na_e) respectively. These high values are due to the high mobility of sodium in layered phases. The occupancies of the transition metal and oxygen sites were fixed to 1.0 and the associated ADP show more usual values of 0.29(3) Å² (Fe and Mn in 2a site) and 0.7(1) Å² (O in 4f site). We also tried to refine the transition metal site occupancy as previous work on P2-$Na_{0.7}MnO_2$ materials showed that some transition metal vacancies could occur [5, 52, 114]. However, any attempt to include transition metal vacancies into the MO_2 slabs did not lead to significant improvement of the refinement.

[14] In collaboration with Dr. M. Suchomel, Argonne Photon Source, Argonne National Laboratory, IL, USA. Beamline: 11BM.

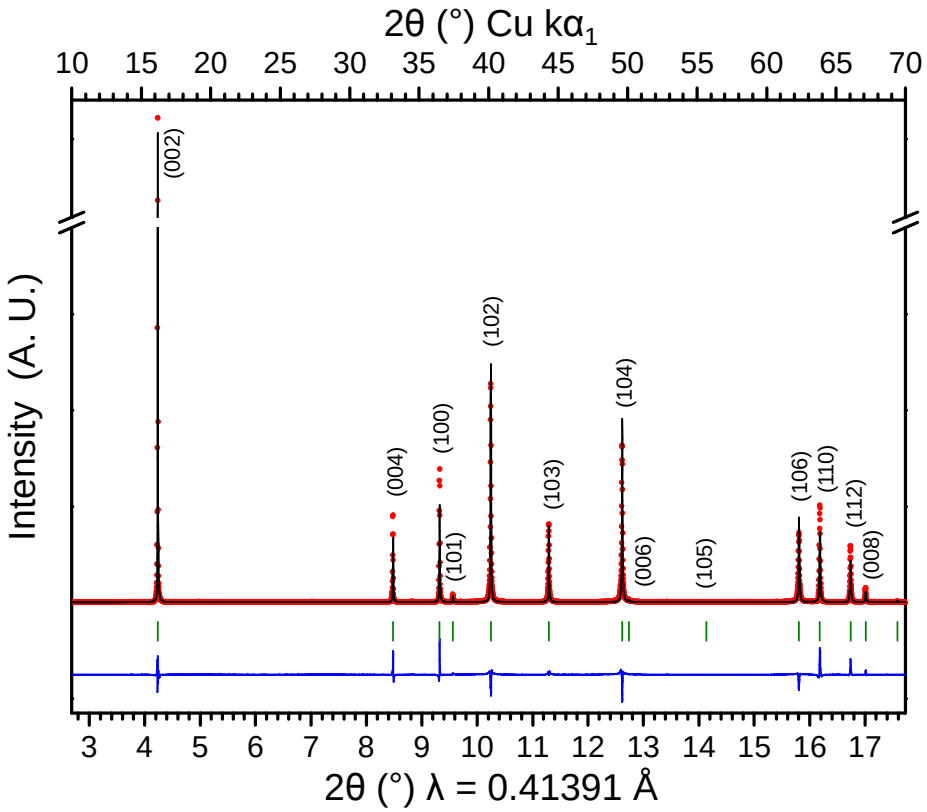

Figure A-III.1: Observed and calculated (Rietveld method) synchrotron XRPD patterns of P2-$Na_{0.62}Mn_{1/2}Fe_{1/2}O_2$. Red dots: experimental, black line: calculated, blue line: difference and green bars: Bragg positions.

Space group: **$P6_3/mmc$** $a_{hex.}$ = 2.9405(1) Å, $c_{hex.}$ = 11.1957(2) Å						
Atom	Wyckoff		Coordinates		Occupancy	ADP (Å²)
Na_f	2d	0	0	1/4	0.18(1)	1.8(7)
Na_e	2b	2/3	1/3	1/4	0.44(2)	1.9(4)
Mn	2a	0	0	0	1	0.29(3)
Fe	2a	0	0	0		
O	4f	1/3	2/3	0.093(1)	1	0.7(1)
Distances:	M-O		Na-O			
	6 * 1.99(1) Å		6 * 2.44(1) Å			
Rwp = 15.33%; R_B = 8.93%						

Table A-III.1: Structural parameters and reliability factors calculated from the synchrotron XRPD pattern of P2-$Na_{0.62}Mn_{1/2}Fe_{1/2}O_2$.

Neutron powder diffraction

Because of the 1:1 ratio between the $Mn^{3+/4+}$ and Fe^{3+} ions, we considered the possibility of an ordering within the transition metal layer and the material was studied by neutron diffraction at ILL[15].

The neutron powder diffraction pattern of the pristine material is shown in **Figure A-III.2**. As no superstructure peak appears on the neutron diffraction pattern, we concluded that P2-$Na_{0.62}Mn_{1/2}Fe_{1/2}O_2$ does not exhibit any long-range ordering between the transition metal ions. The structure of the material is refined from the XRPD and neutron diffraction data using Pseudo-Voigt functions to describe each pattern as shown in **Figure A-III.2**. The corresponding cell and atomic parameters are given in **Table A-III.2**. This combined refinement leads to a structure in very good agreement with the structural model obtained from synchrotron XRPD and gives a final content of 0.500(1) Fe and 0.500(1) Mn, in good agreement with the expected Mn : Fe ratio. The sodium content is equal to 0.60 and is very close to the one deduced by synchrotron XRPD (x = 0.62).

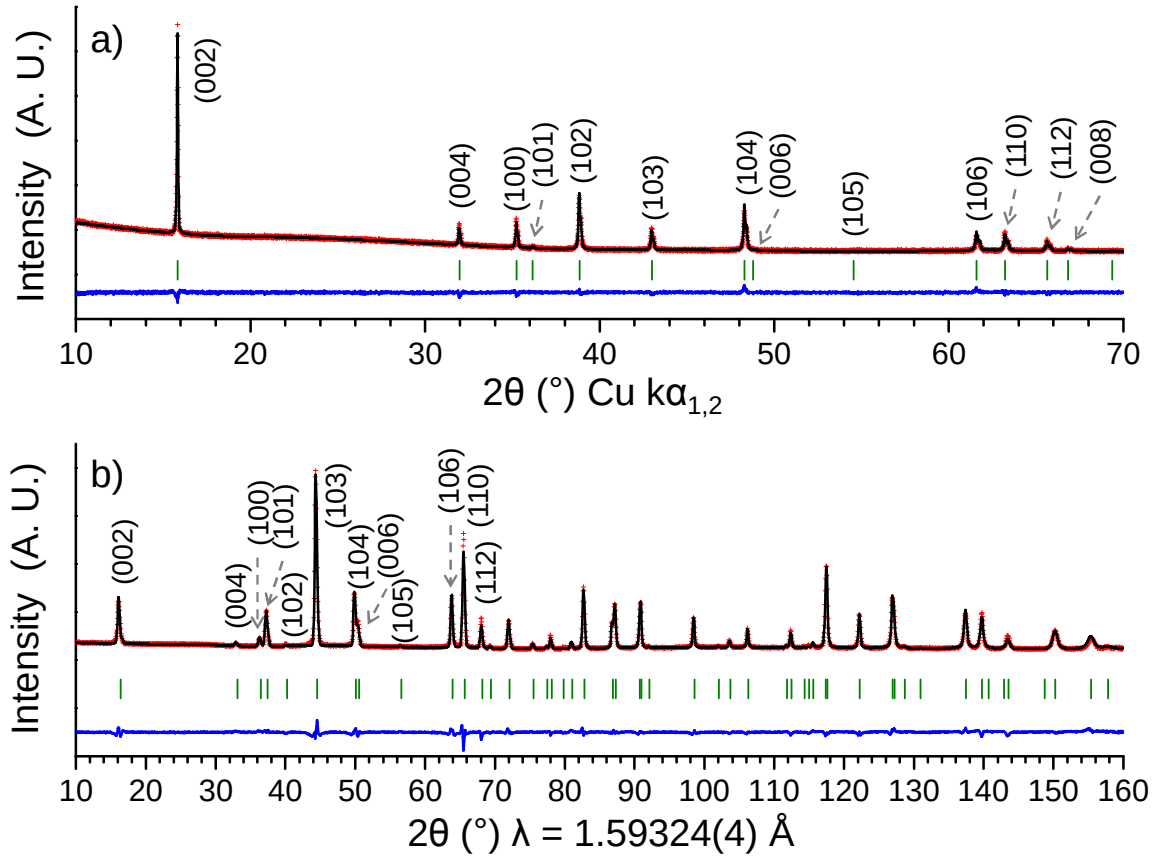

Figure A-III.2: Observed and calculated (Rietveld method) (a) XRPD and (b) neutron powder diffraction patterns of P2-$Na_{0.62}Mn_{1/2}Fe_{1/2}O_2$. Red crosses: experimental, black line: calculated, blue line: difference and green bars: Bragg positions.

[15] In collaboration with Dr. Suard, ILL, Grenoble, France. Beamline: D2B.

		XRPD			Neutron diffraction	
Cell parameters (S.G.: **$P6_3/mmc$**)	$a_{hex.}$ (Å)	2.9384(1)				
	$c_{hex.}$ (Å)	11.1888(2)				
Wavelength (Å)		Cu k$\alpha_{1,2}$			1.59309(5)	
Atomic parameters:		x	y	z	Occ	ADP (Å²)
	Na_f	0	0	1/4	0.19(3)	1.1(1)
	Na_e	2/3	1/3	1/4	0.41(3)	2.26(6)
	Mn (3a)	0	0	0	0.500(1)	0.34(2)
	Fe (3a)	0	0	0	0.500(1)	
	O (6c)	1/3	2/3	0.0921(1)	1.0	0.87(1)
R_{wp} (%)		2.15			4.89	
Global R_{wp} (%)		2.90				

Table A-III.2: Structural parameters and reliability factors calculated from the combined refinement of P2-$Na_{0.62}Mn_{1/2}Fe_{1/2}O_2$ from the XRPD and neutron powder diffraction patterns.

A-III.1.b. Electrochemistry

Influence of the cut-off voltage

The electrochemical properties of P2-$Na_{0.62}Mn_{1/2}Fe_{1/2}O_2$ as a positive electrode material in Na cells were studied in various potential ranges at C/20: 1.5 – 3.8 V (**Figure A-III.3a-b**), 1.5 – 4.0 V (**Figure A-III.3c-d**) and 1.5 – 4.3 V (**Figures A-III.3e-f**). The experiments started by a discharge and the first cycles are highlighted in red in **Figures A-III.3a**, **A-III.3c** and **A-III.3e**. The evolution of the shape of the E = f(x) curves at the 1st, 25th and 50th cycles are shown in **Figures A-III.3b**, **A-III.3d** and **A-III.3f**.

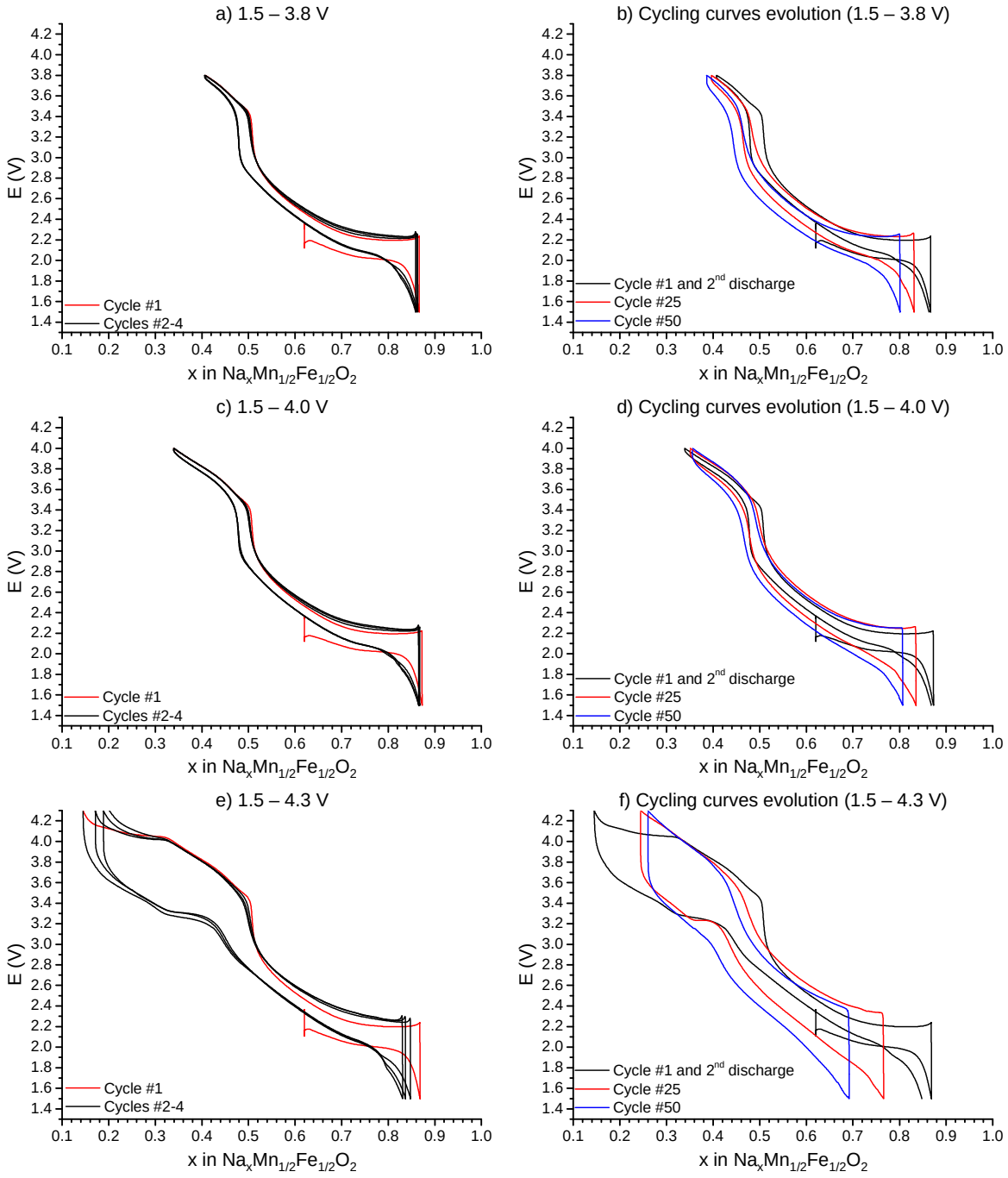

Figure A-III.3: Galvanostatic cycling curves associated to the $Na_xMn_{1/2}Fe_{1/2}O_2$ system and recorded (a,b) between 1.5 and 3.8 V, (c,d) between 1.5 and 4.0 V) and (e,f) between 1.5 and 4.3 V at C/20.

The shape of the E = f(x) curves are similar to those reported in the literature for the 1.5 – 3.8 V and 1.5 - 4.0 V ranges (**Figures A-III.3a** and **A-III.3c**) [26]. During the initial discharge from P2-$Na_{0.62}Mn_{1/2}Fe_{1/2}O_2$, a short voltage plateau is observed at ≈ 2.05 V, suggesting that a phase transition occurs at the end of the discharge. During Na deintercalation, the same plateau is observed at ≈ 2.2 V (thus reversible). Upon further deintercalation, the E = f(x) curves exhibit a solid solution behavior and undergo a sudden voltage jump at x ≈ 0.5. Note that the first cycle is always slightly different from the following ones. From the second cycle the cycling process is reversible and the cells exhibit quite a low polarization when cycled up to 3.8 or 4.0 V. When the upper cut-off voltage is increased to 4.3 V, a second plateau is observed at approximately 4.0 V. During the following discharge, this plateau is not visible anymore and instead an important increase of the polarization is observed. Then, once the cell voltage reaches 3.2 V during discharge, the process seems again fully reversible.

The importance of the upper cut-off voltage on the long-term electrochemical cycling is shown on **Figures A-III.3b**, **A-III.3d** and **A-III.3f**. When the cut-off voltage is set to 3.8 V (**Figure A-III.3a-b**) or 4.0 V (**Figure A-III.3c-d**), the 25th and 50th cycles do not show any significant evolution compared to the first cycle followed by the second discharge (the initial discharge is not considered), besides a progressive decrease of the capacity and a small increase of the polarization. On the other hand, when the cut-off voltage is set to 4.3 V (**Figure A-III.3e-f**), the shape of the cycling curves exhibit drastic evolutions upon cycling: i) the polarization of the curve increases, ii) a smoothing of the voltage jump at x = 0.5 is observed and iii) the 2nd plateau observed at ≈ 3.3 V in discharge decreases in length (x) at the 25th cycle and disappears at the 50th cycle. These changes in behavior result in a strong decrease of the capacity upon cycling: while 0.70 Na^+ ions per formula unit are reintercalated between the first charge and the second discharge, only 0.52 and 0.44 Na^+ ions are reversibly cycled in the 25th and 50th cycles respectively.

The evolution of the discharge capacity along with the cycle number for the different cut-off voltages was also studied and is shown in **Figure A-III.4**.

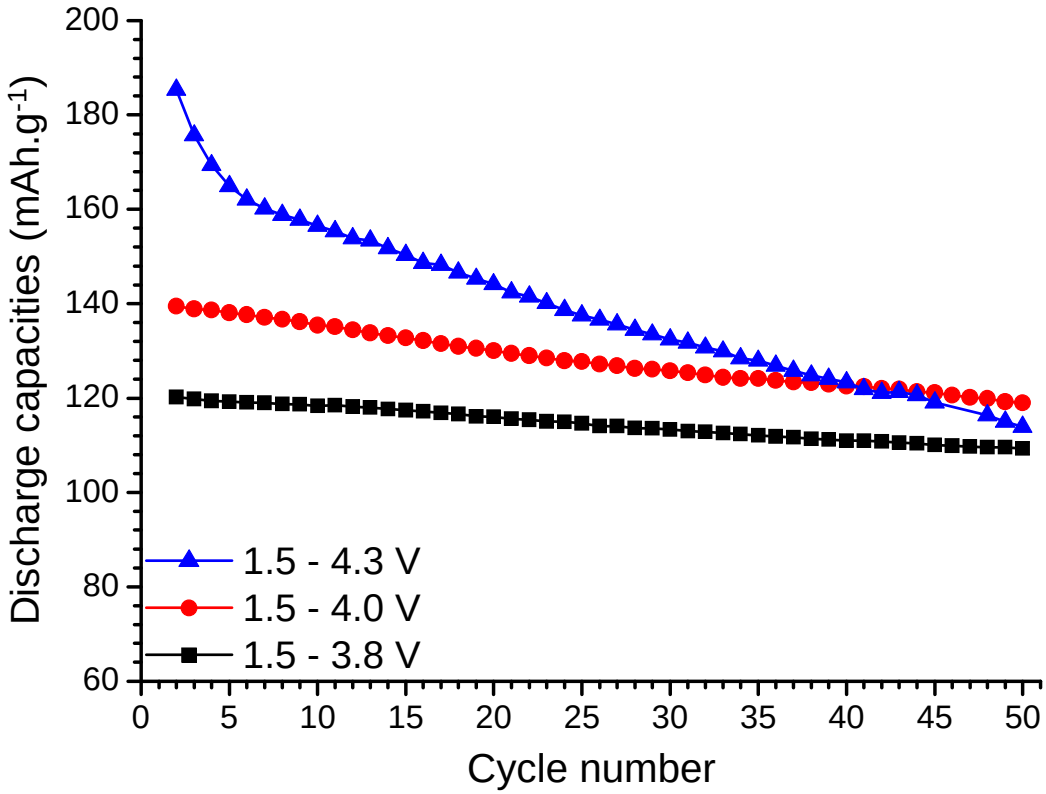

Figure A-III.4: Discharge capacities associated to the galvanostatic curves of the $Na_xMn_{1/2}Fe_{1/2}O_2$ system recorded in the different voltage ranges (**Figure A-III.3**).

Whereas the second cycle discharge capacities increase with the upper cut-off voltage (120 $mAh.g^{-1}$, 140 $mAh.g^{-1}$ and 185 $mAh.g^{-1}$ respectively for $E_{cut\text{-}off}$ = 3.8 V, 4.0 V and 4.3 V), the capacity retention at the 50th cycle is inversely proportional (91 %, 85 % and 60 % retention for $E_{cut\text{-}off}$ = 3.8 V, 4.0 V and 4.3 V respectively). One can observe that using a high 4.3 V cut-off voltage does not lead to a capacity improvement for long term cycling, since after about 40 cycles the capacity value of the cells with $E_{cut\text{-}off}$ = 4.0 V is reached (125 $mAh.g^{-1}$).

To have more insight about the reversibility of the cycling up to 4.3 V, another experiment was made: after three cycles in the 1.5 – 4.3 V range, the upper voltage limit was changed down to 4.0 V. The resulting galvanostatic curves are shown on **Figure A-III.5**.

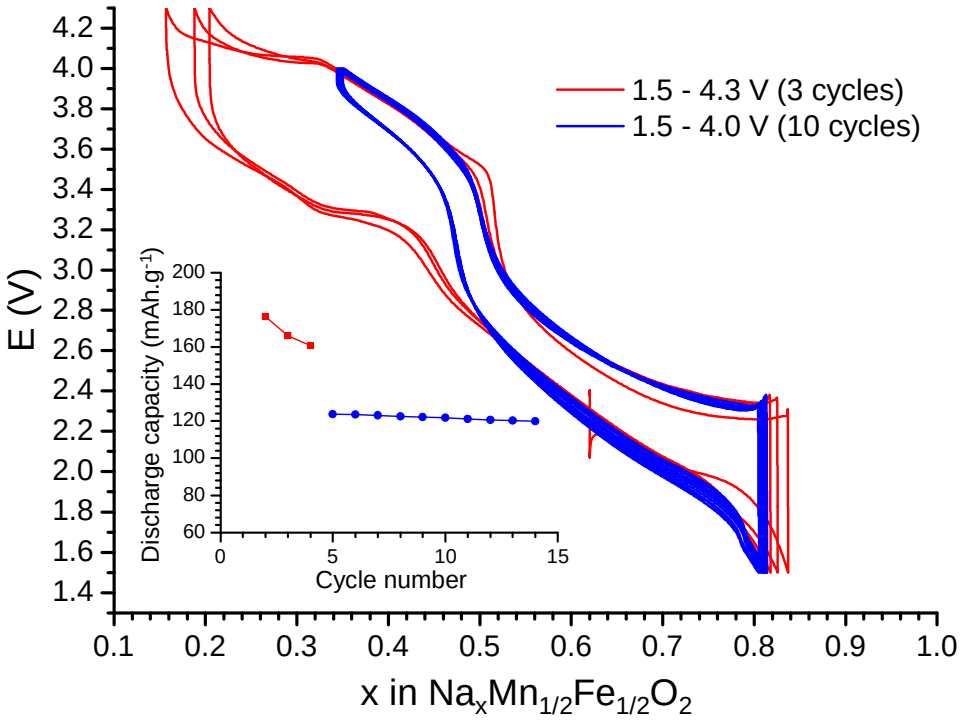

Figure A-III.5: Galvanostatic curves recorded at a C/20 rate between 1.5 – 4.3 V (in red) and then between 1.5 – 4.0 V (in blue) for the $Na_xMn_{1/2}Fe_{1/2}O_2$ system. The insert represents the evolution of the associated discharge capacities.

As shown in **Figure A-III.5** the shape of the curve is similar to the one obtained directly using the 1.5 – 4.0 V range (**Figure A-III.3c**). This result shows that the structural modification occurring above 4.0 V is completely reversible. It also shows that a significant amount of sodium has to be reintercalated to induce the reversible phase transition. The large polarization and the large hysteresis of the process show that a lot of energy is involved.

To better understand the impact of the upper cut-off voltage on the material, we realized a series of SEM micrographs of an un-cycled electrode (**Figure A-III.6a-b**) and of electrodes collected at ≈ 2.6 V after three cycles in the 2.0 – 4.0 V range (**Figure A-III.6c-d**) and in the 2.0 – 4.3 V one (**Figure A-III.6e-f**). However, the comparison between the different SEM micrographs presented in **Figure A-III.6** does not highlight any evolution of the surface of the material after cycling as monolithic grains are still observed.

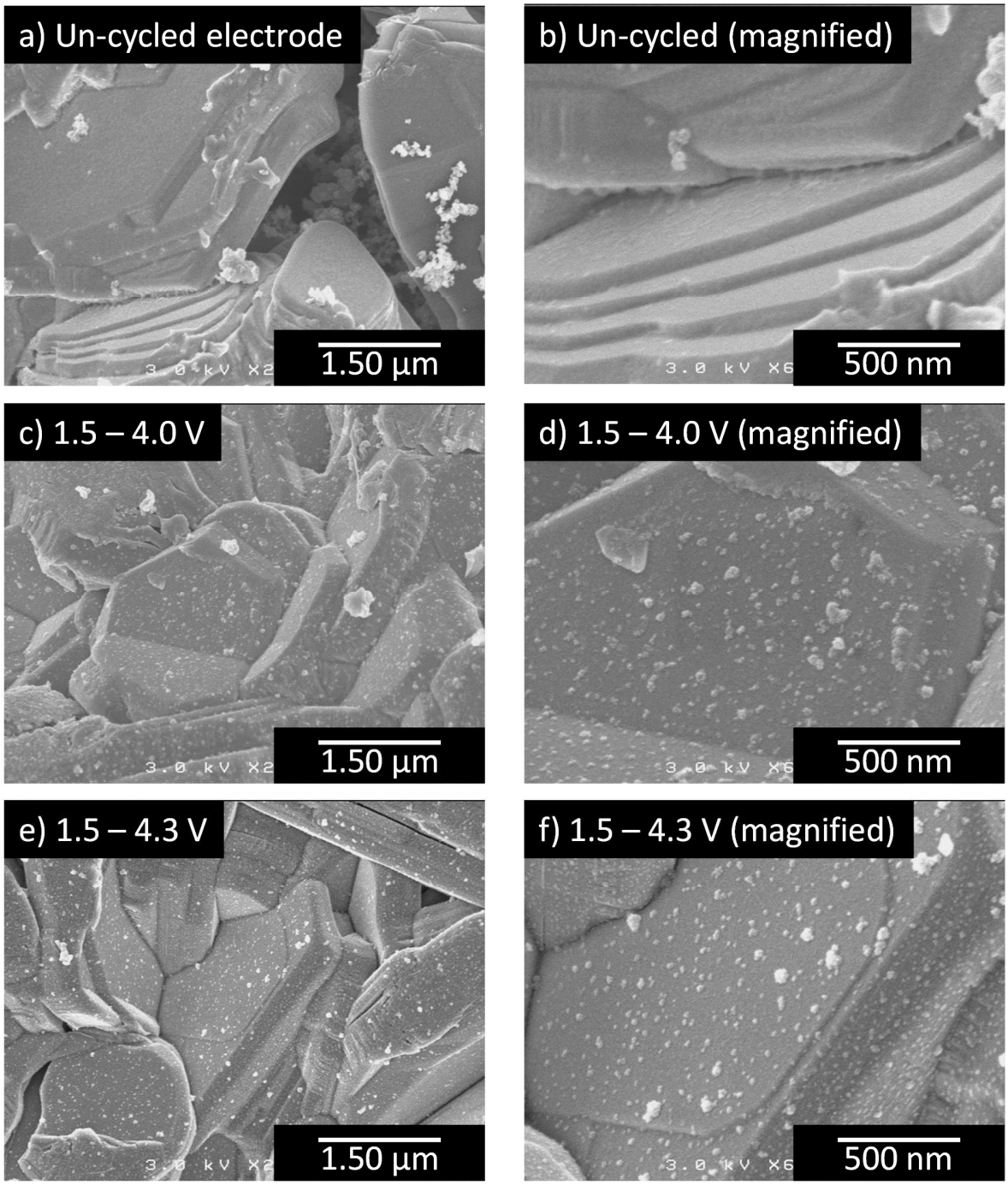

Figure A-III.6: SEM micrographs of (a, b) an un-cycled electrode involving the P2-$Na_{0.62}Mn_{1/2}Fe_{1/2}O_2$ material and similar electrodes cycled 3 times in the (c, d) 2.0 – 4.0 V range and in the (e, f) 2.0 – 4.3 V one.

GITT cycling

We then characterized the material in its relaxed state by carrying out a Galvanostatic Intermittent Titration Technique (GITT) experiment whose result is reported in **Figure A-III.7**.

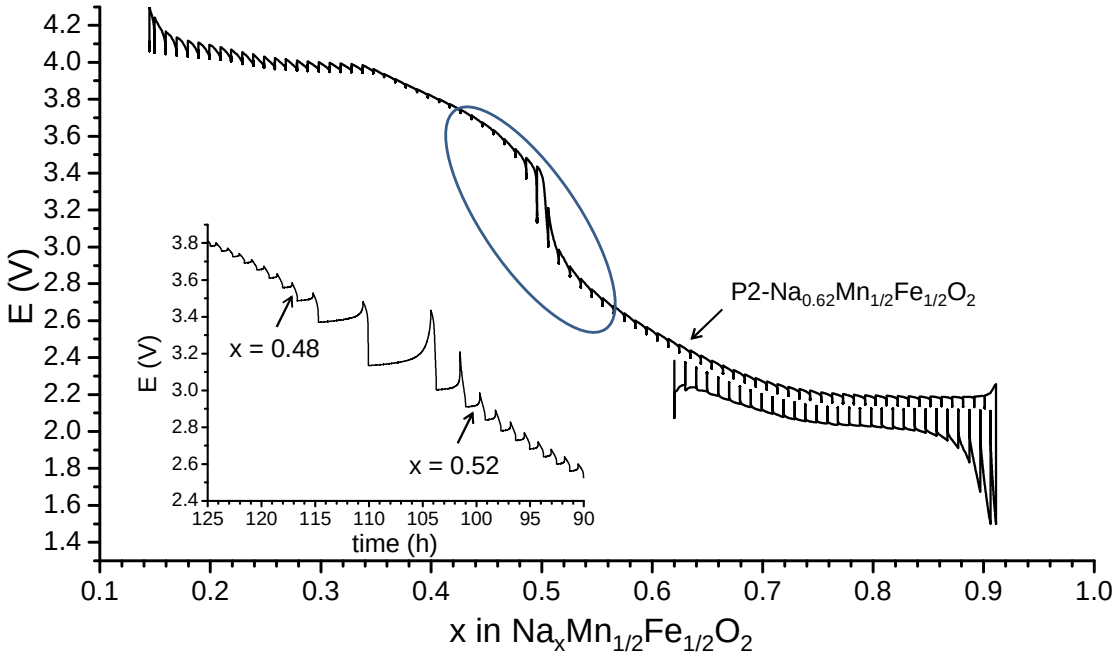

Figure A-III.7: GITT cycling of the $Na_xMn_{1/2}Fe_{1/2}O_2$ system recorded with steps of ≈0.01 Na per formula unit. Relaxation condition: $\Delta V < 4$ mV.h^{-1}.

The shape of the obtained GITT cycling curve is similar to the ones of the galvanostatic experiments and exhibits a first plateau at 2.1 V for $0.82 \leq x \leq 0.90$. Upon charge, we observe a continuous decrease of the polarization until x = 0.52 (ΔE = 74 mV at x = 0.52). For $x \leq 0.48$ the polarization is very low (ΔE = 42 mV for x = 0.48) down to x = 0.33 (4.0 V), as shown in the insert of **Figure A-III.7**. Upon further deintercalation, a second plateau is observed at ≈ 4.0 V for $0.25 < x < 0.33$. On this plateau the polarization continuously increases along with the voltage up to 4.3 V.

If we attribute the Mn^{4+}/Mn^{3+} redox couple to the low voltage region and the Fe^{4+}/Fe^{3+} redox couple to the high voltage region, one can assume the following distribution of cations in the starting material: $Na_{0.62}Mn^{4+}_{0.38}Mn^{3+}_{0.12}Fe^{3+}_{0.50}O_2$. Therefore, during the first discharge almost all Mn^{4+} ions are reduced to the trivalent state and then they are re-oxidized during the first charge. The rapid cell voltage increase for x = 0.50 suggests that trivalent manganese ions are oxidized for $0.50 \leq x \leq 1.0$ and then the trivalent iron ions are oxidized for x < 0.50. As shown in the insert of **Figure A-III.7** the polarization is very different on both sides of the x = 0.5 composition which can be related to the electronic transfer between the involved cations. For x > 0.5 the Mn^{3+}/Mn^{4+} hopping is involved, while the Fe^{3+}/Fe^{4+} couple is only active for x < 0.50. The change in polarization is due to the easier electronic transfer in the case of the iron couple.

Moreover for x = 0.5 the polarization is quite high because, at this exact composition, there is only Mn^{4+} and Fe^{3+} in the material which prevents from an easy electronic transfer.

Influence of the rate

As the P2-$Na_xMn_{1-y}Fe_yO_2$ materials are more suitable for electrochemical applications than the O3 ones [26], the influence of the rate was studied for the P2-$Na_{0.62}Mn_{1/2}Fe_{1/2}O_2$ material. To carry this experiment, three cycles were successively realized at the following rates in the 1.5 – 4.0 V range: C/20, C/10, C/5, C/2, C, 2C and again at C/20. The evolution of the associated discharge capacities is shown in **Figure A-III.8**.

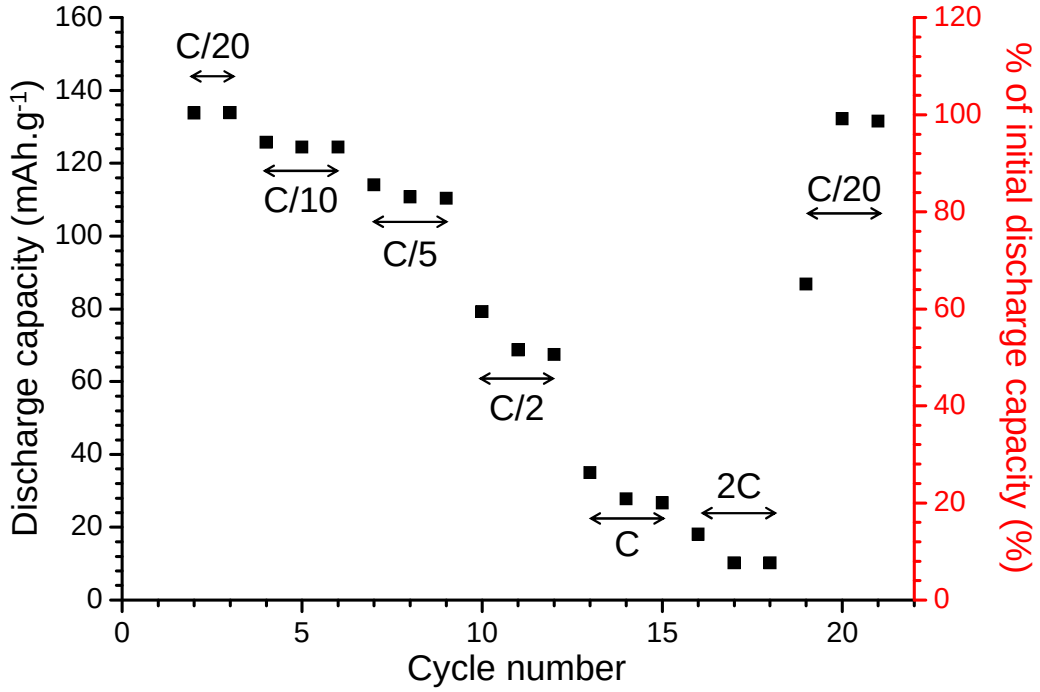

Figure A-III.8: Evolution of the discharge capacity of the $Na_xMn_{1/2}Fe_{1/2}O_2$ system for several rate values.

As one can see, increasing the rate to C/10 or C/5 does not induce an important capacity loss, as 92 % and 82 % of the initial discharge capacity at C/20 are maintained, respectively. On the other hand, cycling at higher rate values induce an important decrease of the discharge capacity (50 %, 20 % and 8 % of the initial discharge capacity are still accessible when the rate is set to C/2, C and 2C). However, the cycling back to C/20 exhibits a discharge capacity close to the initial one (≈ 99 %), which indicates that the material is not damaged during the cycling carried out at higher rates and that the discharge capacity loss is only due to kinetic effects. The low discharge capacity reached at the 19th cycle at C/20 is due to the low amount of Na^+ ions intercalated during the previous charge carried out at 2C.

A-III.1.c. *Operando in situ* study during Na deintercalation

To study the structural rearrangements occurring in the material upon cycling, we carried out an *operando in situ* XRPD experiment during the charge of a $Na_xMn_{1/2}Fe_{1/2}O_2$//Na battery. The experimental conditions were optimized in order to record XRPD patterns in the 13 – 20° and 30 – 43° 2θ ranges every 0.01 Na^+ per formula unit. The evolution of the XRPD patterns along with the complete charge of the battery is shown in **Figures A-III.9** and **A-III.10** in reverse order.

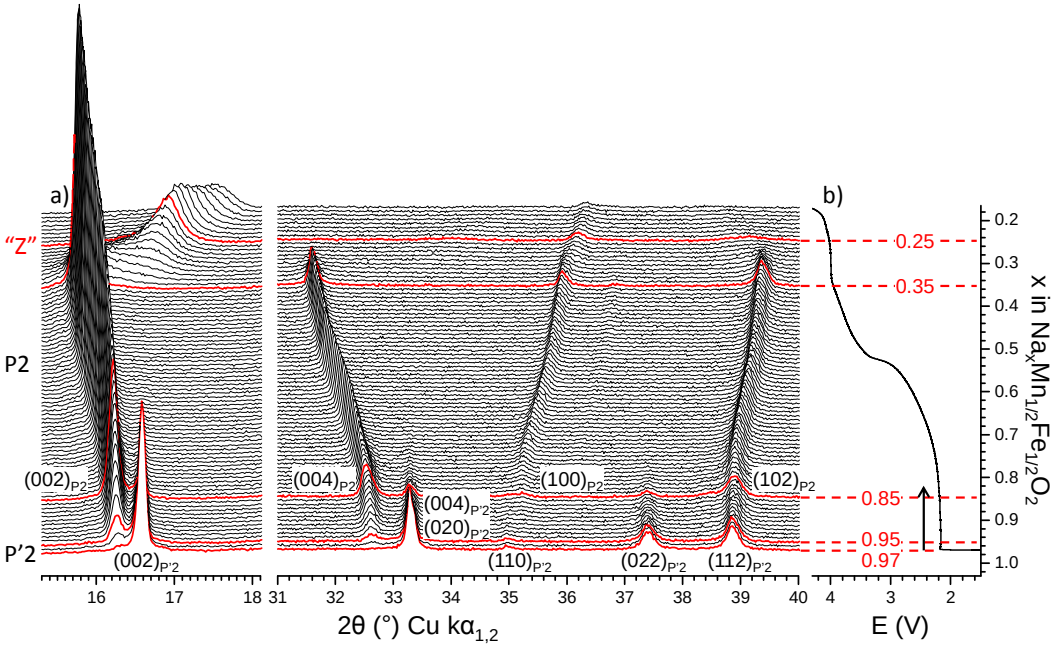

Figure A-III.9: (a) XRPD patterns recorded *in situ* (*operando* mode) during the charge of a $Na_xMn_{1/2}Fe_{1/2}O_2$/$NaPF_6$ in PC (1M) + 2 wt% FEC/Na cell along with (b) the corresponding galvanostatic curve. The red XRPD patterns correspond to the limits of the different structural domains.

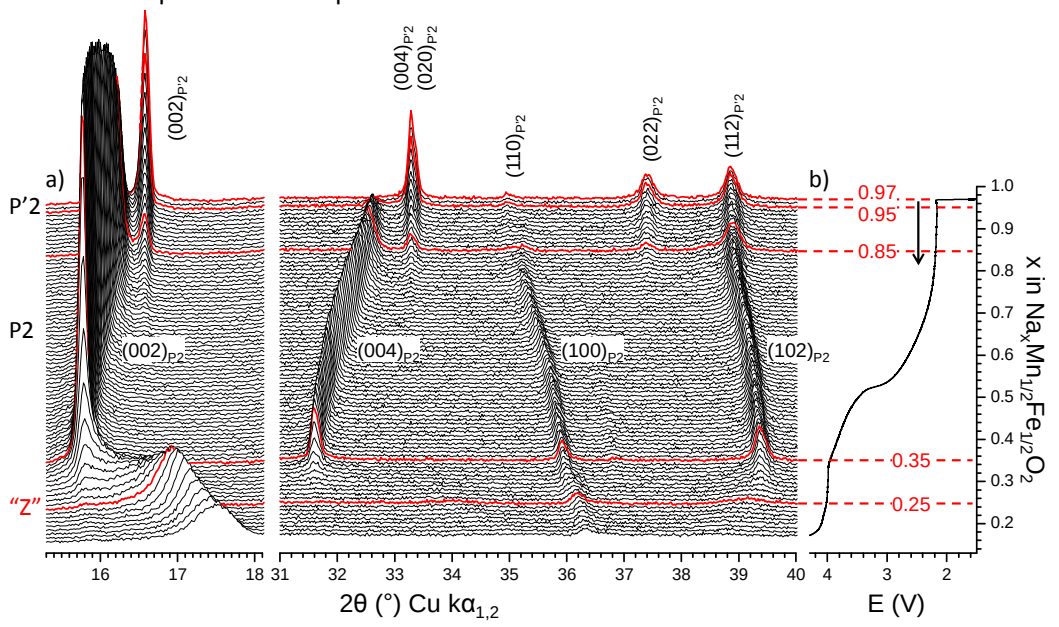

Figure A-III.10: Inverse representation of Figure **A-III.9**: (a) XRPD patterns and (b) corresponding galvanostatic curve. The red XRPD patterns correspond to the limits of the different structural domains.

The experiment starts from the material in the fully intercalated state which corresponds to the $Na_{0.97}Mn_{1/2}Fe_{1/2}O_2$ composition. On its diffraction pattern, two diffraction peaks - observed at approximately 37.4° and 38.8° - cannot be indexed using the hexagonal symmetry of the pristine material. Instead, an orthorhombic cell should be used to index the pattern as for P'2-$Na_{0.7}MnO_2$ [114]. According to the structural classification of Na_xMO_2 phases, we will refer to this phase as P'2 type structure. Therefore, these two diffraction peaks correspond respectively to the $(022)_{P'2}$ and $(112)_{P'2}$ reflections in the orthorhombic symmetry and arise from the splitting of the $(102)_{P2}$ reflection in the hexagonal symmetry. The P'2 type structure is observed as a single phase only for a narrow Na-range: $0.95 < x \leq 0.97$. For $x \leq 0.95$, a second phase is formed (**Figure A-III.9**). It is clearly visible with the appearance of two diffraction peaks at approximately 16.3° and 32.6° that correspond to the $(002)_{P2}$ and $(004)_{P2}$ reflections in the hexagonal cell (P2 type structure), respectively. The biphasic domain between the P2 and P'2 phases is observed for a Na content comprised between $0.85 < x \leq 0.95$.

Upon further charging, only a single phase with P2 type structure is present down to $x \approx 0.35$. For $0.25 < x \leq 0.35$ the intensity of the P2 diffraction lines decreases (**Figure A-III.10**). Simultaneously, a broadening of the $(002)_{P2}$ diffraction peak is observed on the high angle side and a new diffraction peak appears in the $16.7 \leq 2\theta \leq 16.9$ ° region. This behavior is very similar to the one observed in **Chapter A-II** for the O3-based systems at the end of charge. We assume that stacking faults consisting in layers of NaO_6 octahedrons are created among the P2 layers in the material for $0.25 < x \leq 0.35$. For $x < 0.25$, only one diffraction lines is observed in 15.3 – 18.1 ° 2θ range, indicating that only one stacking prevails. The important broadening supposes a loss in the long-range order of the material. An indexation of the XRPD diagram at the end of charge is not possible as only two diffraction peaks are observed. However, we suspect that the MO_2 layers glided upon sodium deintercalation imposes an octahedral environment for sodium ions as it was suggested by several authors in other P2-Na_xMO_2 materials [26, 72]. Therefore, as we do not have any data about the packing type, we will refer to this deintercalated phase as "Z phase".

Two characteristic distances of layered oxide structures can be deduced from the indexation of the XRPD patterns recorded during the *in situ* experiment. The first one is the interslab distance which is the distance between two successive MO_2 layers while the second one is the in-plane M-M distance. For both phases with P'2 and P2 type structures, the interslab distance is equal to half the c parameter. For the P2 type structure, there is only one in-plane M-M distance, equal to the $a_{hex.}$ parameter whereas for the P'2 type one, two different in-plane M-M distances can be found: one is equal to the $a_{orth.}$ parameter and one is equal to $\sqrt{(a_{orth.}^2 + b_{orth.}^2)}/2$. The variation of the interslab distance is reported in **Figure A-III.11a** while the variation of the $a_{hex.}$, $a_{orth.}$ and $b_{orth.}$ cell parameters (P2 and P'2 phases) or of the M-M distance ("Z" phase) are reported in **Figure A-III.11b**. The main feature concerns the interslab distance which increases continuously for the P2 type, then it decreases when the "Z" phase is formed.

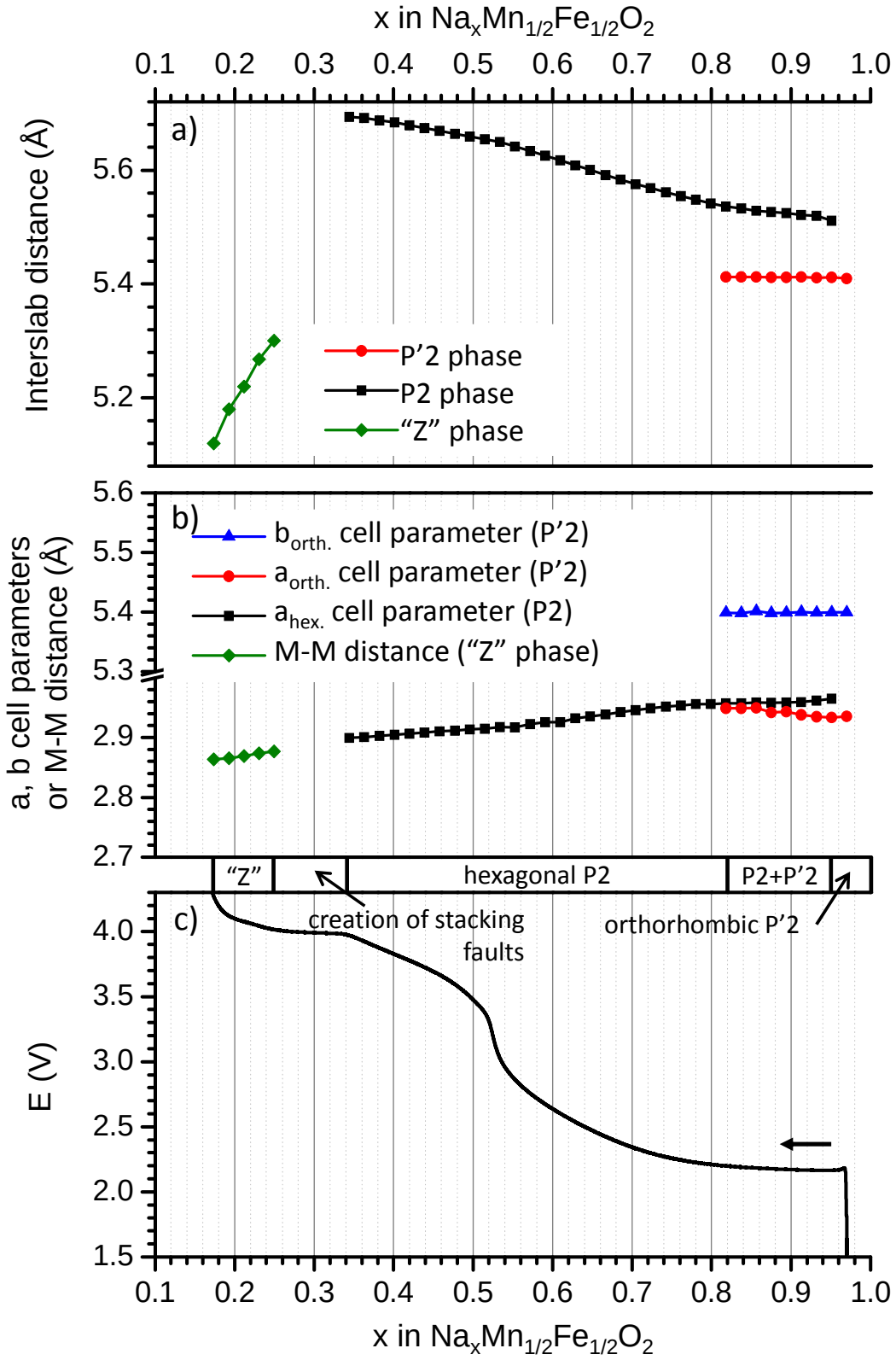

Figure A-III.11: Evolution of (a) the interslab distance and (b) the a and b cell parameters (P'2 and P2 phases) or M-M distance ("Z" phase) of the $Na_xMn_{1/2}Fe_{1/2}O_2$ phases upon sodium deintercalation. The galvanostatic curve versus x is shown as a guide in (c).

Concerning the “Z” phase appearing at high voltage for which the XRPD patterns could not be indexed; only two diffraction lines are seen on the XRPD patterns. As they are very close to the $(002)_{P2}$ and $(100)_{P2}$ ones, one can assume that this material presents for the x = 0.25 composition an interslab distance of 5.3 Å and an in plane M-M distance equal to 2.88 Å. The absence of well-defined diffraction peaks shows that there is no long range ordering in the MO_2 slab packing.

For a very general point of view, when the number of alkali ions in the interslab space is very small, the covalence of the bonds in the MO_2 slab increases thanks to the transition metal oxidation. This leads to a decrease of the interslab thickness. In the case of P2 type phases this decrease will increases the repulsions between the oxygen layers of the NaO_6 trigonal prism which is then strongly destabilized. To accommodate this interslab thickness contraction and to decrease the O-O repulsions, a shift of the slab occurs with formation of octahedral sites in the interslab space. Upon deintercalation, the M-M distance decreases continuously as a result of the transition metal oxidation.

The second important feature concerns the P’2 type phase and is highlighted by two distinct in plane M-M distances of approximately 2.93 and 3.07 Å (**Figure A-III.11b**). This huge difference in distance implies that the triangular lattice formed by Mn and Fe atoms is highly distorted.

After the *operando in situ* XRPD experiment and the charge up to 4.3 V, the cell was discharged again down to 1.5 V and maintained at this voltage until a negligible residual current was observed. The XRPD pattern recorded after this second discharge is compared to the one recorded after the first discharge in **Figure A-III.12**.

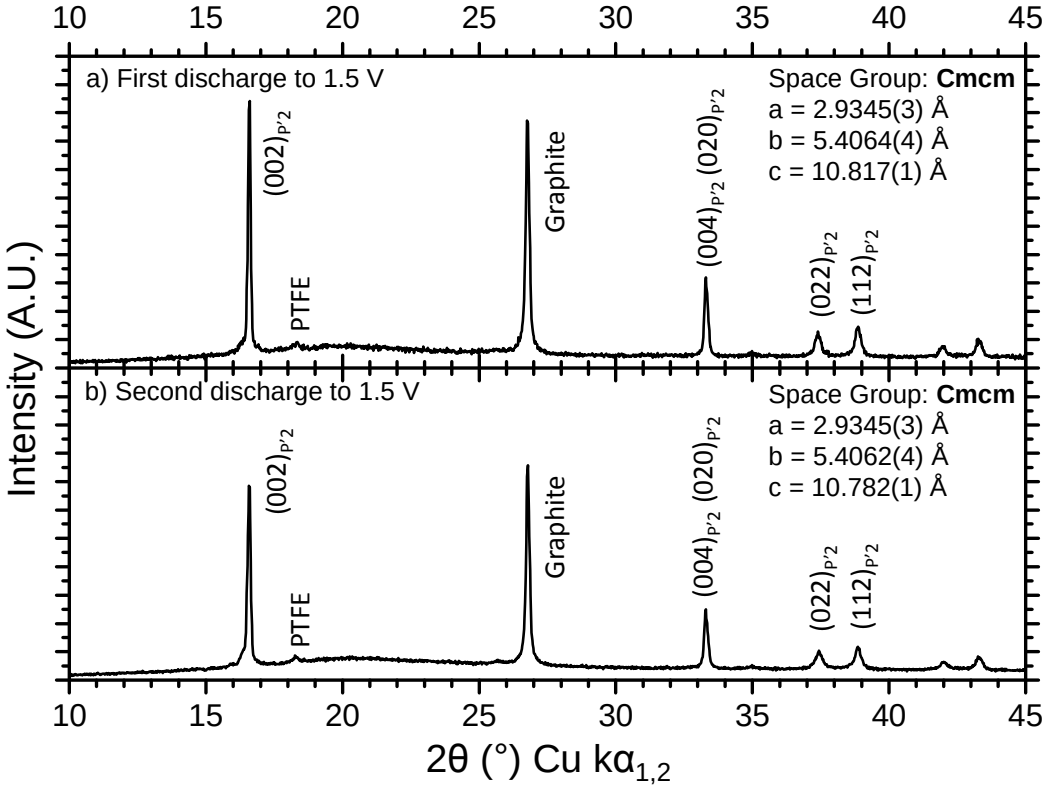

Figure A-III.12: Comparison of the XRPD patterns of P'2 $Na_xMn_{1/2}Fe_{1/2}O_2$ phases recorded after (a) the first and (b) second discharge at 1.5 V, and maintained at the voltage until a negligible current was observed.

As suggested by the cycling curve (**Figure A-III.5**), the XRPD pattern recorded after the second discharge is again characteristic of a well crystallized phase with well-defined diffraction peaks which confirms that sodium electrochemical intercalation is still very reversible even after the charge up to high voltage. Both patterns are indexed in an orthorhombic cell and they have very close cell parameters. The pattern corresponding to the second discharge (**Figure A-III.12b**) exhibits slightly broader diffraction. This slight broadening of the diffraction peaks remains unexplained as it is not correlated to any macroscopic observation on the SEM micrographs (**Figure A-III.6**).

A-III.1.d. *Ex situ* Synchrotron X-ray powder diffraction study of the P'2-$NaMn_{1/2}Fe_{1/2}O_2$ phase

A sample of the fully intercalated phase was prepared by the potentiostatic method. Once recovered and washed, the powder was analyzed by synchrotron XRPD[16]. The experimental and calculated (Rietveld method) patterns are shown in **Figure A-III.13**. The corresponding cell and atomic parameters are given in **Table A-III.3**.

[16] In collaboration with Dr. C. Drathen, ESRF, Grenoble, France.

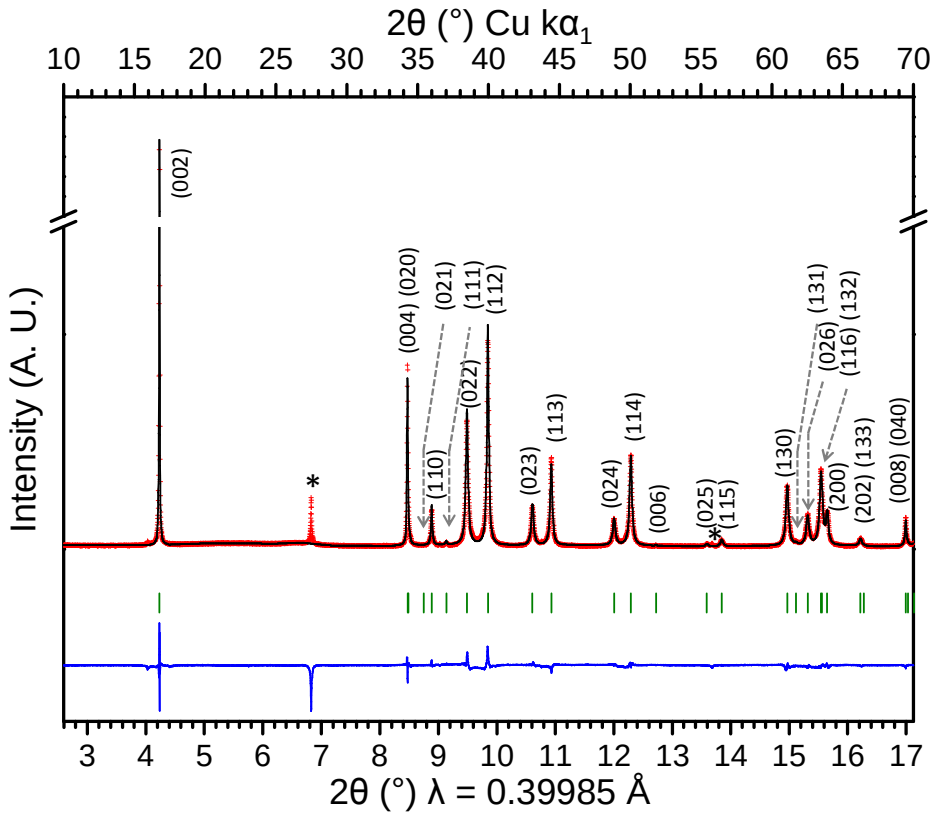

Figure A-III.13: Observed and calculated (Rietveld method) synchrotron XRPD patterns of the P'2-$Na_{\approx 1}Mn_{1/2}Fe_{1/2}O_2$ phase. Red crosses: experimental, black line: calculated, blue line: difference and green bars: Bragg positions. The * symbol indicates the graphite diffraction lines which were excluded for the refinement.

Space group: **Cmcm** $a_{orth.}$ = 2.9367(2) Å, $b_{orth.}$ = 5.4015(5) Å, $c_{orth.}$ = 10.8248(8) Å $b_{orth.}/a_{orth.}$ = 1.84						
Atom	Wyckoff		Coordinates		Occupancy	ADP (Å²)
Na_e	4c	0	0.683(2)	1/4	1.0(2)	0.7(2)
Mn	4a	0	0	0	1	0.60(5)
Fe	4a	0	0	0		
O	8f	0	0.648(2)	0.901(1)	1	0.5(2)
Distances :	M-O		Na-O			
	4 * 1.99(1) Å 2 * 2.18(1) Å		4 * 2.38(1) Å 2 * 2.42(1) Å			
Rwp = 8.40 %; R_B = 7.13 % with excluded regions (graphite)						

Table A-III.3: Structural parameters and reliability factors calculated from the synchrotron XRPD pattern of the P'2- $Na_{\approx 1}Mn_{1/2}Fe_{1/2}O_2$ phase.

The synchrotron XRPD pattern is successfully indexed in the Cmcm orthorhombic space group of the P'2 structures. The refined Na content is equal to 1.0(2), in agreement with the one obtained from electrochemical characterizations. The $b_{orth.}/a_{orth.}$ ratio (1.84) shows the distortion induced by the cooperative Jahn-Teller effect. It is confirmed by the distortion of the MO_6 octahedra which possess 4 short M-O distances (1.99(6) Å) and 2 long ones (2.18(1) Å) (**Table A-III.3**).

It is noteworthy that whereas two crystallographic sites can be occupied by the Na^+ ions in the P'2 orthorhombic structure in the Cmcm space group [114], only the one sharing edges with the surrounding MO_6 octahedra is occupied here. Generally in P2 and P'2 types structure both Na_e and Na_f sites are simultaneously occupied with a ratio close to 2 : 1 [36, 114]. This distribution results from the strong Na^+-Na^+ repulsion which is prevailing to the Na^+-$M^{3+/4+}$ one. As adjacent Na_e and Na_f sites cannot be occupied simultaneously, the $Na_1Mn_{1/2}Fe_{1/2}O_2$ stoichiometry can only be reached if all Na^+ ions are located in one site. Therefore the most stable one - *i.e* Na_e (4c position) - is occupied as shown in **Figure A-III.14**. The ADP value for the Na^+ ions in the P'2 phase is lower (0.7(2) Å²) than for those of the P2-$Na_{0.62}Mn_{1/2}Fe_{1/2}O_2$ phase (1.9(3) Å²), in agreement with the fact that the Na^+ ions should be much less mobile for a stoichiometry close to $Na_1Mn_{1/2}Fe_{1/2}O_2$.

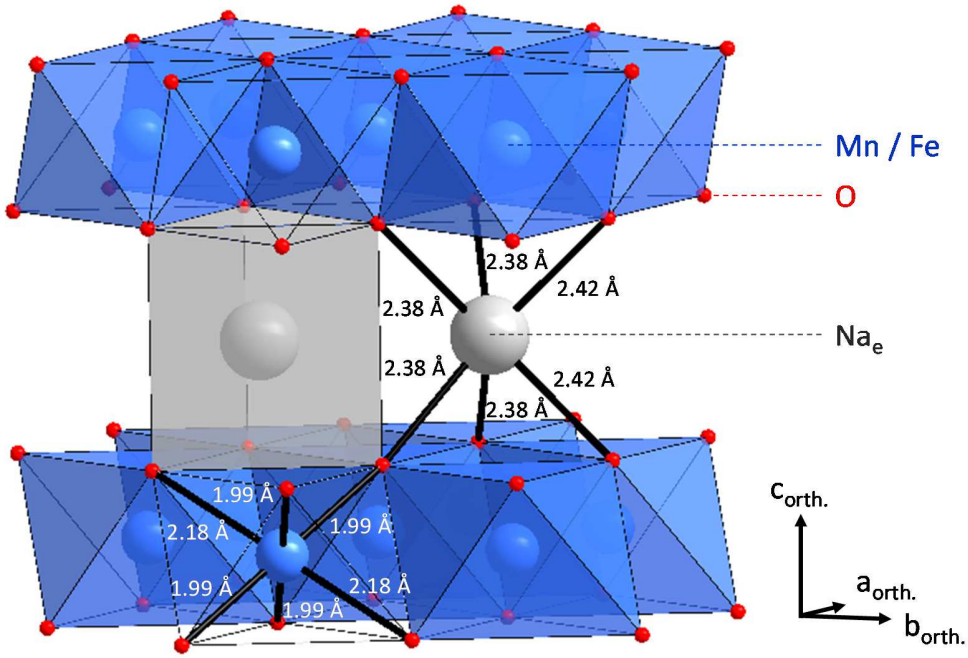

Figure A-III.14: Representation of the MO_6 and NaO_6 polyhedra in the P'2-$Na_{\approx 1}Mn_{1/2}Fe_{1/2}O_2$ phase.

A-III.2. The $Na_xMn_{2/3}Fe_{1/3}O_2$ system

To emphasize the effect of the Mn / Fe ratio on the electrochemical and structural properties, several studies were carried out on the $Na_xMn_{2/3}Fe_{1/3}O_2$ system.

A-III.2.a. Synchrotron X-ray and neutron powder diffraction studies of the pristine material

Synchrotron X-ray Powder Diffraction

The synchrotron XRPD pattern[17] of P2-$Na_{0.77}Mn_{2/3}Fe_{1/3}O_2$ is shown in **Figure A-III.15** along with the calculated pattern (Rietveld method). The corresponding cell and atomic parameters are reported in **Table A-III.4**.

As for the P2-$Na_{0.62}Mn_{1/2}Fe_{1/2}O_2$ material, the pattern can be refined in the hexagonal $P6_3/mmc$ space group using a Pseudo-Voigt function. The refined cell parameters ($a_{hex.}$ = 2.9400(1) Å and $c_{hex.}$ = 11.1812(2) Å) are close to the literature on P2-$Na_{2/3}Mn_{2/3}Fe_{1/3}O_2$: $a_{hex.}$ = 2.913 Å and $c_{hex.}$ = 11.262 Å [32]. The overall sodium content is equal to 0.66(4), which is lower than the expected one (x = 0.77) and the one from the formula determined by ICP-AES ($Na_{0.77}Mn_{0.64}Fe_{0.36}O_2$). This indicates that a more significant part of the Na^+ ions was expelled during the air quenching of the material than for the other studied materials. One can link the sodium loss to the high Mn^{3+} content and its instability at low temperature: a more important part of the transition metal ions are susceptible to be oxidized to Mn^{4+}, expelling more Na^+ ions at the surface of the material in the process. In the following we will refer to the material as P2-$Na_{0.66}Mn_{2/3}Fe_{1/3}O_2$. The global ADP value associated to the sodium sites is high (2.9(5) Å) and can be associated to a high disorder into the sodium layers. Any attempt to refine separately the ADP of the Na sites led to the divergence of the refinement. Occupancies of the transition metal and oxygen sites were fixed to 1.0 and the associated ADP's are equal to 0.65(4) Å² (Fe and Mn in 2a site) and 1.1(1) Å² (O in 4f site). By comparison to P2-$Na_{0.62}Mn_{1/2}Fe_{1/2}O_2$, we note higher ADP values, which imply a higher disorder in P2-$Na_{0.66}Mn_{2/3}Fe_{1/3}O_2$. This can be related to the higher amount of Jahn Teller active Mn^{3+} ions in the pristine material which induce local distortions in the MO_2 slabs, even if the structure is not distorted at the macroscopic scale. We also tried refining the transition metal site occupancy to verify the possibility of transition metal vacancies. However, any attempt to include transition metal vacancies into the MO_2 slabs did not lead to significant improvement of the refinement.

[17] In collaboration with Dr. M. Suchomel, Argonne Photon Source, Argonne National Laboratory, IL, USA.

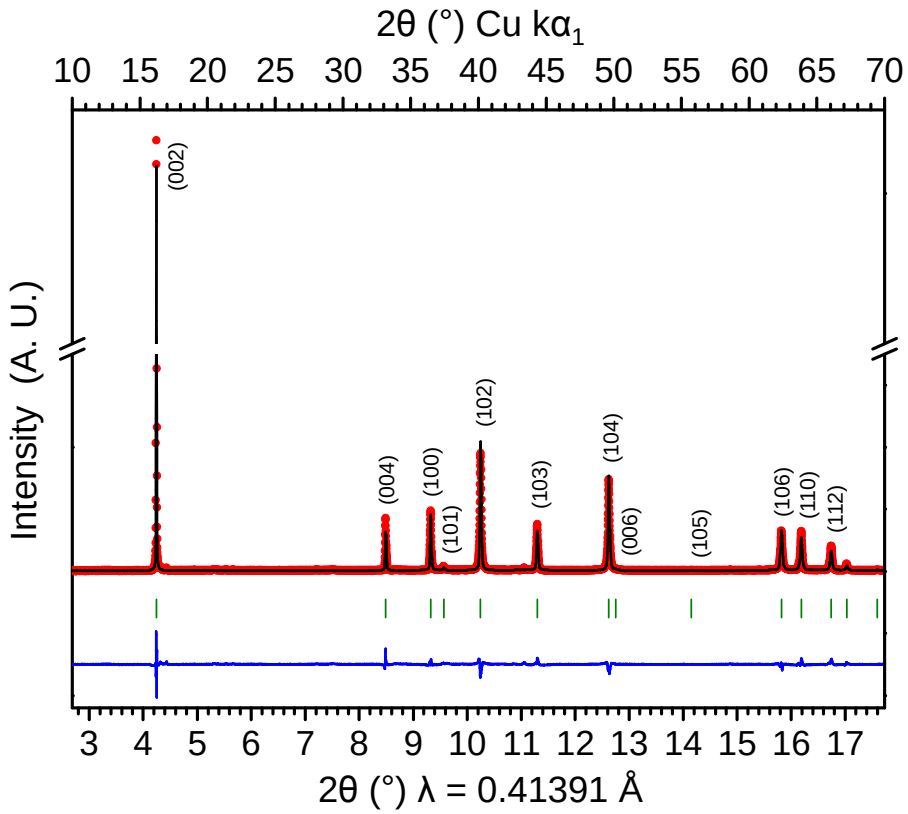

Figure A-III.15: Observed and calculated (Rietveld method) synchrotron XRPD patterns for the P2-$Na_{0.66}Mn_{2/3}Fe_{1/3}O_2$ pristine material. Red dots: experimental, black line: calculated, blue line: difference and green bars: Bragg positions.

Space group: **$P6_3/mmc$** $a_{hex.}$ = 2.9400(1) Å, $c_{hex.}$ = 11.1812(6) Å						
Atom	Wyckoff	Coordinates			Occupancy	ADP (Å²)
Na_f	2d	0	0	1/4	0.20(2)	2.9(5)
Na_e	2b	2/3	1/3	1/4	0.46(2)	
Mn	2a	0	0	0	1	0.65(4)
Fe	2a	0	0	0		
O	4f	1/3	2/3	0.093(1)	1	1.1(1)
Distances:	M-O		Na-O			
	6 * 1.99(1) Å		6 * 2.44(1) Å			
Rwp = 13.29%; R_B = 5.73%						

Table A-III.4: Structural parameters and reliability factors calculated from the synchrotron XRPD pattern of the P2- $Na_{0.66}Mn_{2/3}Fe_{1/3}O_2$ pristine material.

Neutron Powder Diffraction

The 2:1 ratio between the Mn and Fe transition metal led us to consider the existence of a possible ordering within the MO_2 slabs. To investigate this feature, we carried out neutron diffraction measurements at ILL[18] in order to differentiate the Mn and Fe species. The structure of the material was refined from the laboratory XRPD and neutron powder diffraction patterns as shown in **Figure A-III.16**. The atomic and cell parameters deduced from the Rietveld refinements of the structure are given in **Table A-III.5**.

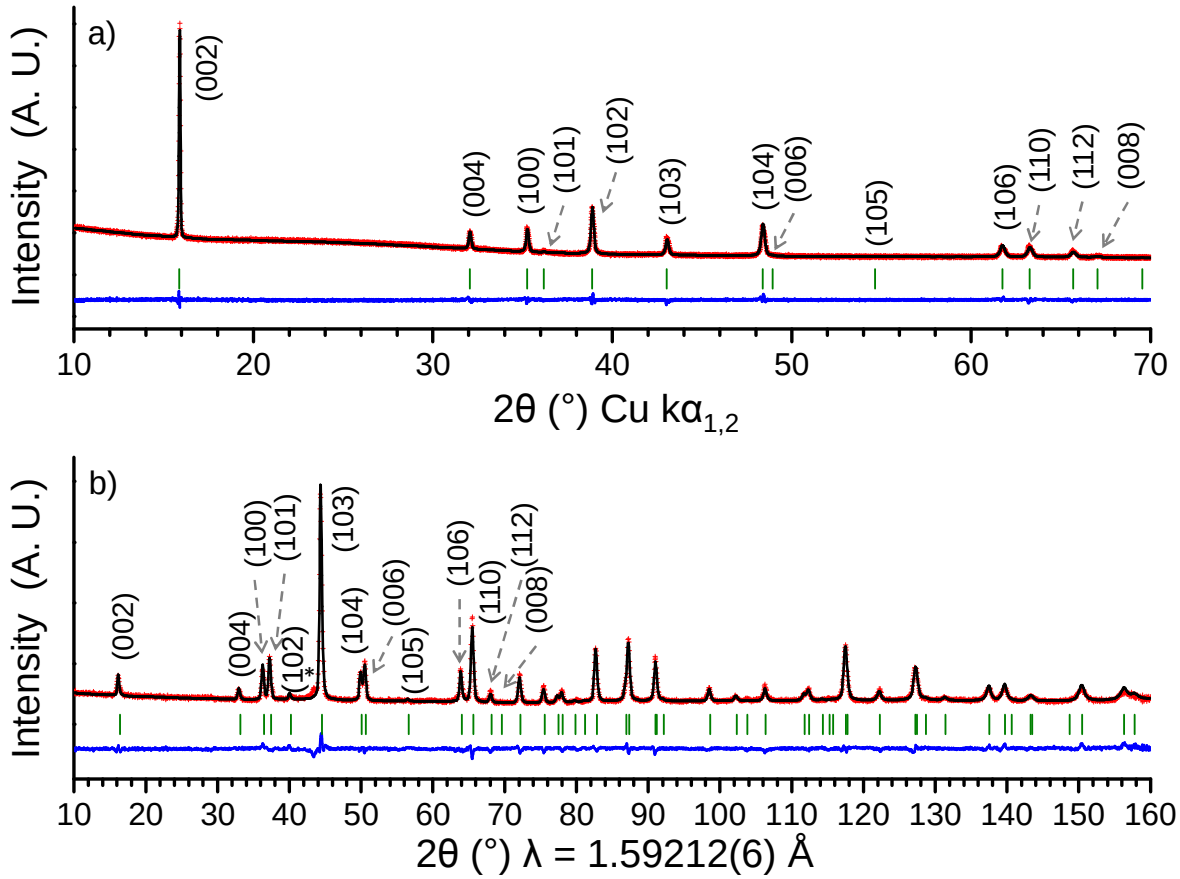

Figure A-III.16: Observed and calculated (Rietveld method) (a) XRPD and (b) neutron powder diffraction patterns for the P2-$Na_{0.662}Mn_{2/3}Fe_{1/3}O_2$ pristine material. Red crosses: experimental, black line: calculated, blue line: difference and green bars: Bragg positions. The * symbol on the neutron powder diffraction pattern indicates a diffraction peak from the vanadium sample container.

[18] In collaboration with Dr. E. Suard, ILL, Grenoble, France.

		XRPD			Neutron diffraction	
Cell parameters (S.G.: **$P6_3/mmc$**)	$a_{hex.}$ (Å)	2.9371(1)				
	$c_{hex.}$ (Å)	11.1588(3)				
Wavelength (Å)		Cu k$\alpha_{1,2}$			1.59212(6)	
Atomic parameters:		x	y	z	Occ	ADP (Å²)
	Na_f	0	0	1/4	0.24(1)	3.4(1)
	Na_e	2/3	1/3	1/4	0.49(1)	
	Mn (3a)	0	0	0	0.655(1)	0.53(3)
	Fe (3a)	0	0	0	0.345(1)	
	O (6c)	1/3	2/3	0.0914(1)	1.0	1.27(1)
R_{wp} (%)		2.50			3.74	
Global R_{wp} (%)		2.74				

Table A-III.5: Structural parameters and reliability factors calculated from the combined refinement of the P2-$Na_{0.66}Mn_{2/3}Fe_{1/3}O_2$ pristine material from the XRPD and neutron powder diffraction patterns.

As for the other $Na_xMn_{1-y}Fe_yO_2$ materials, we do not observe any extra diffraction peak on the neutron powder diffraction pattern. The existence of a long-range ordering between the Mn and Fe species is therefore excluded. The refined Mn and Fe contents are equal to 0.655(1) and 0.345(1) respectively and are close to the targeted ones. There is an important difference between the overall sodium content deduced from the synchrotron XRPD (x = 0.66) and the one deduced from the combined refinement (x = 0.73). We explain this difference by the duration separating the various analyses: the synchrotron XRPD pattern was recorded six months after the neutron and laboratory XR diffraction patterns and the material probably reacted with moisture traces in the glovebox. This hypothesis is coherent with the increase of the $c_{hex.}$ parameters deduced from the neutron diffraction pattern ($c_{hex.}$ = 11.1588(3) Å) and from the synchrotron XRPD pattern ($c_{hex.}$ = 11.1812(6) Å).

A-III.2.b. Electrochemistry

Influence of the cut-off voltage

In order to have a better understanding of the performances and limitations of P2-$Na_{0.66}Mn_{2/3}Fe_{1/3}O_2$ as a positive electrode material for Na batteries, we carried out several electrochemical characterizations including cycling into various voltage ranges. The galvanostatic E = f(x) curves obtained in the 1.5 – 3.8 V, 1.5 – 4.0 V and 1.5 – 4.3 V ranges are given in **Figures A-III.17a-c**, respectively with the first cycle highlighted in red. The evolution of the discharge capacities along with the cycle number is reported in **Figure A-III.17d**.

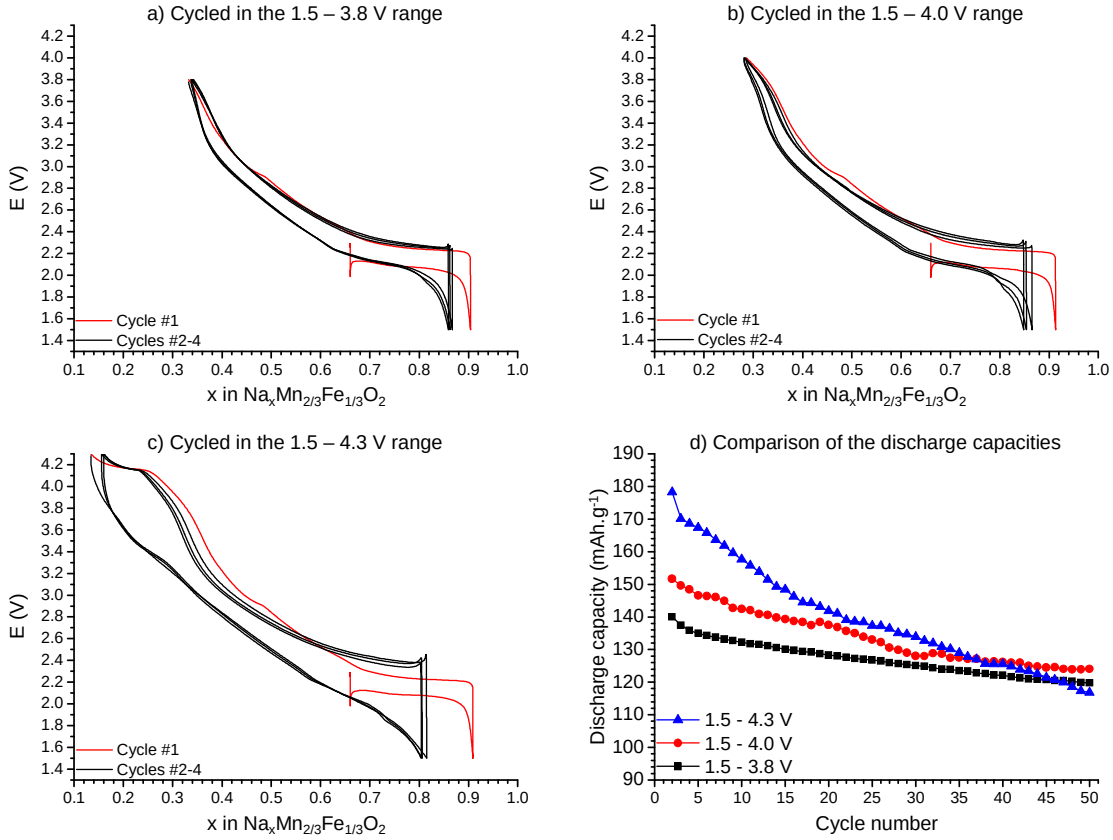

Figure A-III.17: Galvanostatic cycling curves associated to the $Na_xMn_{2/3}Fe_{1/3}O_2$ system and recorded (a) between 1.5 and 3.8 V, (b) between 1.5 and 4.0 V and (c) between 1.5 and 4.3 V at C/20. (d) Associated discharge capacities. The capacities of the first cycle are not shown in (d) as they correspond to the partially intercalated state.

During the first discharge a short voltage plateau is observed at ≈ 2.2 V and at ≈ 2.1 V upon following charge. Then the voltage continuously increases upon deintercalation. If the cut-off voltage is set to 3.8 or 4.0 V, the following discharge shows the reversibility of the Na (de)intercalation process. When the cut-off voltage in increased to 4.3 V a second voltage plateau is observed at ≈ 4.15 V. This plateau is not visible on the consecutive discharge curve and instead an increase of the polarization is observed.

Then the (de)intercalation process is reversible for E < 3.2 V. For every experiment, the 2nd, 3rd and 4th cycles are very similar. Our observations are in agreement with the literature on the same system when cycled in the 1.5 – 3.8 V [66] and 1.5 – 4.3 V ranges [32].

The evolution of the discharge capacities was also studied as shown in **Figure A-III.17d**. Logically, the increase of the upper cut-off voltage induces an extra capacity for the second cycle from 140 mAh.g^{-1} (1.5 – 3.8 V) to 152 mAh.g^{-1} (1.5 – 4.0 V) or 178 mAh.g^{-1} (1.5 – 4.3 V). If the discharge capacity retention at the 50th cycle are comparable for the experiments carried out in the 1.5 – 3.8 V and 1.5 – 4.0 V ranges (86 and 82%, respectively), increasing cycling in the 1.5 – 4.3 V range leads to poor capacity retention (66%) after 50 cycles. We can observe that the discharge capacities in the 1.5 – 4.0 V and 1.5 – 4.3 V range experiments are identical at the 37th cycle. The discharge capacity of the 1.5 – 4.3 V experiment then continues to decrease and matches the discharge capacity value of the battery cycled up to 3.8 V at the 46th cycle.

GITT cycling

In order to have an insight of the phenomenon occurring during the cycling, a GITT experiment was performed, as shown in **Figure A-III.18a**. For comparison purposes, the GITT cycling curve of the $Na_xMn_{1/2}Fe_{1/2}O_2$ material is given in **Figure A-III.18b**.

Starting with a discharge from x = 0.66, the material exhibits a plateau at low voltage for 0.76 ≤ x < 0.88. The same plateau is then observed in charge, confirming the reversibility of the process. Upon further Na deintercalation the voltage continuously increases until a second plateau is observed for 0.22 ≤ x ≤ 0.27. This second plateau is accompanied by an increase of the cell polarization. Deintercalation down to x = 0.13 is accompanied by a continuous voltage increase. Looking closely at the GITT cycling curve during charge, one can see slight slope variation at x ≈ 2/3 and x ≈ 1/2 (red arrows in **Figure A-III.18a**). We do not have any explanation for this phenomenon that is also observed in galvanostatic cycling and only during the first cycle.

Furthermore, one can be surprised that no significant voltage jump is observed at x = 1/3 contrarily to the $Na_xMn_{1/2}Fe_{1/2}O_2$ system where a strong voltage jump is observed for x = 1/2. Instead, a small increase of the polarization of the cell is observed at E = 3.4 V (x ≈ 0.37). In the P2-based $Na_xMn_{1/2}Fe_{1/2}O_2$ system, the same increase of the polarization occurs at the voltage jump, also at E = 3.4 V (**Figure A-III.18b**). One can see the signature of the change of redox process, from $Mn^{3+} \rightarrow Mn^{4+}$ to $Fe^{3+} \rightarrow Fe^{4+}$.

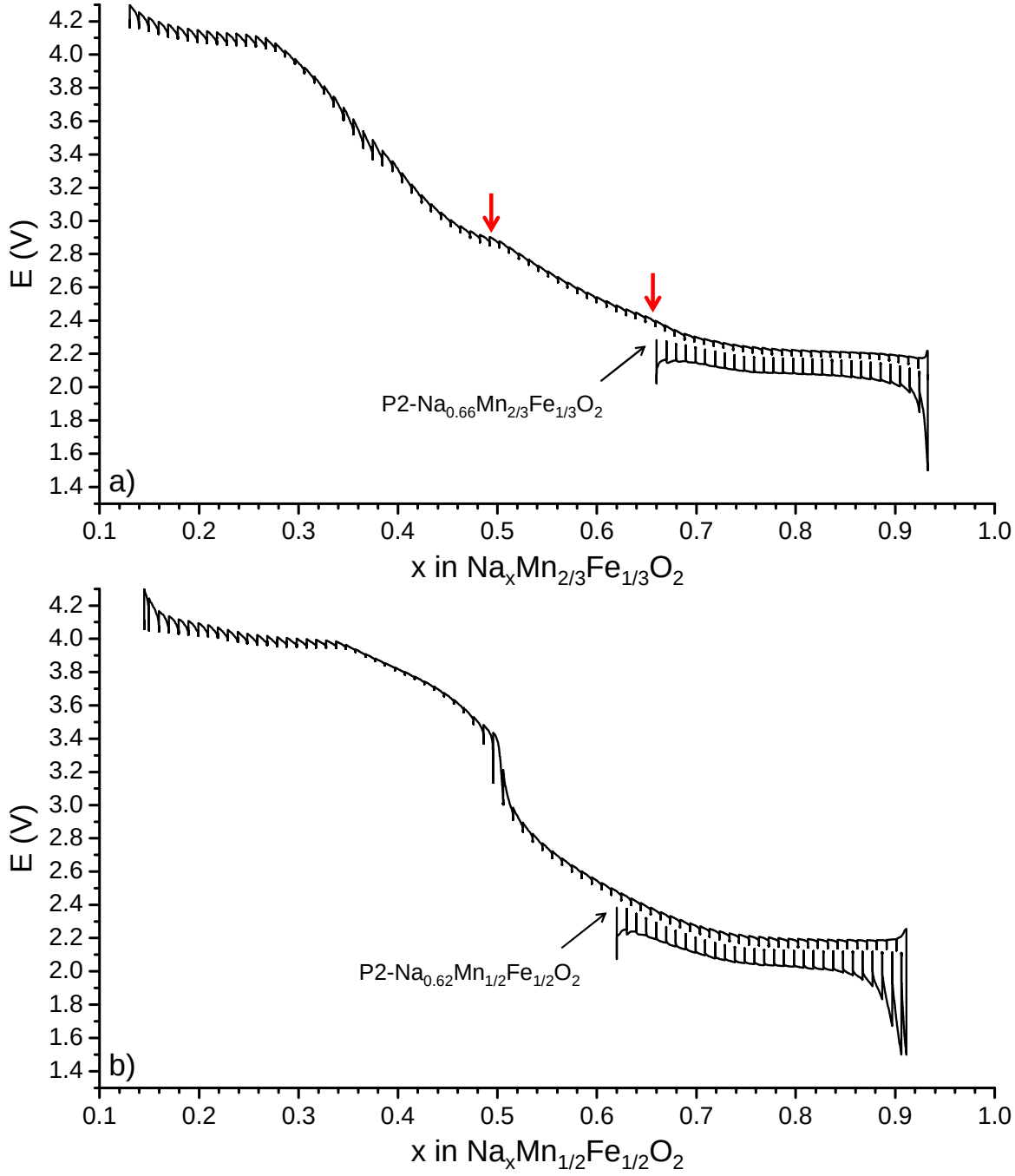

Figure A-III.18: GITT cycling curve recorded with steps of ≈ 0.01 Na^+ per formula unit and a $\Delta V < 4$ mV.h^{-1} relaxation condition for the $Na_xMn_{2/3}Fe_{1/3}O_2$ system (a). The red arrows indicate slight variation in the slope of the curve. The GITT cycling curve recorded for the $Na_xMn_{1/2}Fe_{1/2}O_2$ system is given in (b) as a comparison.

Influence of the rate

We then studied the influence of the rate on the discharge capacity of the P2-$Na_{0.66}Mn_{2/3}Fe_{1/3}O_2$ material. The experiment consisted in different series of 3 cycles, realized with the following rate values: C/20, C/10, C/5, C/5, C, 2C and again at C/20. The corresponding evolution of the discharge capacity is shown in **Figure A-III.19**.

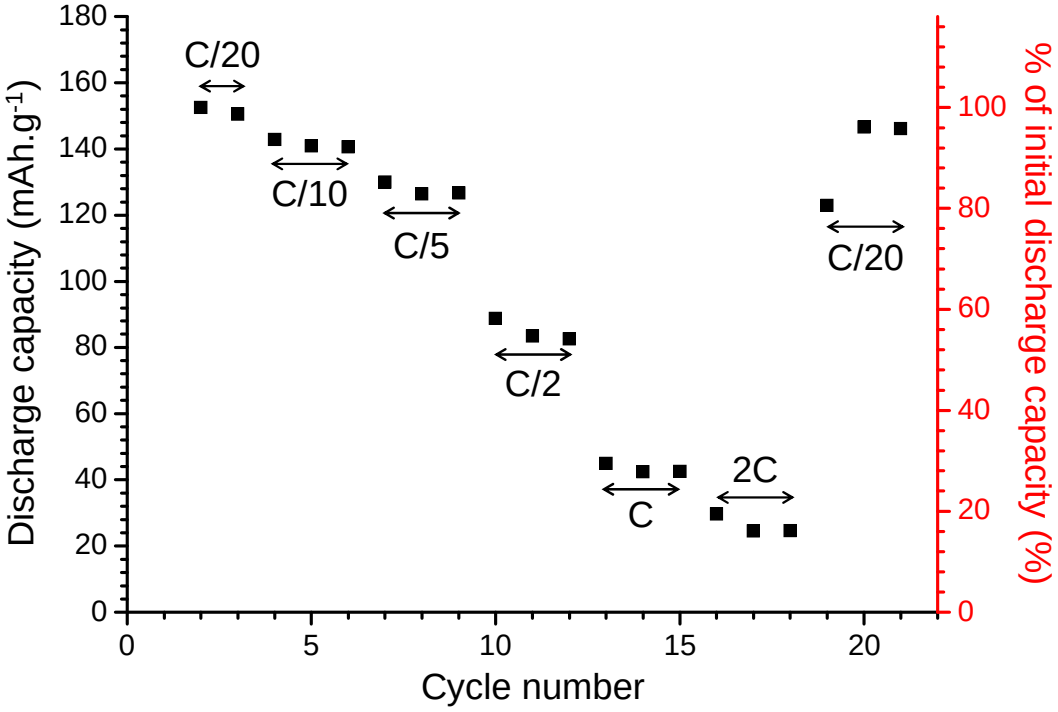

Figure A-III.19: Evolution of the discharge capacity of the $Na_xMn_{2/3}Fe_{1/3}O_2$ system for several rate values.

As for the P2-$Na_xMn_{1/2}Fe_{1/2}O_2$ system, increasing the rate to C/10 or C/5 does not induce an important capacity loss, and 84% of the initial discharge capacity is still accessible at C/5. On the other hand, cycling at higher rate values leads to an important capacity loss as only 56 %, 28 % and 16 % of the initial discharge capacity are reached at C/2, C and 2C. When the material is cycled back at C/20, 92% of the initial discharge capacity is reached after one cycle. This indicates that the material does not undergo any damage upon cycling at high rate. The observed capacity loss is therefore only due to kinetic effects. The low discharge capacity reached at the 19th cycle at C/20 is due to the low amount of Na^+ ions intercalated during the previous charge carried out at 2C.

A-III.2.c. *In situ* studies of the $Na_xMn_{2/3}Fe_{1/3}O_2$ phase diagram

The structural behavior of the material upon cycling was studied by *in situ* XRPD: first during the full charge of the battery, from 1.5 V to 4.3 V in *operando* mode, and then upon discharge from the pristine material, in the GITT mode.

Operando in situ study during the Na deintercalation

The experimental conditions of the *operando in situ* experiment were optimized in order to record XRPD patterns in the 13 – 20° and 30 – 43° 2θ ranges every 0.01 Na^+ per formula unit. The evolution of the XRPD patterns along with the complete charge of the battery is shown in **Figures A-III.20** and **A-III.21**, in reverse order.

The experiment starts from the intercalated state of the material whose corresponding formula is $Na_{0.96}Mn_{2/3}Fe_{1/3}O_2$. This phase can be indexed in the orthorhombic system (Cmcm space group, P'2 structure). The orthorhombic distortion is clearly emphasized by the splitting of the $(102)_{P2}$ diffraction line into the $(022)_{P'2}$ and $(112)_{P'2}$ ones. The P'2-$Na_xMn_{2/3}Fe_{1/3}O_2$ structure is observed alone for a narrow Na range: $0.94 < x \leq 0.96$.

For $x \leq 0.94$, a new set of diffraction lines appears at 16.3° and 38.1 °. These diffraction peaks correspond to the $(002)_{P'2}$ and $(022)_{P'2}$ reflections of a newly formed P'2 phase. To differentiate the two P'2 phases, they will be referred to as the "fully-intercalated $P'2_f$ phase" and as the "intermediate $P'2_i$ phase". The biphasic domain between the two P'2 phases is observed for $0.76 < x \leq 0.96$. Then, the intermediate $P'2_i$ phase is observed alone in a very short range: $0.74 \leq x \leq 0.76$.

Upon further deintercalation, a new phase appears with the P2 structure, leading to a biphasic domain in the $0.68 < x \leq 0.74$ range between the $P'2_i$ intermediate phase and the P2 phase. Surprisingly, the P2 phase and the intermediate $P'2_i$ one share the same interslab distance as shown by the position of their (00*l*) diffraction lines in **Figures A-III.20** and **A-III.21**. A P2 solid solution domain is then observed for $0.20 < x \leq 0.68$.

From x = 0.20, two broad diffraction peaks are observed in the $15.3 \leq 2\theta \leq 18.1$ ° range. One comes from the $(002)_{P2}$ diffraction line and the other one appears at approximatively 17 °. These two diffraction lines remain up to 4.3 V ($x \approx 0.1$), end of the experiment. The shift of the diffraction peak at ≈ 17 ° continuously shifts towards high angle values, indicating a decrease of the interslab similar to the one observed in the other systems.

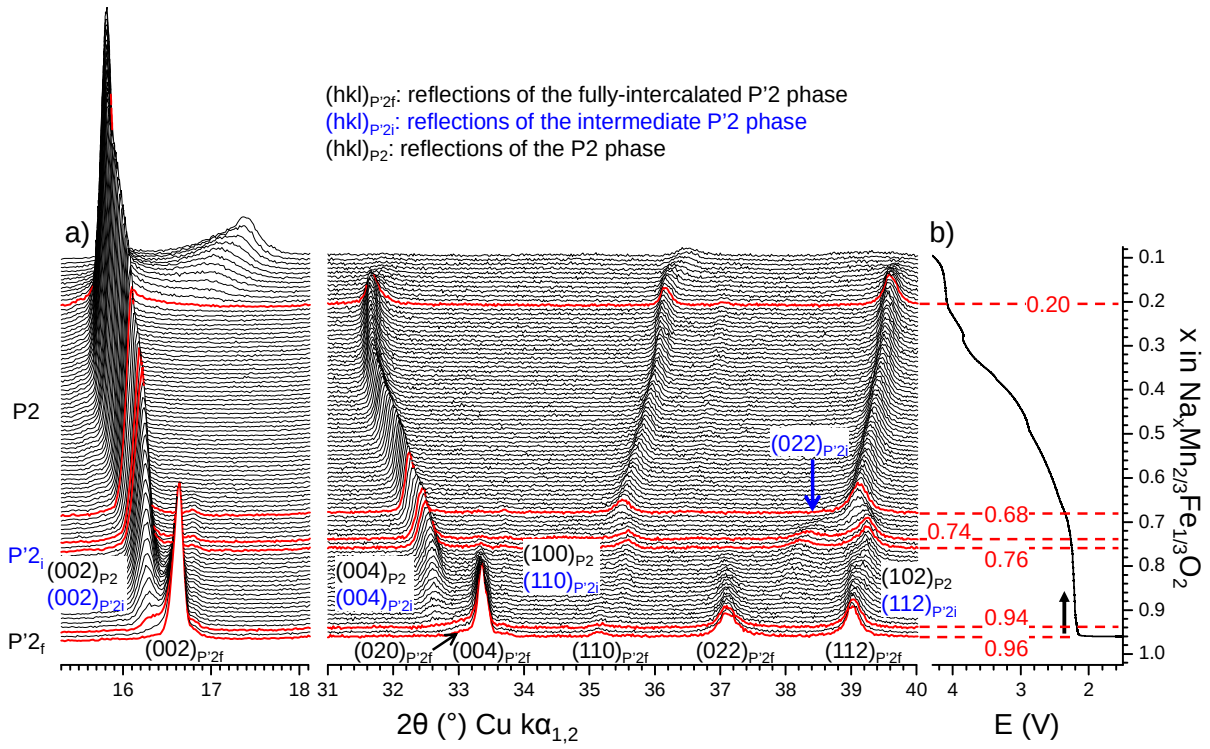

Figure A-III.20: (a) XRPD patterns of the $Na_xMn_{2/3}Fe_{1/3}O_2$ material recorded *in situ* (*operando* mode) during the charge of a $Na_xMn_{2/3}Fe_{1/3}O_2/NaPF_6$ in PC (1M) + 2 wt% FEC/Na cell along with (b) the corresponding cycling curve. The red XRPD patterns correspond to the limits of the different structural domains.

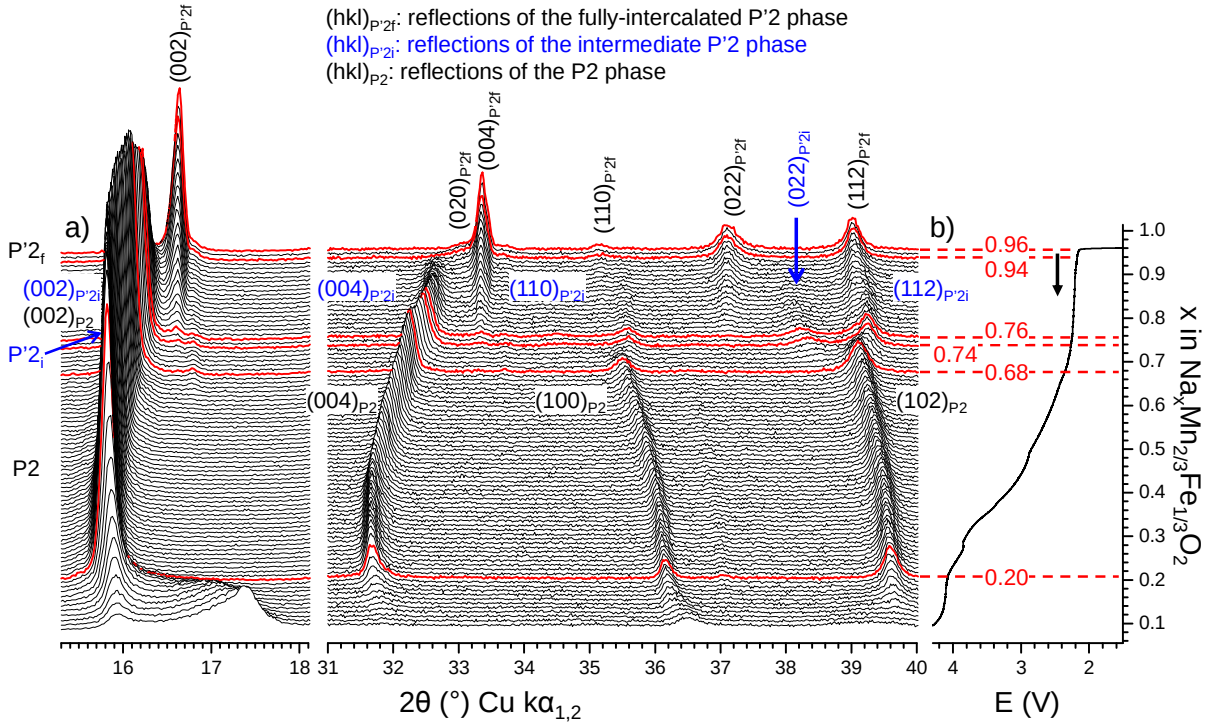

Figure A-III.21: Inversed representation of the *operando in situ* XRPD experiment carried out on the $Na_xMn_{2/3}Fe_{1/3}O_2$ system: (a) XRPD patterns and (b) corresponding cycling curve. The red XRPD patterns correspond to the limits of the different structural domains.

The comparison of this *in situ* experiment with the one carried out on $Na_xMn_{1/2}Fe_{1/2}O_2$ shows that both systems exhibit similar behavior. The only difference is the occurrence of the intermediate $P'2_i$ phase between the $P'2_f$ fully intercalated and P2 ones.

The indexation of the XRPD diagrams presented in **Figures A-III.20** and **A-III.21** allows an estimation of the interslab distances and cell parameters of the different phases. These distances are shown in **Figure A-III.22a** (interslab distances) and **A-III.22b** (cell parameters), along with the galvanostatic curve (**Figure A-III.22c**).

The evolution of the interslab distances (**Figure A-III.22a**) does not show any significant variation in the intermediate $P'2_i$ phase + intercalated $P'2_f$ phase biphasic domain ($0.76 < x \leq 0.96$). The comparison of the cell parameters for the P'2 phases show that the intercalated one is more distorted, as the two M-M distances in the MO_2 slabs are approximatively equal to 2.91 and 3.10 Å *vs.* 2.90 Å and 2.99 Å in the intermediate $P'2_i$ phase. This is due to the higher Mn^{3+} content of the intercalated $P'2_f$ phase which leads to an increase of the cooperative Jahn Teller effect. The lower interslab distance of the intercalated P2 phase (5.40 Å *vs.* 5.45 Å for the intermediate $P'2_i$ phase) confirms this assumption as it implies a higher Na^+ - and thus Mn^{3+}- content.

In the intermediate $P'2_i$ phase + P2 phase biphasic domain, the two phases share identical interslab distance, in agreement with the observation of the (00*l*) diffraction lines (**Figures A-III.20** and **A-III.21**). As already discussed, in the P2 solid solution domain the interslab distance continuously increases as Na^+ ions are involved in the screening effect between the O planes. On the other hand the value of the $a_{hex.}$ cell parameter continuously decreases, due to the contraction of the MO_6 octahedra upon the $M^{3+} \rightarrow M^{4+}$ redox process, the M^{4+}-O bonds being more covalent than the M^{3+}-O ones. For $x < 0.20$, we observe a continuous decrease of the intensity of the diffraction lines of the P2 phase. Simultaneously, a broadening of the $(002)_{P2}$ diffraction peak is observed on the high angle side and a new diffraction peak appears in the $16.7 \leq 2\theta \leq 16.9$ ° region. This behavior is very similar to the one observed in the other P2 and O3-based systems at the end of charge. As for the P2-based $Na_xMn_{1/2}Fe_{1/2}O_2$ system, we assume that stacking faults consisting in layers of NaO_6 octahedrons are created among the P2 layers in the material for $x < 0.20$. Contrarily to the other systems, we do not reach the deintercalation state where the diffraction lines merge to create the pure "Z" (P2-based systems) or "X" (O3-based systems) phases.

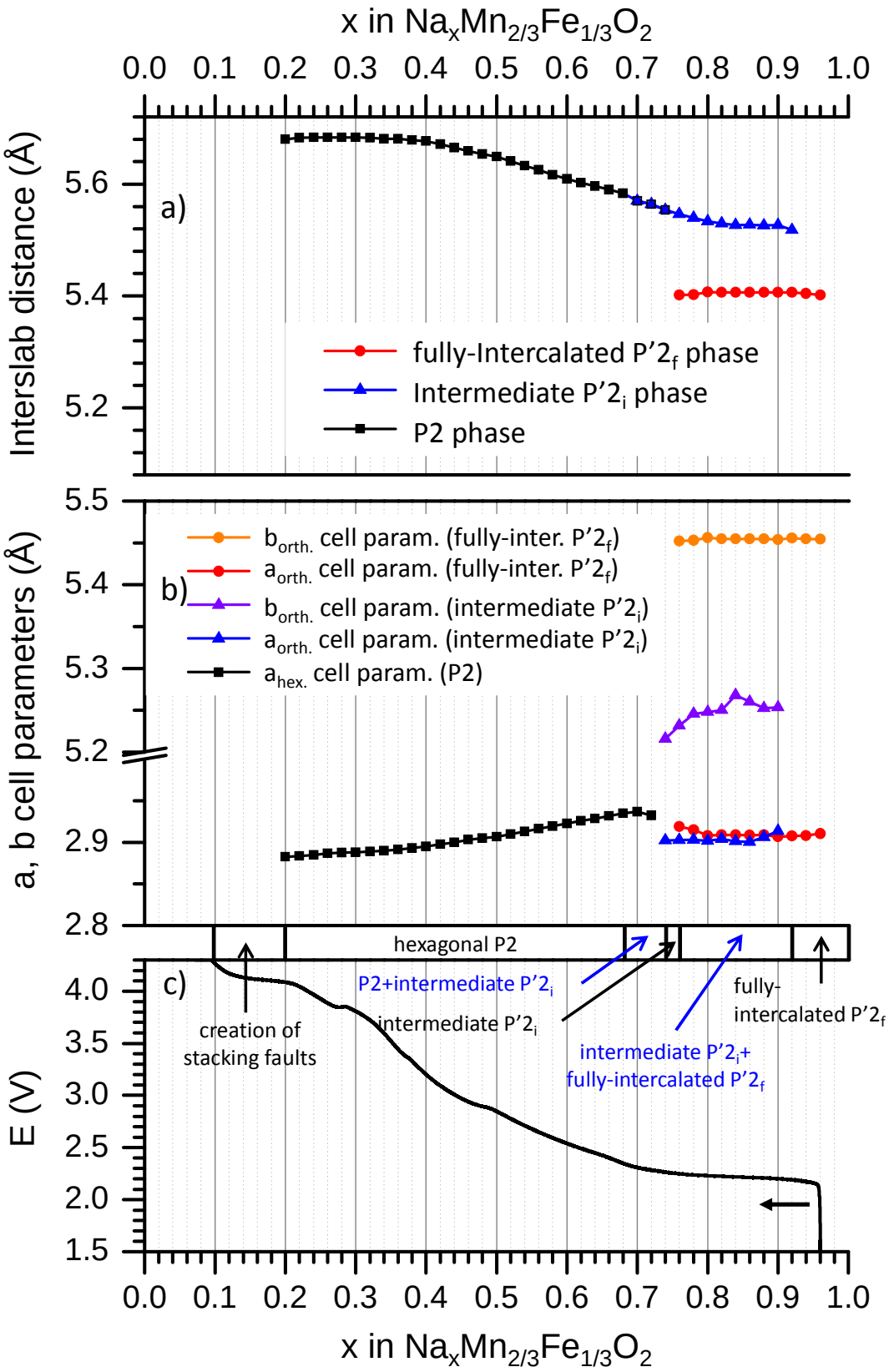

Figure A-III.22: Evolution of the (a) interslab distance and (b) a and b cell parameters of the different $Na_xMn_{2/3}Fe_{1/3}O_2$ phases upon sodium deintercalation. The galvanostatic curve versus x is also shown as a guide in (c).

After the *operando in situ* experiment, the cell was discharged again down to 1.5 V and the voltage was maintained until a negligible residual current was observed. The XRPD pattern was then recorded under constant voltage, and is compared to the one recorded after the first discharge in **Figure A-III.23**.

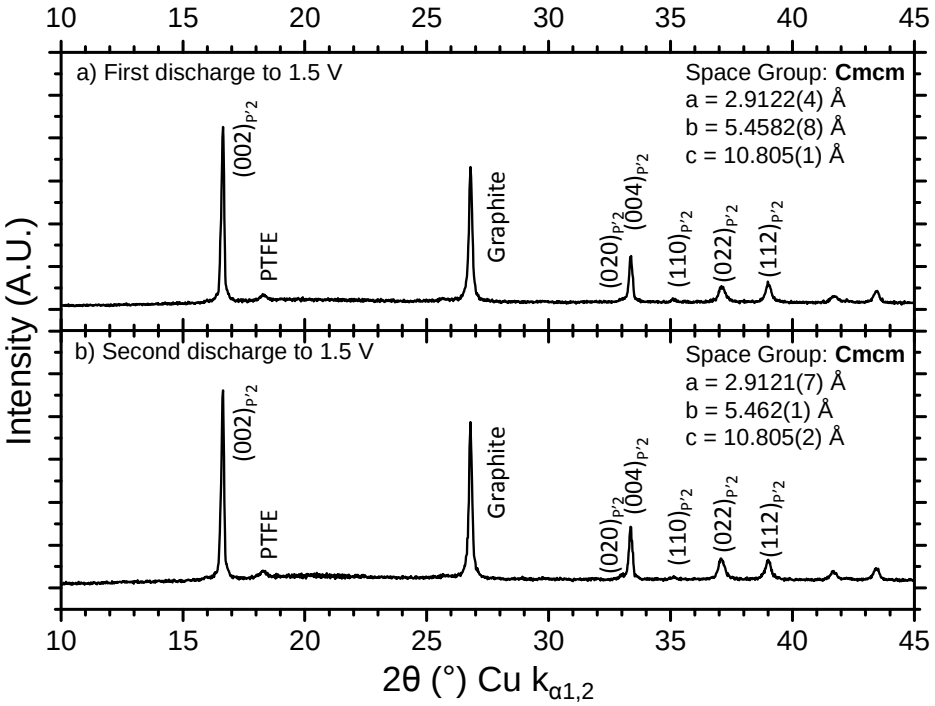

Figure A-III.23: Comparison of the XRPD patterns recorded for the P'2-$Na_xMn_{2/3}Fe_{1/3}O_2$ phases after (a) the first and (b) second discharge at 1.5 V, and maintained at the voltage until a negligible current was observed.

As one can see, the two XRPD patterns exhibit well-defined diffraction peaks, which indicate that the cycling up to 4.3 V does not damage the material after one cycle. Both patterns are indexed in the Cmcm space group (P'2 phase) and show very close cell parameters. No noticeable broadening of the diffraction peaks is observed between the two patterns.

GITT in situ study during the Na intercalation from P2-$Na_{0.66}Mn_{2/3}Fe_{1/3}O_2$

This experiment carried out during a GITT discharge aimed to confirm the behavior we observed in the operando mode at low voltage (formation of the P'2 intermediate phase). Current pulses (C/50) corresponding to a sodium step of + 0.03 Na^+ ions per formula unit were applied. An open current voltage (or relaxation) period was then set for 5 hours in order to reach equilibrium. The XRPD pattern was recorded during the last 90 minutes of the relaxation period between 15° and 45° (2θ Cu kα_1). The collected XRPD patterns are shown in **Figure A-III.24** along with the GITT curve. A magnification in the 30° - 45° 2θ region is given in **Figure A-III.25**.

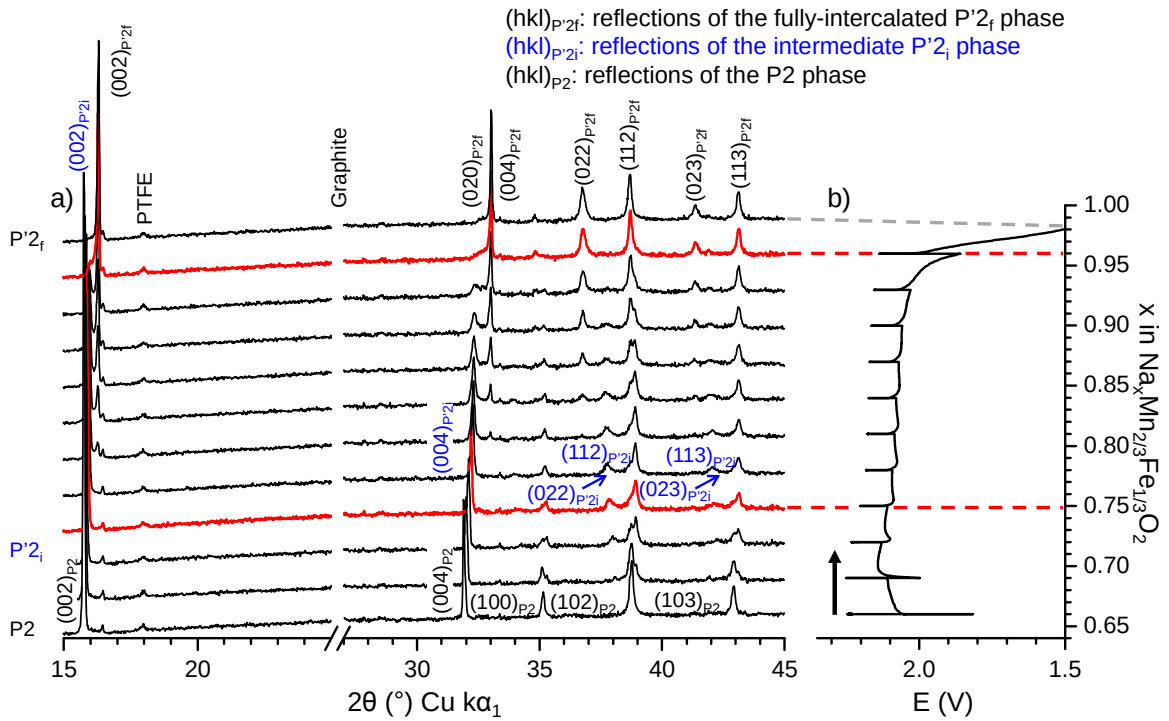

Figure A-III.24: (a) XRPD patterns recorded *in situ* during the relaxation periods of a $Na_xMn_{2/3}Fe_{1/3}O_2$/$NaPF_6$ in PC (1M) + 2 wt% FEC /Na cell along with (b) the corresponding GITT curve. Only the most important reflections are labeled for clarity purposes.

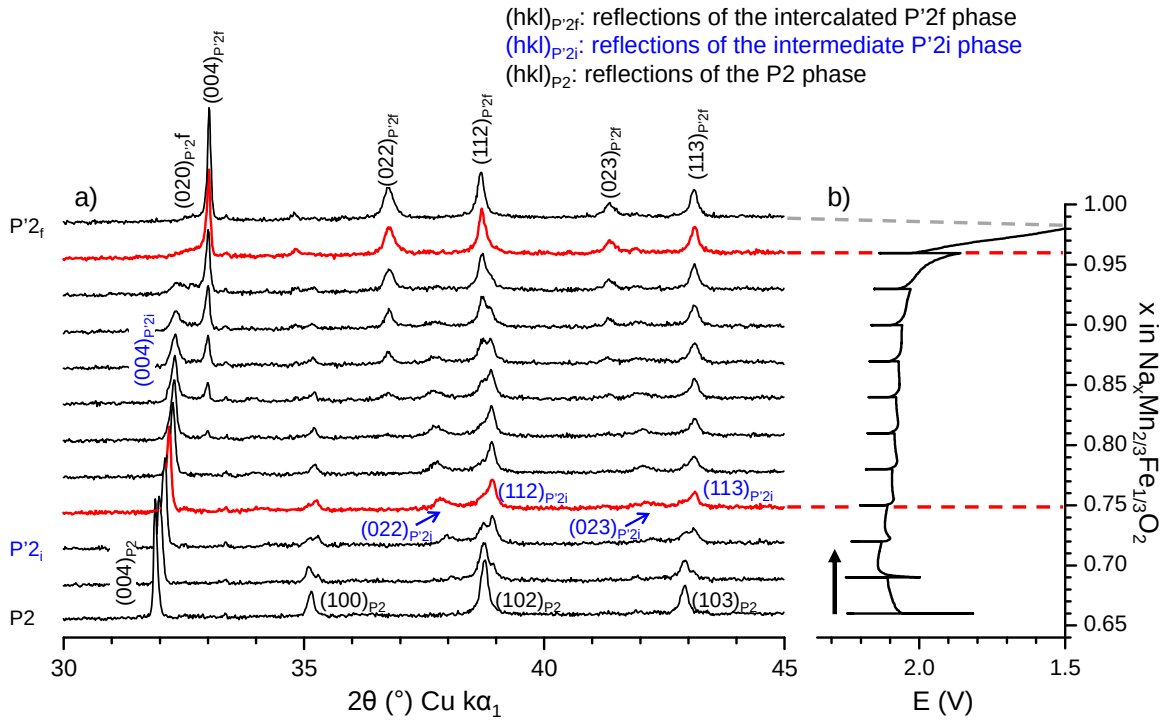

Figure A-III.25: (a) Zoom in the 30 – 45 ° region of the XRPD patterns recorded *in situ* during the relaxation periods of a $Na_xMn_{2/3}Fe_{1/3}O_2$/$NaPF_6$ in PC (1M) + 2 wt% FEC /Na cell along with (b) the corresponding GITT curve. Only the most important reflections are labeled for clarity purposes.

The intercalation of a small amount of Na from the pristine material (x = 0.66) leads to the apparition of the intermediate $P'2_i$ phase at x = 0.69. The intermediate $P'2_i$ phase and P2 phase are observed simultaneously for $0.69 \leq x < 0.75$. At x = 0.75, the intermediate $P'2_i$ phase is observed alone. Further intercalation leads to the formation of the fully-intercalated $P'2_f$ phase and the biphasic domain between the two P'2 phases is observed in the $0.78 < x < 0.96$ range. Then, for $x \geq 0.96$, the fully-intercalated $P'2_f$ phase is observed alone.

The refinement of the XRPD patterns allows determining the interslab distances and cell parameters, as shown in **Figure A-III.26**. As one can see, the interslab distances of the P2 and intermediate $P'2_i$ phase decreases upon Na^+ intercalation, indicating that both phases are involved in a solid solution process in this limited composition domain. This feature could not be observed on the *in situ operando* experiment or in the GITT curve (**Figure A-III.18a**). The interslab distance of both phases does not evolve much upon Na intercalation, indicating equilibrium between the intermediate $P'2_i$ and fully-intercalated $P'2_f$ phases. Then, the fully-intercalated $P'2_f$ phase is observed alone for x = 0.98. Looking closely on the GITT curves in **Figures A-III.24b** and **A-III.25b**, we notice two voltage plateaus. The first one is located at $E \approx 2.25$ V ($0.66 < x \leq 0.69$) and the second one at $E \approx 2.17$ V ($0.81 \leq x \leq 0.93$). Due to the small gap between the two voltage plateaus, we do not expect the intermediate $P'2_i$ phase ($E_{eq} \approx 2.20$ V) to exhibit important thermodynamic stability.

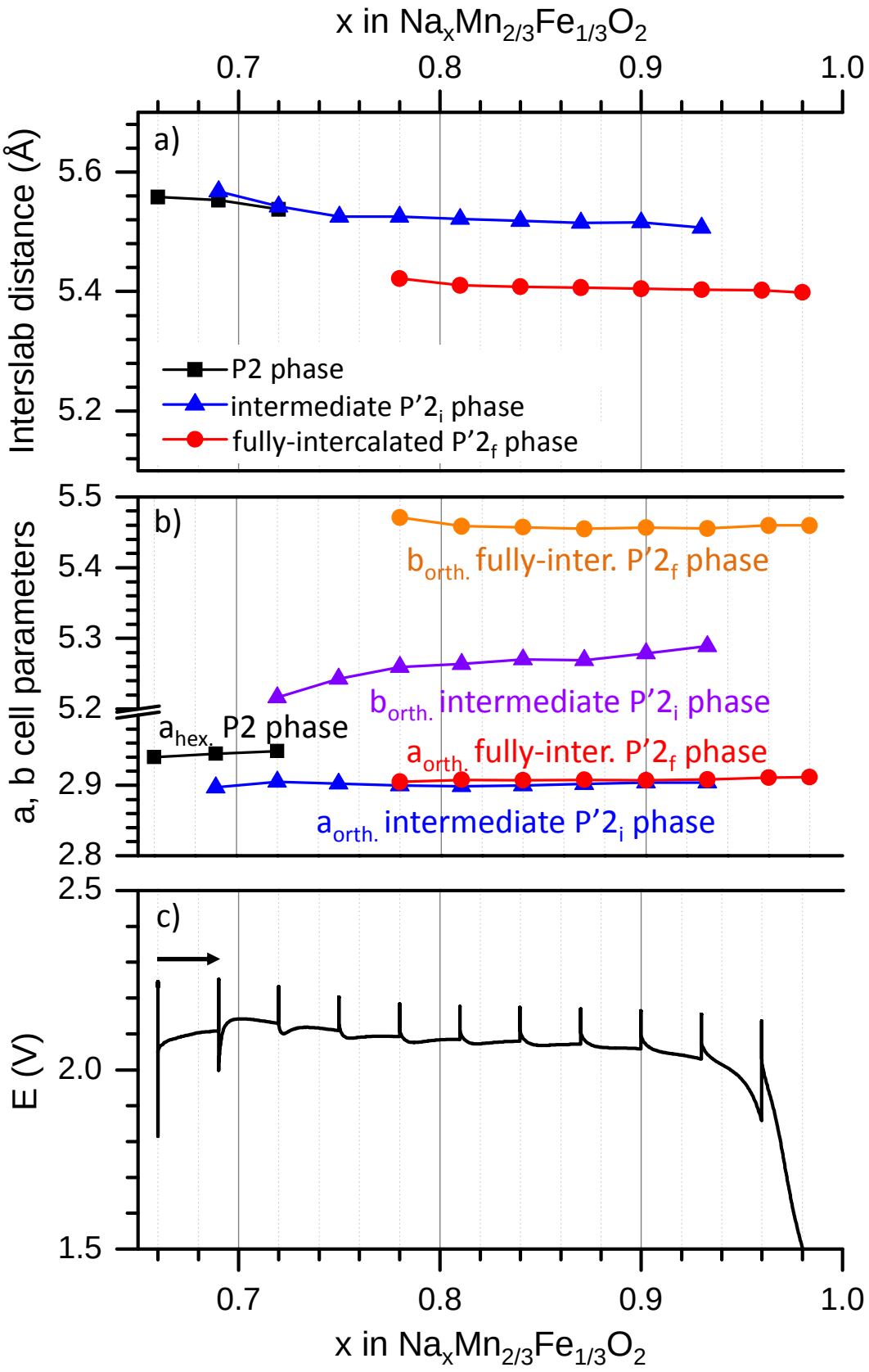

Figure A-III.26: Evolution of the (a) interslab distance and (b) a and b cell parameters of the P2 and P'2-$Na_xMn_{2/3}Fe_{1/3}O_2$ phases upon sodium intercalation. The GITT E = f(x) curve is also shown as a guide in (c).

A-III.2.d. *Ex situ* X-ray powder diffraction study of P'2-$Na_{0.96}Mn_{2/3}Fe_{1/3}O_2$

A sample of the intercalated P'2 phase was prepared by the potentiostatic method. Once recovered and washed, the powder was analyzed by XRPD. The experimental and calculated (Rietveld method) patterns are shown in **Figure A-III.27**. The corresponding cell and atomic parameters are given in **Table A-III.6**.

Due to the limitations of laboratory XRPD (signal/noise ratio, Fe fluorescence under the Cu kα radiation…), it was not possible to refine as many atomic parameters as synchrotron XRPD data allows to. Therefore we fixed the sodium content to 0.96 from the electrochemical curve, and we fixed reasonable ADP values for the Na, Mn, Fe and O atoms (1.0, 0.5, 0.5 and 0.8 Å², respectively).

Nonetheless, the XRPD pattern of the intercalated P'2 phase is successfully indexed in the orthorhombic symmetry (Cmcm space group). The $b_{orth.}/a_{orth.}$ ratio is equal to 1.88 and shows that the cooperative Jahn Teller distortion is higher than in the P2-$Na_{\approx 1}Mn_{1/2}Fe_{1/2}O_2$ phase ($b_{orth.}/a_{orth.}$ = 1.84). The cooperative Jahn Teller effect is confirmed by the distortion of the MO_6 octahedra which exhibits 4 short M-O distances (2.01(1) Å) and 2 long ones (2.25(2) Å).

As observed in the P'2-$Na_{\approx 1}Mn_{1/2}Fe_{1/2}O_2$ phase, only the Na_e site which shares edges with the surrounding MO_6 octahedron is occupied in order to minimize the Na^+-Na^+ repulsions.

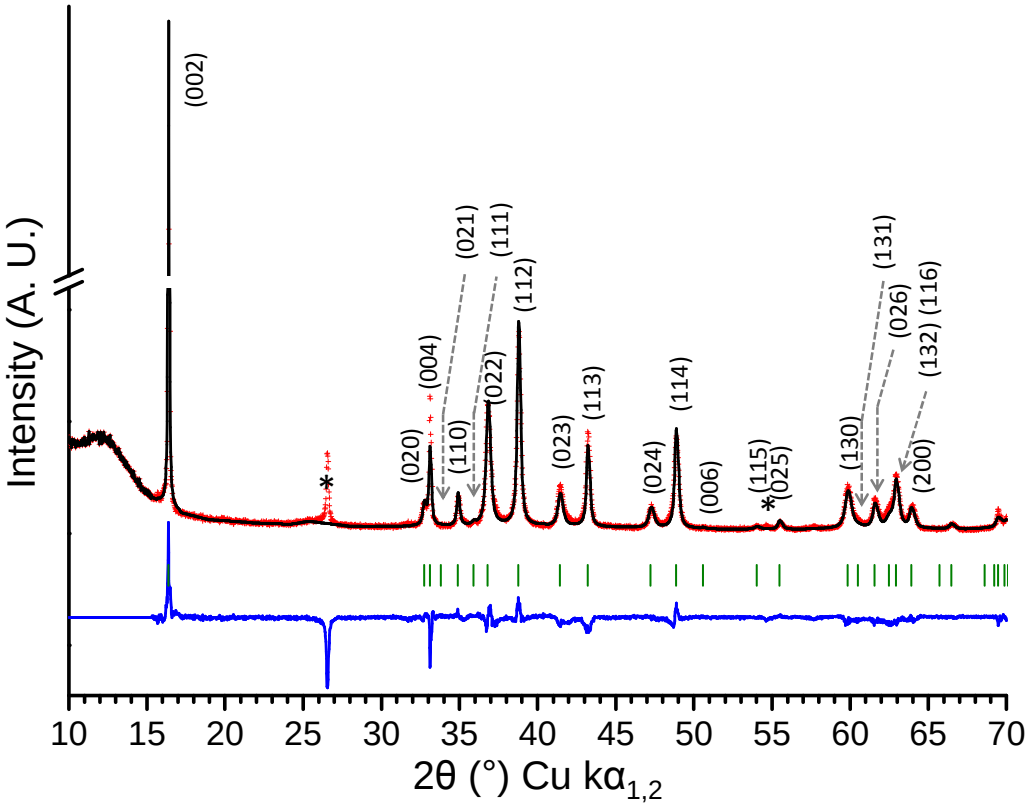

Figure A-III.27: Observed and calculated (Rietveld method) XRPD patterns of the intercalated P'2-$Na_{0.96}Mn_{2/3}Fe_{1/3}O_2$ phase. Red crosses: experimental, black line: calculated, blue line: difference and green bars: Bragg positions. The * symbol indicates the position of the graphite diffraction lines.

Space group: **Cmcm** $a_{orth.}$ = 2.9109(7) Å, $b_{orth.}$ = 5.467(2) Å, $c_{orth.}$ = 10.817(3) Å $b_{orth.}/a_{orth.}$ = 1.88						
Atom	Wyckoff		Coordinates		Occupancy	ADP (Å²)
Na_e	4c	0	0.687(4)	1/4	0.96	1.0
Mn	4a	0	0	0	1	0.5
Fe	4a	0	0	0		
O	8f	0	0.644(5)	0.895(2)	1	0.8
Distances :	M-O		Na-O			
	4 * 2.01(1) Å 2 * 2.25(2) Å		4 * 2.33(2) Å 2 * 2.40(1) Å			
Rwp = 14.36 %; R_B = 9.37 % with excluded regions (graphite)						

Table A-III.6: Structural parameters and reliability factors calculated from the XRPD diagram of the P'2-$Na_{0.96}Mn_{2/3}Fe_{1/3}O_2$ phase.

A-III.3. Study of the Redox mechanisms during Na deintercalation for the P2-based $Na_xMn_{1/2}Fe_{1/2}O_2$ and $Na_xMn_{2/3}Fe_{1/3}O_2$ systems

As for the O3-based systems, we studied the redox mechanisms involved during Na^+ deintercalation for both P2-based systems. The open current voltage charge curves extracted from the GITT cycling ones are shown in **Figure A-III.28**. If the voltage jump is located at x ≈ 0.50 on the cycling curve of the $Na_xMn_{1/2}Fe_{1/2}O_2$ system (**Figure A-III.28**), no well-defined voltage jump is observed on the $Na_xMn_{2/3}Fe_{1/3}O_2$ curve, preventing any comparison. By comparison to the O3-based systems we expect the Mn^{4+}/Mn^{3+} redox couple to be active in the low voltage region and the Fe^{4+}/Fe^{3+} redox couple to be active in the high voltage region. To confirm this assumption, we carried out *operando in situ* X-ray absorption spectroscopy on the $Na_xMn_{1/2}Fe_{1/2}O_2$ system only and *ex situ* ^{57}Fe Mössbauer spectroscopy measurements on the $Na_xMn_{1/2}Fe_{1/2}O_2$ and $Na_xMn_{2/3}Fe_{1/3}O_2$ systems.

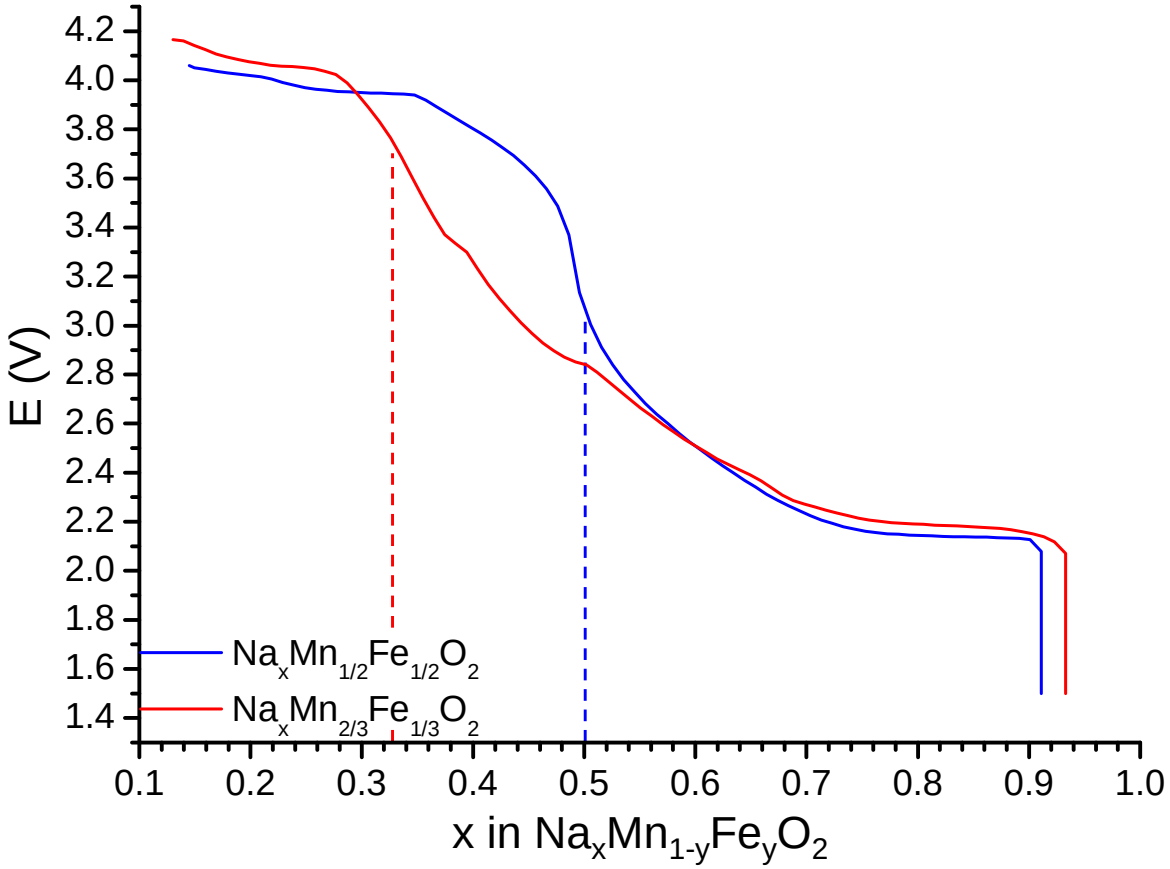

Figure A-III.28: Open current voltage charging curves extracted from the GITT cycling cones for (blue) $Na_xMn_{1/2}Fe_{1/2}O_2$ and (red) $Na_xMn_{2/3}Fe_{1/3}O_2$. The dashed lines represent the expected position of the voltage jump associated to the change of redox process during charge if the redox potentials of Fe^{4+}/Fe^{3+} and Mn^{4+}/Mn^{3+} are well separated.

A-III.3.a. *Operando in situ* x-ray absorption near edge spectroscopy study of the $Na_xMn_{1/2}Fe_{1/2}O_2$ system

The *operando in situ* X-ray absorption spectroscopy study was performed on the $Na_xMn_{1/2}Fe_{1/2}O_2$ system[19], starting from the intercalated state of the material. The evolution of the X-ray absorption near edge spectroscopy parts of the spectrum are shown in **Figures A-III.29a** (Mn K-edge) and **A-III.29b** (Fe K-edge). The spectrum of the Mn and Fe references are shown in **Figures A-III.29c** and **A-III.29d**, respectively. Unfortunately, we do not have X-ray absorption spectroscopy data for the $Na_xMn_{2/3}Fe_{1/3}O_2$ system yet.

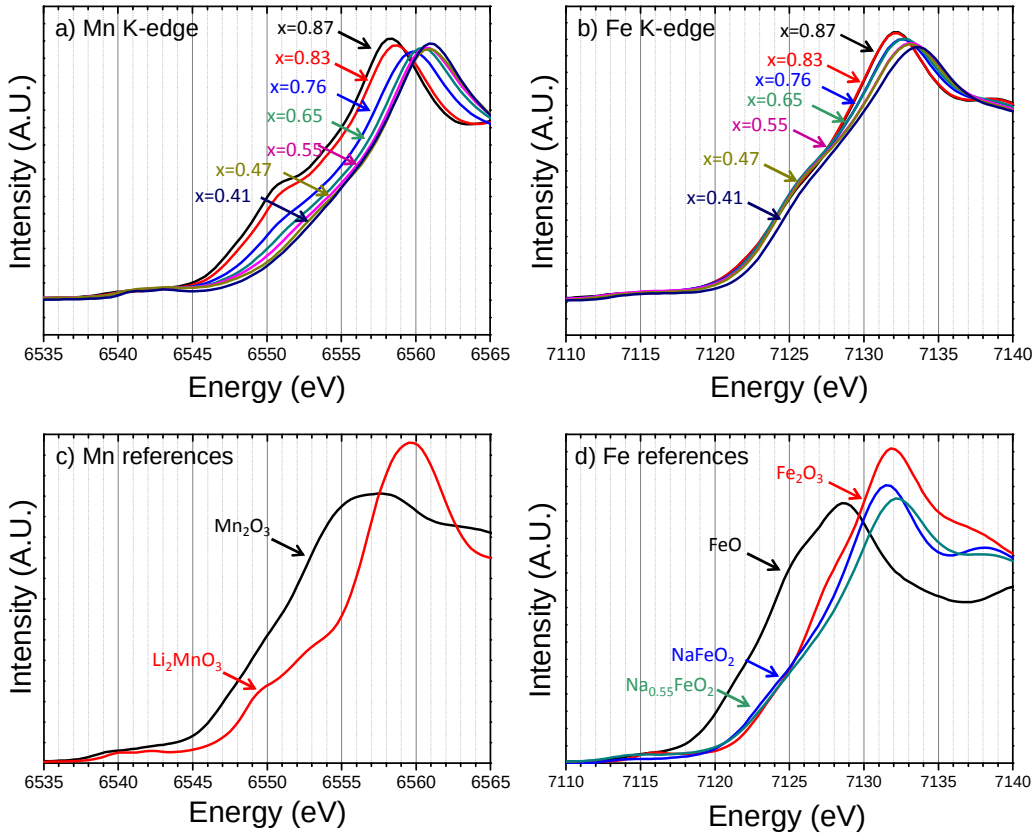

Figure A-III.29: X-ray absorption near edge spectroscopy spectra recorded *in situ* and corresponding to the (a) Mn and (b) Fe K-edges of a $Na_xMn_{1/2}Fe_{1/2}O_2$ electrode. The spectra of the (c) Mn and (d) Fe references compounds are also given.

As shown in **Figure A-III.29a**, the Mn K-edge exhibits an important shift towards higher energies upon deintercalation in the $0.87 \geq x > 0.47$ range. The comparison to the Mn references (**Figure A-III.29c**) associates this shift to the $Mn^{3+} \rightarrow Mn^{4+}$ redox process. In the same range, a small continuous shift is observed on the Fe K-edge spectra. As the same phenomenon was observed for the O3-$Na_xMn_{1/2}Fe_{1/2}O_2$

[19] In collaboration with Pr. Bing-Joe Hwang, NTUST / NSRRC, Taiwan, R.O.C.

system (**Chapter A-II**), one can suppose that the higher Mn content of these materials leads to the oxidation of isolated Fe^{3+} cations surrounded by more Mn^{4+} cations.

For $x \leq 0.47$, no significant shift is observed for the spectra of the Mn K-edge. On the other hand a more important shift towards the higher energy region is observed for the Fe K-edge spectra. The comparison to the Fe references (**Figure A-III.29d**) strongly suggests that the $Fe^{3+} \rightarrow Fe^{4+}$ redox process is involved in the high voltage region.

A-III.3.b. *Ex situ* ^{57}Fe Mössbauer study

Ex situ ^{57}Fe Mössbauer study of the P2-based $Na_xMn_{1/2}Fe_{1/2}O_2$ system

To confirm the $Fe^{3+} \rightarrow Fe^{4+}$ redox process and to study the structure of the materials using the Fe atoms as a local probe, we carried out ^{57}Fe Mössbauer spectroscopy measurements. The spectrum of the P2-$Na_{0.62}Mn_{1/2}Fe_{1/2}O_2$ pristine material was recorded and is shown in **Figure A-III.30**. The Mössbauer parameters corresponding to the fit of the spectrum are given in **Table A-III.7**. The spectrum corresponds to a quadrupole doublet whose isomeric shift (δ_{Fe3+} = 0.356 mm.s^{-1}) is typical of high spin Fe^{3+} ions in octahedral sites. The Lorentzian fit (**Figure A-III.30a**) highlight a quite high FWHM value (Γ = 0.35 mm.s^{-1}) and a high quadrupole splitting (Δ_{Fe3+} = 0.67 mm.s^{-1}). A distribution fit (**Figure A-III.30b**) based on fixed isomeric shift and FWHM values (**Table A-III.7b**) highlight the existence of a distribution of the quadrupole splittings (Δ^*) which are too close to be separated (**Figure A-III.30c**). This implies that the presence of 12% of $Mn^{3+}O_6$ octahedra is enough to impact the FeO_6 ones (distribution of the surroundings).

a) Lorentzian fit				
Site	**δ (mm.s^{-1})**	**FWHM (mm.s^{-1})**	**Δ (mm.s^{-1})**	**P (%)**
Fe^{3+}(A)	0.356	0.35	0.67	100
b) Distribution fit				
Site	**δ (mm.s^{-1})**	**FWHM (mm.s^{-1})**	**Δ* (mm.s^{-1})**	**P (%)**
Fe^{3+}(1)	0.356 (fixed)	0.25 (fixed)	0.70	100

Table A-III.7: Mössbauer parameters deduced from the Lorentzian and Distribution fits of the Mössbauer spectrum of the P2-$Na_{0.62}Mn_{1/2}Fe_{1/2}O_2$ pristine material.

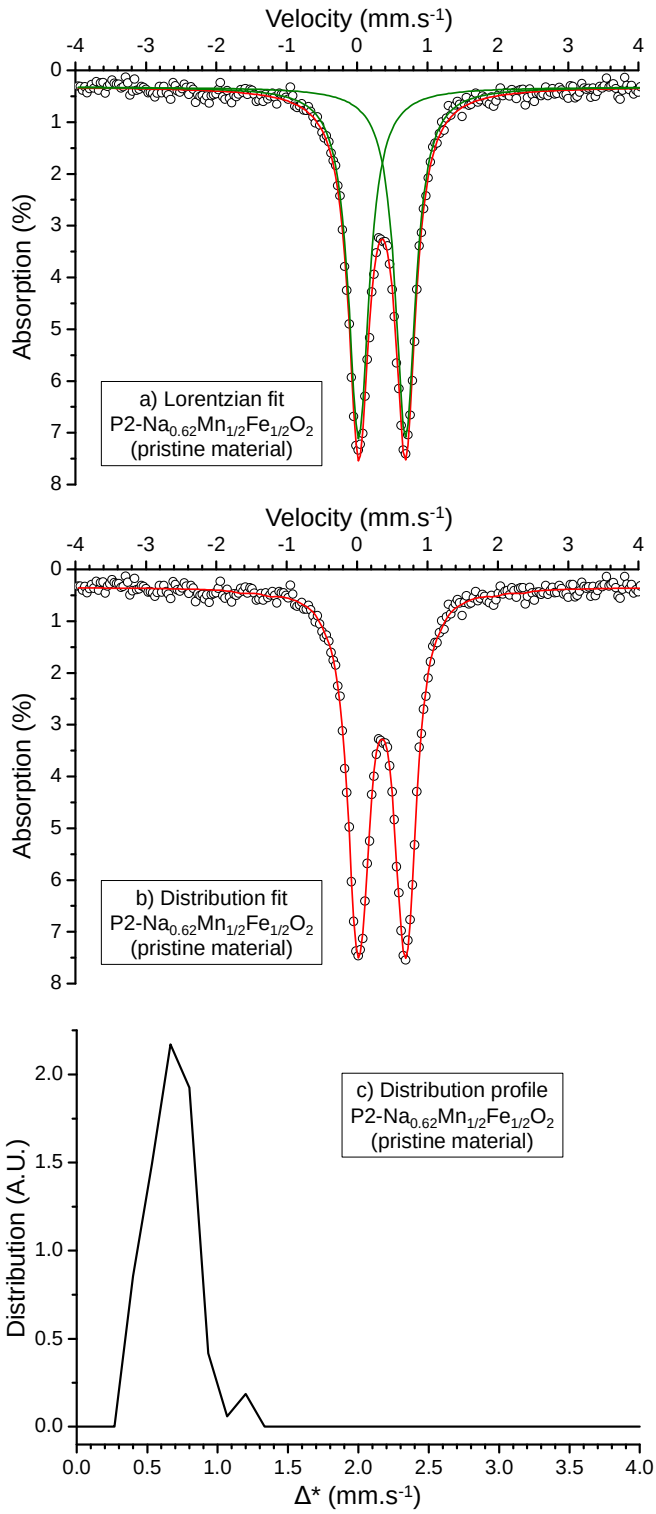

Figure A-III.30: (a) Lorentzian and (b) distribution fits of the Mössbauer spectrum of the P2-$Na_{0.62}Mn_{1/2}Fe_{1/2}O_2$ pristine material. (c) Distribution profile corresponding to the distribution fit.

Then several $Na_xMn_{1/2}Fe_{1/2}O_2$ materials were prepared following the potentiostatic route in order to obtain precise sodium contents: x ≈ 1.0 (E_{eq} = 1.5 V), x = 0.5 (E_{eq} = 3.2 V), x = 0.45 (E_{eq} = 3.8 V), x = 0.24 (E_{eq} = 4.0 V) and x = 0.14 (E_{eq} = 4.3 V). The corresponding Mössbauer spectra are shown in **Figure A-III.31** and compared altogether in **Figure A-III.32**. The developed formulas and awaited Fe^{n+} populations of the (dis)charged materials are given in **Table A-III.8** along with the Mössbauer parameters of the fit of the spectra.

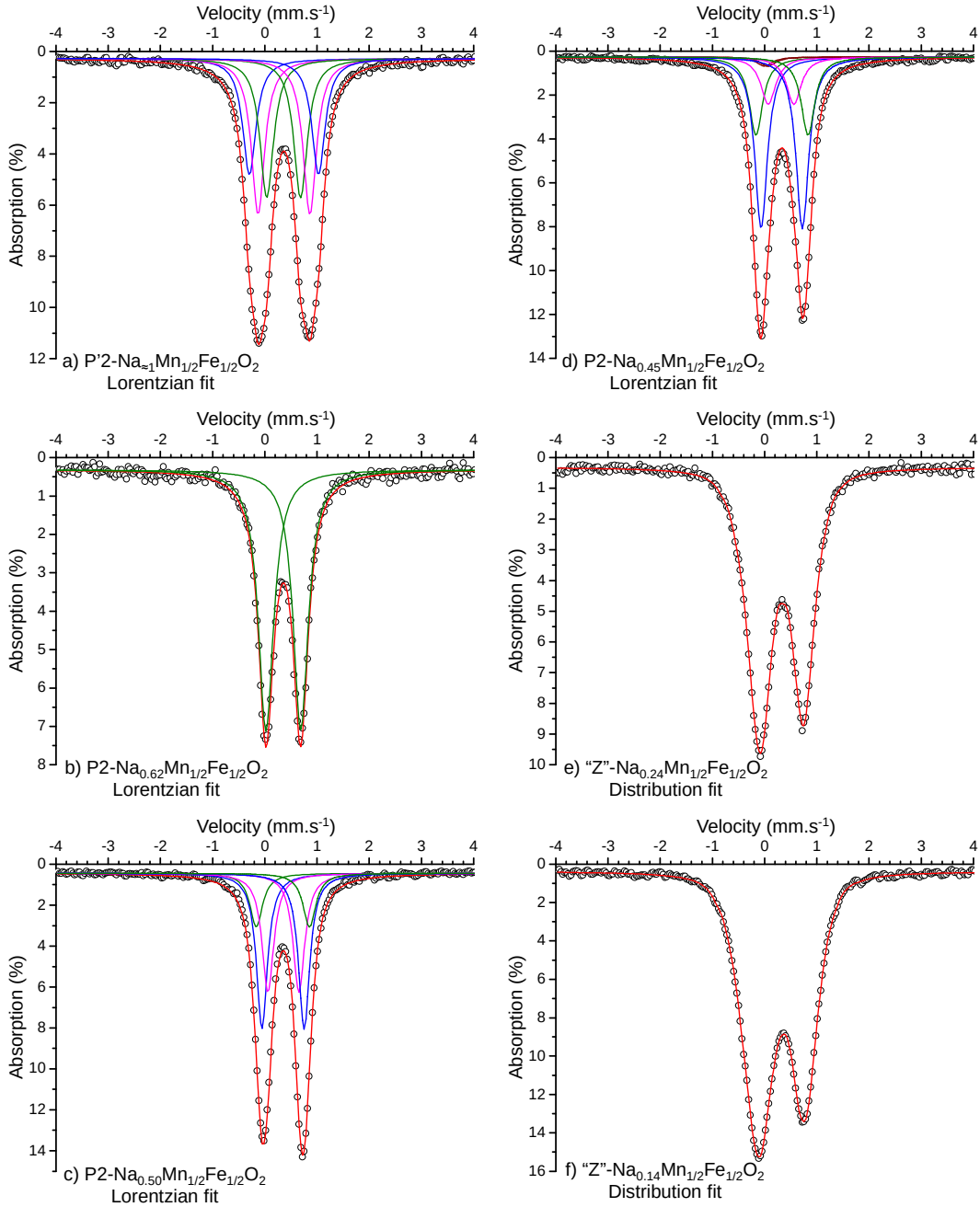

Figure A-III.31: ^{57}Fe Mössbauer spectra of (a) P'2-$Na_{\approx1}Mn_{1/2}Fe_{1/2}O_2$, (b) P2-$Na_{0.62}Mn_{1/2}Fe_{1/2}O_2$, (c) P2-$Na_{0.5}Mn_{1/2}Fe_{1/2}O_2$, (d) P2-$Na_{0.45}Mn_{1/2}Fe_{1/2}O_2$, (e) "Z"-$Na_{0.24}Mn_{1/2}Fe_{1/2}O_2$ and (f) "Z"-$Na_{0.14}Mn_{1/2}Fe_{1/2}O_2$. Black circles: experimental and red line: calculated. Blue, pink, green and brown lines: ^{57}Fe Mössbauer sites (Lorentzian fits only).

Awaited results from electrochemistry			Mössbauer results (Lorentzian fit)																			
Developed formula	%Fe^{3+}	%Fe^{4+}	Fe^{3+}(A)				Fe^{3+}(B)				Fe^{3+}(C)										%Fe^{3+}	%Fe^{4+}
			δ ($mm.s^{-1}$)	Δ ($mm.s^{-1}$)	Γ ($mm.s^{-1}$)	P (%)	δ ($mm.s^{-1}$)	Δ ($mm.s^{-1}$)	Γ ($mm.s^{-1}$)	P (%)	δ ($mm.s^{-1}$)	Δ ($mm.s^{-1}$)	Γ ($mm.s^{-1}$)	P (%)								
$Na_{1.0}Mn^{3+}_{0.50}Mn^{4+}_{0.00}Fe^{3+}_{0.50}Fe^{4+}_{0}O_2$	100	0	0.363	0.66	0.33	37	0.366	1.33	0.30	24	0.367	1.01	0.31	39							100	0
$Na_{0.62}Mn^{3+}_{0.12}Mn^{4+}_{0.38}Fe^{3+}_{0.50}Fe^{4+}_{0}O_2$	100	0	0.356	0.67	0.35	100																
$Na_{0.50}Mn^{3+}_{0.00}Mn^{4+}_{0.50}Fe^{3+}_{0.50}Fe^{4+}_{0}O_2$	100	0	0.346	1.02	0.29	18	0.350	0.81	0.26	45	0.358	0.59	0.27	37							100	0
Developed formula	%Fe^{3+}	%Fe^{4+}	Fe^{3+}(A)				Fe^{3+}(B)				Fe^{4+}				$Fe^{(3+z)+}$						%Fe^{3+}	%Fe^{4+}
			δ ($mm.s^{-1}$)	Δ ($mm.s^{-1}$)	Γ ($mm.s^{-1}$)	P (%)	δ ($mm.s^{-1}$)	Δ ($mm.s^{-1}$)	Γ ($mm.s^{-1}$)	P (%)	δ ($mm.s^{-1}$)	Δ ($mm.s^{-1}$)	Γ ($mm.s^{-1}$)	P (%)	δ ($mm.s^{-1}$)	Δ ($mm.s^{-1}$)	Γ ($mm.s^{-1}$)	P (%)	Repartition between Fe^{3+} (%)	Repartition between Fe^{4+} (%)		
$Na_{0.45}Mn^{3+}_{0}Mn^{4+}_{0.50}Fe^{3+}_{0.45}Fe^{4+}_{0.05}O_2$	90	10	0.333	0.93	0.31	44	0.335	0.76	0.23	23	0.00	0.14	0.40	2	0.319	0.60	0.38	31	30	1	97	3
Mössbauer results (Distribution fit)																						
Developed formula	%Fe^{3+}	%Fe^{4+}	Fe^{3+}								Fe^{4+}				$Fe^{(3+z)+}$						%Fe^{3+}	%Fe^{4+}
			δ ($mm.s^{-1}$)	Δ* ($mm.s^{-1}$)	Γ ($mm.s^{-1}$)	P (%)					δ ($mm.s^{-1}$)	Δ ($mm.s^{-1}$)	Γ ($mm.s^{-1}$)	P (%)	δ ($mm.s^{-1}$)	Δ* ($mm.s^{-1}$)	Γ ($mm.s^{-1}$)	P (%)	Repartition between Fe^{3+} (%)	Repartition between Fe^{4+} (%)		
$Na_{0.24}Mn^{3+}_{0}Mn^{4+}_{0.50}Fe^{3+}_{0.24}Fe^{4+}_{0.26}O_2$	46	54	0.35	0.85	0.25	65					-0.05	0.17	0.25	6	0.17	0.86	0.25	29	16	13	81	19
$Na_{0.14}Mn^{3+}_{0}Mn^{4+}_{0.50}Fe^{3+}_{0.14}Fe^{4+}_{0.36}O_2$	28	72	0.35	0.90	0.25	55					-0.05	0.17	0.25	12	0.17	0.90	0.25	33	17	15	73	27

Table A-III.8: Developed formulas, awaited Fe^{n+} populations and Mössbauer parameters corresponding to the fit of the spectra of the $Na_xMn_{1/2}Fe_{1/2}O_2$ system presented in **Figure A-III.31**. The standard deviations on the isomer shift values are equal to 0.002 $mm.s^{-1}$. The population of the $Fe^{(3+z)+}$ is distributed into the Fe^{3+} and Fe^{4+} sites by the formula: $P(Fe^{3+}) = (\delta(Fe^{3+z})-\delta(Fe^{4+})) / (\delta(Fe^{3+})-\delta(Fe^{4+}))$.

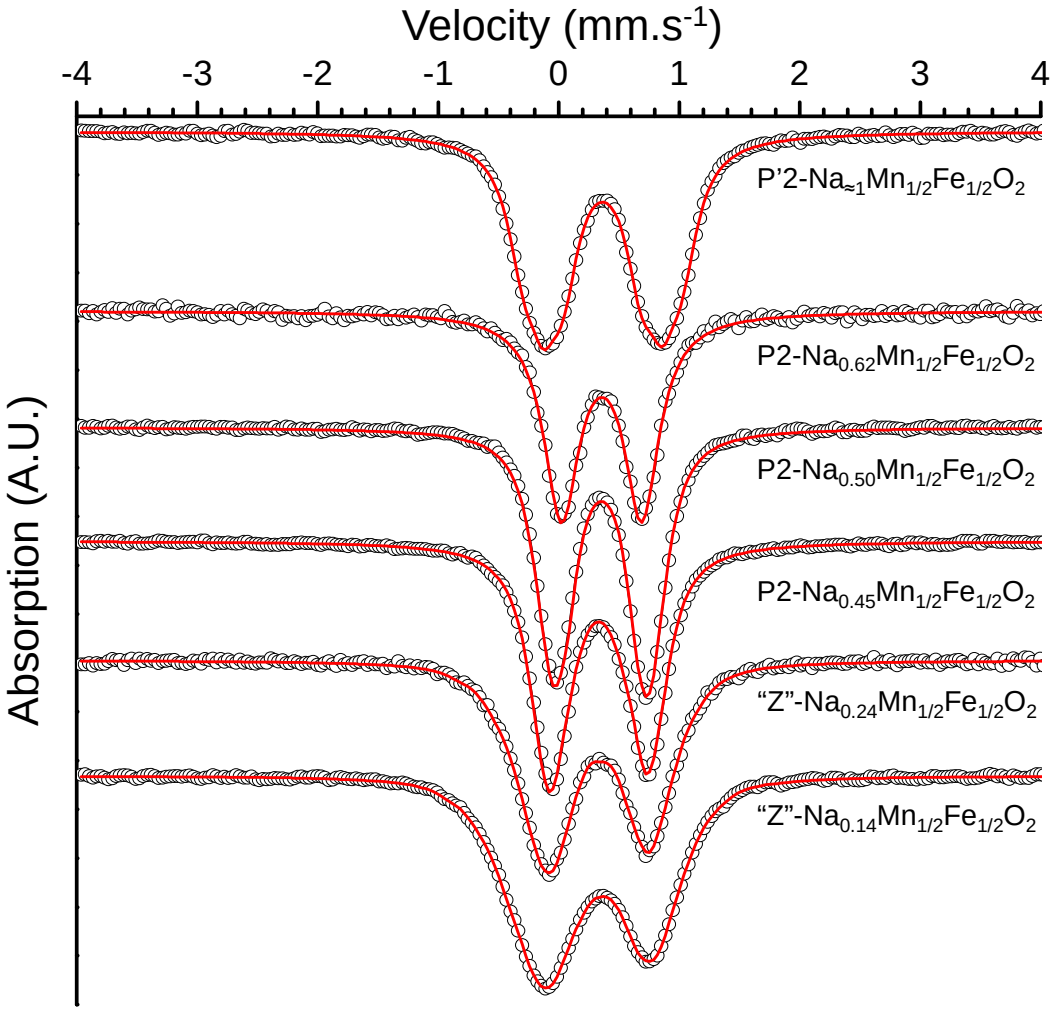

Figure A-III.32: Comparison of the Mössbauer spectra recorded in the P2-based $Na_xMn_{1/2}Fe_{1/2}O_2$ system. Black circles: experimental and red line: calculated.

As shown in **Figures A-III.31** and **A-III.32**, all spectra exhibit a quadrupole doublet whose FWHM increase continuously from x = 0.62 to x = 0.14. The Mössbauer spectra can be separated into two groups depending on the redox process: $Mn^{3+} \rightarrow Mn^{4+}$ ($x \geq 0.5$) or $Fe^{3+} \rightarrow Fe^{4+}$ ($x < 0.5$).

The spectrum of the intercalated material (**Figure A-III.31a**) is characterized by a very broad quadrupole doublet which can be described by three Mössbauer sites in a Lorentzian fit. The isomer shifts of these three sites are really close ($\delta_{Fe3+(A)}$ = 0.363 mm.s^{-1}, $\delta_{Fe3+(B)}$ = 0.366 mm.s^{-1} and $\delta_{Fe3+(C)}$ = 0.367 mm.s^{-1}) and correspond to Fe^{3+} ions in octahedral sites. If their FWHM values are also similar and approximatively equal to 0.31 mm.s^{-1}, the three sites show important disparities in their quadrupole splitting values ($\Delta_{Fe3+(A)}$ = 0.66 mm.s^{-1}, $\Delta_{Fe3+(B)}$ = 1.33 mm.s^{-1} and $\Delta_{Fe3+(C)}$ = 1.01 mm.s^{-1}, respectively). These disparities imply that some FeO_6 octahedra are located in a much distorted environment, resulting from the cooperative Jahn-Teller effect of the Mn^{3+} ions.

The spectrum of P2-$Na_{0.50}Mn_{1/2}Fe_{1/2}O_2$ (**Figure A-III.31c**) also requires three quadrupole doublets to be described. They exhibit smaller isomeric shifts that for the intercalated material ($\delta_{Fe3+(A)}$ = 0.346 mm.s^{-1}, $\delta_{Fe3+(B)}$ = 0.350 mm.s^{-1} and $\delta_{Fe3+(C)}$ = 0.358 mm.s^{-1}) in agreement with the increase of the average Mn oxidation state from +III to +IV. The disappearance of the Mn^{3+} ions and of the cooperative Jahn-Teller effect lowers the distortion of the FeO_6 octahedra, as shown by the decreasing average FWHM ($\Gamma \approx$ 27.3 mm.s^{-1}) and quadrupole splitting of the different sites ($\Delta_{Fe3+(A)}$ = 1.02 mm.s^{-1}, $\Delta_{Fe3+(B)}$ = 0.81 mm.s^{-1} and $\Delta_{Fe3+(C)}$ = 0.59 mm.s^{-1}, respectively).

The existence of the three Mössbauer sites in the $x \approx 1$ and x = 0.50 samples suggests that three sites are also present in the pristine material. However, they are too close to be separated in a Lorentzian or distribution fit.

For $x < 0.5$, we expect all the Mn^{3+} ions to be oxidized to Mn^{4+} ions. The spectrum of the P2-$Na_{0.45}Mn_{1/2}Fe_{1/2}O_2$ material can be fitted by four quadrupole doublets in a Lorentzian fit: two Fe^{3+} sites, a $Fe^{(3+z)+}$ site and a Fe^{4+} one. Once again the two Fe^{3+} sites show very close isomer shift values ($\delta_{Fe3+(A)}$ = 0.333 mm.s^{-1} and $\delta_{Fe3+(B)}$ = 0.335 mm.s^{-1}) whose corresponding quadrupole splitting implies a highly distorted Fe^{3+} site ($\Delta_{Fe3+(A)}$ = 0.93 mm.s^{-1}) and a less distorted one ($\Delta_{Fe3+(B)}$ = 0.76 mm.s^{-1}). The associated FWHM values show the same tendency as the first one is broader ($\Gamma_{Fe3+(A)}$ = 0.31 mm.s^{-1}) than the second ($\Gamma_{Fe3+(B)}$ = 0.23 mm.s^{-1}). As expected, we note the apparition of a Fe^{4+} quadrupole doublet at δ_{Fe4+} = 0.00 mm.s^{-1}, confirming the $Fe^{3+} \rightarrow Fe^{4+}$ redox process. However, we cannot conclude on the spin state of the Fe^{4+} ions. As for the ^{57}Fe Mössbauer study of the O3-based materials, a $Fe^{(3+z)+}$ site is also needed to describe the spectrum. It is characterized intermediate values of the isomer shift ($\delta_{Fe(3+z)+}$ = 0.319 mm.s^{-1}), quadrupole splitting ($\Delta_{Fe(3+z)+}$ = 0.60 mm.s^{-1}) and FWHM ($\Gamma_{Fe(3+z)+}$ = 0.38 mm.s^{-1}). Mössbauer spectroscopy gives the

following formula for the material: $Na_{0.48}Mn_{1/2}Fe_{1/2}O_2$. We note a small gap to the formula expected from electrochemistry ($Na_{0.45}Mn_{1/2}Fe_{1/2}O_2$).

The next two spectra correspond to the "Z" phase and show a broad quadrupole doublet which can only be described using a distribution fitting involving three Fe sites: Fe^{3+}, Fe^{4+} and $Fe^{(3+z)+}$. The FWHM have been fixed to reasonable values for the fit (0.25 $mm.s^{-1}$) and so were the isomeric shifts (δ_{Fe3+} = 0.35 $mm.s^{-1}$, $\delta_{Fe(3+z)+}$ = 0.17 $mm.s^{-1}$ and δ_{Fe4+} = -0.05 $mm.s^{-1}$). The fit of the spectra give increasing quadrupole splitting values (from 0.85 to 0.90 $mm.s^{-1}$ for Δ_{Fe3+} and from 0.86 to 0.90 $mm.s^{-1}$ for $\Delta_{Fe(3+z)+}$) highlighting an increasing disorder in the material, in agreement with the *operando in situ* XRPD results.

The determined formulae are $Na_{0.41}Mn_{1/2}Fe_{1/2}O_2$ and $Na_{0.36}Mn_{1/2}Fe_{1/2}O_2$ while the expected ones from electrochemistry $Na_{0.24}Mn_{1/2}Fe_{1/2}O_2$ and $Na_{0.14}Mn_{1/2}Fe_{1/2}O_2$, respectively. These sodium contents are again significantly lower than the expected ones. As for the O3-based $Na_xMn_{1/2}Fe_{1/2}O_2$ system, underestimation of the Na content, which lead to an overestimation of the Fe^{4+} one, would explain the differences between the expected formulae and the ones deduced from Mössbauer spectroscopy.

Furthermore, the most deintercalated samples (x = 0.24 and x = 0.14) correspond to an unknown part of the phase diagram where the "Z" phase appears and where a strange phenomenon involving a lot of energy is evidenced on the galvanostatic curve (**Chapter A-III.1.b**). As the experimental Fe^{3+} : Fe^{4+} ratio does not evolve much between the samples prepared at 4.0 V ($x_{th.}$ = 0.24) and 4.3 V ($x_{th.}$ = 0.14), one can also suppose the participation of another redox couple for E > 4.0 V. Further experiments are required before we can conclude on this topic.

The Mössbauer results obtained on the P2-based $Na_xMn_{1/2}Fe_{1/2}O_2$ system are very similar to the ones of the O3-based $Na_xMn_{1/2}Fe_{1/2}O_2$ system. They show that the $Mn^{4+/3+}$ and $Fe^{4+/3+}$ redox couples are successively involved during the electrochemical deintercalation, in agreement with the X-ray absorption spectroscopy study.

Ex situ ^{57}Fe Mössbauer study of the P2-based $Na_xMn_{2/3}Fe_{1/3}O_2$ system

The $Na_xMn_{2/3}Fe_{1/3}O_2$ system was also investigated by ^{57}Fe Mössbauer spectroscopy. The spectrum of the pristine material and is shown in **Figure A-III.33**. It consists in a quadrupole doublet whose isomeric shift (δ_{Fe3+} = 0.35 mm.s^{-1}) is typical of high spin Fe^{3+} ions in octahedral sites. As for the $Na_xMn_{1/2}Fe_{1/2}O_2$ system the Lorentzian fit (**Figure A-III.33a** and **Table A-III.9a**) highlight quite high FWHM and quadrupole splitting values (Γ = 0.34 mm.s^{-1} and Δ_{Fe3+} = 0.71 mm.s^{-1}). A distribution fit highlight the existence of a distribution of the quadrupole splittings for an average Δ^* = 0.72 mm.s^{-1} (**Figure A-III.33b**). The fit based on fixed isomeric shift and FWHM values (**Table A-III.9b**). Contrarily to the other P2-based system, the distribution profile shows three separated contributions for Δ^*_1 = 0.47 mm.s^{-1} (Population ≈ 33%), Δ^*_2 = 0.70 mm.s^{-1} (Population ≈ 50%) and Δ^*_3 = 0.93 mm.s^{-1} (Population ≈ 17%). This better separation is probably correlated to the higher fraction of distorted FeO_6 octahedra which are surrounded by a more important fraction of Jahn-Teller $Mn^{3+}O_6$ octahedra (33 % of the MO_6 octahedra). In P2-$Na_{0.62}Mn_{1/2}Fe_{1/2}O_2$ only 12 % of MO_6 octahedra are distorted.

a) Lorentzian fit				
Site	**δ (mm.s^{-1})**	**FWHM (mm.s^{-1})**	**Δ (mm.s^{-1})**	**P (%)**
Fe^{3+}(A)	0.35	0.34	0.71	100
b) Distribution fit				
Site	**δ (mm.s^{-1})**	**FWHM (mm.s^{-1})**	**Δ* (mm.s^{-1})**	**P (%)**
Fe^{3+}(1)	0.35 (fixed)	0.25 (fixed)	0.72	100

Table A-III.9: Mössbauer parameters deduced from the Lorentzian and Distribution fits of the Mössbauer spectrum of the P2-$Na_{0.66}Mn_{2/3}Fe_{1/3}O_2$ pristine material.

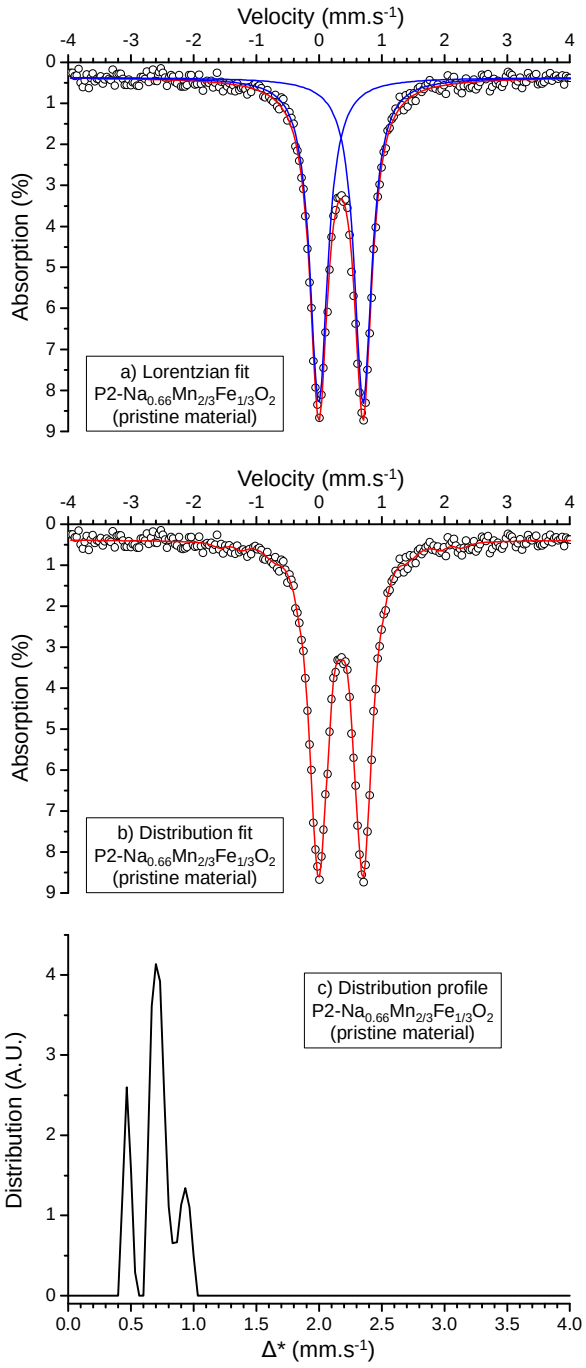

Figure A-III.33: (a) Lorentzian and (b) distribution fits of the Mössbauer spectrum of the P2-$Na_{0.66}Mn_{2/3}Fe_{1/3}O_2$ pristine material. (c) Distribution profile corresponding to the distribution fit.

Finally, P'2-$Na_{0.96}Mn_{2/3}Fe_{1/3}O_2$ and $Na_{0.26}Mn_{2/3}Fe_{1/3}O_2$ materials were prepared by the potentiostatic route (E_{eq} = 1.5 V and 4.3 V, respectively) and their spectra were collected as shown in **Figure A-III.34**. The developed formulas and awaited Fe^{n+} populations of the (dis)charged materials are given in **Table A-III.10** along with the Mössbauer parameters of the fit of the spectra.

The spectrum of P'2-$Na_{0.96}Mn_{2/3}Fe_{1/3}O_2$ exhibits a quadrupole doublet that a preliminary Lorentzian fit attributes to HS Fe^{3+} ions (δ_{Fe3+} = 0.351 mm.s^{-1}). The distribution fit reveals high FWHM and quadrupole splitting values (Γ = 0.30 mm.s^{-1} and Δ^* = 1.31 mm.s^{-1}) thus indicating an important distortion of the FeO_6 octahedra, due to the high cooperative Jahn-Teller effect of the Mn^{3+} ions (64 % of the transition metal ions).

The spectrum of the deintercalated material: $Na_{0.26}Mn_{2/3}Fe_{1/3}O_2$ exhibits a broad quadrupole doublet resulting from the contribution of Fe^{3+} (δ_{Fe3+} = 0.35 mm.s^{-1}) and Fe^{4+} (δ_{Fe4+} = -0.05 mm.s^{-1}) ions. Electron hopping is involved between a fraction of these two ions as an third isomeric shift with intermediate value is required to fit the spectrum ($\delta_{Fe(3+z)+}$ = 0.17 mm.s^{-1}). The high quadrupole splitting values (Δ^*_{Fe3+} = 0.79 mm.s^{-1}, Δ^*_{Fe4+} = 0.47 mm.s^{-1} and $\Delta^*_{Fe(3+z)+}$ = 0.92 mm.s^{-1}) imply high disorder within the material, in agreement with *in situ* XRPD results (both P2 and "Z" phases are expected in this material). The formula deduced from the Mössbauer data is similar to the expected one from electrochemistry ($Na_{0.25}Mn_{2/3}Fe_{1/3}O_2$ *vs.* $Na_{0.26}Mn_{2/3}Fe_{1/3}O_2$).

The Mössbauer results obtained on the P2-based $Na_xMn_{2/3}Fe_{1/3}O_2$ system show that the $Mn^{4+/3+}$ and $Fe^{4+/3+}$ redox couples are successively involved during the electrochemical deintercalation, as for the other $Na_xMn_{1-y}Fe_yO_2$ systems. This conclusion is in agreement with the small increase of the polarization observed for x ≈ 1/3 on the GITT cycling curve (**Figure A-III.18a**).

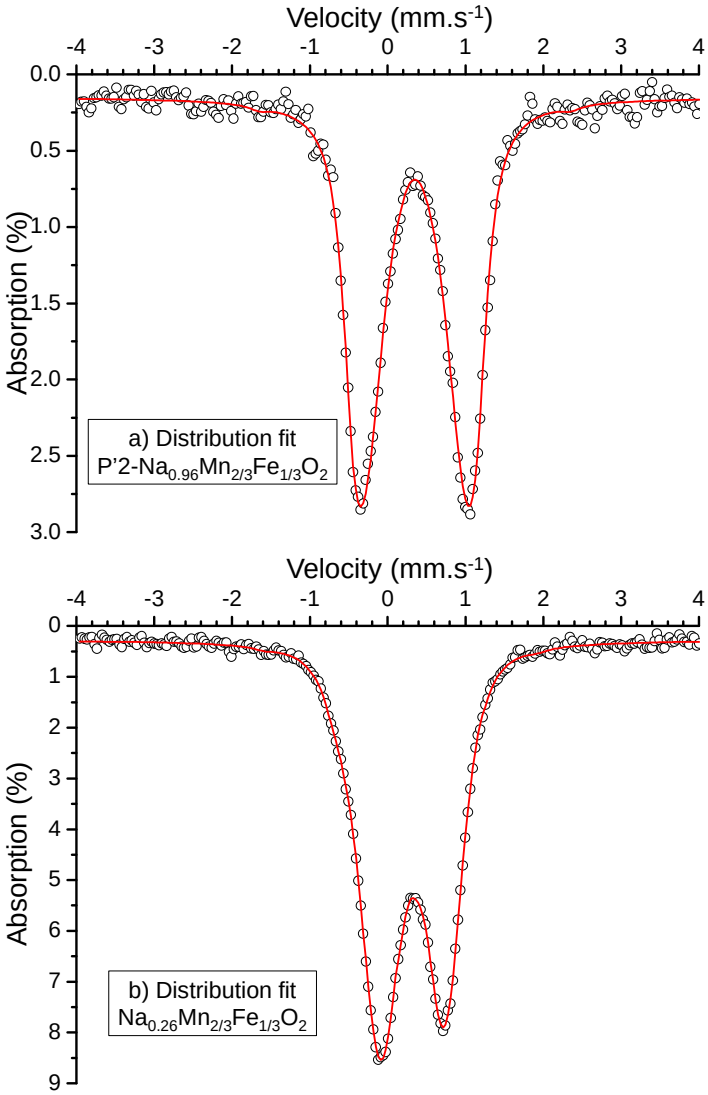

Figure A-III.34: ^{57}Fe Mössbauer spectra of (a) P'2-$Na_{0.96}Mn_{2/3}Fe_{1/3}O_2$, (b) $Na_{0.26}Mn_{2/3}Fe_{1/3}O_2$. Black circles: experimental and red line: calculated.

Awaited results from electrochemistry			Mössbauer results (Distribution fit)															
Developed formula	%Fe^{3+}	%Fe^{4+}	Fe^{3+}				Fe^{4+}				$Fe^{(3+z)+}$						%Fe^{3+}	%Fe^{4+}
			δ ($mm.s^{-1}$)	Δ* ($mm.s^{-1}$)	Γ ($mm.s^{-1}$)	P (%)	δ ($mm.s^{-1}$)	Δ* ($mm.s^{-1}$)	Γ ($mm.s^{-1}$)	P (%)	δ ($mm.s^{-1}$)	Δ* ($mm.s^{-1}$)	Γ ($mm.s^{-1}$)	P (%)	Repartition between Fe^{3+} (%)	Repartition between Fe^{4+} (%)		
$Na_{0.96}Mn^{3+}_{0.62}Mn^{4+}_{0.04}Fe^{3+}_{0}Fe^{4+}_{0}O_2$	100	0	0.351	1.31	0.30	100											100	0
$Na_{0.26}Mn^{3+}_{0}Mn^{4+}_{0.67}Fe^{3+}_{0.26}Fe^{4+}_{0.07}O_2$	79	21	0.35	0.79	0.25	57	-0.05	0.47	0.25	9	0.17	0.92	0.25	34	19	15	76	24

Table A-III.10: Developed formulas, awaited Fe^{n+} populations and Mössbauer parameters corresponding to the fit of the spectra of the $Na_xMn_{2/3}Fe_{1/3}O_2$ system presented in **Figure A-III.34**. The standard deviations on the isomer shift values are equal to 0.002 $mm.s^{-1}$. The population of the $Fe^{(3+z)+}$ is distributed into the Fe^{3+} and Fe^{4+} sites by the formula: $P(Fe^{3+}) = (\delta(Fe^{3+z})-\delta(Fe^{4+})) / (\delta(Fe^{3+})-\delta(Fe^{4+}))$.

A-III.4. Conclusion on the P2-based $Na_xMn_{1-y}Fe_yO_2$ systems

In this chapter were further investigated the electrochemical and structural properties of the P2-based $Na_xMn_{1-y}Fe_yO_2$ materials.

As mentioned in **Chapter A-I**, the P2-based systems exhibit the best electrochemical properties among the P2/O3 based $Na_xMn_{1-y}Fe_yO_2$ systems. Batteries cycled in the 1.5 – 4.0 V range showed interesting second discharge capacities of 140 $mAh.g^{-1}$ (P2-based $Na_xMn_{1/2}Fe_{1/2}O_2$ system) and 152 $mAh.g^{-1}$ (P2-based $Na_xMn_{2/3}Fe_{1/3}O_2$ system). The associated capacity retentions at the 50^{th} cycle showed interesting values of 85 % (P2-based $Na_xMn_{1/2}Fe_{1/2}O_2$ system) and 82 % (P2-based $Na_xMn_{2/3}Fe_{1/3}O_2$ system).

In situ XRPD during the charge of Na-cells showed that the P2-based materials undergo three structural transitions: P'2 → P2 → "Z" from the fully intercalated state to the deintercalated ones (up to 4.3 V). Contrarily to the O3-based materials, no residual phases were observed.

Thanks to X-ray absorption spectroscopy and Mössbauer spectroscopy, we showed that the Mn^{3+} → Mn^{4+} redox process is active at low voltage and that the Fe^{3+} → Fe^{4+} one is active at high voltage, upon Na^+ deintercalation. The same observation was made concerning the O3-based systems.

Chapter A-IV: Influence of the Mn / Fe ratio on the electrochemical and structural properties

Table of contents

This last chapter on the $Na_xMn_{1-y}Fe_yO_2$ (y = 1/3, 1/2 and 2/3) presents a discussion on the impact of the Mn / Fe ratio on the O3 and P2 materials, based on the results presented in **chapters A-I to A-III**. The evolution of the electrochemical properties is investigated first and then the evolution of the structural properties is discussed.

A-IV.1. Effect on the electrochemical properties

In **Chapter A-I**, we already studied the impact of the Mn content on the discharge capacities of the $Na_xMn_{1-y}Fe_yO_2$ materials, when cycled between 1.5 and 3.8 V in Na cells. The conclusions of this study are reminded below:

(1) In P2 materials, increasing the Mn content leads to better second discharge capacities.
(2) In O3 materials, increasing the Mn content decreases the second discharge capacity but leads to better capacity retention.
(3) The comparison between the P2 and O3 $Na_xMn_{1/2}Fe_{1/2}O_2$ materials shows that the P2 material exhibit higher discharge capacity and better capacity retention.

In **Chapters A-II** and **A-III**, we investigated the impact of the upper cut-off voltage on the galvanostatic curves of the different materials. We now compare these results for different Mn / Fe ratios, first on the O3 systems and then on the P2 systems.

A-IV.1.a. Impact on the O3 systems

The electrochemical profile up to 4.0 V and 4.3 V are reminded in **Figure A-IV.1** for the O3-based $Na_xMn_{1/3}Fe_{2/3}O_2$ and $Na_xMn_{1/2}Fe_{1/2}O_2$ systems.

The main influence of the higher Mn / Fe ratio (from 1 / 2 to 1 / 1) is to delay the sudden voltage jump associated to the change of active redox couple. Furthermore, one can see that increasing the Mn / Fe ratio allows deintercalating more Na^+ ions when the cut-off voltage is increased from 4.0 V to 4.3 V (+ 0.02 Na^+ ions per formula unit in the O3-based $Na_xMn_{1/3}Fe_{2/3}O_2$ system *vs.* +0.14 Na^+ ions per formula unit in the O3-based $Na_xMn_{1/2}Fe_{1/2}O_2$ one). This leads to higher discharge capacities when cycling the O3-based $Na_xMn_{1/3}Fe_{2/3}O_2$ material up to 4.0 or 4.3 V compared to the cycling in the 1.5 – 3.8 V range, as evidenced in **Figure A-IV.2**. The higher Mn / Fe ratio also induce the second voltage plateau to occur at higher voltage (≈ 4.0 V *vs.* ≈ 3.9 V for O3-based $Na_xMn_{1/3}Fe_{2/3}O_2$). As a consequence, the capacity retention of the batteries cycled in the 1.5 – 4.0 V is higher for the O3-based $Na_xMn_{1/2}Fe_{1/2}O_2$ system (91 % after 29 cycles) than for the $Na_xMn_{1/3}Fe_{2/3}O_2$ one (74 % after 29 cycles).

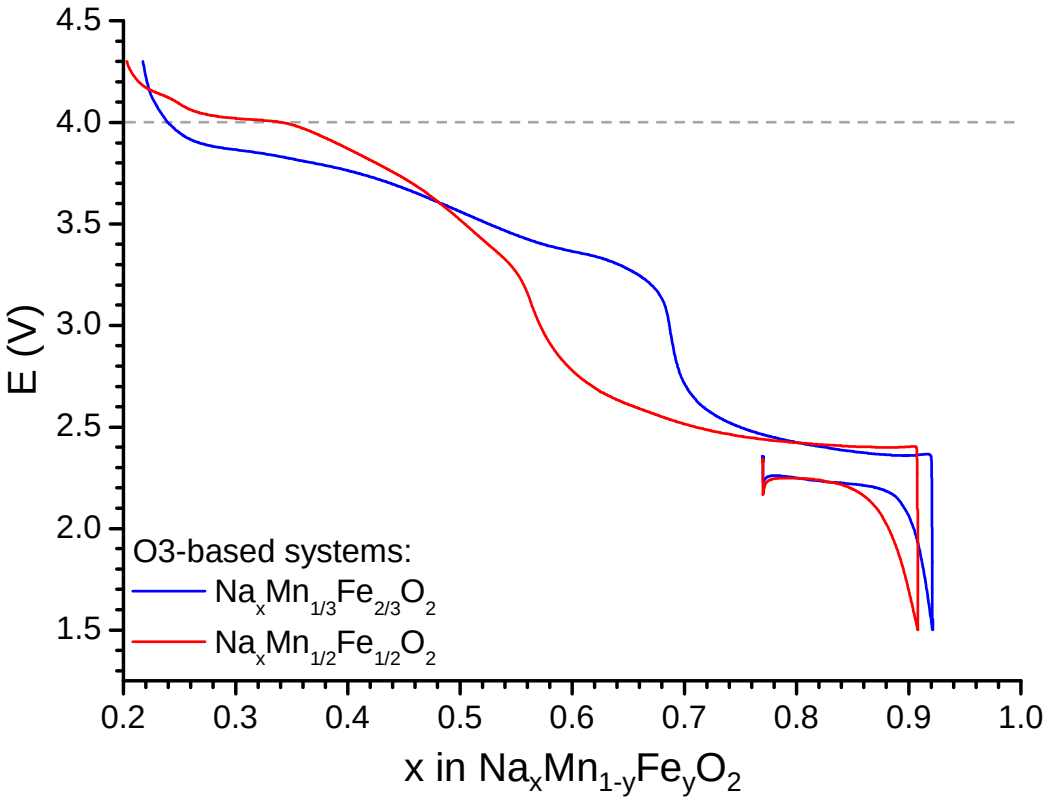

Figure A-IV.1: Evolution of the galvanostatic curves recorded at C/50 for the O3-based $Na_xMn_{1/3}Fe_{2/3}O_2$ (red line) and $Na_xMn_{1/2}Fe_{1/2}O_2$ (blue line) systems while cycled up to 4.3 V. The dashed grey line corresponds to the E = 4.0 V voltage value.

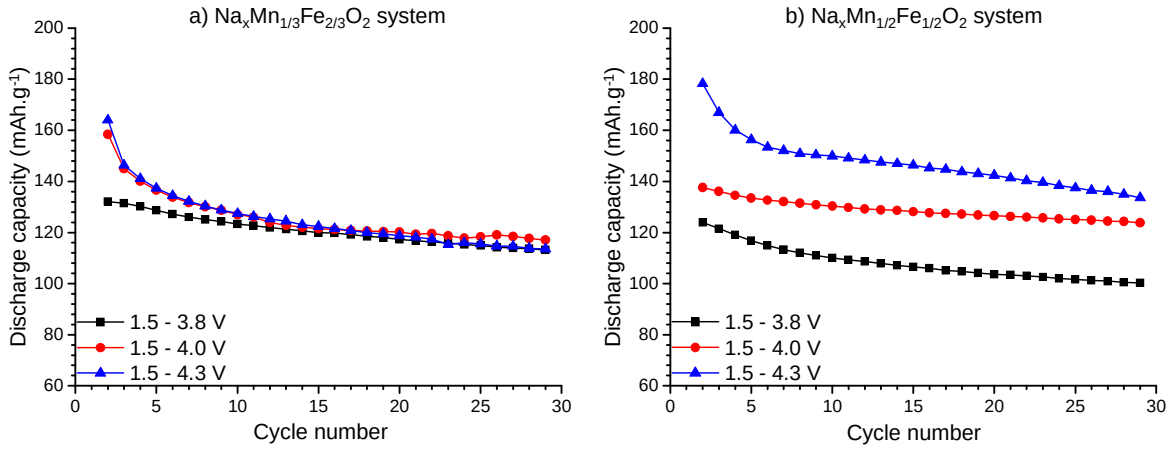

Figure A-IV.2: Evolution of the discharge capacity for the O3-based (a) $Na_xMn_{1/3}Fe_{2/3}O_2$ and (b) $Na_xMn_{1/2}Fe_{1/2}O_2$ systems in the 1.5 – 3.8 V, 1.5 – 4.0 V and 1.5 – 4.3 V ranges at C/50.

A-IV.1.b. Impact on the P2 systems

The electrochemical profiles up to 4.0 V and 4.3 V are reminded in **Figure A-IV.3** for the P2-based $Na_xMn_{1/2}Fe_{1/2}O_2$ and $Na_xMn_{2/3}Fe_{1/3}O_2$ systems.

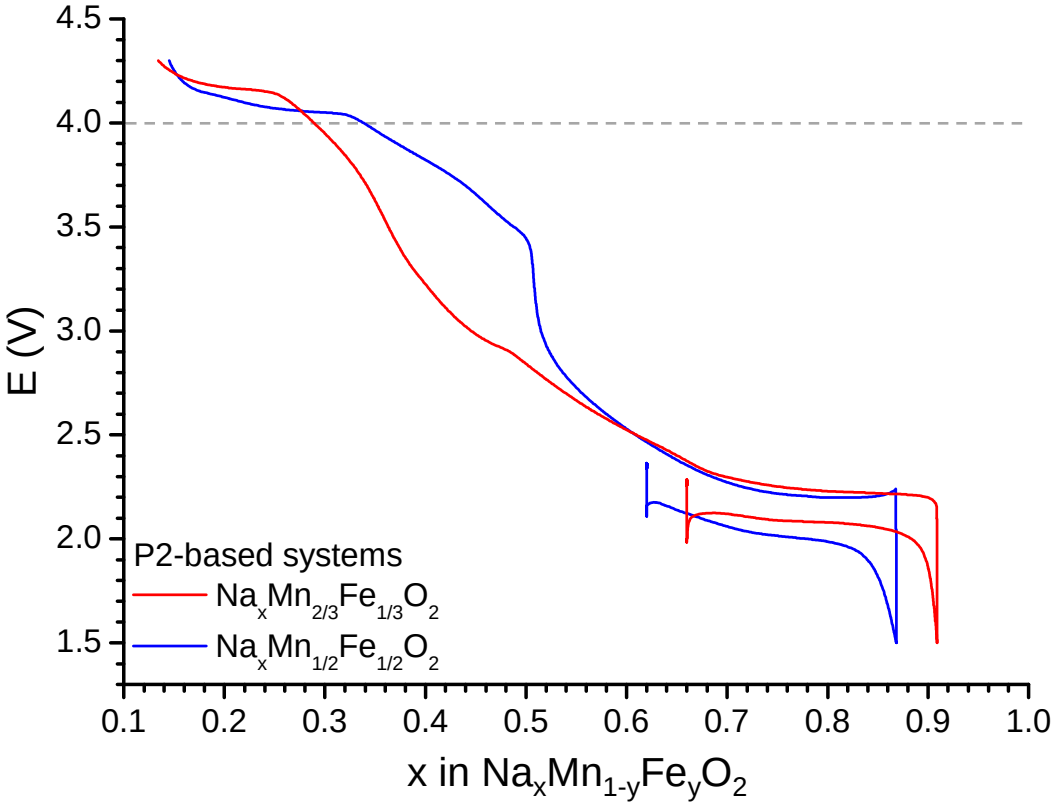

Figure A-IV.3: Evolution of the galvanostatic curves recorded at C/20 for the P2-based (a) $Na_xMn_{1/2}Fe_{1/2}O_2$ and (b) $Na_xMn_{2/3}Fe_{1/3}O_2$ systems while cycled up to 4.0 V (black lines) and up to 4.3 V (red lines).

As observed for the O3 structures, the increase of the Mn / Fe ratio increases the voltage of the plateau from ≈ 4.05 V ($Na_xMn_{1/2}Fe_{1/2}O_2$) to ≈ 4.15 V ($Na_xMn_{2/3}Fe_{1/3}O_2$). If one assumes that cycling beyond the plateau is the origin of the capacity fading discussed in **Chapter A-III**, we can explain the interesting discharge capacities retentions reached in the 1.5 – 4.0 V for both materials (80 – 85 % after 50 cycles). As shown in **Figure A-IV.4** the second cycle discharge capacity in the 1.5 – 4.0 V range is slightly higher for $Na_xMn_{2/3}Fe_{1/3}O_2$ (152 $mAh.g^{-1}$) than for $Na_xMn_{1/2}Fe_{1/2}O_2$ (140 $mAh.g^{-1}$). However, it is difficult to highlight a better candidate for Na-ion batteries based only on the discharge capacity values.

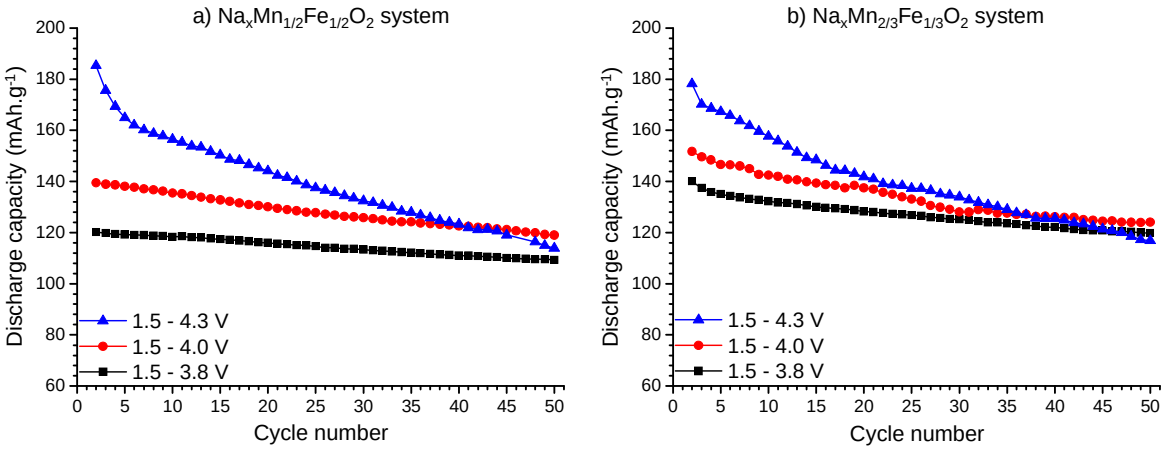

Figure A-IV.4: Evolution of the discharge capacities for the P2-based (a) $Na_xMn_{1/2}Fe_{1/2}O_2$ and (b) $Na_xMn_{2/3}Fe_{1/3}O_2$ systems in the 1.5 – 3.8 V, 1.5 – 4.0 V and 1.5 – 4.3 V ranges at C/20.

The influence of the rate on the discharge capacities of the P2 materials was also studied (**Chapter A-III**) and is reminded in **Figure A-IV.5**. As previously discussed, we observe an important decrease of the discharge capacity when the rate is higher than C/5 for both materials. However, comparing the two materials, the $Na_xMn_{2/3}Fe_{1/3}O_2$ system appears more suitable to handle high C-rate cycling than the $Na_xMn_{1/2}Fe_{1/2}O_2$ one: 28 % and 16 % of the capacity at C/20 are still accessible at C and 2C rates *vs.* 20 % and 8 % for the $Na_xMn_{1/2}Fe_{1/2}O_2$ system. Based on this observation, the $Na_xMn_{2/3}Fe_{1/3}O_2$ system seems more suitable to handle the important rate variations and thus to constitute the positive electrode active material of hypothetical Na-ion cells. Furthermore, we can consider increasing the discharge capacity and the power density by cycling the $Na_xMn_{2/3}Fe_{1/3}O_2$ system up to 4.1 V (before reaching the high voltage plateau).

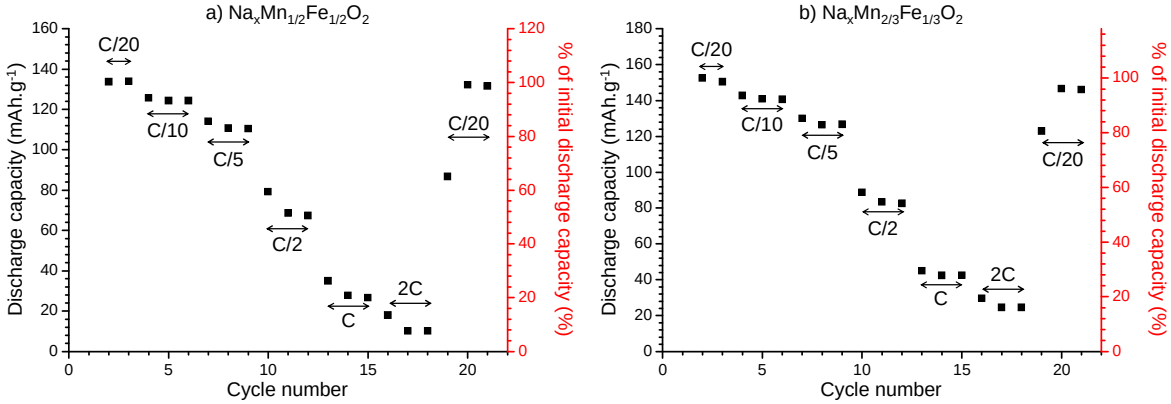

Figure A-IV.5: Evolution of the discharge capacity for different C-rate values for P2-based (a) $Na_xMn_{1/2}Fe_{1/2}O_2$ and (b) $Na_xMn_{2/3}Fe_{1/3}O_2$.

A-IV.2. Effect of the Mn content on the structural properties

A-IV-2.a. Impact on the phase diagrams

The shape of the galvanostatic curves discussed in **Chapters A-I to A-III** highlight the existence of a plateau at low voltage that the *operando in situ* XRPD studies carried out during the charge of Na cells associated to biphasic domains involving the undistorted (O3/P2) distorted phases (O'3/P'2). The origin of the distorted phases for the almost fully intercalated states is attributed to the Jahn-Teller active Mn^{3+} ions. From the *in situ* experiments, we also established the phase diagrams for every system as compared in **Figure A-IV.6**.

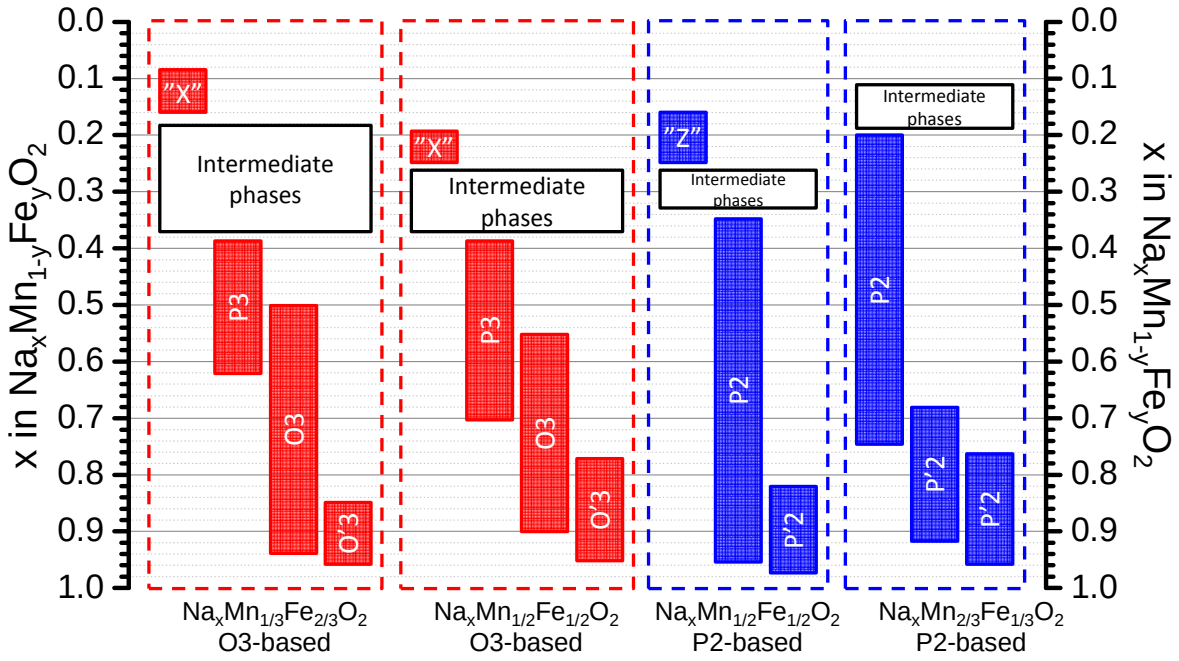

Figure A-IV.6: Domains of observation of the O'3, O3, P3 and "X" phases (O3-type materials) and of the P'2, P2 and "Z" phases (P2-type materials).

Concerning the O3-type materials, we observe that increasing the Mn / Fe ratio from 1 / 2 to 1 / 1 leads to the observation of the O'3-type phase on a wider x range, in agreement with the higher Mn^{3+} content expected. Increasing the Mn content also leads to the apparition of the P3-type phase for higher x values (x = 0.7 for the $Na_xMn_{1/2}Fe_{1/2}O_2$ system *vs.* x = 0.62 for the $Na_xMn_{1/3}Fe_{2/3}O_2$ system). The P3-type phase is also observed in a wider range in the O3-based $Na_xMn_{1/2}Fe_{1/2}O_2$ system ($0.39 \leq x \leq 0.7$ *vs.* $0.39 \leq x \leq 0.62$ in the $Na_xMn_{1/3}Fe_{2/3}O_2$ system). For both O3-based systems, stacking faults are created for $x < 0.39$ and lead to the "X" phase.

Concerning the P2-type materials, increasing the Mn / Fe ratio from 1 / 1 to 2 / 1 leads to the observation of the P'2 phase(s) on a wider x range. A second P'2 domain is also observed for the $Na_xMn_{2/3}Fe_{1/3}O_2$ system and delays the apparition of the P2-type phase (x = 74 *vs.* x = 0.95 in the $Na_xMn_{1/2}Fe_{1/2}O_2$ system). Because of that, the P2-type phase is observed on a wider domain in the $Na_xMn_{1/2}Fe_{1/2}O_2$ system ($0.26 \leq x \leq 0.95$) than in the $Na_xMn_{2/3}Fe_{1/3}O_2$ one ($0.1 \leq x \leq 0.74$). Contrarily to the O3 based materials, increasing the Mn content prevent the appearance of a pure "Z" phase up to 4.3 V for the P2 based $Na_xMn_{2/3}Fe_{1/3}O_2$ system while it appears at x = 0.25 in the P2-based $Na_xMn_{1/2}Fe_{1/2}O_2$ one.

In both systems the formation of the "X" or "Z" phases in charge is achieved through the apparition of stacking faults. In the O3-based systems stacking faults are occurring simultaneously for the P3 and O3 phases and presumably consist in the appearance of octahedral surroundings for some NaO_6 ions from the P3 phase or in the appearance of O1 planes among the O3 phase. In the P2-based materials, the "Z" phase also appears through the apparition of stacking faults (NaO_6 octahedra planes) in the P2 phase.

As both "X" and "Z" phases show octahedral surroundings of the Na^+ ions and appear for comparable sodium contents ($0.16 \leq x \leq 0.25$), one can expect them to show similar interlayer distance. This is confirmed in **Figure A-IV.7** which compares the XRPD patterns of "X"-$Na_{0.16}Mn_{1/3}Fe_{2/3}O_2$, "X"-$Na_{0.25}Mn_{1/2}Fe_{1/2}O_2$ and "Z"-$Na_{0.25}Mn_{1/2}Fe_{1/2}O_2$ recorded during the XRPD experiments during charge of corresponding Na-cells. As expected, the (00*l*) diffraction peak of every phase is located at similar position ($2\theta \approx 17°$).

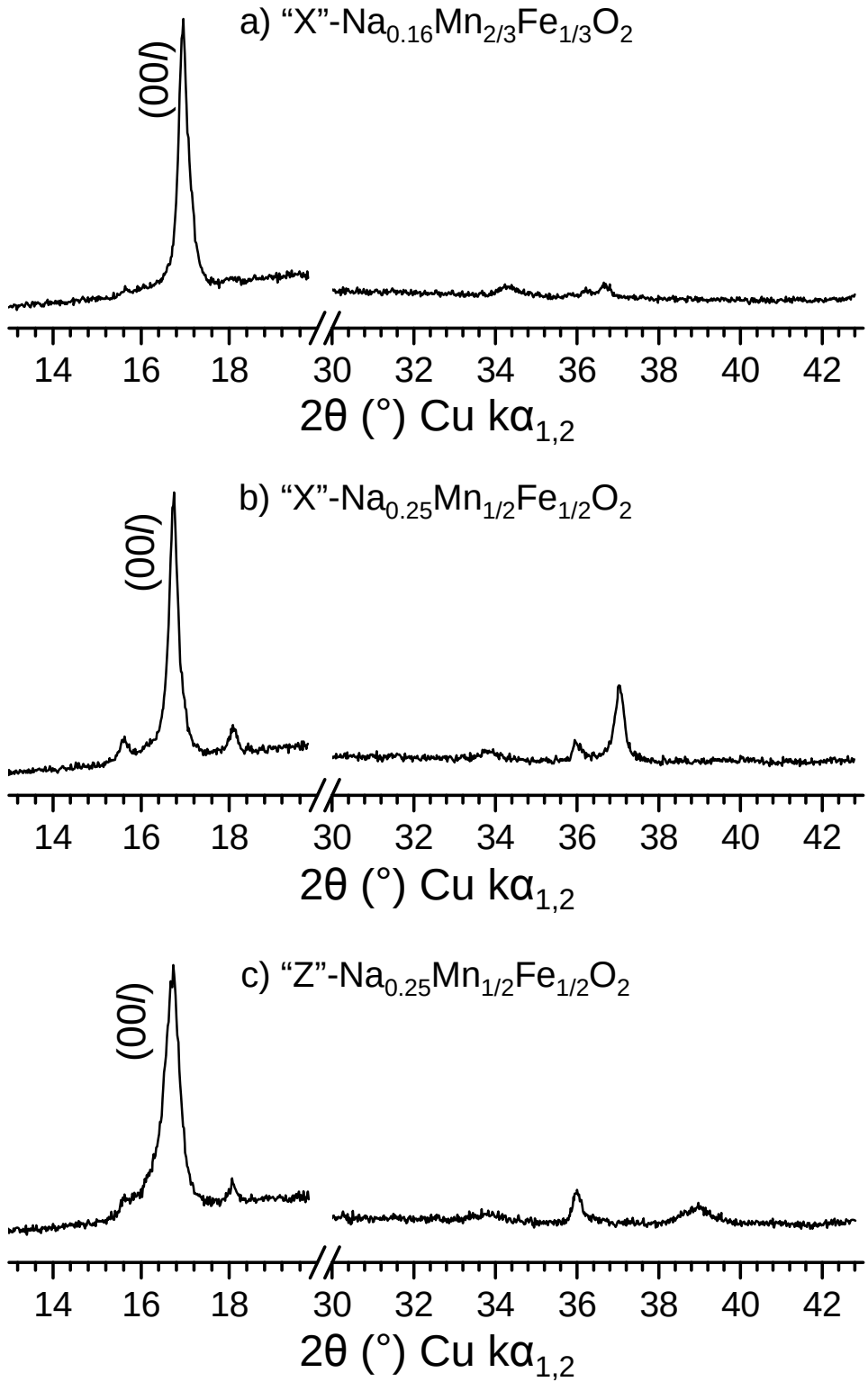

Figure A-IV.7: Comparison of the XRPD patterns recorded *in situ* during the charge of corresponding Na-cells of (a) "X"-$Na_{0.16}Mn_{1/3}Fe_{2/3}O_2$, (b) "X"-$Na_{0.25}Mn_{1/2}Fe_{1/2}O_2$ and (c) "Z"-$Na_{0.25}Mn_{1/2}Fe_{1/2}O_2$. The zero shifts have been corrected for each pattern.

A-IV-2.b. Impact on the intercalated state and on the cooperative Jahn-Teller effect

As discussed along with **Figure A-IV.6**, increasing the Mn content leads to the observation of the distorted phase on wider range, because of the cooperative Jahn-Teller effect induced by the Mn^{3+} ions. To study the evolution of the cooperative Jahn-Teller effect with the Mn / Fe ratio, we first study the evolution of the $a_{mon.}/b_{mon.}$ or $b_{orth.}/a_{orth.}$ ratios along with the Mn content in the $Na_xMn_{1-y}Fe_yO_2$ materials. This evolution is shown in **Figure A-IV.8**. In order to make the interpretation easier, we considered all the Mn^{n+} ions to be in the +III oxidation state. The data for the O3-$NaFeO_2$ and O'3-$NaMnO_2$ phase have been added from the literature [35, 44] for comparison purposes.

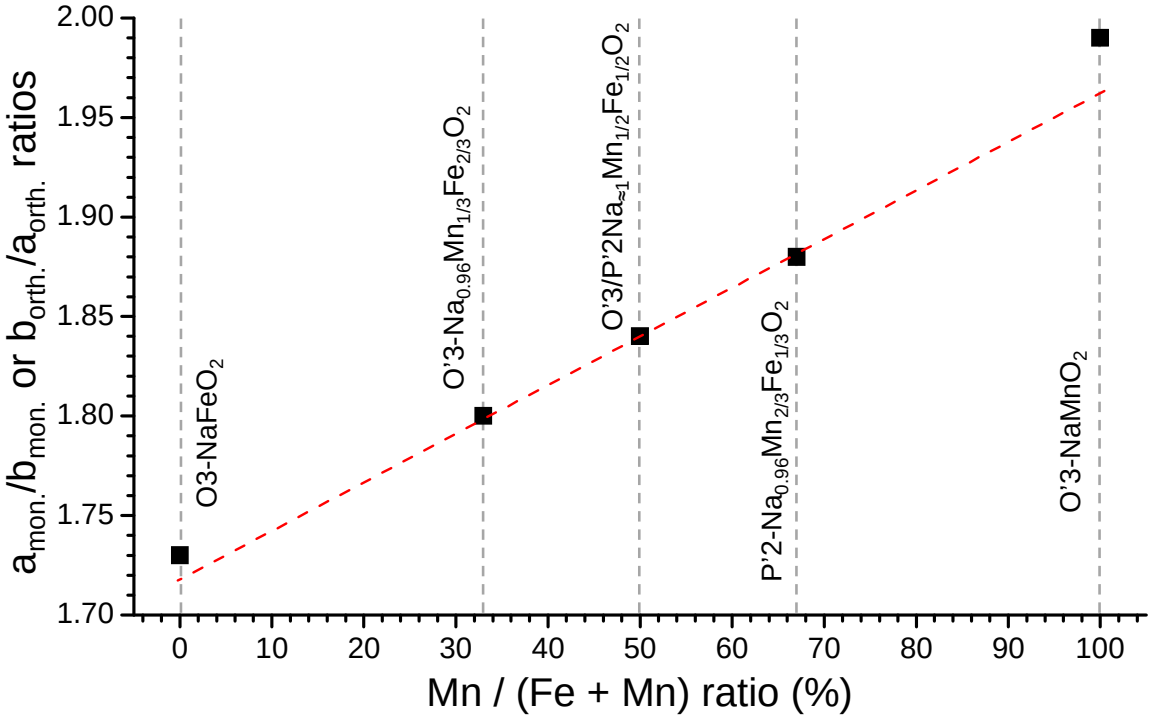

Figure A-IV.8: Evolution of the $a_{mon.}/b_{mon.}$ or $b_{orth.}/a_{orth.}$ ratios along with the Mn content in the $Na_xMn_{1-y}Fe_yO_2$ materials. O3-$NaFeO_2$: data from [35], O'3-$NaMnO_2$: data from [44].

As one can see, the evolution of the $a_{mon.}/b_{mon.}$ or $b_{orth.}/a_{orth.}$ ratios is linear for our experimental results ($Na_xMn_{1-y}Fe_yO_2$ with y = 1/3, 1/2 and 2/3) with the increase of the Mn content. The structure type seems to have no impact on the distortion as the $a_{mon.}/b_{mon.}$ (O'3) and the $b_{orth.}/a_{orth.}$(P'2) ratios in the $Na_{\approx1}Mn_{1/2}Fe_{1/2}O_2$ systems are both equal to 1.84. To verify this hypothesis, we reported the evolution of the M-O distances in the MO_6 octahedra in **Figure A-IV.9**:

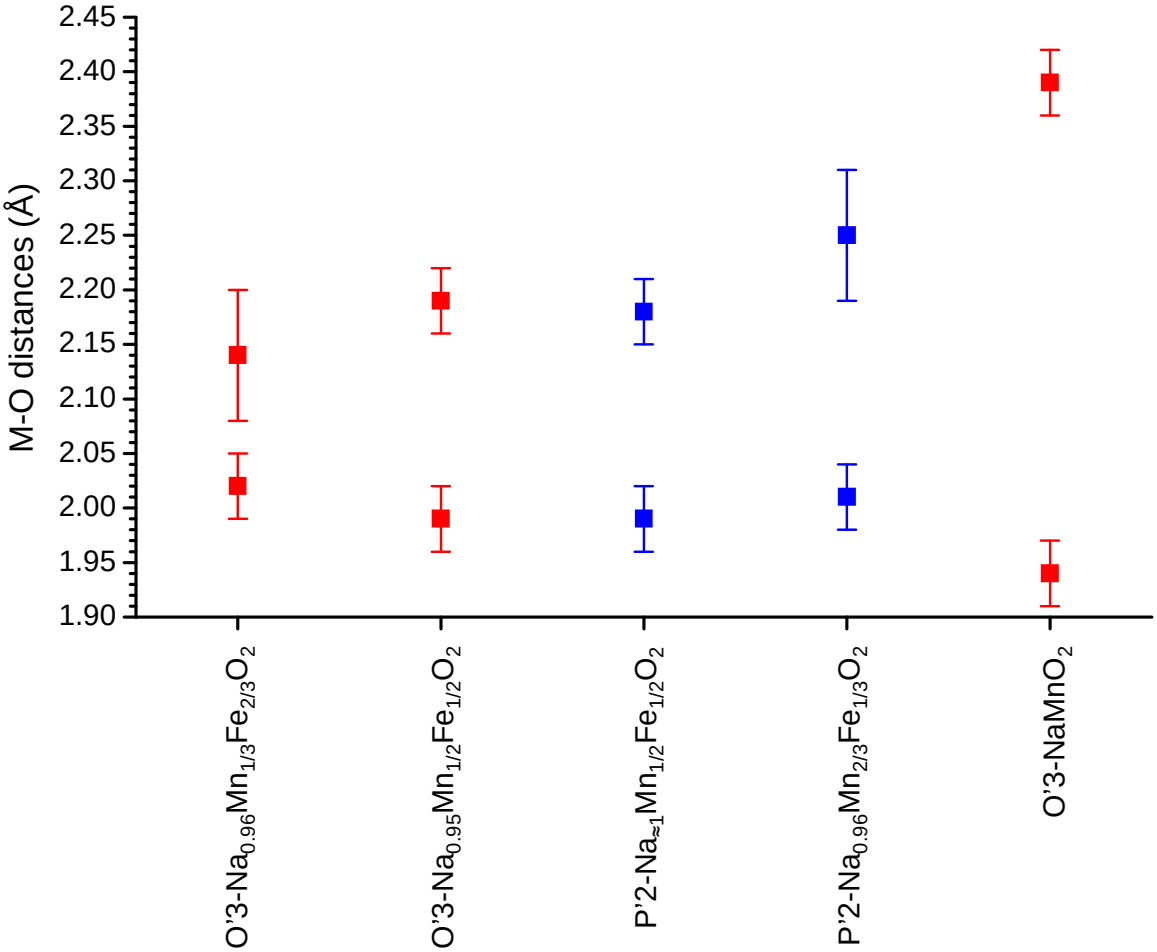

Figure A-IV.9: Evolution of the M-O distances in the MO_6 octahedra in P'2 and O'3-$Na_{\approx 1}Mn_{1-y}Fe_yO_2$ phases. O'3-$NaMnO_2$: data from [44].

As highlighted in **Figure A-IV.9**, the O'3 and P'2 $Na_{\approx 1}Mn_{1/2}Fe_{1/2}O_2$ materials show the same distortion of the octahedra with M-O distances equal to 4 x 1.99 Å and 2 x 2.19 Å (O'3 material) and 4 x 1.99 Å and 2 x 2.18 Å (P'2 material). We also observe that the MO_6 octahedra are more distorted when the Mn^{3+} content increase as the M-O distances are equal to 4 x 2.02 Å and 2 x 2.14 Å (O'3-$Na_{\approx 1}Mn_{1/3}Fe_{2/3}O_2$) and to 4 x 1.94 Å and 2 x 2.39 Å (O'3-$NaMnO_2$), in agreement with the higher quantity of Mn^{3+} ions.

Part B

O'3-$NaNiO_2$ and the Na_xNiO_2 phase diagram

Chapter B-I: O'3-$NaNiO_2$ and the Na_xNiO_2 phase diagram

Table of contents

This second part focuses on the O'3-$NaNiO_2$ material and on the Na_xNiO_2 phase diagram. A state of art on the O'3-$NaNiO_2$ material is first presented along with the reasons that motivated our choice to study this material. Then, the synthesis of O'3-$NaNiO_2$ is given before the electrochemical and structural characterizations. Finally the Na_xNiO_2 phase diagram is investigated in the $1/3 \leq x \leq 1$ range.

B-I.1. O'3-$NaNiO_2$ in the literature

The first synthesis of O'3-$NaNiO_2$ by solid state reaction of Na_2O and NiO is attributed to Dyer et al. in 1954 [2]. O'3-$NaNiO_2$ (monoclinic) was mostly studied for its magnetic [43, 124-132] and physical [133] properties or for its reversible transition towards O3-$NaNiO_2$ (rhombohedric) for T > 220°C [2, 43].

The electrochemical properties of O'3-$NaNiO_2$ as a positive electrode in a Na battery were only studied in 1982 by Braconnier et al. [38] who highlighted the existence of several ordered phases within border of biphasic domains: P'3-$Na_{0.91}NiO_2$, P''3-$Na_{0.84}NiO_2$, O''3-$Na_{0.81}NiO_2$ and O'''3-$Na_{0.79}NiO_2$. In 2013, Vassiliaras et al. reported a study on the cyclability of O'3-$NaNiO_2$ [34]. Despite the interesting initial charge capacity of ≈ 150 $mAh.g^{-1}$ when cycled between 1.25 and 3.75 V, the reversibility is limited by the formation of an intermediate phase in discharge that seems to prevent the formation of the original O'3-$NaNiO_2$ phase. Therefore, the subsequent discharge capacity decreases to 120 $mAh.g^{-1}$. The different structural transitions and the formation of the intermediate phase in discharge were observed *in situ* by Han et al. in 2014 who confirmed the existence of peculiar compositions, separated by biphasic domains [134].

Following the work of Vassiliaras and her collaborators' [34], we decided to reinvestigate the Na_xNiO_2 phase diagram by *in situ* XRPD during the charge of a corresponding battery. Several sodium / vacancy orderings were expected, by comparison to other Na_xMO_2 systems studied at the ICMCB and in the literature [48, 55, 56, 64, 135]. The synthesis and optimization of the materials as well as the first electrochemical characterizations were carried out by T. Phraewphiphat during two Ph.D. training periods in our laboratory.

B-I.2. Synthesis of the O'3-$NaNiO_2$ pristine materials

Several synthesis routes are reported for the synthesis of O'3-$NaNiO_2$ such as classic solid state [2, 34, 38, 43, 124, 125, 127, 128, 131, 133, 134], molten hydroxide method [129, 130] or single crystal growth [132]. In the present work, we followed the protocol described by Braconnier et al. [38] in 1982, as the synthesis duration (less than 24 hours) allows us to prepare the material rapidly and to obtain it in powder-form, which is more adapted for electrochemical cycling. The protocol consists in mixing and grinding Na_2O and NiO (prepared from $Ni(NO_3)_2.6\,H_2O$) altogether in a mortar under Ar atmosphere. 10 wt% excess of Na are added in order to compensate the high volatility of Na oxides. The mixture is then placed into a gold boat introduced in a furnace and heated at 650 °C during 15 hours under O_2 atmosphere (heating ramp: +2 °C.min^{-1}). After the heat treatment, the gold boat is quenched under air and directly placed under vacuum before entering the glovebox (Ar atmosphere).

Then, we tried several synthesis conditions by varying the excess Na amount and the duration of the heat treatment. After XRPD characterization of the resulting materials, three of them were selected. The corresponding conditions are resumed in **Figure B-I.1** and **Table B-I.1**. The name of the different samples ("large grains", "medium grains" and "small grains") were attributed based on the scanning electron microscopy micrographs discussed in the later.

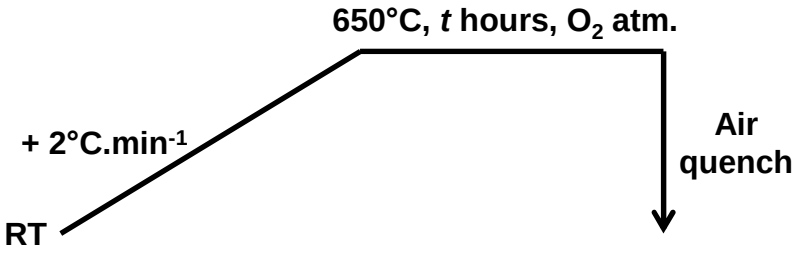

Sample	Na excess	Synthesis duration (t)
Large grains	10 %	15 hours
Medium grains	0 %	15 hours
Small grains	0 %	3 hours

Figure B-I.1 and Table B-I.1: Synthesis conditions of the three studied O'3-$NaNiO_2$ materials.

B-I.3. Structure and Morphology

B-I.3.a. Confirmation of the samples purity

The purity of the various samples was confirmed by XRPD. The different patterns are represented in **Figure B-I.2**.

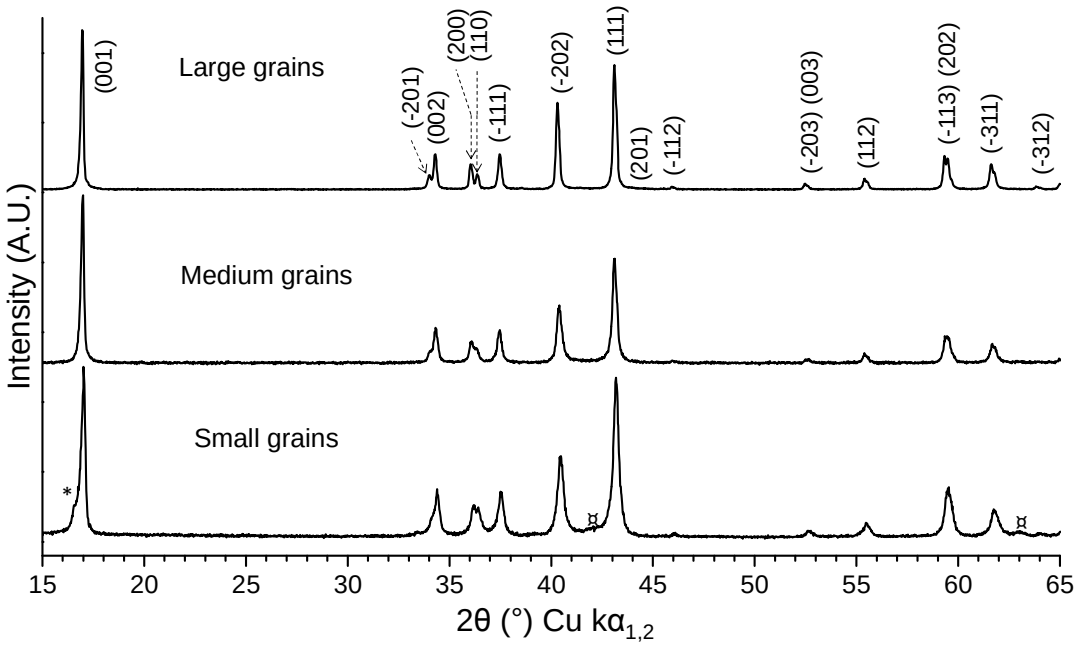

Figure B-I.2: XRPD patterns of the three O'3-$NaNiO_2$ samples: (top) large, (middle) medium and (bottom) small grain sizes. ¤ symbol: NiO traces and * symbol: $Na_{\approx 0.8}NiO_2$. The Miller indexes correspond to the indexation in the monoclinic cell (S.G.: C2/m).

The XRPD patterns are successfully indexed in the C2/m space group of the O'3 structure. We observe the appearance of extra diffraction lines only in the XRPD pattern of the "small grains" sample. Two of them correspond to un-reacted NiO, indicated by the ¤ symbol in Figure B-I.2. Another extra diffraction peak (* symbol in **Figure B-I.2**) is observed at $2\theta \approx 16.5°$ and is very close to the $(001)_{O'3}$ reflection. Its origin will be explained later.

As one can see, every sample exhibits well defined diffraction peaks but show different widths at half maximum. In XRPD, the broadening of the diffraction peaks is strongly correlated to the decrease of the coherent lengths. This observation suggests that our materials have different particle sizes.

The cell parameters of the different samples were determined by LeBail refinement of the profiles and are given in **Table B-I.2**. As one can see all materials exhibit very similar cell parameters and identical $a_{mon.}/b_{mon.}$ ratios.

Sample	$a_{mon.}$ (Å)	$b_{mon.}$ (Å)	$c_{mon.}$ (Å)	$\beta_{mon.}$ (°)	$a_{mon.}/b_{mon.}$
Large grains	5.321(1)	2.844(1)	5.582(1)	110.84(2)	1.87
Medium grains	5.309(1)	2.845(1)	5.570(1)	110.41(6)	1.87
Small grains	5.308(2)	2.845(1)	5.571(2)	110.40(2)	1.87

Table B-I.2: Cell parameters and $a_{mon.}/b_{mon.}$ ratios deduced from the LeBail refinement of the profiles of the different O'3-$NaNiO_2$ samples from the XRPD patterns.

B-I.3.b. Morphology: Scanning Electron Microscopy

The various samples were then analyzed by Scanning Electron Microscopy. The resulting micrographs are given in **Figure B-I.3**.

The SEM micrographs show that the sample involving an excess Na content and heated during 15 hours (**Figure B-I.3a**) exhibits the largest particles with well-defined shape whose sizes are comprised between 500 nm and 1.50 µm. Several imperfections are observed at the surface of the material and probably correspond to Na salts or un-reacted Na oxides due to the 10 wt% Na excess used. They are not observed on the XRPD pattern and represent a clear minority of the sample.

The sample heated during 15 hours with no Na excess (**Figure B-I.3b**) exhibits smaller grains whose sizes are comprised between 250 nm and 650 nm. Contrarily to the "large grains" sample, no noticeable imperfections are observed at the surface of the material which still exhibits well-defined particles. As commonly observed the excess Na amount facilitates the particle growth in the "large grains" sample.

Finally, the sample prepared through a 3 hours heat-treatment (**Figure B-I.3c**) is characterized by poorly-defined and small particles (≈ 100 nm) which are agglomerated (1 – 2 µm). No imperfections are observed at the surface of this material either.

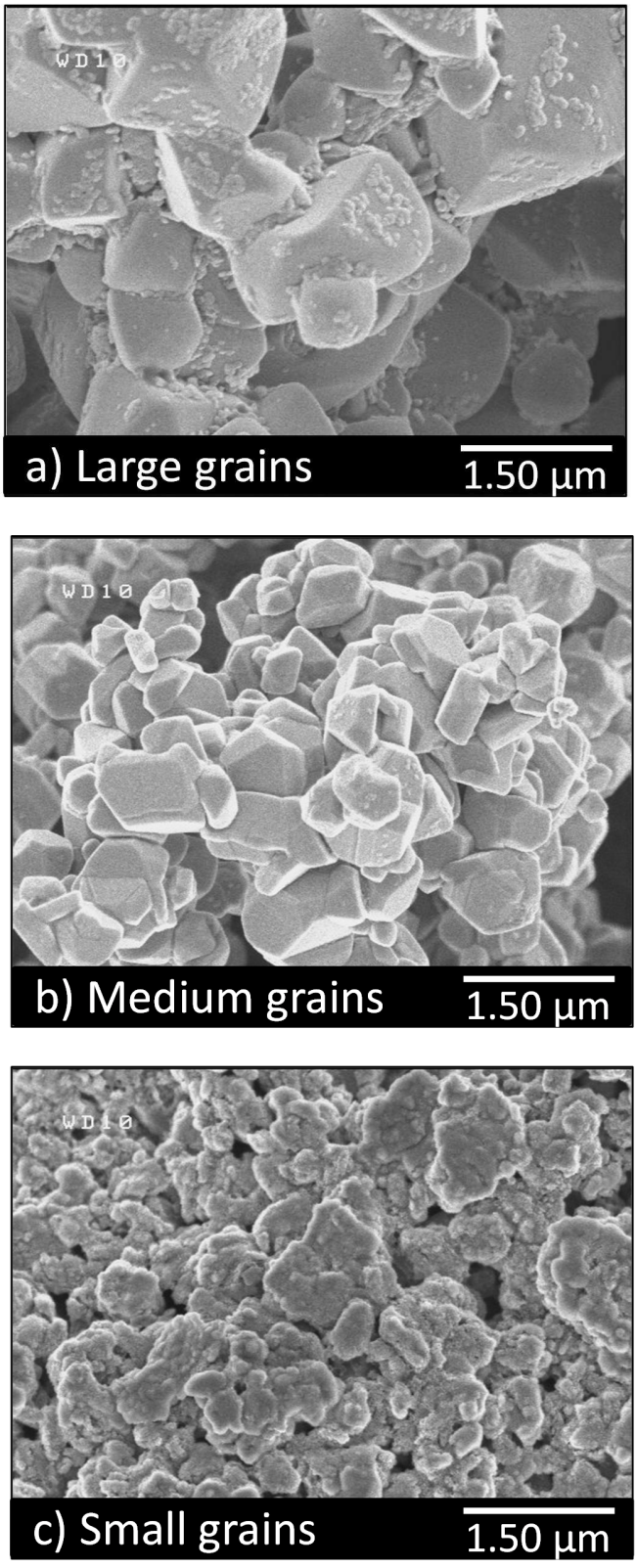

Figure B-I.3: Scanning Electron Microscopy micrographs of the (a) large grains, (b) medium grains and (c) small grains samples of the O'3-$NaNiO_2$ material.

B-I.3.c. Rietveld refinement of the structure

Due to the similitudes between the different materials, only one Rietveld refinement of the structure was carried out from the XRPD pattern of the "large grain" sample. The observed and calculated XRPD patterns are presented in **Figure B-I.4**. The corresponding atomic and cell parameters are given in **Table B-I.3**.

As observed in **Figure B-I.4**, the diffraction peaks can be indexed in the monoclinic system (C2/m space group). The $a_{mon.}/b_{mon.}$ ratio is equal to 1.87 and confirms that the O'3 packing results from the cooperative Jahn-Teller effect of the Ni^{3+} ions leading to two long Ni-O distances (2.14(1) Å) and four short ones (1.92(1) Å).

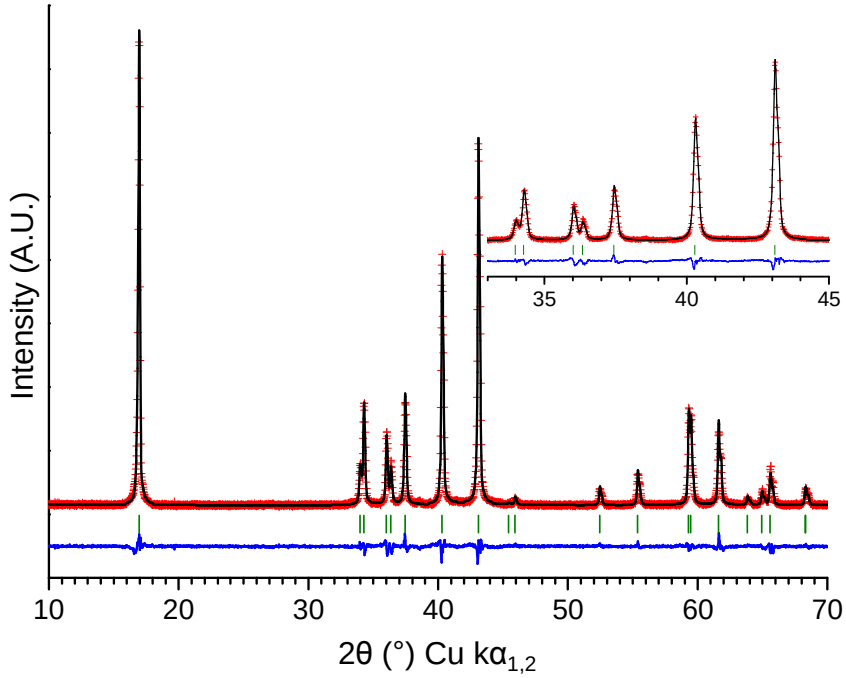

Figure B-I.4: Observed and Calculated (Rietveld method) XRPD patterns of the "large grains" O'3-$NaNiO_2$ sample. Red crosses: observed, black line: calculated, blue line: difference and green bars: Bragg positions.

O'3-$NaNiO_2$ Space group : C2/m $a_{mon.}$ = 5.3205(2) Å, $b_{mon.}$ = 2.8444(1) Å, $c_{mon.}$ = 5.5822(2) Å, $\beta_{mon.}$ = 110.48(1)° $a_{mon.}/b_{mon.}$ = 1.87						
Atom	Wyckoff	Coordinates			Occupancy	ADP (Å²)
Na	2c	0	0	1/2	0.99(1)	1.7(1)
Ni	2b	0	1/2	0	1	1.3(1)
O	4i	0.220(1)	0	0.197(1)	1	1.4(1)
Ni-O distances		4 * 1.92(1) Å		2 * 2.14(1) Å		
Rwp = 6.69%; R_B = 2.77% (with excluded regions)						

Table B-I.3: Structural parameters and reliability factors calculated from the XRPD pattern of the O'3-$NaNiO_2$ sample (large grains).

B-I.4. Electrochemistry

B-I.4.a. Galvanostatic cycling

The materials were used as positive electrode in Na//Na_xNiO_2 batteries which were galvanostatically cycled between 1.5 and 3.8 V at C/50. Every experiment started by a discharge to 1.5 V in order to confirm the initial sodium content (x = 1). The obtained galvanostatic curves are presented in **Figure B-I.5** for the large (**Figure B-I.5a**), medium (**Figure B-I.5b**) and small (**Figure B-I.5c**) grains samples.

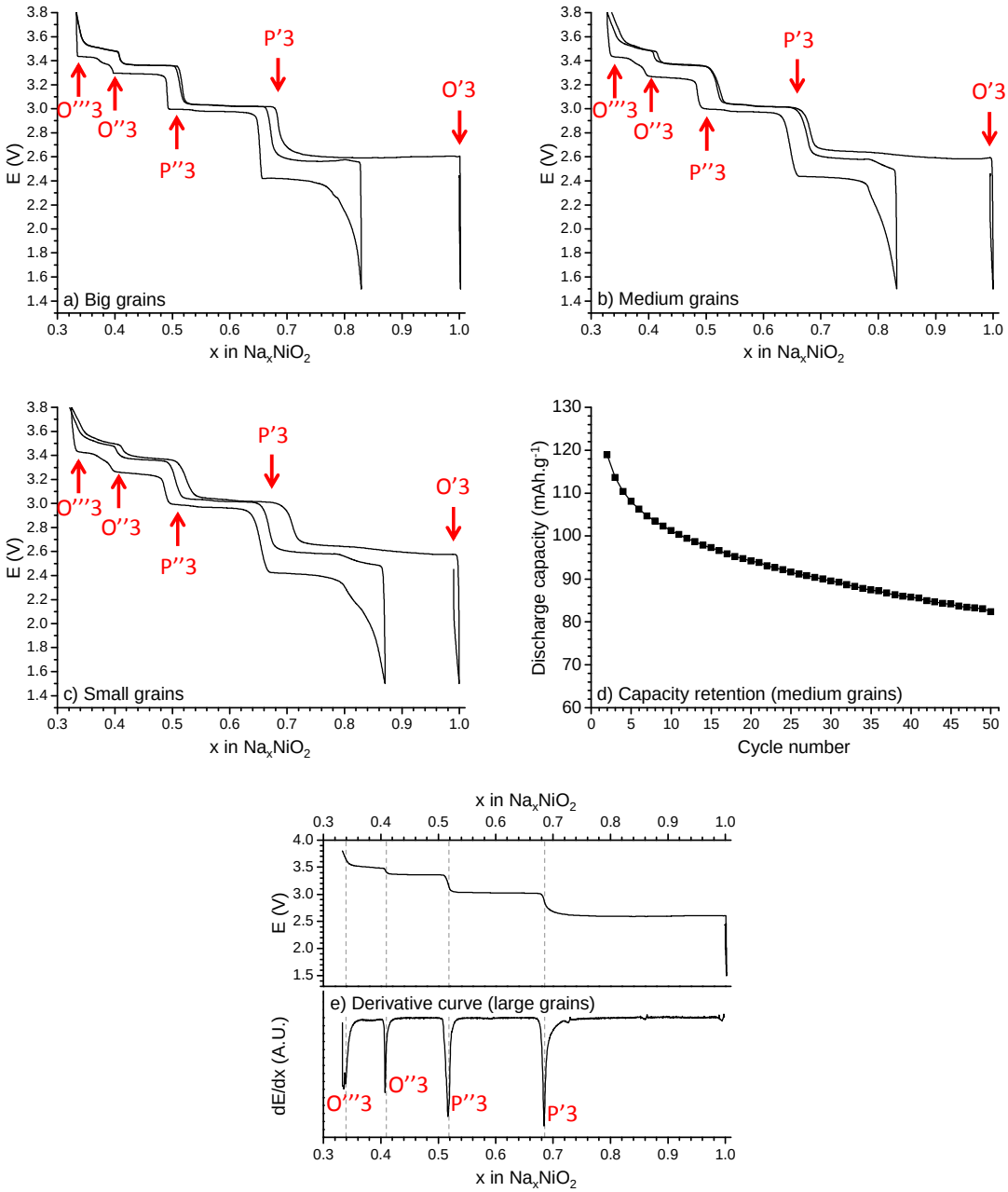

Figure B-I.5: Galvanostatic cycling curves recorded at C/50 between 1.5 and 3.8 V for the (a) large, (b) medium and (c) small grain sized O'3-$NaNiO_2$ materials. The evolution of the discharge capacity as a function of the cycle number is given in (d) for the medium grains sample. The derivative dE/dx curve highlighting the voltage jumps is given in (e) for the "large grains" sample.

During the first discharge, no significant amount of Na^+ ions is inserted in the materials exhibiting large or medium grains. On the other hand, we observe that ≈ 0.01 Na^+ ions are inserted in the "small grains" sample. In the consecutive charge, the electrochemical profile exhibits several potential plateaus within the borders of peculiar compositions for x = 1, 2/3, 1/2 and 2/5. A solid solution behavior is then observed in the 1/3 < x < 2/5 range. The peculiar compositions observed at x = 2/3, 1/2, 2/5 and 1/3 correspond to the ones observed at x' = 0.91, 0.84, 0.81 and 0.79 in [38], respectively. They are highlighted in the dE/dx curve (**Figure B-I.5e**). The difference between the sodium intercalation amounts could come from the more reliable characterization techniques we used for our study. Depending on the particle size, the voltage plateau observed in the 2/3 < x < 1 range is slightly different and can be divided in one (large grains) or two (medium and small grains) parts. This point will be further discussed along with the GITT cycling curves. As discussed later, the O'3 / P'3 stacking types determined by the authors of [38] for x = 2/3, 1/2, 2/5 and 1/3 (highlighted in red in **Figure B-I.5**) were confirmed by synchrotron XRPD and XRPD measurements. The phases were labelled (P'3, P''3…) accordingly to [38].

Upon the second discharge, we notice the partial reversibility of the (de)intercalation process. The curves exhibit two differences with the first charge ones: (i) the voltage jump observed at x ≈ 2/5 in charge is characterized by two smaller jumps in discharge and (ii) the maximal intercalated content in the second discharge curves is reached at x ≈ 0.83 (large and medium grains) or x ≈ 0.87 (small grains) instead of x ≈ 1. This phenomenon was already observed by Vassilliaras et al. [34]. The following charge shows the apparition of a solid solution domain whose range varies depending on the particle size: 0.80 < x ≤ 0.83 (large grains), 0.78 ≤ x ≤ 0.83 (medium grains) or 0.79 < x ≤ 0.88 (small grains). Then the first and second charge curves show the same profile for x > 2/3. After 50 cycles, all materials exhibit poor discharge capacity retention of ≈ 70 %, in agreement with literature [34].

B-I.4.b. GITT cyclings

To have a better understanding of the electrochemical behavior of O'3-$NaNiO_2$ upon Na^+ deintercalation, we carried out a GITT measurement during the charge of a Na_xNiO_2/$NaPF_6$ in PC (1M) + 2 wt% FEC/Na battery as reported in **Figure B-I.6**. The sodium deintercalation step was 0.005 Na^+/formula unit (C-rate: C/50) and the relaxation time was fixed to 30 minutes. The "medium grains" sample was selected as it represents the best compromise between the particle size (see SEM micrographs in **Figure B-I.3**) and the purity (see XRPD patterns in **Figure B-I.2**).

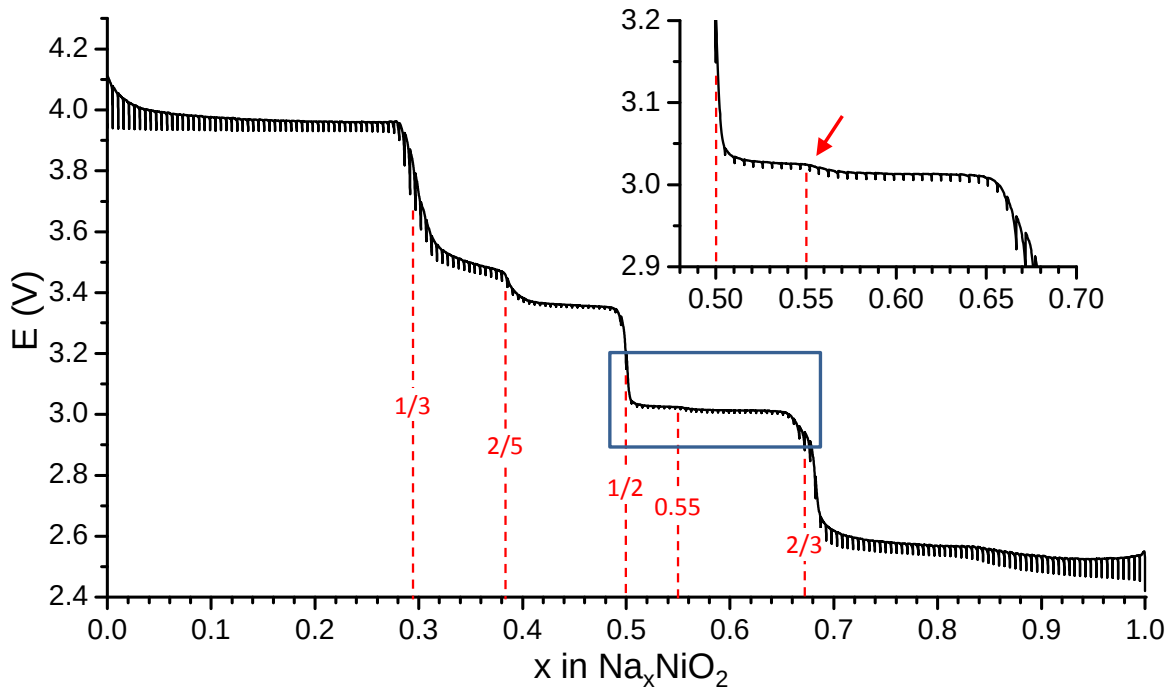

Figure B-I.6: GITT cycling curve recorded with steps of 0.005 Na per formula unit (C/50) followed by a 30 minutes relaxation time for a Na_xNiO_2/ $NaPF_6$ in PC (1M) + 2 wt% FEC /Na battery ("medium grains" sample).

The GITT cycling curve corresponding to the charge of the battery shows an altering between peculiar compositions and biphasic domains, as previously stated. In the $2/3 \leq x \leq 1.0$ range, two voltage pseudo-plateaus are observed. This phenomenon will be detailed later for the three materials. In the $1/2 \leq x \leq 2/3$ range, we note the appearance of an intermediate plateau in the GITT cycling curve, indicating a new phenomenon at $x \approx 0.55$, that is hardly evidenced on the galvanostatic curve. This feature is highlighted on the insert of **Figure B-I.6**. One more plateau is finally observed between the $x = 1/2$ and $x = 2/5$ compositions while further deintercalation leads to a solid solution behavior down to $x = 1/3$. For $E > 3.9$ V ($x > 1/3$), no more variation on the voltage is observed and only a long plateau -cut for representation purposes- is visible. One can suppose the origin of this plateau to be the decomposition of the electrolyte in the battery. Nonetheless, one can observe an increase of the voltage at $x \approx 0$, indicating the beginning of a new reaction.

Concerning the evolution of the polarization of the battery, we note the higher polarization for $x > 0.8$ (250 mV $\leq \Delta E \leq$ 500 mV). The $2/3 \geq x \geq 2/5$ region of the curve exhibits a very low polarization ($\Delta E \approx$ 10 mV). In the literature, Braconnier et al. highlighted the existence of P'3 structure types for the $x = 2/3$ and $x = 1/2$ compositions [38]. The decrease of the polarization is in agreement with this result as a higher ionic conductivity is expected from the P'3 phases [113]. For $x < 2/5$ the polarization increases to $\Delta E \approx 30$ mV, in agreement with the O'3 type structure observed by Braconnier et al. [38].

To further study the electrochemical behavior in the 2/3 ≤ x ≤ 1.0 range, we recorded the GITT cycling curves for all materials, as shown in **Figure B-I.7**.

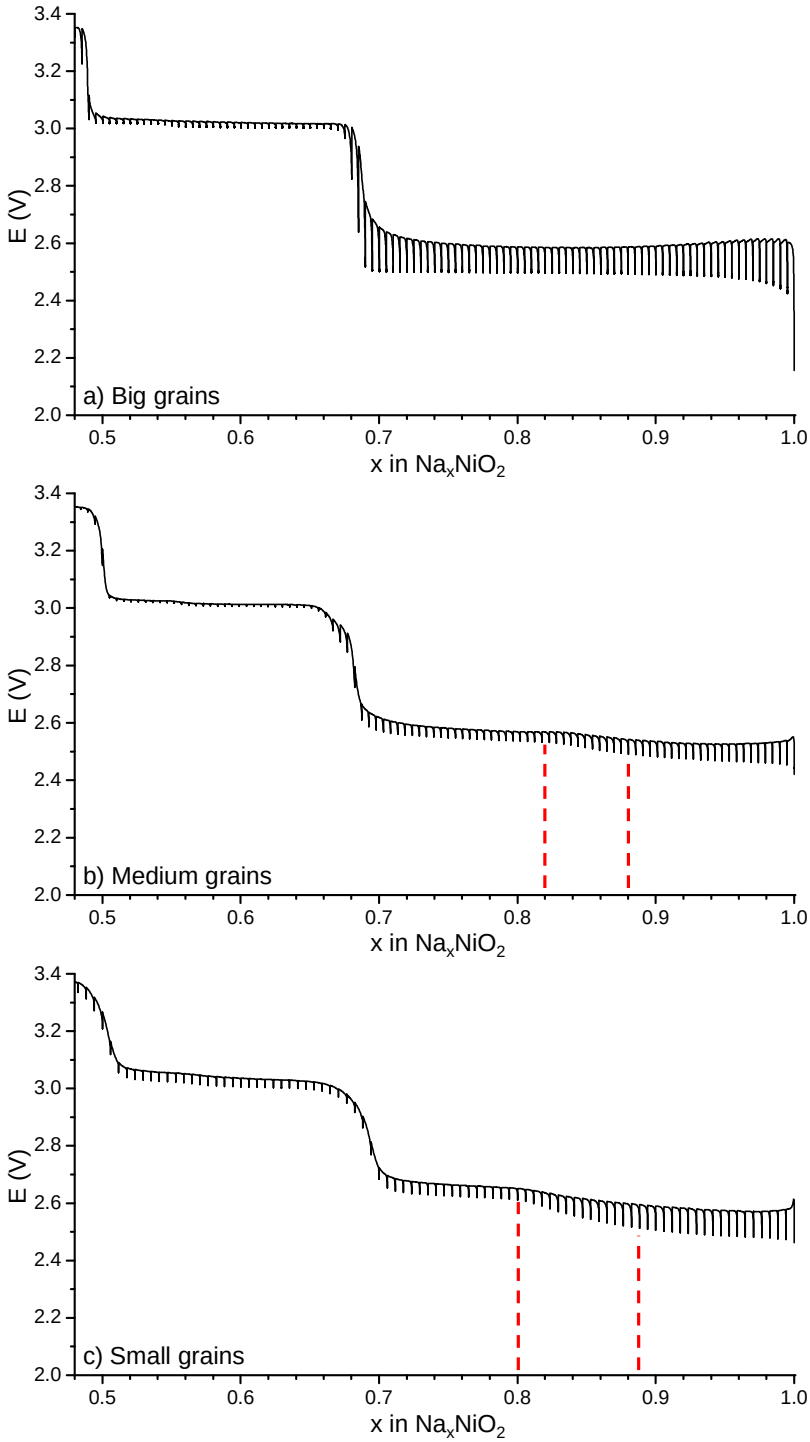

Figure B-I.7: GITT cyclings in the 0.5 < x < 1.0 range recorded with steps of ≈ 0.005 Na per formula unit (C/50) followed by a 60 (a) or 30 (b,c) minutes relaxation time for Na_xNiO_2/ $NaPF_6$ in PC (1M) + 2 wt% FEC /Na batteries for the (a) large, (b) medium and (c) small grains samples.

In the 2/3 ≤ x ≤ 1 range, the “large grains” sample shows only one voltage plateau associated to a high polarization (ΔE ≈ 90 mV) whereas the “medium grains” and “small grains” materials exhibit two distinct voltage plateaus separated by a small solid solution domain for 0.82 < x < 0.88 (“medium grains” curve values). As expected the polarization varies in the same way for the three materials. It decreases from the “large grains” sample to the “medium grains” one. Surprisingly, decreasing the grains size leads to an increase of the polarization. One can suppose this polarization increase to result from the grain boundaries resistances, more numerous in the case of the “small grains” sample. The voltage variation during Na^+ diffusion (end of relaxation step) is comparable to the one of the “medium grains” material.

B-I.5. The Na_xNiO_2 phase diagram

B-I.5.a. *In situ* XRPD during full charge of the battery

To follow the structural changes that Na_xNiO_2 undergoes during Na^+ deintercalation, we carried out an *in situ* XRPD study during the charge of a $Na_xNiO_2/NaPF_6$ in PC (1M) + 2wt% FEC/Na battery on the “medium grains” sample. Due to the expected Na/vacancy orderings for precise Na contents, we carried out the experiment in the GITT mode to obtain each XRPD pattern at the equilibrium with a satisfying signal/noise ratio. The XRPD patterns were recorded between 15° and 45° (2θ) using the monochromatic Cu $k\alpha_1$ incident wavelength to better distinct close diffraction peaks. The XRPD patterns recorded during the experiment are shown in **Figure B-I.8**. Because of a parasitic current associated to the electrochemical cell, the recorded E = f(x) curve is severely shifted towards low x values and we are unable to provide the associated GITT cycling curve.

The peculiar compositions observed alone for x = 1 (pristine material), ≈ 0.8, 2/3, 1/2, 2/5 and 1/3 (end of experiment) are highlighted in red in **Figure B-I.8**. Surprisingly a single phase domain at x ≈ 0.8 is observed during the first charge. In the following, this phase will be referred to as “$Na_{\approx 0.8}NiO_2$”. Its existence is clearly shown in the zoom of the 15.5 – 17.3° 2θ region presented in **Figure B-I.9** where one can follow the variation of the $(001)_{mon.}$ diffraction line for each phase upon deintercalation. In the literature, the $Na_{\approx 0.8}NiO_2$ phase was only observed *in situ* during the discharge and not during the first charge [134]. We believe this is due to the *operando* mode the authors used.

The interslab distances deduced from the position of the $(001)_{mon.}$ diffraction peaks were calculated and are reported in **Figure B-I.10**.

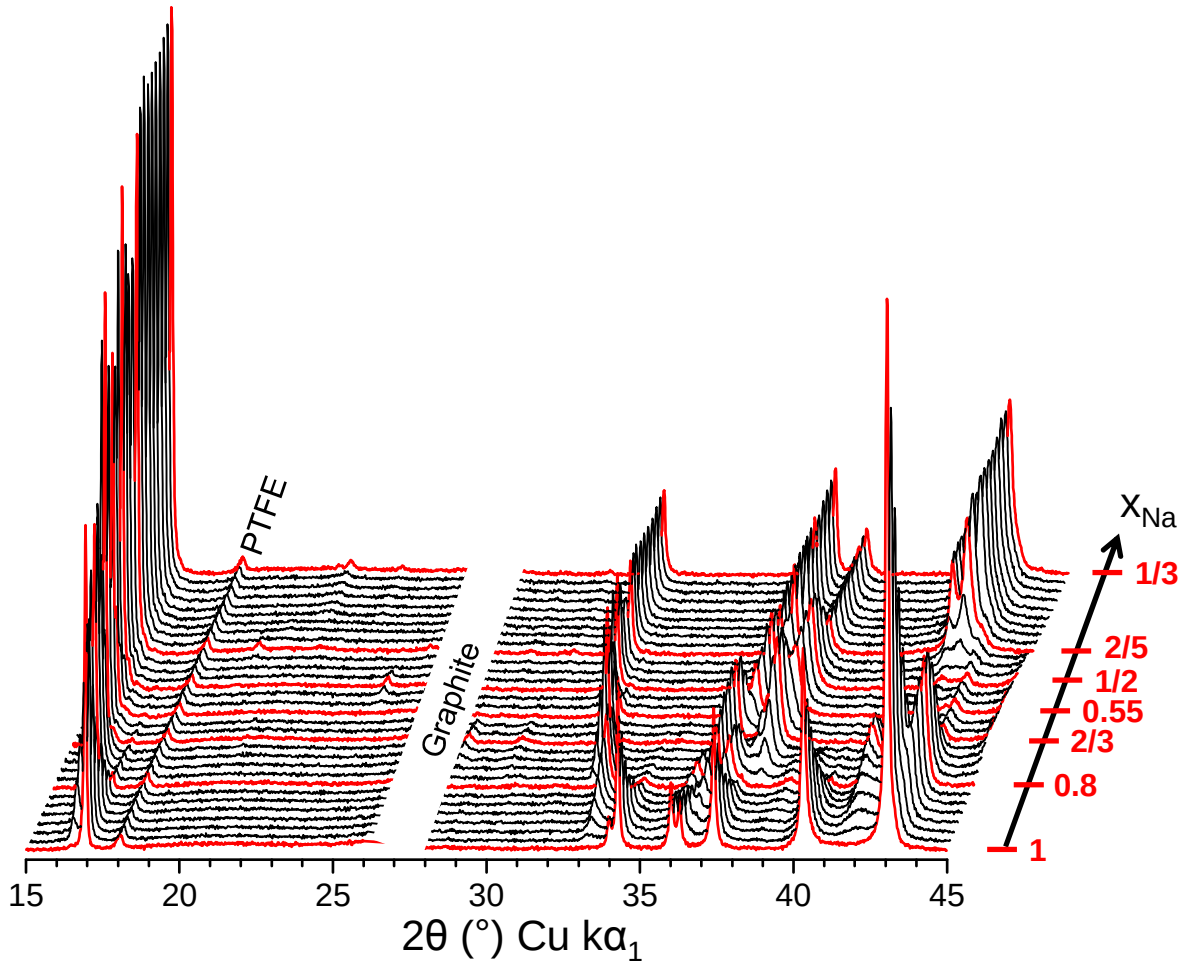

Figure B-I.8: Evolution of the XRPD patterns recorded *in situ* during the charge of a $NaNiO_2/NaPF_6$ in PC (1M) + 2 wt% FEC/Na cell (medium grains sample). The red XRPD patterns highlight the peculiar compositions.

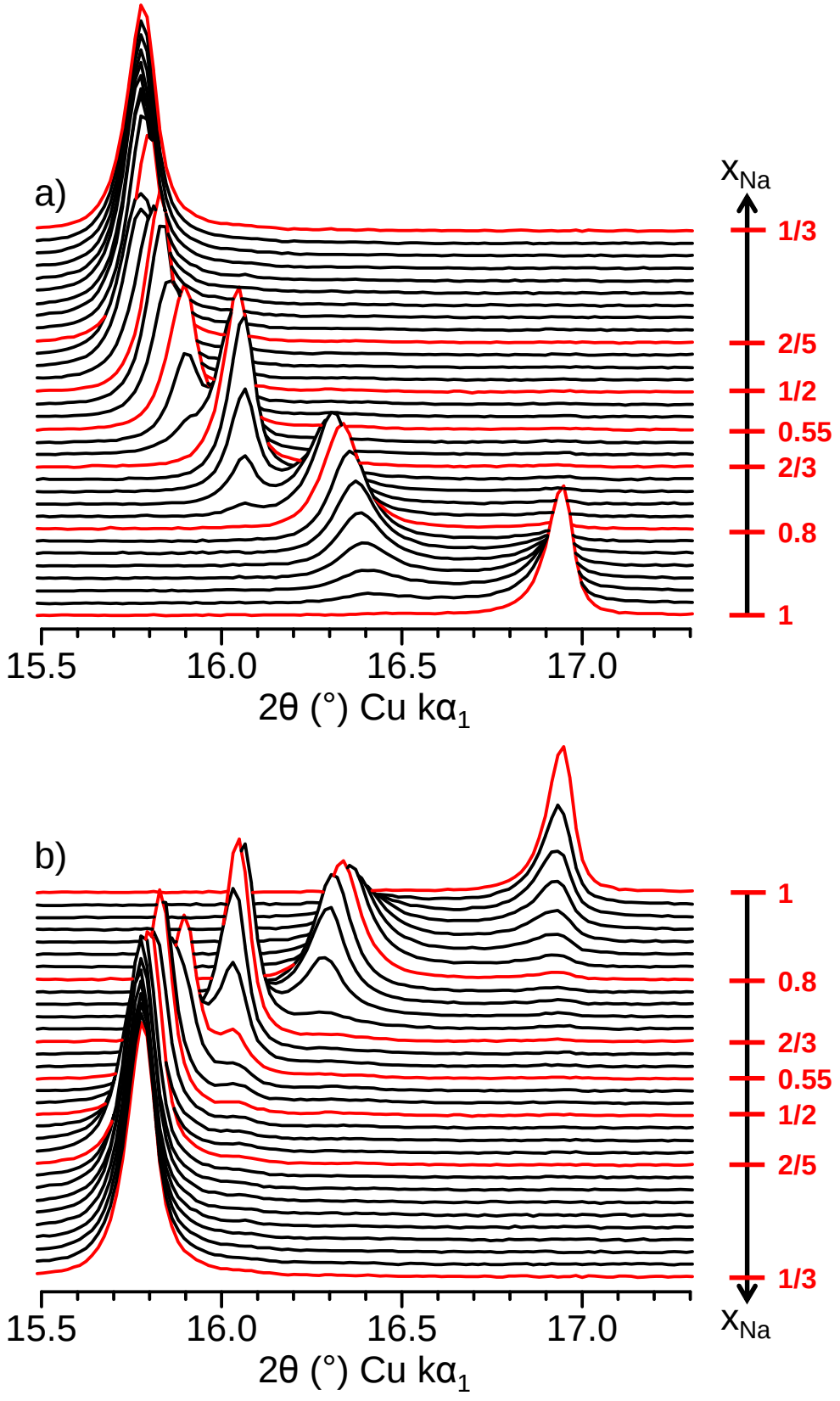

Figure B-I.9: (a) Zoom in the 15.5 – 17.3° 2θ region of the XRPD patterns recorded during the *in situ* experiment carried out on the Na_xNiO_2 system (medium grains sample). (b) Inversed representation. The red XRPD patterns highlight the peculiar compositions.

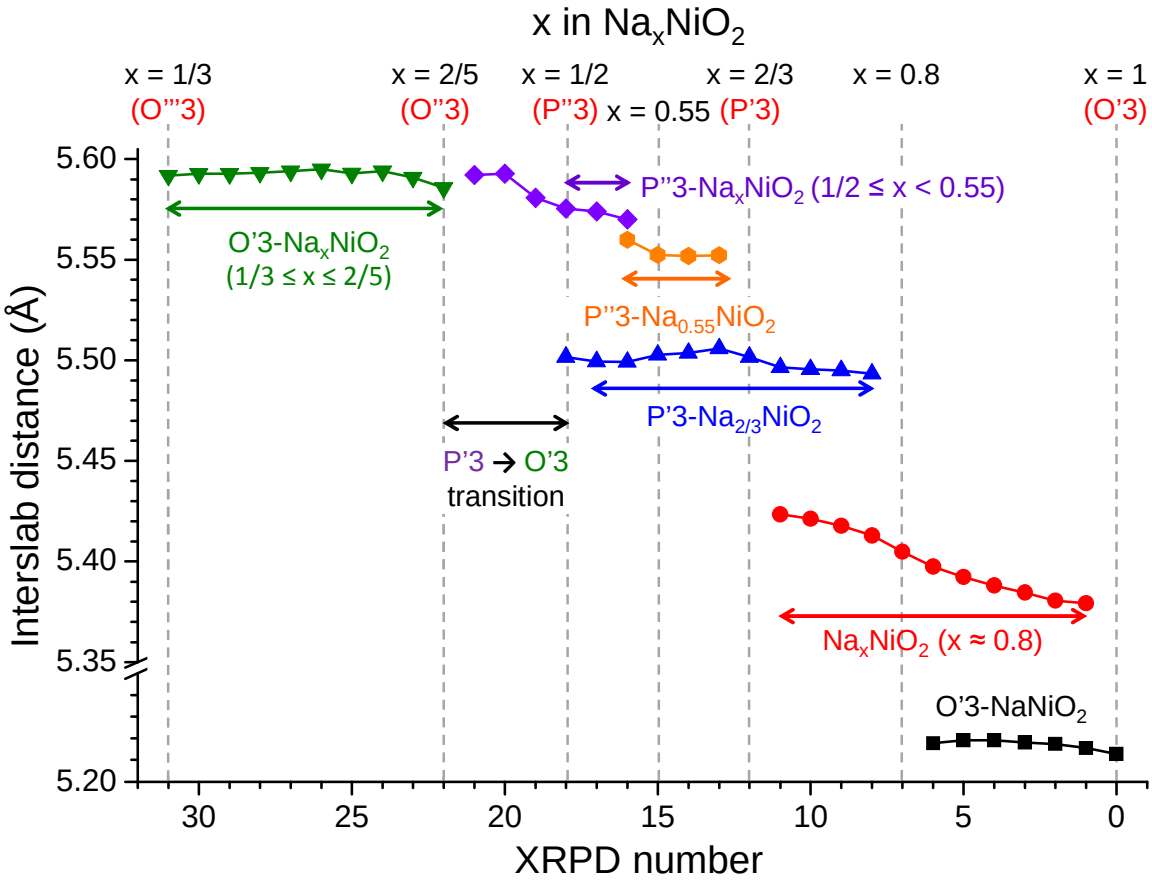

Figure B-I.10: Evolution of the interslab distances of the different Na_xNiO_2 phases deduced from the position of the $(001)_{mon.}$ diffraction lines and after correction of the "zero shift".

In the 0.8 < x < 1 range, the intensity of the $(001)_{mon.}$ diffraction peak of the $Na_{\approx 0.8}NiO_2$ phase increases while the intensity of the $(001)_{mon.}$ diffraction peak of O'3-$NaNiO_2$ decreases. The evolution of the interslab distances shows no significant variation for the O'3-$NaNiO_2$ phase while it shows a small increase upon deintercalation for the $Na_{\approx 0.8}NiO_2$ phase. This indicates a solid solution behavior of the $Na_{\approx 0.8}NiO_2$ phase in the $Na_{\approx 0.8}NiO_2$ + O'3-$NaNiO_2$ biphasic domain. Then, the $Na_{\approx 0.8}NiO_2$ phase is observed alone in a narrow range, around x ≈ 0.8 (**Figure B-I.9**).

In the 2/3 < x < 0.8 range a biphasic behavior is observed between the P'3-$Na_{2/3}NiO_2$ phase and the $Na_{\approx 0.8}NiO_2$ one. While the interslab distance of the P'3-$Na_{2/3}NiO_2$ phase does not evolve, we note a small evolution of the interslab distance of the $Na_{\approx 0.8}NiO_2$ phase which is, once more, involved in a solid solution behavior inside the biphasic domain.

In the 1/2 < x < 2/3 range, two biphasic domains are observed. For the higher sodium contents (XRPD patterns #13 → 15), a biphasic behavior is observed between P'3-$Na_{2/3}NiO_2$ and P''3-$Na_{0.55}NiO_2$. The P''3-$Na_{0.55}NiO_2$ phase corresponds to the small voltage increase observed on the GITT cycling curve and evidenced by the red arrow in **Figure B-I.6**.

For lower sodium contents (XRPD patterns #16 → 18) the P''3-$Na_{1/2}NiO_2$ phase appears while the intensity of the diffraction peaks of the P''3-$Na_{0.55}NiO_2$ and P'3-$Na_{2/3}NiO_2$ phases decrease. The presence of the P'3-$Na_{2/3}NiO_2$ phase in the $1/2 < x < 0.55$ implies slow kinetics for the P'3-$Na_{2/3}NiO_2$ phase.

For $2/5 < x < 1/2$, the $(001)_{mon.}$ diffraction line shows an important broadening. A zoom of the $(001)_{mon.}$ diffraction peak position of the XRPD patterns around the $2/5 \leq x \leq 1/2$ range is given in **Figure B-I.11**.

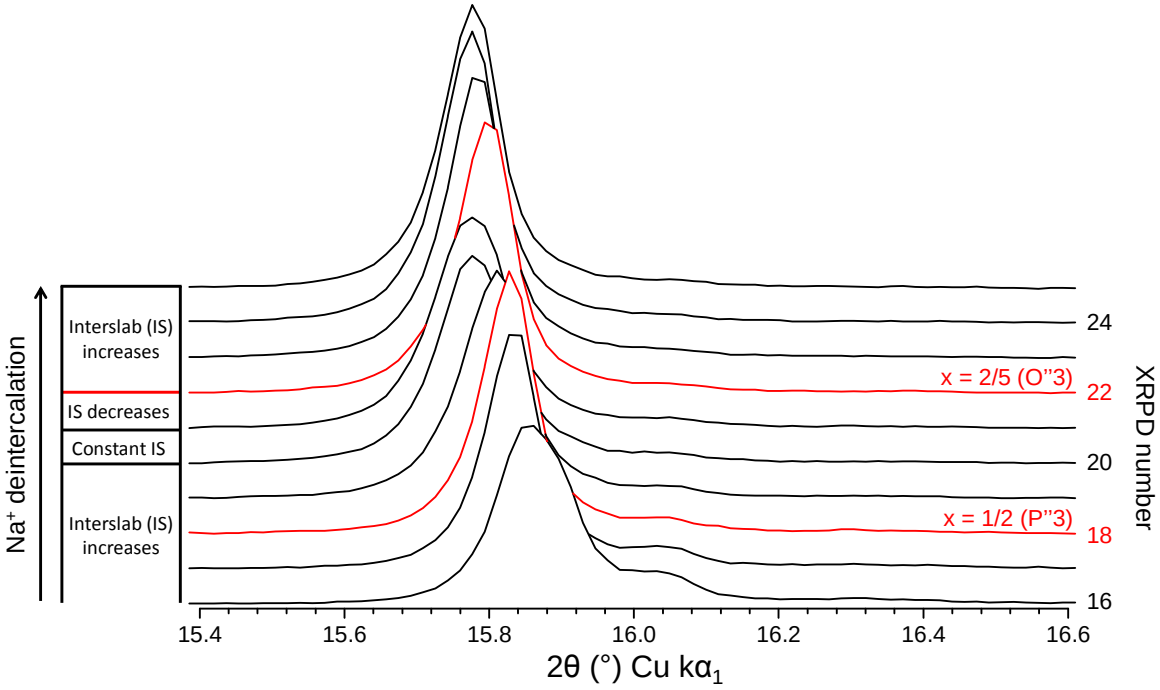

Figure B-I.11: Zoom in the 15.4 – 16.6° 2θ region of the XRPD patterns recorded around the $2/5 \leq x \leq 1/2$ range during the *in situ* experiment.

Upon deintercalation, one would expect the interslab distance of the material to continuously increase for a given phase. However, its value is very similar between P''3-$Na_{1/2}NiO_2$ (≈ 5.58 Å) and O''3-$Na_{2/5}NiO_2$ (≈ 5.59 Å) which is explained by the evolution of the NaO_6 surrounding from a prismatic site to a more compact octahedral one. Between the two compositions a complex behavior is observed: first the interslab distance increases between pattern #18 (x = 1/2) and pattern #20. The interslab is then constant from patterns #20 to #21. It then decreases from pattern #21 to #22. In fact two opposite effects are in competition from pattern #18 to #22:

(1) The deintercalation from P''3-$Na_{1/2}NiO_2$ which implies an increase of the interslab distance.

(2) The formation of an octahedral environment for some NaO_6 polyhedra slabs which leads to a decrease of the interslab distance.

From patterns #18 (x = 1/2) to #20, the deintercalation from P''3-$Na_{1/2}NiO_2$ prevails, and the interslab distance of the material increases. From patterns #20 to #21, the deintercalation and the creation of stacking faults compensate each other and no variation of the interslab is observed. The broader (001) diffraction peak in pattern #21 involve the increase of the stacking fault amount. From pattern #21 to# 22, the formation of NaO_6 octahedral slabs is prevailing and the interslab distance decreases as more and more sodium ions are located in octahedral environments. The coexistence of prismatic and octahedral environments of the Na^+ ions is the origin of the broadening of the diffraction peak for $2/5 < x < 1/2$ range. From x = 2/5 (pattern #22), all sodium ions are located in NaO_6 octahedrons and the interslab distance decreases. Upon further deintercalation, the material goes through a solid solution process and the interslab distance increases down to x = 1/3, in agreement with lower sodium content.

Looking closely at the XRPD patterns in the 17 – 30° 2θ range, we observe the reversible appearance of extra diffraction peaks of lower intensity. This feature is highlighted in **Figure B-I.12** which displays the XRPD patterns recorded for x = 1, 0.8, 2/3, 1/2 and 1/3 in the 15 – 35° 2θ domain.

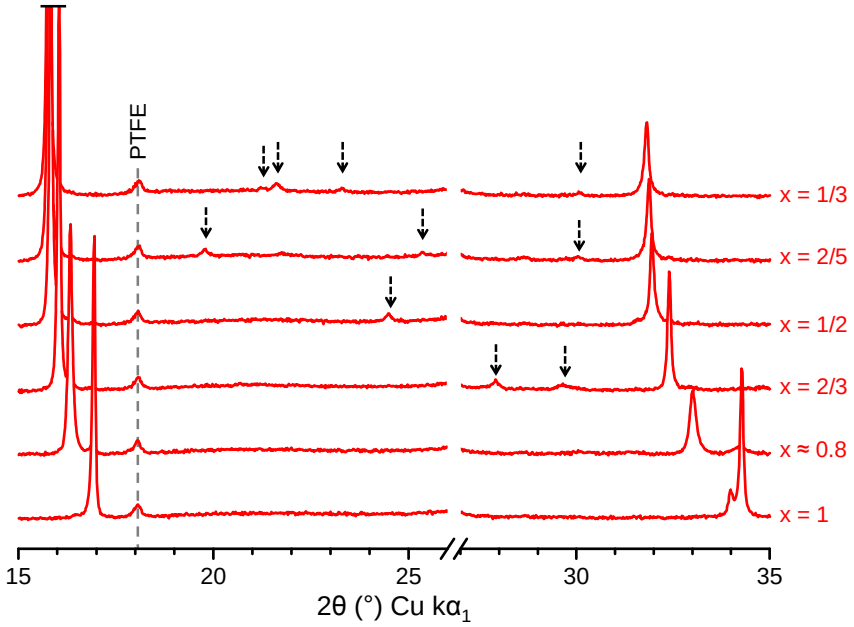

Figure B-I.12: XRPD patterns of the x = 1, 0.8, 2/3, 1/2, 2/5 and 1/3 recorded *in situ* during the charge of a $Na_xNiO_2/NaPF_6$ in PC (1M) + 2 wt % FEC/Na battery. The black dashed arrows highlight the appearance of new diffraction peaks.

As one can see, the XRPD patterns of the x = 2/3, 1/2, 2/5 and 1/3 compositions all exhibit extra diffraction peak(s). In Na_xMO_2 oxides, such a phenomenon is commonly observed for peculiar compositions and is the consequence of long-range Na/vacancies ordering between the MO_2 layers [48, 56, 64]. Including the extra-diffraction peaks in the LeBail refinement of the profile require determining new cell parameters for the *supercell*, based on the ones of the *subcell*. Note that the supercell and subcell do not always share the same space group.

B-I.5.b. Influence of particle size on the deintercalation processes

Consecutively to the GITT study in the $2/3 \leq x \leq 1$ range for the large, medium and small grain sized materials, we carried out the same experiment *in situ*, recording a XRPD pattern at the end of each relaxation period. The sodium step was originally 0.025 Na^+ ions per formula unit. However some parasitic current due to the electrochemical cell slightly shifted the galvanostatic curves. **Figure B-I.13** shows the evolution of the XRPD patterns recorded *in situ* during the GITT charge of the $Na_xNiO_2/NaPF_6$ in PC (1M) + 2 wt% FEC/Na cells along with the corresponding GITT cycling curves. The interslab distances of O'3-$NaNiO_2$, $Na_{\approx 0.8}NiO_2$ and P'3-$Na_{2/3}NiO_2$ are reported in **Figure B-I.14**. The Na contents have been corrected by linear regression between x = 1 (starting point of the experiment) and x = 2/3 (E = 2.85 V).

As shown in **Figure B-I.13** the "large grains" and "medium grains" samples show a pure O'3-$NaNiO_2$ phase in the pristine material. On the other hand, the "small grains" sample exhibits a small portion of $Na_{\approx 0.8}NiO_2$ in the starting material which is the origin of the extra diffraction peak observed on the XRPD pattern recorded after the synthesis (**Figure B-I.2**). Upon slight Na^+ deintercalation ($x \approx 0.97$), the O'3-$NaNiO_2$ and the $Na_{\approx 0.8}NiO_2$ phases are observed simultaneously for all materials. Further deintercalation leads to the apparition of the P'3-$Na_{2/3}NiO_2$ phase in the "large grains" samples and the three phases are observed simultaneously down to $x \approx 0.7$. Then, for x = 2/3, only the P'3-$Na_{2/3}NiO_2$ phase and a small part of the O'3-$NaNiO_2$ phase are observed. We note that there is no variation of the interslab distances for any of the three phases in the $2/3 \leq x \leq 0.945$ range for the "large grains" sample.

The behavior of the "medium grains" and "small grains" samples is identical to the one described during the full charge of the battery on the "medium grains" material: the O'3-$NaNiO_2$ and $Na_{\approx 0.8}NiO_2$ phases are observed for the higher sodium contents ($0.835 \leq x < 0.96$ and $0.835 \leq x \leq 1.0$ for the "medium grains" and "small grains" samples respectively). While no variation of interslab distance of the O'3-$NaNiO_2$ phase is observed, the $Na_{\approx 0.8}NiO_2$ phase shows a progressive increase of its interslab parameter typical of a solid solution (**Figure B-I.14**). The solid solution behavior of the $Na_{\approx 0.8}NiO_2$ phase is observed alone in a narrow range ($0.80 \leq x < 0.835$) for both samples. Further deintercalation leads to the appearance of the P'3-$Na_{2/3}NiO_2$ phase which exhibits a constant interslab distance while the one of the $Na_{\approx 0.8}NiO_2$ phase continuously increases. For x = 2/3, only the P'3-$Na_{2/3}NiO_2$ phase is observed for the "medium grains" and "small grains" samples.

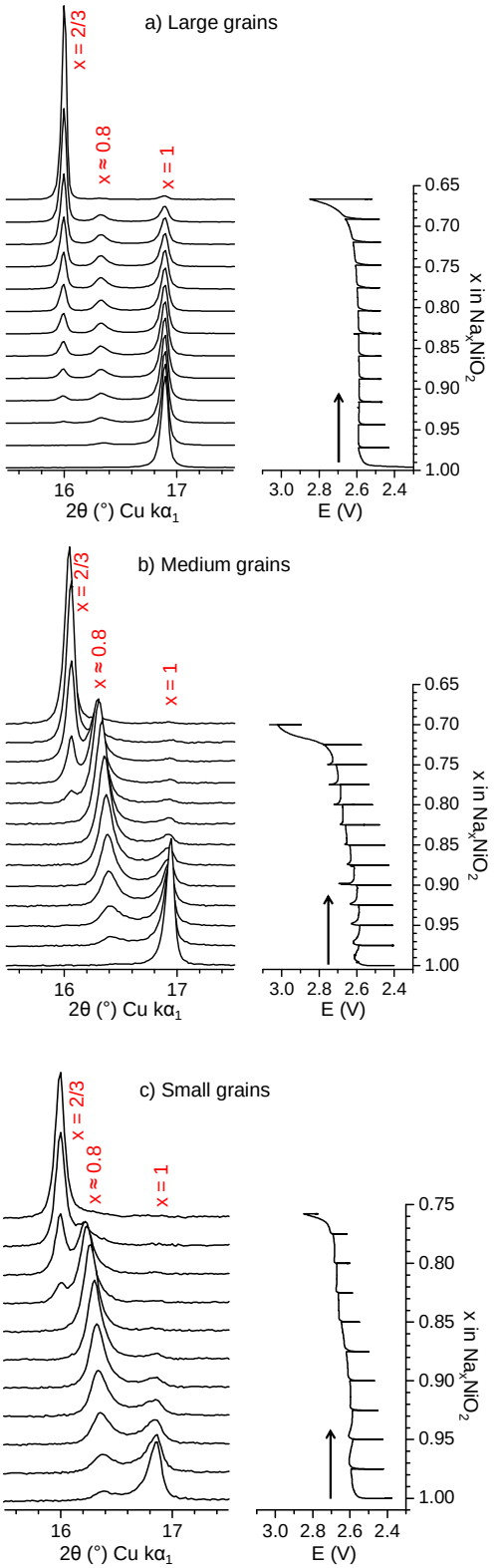

Figure B-I.13: Evolution of the XRPD patterns in the 15.5 – 17.5 2θ range recorded *in situ* during the charge of $NaNiO_2/NaPF_6$ in PC (1M) + 2 wt% FEC/Na cells involving the different samples: (a) "large grains", (b)"medium grains" and (c) "small grains".

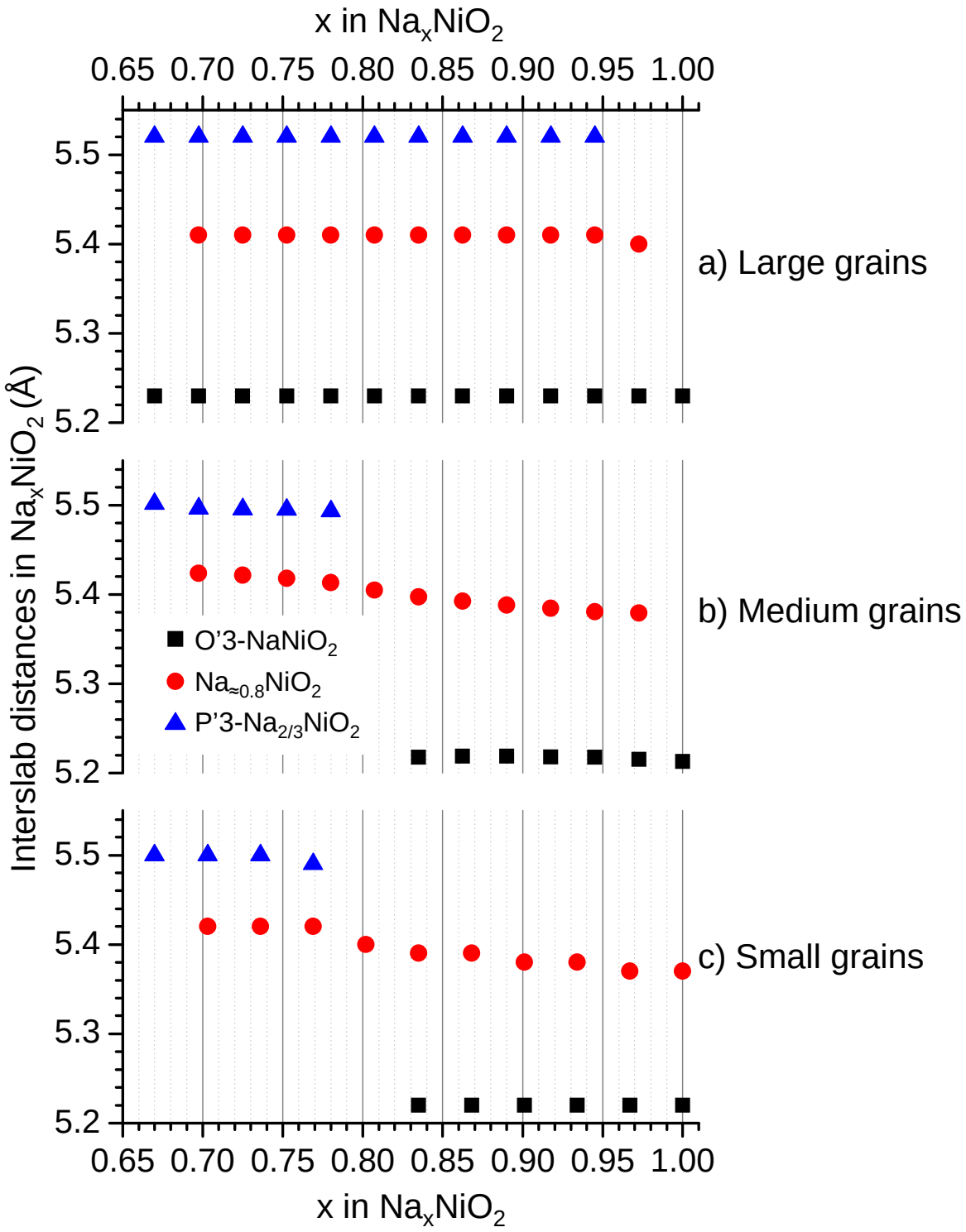

Figure B-I.14: Evolution of the interslab distances deduced from the XRPD patterns recorded *in situ* during charge of the Na_xNiO_2/ $NaPF_6$ in PC (1M) + 2 wt% FEC /Na cells with the (a) "large grains", (b) "medium grains" and (c) "small grains" samples.

The behavior of the "large grains" sample shows that there are large kinetic differences between the O'3-$NaNiO_2$, $Na_{\approx 0.8}NiO_2$ and P'3-$Na_{2/3}NiO_2$ phases. As soon as the $Na_{\approx 0.8}NiO_2$ phase is formed, it transforms rapidly into P'3-$Na_{2/3}NiO_2$. Due to the very small voltage difference between the pseudo-plateaus, and the high polarization in the case of the "large grains" sample, the cell voltage is always above the $Na_{\approx 0.8}NiO_2$ → P'3-$Na_{2/3}NiO_2$ redox potential. In the case of the "medium grains" and "small grains" samples, there is a small polarization and, therefore, the O'3-$NaNiO_2$ → $Na_{\approx 0.8}NiO_2$ and $Na_{\approx 0.8}NiO_2$ → P'3-$Na_{2/3}NiO_2$ phenomenons are separated.

B-I.5.c. Investigation of the deintercalated phases

The P'3-$Na_{2/3}NiO_2$, P''3-$Na_{1/2}NiO_2$ and O''3-$Na_{2/5}NiO_2$ phases

To further study the structure of the Na_xNiO_2 materials we recorded their synchrotron XRPD patterns at the ESRF[20] as shown in **Figure B-I.15**.

As the only differences between the two structures are the O and Na atomic positions, it is easy to discriminate the P'3 structure from the O'3 one based on the relative intensities of selected diffraction peaks. Typically, the XRPD patterns of P'3 structures exhibit (111) and (-202) diffraction peaks of weak intensity while the (201) and (-112) diffraction peaks show strong intensity. The opposite phenomenon is observed on the XRPD patterns of O'3 structures which show (111) and (-202) diffraction peaks of strong intensity while the (201) and (-112) diffraction peaks show weak intensity. Looking at the (111), (-202), (201) and (-112) diffraction peaks on the synchrotron XRPD patterns (see black Miller indexes in grey areas of **Figure B-I.15**), we are able to confirm the structures of the peculiar compositions: P'3-$Na_{2/3}NiO_2$, P''3-$Na_{1/2}NiO_2$ and O''3-$Na_{2/5}NiO_2$.

Unfortunately, we could not prepare a sample of O'''3-$Na_{1/3}NiO_2$ on time for the synchrotron experiment. However, it is possible to confirm the O'3 stacking in this material looking at the *in situ* XRPD pattern in **Figure B-I.8** as the (111) and (-202) diffraction peaks ($42 \leq 2\theta \leq 45°$) exhibit high intensity similar to those of O''3-$Na_{2/5}NiO_2$.

The better signal / noise ratio of the synchrotron XRPD patterns allows better distinction of the *superstructure* peaks. Therefore, we tried to find the superstructure cells of P'3-$Na_{2/3}NiO_2$, P''3-$Na_{1/2}NiO_2$ and O''3-$Na_{2/5}NiO_2$ from the synchrotron XRPD patterns. The first step was to index the subcell in the monoclinic symmetry (space group C2/m) independently of the stacking type (P'3 or O'3). The cell parameters determined for P'3-$Na_{2/3}NiO_2$, P''3-$Na_{1/2}NiO_2$ and O''3-$Na_{2/5}NiO_2$ are reported in **Table B-I.4**.

[20] In collaboration with Dr. C. Drathen, ESRF, Grenoble, France (ID31 beamline).

Then we tried fitting the synchrotron XRPD patterns with various supercells whose cell parameters were based on the subcell ones. The centrosymmetric space group of lowest symmetry (P-1) was considered for this step. After we determined the only possible supercell parameters, we deduced the space group (monoclinic symmetry) based on the reflection conditions. For every material, we found only one possible space group to fit the pattern. The result of the LeBail refinement of the profiles considering the supercell are displayed in **Figure B-I.15** for P'3-$Na_{2/3}NiO_2$, P''3-$Na_{1/2}NiO_2$ and O''3-$Na_{2/5}NiO_2$. The space groups and cell parameters of the supercells are given in **Table B-I.5**.

Material	**$a_{mon.}$ (Å)**	**$b_{mon.}$ (Å)**	**$c_{mon.}$ (Å)**	**$\beta_{mon.}$ (°)**
P'3-$Na_{2/3}NiO_2$	4.970(5)	2.862(3)	5.742(4)	105.9(1)
P''3-$Na_{1/2}NiO_2$	4.919(6)	2.832(3)	5.816(7)	105.6(1)
O''3-$Na_{2/5}NiO_2$	4.941(3)	2.809(2)	5.858(6)	106.52(7)

Table B-I.4: Subcell parameters deduced from the LeBail refinement of the profiles of P'3-$Na_{2/3}NiO_2$, P'3-$Na_{1/2}NiO_2$ and O'3-$Na_{2/5}NiO_2$.

Material	**Space Group**	**Supercell parameters**				**$a_{sub.}/b_{sub.}$**
		$a_{sup.}$ (Å)	**$b_{sup.}$ (Å)**	**$c_{sup.}$ (Å)**	**$\beta_{sup.}$ (°)**	
P'3-$Na_{2/3}NiO_2$	$P2_1/a$	4.9715(4) = **$a_{sub.}$**	8.589(1) = **3 x $b_{sub.}$**	5.7391(5) = **$c_{sub.}$**	105.84(1) = **$\beta_{sub.}$**	1.74
P''3-$Na_{1/2}NiO_2$	$P2_1/m$	4.918(1) = **$a_{sub.}$**	5.6633(7) = **2 x $b_{sub.}$**	5.8155(8) = **$c_{sub.}$**	105.52(1) = **$\beta_{sub.}$**	1.74
O''3-$Na_{2/5}NiO_2$	C2/m	4.941(3) = **$a_{sub.}$**	14.046(8) = **5 x $b_{sub.}$**	5.856(5) = **$c_{sub.}$**	106.53(8) = **$\beta_{sub.}$**	1.76

Table B-I.5: Supercells and space groups used to describe the P'3-$Na_{2/3}NiO_2$, P'3-$Na_{1/2}NiO_2$ and O'3-$Na_{2/5}NiO_2$ peculiar compositions (and thus including the extra diffraction peaks).

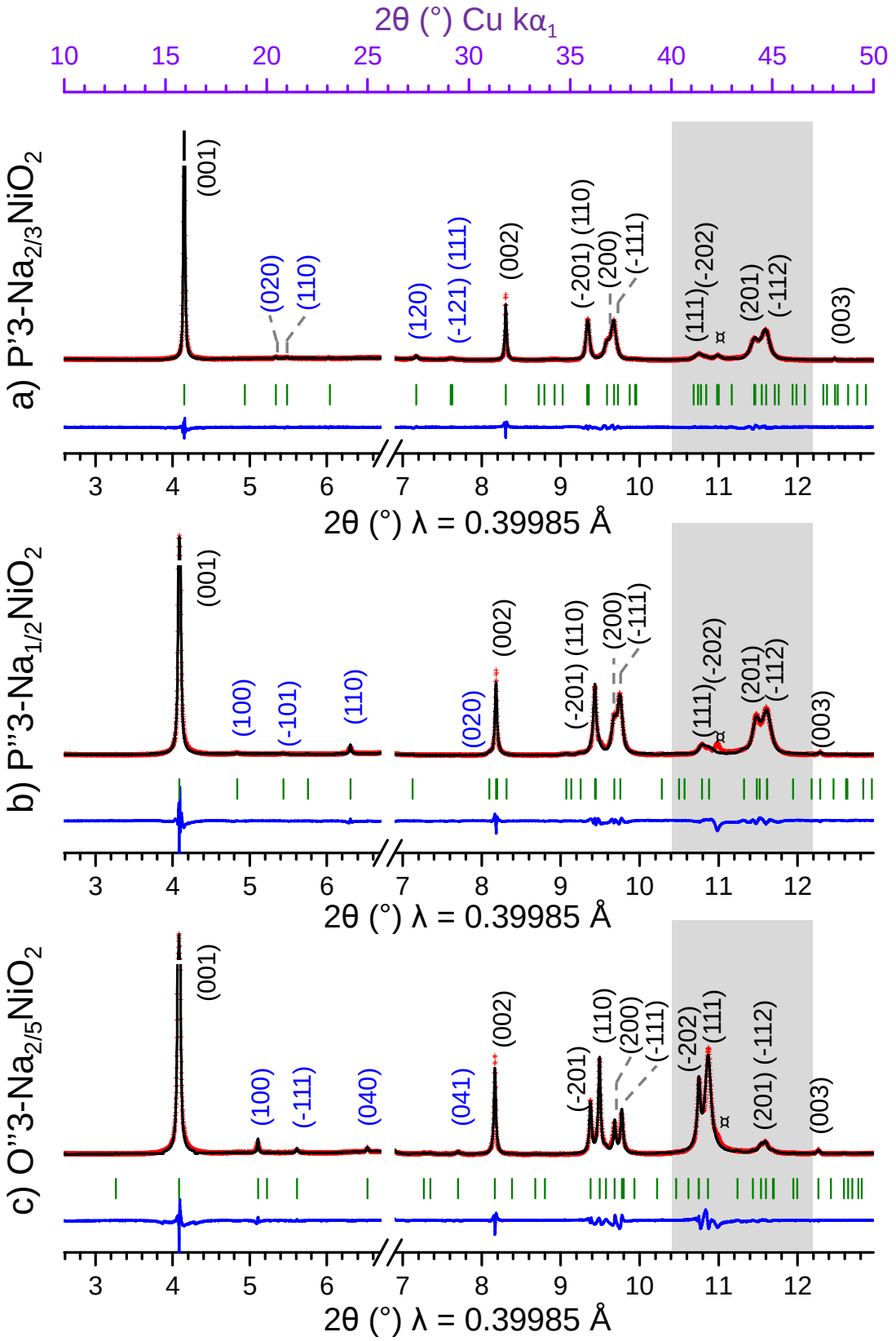

Figure B-I.15: LeBail refinement of the XRPD profiles of (a) P'3-$Na_{2/3}NiO_2$, (b) P'3-$Na_{1/2}NiO_2$ and (c) O'3-$Na_{2/5}NiO_2$. The ¤ symbol indicates the NiO diffraction peak. Black Miller indexes: subcell indexation. Blue Miller indexes: indexation of the superstructure peaks in the supercell.

As shown in **Table B-I.5**, the supercell of every material necessitates multiplying the $b_{sub.}$ cell parameter. The $a_{sub.}/b_{sub.}$ ratio is close to $\sqrt{3}$ (≈ 1.73). Therefore, no cooperative Jahn-Teller effect induced by the Ni^{3+} ions is expected. As all materials contain a significant amount of Ni^{4+} ions, one can assume that electronic transfer occurs between the Ni^{3+} and Ni^{4+} ions, preventing from the cooperative distortion of the cell. Electrical measurements are in progress to confirm this hypothesis.

The $Na_{\approx 0.8}NiO_2$ phase

As highlighted in **Figure B-I.16** the XRPD pattern of the $Na_{\approx 0.8}NiO_2$ phase does not exhibits any weaker reflection in the 15 – 35° 2θ range. On the other hand, it presents several extra reflections apparently arising from the splitting of the monoclinic symmetry diffraction peaks of O'3-$NaNiO_2$ and a triclinic symmetry is therefore awaited. However, any attempt to index this diagram failed, in part due to the broadening of the diffraction peaks. An indexation based on the monoclinic cell parameters as described in [134] was not successful either.

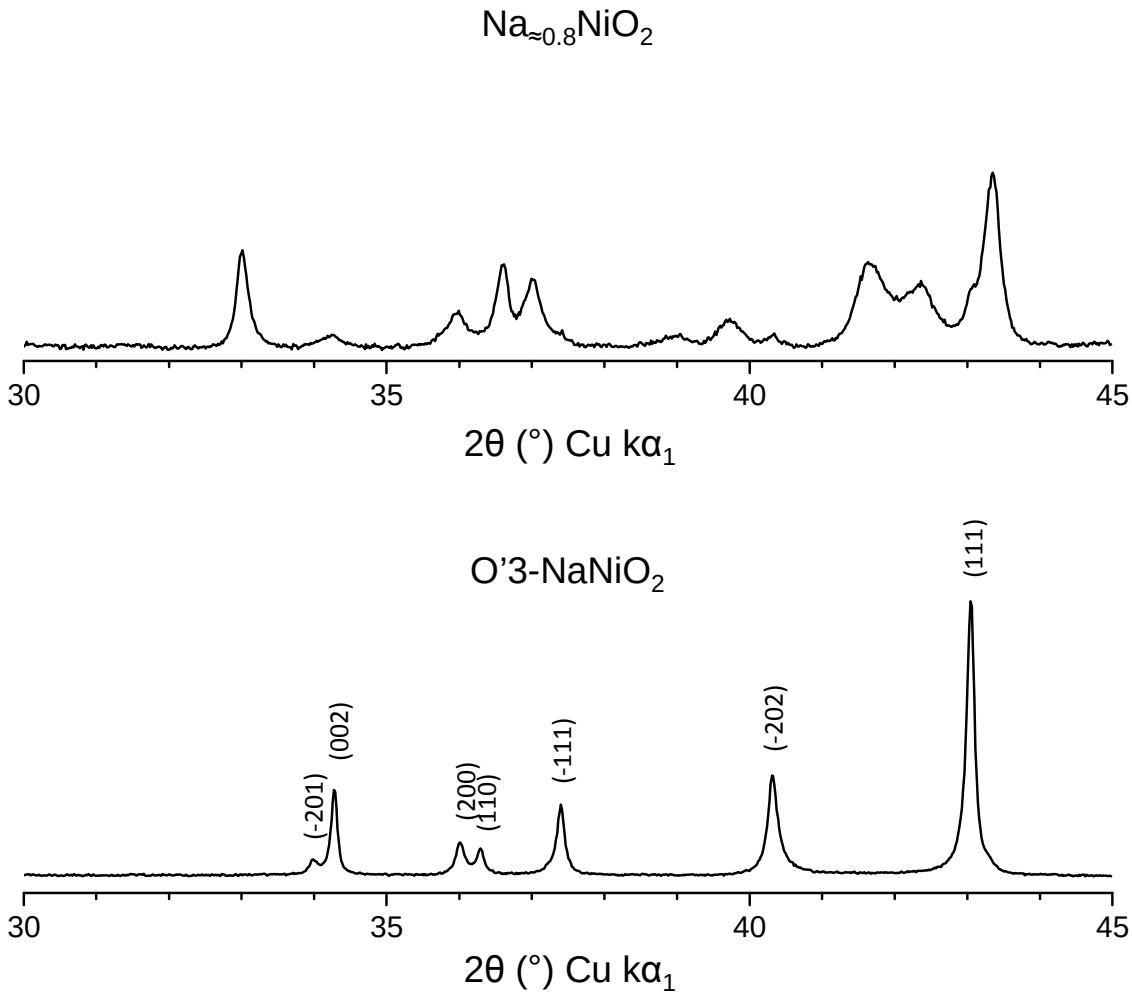

Figure B-I.16: Comparison of the XRPD patterns of the (top) $Na_{\approx 0.8}NiO_2$ and (bottom) O'3-$NaNiO_2$ phases. The intensity scale is different for both patterns.

General Conclusion and perspective work

The present work is a study of the structural and electrochemical properties of $Na_xMn_{1-y}Fe_yO_2$ and Na_xNiO_2 materials as positive electrodes for Na-ion batteries.

The first part concerned the preparation by a self-combustion type synthesis of four materials in the $Na_xMn_{1-y}Fe_yO_2$ system: the P2-$Na_{0.66}Mn_{0.66}Mn_{1/3}Fe_{2/3}O_2$, P2-$Na_{0.62}Mn_{1/2}Fe_{1/2}O_2$, (O3+O'3)-$Na_{0.77}Mn_{1/2}Fe_{1/2}O_2$ and O3-$Na_{0.77}Mn_{1/3}Fe_{2/3}O_2$ ones. Experimentally, we showed that a high Mn / Fe ratio stabilizes P2 structures while a low Mn / Fe ratio stabilizes O3 ones. In parallel to this thesis, several studies were released on P2 and O3-$Na_xMn_{1-y}Fe_yO_2$ materials. If the P2 phases are similar to the one we obtained, our O3-type materials are definitely different, probably because of (i) the lower initial Na content (x = 0.77) compared to the literature (x = 1.0) and/or (ii) the higher synthesis temperature.

The electrochemical characterizations carried out on the $Na_xMn_{1-y}Fe_yO_2$ materials showed that all materials are capable of reversibly (de)intercalate Na^+ ions in Na cells in the 1.5 – 3.8 V, 1.5 – 4.0 V and 1.5 – 4.3 V ranges. Among our materials, the most interesting electrochemical properties were obtained for the P2 materials which show higher discharge capacities and capacity retentions. The lower polarizations observed on the galvanostatic curves of the P2 materials imply a higher ionic conductivity and explain why they can handle cycling at higher rate values. For both O3 and P2 materials increasing the Mn / Fe ratio has a tremendous effect on the electrochemical properties. Concerning O3 materials, it increases the capacity retention on the long-term cycling of the batteries. Among P2 phases, increasing the Mn content slightly increases the available discharge capacity but also allows cycling at higher rate values.

The sodium deintercalation process is accompanied by the $Mn^{3+} \rightarrow Mn^{4+}$ (low voltage region) and $Fe^{3+} \rightarrow Fe^{4+}$ (high voltage region) redox processes. Among the $Na_xMn_{1/2}Fe_{1/2}O_2$ systems, the transition from a redox process to another seems to occur distinctively in the P2 material while both Mn^{3+} and Fe^{3+} ions could be oxidized in a short range in the O3 one.

Upon cycling, all systems undergo several structural transitions that were investigated by *in situ* X-ray powder diffraction during Na deintercalation from the fully intercalated state and up to 4.3 V. The results highlighted the cooperative Jahn-Teller effect of the Mn^{3+} ions for the most intercalated states. Upon deintercalation, the O3-type systems go through several phase transitions (O'3 → O3 → P3 → "X") whose existence domain is strongly correlated to the Mn / Fe ratio. At the end of the charge the apparition of a poorly ordered phase, noted "X", was evidenced and is correlated to the capacity loss observed when cycling at high voltage. Further experiments are required to investigate the origin of the deintercalated phase which could be explained by stacking defaults between the layers (altering of NaO_6 prisms and octahedrons). This hypothesis is reinforced by the ^{57}Fe Mössbauer spectroscopy experiments which highlighted an important disorder in the materials for low Na contents.

Similarly, the P2-type systems show an orthorhombic distortion for the most intercalated states of both systems. Na^+ deintercalation from $x \approx 1$ quickly lead to the apparition of the P2 phase which is observed on a wide sodium content range. Further deintercalation lead to the observation of a poorly ordered phase for the most deintercalated states of the materials. The origin and structure of this new phase are still uncertain. The *in situ* X-ray powder diffraction results allow us to optimize the voltage range, based on the stability domain of the different materials. Concerning potential applications, the next step would be the optimization of the Mn : Fe ratio in P2 phases and the partial substitution by other transition metals such as Al, Ni, Co… as it was already started in the literature.

The second part of this work reports the preparation of O'3-$NaNiO_2$ materials of very reasonable purity by solid state synthesis. By adding –or not– an excess sodium amount and varying the synthesis temperature, we were able to prepare O'3-$NaNiO_2$ with different grain sizes, labelling the corresponding samples as "large grains", "medium grains" and "small grains". The electrochemical study of these samples revealed different behaviors in the $2/3 \leq x \leq 1$ range and *in situ* XRPD carried out during the relaxation of corresponding batteries revealed the existence of three phases: O'3-$NaNiO_2$ (the pristine one), "$Na_{\approx 0.8}NiO_2$" and P'3-$Na_{2/3}NiO_2$. Due to the important particle size (0.50 – 1.50 µm) in the "large grain sample", all three phases are observed simultaneously while only two phases are observed at the same time in the "medium grains" and "small grains samples". The "$Na_{\approx 0.8}NiO_2$" phase is characterized by a splitting of the monoclinic diffraction peaks of the pristine material suggesting a triclinic symmetry. The important broadening of the peaks prevented any description of the structure from the XRPD patterns.

The *in situ* XRPD carried out during the relaxation of a battery assembled from the "medium grains" samples in the $1/3 \leq x \leq 1$ range confirmed the phase transitions between several O'3 and P'3 structures first mentioned by Braconnier et al. in 1982 [38]. These transitions are facilitated as they only require MO_2 slabs gliding. The *in* situ study revealed a complex behavior, especially between the P'3-$Na_{1/2}NiO_2$ and the O'3-$Na_{2/5}NiO_2$ phases with the formation of an O'3/P'3 intermediate phase. The XRPD patterns of the x = 2/3, 1/2, 2/5 and 1/3 peculiar compositions show extra-diffraction lines, which are characteristic of long-range Na/vacancy orderings. Due to the few number of peaks available the study of the Na/vacancy orderings is difficult to carry out on laboratory XRPD patterns. For that purpose, synchrotron XRPD patterns were recorded at the ESRF to facilitate the resolution of the structures of P'3-$Na_{2/3}NiO_2$, P'3-$Na_{1/2}NiO_2$ and O'3-$Na_{2/5}NiO_2$. This work is completed by DFT and ^{23}Na NMR studies carried out by Dr. S Kumara Swamy at ICMCB.

Résumé étendu

Résumé étendu

Table des matières

Introduction générale

La maitrise de l'énergie et de sa production furent les étapes nécessaires à l'établissement de la société moderne. Depuis que l'électricité est produite puis acheminée vers les foyers et installations publiques, nous vivons plus longtemps, en meilleure santé et avons un accès direct à l'information et aux gens. Aujourd'hui, notre mode de vie nomade nécessite que l'on soit accompagné de nos appareils de communication. Pour rendre cela possible, il a fallu non seulement miniaturiser les composants électroniques constituant nos appareils mais également les doter d'une source d'énergie portable : les batteries[21] (Nickel-Cadmium, Nickel-hydrure métallique). Cependant, les besoins d'énergie croissants d'appareils toujours plus performants ont nécessité le développement d'une nouvelle technologie capable de délivrer de hautes densités d'énergie : la technologie Li-ion.

Les oxydes lamellaires de formule A_xMO_2 (A = Li ou Na, M = métal de transition et $x \leq 1$) sont des matériaux connus et étudiés pour leurs propriétés physiques depuis les années 1950 [1-9]. Devant la nécessité de développer une nouvelle technologie de batteries, beaucoup de systèmes A_xMO_2 ont été étudiés à nouveau, pour leurs propriétés de (dés)intercalation réversible des ions alcalins (A^+). Parmi ces études, la découverte de l'activité électrochimique de $LiCoO_2$ en batteries Li par l'équipe de Goodenough en 1980 [10] allait se révéler marquante et la première batterie Li-ion fut commercialisée en 1991 par Sony©. Faisant suite à la découverte de Goodenough, une majeure partie des recherches se focalisèrent sur les matériaux pour batteries Li-ion, la technologie Na-ion ne pouvant tenir la comparaison pour des applications à haute densité d'énergie. En effet, le sodium possède une masse molaire plus de trois fois supérieure à celle du lithium (22,99 $g.mol^{-1}$ *vs.* 6,941 $g.mol^{-1}$) et est également plus volumineux (les rayons ioniques des espèces Na^+ est Li^+ sont respectivement égales à 1.02 Å et 0.76 Å), impliquant des densités d'énergies volumiques et massiques faibles pour la technologie Na-ion. De plus, le potentiel du couple redox Na^+/Na, supérieur de 0,3 V à celui du lithium ($E°_{(Na+/Na)}$ = -2, 71 V *vs.* ENH[22] et $E°_{(Li+/Li)}$ = -3,01 V *vs.* ENH [11]), entraine une perte d'énergie. Depuis les années 1990, les matériaux d'électrode positive de la famille des $LiMO_2$ ont gagné en sécurité et en complexité. De nos jours, des matériaux de type Li(Ni, Co, Al)O_2 [12-15] et Li(Ni, Mn, Co)O_2 [16, 17] équipent les nouveaux véhicules électriques. D'autres matériaux de structures dites « spinelle » ($LiMn_2O_4$) et « olivine » ($LiFePO_4$) sont également de potentiels candidats au remplacement des $LiMO_2$, pour des raisons de sureté accrue et de toxicité moindre [18-21].

Cependant, le monde des années 2010 doit toujours faire faces à de nombreux problèmes énergétiques. Si les pays développés ont un accès quotidien à l'énergie, ce n'est pas le cas des pays

[21] Contrairement au terme « battery » en anglais, le mot « batterie » implique un système réversible et donc rechargeable, contrairement aux piles, qui ne le sont pas.
[22] ENH : Electrode Normale à Hydrogène.

émergents et si ces derniers choisissent d'adopter des technologies polluantes telles que le charbon, le bilan écologique pourrait être lourd. Une solution à ce problème serait d'encourager la transition vers des énergies plus « vertes » telles que les énergies éolienne ou solaire. Cependant, l'intermittence de ces sources d'énergies empêche leur déploiement à grande échelle et si l'emploi de batteries Li-ion fut un temps envisagé pour réguler la production, le prix des matières premières et les coûts énergétiques élevés de fabrication suffiraient à annuler tout impact positif apporté par des énergies « vertes ».

C'est dans ce contexte que la technologie Na-ion fut à nouveau étudiée dans les années 2000. Comme la régulation de la production d'énergie ne nécessite « que » des batteries stationnaires, les faibles densités d'énergie massique et volumiques de la technologie Na-ion ne représentent plus un critère d'exclusion. De nouveaux critères de sélection firent leur apparition tels que le prix, l'abondance et l'éco-compatibilité des matières premières [22]. Cela faisant, de nombreuses études portant sur des matériaux Na_xMO_2 basés sur des métaux de transition peu polluants (M = Mn, Fe, Ni…) furent publiées depuis les années 2000 [22-25]. Dans ce manuscrit, nous nous sommes intéressés à deux systèmes se basant sur ces éléments :

Etude du (des) système(s) $Na_xMn_{1-y}Fe_yO_2$. Cette étude constitue le corps de ce manuscrit. Parmi les matériaux Na_xMO_2, le système $Na_xMn_{1-y}Fe_yO_2$ n'avait jamais été étudié pour ses propriétés électrochimiques au début de nos travaux. La publication d'une étude sur des phases $Na_xMn_{1/2}Fe_{1/2}O_2$ par Yabuuchi et al. en 2012 [26] a propulsé ces matériaux sur le devant de la scène et de nombreuses études portant sur le système $Na_xMn_{1-y}Fe_yO_2$ en tant que matériau d'électrode pour batteries Na-ion furent publiées [27-33].

Les matériaux que nous avons synthétisés dans le système $Na_xMn_{1-y}Fe_yO_2$ (y = 1/3, 1/2 ou 2/3) ont été préparé par synthèse de type auto-combustion. Selon les rapports Na : (Mn + Fe) et Mn : Fe visés, les composés adoptent un empilement de type P2 ou O3 (cf. **Figure R.1**). Tous les matériaux obtenus se sont montrés capables de réversiblement (dés)intercaler les ions Na^+ quand employés en tant qu'électrode positive dans des batteries Na. Cependant, les propriétés électrochimiques se sont montrées dépendantes des rapports Mn / Fe, des empilements adoptés ou encore des limites en potentiel fixées pour le cyclage électrochimique. Pour ces raisons, une part importante de ce travail fut de comprendre les mécanismes structuraux et redox accompagnant la (dés)intercalation des ions Na^+. Pour cela nous avons eu recours à plusieurs techniques *in* et *ex situ* : diffraction des rayons-X, spectroscopie Mössbauer du ^{57}Fe…

Etude de O'3-$NaNiO_2$ et du diagramme de phase Na_xNiO_2. Comme nous l'avons mentionné auparavant, les matériaux de type Na_xMO_2 ont longtemps été étudiés pour leurs propriétés physiques ainsi que structurales. Suivant une approche similaire à celle déjà menée au laboratoire sur des matériaux Na_xMO_2 [48, 55, 56, 64], nous avons choisi d'étudier le diagramme de phases de Na_xNiO_2 par diffraction des rayons-X *in situ*. Ce choix a suivi l'étude concernant les propriétés électrochimiques de O'3-NaNiO menée par Vassilliaras et al. [34] en 2012.

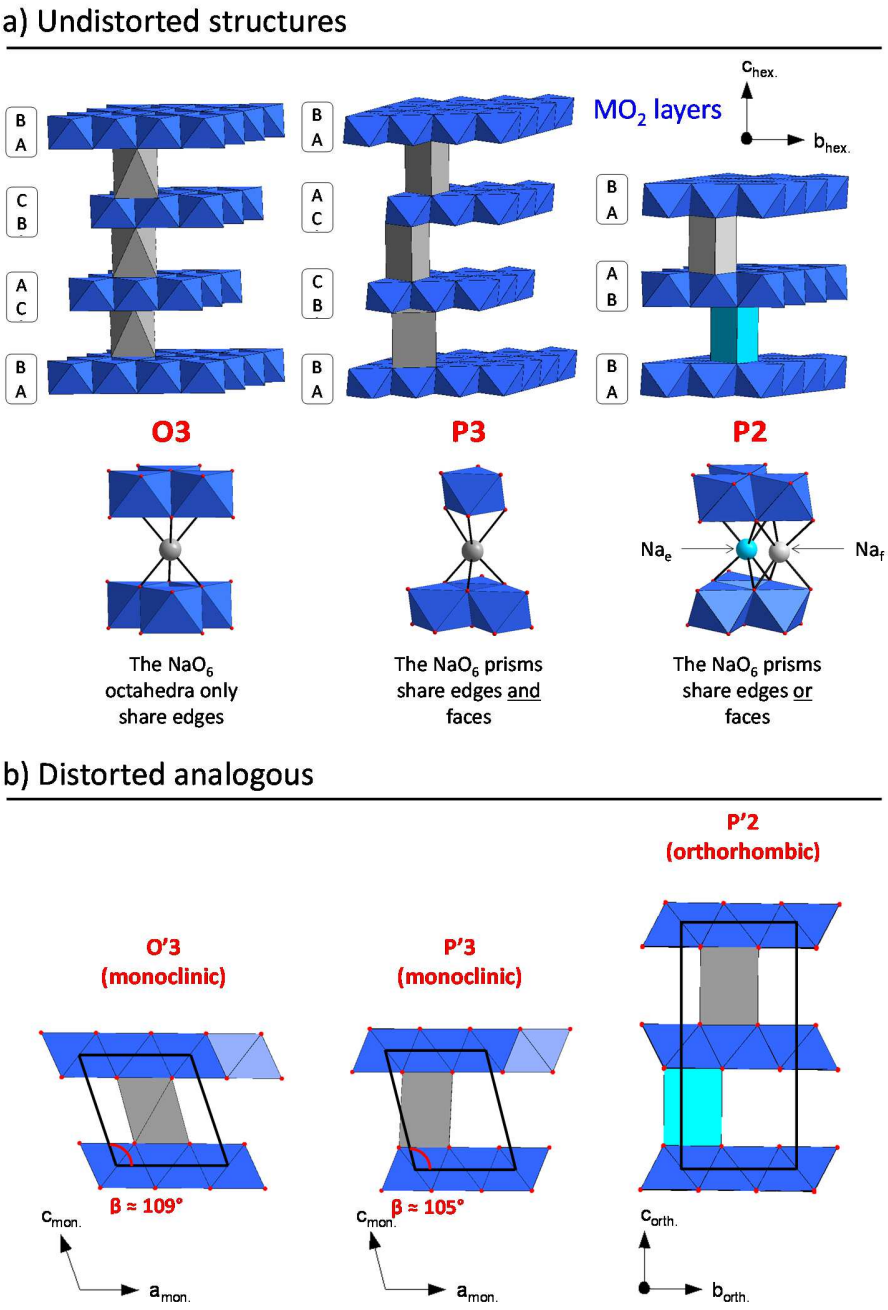

Figure R.1 : (a) Structures des phases dites « O3 », « P3 » et « P2 », d'après [36]. Les différents environnements autour des ions Na sont également représentés. (b) Structures distordues (« O'3 », « P'3 » et « P'2 ») dérivant des structures « O3 », « P3 » et « P2 ».

R.1. Le(s) système(s) $Na_xMn_yFe_{1-y}O_2$

R.1.a. Synthèse des matériaux

Les matériaux $Na_xMn_{1-y}Fe_yO_2$ ont été synthétisés par une voie de type auto-combustion qui consiste en une réaction redox entre une (des) espèce(s) oxydante(s) (généralement des nitrates de métaux de transition ou d'alcalins) et un combustible tel que la glycine qui joue également le rôle d'agent complexant [112].Ce type de synthèse est caractérisée par la très haute température de flamme rapidement atteinte, généralement supérieure à 1000°C [109], et par l'obtention d'un précurseur de petite taille et / ou peu cristallisé [111]. Nous justifions l'utilisation de cette voie de synthèse par notre volonté d'obtenir des précurseurs avec une bonne distribution entre les espèces fer et manganèse.

Suivant le protocole présenté ci-dessus, nous avons préparé les matériaux $Na_xMn_{1-y}Fe_yO_2$ en dissolvant des nitrates de manganèse, fer et sodium (Alfa Aesar $Mn(NO_3)_2.4H_2O$ (97% pureté), $Fe(NO_3)_3.9H_2O$ (98%) and $NaNO_3$ (99%) respectivement) dans de l'eau distillée. Un excès massique de 10 % de $NaNO_3$ a été ajouté afin de prendre en compte la volatilité du sodium lors du traitement thermique à suivre. Après dissolution totale des nitrates, de la glycine est ajoutée selon un rapport nitrate / glycine égal à 8 / 1. Le large excès de nitrate permet de diminuer la température et la violence de la réaction. La solution est ensuite versée dans un récipient en céramique placé dans un bain de sable dont la température est maintenue à 480 °C afin d'évaporer l'eau. Après 4 – 5 heures, l'auto combustion se produit et une fine poudre noire est obtenue. L'analyse de son diffractogramme des rayons-X a montré qu'elle contient une phase de type bixbyite $Mn_{1-y}Fe_yO_3$ et du $NaNO_3$ n'ayant pas réagi.

Le précurseur obtenu est ensuite recuit dans une nacelle en or placée dans un four tubulaire, d'abord à 700 °C pendant 20 h afin de (i) décomposer les nitrates restants et (ii) d'amorcer la réaction entre $Mn_{1-y}Fe_yO_2$ et $NaNO_3$, puis à 1000°C pendant 5 h sous flux d'oxygène afin de cristalliser le matériau. Après le recuit les échantillons sont trempés à température ambiante et stockés en boîte à gants sous atmosphère inerte (Ar).

En variant les rapports Mn / Fe et Na / (Mn + Fe), nous sommes parvenus à obtenir quatre phases : P2-$Na_{0.67}Mn_{2/3}Fe_{1/3}O_2$, P2-$Na_{0.62}Mn_{1/2}Fe_{1/2}O_2$, (O3+O'3)-$Na_{0.77}Mn_{1/2}Fe_{1/2}O_2$ et O3-$Na_{0.77}Mn_{1/3}Fe_{2/3}O_2$.

R.1.b. Pureté, morphologie et électrochimie des matériaux de départ

Diffraction des rayons-X

Les diffractogrammes de rayons-X des différentes phases sont donnés sur la **Figure R.2**. Les paramètres de maille et distances inter-feuillets sont donnés dans le **Tableau R.1**.

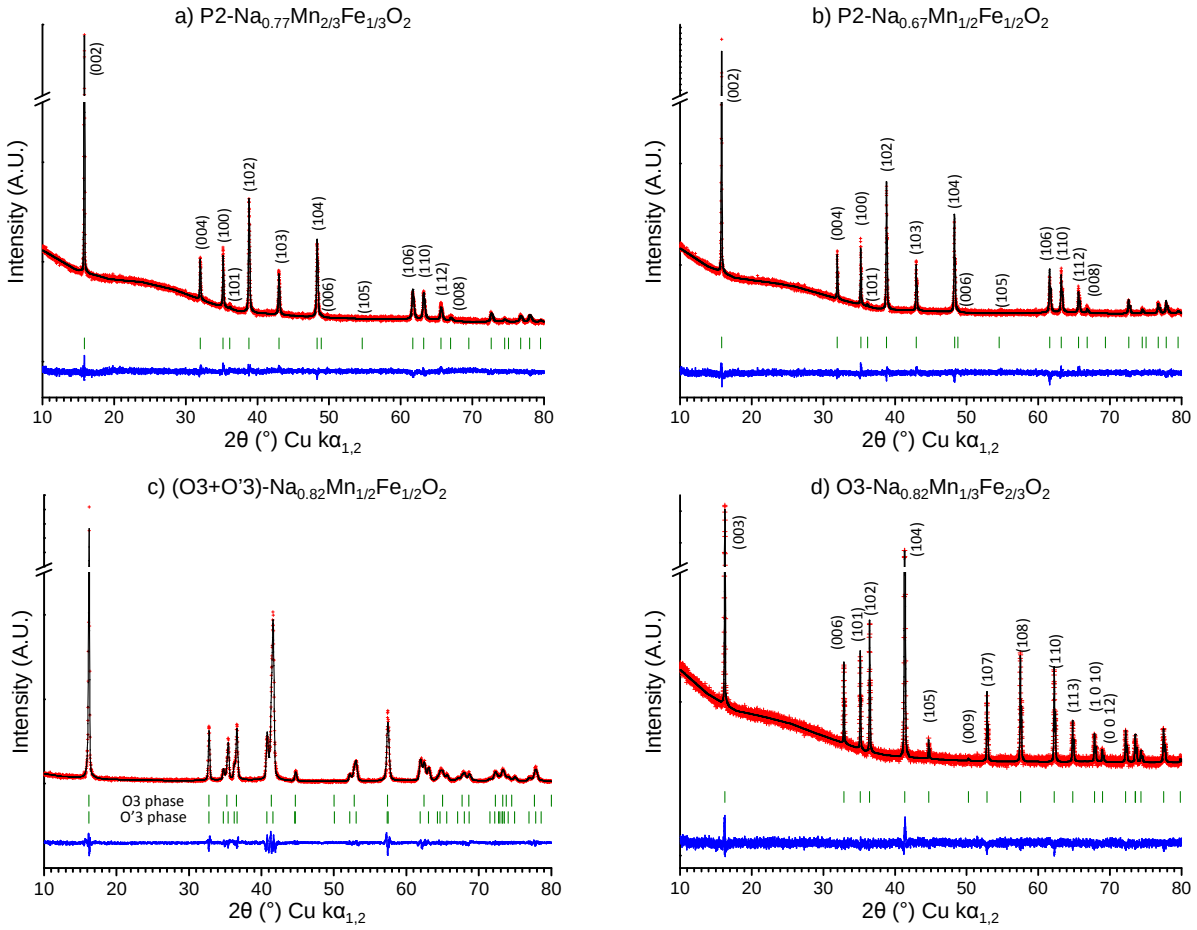

Figure R.2 : Diffractogrammes de rayons-X expérimentaux et calculés pour (a) P2-$Na_{0.77}Mn_{2/3}Fe_{1/3}O_2$, (b) P2-$Na_{0.67}Mn_{1/2}Fe_{1/2}O_2$, (c) (O3+O'3)$Na_{0.82}Mn_{1/2}Fe_{1/2}O_2$ et (d) O3-$Na_{0.82}Mn_{1/3}Fe_{2/3}O_2$ phases. Croix rouges : observé, ligne noire : calculé, ligne bleue: différence et barres vertes : Bragg. (a, b, d) : affinement de type Rietveld et (c) : affinement de type LeBail.

	P2-$Na_{0.77}Mn_{2/3}Fe_{1/3}O_2$	**P2-$Na_{0.67}Mn_{1/2}Fe_{1/2}O_2$**	**(O3+O'3)$Na_{0.82}Mn_{1/2}Fe_{1/2}O_2$**		**O3-$Na_{0.82}Mn_{1/3}Fe_{2/3}O_2$**
Space group	$P6_3/mmc$	$P6_3/mmc$	R-3m (O3)	C2/m (O'3)	R-3m
a (Å)	2.9392(1)	2.9386(1)	2.9730(3)	5.2170(7)	2.9805(1)
b (Å)	/	/	/	2.9462(3)	/
c (Å)	11.1648(6)	11.1884(4)	16.396(4)	5.7515(8)	16.3264(5)
β (°)	/	/	/	108.24(1)	/
Interslab distance (Å)	5.5824(6)	5.5942(4)	5.465(4)	5.463(3)	5.4421(5)

Tableau R.1 : Paramètres de maile et distances inter-feuillet des phases P2-$Na_{0.77}Mn_{2/3}Fe_{1/3}O_2$, P2-$Na_{0.67}Mn_{1/2}Fe_{1/2}O_2$, (O3+O'3), $Na_{0.82}Mn_{1/2}Fe_{1/2}O_2$ et O3-$Na_{0.82}Mn_{1/3}Fe_{2/3}O_2$.

Les diffractogrammes de rayons-X montrent des phases pures et bien cristallisées. Les affinements des structures (LeBail ou Rietveld) conduisent à des paramètres de maille proches de la littérature [26]. Comme attendu des différents empilements, les phases P2 ont une distance inter-feuillet supérieure à celle des phases O3. Cela est dû à la grande taille des sites prismatiques NaO_6.

L'origine de la phase O'3 dans le mélange (O3 + O'3)-$Na_{0.77}Mn_{1/2}Fe_{1/2}O_2$ peut être attribuée à l'effet Jahn-Teller coopératif des ions Mn^{3+}. Cela est confirmé par le rapport $a_{mon.}/b_{mon.}$ égal à 1.77 (et donc supérieur à 1.73, valeur obtenue en absence d'effet Jahn-Teller coopératif [5]). La phase O'3 devrait donc avoir un taux d'ions Mn^{3+} plus important que la phase O3 (et donc un taux de sodium plus élevé). Les rapports Mn / Fe et Na / (Mn + Fe) ont été confirmés par analyse élémentaire ICP-AES. Les rapports Na / (Mn + Fe) ont par ailleurs été confirmé par diffraction des rayons-X synchrotron.

Morphologie

La morphologie des différents matériaux a été étudiée par microscopie électronique à balayage. Les micrographes obtenus pour les phases P2-$Na_{0.62}Mn_{1/2}Fe_{1/2}O_2$ et O3-$Na_{0.77}Mn_{1/3}Fe_{2/3}O_2$, donnés **Figure R.3**, sont représentatifs des matériaux de type P2 et O3.

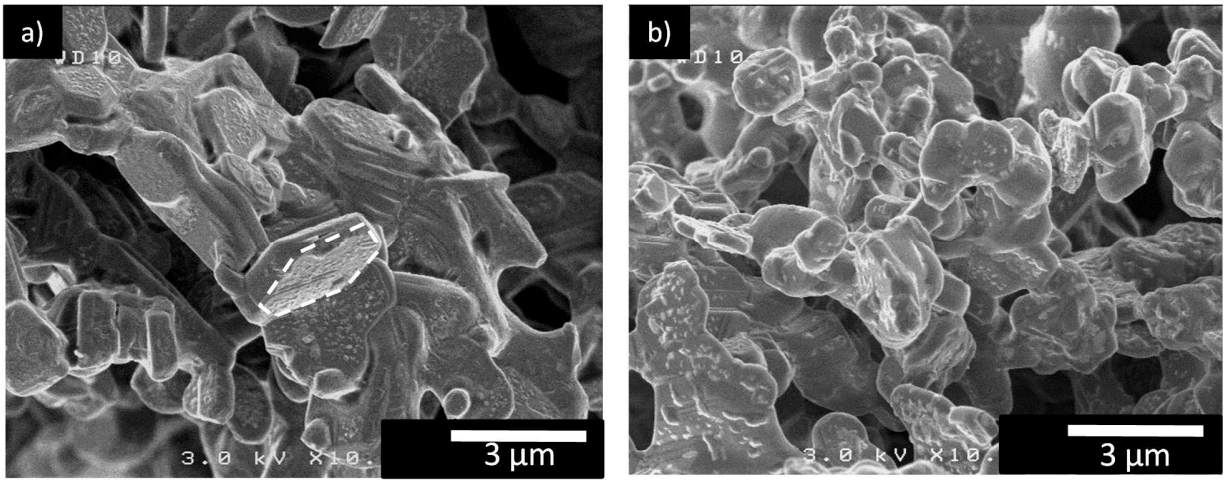

Figure R.3 : Micrographes (MEB) des phases (a) P2-$Na_{0.67}Mn_{1/2}Fe_{1/2}O_2$ et (b) O3-$Na_{0.82}Mn_{1/3}Fe_{2/3}O_2$.

Les matériaux de type P2 se présentent sous forme de particules bien définies d'un diamètre moyen de 3.4 µm et d'une épaisseur moyenne de 200 nm (**Figure R.3a**). Les matériaux de type O3 se présentent sous forme de particules plus arrondies de diamètre moyen égal à 3 µm (**Figure R.3b**). Les imperfections présentes à la surface des matériaux sont dues à leur exposition à l'air durant la préparation des échantillons. Leur nombre et importance augmentant avec la durée de l'exposition. Nous pensons qu'il s'agit des composés NaOH et/ou Na_2CO_3, formés par réaction avec l'eau et le dioxyde de carbone de l'atmosphère ambiante. Les micrographes montrent une forte agglomération des particules dont la taille est nettement supérieure à celle observée dans la littérature, typiquement de l'ordre de 500 nm [26]. Cela est certainement dû à la température de synthèse plus élevée de nos matériaux (1000 °C *vs.* 700 °C [26, 66]).

Electrochimie

L'activité électrochimique des différents matériaux (*i.e.* leur habilité à réversiblement (dés)intercaler les ions Na^+) a été étudiée en batteries Na/ $NaPF_6$ in PC (1 M) + 2 wt% FEC /$Na_xMn_{1-y}Fe_yO_2$ à un régime fixé à C/50. L'évolution du potentiel des batteries en fonction du taux de sodium entre 1.5 et 3.8 V est donnée sur la **Figure R.4**.

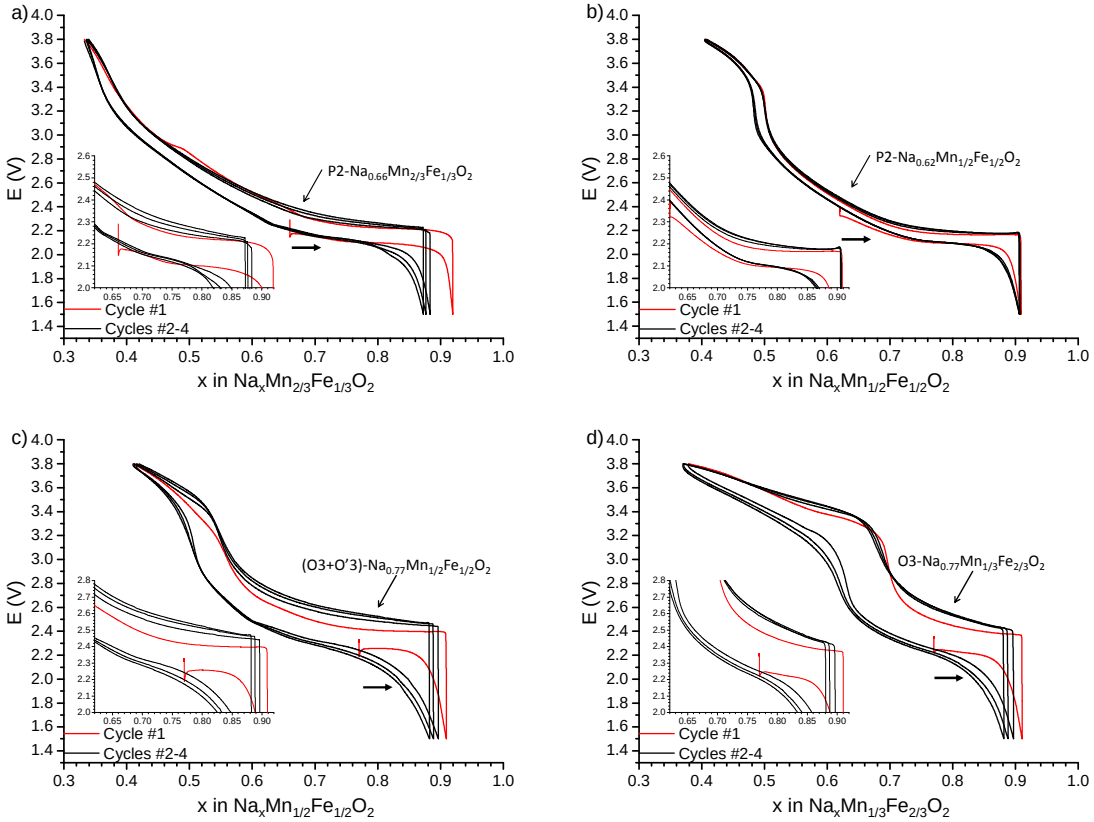

Figure R.4 : Courbes de cyclage galvanostatique (C/50) de batteries enregistrées entre 1.5 et 3.8 V : (a) P2-$Na_xMn_{0.66}Mn_{1/3}Fe_{2/3}O_2$, (b) P2-$Na_{0.62}Mn_{1/2}Fe_{1/2}O_2$, (c) (O3+O'3)-$Na_{0.77}Mn_{1/2}Fe_{1/2}O_2$ et (d) O3-$Na_{0.77}Mn_{1/3}Fe_{2/3}O_2$. Un agrandissement autour du point de départ est donné pour chacune des courbes.

Les mêmes comportements ont été observés que la batterie commence par une charge ou par une décharge et seules les courbes commençant par une décharge sont montrées ici. Pour chaque matériau, les courbes de charge et de décharge sont similaires, indiquant la réversibilité de la (dés)intercalation. Les différentes courbes montrent les mêmes tendances : lors de la première décharge, un plateau en potentiel apparaît et indique un domaine biphasé avec la phase la plus intercalée. Le potentiel de ce plateau est supérieur de 0.2 V pour les phases de type O3 par rapport aux phases de type P2. Cela indique qu'une plus grande énergie est nécessaire pour (dés)intercaler les ions Na^+ dans les phases de type O3.

Comme on peut le voir sur la **Figure R.4c**, le point de départ de la phase (O3 + O'3)- $Na_{0.77}Mn_{1/2}Fe_{1/2}O_2$ se situe sur le plateau. Nous pouvons donc supposer que ce plateau correspond à un équilibre entre des phases de type O3 et O'3 et que l'état intercalé des matériaux de type O3 correspond à une phase O'3. Par analogie, une structure distordue (P'2) est attendue pour les matériaux de type P2 en fin de décharge.

Lors de la charge consécutive le même plateau en potentiel est observé, indiquant la bonne réversibilité du processus. Le potentiel augmente ensuite de façon continu et décrit un saut en potentiel pour $x \approx y_{Fe}$ pour les matériaux pour lesquels le rapport Mn / Fe est égal à 1 / 1 ou 1 /2. Ces sauts correspondent au changement de processus redox (de $Mn^{3+} \rightarrow Mn^{4+}$ à $Fe^{3+} \rightarrow Fe^{4+}$) comme cela a été montré dans la littérature par spectroscopie d'absorption des rayons-X et spectroscopie Mössbauer [26, 28]. Si pour les systèmes de type P2 la première décharge est similaire aux suivantes, nous pouvons observer une augmentation de la polarisation en fonction du nombre de cycles pour les systèmes de type O3.

L'évolution de la capacité en décharge a été extraite pour chaque courbe et est reportée **Figure R.5** pour les différents matériaux.

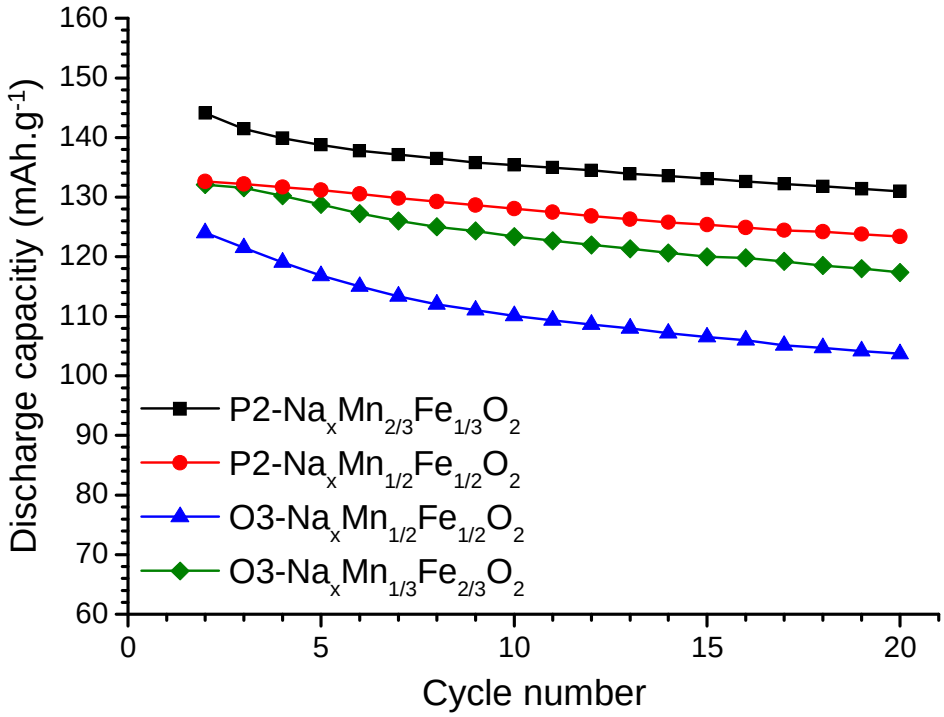

Figure R.5 : Capacités en décharge extraites des courbes galvanostatiques (**Figure R.4**) : P2-$Na_{0.66}Mn_{2/3}Fe_{1/3}O_3$ (noir), P2-$Na_{0.62}Mn_{1/2}Fe_{1/2}O_2$ (bleu), (O3+O'3)-$Na_{0.77}Mn_{1/2}Fe_{1/2}O_2$ (rouge) et O3-$Na_{0.77}Mn_{1/3}Fe_{2/3}O_2$ (vert).

La comparaison des capacités en décharge aux seconds cycles montre un maximum pour la phase P2-$Na_{0.66}Mn_{2/3}Fe_{1/3}O_2$ (144 $mAh.g^{-1}$). La diminution du rapport Mn / Fe pour les systèmes de type P2 entraine une diminution de la capacité (133 $mAh.g^{-1}$). Le phénomène contraire est observé pour les systèmes de type O3 et diminuer le rapport Mn / Fe entraine une augmentation de la capacité en décharge au second cycle (de 124 $mAh.g^{-1}$ pour $Na_xMn_{1/2}Fe_{1/2}O_2$ à 133 $mAh.g^{-1}$ pour $Na_xMn_{1/3}Fe_{2/3}O_2$). La comparaison des systèmes P2 et O3 montre que les capacités en décharges sont plus élevées pour les phases de type P2, en accord avec la littérature [26].

Les évolutions des capacités en décharge en fonction du nombre de cycle montrent des rétentions de capacité similaires après 20 cycles pour les différents matériaux : 91 % (P2-$Na_xMn_{2/3}Fe_{1/3}O_2$), 93 % (P2-$Na_xMn_{1/2}Fe_{1/2}O_2$), 91 % (O3-$Na_xMn_{1/2}Fe_{1/2}O_2$) et 89 % (O3-$Na_xMn_{1/3}Fe_{2/3}O_2$). Bien que montrant une capacité en décharge supérieure au second cycle, le système de type O3-$Na_xMn_{1/3}Fe_{2/3}O_2$ possède une stabilité moindre que le système $Na_xMn_{1/2}Fe_{1/2}O_2$.

Si les capacités en décharge de nos systèmes de type P2 sont similaires avec la littérature, il est remarquable que nos systèmes de type O3 montrent des valeurs supérieures à celles reportées (respectivement 124 mAh.g^{-1} *vs.* ≈ 110 mAh.g^{-1} pour O3-$Na_xMn_{1/2}Fe_{1/2}O_2$ et ≈ 132 mAh.g^{-1} *vs.* 90 mAh.g^{-1} pour O3-$Na_xMn_{1/3}Fe_{2/3}O_2$) et ce malgré le potentiel limite inférieur utilisé pour notre étude. Ces différences peuvent venir des différentes conditions de synthèse de nos matériaux, que nous avons préparés avec un rapport Na / M inférieur à 1.0 (*vs.* 1.0 pour [26, 66]) et qui ont été recuits à 1000 °C (au lieu de 700 °C pour [26, 66]). De plus, les systèmes préparés à plus basse température dans la littérature pourraient présenter des lacunes en métaux de transition, stabilisant ainsi des ions Mn^{4+}. Un tel phénomène a déjà été observé pour des matériaux de type P'2-Na_xMnO_2 [114]. Le cas échéant, la formule devrait alors être réécrite : $Na_{2x/(2+y)}(Mn,Fe)_{2/(2+y)}\square_{y/(2+y)}O_2$.

R.1.c. Focus sur le système de type O3-$Na_xMn_{1/3}Fe_{2/3}O_2$

Afin de comprendre l'évolution des propriétés structurales et redox des matériaux pendant le cyclage électrochimique, nous avons utilisé plusieurs techniques *in situ* et *ex situ*. Nous proposons ici de suivre le cas du système de type O3-$Na_xMn_{1/3}Fe_{2/3}O_2$ qui est le matériau présentant le plus haut taux de Fe (et étant donc le plus adapté à la spectroscopie Mössbauer) ainsi que celui présentant la moins bonne stabilité électrochimique (et mettant donc davantage en évidence les mécanismes de dégradation).

Diffraction des rayons-X pendant la désintercalation électrochimique

Les changements structuraux accompagnant la désintercalation ont été étudiés par diffraction des rayons-X *in situ* (*operando*) pendant la charge d'une batterie $Na_xMn_{1/3}Fe_{2/3}O_2$//Na. La cellule a été préalablement déchargée jusqu'à la composition limite $Na_{0.96}Mn_{1/3}Fe_{2/3}O_2$. Afin de s'assurer d'être au maximum d'intercalation, la décharge a été suivie d'une étape potentiostatique à 1.5 V jusqu'à ce que le courant résiduel soit proche de 0 mA. Après enregistrement d'un premier diffractogramme, la cellule fut chargée à C/80. Les conditions de l'expérience ont été optimisées afin d'enregistrer un diffractogramme tous les 0.013 Na^+ désintercalés. Certaines parties des diffractogrammes enregistrés sont présentées sur la **Figures R.6**. Comme la superposition des diffractogrammes empêche la bonne observation de certains phénomènes, la même expérience est présentée en sens contraire **Figure R.7**.

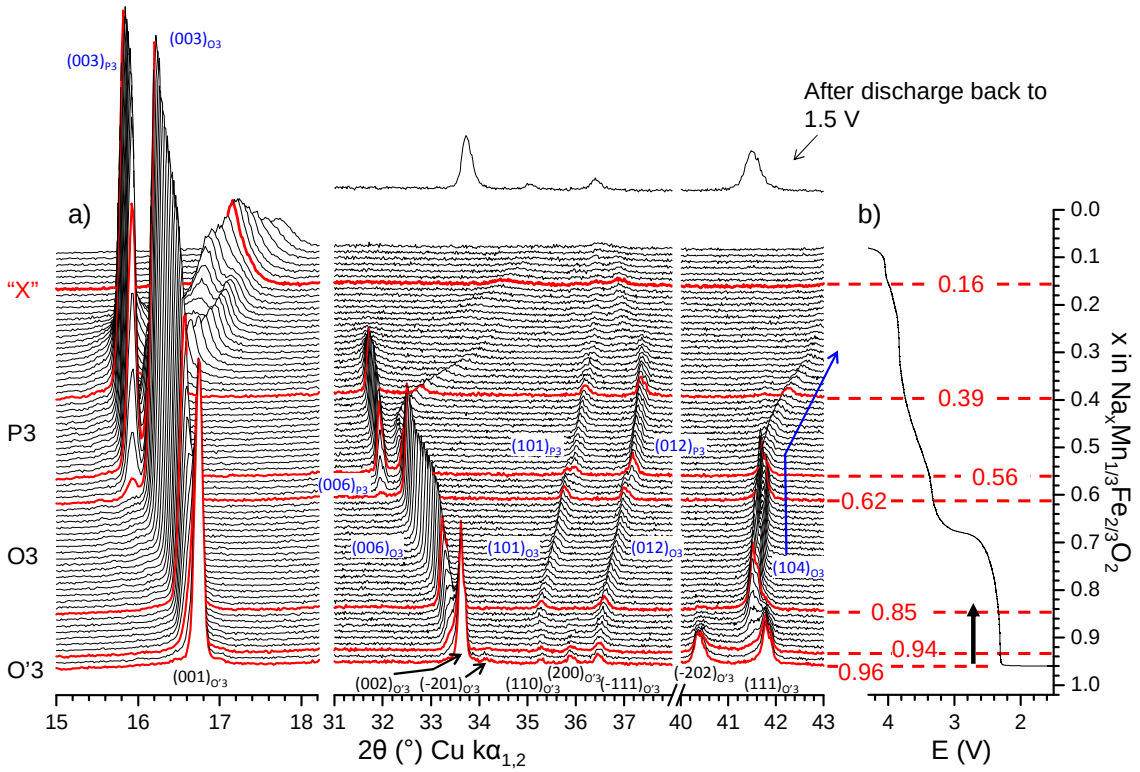

Figure R.6 : (a) Diffractogrammes de rayons-X enregistrés *in situ* (*operando*) pendant la charge d'une cellule $Na_xMn_{1/2}Fe_{1/2}O_2/NaPF_6$ in PC (1M)/Na. Les diffractogrammes rouges correspondent aux limites des différents domaines structuraux. (b) Courbe galvanostatique correspondante.

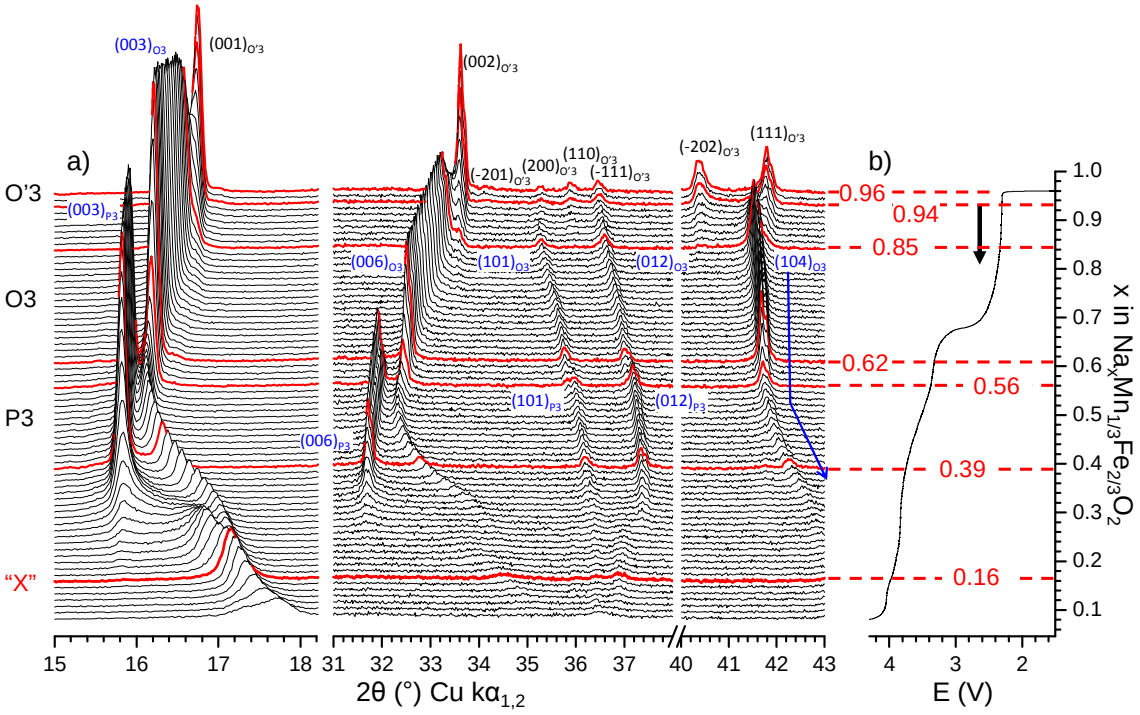

Figure R.7 : Représentation inverse de la **Figure R.6**. (a) Diffractogrammes de rayons-X enregistrés *in situ* (*operando*) pendant la charge d'une cellule $Na_xMn_{1/2}Fe_{1/2}O_2/NaPF_6$ in PC (1M)/Na. Les diffractogrammes rouges correspondent aux limites des différents domaines structuraux. (b) Courbe galvanostatique correspondante.

Comme nous le détaillerons plus tard, plusieurs changements structuraux sont observés au cours de la charge. La phase intercalée présente une distorsion monoclinique et une structure O'3. La désintercalation conduit à l'apparition d'une phase de type O3 (structure du matériau de départ) à travers un domaine biphasé pour $0.85 \leq x < 0.94$. Pour $x < 0.62$, une phase de type P3 apparaît. Elle possède une distance inter-feuillet supérieure à celle de la phase O3 comme le montrent les positions des pics de diffraction $(003)_{P3}$ et $(003)_{O3}$, ce qui s'explique par la géométrie prismatique des polyèdres NaO_6 (contrairement à la géométrie octaédrique dans la phase O3). Cette modification structurale est confirmée par la disparition du pic $(104)_{P3}$ dont l'intensité est très faible sur les diffractogrammes des phases de type P3 comparée aux phases de type O3.

Il est remarquable que la phase O3 ne disparaisse pas entièrement pendant la charge. A défaut de disparaître, la position des pics $(00l)_{O3}$ montre une diminution importante de la distance inter-feuillet. Ce résultat inattendu est reproductible et réversible si la cellule est déchargée. Afin de vérifier si ce phénomène n'était pas induit par le mode « *operando* », une expérience similaire a été réalisée à l'équilibre et a montré les mêmes résultats. Indubitablement pour $x < 0.62$ il y a coexistence de deux systèmes qui sont désintercalés simultanément, comme nous le verrons plus tard.

A partir des paramètres de maille déduits des diffractogrammes il est possible d'estimer les distances inter-feuillet. Les évolutions de ces distances ainsi que des paramètres de maille sont données **Figure R.8**.

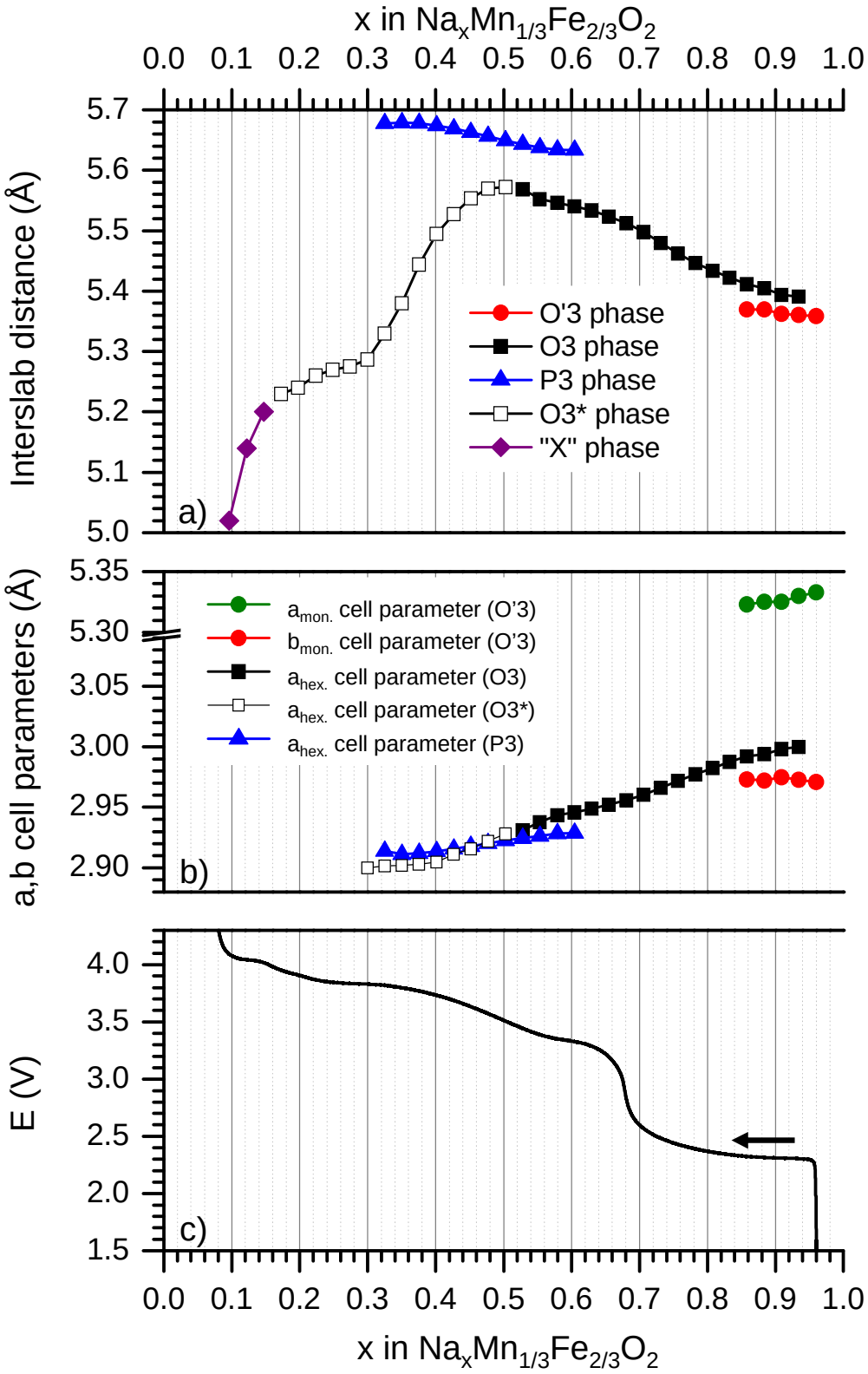

Figure R.8 : Evolution de (a) la distance inter-feuillet et (b) les paramètres de maille a et b des phases O'3, O3 et P3-$Na_xMn_{1-y}Fe_yO_2$ au cours de la désintercalation électrochimique. (c) Courbe galvanostatique correspondante.

Le diffractogramme de la phase intercalée $Na_{0.96}Mn_{1/3}Fe_{2/3}O_2$ peut être indexé dans le système monoclinique (groupe d'espace C2/m, structure O'3). La distorsion monoclinique est clairement visible *via* le dédoublement des pics $(012)_{hex.}$ et $(104)_{hex.}$ de la structure O3 en $(-111)_{mon.}$ + $(200)_{mon.}$ et $(-202)_{mon.}$ + $(111)_{mon.}$ de la structure O'3. La phase O'3 est observée dans un domaine restreint : $0.94 < x < 0.96$. Ce domaine est ensuite suivi par un domaine biphasé O3 + O'3 ($0.85 \leq x \leq 0.94$), correspondant au plateau en potentiel observé sur la courbe galvanostatique. La position relative des pics (00*l*) montre une distance inter-feuillet supérieure pour la phase O3. Cela s'explique par le taux de sodium inférieur dans cette phase, qui diminue l'écrantage exercé par les ions Na^+ sur les atomes d'oxygène environnants.

Pour $0.62 < x < 0.85$, le système présente une solution solide (O3). Pour la raison que celle énoncée précédemment, la distance inter-feuillet augmente lors de la désintercalation. Simultanément, la distance M-M au sein d'un même feuillet (paramètre $a_{hex.}$) diminue, tout comme le rayon ionique moyen des cations M^{n+} dans les feuillets MO_2.

Pour $x < 0.62$, une nouvelle phase présentant un empilement de type P3 apparaît. Dans le même temps, l'intensité des pics de la phase O3 diminue. Comme nous l'avons déjà mentionné auparavant, une quantité non négligeable de la phase O3 est toujours observée. Le pic $(003)_{O3}$ continue de se déplacer vers des angles plus petits jusqu'à $x = 0.50$. Elle se déplace ensuite vers des angles plus grands pour $x < 0.50$. Ce domaine sera appelé O3* par la suite. La position du pic $(003)_{O3}$ montre que la distance inter-feuillet augmente lors de la désintercalation puis diminue à la fin de la charge, comme observé pour tous les matériaux de type O3-A_xMO_2 (A = Li, Na) [116]. Dans les systèmes Li_xNiO_2 et Li_xCoO_2, la délithiation complète conduit à des structures de type O1 [117].

Pour $x \leq 0.16$ une nouvelle phase, notée « X » est observée. On observe que la position du pic $(00l)_X$ se déplace continument vers de plus fortes valeurs d'angle 2θ, ce qui traduit une diminution de la distance inter-feuillet.

Comme nous pouvons le voir sur les **Figures R.7** et **R.9b**, la position du pic $(003)_{P3}$ n'évolue pas pour $0.56 < x < 0.62$ comme nous pouvions l'attendre d'un mécanisme biphasé. Le pic $(003)_{P3}$ se décale vers des angles 2θ inférieurs, ce qui indique un comportement de type solution solide ($0.39 < x < 0.56$). Dans le domaine $0.39 < x < 0.50$, deux solutions solides (O3* et P3) sont donc clairement impliquées.

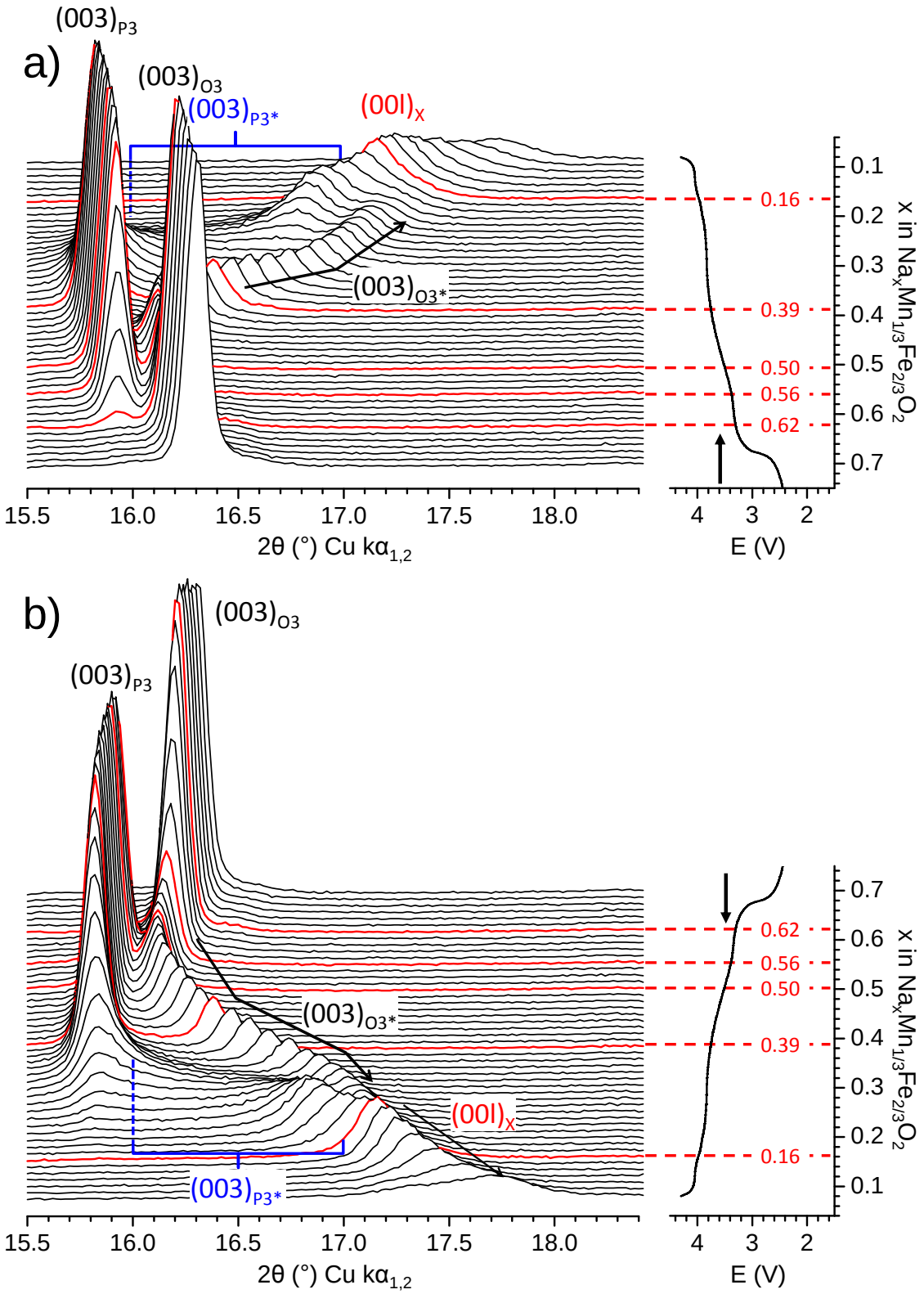

Figure R.9 : (a,b) Agrandissement de la région 0.3 ≤ x ≤ 0.7 des diffractogrammes de rayons-X enregistrés *in situ* (*operando*) lors de l'expérience menée sur le système de type O3 $Na_xMn_{1/3}Fe_{2/3}O_2$. Les lignes rouges mettent en évidence les limites des différents domaines structuraux.

Pour x < 0.39, la position du pic $(003)_{P3}$ ne varie plus et l'intensité du pic décroit. Simultanément, un élargissement du côté du pic situé à plus grand angle 2θ est observée et suggère la formation de fautes d'empilement au sein de la phase P3. Nous pouvons supposer que quand un très grand nombre d'ions sodium sont désintercalés de la phase P3 certains feuillets MO_2 glissent les uns par rapport aux autres, créant ainsi un environnement octaédrique pour les ions Na^+ restants. Cette phase P3 incluant des fautes d'empilement sera notée P3* dans la suite. Le nombre de feuillets ainsi affectés augmente continument au cours de la désintercalation, en accord avec le shift continu du pic $(003)_{P3*}$ vers des angles 2θ inférieurs.

Pour x = 0.16, les pics issus des phases O3* et P3* ont fusionnés en une nouvelle phase notée « X ». De par la symétrie et la faible largeur à mi-hauteur du pic $(00l)_X$ aucune faute d'empilement n'est attendue dans cette phase. Pour x < 0.10, un nouveau pic de diffraction apparaît à 2θ ≈ 17.3°, indiquant un nouveau domaine biphasé impliquant une phase inconnue ou la formation de nouvelles fautes d'empilement. D'autres expériences seraient nécessaires pour pouvoir confirmer l'une de ces hypothèses. Un schéma récapitulatif du diagramme de phases de $Na_xMn_{1/3}Fe_{2/3}O_2$ est proposé **Figure R.10**.

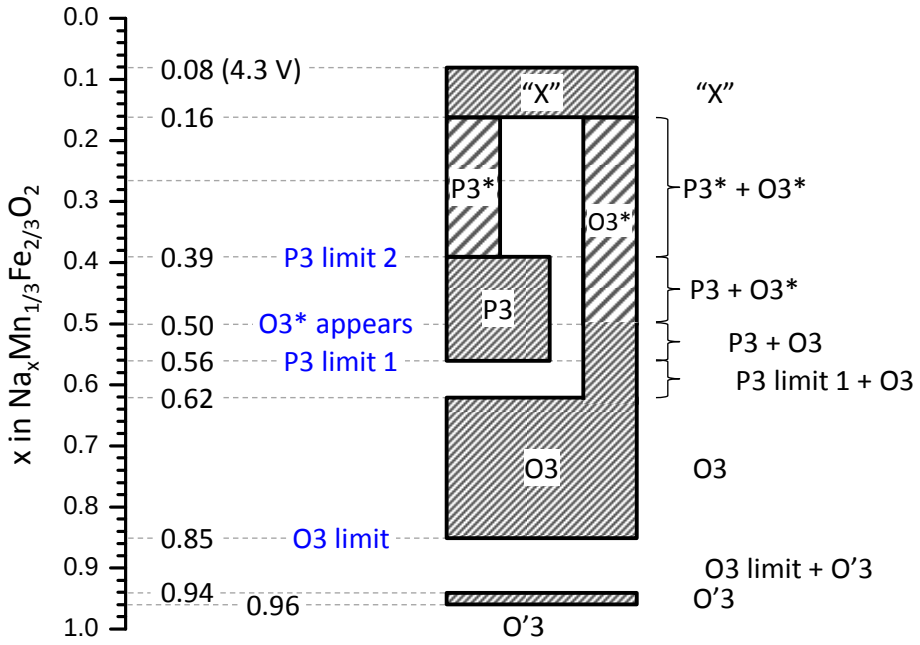

Figure R.10 : Représentation schématique de l'évolution du diagramme de phase de $Na_xMn_{1-3}Fe_{2/3}O_2$ au cours de la désintercalation électrochimique déduit de l'expérience *in situ*.

La présence simultanée de phases présentant des empilements O3 et P3 lors de la désintercalation électrochimique est difficile à envisager. Afin de l'expliquer, nous pouvons supposer des fluctuations de compositions dans le matériau initial, indétectables par diffraction des rayons-X. Ces fluctuations peuvent être dues à (i) la coexistence de particules avec des rapports Mn / Fe légèrement différents ou (ii) la coexistence de particules avec et sans lacunes de Mn. La littérature montre que la stabilité relative des empilements O3 et P3 est directement corrélée à la covalence des liaisons dans les feuillets MO_2 et au taux d'intercalation [36]. Suivant cette hypothèse, une partie de la phase O3 serait désintercalée à *via* un mécanisme de type solution solide pendant que l'autre serait transformée en P3. Il est impossible de conclure sur ce point sans réaliser davantage d'expériences.

Afin d'étudier la réversibilité des différentes transitions structurelles la cellule *in situ* a été à nouveau déchargée à 1.5 V et un diffractrogramme de rayons-X a été enregistré sous potentiel constant et avec les mêmes paramètres d'acquisition que pour l'expérience *in situ*. Les diffractogrammes collectés après la première et seconde décharge sont comparés **Figure R.11**. Etonnamment, la distorsion monoclinique n'est pas observée après la seconde décharge. Ceci est expliqué par le plus faible taux d'intercalation atteint après la seconde décharge ($x \approx 0.8$). La fraction d'ions Mn^{3+} ne représente plus que 13 % des ions M^{n+} ce qui est insuffisant pour induire un effet Jahn-Teller coopératif. La grande différence entre les taux d'intercalation atteints après la première et la seconde décharge implique que le matériau a subit des transitions structurelles irréversibles pendant la charge, qui peuvent être dues à nos conditions de cyclage. La migration du fer dans l'espace inter-feuillet, déjà considérée pour Na_xFeO_2 [35] est une explication envisageable.

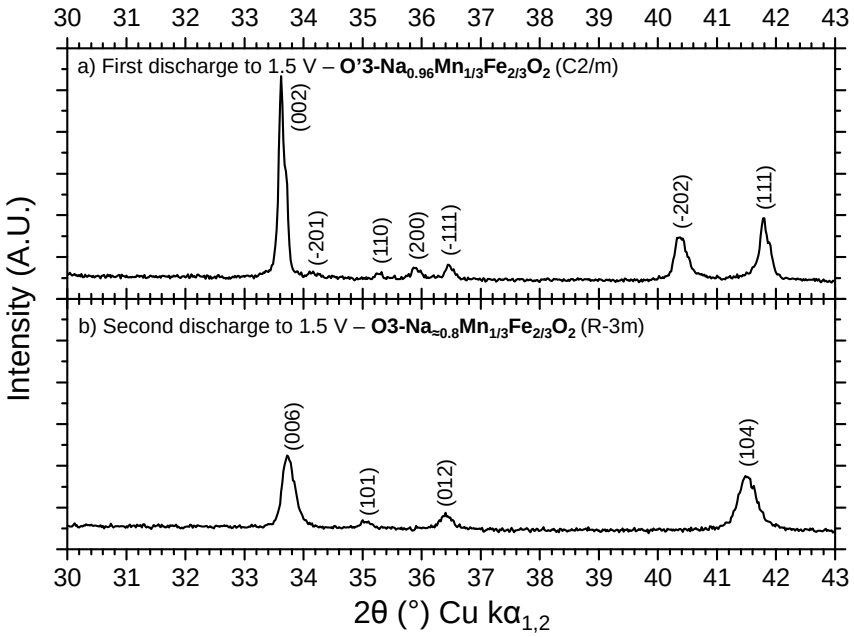

Figure R.11 : Diffractogrammes de rayons-X enregistrés *in situ* pendant une étape potentiostatique (1.5 V) après les (a) première et (b) seconde décharges de l'expérience sur le système $Na_xMn_{1/3}Fe_{2/3}O_2$.

Etude des mécanismes Redox pendant la désintercalation électrochimique

La courbe galvanostatique de O3-$Na_{0.77}Mn_{1/3}Fe_{2/3}O_2$ (**Figure R.4d**) montre un saut de potentiel marqué à x ≈ 2/3, ce qui correspond au taux de fer dans le matériau et donne une première idée des domaines d'activité des couples redox Fe^{4+}/Fe^{3+} (haut potentiel, x < 2/3) et Mn^{4+}/Mn^{3+} (bas potentiel, x > 2/3). Afin de confirmer ces attributions, deux techniques spectroscopiques ont été utilisés *in situ* pendant la désintercalation électrochimique : la spectroscopie d'absorption des rayons-X et la spectroscopie Mössbauer du ^{57}Fe.

Operando *in situ* X-ray Absorption Near Edge Spectroscopy (XANES)

Les limites de temps imposées par l'utilisation d'une ligne synchrotron[23] nous ont conduits à mener l'expérience *in situ* (*operando*). L'évolution des spectres XANES enregistrés aux seuils K du fer et du manganèse pour le système de type O3-$Na_xMn_{1/3}Fe_{2/3}O_2$ est donnée sur la **Figure R.12**.

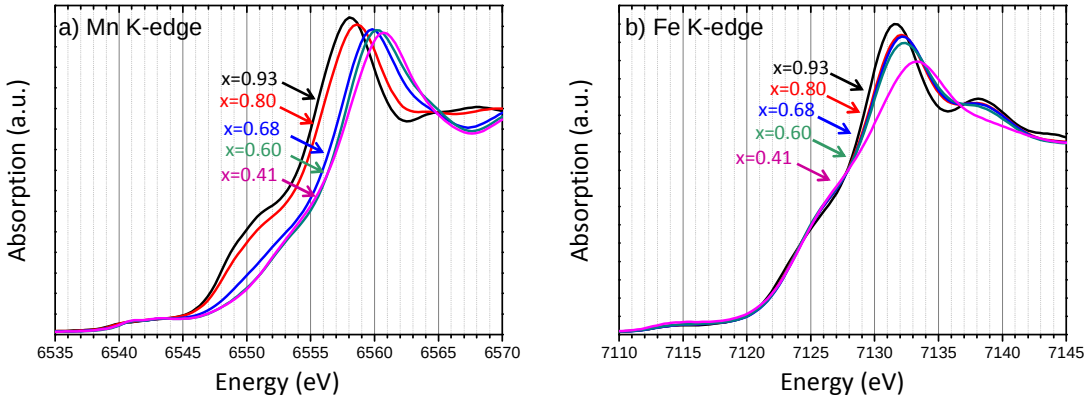

Figure R.12. Spectres XANES enregistrés aux seuils K du Mn et de Fe *in situ* (*operando*) pendant la charge d'une cellule $Na_xMn_{1-y}Fe_yO_2$//Na. La cellule a été préalablement déchargée.

Dans le domaine 2/3 ≤ x < 1, un décalage important du maximum d'absorption au seuil K du manganèse vers de plus hautes énergies est observé. Ce décalage est associé à la réaction redox $Mn^{3+} \rightarrow Mn^{4+}$ comme l'a confirmé la comparaison avec les composés de référence. Dans le même domaine de composition aucun décalage notable du maximum d'absorption au seuil K du fer n'est observé. Ainsi, seul le couple Mn^{4+}/Mn^{3+} est impliqué à bas potentiel.

Pour x < 0.67, aucun décalage notable du maximum d'absorption au seuil K du manganèse n'est observé. Simultanément, un léger décalage du maximum d'absorption au seuil K du fer vers les énergies plus élevées est observé. Des références que nous avions préparées (O3-$NaFeO_2$ et $Na_{0.55}FeO_2$) ont montré la même tendance lorsque le degré d'oxydation du fer augmente. Il est ainsi fortement suggéré que le procédé redox $Fe^{3+} \rightarrow Fe^{4+}$ soit impliqué à haut potentiel. La spectroscopie Mössbauer a donc été utilisée pour confirmer cette attribution.

[23] En collaboration avec l'équipe du Pr. Hwang, NTUST/NSRRC, Taiwan, R.O.C. Beamline (NSRRC): 17C.

Spectroscopie Mössbauer du ^{57}Fe *in* et *ex situ*

Le spectre Mössbauer du ^{57}Fe de la phase initiale O3-$Na_{0.77}Mn_{1/3}Fe_{2/3}O_2$ est donné **Figure R.13a**. Le spectre montre un doublet quadripolaire qui peut être décrit par un profil de type Lorentzien. L'affinement nécessite deux sites Mössbauer (**Tableau R.2**). Les déplacements isomériques correspondent à des ions Fe^{3+} à haut spin dans des environnements octaédriques. Ces sites, appelés Fe^{3+} (A) et Fe^{3+} (B), sont représentés respectivement par des lignes bleues et vertes sur la **Figure R.13a**, respectivement. L'important éclatement quadripolaire associé au site Fe^{3+} (A) (Δ_A = 0.88 mm.s^{-1}) indique que l'environnement de ces octaèdre FeO_6 de ce site est davantage soumis au désordre environnant que pour le site Fe^{3+} (B) (Δ_B = 0.58 mm.s^{-1}). Les populations associées montrent qu'une nette majorité du fer est localisé dans le site Fe^{3+} (B) (75 %). Dans la littérature, Yabuuchi et al. ont également utilisé deux sites Fe^{3+} pour décrire le spectre de P2-$Na_{2/3}Mn_{1/2}Fe_{1/2}O_2$ [26].

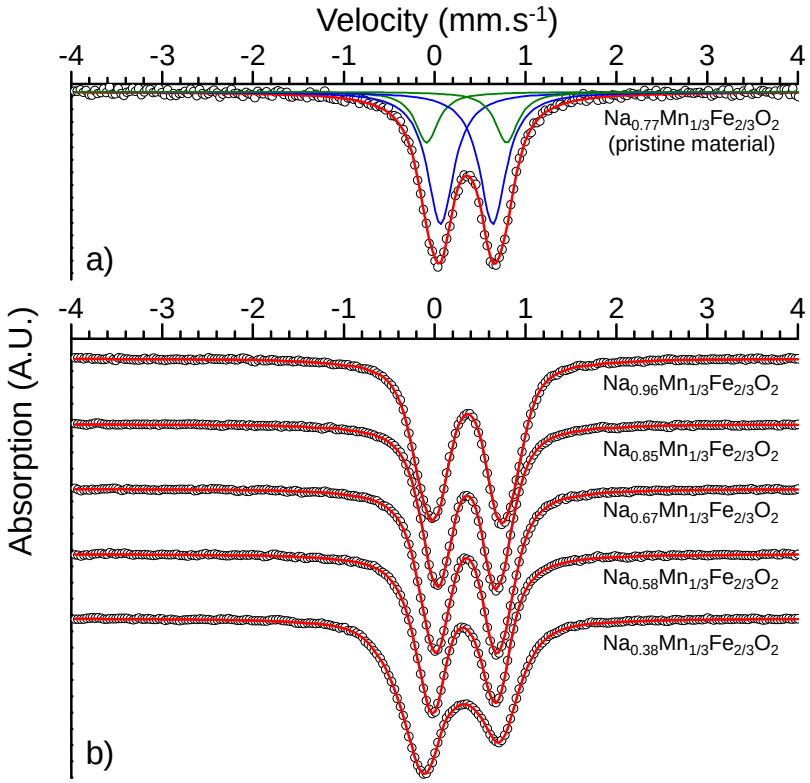

Figure R.12. Spectres XANES enregistrés aux seuils K du Mn et de Fe *in situ* (*operando*) pendant la charge d'une cellule $Na_xMn_{1-y}Fe_yO_2$//Na. La cellule a été préalablement déchargée.

Site	δ (mm.s^{-1})	FWHM (mm.s^{-1})	Δ (mm.s^{-1})	P (%)
Fe^{3+}(A)	0.353	0.30	0.88	25
Fe^{3+}(B)	0.354	0.35	0.58	75

Tableau R.2 : Paramètres Mössbauer correspondant au spectre de O3-$Na_{0.77}Mn_{1/3}Fe_{2/3}O_2$.

Nous avons ensuite réalisé l'étude *in situ*. Les spectres des phases $Na_xMn_{1/3}Fe_{2/3}O_2$ ont été enregistrés pour des valeurs d'intercalation sélectionnées : x = 0.96, 0.85, 0.67, 0.58 et 0.38. Ces spectres ont été enregistrés pendant la charge de la cellule faisant suite à une décharge préalable. Les spectres enregistrés à potentiel constant sont donnés **Figure R.13b**. Comme nous pouvons le voir, il n'y a pas de décalage dans la position des pics dans le domaine $0.96 \geq x \geq 0.67$. Au contraire, un décalage significatif vers les vitesses les plus basses est observé pour les spectres correspondant aux compositions x = 0.58 et x = 0.38. Ce décalage indique une évolution de l'état d'oxydation des ions Fe^{3+}. Comme pour le spectre du matériau initial, tous les spectres enregistrés *in situ* se présentent sous la forme d'un doublet quadripolaire dont l'asymétrie et la largeur à mi-hauteur augmentent lors de la désintercalation électrochimique.

Un premier affinement de type Lorentzien a été réalisé afin de déterminer le nombre de sites présents pour chaque composition (**Tableau R.3**). Dans le domaine $0.67 \leq x < 1$, deux sites Fe^{3+} ($\delta \approx 0.34 – 0.37$ mm.s^{-1}) sont nécessaires pour décrire les spectres. Les déplacements isomériques associés n'évoluant pas de façon notable dans le domaine $0.67 \leq x < 1$ confirment que les ions Fe^{3+} ne participent pas au processus redox à bas potentiel et que seuls les ions Mn^{3+} sont oxydés. Pour $x < 0.67$, on observe l'apparition des sites Fe^{4+} ($\delta \approx 0$ mm.s^{-1}) et $Fe^{(3+z)+}$ ($\delta \approx 0.10 – 0.18$ mm.s^{-1}) ce qui confirme l'oxydation des ions Fe^{3+} à haut potentiel.

Un important élargissement des pics est observé au cours de la désintercalation de x = 0.96 à x = 0.38 ce qui est en accord avec l'apparition de nouveaux sites Fe^{n+}. Cela suggère également une augmentation du désordre dans le matériau au cours de la désintercalation. Afin de prendre en compte ce phénomène nous avons réalisé un second type d'affinement, dit en distribution, se basant sur des valeurs de déplacement isomériques fixées d'après les affinements Lorentziens. Les largeurs à mi-hauteur ont été fixées à 0.20 mm.s^{-1} (x = 0.96 et x = 0.85), 0.25 mm.s^{-1} (x = 0.67) et 0.30 mm.s^{-1} (x = 0.58 et x = 0.38) afin de prendre en compte l'augmentation du désordre dans le matériau au cours de la désintercalation. Grâce à ces affinements en distribution, nous avons pu déterminer l'éclatement quadripolaire moyen (Δ^*) et la population des différents sites. Ces résultats sont donnés dans le **Tableau R.3** avec les formules développées des matériaux et les populations attendues pour les différents sites.

Les résultats peuvent être séparés en deux groupes selon le procédé redox actif : $Mn^{3+} \rightarrow Mn^{4+}$ ($x \geq 2/3$) et $Fe^{3+} \rightarrow Fe^{4+}$ ($x < 2/3$). Les spectres correspondant aux compositions x = 0.96, 0.85 et 0.67 sont similaires et peuvent être affinés en utilisant deux sites Fe^{3+}, comme pour le matériau initial. Ces sites sont appelés Fe^{3+} (1) et Fe^{3+} (2) afin d'éviter toute confusion avec les sites déduits de l'affinement Lorentzien. Les signaux associés à ces sites correspondent à des doublets quadripolaires qui montrent des déplacements isomériques similaires (δ = 0.355 mm.s^{-1} et 0.365 mm.s^{-1} pour la composition x = 0.96). Les

éclatements quadripolaires des deux sites correspondant à la phase O'3 (x = 0.96) sont différents (Δ* = 1.00 mm.s^{-1} et 0.71 mm.s^{-1} pour les sites Fe^{3+} (1) et Fe^{3+} (2) respectivement). La plus haute valeur de l'éclatement quadripolaire pour le site Fe^{3+} (1) indique qu'il est davantage affecté par l'effet Jahn-Teller coopératif des ions Mn^{3+} environnants. De plus, quand la structure évolue vers un empilement de type O3 (x = 0.85 puis x = 0.67), la valeur de l'éclatement quadripolaire du site Fe^{3+} (1) diminue continuellement alors que l'éclatement quadripolaire du site Fe^{3+} (2) reste constant. Nous pouvons donc conclure que le site Fe^{3+} (1) correspond à des ions Fe^{3+} principalement entourés d'ions Mn^{n+} (incluant une distribution d'environnements) alors que le site Fe^{3+} (2) correspond à des ions Fe^{3+} principalement entourés d'autres ions Fe^{3+}. Les populations des deux sites donnent un rapport Fe^{3+} (1) : Fe^{3+} (2) égal à 40 : 60 qui est maintenu dans le domaine $0.96 \geq x \geq 0.67$. Dans ce même domaine, les déplacements isomériques diminuent suivant la désintercalation électrochimique, ce qui est en accord avec l'augmentation de l'état d'oxydation moyen des ions Mn^{n+} environnants.

Dans le domaine $x < 0.67$, tous les ions Mn^{3+} ont été oxydés, d'après les mesures d'absorption des rayons-X, et le procédé redox actif est maintenant $Fe^{3+} \rightarrow Fe^{4+}$. Trois sites sont maintenant nécessaires pour pouvoir décrire les spectres. Le premier site est caractérisé par un déplacement isomérique égal à 0.336 – 0.321 mm.s^{-1} et correspond à des ions Fe^{3+} à haut spin en environnement octaédrique. Le deuxième site montre un déplacement isomérique proche de 0 mm.s^{-1}, caractéristique d'ions Fe^{4+} en environnement octaédrique. L'ion Fe^{4+} a déjà été observé dans des oxydes lamellaires aux états haut-spin [121] et bas spin [122, 123]. L'état de spin du Fe^{4+} dans notre matériau n'a, en revanche, pas encore été déterminé. Si l'existence ces ions Fe^{3+} et Fe^{4+} était prévisible, la présence d'un troisième site d'état d'oxydation intermédiaire $Fe^{(3+z)+}$ l'était moins. Ce troisième site possède un déplacement isomérique de valeur intermédiaire entre celles des sites Fe^{3+} et Fe^{4+}. Une origine possible de cet état d'oxydation moyen est l'existence d'un mécanisme de « Fast Electron Hopping » entre les espèces Fe^{3+} et Fe^{4+}, comme cela a déjà été observé dans les systèmes $Li_xNi_{0.70}Fe_{0.15}Co_{0.15}O_2$ [121] et $Ni_{1-y}Fe_yOOH_x$ / $Ni_{1-y}Fe_y(OH)_2$, *ex situ* [122] et *in situ* [123]. La population du site $Fe^{(3+z)+}$ peut être répartie entre les espèces Fe^{3+} et Fe^{4+} si l'on considère la somme des populations Fe^{3+} et Fe^{4+} égale à 1. Cette répartition est donnée dans le **Tableau R.3**.

On peut observer une bonne concordance entre les compositions déduites des spectres Mössbauer ($Na_{0.58}Mn_{1/3}Fe_{2/3}O_2$ et $Na_{0.40}Mn_{1/3}Fe_{2/3}O_2$) et celles déduites de l'électrochimie ($Na_{0.58}Mn_{1/3}Fe_{2/3}O_2$ et $Na_{0.38}Mn_{1/3}Fe_{2/3}O_2$, respectivement). Parallèlement, l'éclatement quadripolaire moyen augmente lors de la désintercalation, notamment pour le site Fe^{4+} (Δ* = 0.19 mm.s^{-1} et 0.55 mm.s^{-1} pour x = 0.58 et x = 0.38, respectivement). Cela indique une fois de plus une augmentation du désordre dans le matériau lors de la désintercalation, et corrobore les résultats obtenus par diffraction des rayons-X qui montraient la coexistence de deux phases : P3 (majoritaire) et O3 (minoritaire).

Awaited results from electrochemistry			Mössbauer results											
Developed formula	%Fe^{3+}	%Fe^{4+}	Fe^{3+} (1)			Fe^{3+} (2)							Δ_{max} ($mm.s^{-1}$)	%Fe^{3+}	%Fe^{4+}
			δ ($mm.s^{-1}$)	Δ* ($mm.s^{-1}$)	P (%)	δ ($mm.s^{-1}$)	Δ* ($mm.s^{-1}$)	P (%)						
$Na_{0.96}Mn^{3+}_{0.29}Mn^{4+}_{0.04}Fe^{3+}_{0.67}Fe^{4+}_{0}O_2$	100	0	0.355	1.00	40	0.365	0.71	60					0.93	100	0
$Na_{0.85}Mn^{3+}_{0.15}Mn^{4+}_{0.18}Fe^{3+}_{0.67}Fe^{4+}_{0}O_2$	100	0	0.351	0.81	39	0.360	0.61	61					0.80	100	0
$Na_{0.67}Mn^{3+}_{0}Mn^{4+}_{0.33}Fe^{3+}_{0.67}Fe^{4+}_{0}O_2$	100	0	0.341	0.78	41	0.360	0.67	59					0.67	100	0
Developed formula	%Fe^{3+}	%Fe^{4+}	Fe^{3+}			Fe^{4+}			$Fe^{(3+z)+}$				Δ_{max} ($mm.s^{-1}$)	%Fe^{3+}	%Fe^{4+}
			δ ($mm.s^{-1}$)	Δ* ($mm.s^{-1}$)	P (%)	δ ($mm.s^{-1}$)	Δ* ($mm.s^{-1}$)	P (%)	δ ($mm.s^{-1}$)	Δ* ($mm.s^{-1}$)	P (%)	Repartition between			
												Fe^{3+}(%)	Fe^{4+}(%)		
$Na_{0.58}Mn^{3+}_{0}Mn^{4+}_{0.33}Fe^{3+}_{0.58}Fe^{4+}_{0.09}O_2$	87	13	0.336	0.70	78	0.04	0.19	3	0.175	0.68	19	9	10	0.70	87	13
$Na_{0.38}Mn^{3+}_{0}Mn^{4+}_{0.33}Fe^{3+}_{0.38}Fe^{4+}_{0.29}O_2$	57	43	0.321	0.87	57	0.048	0.55	24	0.107	0.77	19	4	15	0.87	61	39

Tableau R.3 : Formules développées et paramètres Mössbauer correspondant aux affinements des spectres présentés **Figure R.13**. Les écarts-types sur les valeurs des déplacements isomériques sont égaux à 0.002 $mm.s^{-1}$. La population du site $Fe^{(3+z)+}$ est redistribuée entre les sites Fe^{3+} et Fe^{4+} selon la formule : $P(Fe^{3+}) = (\delta(Fe^{3+z})-\delta(Fe^{4+})) / (\delta(Fe^{3+})-\delta(Fe^{4+}))$.

R.1.d. Comparaison des différents systèmes $Na_xMn_{1-y}Fe_yO_2$

Comparaison des diagrammes de phase

Les diagrammes de phase des différents systèmes P2 et O3-$Na_xMn_{1-y}Fe_yO_2$ déduits par diffraction des rayons-X menée *in situ* pendant la charge complète de batteries Na sont donnés **Figure R.14**.

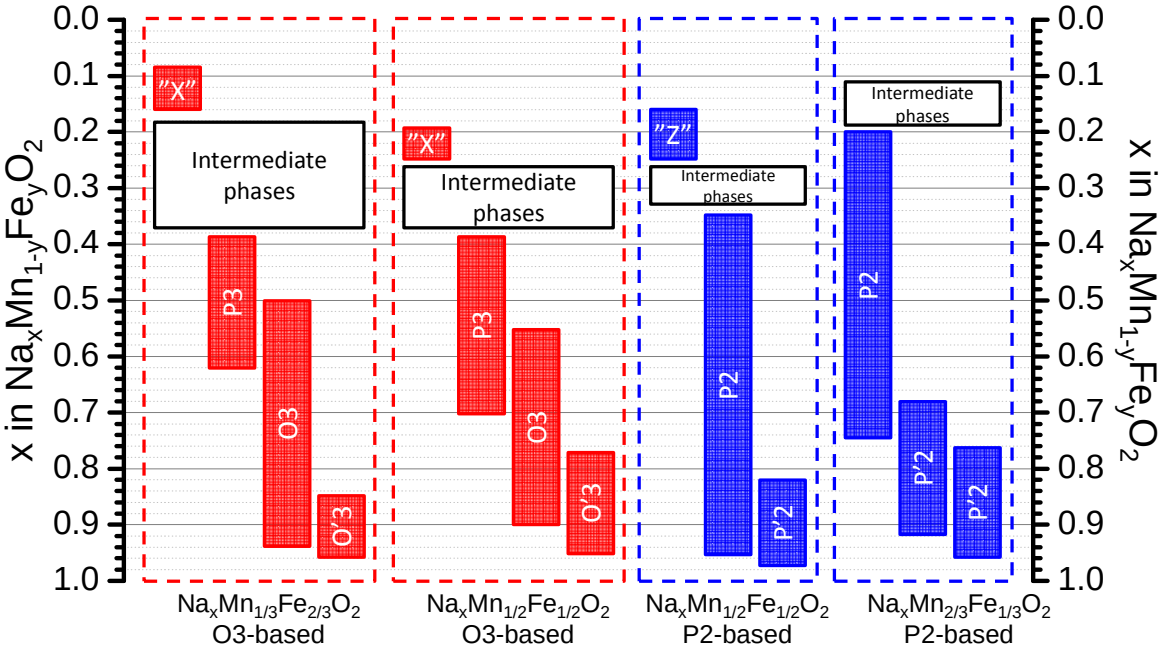

Figure R.14 : Domaines d'observation des phases O'3, O3, P3 et « X » (systèmes de type O3) et des phases P'2, P2 et « Z » (systèmes de type P2) en fonction du taux de Na.

Tous les systèmes (P2 ou O3) montrent un comportement similaire (i) une phase distordue (P'2 ou O'3) pour les états les plus intercalés et (ii) une importante perte de cristallinité pour les états les plus désintercalés (E ≈ 4.3 V).

Concernant les systèmes de type O3, l'augmentation du rapport Mn : Fe de 1 : 2 à 1 : 1 entraine (i) un domaine d'observation de la phase O'3 plus étendu et (ii) une apparition plus rapide de la phase P3 (pour x = 0.7 ($Na_xMn_{1/2}Fe_{1/2}O_2$) *vs.* x = 0.62 ($Na_xMn_{2/3}Fe_{1/3}O_2$). Cette phase P3 est d'ailleurs observée sur un domaine plus étendu dans le cas du système $Na_xMn_{1/2}Fe_{1/2}O_2$ ($0.39 \leq x \leq 0.7$) que dans le cas du système $Na_xMn_{1/3}Fe_{2/3}O_2$ ($0.39 \leq x \leq 0.62$).

Concernant les systèmes de type P2, l'augmentation du rapport Mn : Fe de 1 : 1 à 2 : 1 conduit à l'observation de la phase P'2 (des phases P'2) sur un domaine de composition en sodium plus étendu. Un second domaine P'2 est observé pour le système $Na_xMn_{2/3}Fe_{1/3}O_2$ et retarde donc l'apparition de la phase P2 (x = 0.74 ($Na_xMn_{2/3}Fe_{1/3}O_2$) *vs.* x = 0.95 ($Na_xMn_{1/2}Fe_{1/2}O_2$)). La phase P2 est observée sur un domaine de composition plus étendu dans le cas du système $Na_xMn_{1/2}Fe_{1/2}O_2$ ($0.26 \leq x \leq 0.95$) que dans le cas du

système $Na_xMn_{2/3}Fe_{1/3}O_2$ ($0.1 \leq x \leq 0.74$). L'augmentation du rapport Mn : Fe prévient ici l'apparition de la phase peu cristallisée, notée « Z », jusqu'à 4.3 V pour le système $Na_xMn_{2/3}Fe_{1/3}O_2$.

Dans les phases de type P2 et O3, la formation des phases « X » et « Z » en charge se produit *via* la création de fautes d'empilement. Dans les systèmes de type O3 les fautes d'empilement sont simultanément créées dans les phases O3 et P3. Ces fautes sont hypothétiquement l'apparition de plans d'octaèdres NaO_6 dans la phase P3 ou l'apparition de plans O1 dans la phase O3. Dans les systèmes de type P2, la phase dite « Z » se forme également *via* l'apparition de plans d'octaèdres NaO_6 dans la phase P2.

Influence du rapport Mn : Fe sur l'état intercalé

Comme nous l'avons discuté avec la **Figure R.14**, l'effet Jahn-Teller coopératif des ions Mn^{3+} conduit à l'apparition d'une phase distordue (O'3 ou P'2) pour les plus hauts taux d'intercalation. De plus, augmenter le rapport Mn : Fe conduit à l'observation de ces phases distordues sur un domaine en composition plus étendu. Afin d'étudier l'évolution de l'effet Jahn-Teller coopératif avec le rapport Mn : Fe, nous avons tout d'abord étudié l'évolution des rapports $a_{mon.}/b_{mon.}$ (phases O'3) et $b_{orth.}/a_{orth.}$ (phases P'2). Cette évolution est donnée **Figure R.15**. Afin d'en faciliter l'interprétation, nous avons considéré tous les ions Mn^{n+} au degré d'oxydation +III.

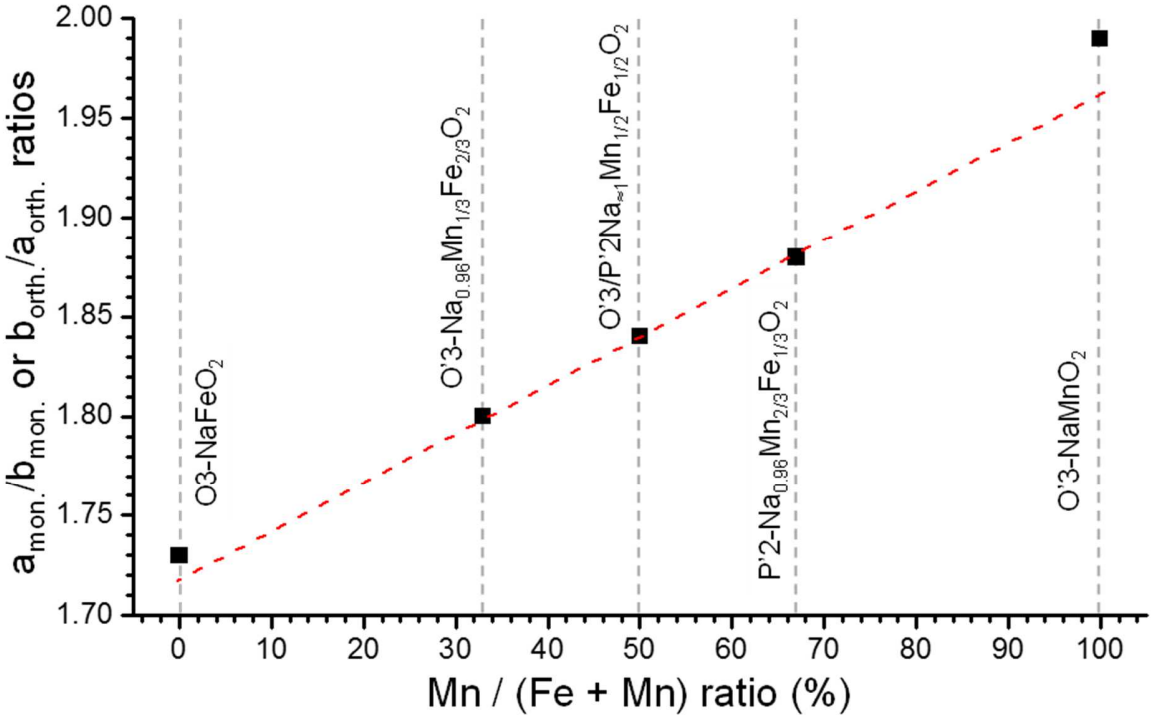

Figure R.15 : Evolution des rapports $a_{mon.}/b_{mon.}$ (phases O'3) et $b_{orth.}/a_{orth.}$ (phases P'2) en fonction du rapport Mn : Fe. O3-$NaFeO_2$: données provenant de [35]. O'3-$NaMnO_2$: données provenant de [44].

Comme l'on peut le voir l'évolution des rapports entre les paramètres de maille est linéaire pour nous résultats expérimentaux. De plus, l'empilement (O'3 ou P'2) ne semble pas avoir d'impact sur la distorsion à la vue des rapports $a_{mon.}/b_{mon.}$ (O'3) et $b_{orth.}/a_{orth.}$ (P'2) qui sont égaux (1.84) pour les deux polytypes $Na_{\approx 1}Mn_{1/2}Fe_{1/2}O_2$. Afin de vérifier cette hypothèse, nous avons également étudié l'évolution des distances M-O (polyèdres MO_6) sur la **Figure R.16** :

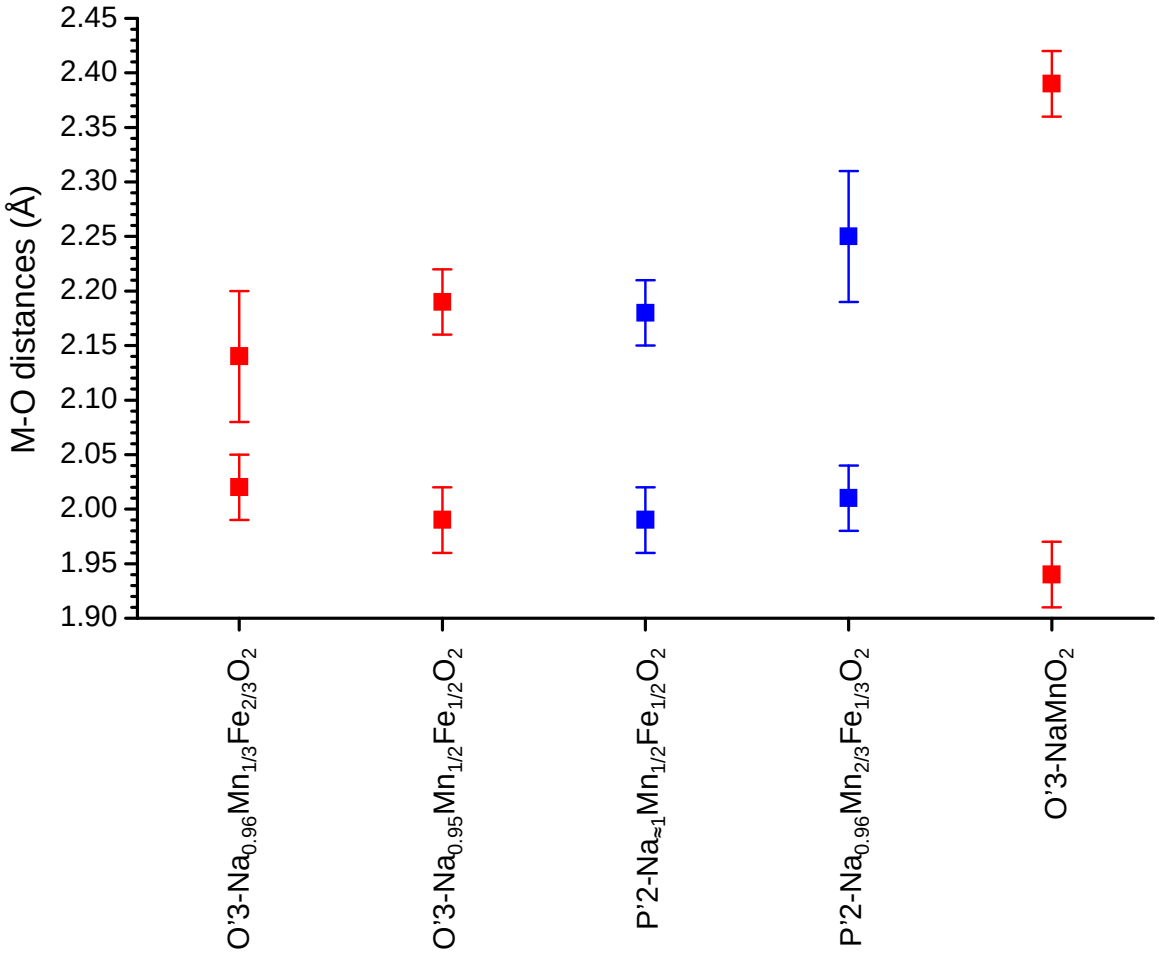

Figure R.16 : Evolution des distances M-O des octaèdres MO_6 dans les phases P'2 et O'3-$Na_{\approx 1}Mn_{1-y}Fe_yO_2$. O'3-$NaMnO_2$: données provenant de [44].

La **Figure R.16** confirme bien que la distorsion des octaèdres MO_6 est identique pour les phases O'3-$Na_{\approx 1}Mn_{1/2}Fe_{1/2}O_2$ (distances M-O égales à 4 x 1.99 Å et 2 x 2.19 Å) et P'2-$Na_{\approx 1}Mn_{1/2}Fe_{1/2}O_2$ (distances M-O égales à 4 x 1.99 Å et 2 x 2.18 Å). On observe également que les octaèdres MO_6 sont davantage distordus lorsque la quantité d'ions Mn^{3+} augmente (distances M-O égales à 4 x 2.02 Å et 2 x 2.14 Å pour O'3-Na $Na_{\approx 1}Mn_{1/3}Fe_{2/3}O_2$ *vs.* 4 x 1.94 Å et 2 x 2.39 Å pour O'3-$NaMnO_2$).

R.2. $NaNiO_2$ et le diagramme de phases de Na_xNiO_2 ($1/3 \leq x \leq 1$)

R.2.a. Contexte de l'étude

Les premières recherches portant sur O'3-NaNiO2 datent de 1954 et sont attribuées à Dyer et al [2]. Depuis, O'3-$NaNiO_2$ a principalement été étudié pour ses propriétés magnétiques [43, 124-132], physiques [133] et structurales [2, 43].

La première étude montrant la possibilité de désintercaler réversiblement les ions sodium de O'3-$NaNiO_2$ fut menée par Braconnier et al. en 1982 [38]. Cette étude révèle que la (dés)intercalation électrochimique se produit suivant une succession de mécanismes biphasés entre plusieurs composés définis : P'3-$Na_{0.91}NiO_2$, P''3-$Na_{0.84}NiO_2$, O''3-$Na_{0.81}NiO_2$ and O'''3-$Na_{0.79}NiO_2$. En 2013, Vassiliaras et al. ont publié une étude concernant la cyclabilité sur le long terme de O'3-$NaNiO_2$ [34]. Malgré une capacité de première charge égale à 150 $mAh.g^{-1}$ pour des batteries Na cyclées entre 1,25 et 3,75 V, la réversibilité du matériau est grandement limitée par la formation d'une phase intermédiaire au cours de la première décharge, qui empêche la réversibilité vers O'3-$NaNiO_2$. Cette phase intermédiaire ainsi que les différentes transitions de phases furent observées *in situ* par Han et al. en 2014 [134].

Nos travaux sur le système Na_xNiO_2 firent suite à ceux de Vassiliaras et al., notre but étant d'étudier le diagramme de phases de Na_xNiO_2 par diffraction des rayons-X *in situ*. Par comparaison avec d'autres systèmes Na_xMO_2 étudiés à l'ICMCB et dans la littérature, nous nous attendions à observer des ordres sodium – lacunes pour les différents composés définis [48, 55, 56, 64].

Les premiers travaux de synthèse et de caractérisation sur ce système furent réalisés par T. Phraewphiphat au cours de deux stages doctoraux réalisés à l'ICMCB en 2013 et 2014.

R.2.b. Synthèse de O'3-$NaNiO_2$ dit « moyens grains »

O'3-$NaNiO_2$ a été préparé suivant le mode opératoire décrit par Braconnier et al. [38]. Ce protocole consiste à mélanger et broyer les oxydes Na_2O et NiO (préparé par décomposition thermique de $Ni(NO_3)_2 .6\,H_2O$) dans un mortier sous atmosphère inerte. Le mélange est ensuite placé dans une nacelle en or, introduite dans un four tubulaire et chauffée à 650°C pendant 15h sous oxygène. Le matériau est ensuite trempé à l'air et directement placé sous vide avant d'être introduit en boite à gants. La différence majeure avec les conditions de synthèse décrites par Braconnier et al. [38] est le non-ajout d'excès de sodium au cours de la synthèse, qui avait pour effet d'augmenter la taille des grains et d'introduire des limites de diffusion ionique dans le matériau.

La pureté de O'3-$NaNiO_2$ ainsi obtenu a été confirmé par diffraction des rayons-X (**Figure R.17**).

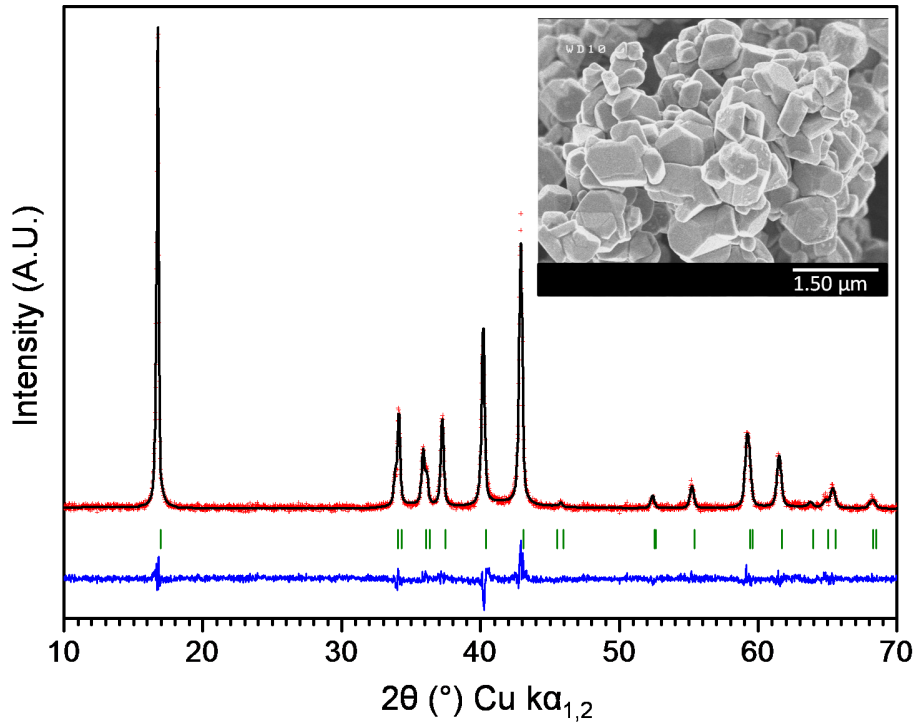

Figure R.17 : diffractogrammes observés et calculés (affinement de type Rietveld) de la phase O'3-$NaNiO_2$ (moyens grains). Croix rouges : observé, ligne noire : calculé, ligne bleue : différence et traits verticaux verts : réflexions. Insert : cliché MEB du même échantillon.

O'3-$NaNiO_2$ Space group : C2/m $a_{mon.}$ = 5.3087(7) Å, $b_{mon.}$ = 2.8453(3) Å, $c_{mon.}$ = 5.5695(7) Å, $\beta_{mon.}$ = 110.41(1)° $a_{mon.}/b_{mon.}$ = 1.87						
Atom	Wyckoff	Coordinates			Occupancy	ADP (Å²)
Na	2c	0	0	1/2	0.99(3)	0.6(4)
Ni	2b	0	1/2	0	1	0.8(3)
O	4i	0.224(2)	0	0.192(2)	1	0.5(5)
Ni-O distances		4 * 1.93(1) Å		2 * 2.11(1) Å		
Rwp = 12.51%; R_B = 4.09%						

Tableau R.4 : Paramètres structuraux et facteurs de mérite calculés à partir du diffractogramme de O'3-$NaNiO_2$ (moyens grains).

Le diffractogramme obtenu est correctement indexé dans le groupe d'espace C2/m des structures de type O'3. Les paramètres de maille sont similaires à la littérature et donnent un rapport $a_{mon.}/b_{mon.}$ égal à 1,87 qui est dû à l'effet Jahn-Teller coopératif des ions Ni^{3+}. Cet effet est confirmé par l'existence de deux liaisons longues (2 x 2.11 Å) et de quatre liaisons courtes (4 x 1.93 Å) dans les octaèdres NiO_6 (**Tableau R.4**).

Les pics de diffraction sont bien définis impliquant un matériau bien cristallisé. Ceci a été confirmé par microscopie électronique à balayage (insert de la **Figure R.17**) qui fait état d'une taille de cristallites comprise entre 250 et 650 nm.

R.2.c. Electrochimie

Le comportement électrochimique de O'3-$NaNiO_2$ « moyens grains » a été étudié en batteries Na entre 1,5 et 3,8 V à C/50. Les résultats de cette expérience sont illustrés sur la **Figure R.18** ci-après :

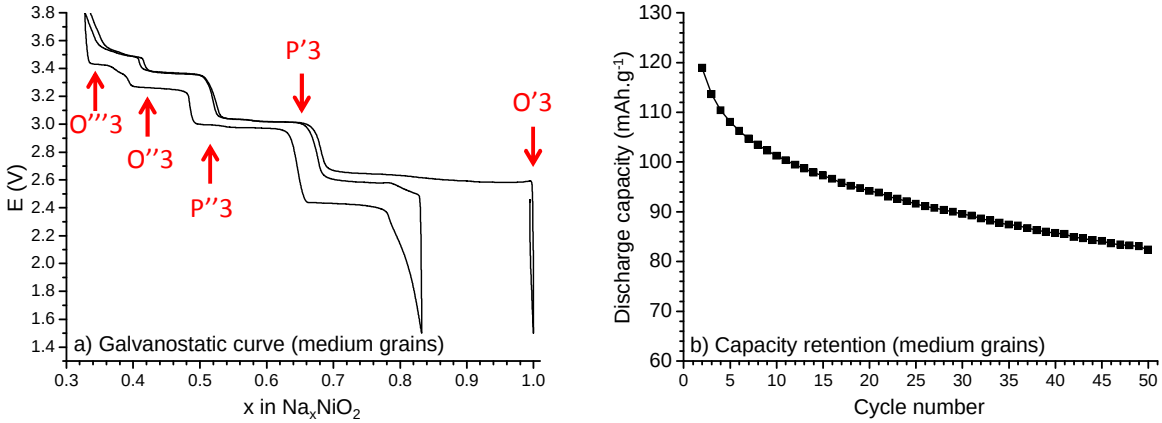

Figure R.18 : (a) courbe galvanostatique et (b) évolution de la capacité en décharge pour une batterie Na_xNiO_2 (moyens grains) / $NaPF_6$ in PC (1M) + 2 wt% FEC / Na. Régime : C/50.

La première décharge confirme l'état d'intercalation maximal du matériau de départ. Le profil de charge consiste en une succession de plateaux et de sauts de potentiels entre les compositions x = 1 ; 2/3 ; 1/2 et 2/5. Un comportement de type « solution solide » est observé entre x = 2/5 et x = 1/3. Les composés définis observés pour x = 2/3 ; 1/2 ; 2/5 et 1/3 correspondent à ceux observés pour x' = 0,91 ; 0,84 ; 0,81 et 0,79 dans l'étude de Braconnier et al. [38]. Cette différence entre les taux de sodium vient probablement des meilleurs moyens matériels mis à notre disposition pour cette étude. Lors de la seconde décharge une réversibilité partielle est observée. Deux différences majeures affectent la courbe de deuxième décharge : (i) le saut de potentiel observé à x = 2/5 en charge est remplacé par deux sauts de potentiel successifs en décharge et (ii) l'état d'intercalation maximal est atteint pour x = 0,83. Ce deuxième phénomène avait déjà été observé par Vassiliaras et al. [34].

Au cours de la seconde charge, un domaine de type « solution solide » est observé pour $0.78 \leq x \leq 0.83$. Les courbes de première et de seconde charge sont ensuite identiques pour $x > 2/3$. Après 50 cycles, le matériau montre une faible rétention de capacité en décharge (≈ 70 %) en accord avec la littérature.

Des mesures en mode GITT ont également été conduites afin d'avoir une meilleure compréhension des comportements électrochimiques. Les résultats obtenus sont donnés sur la **Figure R.19** et montrent une succession de sauts et de plateaux en potentiel comme nous l'avons vu précédemment. Dans le domaine $2/3 \leq x \leq 1$, on observe deux pseudo-plateaux en potentiel qui sont séparés par un domaine « solution solide » ($0.82 \leq x \leq 0.88$). Pour $1/2 \leq x \leq 2/3$, les mesures GITT montrent à nouveaux deux plateaux en potentiel, indiquant la présence d'un nouveau composé défini pour $x \approx 0.55$. Ce phénomène est davantage mis en évidence sur l'insert de la **Figure R.19**. Un dernier plateau est observé

entre les compositions x = 1/2 et x = 2/5. Un comportement de type solution solide sépare ensuite les compositions x = 2/5 et x = 1/3. Pour E > 3.9 V (x > 1/3), seul un long plateau est observé. Son origine se trouve probablement dans la décomposition de l'électrolyte de la batterie Na. L'augmentation du potentiel pour x ≈ 0 indique la présence d'une nouvelle réaction.

Au cours de la mesure GITT, on remarque une diminution continue de la polarisation pour 2/5 ≤ x ≤ 1. Cette observation est cohérente avec le changement de structure attendu (O'3 → P'3) [38], les matériaux de type P3 / P'3 se montrant de meilleures conducteurs ioniques [113]. L'augmentation de la polarisation observée pour x ≤ 2/5 résulte de la transition structurale P'3 → O'3 [38].

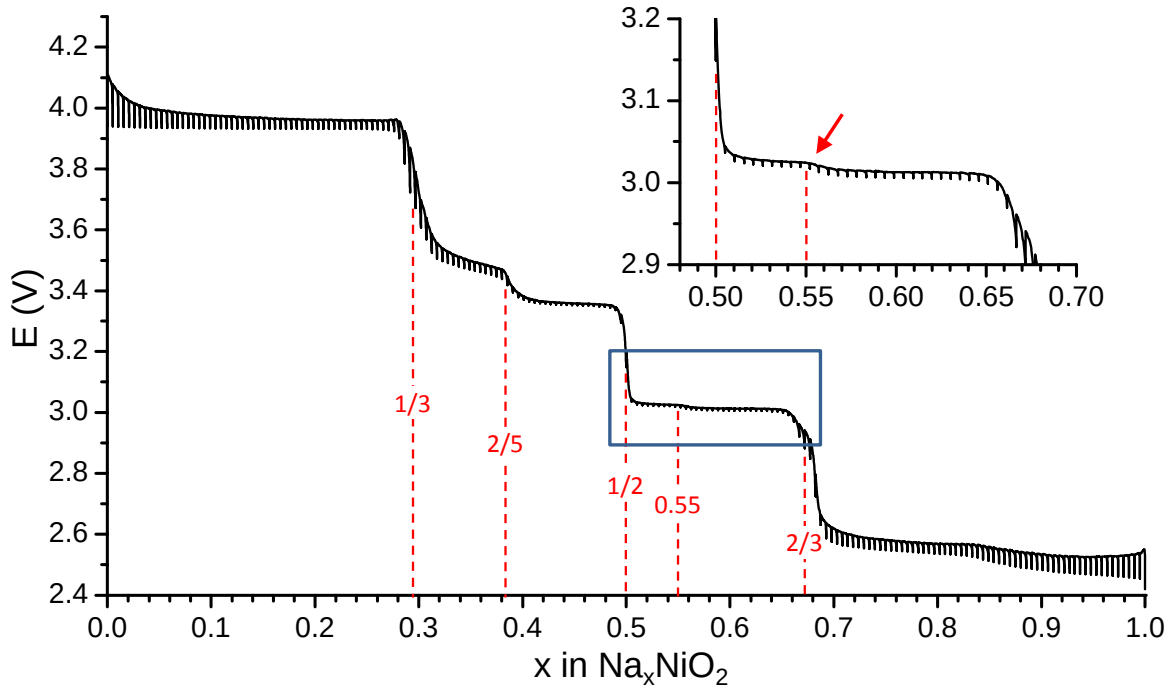

Figure R.19 : Courbe de cyclage en mode GITT enregistrée pour une batterie Na_xNiO_2 (moyens grains) / $NaPF_6$ in PC (1M) + 2 wt% FEC / Na. Régime : C/50 (pas de 0.005 Na^+ / unité formulaire), temps de relaxation : 30 minutes.

R.2.d. Le diagramme de phase de Na_xNiO_2

Le diagramme de phase de Na_xNiO_2 a été étudié *in situ* lors de la charge d'une batterie Na_xNiO_2//Na. L'expérience s'est déroulée en mode GITT afin de pouvoir mieux caractériser de probables phases ordonnées. Les diffractogrammes de rayons-X issus de l'expérience sont donnés sur la **Figure R.20**. Les diffractogrammes correspondant aux composés définis (x = 1 ; ≈ 0,8 ; 2/3 ; 1/2 ; 2/5 et 1/3 (fin de l'expérience)) sont tracés en rouge. Par rapport à la littérature un nouveau domaine monophasé est observé pour x ≈ 0.80. Par la suite nous nous réfèrerons à la phase correspondante en tant que « $Na_{\approx 0.80}NiO_2$ ». Son existence est mise en évidence sur les zooms des pics de diffraction $(001)_{mon.}$ présentés sur la **Figure R.21**, et qui permettent de suivre l'évolution de ces mêmes pics pour chaque phase au cours

de la désintercalation. Dans la littérature, la phase $Na_{\approx 0.80}NiO_2$ n'a été observée *in situ* qu'en décharge [134], certainement à cause du mode *operando* choisi par les auteurs.

Les distances inter-feuillet déduites de la position des pics de diffraction $(001)_{mon.}$ sont données **Figure R.22**.

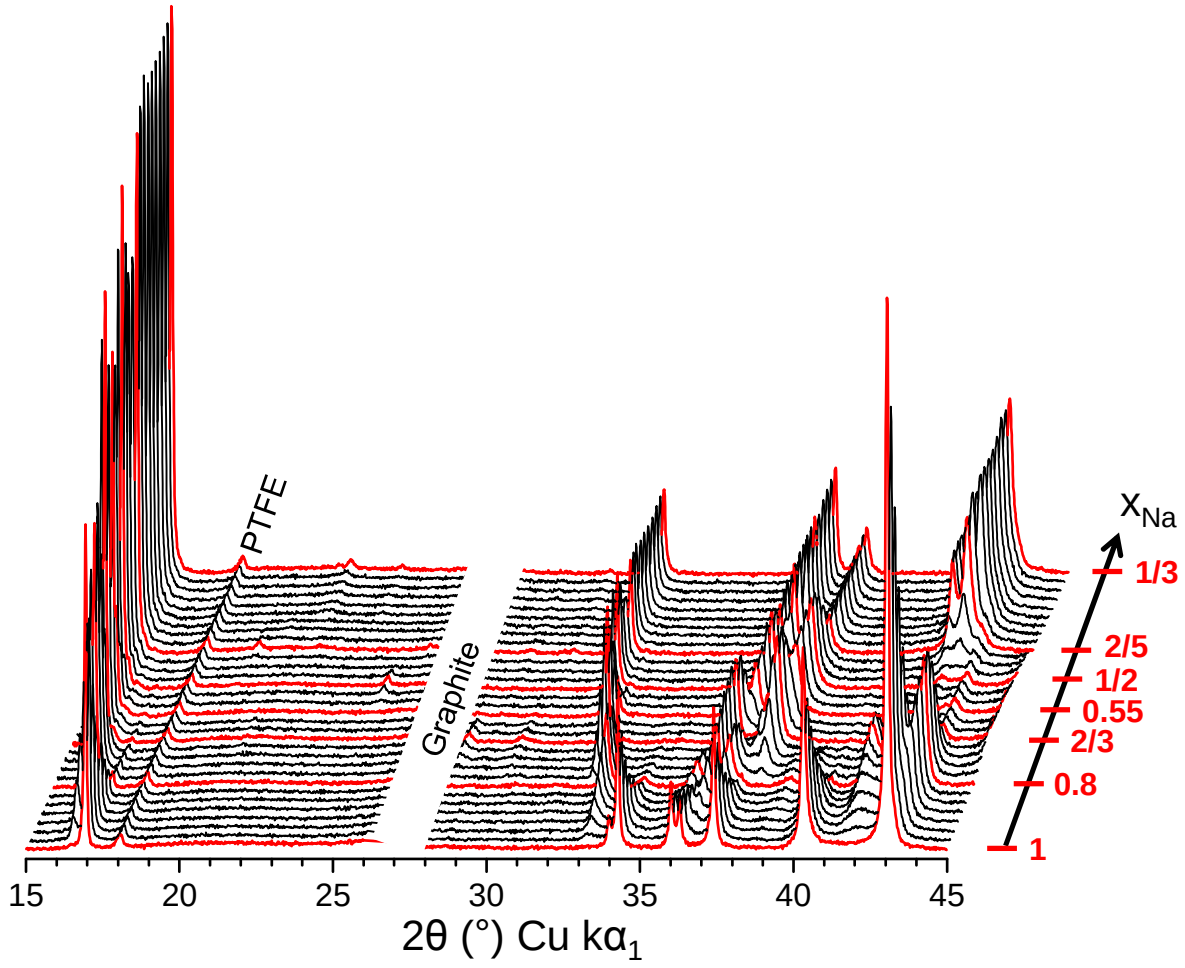

Figure R.20 : Evolution des diffractogrammes de rayons-X enregistré *in situ* pendant la charge d'une batterie Na_xNiO_2 (moyens grains) / $NaPF_6$ in PC (1M) + 2 wt% FEC / Na. Les diffractogrammes représentés en rouge correspondent aux composés définis.

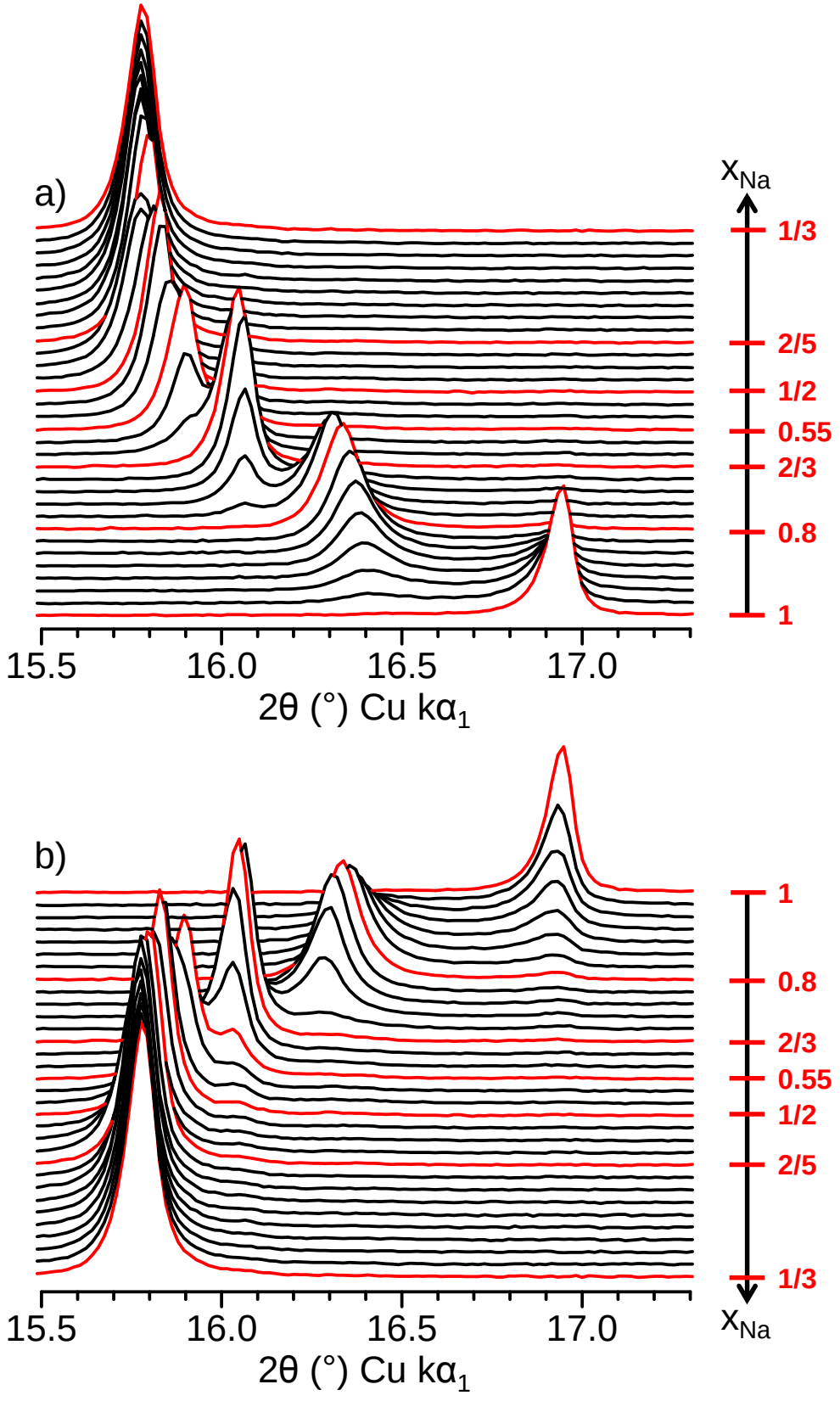

Figue R.21 : (a,b) Zooms dans le domaine 15,5 – 17,3° (2θ Cu $k\alpha_1$) des diffractogrammes présentés **Figure R.20**.

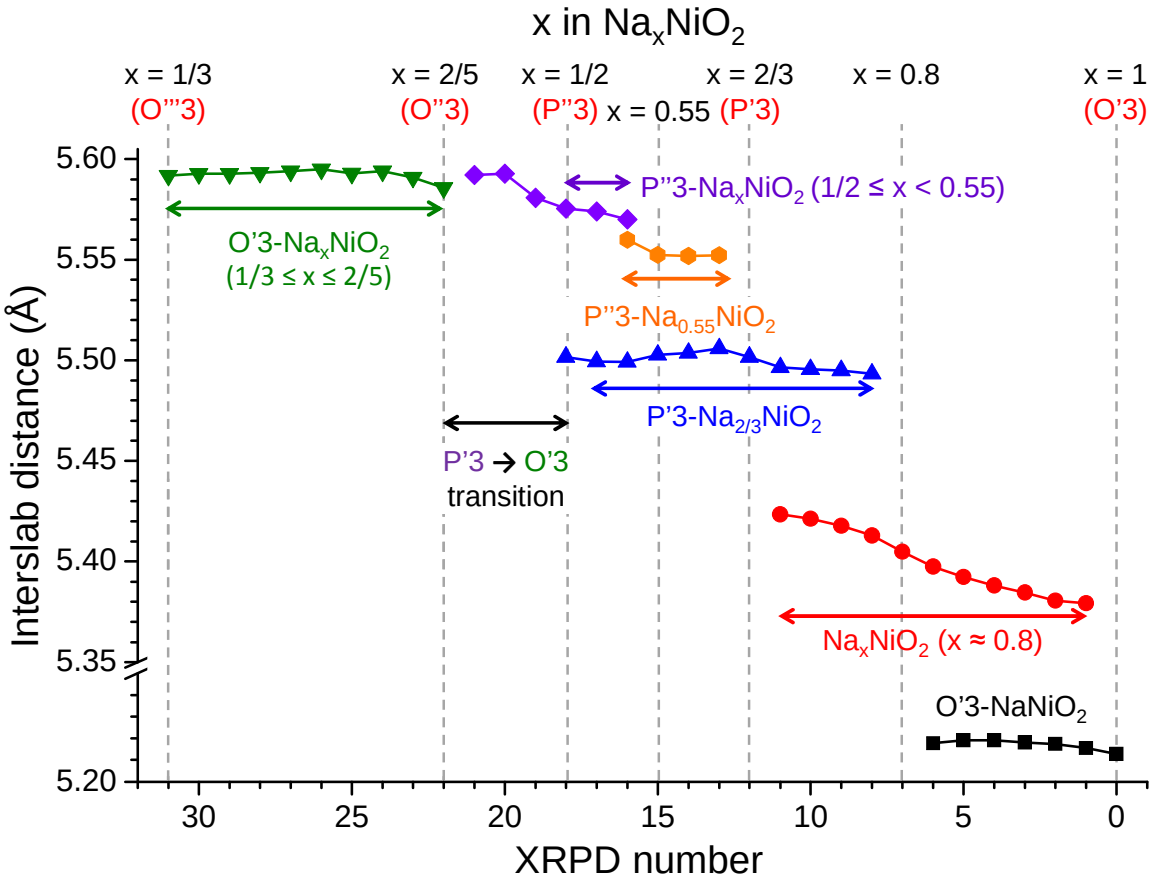

Figure R.22 : Evolution des distances inter-feuillets déduites de la position des pics de diffraction $(001)_{mon.}$ pour les différentes phases Na_xNiO_2.

Dans le domaine 0.8 < x < 1, l'intensité du pic $(001)_{mon.}$ correspondant à la phase $Na_{\approx 0.80}NiO_2$ augmente pendant que l'intensité du pic $(001)_{mon.}$ de la phase O'3-$NaNiO_2$ diminue. Alors qu'aucune variation de la distance inter-feuillet n'est observée pour la phase O'3-$NaNiO_2$, la phase $Na_{\approx 0.80}NiO_2$ montre une légère augmentation de sa distance inter-feuillet. Cela indique que la phase $Na_{\approx 0.80}NiO_2$ est impliquée dans une solution solide au sein du domaine biphasé O'3-$NaNiO_2$ + $Na_{\approx 0.80}NiO_2$. La phase $Na_{\approx 0.80}NiO_2$ est observée seule pour x ≈ 0.8.

Un domaine biphasé séparé également les compositions x = 2/3 et x = 0.8. Alors que la distance inter-feuillet de la phase P'3-$Na_{2/3}NiO_2$ n'évolue pas, on remarque que celle de la phase $Na_{\approx 0.80}NiO_2$ augmente légèrement. La phase $Na_{\approx 0.80}NiO_2$ est donc à nouveau impliquée dans une solution solide au sein du domaine biphasé $Na_{\approx 0.80}NiO_2$ + P'3-$Na_{2/3}NiO_2$.

Dans le domaine 1/2 < x < 2/3, deux domaines biphasés sont observés. Pour les plus hauts taux de sodium (diffractogrammes #13 à 15), un premier domaine biphasé sépare les phases P'3-$Na_{2/3}NiO_2$ et P''3-$Na_{0.5}NiO_2$. Cette dernière phase correspond au léger saut de potentiel observé lors des mesures GITT, mis en évidence par une flèche rouge sur la **Figure R.19**. Pour des taux d'intercalation plus faibles

(diffractogrammes #16 à 18), la phase P''3-$Na_{1/2}NiO_2$ apparaît pendant que l'intensité des pics correspondant aux phases P''3-$Na_{0.55}NiO_2$ et P''3-$Na_{2/3}NiO_2$ diminuent. La présence de la phase P''3-$Na_{2/3}NiO_2$ dans le domaine 1/2 < x < 0.55 implique des limitations cinétiques importantes.

Dans le domaine 2/5 < x < 1/2, le pic de diffraction $(001)_{mon.}$ s'élargit considérablement. Afin de mieux comprendre les phénomènes impliqués, un zoom des diffractogrammes autour du domaine 2/5 ≤ x ≤ 1/2 est donné **Figure R.23**.

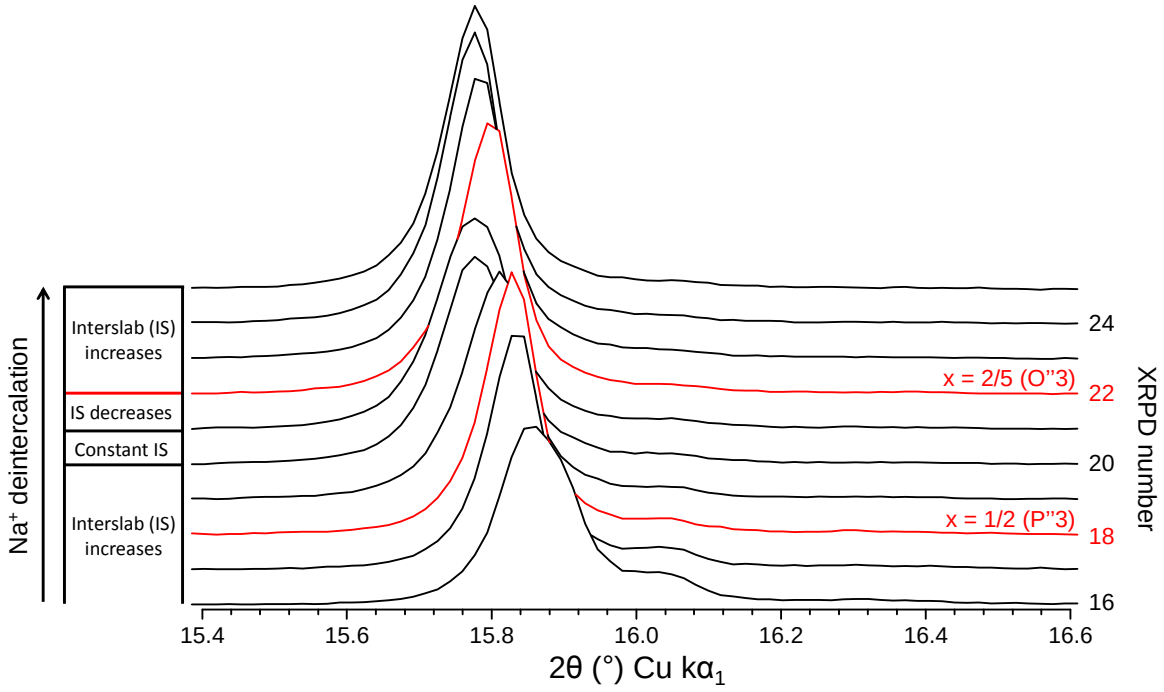

Figure R.23 : Zoom dans le domaine 15,4 – 16,6° (2θ Cu $k\alpha_1$) des diffractogrammes dans le domaine 2/5 ≤ x ≤ 1/2.

Lors de la désintercalation, une augmentation continue de la distance inter-feuillet est normalement attendue. Cependant, la distance inter-feuillet des phases P''3-$Na_{1/2}NiO$ et O''3-$Na_{2/5}NiO_2$ est similaire (≈ 5.59 Å). Cette similitude est expliquée par l'évolution de la géométrie des sites NaO_6, de prismatique à octaédrique, plus compacte. Entre les compositions x = 1/2 et x = 2/5, un comportement complexe est observé : d'abord la distance inter-feuillets augmente des diffractogrammes #18 (x = 1/2) à #20. Elle reste ensuite constante pour les diffractogrammes #20 à #21 et décroit des diffractogrammes #21 à #22. Cela peut être expliqué par la compétition entre deux effets opposés :

(1) La désintercalation à partir de P''3-$Na_{1/2}NiO_2$ qui entraine une augmentation de la distance inter-feuillets.

(2) La formation d'un environnement octaédrique pour certains feuillets NaO_6 qui entraine une diminution de la distance inter-feuillets.

Entre les diffractogrammes #18 (x = 1/2) et #20, la désintercalation à partir de la phase P''3-$Na_{1/2}NiO_2$ est le phénomène prédominant et la distance inter-feuillet augmente. Entre les diffractogrammes #20 et #21, les deux phénomènes se compensent et aucun déplacement du pic $(001)_{mon.}$ n'est observé. L'élargissement du pic $(001)_{mon.}$ visible sur le diffractogramme #21 implique l'augmentation du nombre de fautes d'empilement. Ce phénomène prédomine jusqu'au diffractogramme #22, entrainant une diminution de la distance inter-feuillet. La coexistence des feuillets d'octaèdres et de prismes NaO_6 est à l'origine de l'élargissement du pic $(001)_{mon.}$ dans le domaine $2/5 < x < 1/2$. Pour $x \leq 2/5$ (diffractogramme #22), tous les ions sodium sont dans une coordination octaédrique et la distance inter-feuillet augmente de façon continue jusqu'à x = 1/3, confirmant le mécanisme de type « solution solide ».

Si l'on regarde de plus près les diffractogrammes correspondant aux phases définies dans le domaine 17 – 30 °, on peut observer l'apparition réversible de pics de diffraction supplémentaires. Cette observation est facilitée sur la **Figure R.24**.

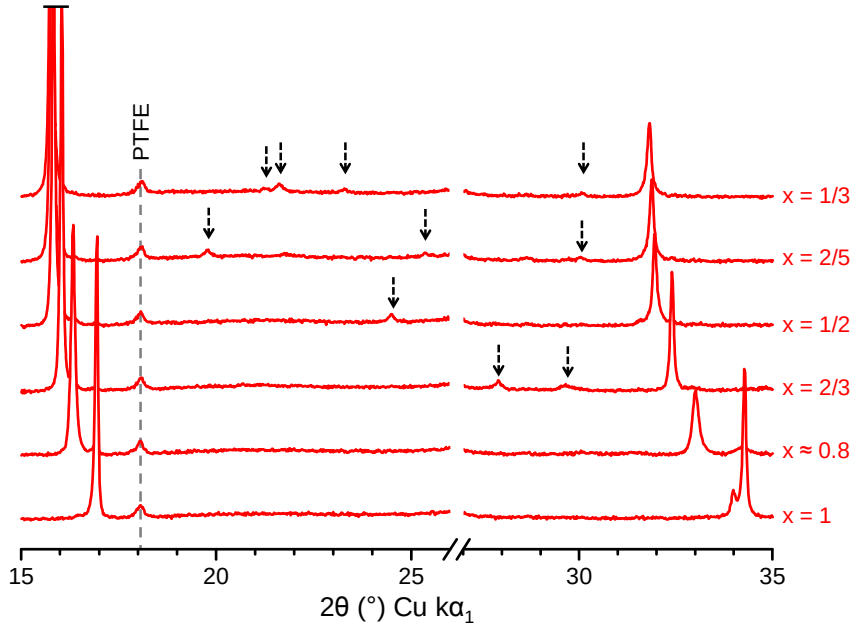

Figure R.24 : Diffractogrammes correspondant aux composés définis observés pour x = 1, 0.8, 2/3, 1/2, 2/5 et 1/3. Les flèches noires mettent en évidence la présence de pics de diffraction supplémentaires.

Dans les oxydes lamellaires Na_xMO_2, un tel phénomène est généralement associé à l'existence d'ordres Na^+ / lacunes entre les feuillets MO_2 [48, 55, 56, 64]. Inclure ces pics de diffraction supplémentaires dans un affinement de type LeBail nécessite la détermination de nouveaux paramètres de maille pour la *sur-maille*, le plus souvent se basant sur ceux de la *sous-maille*. La *sur-maille* et la *sous-maille* ne partagent pas toujours la même symétrie ni le même groupe d'espace.

Les phases ordonnées P'3-$Na_{2/3}NiO_2$, P''3-$Na_{1/2}NiO_2$ et O''3-$Na_{2/5}NiO_2$

Afin d'étudier les structures des phases P'3-$Na_{2/3}NiO_2$, P''3-$Na_{1/2}NiO_2$ et O''3-$Na_{2/5}NiO_2$, nous avons conduit des mesures de diffraction des rayons-X synchrotron haute résolution à l'ESRF[24] (**Figure R.25**).

La type d'empilement des différentes phases est déterminée par les intensités relatives des pics de diffraction $(111)_{mon.}$ et $(-202)_{mon.}$ par rapport aux pics $(201)_{mon.}$ et $(-112)_{mon.}$ dans la sous-maille. Les diffractogrammes associés aux phases de type O'3 montrent des pics de diffraction $(111)_{mon.}$ et $(-202)_{mon.}$ très intenses par rapport aux pics $(201)_{mon.}$ et $(-112)_{mon.}$. Le phénomène inverse est observé sur les diffractogrammes des phases P'3. Ainsi les diffractogrammes présentés **Figure R.25** nous permettent bien de confirmer les structures des phases P'2-$Na_{2/3}NiO_2$, P''3-$Na_{1/2}NiO_2$ et O''3-$Na_{2/5}NiO_2$.

Le meilleur rapport signal / bruit obtenu grâce aux mesures synchrotron permettent une meilleure distinction des pics de sur-structure que nous avons essayé d'inclure dans une sur-maille. Pour cela, nous avons d'abord indexé la sous-maille en utilisant une symétrie monoclinique (C2/m). Plusieurs sur-mailles dont les paramètres étaient multiples de ceux de la sous-maille ont ensuite été considérées pour inclure les pics de sur-structure dans la symétrie P-1. Une fois les meilleurs paramètres de maille identifiés (*i.e.* les paramètres les plus petits permettant d'inclure tous les pics de diffraction de la sur-structure), nous avons identifié les groupes d'espaces possibles en se basant sur les conditions de réflexion et en considérant une symétrie monoclinique. Pour chaque matériau, un seul groupe d'espace est possible. Les résultats des affinements de profils de type LeBail pour les super-mailles sont montrés sur la **Figure R.25**. Les groupes d'espaces et paramètres de maille des super-mailles sont reportés dans le **Tableau R.5**. Les relations entre les paramètres des sous-mailles et des sur-mailles y sont également données.

[24] En collaboration avec Dr. C. Drathen, ESRF, Grenoble, France (ligne ID31).

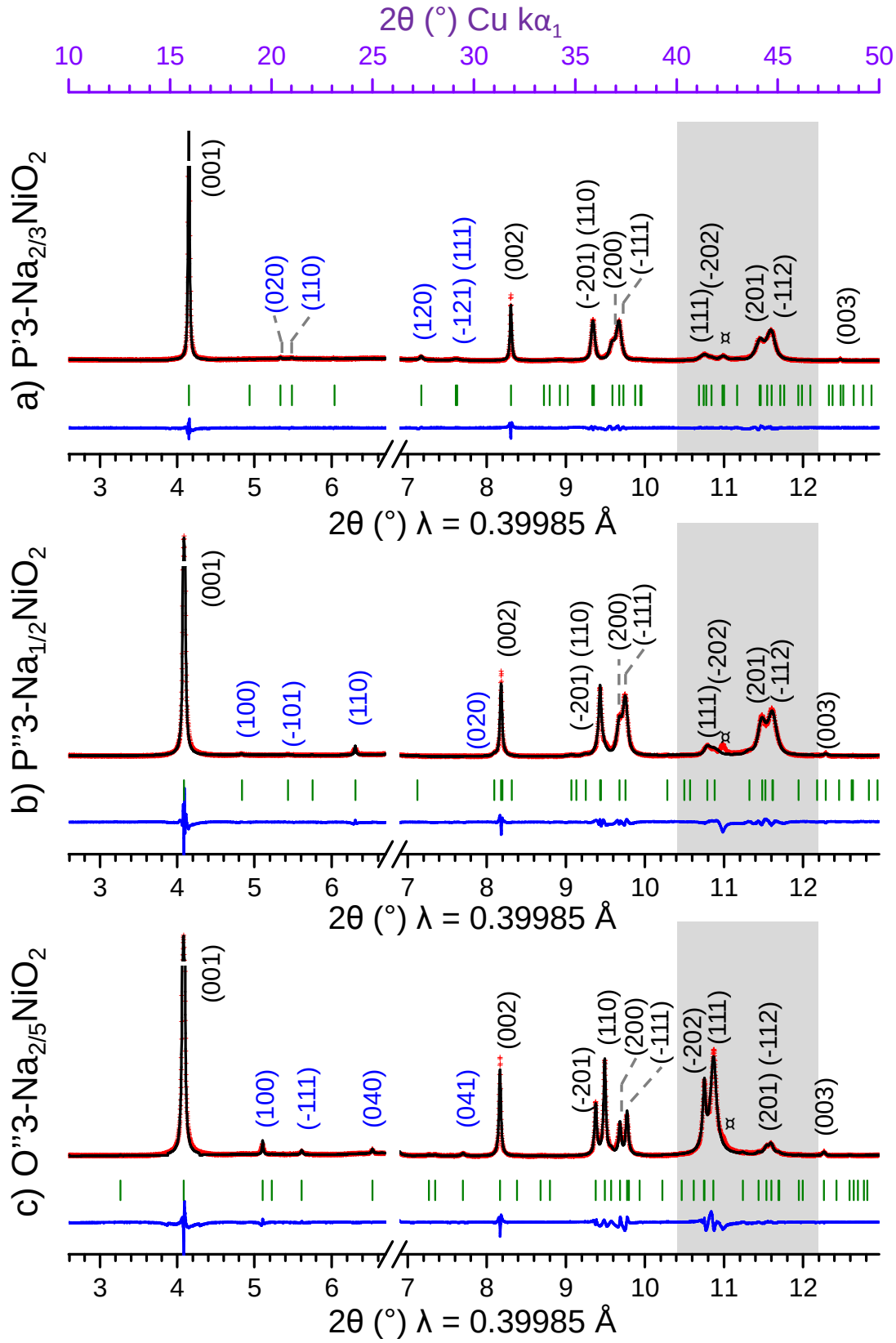

Figure R.25 : Affinements de type LeBail des profils pour les phases (a) P'3-$Na_{2/3}NiO_2$, (b) P''3-$Na_{1/2}NiO_2$ et (c) O'3-$Na_{2/5}NiO_2$. Le symbole ¤ correspond aux pics de diffractions de NiO. Les indices de Miller noirs et bleus correspondent respectivement aux indexations de la sous-maille et de la sur-maille.

Material	Space Group	Supercell parameters				$a_{sub.}/b_{sub.}$
		$a_{sup.}$ (Å)	$b_{sup.}$ (Å)	$c_{sup.}$ (Å)	$\beta_{sup.}$ (°)	
P'3-$Na_{2/3}NiO_2$	$P2_1/a$	4.9715(4) = $\mathbf{a_{sub.}}$	8.589(1) = **3 x** $\mathbf{b_{sub.}}$	5.7391(5) = $\mathbf{c_{sub.}}$	105.84(1) = $\mathbf{\beta_{sub.}}$	1.74
P''3-$Na_{1/2}NiO_2$	$P2_1/m$	4.918(1) = $\mathbf{a_{sub.}}$	5.6633(7) = **2 x** $\mathbf{b_{sub.}}$	5.8155(8) = $\mathbf{c_{sub.}}$	105.52(1) = $\mathbf{\beta_{sub.}}$	1.74
O''3-$Na_{2/5}NiO_2$	C2/m	4.941(3) = $\mathbf{a_{sub.}}$	14.046(8) = **5 x** $\mathbf{b_{sub.}}$	5.856(5) = $\mathbf{c_{sub.}}$	106.53(8) = $\mathbf{\beta_{sub.}}$	1.76

Tableau R.5 : Paramètres de maille et groupes d'espaces des super-mailles des composés définis P'3-$Na_{2/3}NiO_2$, P'3-$Na_{1/2}NiO_2$ et O'3-$Na_{2/5}NiO_2$. Les relations entre les paramètres des sur-mailles et des sous-mailles sont indiquées en gras.

La phase $Na_{\approx 0.8}NiO_2$

Comme il est rappelé sur la **Figure R.26**, le diagramme de diffraction de la phase $Na_{\approx 0.8}NiO_2$ ne montre aucun pic de diffraction supplémentaire dans le domaine 15 – 35 ° (2θ Cu $k\alpha_1$). Cependant, plusieurs pics de diffraction dont l'origine semble être une séparation de pics existants de la symétrie monoclinique sont observés. Une symétrie triclinique est donc attendue pour la phase $Na_{\approx 0.8}NiO_2$. Malheureusement, toute tentative d'indexation de ce diffractogramme a échoué, en partie à cause de l'élargissement des pics de diffraction. Une indexation basée sur les paramètres de maille monocliniques reportés dans [134] n'a également pas donné de résultats plus satisfaisants.

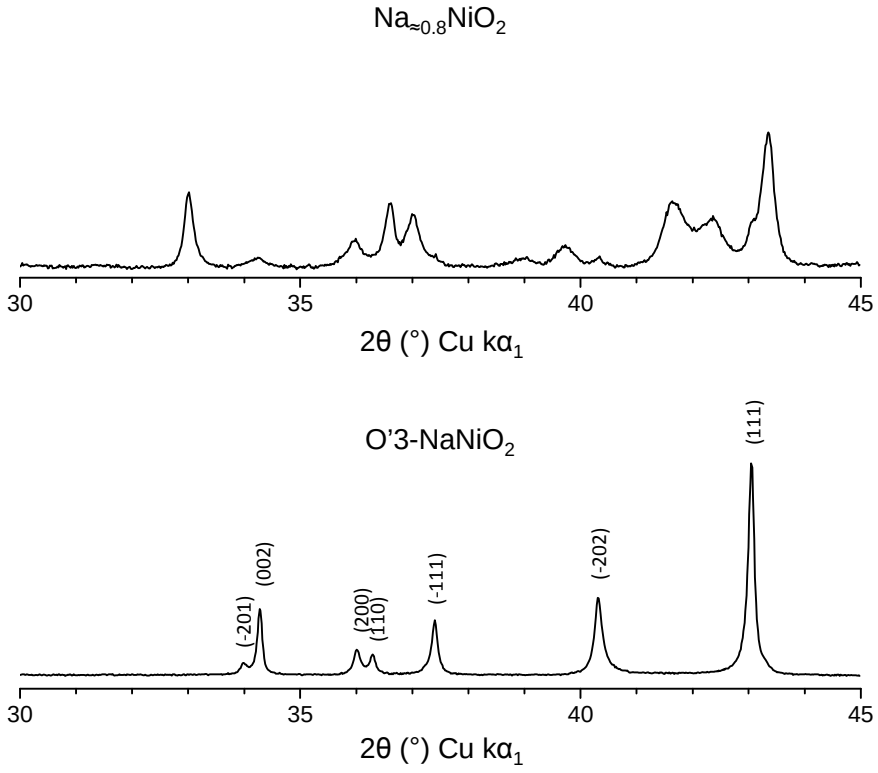

Figure R.26 : Comparaison des diffractogrammes enregistrés lors de l'expérience *in situ* pour les composés définis (haut) $Na_{\approx 0.8}NiO_2$ et (bas) O'3-$NaNiO_2$. Les échelles d'intensité des deux diffractogrammes ne sont pas identiques.

Conclusion générale

Ces travaux représentent une étude des propriétés structurales et électrochimiques des systèmes $Na_xMn_{1-y}Fe_yO_2$ et Na_xNiO_2 utilisés en tant qu'électrodes positives en batteries Na-ion.

La première partie de ce manuscrit concerne la préparation par synthèse de type auto-combustion de quatre phases du système $Na_xMn_{1-y}Fe_yO_2$: P2-$Na_{0.66}Mn_{2/3}Fe_{1/3}O_2$, P2-$Na_{0.62}Mn_{1/2}Fe_{1/2}O_2$, (O3 + O'3)-$Na_{0.77}Mn_{1/2}Fe_{1/2}O_2$ et O3-$Na_{0.77}Mn_{1/3}Fe_{2/3}O_2$. Nous avons montré qu'un rapport Mn : Fe élevé stabilisait l'empilement de type P2 tandis qu'un rapport Mn : Fe faible stabilisait l'empilement de type O3. Parallèlement à ces travaux de thèse, plusieurs études traitant des phases P2 et O3 $Na_xMn_{1-y}Fe_yO_2$ sont sorties. Si les résultats de ces études portant sur les phases de type P2 sont en accord avec nos travaux, nos matériaux de type O3 se sont révélés différents. Cela est probablement dû à (i) un taux de sodium inférieur dans nos matériaux par rapport à la littérature (x = 0.77 *vs.* 1.0) et/ou (ii) à la plus haute température de synthèse employée.

Les caractérisations électrochimiques menées sur les matériaux du système $Na_xMn_{1-y}Fe_yO_2$ ont montré que tous étaient capables de (dés)intercaler réversiblement les ions Na^+ entre 1.5 et 3.8 - 4.3 V. Les matériaux de type P2 se sont montrés les plus performants en terme de capacité, de rétention de capacité et de conductivité ionique. Pour les matériaux de types P2 et O3, accroître le rapport Mn : Fe permet de modifier l'électrochimie. Dans les matériaux de type O3, un plus haut taux de Mn permet d'accroître la rétention de capacité. Dans les matériaux de type P2 un plus haut taux de Mn permet d'accroître la capacité en décharge mais également de cycler le matériau à un plus haut régime.

La désintercalation est accompagnée par les procédés redox suivants : $Mn^{3+} \rightarrow Mn^{4+}$ (bas potentiel) et $Fe^{3+} \rightarrow Fe^{4+}$ (haut potentiel). Parmi les matériaux de composition $Na_xMn_{1/2}Fe_{1/2}O_2$, la transition entre les procédés redox semble être distincte pour la phase de type P2, tandis que les ions Fe^{3+} et Mn^{3+} pourraient être oxydés simultanément pour un domaine restreint pour la phase de type O3.

Au cours du cyclage, les systèmes $Na_xMn_{1-y}Fe_yO_2$ subissent plusieurs transitions structurales, comme l'ont montré des expériences de diffraction des rayons-X menées *in situ* pendant la charge. Tous les matériaux présentent une structure distordue à bas potentiel (1.5 V) / haut taux d'intercalation, induite par l'effet Jahn-Teller coopératif des ions Mn^{3+}. Lors de la charge, les matériaux de type O3 subissent plusieurs transitions (O'3 → O3 → P3 → « X ») dont les domaines d'observations sont dépendants du rapport Mn : Fe. A la fin de la charge (4.3 V), l'apparition d'une phase de faible cristallinité, notée « X », a été observée et reliée à la perte de capacité induite par des cyclages à haut potentiel. Davantage de mesures seront nécessaires pour étudier l'origine de cette phase désintercalée qui pourrait se trouver dans la création de fautes d'empilements dans les espaces inter-feuillets. Cette hypothèse est davantage

appuyée par des mesures de spectroscopie Mössbauer du ^{57}Fe qui ont montré un désordre croissant dans les phases les plus désintercalées.

De même, les matériaux de type P2 possèdent une structure distordue pour les états les plus intercalés. La désintercalation électrochimique est rapidement accompagnée par l'apparition d'une phase P2 observée sur un vaste domaine en composition. Une désintercalation plus poussée (jusqu'à 4.3 V) conduit à l'apparition d'une nouvelle phase peu cristallisée dont l'origine et la structure sont incertaines. Les expériences de diffraction des rayons-X menées *in situ* permettent d'optimiser les conditions de cyclage pour chaque matériau.

Concernant de futures applications, la prochaine étape serait l'optimisation des rapports Mn : Fe dans les phases P2 ainsi que la substitution partielle par d'autres métaux de transition (Al, Ni, Co,…). Cette approche a déjà été envisagée dans la littérature.

La seconde partie de ce manuscrit concerne la phase O'3-$NaNiO_2$ et le diagramme de phase Na_xNiO_2. En jouant sur l'ajout -ou non- d'un excès de sodium et sur la température de synthèse, nous avons pu obtenir des échantillons avec différentes tailles de cristallites (« gros », « moyen » et « petits »). L'électrochimie de ces matériaux s'est révélée différente dans le domaine $2/3 \leq x \leq 1$ et la diffraction des rayons-X menée *in situ* a révélé que trois phases étaient impliquées : O'3-$NaNiO_2$, $Na_{\approx 0.8}NiO_2$ et P'3-$Na_{2/3}NiO_2$. De par la taille importante des cristallites dans la phase dite « gros grains » (0.50 – 1.50 µm), les trois phases sont observées simultanément alors que seules deux phases le sont dans les échantillons dits « moyens grains » et « petits grains ». Une symétrie triclinique est attendue pour la phase $Na_{\approx 0.8}NiO_2$. Cependant, l'élargissement important des pics de diffraction empêche toute indexation du diffractogramme de rayons-X.

L'étude par diffraction des rayons-X menée *in situ* sur l'échantillon dit « moyens grains » a confirmé les transitions entre plusieurs composés définis de structures P'3 et O'3 reportés par Braconnier et al. en 1982. Ces transitions P'3 ↔ O'3 sont facilitées car elles n'impliquent que des glissements des feuillets MO_2. Cependant l'étude *in situ* a montré des mécanismes complexes, notamment lors de la transition entre les phases P'3-$Na_{1/2}NiO_2$ et O'3-$Na_{2/5}NiO_2$ avec la formation d'une phase de structure intermédiaire P'3/O'3. Les diffractogrammes des composés définis x = 2/3, 1/2, 2/5 et 1/3 ont montré des pics de sur-structures, caractéristiques d'ordres longue distance sodium / lacunes. Ces structures ont été davantage étudiées grâce à des mesures de diffraction de rayons-X synchrotron menées à l'ESRF. Cette étude est complétée par les travaux de Dr. S. Kumara Swamy (DFT et RMN du ^{23}Na).

Table of Figures / Tables

Chapter I: The Na_xMO_2 layered oxides and the Na-ion battery technology

Chapter A-II: Characterizations of the O3-$Na_{0.77}Mn_{1/3}Fe_{2/3}O_2$ and (O3+O'3)-$Na_{0.77}Mn_{1/2}Fe_{1/2}O_2$ systems

Figure A-II.16: Comparison of the distances in the MO_6 and NaO_6 polyedra in a) O'3-$Na_{0.96}Mn_{1/3}Fe_{2/3}O_2$, b) O3-$Na_{2/3}Mn_{1/3}Fe_{2/3}O_2$ and c) P3-$Na_{0.61}Mn_{1/3}Fe_{2/3}O_2$. The MO_2 slab thicknesses are also indicated. For the O3 and P3 type phases, only a part of the stacking sequence is shown for clarity purposes.

Figure A-II.17: Galvanostatic cycling curves associated to the $Na_xMn_{1/2}Fe_{1/2}O_2$ system recorded (a) between 1.5 and 3.8 V, (b) between 1.5 and 4.0 V and (c) between 1.5 and 4.3 V at C/50. (d) Associated discharge capacities. The capacities of the first cycles are not shown on (d) as they correspond to the partially intercalated state of the material.

Figure A-II.18: GITT cyclings with steps of 0.01 Na per formula unit and a $\Delta V < 4$ mV.h^{-1} relaxation condition for the (a) $Na_xMn_{1/2}Fe_{1/2}O_2$ and (b) $Na_xMn_{1/3}Fe_{2/3}O_2$ compositions.

Figure A-II.19: (a) XRPD patterns recorded *in situ* (*operando* mode) during the charge of an $Na_xMn_{1/2}Fe_{1/2}O_2$/$NaPF_6$ in PC (1M)/Na cell along with (b) the corresponding galvanostatic curve. The red XRPD patterns correspond to the limitations of the different structural domains.

Figure A-II.20: Inverse representation of the *operando in situ* experiment carried out on the $Na_xMn_{1/2}Fe_{1/2}O_2$ system: (a) XRPD patterns and (b) corresponding galvanostatic curve. Blue Miller indexes: O3 and P3 phases. The red XRPD patterns correspond to the limitations of the different structural domains.

Figure A-II.21: Evolution of the (a) interslab distances and (b) cell parameters of the different phases observed in the $Na_xMn_{1/2}Fe_{1/2}O_2$ system during the *operando in situ* XRPD study. The galvanostatic curve is shown as a guide on (c).

Figure A-II.22: XRPD patterns recorded *in situ* (*operando* mode) during the charge of an $Na_xMn_{1/2}Fe_{1/2}O_2$/$NaPF_6$ in PC (1M)/Na cell: highlighting of the intermediate phases (green, pink and blue arrow).

Figure A-II.23: Comparison of the XRPD patterns of the $Na_xMn_{1/2}Fe_{1/2}O_2$ system recorded under constant voltage at 1.5 V: (a) at the beginning of the *operando in situ* XRPD experiment and (b) after cycling to 4.3 V and discharge back to 1.5 V.

Figure A-II.24: Observed and calculated (Rietveld Method) synchrotron XRPD patterns of the O'3-$Na_{0.95}Mn_{1/2}Fe_{1/2}O_2$ phase.

Table A-II.6: Structural parameters and reliability factors calculated from the refinement of the structure of the O'3-$Na_{0.95}Mn_{1/2}Fe_{1/2}O_2$ phase from the synchrotron XRPD pattern.

Figure A-II.25: Open current voltage charging curves extracted from the GITT cycling cones for (red) $Na_xMn_{1/2}Fe_{1/2}O_2$ and (blue) $Na_xMn_{1/3}Fe_{2/3}O_2$. The dashed lines represent the expected position of the voltage jump associated to the change of redox process during charge if the redox potentials of Fe^{4+}/Fe^{3+} and Mn^{4+}/Mn^{3+} are well separated.

Figure A-II.26: *Operando In situ* X-ray Absorption Near Edge Spectroscopy (XANES) spectra corresponding to the Mn and Fe K-edges and recorded during the charge of the (a,b) Na//$Na_xMn_{1/3}Fe_{2/3}O_2$ and (c,d) Na//$Na_xMn_{1/2}Fe_{1/2}O_2$ cells. The Mn references for Mn^{3+} (Mn_2O_3) and Mn^{4+} (Li_2MnO_3) are given in (e). The Fe references for Fe^{2+} (FeO), Fe^{3+} (Fe_2O_3, $NaFeO_2$) and $Fe^{3.45+}$ ($Na_{0.55}FeO_2$) are given in (f).

Figure A-II.27: ^{57}Fe Mössbauer spectra (a) of the pristine material and (b) recorded *in situ* during the charge of a $Na_xMn_{1/3}Fe_{2/3}O_2$ //Na battery.

Table A-II.7: Mössbauer parameters corresponding to the spectrum of the O3-$Na_{0.77}Mn_{1/3}Fe_{2/3}O_2$ pristine material.

Figure A-II.28: Superposition of different Mössbauer spectra in the $Na_xMn_{1/3}Fe_{2/3}O_2$ system: (a) x = 0.96 (black line), x = 0.86 (red line) and x = 0.67 (blue line) compositions and (b) x = 0.96 (black line), x = 0.58 (red line) and x = 0.38 (blue line) compositions.

Table A-II.8: Developed formulas, awaited Fe^{n+} populations and Mössbauer parameters corresponding to the fit of the spectra presented in **Figure A-II.27b** for the $Na_xMn_{1/3}Fe_{2/3}O_2$ system. The standard deviations on the isomer shift values are equal to 0.002 mm.s^{-1}. The population of the $Fe^{(3+z)+}$ is distributed into the Fe^{3+} and Fe^{4+} sites by the formula: $P(Fe^{3+}) = (\delta(Fe^{3+z})-\delta(Fe^{4+})) / (\delta(Fe^{3+})-\delta(Fe^{4+}))$.

Figure A-II.29: ^{57}Fe Mössbauer spectra recorded *ex situ* for the $Na_xMn_{1/2}Fe_{1/2}O_2$ system at the (a) x = 0.95, (b) x = 0.67, (c) x = 0.55, (d) x = 0.44 and (e) x = 0.22 compositions. Black circles: experimental and red lines: calculated. The different Mössbauer sites deduced from the Lorentzian fittings are represented by the blue, pink and green lines.

Figure A-II.30: Comparison of the Mössbauer spectra recorded for the $Na_xMn_{1/2}Fe_{1/2}O_2$ system. Black dots: experimental and red line: calculated.

Table A-II.9: Developed formulas, awaited Fe^{n+} populations and Mössbauer parameters corresponding to the fit of the spectra of the $Na_xMn_{1/2}Fe_{1/2}O_2$ system presented in **Figure A-II.29**. The standard deviations on the isomer shift values are equal to 0.002 mm.s^{-1}. The population of the $Fe^{(3+z)+}$ is distributed into the Fe^{3+} and Fe^{4+} sites by the formula: $P(Fe^{3+}) = (\delta(Fe^{3+z})-\delta(Fe^{4+})) / (\delta(Fe^{3+})-\delta(Fe^{4+}))$.

Chapter A-III: Characterizations of the P2-$Na_{0.62}Mn_{1/2}Fe_{1/2}O_2$ and P2-$Na_{0.66}Mn_{2/3}Fe_{1/3}O_2$ systems

Figure A-III.1: Observed and calculated (Rietveld method) synchrotron XRPD patterns of P2-$Na_{0.62}Mn_{1/2}Fe_{1/2}O_2$. Red dots: experimental, black line: calculated, blue line: difference and green bars: Bragg positions.

Table A-III.1: Structural parameters and reliability factors calculated from the synchrotron XRPD pattern of P2-$Na_{0.62}Mn_{1/2}Fe_{1/2}O_2$.

Figure A-III.2: Observed and calculated (Rietveld method) (a) XRPD and (b) neutron powder diffraction patterns of P2-$Na_{0.62}Mn_{1/2}Fe_{1/2}O_2$. Red crosses: experimental, black line: calculated, blue line: difference and green bars: Bragg positions.

Table A-III.2: Structural parameters and reliability factors calculated from the combined refinement of P2-$Na_{0.62}Mn_{1/2}Fe_{1/2}O_2$ from the XRPD and neutron powder diffraction patterns.

Figure A-III.3: Galvanostatic cycling curves associated to the $Na_xMn_{1/2}Fe_{1/2}O_2$ system and recorded (a,b) between 1.5 and 3.8 V, (c,d) between 1.5 and 4.0 V) and (e,f) between 1.5 and 4.3 V at C/20.

Figure A-III.4: Discharge capacities associated to the galvanostatic curves of the $Na_xMn_{1/2}Fe_{1/2}O_2$ system recorded in the different voltage ranges (**Figure A-III.3**).

Figure A-III.5: Galvanostatic curves recorded at a C/20 rate between 1.5 – 4.3 V (in red) and then between 1.5 – 4.0 V (in blue) for the $Na_xMn_{1/2}Fe_{1/2}O_2$ system. The insert represents the evolution of the associated discharge capacities.

Figure A-III.6: SEM micrographs of (a, b) an un-cycled electrode involving the P2-$Na_{0.62}Mn_{1/2}Fe_{1/2}O_2$ material and similar electrodes cycled 3 times in the (c, d) 2.0 – 4.0 V range and in the (e, f) 2.0 – 4.3 V one.

Figure A-III.7: GITT cycling of the $Na_xMn_{1/2}Fe_{1/2}O_2$ system recorded with steps of ≈0.01 Na per formula unit. Relaxation condition: $\Delta V < 4$ mV.h^{-1}.

Figure A-III.8: Evolution of the discharge capacity of the $Na_xMn_{1/2}Fe_{1/2}O_2$ system for several rate values.

Figure A-III.9: (a) XRPD patterns recorded *in situ* (*operando* mode) during the charge of a $Na_xMn_{1/2}Fe_{1/2}O_2$/$NaPF_6$ in PC (1M) + 2 wt% FEC/Na cell along with (b) the corresponding galvanostatic curve. The red XRPD patterns correspond to the limits of the different structural domains.

Figure A-III.10: Inverse representation of Figure **A-III.9**: (a) XRPD patterns and (b) corresponding galvanostatic curve. The red XRPD patterns correspond to the limits of the different structural domains.

Figure A-III.11: Evolution of (a) the interslab distance and (b) the a and b cell parameters (P'2 and P2 phases) or M-M distance ("Z" phase) of the $Na_xMn_{1/2}Fe_{1/2}O_2$ phases upon sodium deintercalation. The galvanostatic curve versus x is shown as a guide in (c).

Figure A-III.12: Comparison of the XRPD patterns of P'2 $Na_xMn_{1/2}Fe_{1/2}O_2$ phases recorded after (a) the first and (b) second discharge at 1.5 V, and maintained at the voltage until a negligible current was observed.

Figure A-III.13: Observed and calculated (Rietveld method) synchrotron XRPD patterns of the P'2-$Na_{\approx 1}Mn_{1/2}Fe_{1/2}O_2$ phase. Red crosses: experimental, black line: calculated, blue line: difference and green bars: Bragg positions. The * symbol indicates the graphite diffraction lines which were excluded for the refinement.

Table A-III.3: Structural parameters and reliability factors calculated from the synchrotron XRPD pattern of the P'2- $Na_{\approx 1}Mn_{1/2}Fe_{1/2}O_2$ phase.

Figure A-III.14: Representation of the MO_6 and NaO_6 polyhedra in the P'2-$Na_{\approx 1}Mn_{1/2}Fe_{1/2}O_2$ phase.

Figure A-III.15: Observed and calculated (Rietveld method) synchrotron XRPD patterns for the P2-$Na_{0.66}Mn_{2/3}Fe_{1/3}O_2$ pristine material. Red dots: experimental, black line: calculated, blue line: difference and green bars: Bragg positions.

Table A-III.4: Structural parameters and reliability factors calculated from the synchrotron XRPD pattern of the P2- $Na_{0.66}Mn_{2/3}Fe_{1/3}O_2$ pristine material.

Figure A-III.16: Observed and calculated (Rietveld method) (a) XRPD and (b) neutron powder diffraction patterns for the P2-$Na_{0.662}Mn_{2/3}Fe_{1/3}O_2$ pristine material. Red crosses: experimental, black line: calculated,

blue line: difference and green bars: Bragg positions. The * symbol on the neutron powder diffraction pattern indicates a diffraction peak from the vanadium sample container.

Table A-III.5: Structural parameters and reliability factors calculated from the combined refinement of the P2-$Na_{0.66}Mn_{2/3}Fe_{1/3}O_2$ pristine material from the XRPD and neutron powder diffraction patterns.

Figure A-III.17: Galvanostatic cycling curves associated to the $Na_xMn_{2/3}Fe_{1/3}O_2$ system and recorded (a) between 1.5 and 3.8 V, (b) between 1.5 and 4.0 V and (c) between 1.5 and 4.3 V at C/20. (d) Associated discharge capacities. The capacities of the first cycle are not shown in (d) as they correspond to the partially intercalated state.

Figure A-III.18: GITT cycling curve recorded with steps of ≈ 0.01 Na^+ per formula unit and a $\Delta V < 4$ mV.h^{-1} relaxation condition for the $Na_xMn_{2/3}Fe_{1/3}O_2$ system (a). The red arrows indicate slight variation in the slope of the curve. The GITT cycling curve recorded for the $Na_xMn_{1/2}Fe_{1/2}O_2$ system is given in (b) as a comparison.

Figure A-III.19: Evolution of the discharge capacity of the $Na_xMn_{2/3}Fe_{1/3}O_2$ system for several rate values.

Figure A-III.20: (a) XRPD patterns of the $Na_xMn_{2/3}Fe_{1/3}O_2$ material recorded *in situ* (*operando* mode) during the charge of a $Na_xMn_{2/3}Fe_{1/3}O_2/NaPF_6$ in PC (1M) + 2 wt% FEC/Na cell along with (b) the corresponding cycling curve. The red XRPD patterns correspond to the limits of the different structural domains.

Figure A-III.21: Inversed representation of the *operando in situ* XRPD experiment carried out on the $Na_xMn_{2/3}Fe_{1/3}O_2$ system: (a) XRPD patterns and (b) corresponding cycling curve. The red XRPD patterns correspond to the limits of the different structural domains.

Figure A-III.22: Evolution of the (a) interslab distance and (b) a and b cell parameters of the different $Na_xMn_{2/3}Fe_{1/3}O_2$ phases upon sodium deintercalation. The galvanostatic curve versus x is also shown as a guide in (c).

Figure A-III.23: Comparison of the XRPD patterns recorded for the P'2-$Na_xMn_{2/3}Fe_{1/3}O_2$ phases after (a) the first and (b) second discharge at 1.5 V, and maintained at the voltage until a negligible current was observed.

Figure A-III.24: (a) XRPD patterns recorded *in situ* during the relaxation periods of a $Na_xMn_{2/3}Fe_{1/3}O_2/NaPF_6$ in PC (1M) + 2 wt% FEC /Na cell along with (b) the corresponding GITT curve. Only the most important reflections are labeled for clarity purposes.

Figure A-III.25: (a) Zoom in the 30 – 45 ° region of the XRPD patterns recorded *in situ* during the relaxation periods of a $Na_xMn_{2/3}Fe_{1/3}O_2/NaPF_6$ in PC (1M) + 2 wt% FEC /Na cell along with (b) the corresponding GITT curve. Only the most important reflections are labeled for clarity purposes.

Figure A-III.26: Evolution of the (a) interslab distance and (b) a and b cell parameters of the P2 and P'2-$Na_xMn_{2/3}Fe_{1/3}O_2$ phases upon sodium intercalation. The GITT E = f(x) curve is also shown as a guide in (c).

Figure A-III.27: Observed and calculated (Rietveld method) XRPD patterns of the intercalated P'2-$Na_{0.96}Mn_{2/3}Fe_{1/3}O_2$ phase. Red crosses: experimental, black line: calculated, blue line: difference and green bars: Bragg positions. The * symbol indicates the position of the graphite diffraction lines.

Table A-III.6: Structural parameters and reliability factors calculated from the XRPD diagram of the P'2-$Na_{0.96}Mn_{2/3}Fe_{1/3}O_2$ phase.

Figure A-III.28: Open current voltage charging curves extracted from the GITT cycling cones for (blue) $Na_xMn_{1/2}Fe_{1/2}O_2$ and (red) $Na_xMn_{2/3}Fe_{1/3}O_2$. The dashed lines represent the expected position of the voltage jump associated to the change of redox process during charge if the redox potentials of Fe^{4+}/Fe^{3+} and Mn^{4+}/Mn^{3+} are well separated.

Figure A-III.29: X-ray absorption near edge spectroscopy spectra recorded *in situ* and corresponding to the (a) Mn and (b) Fe K-edges of a $Na_xMn_{1/2}Fe_{1/2}O_2$ electrode. The spectra of the (c) Mn and (d) Fe references compounds are also given.

Table A-III.7: Mössbauer parameters deduced from the Lorentzian and Distribution fits of the Mössbauer spectrum of the P2-$Na_{0.62}Mn_{1/2}Fe_{1/2}O_2$ pristine material.

Figure A-III.30: (a) Lorentzian and (b) distribution fits of the Mössbauer spectrum of the P2-$Na_{0.62}Mn_{1/2}Fe_{1/2}O_2$ pristine material. (c) Distribution profile corresponding to the distribution fit.

Figure A-III.31: ^{57}Fe Mössbauer spectra of (a) P'2-$Na_{\approx 1}Mn_{1/2}Fe_{1/2}O_2$, (b) P2-$Na_{0.62}Mn_{1/2}Fe_{1/2}O_2$, (c) P2-$Na_{0.5}Mn_{1/2}Fe_{1/2}O_2$, (d) P2-$Na_{0.45}Mn_{1/2}Fe_{1/2}O_2$, (e) "Z"-$Na_{0.24}Mn_{1/2}Fe_{1/2}O_2$ and (f) "Z"-$Na_{0.14}Mn_{1/2}Fe_{1/2}O_2$. Black

circles: experimental and red line: calculated. Blue, pink, green and brown lines: ^{57}Fe Mössbauer sites (Lorentzian fits only).

Table A-III.8: Developed formulas, awaited Fe^{n+} populations and Mössbauer parameters corresponding to the fit of the spectra of the $Na_xMn_{1/2}Fe_{1/2}O_2$ system presented in **Figure A-III.31**. The standard deviations on the isomer shift values are equal to 0.002 $mm.s^{-1}$. The population of the $Fe^{(3+z)+}$ is distributed into the Fe^{3+} and Fe^{4+} sites by the formula: $P(Fe^{3+}) = (\delta(Fe^{3+z})-\delta(Fe^{4+})) / (\delta(Fe^{3+})-\delta(Fe^{4+}))$.

Figure A-III.32: Comparison of the Mössbauer spectra recorded in the P2-based $Na_xMn_{1/2}Fe_{1/2}O_2$ system.

Table A-III.9: Mössbauer parameters deduced from the Lorentzian and Distribution fits of the Mössbauer spectrum of the P2-$Na_{0.66}Mn_{2/3}Fe_{1/3}O_2$ pristine material.

Figure A-III.33: (a) Lorentzian and (b) distribution fits of the Mössbauer spectrum of the P2-$Na_{0.66}Mn_{2/3}Fe_{1/3}O_2$ pristine material. (c) Distribution profile corresponding to the distribution fit.

Figure A-III.34: ^{57}Fe Mössbauer spectra of (a) P'2-$Na_{0.96}Mn_{2/3}Fe_{1/3}O_2$, (b) $Na_{0.26}Mn_{2/3}Fe_{1/3}O_2$. Black circles: experimental and red line: calculated.

Table A-III.10: Developed formulas, awaited Fe^{n+} populations and Mössbauer parameters corresponding to the fit of the spectra of the $Na_xMn_{2/3}Fe_{1/3}O_2$ system presented in **Figure A-III.34**. The standard deviations on the isomer shift values are equal to 0.002 $mm.s^{-1}$. The population of the $Fe^{(3+z)+}$ is distributed into the Fe^{3+} and Fe^{4+} sites by the formula: $P(Fe^{3+}) = (\delta(Fe^{3+z})-\delta(Fe^{4+})) / (\delta(Fe^{3+})-\delta(Fe^{4+}))$.

Chapter A-IV: Influence of the Mn / Fe ratio on the electrochemical and structural properties

Résumé étendu

Figure R.1 : (a) Structures des phases dites « O3 », « P3 » et « P2 », d'après [36]. Les différents environnements autour des ions Na sont également représentés. (b) Structures distordues (« O'3 », « P'3 » et « P'2 ») dérivant des structures « O3 », « P3 » et « P2 ».

Figure R.2 : Diffractogrammes de rayons-X expérimentaux et calculés pour (a) P2-$Na_{0.77}Mn_{2/3}Fe_{1/3}O_2$, (b) P2-$Na_{0.67}Mn_{1/2}Fe_{1/2}O_2$, (c) (O3+O'3)$Na_{0.82}Mn_{1/2}Fe_{1/2}O_2$ et (d) O3-$Na_{0.82}Mn_{1/3}Fe_{2/3}O_2$ phases. Croix rouges : observé, ligne noire : calculé, ligne bleue: différence et barres vertes : Bragg. (a, b, d) : affinement de type Rietveld et (c) : affinement de type LeBail.

Tableau R.1 : Paramètres de maile et distances inter-feuillet des phases P2-$Na_{0.77}Mn_{2/3}Fe_{1/3}O_2$, P2-$Na_{0.67}Mn_{1/2}Fe_{1/2}O_2$, (O3+O'3), $Na_{0.82}Mn_{1/2}Fe_{1/2}O_2$ et O3-$Na_{0.82}Mn_{1/3}Fe_{2/3}O_2$.

Figure R.3 : Micrographes (MEB) des phases (a) P2-$Na_{0.67}Mn_{1/2}Fe_{1/2}O_2$ et (b) O3-$Na_{0.82}Mn_{1/3}Fe_{2/3}O_2$.

Figure R.4 : Courbes de cyclage galvanostatique (C/50) de batteries enregistrées entre 1.5 et 3.8 V : (a) P2-$Na_xMn_{0.66}Mn_{1/3}Fe_{2/3}O_2$, (b) P2-$Na_{0.62}Mn_{1/2}Fe_{1/2}O_2$, (c) (O3+O'3)-$Na_{0.77}Mn_{1/2}Fe_{1/2}O_2$ et (d) O3-$Na_{0.77}Mn_{1/3}Fe_{2/3}O_2$. Un agrandissement autour du point de départ est donné pour chacune des courbes.

Figure R.5 : Capacités en décharge extraites des courbes galvanostatiques (**Figure R.4**) : P2-$Na_{0.66}Mn_{2/3}Fe_{1/3}O_3$ (noir), P2-$Na_{0.62}Mn_{1/2}Fe_{1/2}O_2$ (bleu), (O3+O'3)-$Na_{0.77}Mn_{1/2}Fe_{1/2}O_2$ (rouge) et O3-$Na_{0.77}Mn_{1/3}Fe_{2/3}O_2$ (vert).

Figure R.6 : (a) Diffractogrammes de rayons-X enregistrés *in situ* (*operando*) pendant la charge d'une cellule $Na_xMn_{1/2}Fe_{1/2}O_2/NaPF_6$ in PC (1M)/Na. Les diffractogrammes rouges correspondent aux limites des différents domaines structuraux. (b) Courbe galvanostatique correspondante.

Figure R.7 : Représentation inverse de la **Figure R.6**. (a) Diffractogrammes de rayons-X enregistrés *in situ* (*operando*) pendant la charge d'une cellule $Na_xMn_{1/2}Fe_{1/2}O_2/NaPF_6$ in PC (1M)/Na. Les diffractogrammes rouges correspondent aux limites des différents domaines structuraux. (b) Courbe galvanostatique correspondante.

Figure R.8 : Evolution de (a) la distance inter-feuillet et (b) les paramètres de maille a et b des phases O'3, O3 et P3-$Na_xMn_{1-y}Fe_yO_2$ au cours de la désintercalation électrochimique. (c) Courbe galvanostatique correspondante.

Figure R.9 : (a,b) Agrandissement de la région $0.3 \leq x \leq 0.7$ des diffractogrammes de rayons-X enregistrés *in situ* (*operando*) lors de l'expérience menée sur le système de type O3 $Na_xMn_{1/3}Fe_{2/3}O_2$. Les lignes rouges mettent en évidence les limites des différents domaines structuraux.

Figure R.10 : Représentation schématique de l'évolution du diagramme de phase de $Na_xMn_{1-3}Fe_{2/3}O_2$ au cours de la désintercalation électrochimique déduit de l'expérience *in situ*.

Figure R.11 : Diffractogrammes de rayons-X enregistrés *in situ* pendant une étape potentiostatique (1.5 V) après les (a) première et (b) seconde décharges de l'expérience sur le système $Na_xMn_{1/3}Fe_{2/3}O_2$.

Figure R.12. Spectres XANES enregistrés aux seuils K du Mn et de Fe *in situ* (*operando*) pendant la charge d'une cellule $Na_xMn_{1-y}Fe_yO_2$//Na. La cellule a été préalablement déchargée.

Figure R.12. Spectres XANES enregistrés aux seuils K du Mn et de Fe *in situ* (*operando*) pendant la charge d'une cellule $Na_xMn_{1-y}Fe_yO_2$//Na. La cellule a été préalablement déchargée.

Tableau R.2 : Paramètres Mössbauer correspondant au spectre de O3-$Na_{0.77}Mn_{1/3}Fe_{2/3}O_2$.

Tableau R.3 : Formules développées et paramètres Mössbauer correspondant aux affinements des spectres présentés **Figure R.13**. Les écarts-types sur les valeurs des déplacements isomériques sont égaux à 0.002 $mm.s^{-1}$. La population du site $Fe^{(3+z)+}$ est redistribuée entre les sites Fe^{3+} et Fe^{4+} selon la formule : $P(Fe^{3+}) = (\delta(Fe^{3+z})-\delta(Fe^{4+})) / (\delta(Fe^{3+})-\delta(Fe^{4+}))$.

Figure R.14 : Domaines d'observation des phases O'3, O3, P3 et « X » (systèmes de type O3) et des phases P'2, P2 et « Z » (systèmes de type P2) en fonction du taux de Na.

Figure R.15 : Evolution des rapports $a_{mon.}/b_{mon.}$ (phases O'3) et $b_{orth.}/a_{orth.}$ (phases P'2) en fonction du rapport Mn : Fe. O3-$NaFeO_2$: données provenant de [35]. O'3-$NaMnO_2$: données provenant de [44].

Figure R.16 : Evolution des distances M-O des octaèdres MO_6 dans les phases P'2 et O'3-$Na_{\approx 1}Mn_{1-y}Fe_yO_2$. O'3-$NaMnO_2$: données provenant de [44].

Figure R.17 : diffractogrammes observés et calculés (affinement de type Rietveld) de la phase O'3-$NaNiO_2$ (moyens grains). Croix rouges : observé, ligne noire : calculé, ligne bleue : différence et traits verticaux verts : réflexions. Insert : cliché MEB du même échantillon.
Tableau R.4 : Paramètres structuraux et facteurs de mérite calculés à partir du diffractogramme de O'3-$NaNiO_2$ (moyens grains).
Figure R.18 : (a) courbe galvanostatique et (b) évolution de la capacité en décharge pour une batterie Na_xNiO_2 (moyens grains) / $NaPF_6$ in PC (1M) + 2 wt% FEC / Na. Régime : C/50.
Figure R.19 : Courbe de cyclage en mode GITT enregistrée pour une batterie Na_xNiO_2 (moyens grains) / $NaPF_6$ in PC (1M) + 2 wt% FEC / Na. Régime : C/50 (pas de 0.005 Na^+ / unité formulaire), temps de relaxation : 30 minutes.
Figure R.20 : Evolution des diffractogrammes de rayons-X enregistré *in situ* pendant la charge d'une batterie Na_xNiO_2 (moyens grains) / $NaPF_6$ in PC (1M) + 2 wt% FEC / Na. Les diffractogrammes représentés en rouge correspondent aux composés définis.
Figue R.21 : (a,b) Zooms dans le domaine 15,5 – 17,3° (2θ Cu kα_1) des diffractogrammes présentés **Figure R.20**.
Figure R.22 : Evolution des distances inter-feuillets déduites de la position des pics de diffraction $(001)_{mon.}$ pour les différentes phases Na_xNiO_2.
Figure R.23 : Zoom dans le domaine 15,4 – 16,6° (2θ Cu kα_1) des diffractogrammes dans le domaine $2/5 \leq x \leq 1/2$.
Figure R.24 : Diffractogrammes correspondant aux composés définis observés pour x = 1, 0.8, 2/3, 1/2, 2/5 et 1/3. Les flèches noires mettent en évidence la présence de pics de diffraction supplémentaires.
Figure R.25 : Affinements de type LeBail des profils pour les phases (a) P'3-$Na_{2/3}NiO_2$, (b) P''3-$Na_{1/2}NiO_2$ et (c) O'3-$Na_{2/5}NiO_2$. Le symbole ¤ correspond aux pics de diffractions de NiO. Les indices de Miller noirs et bleus correspondent respectivement aux indexations de la sous-maille et de la sur-maille.
Tableau R.5 : Paramètres de maille et groupes d'espaces des super-mailles des composés définis P'3-$Na_{2/3}NiO_2$, P'3-$Na_{1/2}NiO_2$ et O'3-$Na_{2/5}NiO_2$. Les relations entre les paramètres des sur-mailles et des sous-mailles sont indiquées en gras.
Figure R.26 : Comparaison des diffractogrammes enregistrés lors de l'expérience *in situ* pour les composés définis (haut) $Na_{\approx 0.8}NiO_2$ et (bas) O'3-$NaNiO_2$. Les échelles d'intensité des deux diffractogrammes ne sont pas identiques.

Bibliography

[1] Goldztaub, S. *C. R. Acad. Sci. Paris* **1933,** 196, 280.
[2] Dyer, L. D.; Borie, B. S.; Smith, G. P. *J. Am. Chem. Soc.* **1954,** 76, 1499.
[3] Dodero, M.; Déportes, C. *C. R. Acad. Sci. Paris* **1956,** 242, 2939.
[4] Fouassier, C.; Matejka, G.; Reau, J.-M.; Hagenmuller, P. *J. Solid State Chem.* **1973,** 6, 532.
[5] Parant, J.-P.; Olazcuaga, R.; Devalette, M.; Fouassier, C.; Hagenmuller, P. *J. Solid State Chem.* **1971,** 3, 1
[6] Goodenough, J. B.; Wickham, D. G.; Croft, W. J. *J. Appl. Phys.* **1958,** 29, (3), 382.
[7] Johnston, W. D.; Heikes, R. R.; Sestrich, D. *J. Phys. Chem. Solids* **1958,** 7, (1), 1.
[8] Kobayashi, K.; Kosuge, K.; Kachi, S. *Mater. Res. Bull.* **1969,** 4, (2), 95.
[9] Rüdorff, V. W.; Becker, H. *Z. Naturforsch* **1954,** 9, 614.
[10] Mizushima, K.; Jones, P. C.; Wiseman, P. J.; Goodenough, J. B. *Mater. Res. Bull.* **1980,** 15, 783.
[11] *Handbook of Batteries*. Third ed.; 1995.
[12] Lee, K. K.; Yoon, W. S.; Kim, K. B.; Lee, K. Y.; Hong, S. T. *J. Power Sources* **2001,** 97–98, (0), 308.
[13] Guilmard, M.; Pouillerie, C.; Croguennec, L.; Delmas, C. *Solid State Ionics* **2003,** 160, (1–2), 39.
[14] Madhavi, S.; Subba Rao, G. V.; Chowdari, B. V. R.; Li, S. F. Y. *J. Power Sources* **2001,** 93, (1–2), 156.
[15] Weaving, J. S.; Coowar, F.; Teagle, D. A.; Cullen, J.; Dass, V.; Bindin, P.; Green, R.; Macklin, W. J. *J. Power Sources* **2001,** 97–98, (0), 733.
[16] Lu, Z.; MacNeil, D. D.; Dahn, J. R. *Electrochem. Solid. St.* **2001,** 4, (12), A200.
[17] Ohzuku, T.; Makimura, Y. *Chemistry Letters* **2001**, (7), 642.
[18] Padhi, A. K.; Nanjundaswamy, K. S.; Goodenough, J. B. *J. Electrochem. Soc.* **1997,** 144, (4), 1188.
[19] Tarascon, J. M.; Wang, E.; Shokoohi, F. K.; McKinnon, W. R.; Colson, S. *J. Electrochem. Soc.* **1991,** 138, (10), 2859.
[20] Thackeray, M. M.; Johnson, P. J.; de Picciotto, L. A.; Bruce, P. G.; Goodenough, J. B. *Mater. Res. Bull.* **1984,** 19, (2), 179.
[21] Thackeray, M. M.; David, W. I. F.; Bruce, P. G.; Goodenough, J. B. *Mater. Res. Bull.* **1983,** 18, (4), 461.
[22] Slater, M. D.; Kim, D.; Lee, E.; Johnson, C. S. *Adv. Funct. Mater.* **2013,** 23, (8), 947.
[23] Palomares, V.; Casas-Cabanas, M.; Castillo-Martínez, E.; Han, M. H.; Rojo, T. *Energ. Environ. Sci.* **2013,** 6, (8), 2312.
[24] Palomares, V.; Serras, P.; Villaluenga, I.; Hueso, K. B.; Carretero-González, J.; Rojo, T. *Energ. Environ. Sci.* **2012,** 5, (3), 5884.
[25] Xu, J.; Lee, D. H.; Meng, Y. S. *Func. Mater. Lett.* **2013,** 06, (01), 1330001.
[26] Yabuuchi, N.; Kajiyama, M.; Iwatate, J.; Nishikawa, H.; Hitomi, S.; Okuyama, R.; Usui, R.; Yamada, Y.; Komaba, S. *Nat. Mat.* **2012,** 11, (6), 512
[27] Yoncheva, M.; Stoyanova, R.; Zhecheva, E.; Kuzmanova, E.; Sendova-Vassileva, M.; Nihtianova, D.; Carlier, D.; Guignard, M.; Delmas, C. *J. Mater. Chem.* **2012,** 22, (44), 23418
[28] Thorne, J. S.; Dunlap, R. A.; Obrovac, M. N. *J. Electrochem. Soc.* **2012,** 160, (2), A361
[29] Singh, G.; Acebedo, B.; Cabanas, M. C.; Shanmukaraj, D.; Armand, M.; Rojo, T. *Electrochem. Comm.* **2013,** 37, 61
[30] Kodera, T.; Ogihara, T. *J. Ceram. Soc. Jpn* **2014,** 122, (6), 483
[31] Park, K.; Han, D.; Kim, H.; Chang, W.-s.; Choi, B.; Anass, B.; Lee, S. *R. Soc. Chem. Adv.* **2014,** 4, (43), 22798
[32] Zhao, J.; Xu, J.; Lee, D. H.; Dimov, N.; Meng, Y. S.; Okada, S. *J. Power Sources* **2014,** 264, 235
[33] Zhu, H.; Lee, K. T.; Hitz, G. T.; Han, X.; Li, Y.; Wan, J.; Lacey, S.; Cresce, A.; Xu, K.; Wachsman, E.; Hu, L. *ACS Appl. Mater. Interfaces* **2014,** 6, (6), 4242
[34] Vassilaras, P.; Ma, X.; Li, X.; Ceder, G. *J. Electrochem. Soc.* **2012,** 160, (2), A207.
[35] Takeda, Y.; Nakahara, K.; Nishijima, M.; Imanishi, N.; Yamamoto, O.; Takano, M.; Kanno, R. *Mater. Res. Bull.* **1994,** 29, (6), 659
[36] Delmas, C.; Fouassier, C.; Hagenmuller, P. *Phys. 99B* **1980**, 81
[37] Maazaz, A.; Delmas, C.; Hagenmuller, P. *C. R. Acad. Sci. Paris* **1982,** 295, 759
[38] Braconnier, J.-J.; Delmas, C.; Hagenmuller, P. *Mater. Res. Bull.* **1982,** 17, 993

[39] Barker, M. G.; Hooper, A. J. *J. Chem. Soc., Dalton Trans.* **1973**, 1517.
[40] Jahn, H. A.; Teller, E. *Proc. R. Soc. Lond. A* **1937,** 161, 220.
[41] Cotton, A. F.; Wilkinson, G.; Gaus, P. L., *Basic Inorganic Chemistry*, 3rd Edition ed.; Wiley-Interscience, Ed. 1995; p 538.
[42] Atkins, P.; Overton, T.; Rourke, J.; Weller, M.; Armstrong, F., *Inorg. Chem.*, 4th Edition ed.; Oxford: 2006; p 467.
[43] Chappel, E.; Nùñez-Regueiro, M. D.; Chouteau, G.; Isnard, O.; Darie, C. *E. P. J. B* **2000,** 17, 615.
[44] Ma, X.; Chen, H.; Ceder, G. *J. Electrochem. Soc.* **2011,** 158, (12), A1307
[45] Komaba, S.; Murata, W.; Ishikawa, T.; Yabuuchi, N.; Ozeki, T.; Nakayama, T.; Ogata, A.; Gotoh, K.; Fujiwara, K. *Adv. Funct. Mater.* **2011,** 21, (20), 3859.
[46] Kim, D.; Lee, E.; Slater, M.; Lu, W.; Rood, S.; Johnson, C. S. *Electrochem. Comm.* **2012,** 18, 66
[47] Ponrouch, A.; Goñi, A. R.; Palacín, M. R. *Electrochem. Comm.* **2013,** 27, 85.
[48] Berthelot, R.; Carlier, D.; Delmas, C. *Nat. Mat.* **2011,** 10, (1), 74
[49] Jansen, M.; Hoppe, R. *Z. Anorg. Allg. Chem* **1974,** 408, (2), 104.
[50] Jansen, M.; Hoppe, R. *Naturwissenschaften* **1972,** 59, (5), 215.
[51] Delmas, C.; Braconnier, J.-J.; Fouassier, C.; Hagenmuller, P. *Solid State Ionics* **1981,** 3/4, 165
[52] Mendiboure, A.; Delmas, C.; Hagenmuller, P. *J. Solid State Chem.* **1985,** 57, 323.
[53] Maazaz, A.; Delmas, C.; Hagenmuller, P. *J. Incl. Phenom.* **1983,** 1, 45
[54] Hamani, D.; Ati, M.; Tarascon, J.-M.; Rozier, P. *Electrochem. Comm.* **2011,** 13, (9), 938.
[55] Didier, C.; Guignard, M.; Denage, C.; Szajwaj, O.; Ito, S.; Saadoune, I.; Darriet, J.; Delmas, C. *Electrochem. Solid. St.* **2011,** 14, (5), A75
[56] Guignard, M.; Didier, C.; Darriet, J.; Bordet, P.; Elkaïm, E.; Delmas, C. *Nat. Mat.* **2013,** 12, 74
[57] Komaba, S.; Nakayama, T.; Ogata, A.; Shimizu, T.; Takei, C.; Takada, S.; Hokura, A.; Nakai, I. *ECS Trans.* **2009,** 16, (42), 43.
[58] Komaba, S.; Takei, C.; Nakayama, T.; Ogata, A.; Yabuuchi, N. *Electrochem. Comm.* **2010,** 12, (3), 355.
[59] Xia, X.; Dahn, J. R. *Electrochem. Solid. St.* **2012,** 15, (1), A1.
[60] Ding, J.-J.; Zhou, Y.-N.; Sun, Q.; Fu, Z.-W. *Electrochem. Comm.* **2012,** 22, 85.
[61] Caballero, A.; Hernán, L.; Morales, J.; Sánchez, L.; Santos Peña, J.; Aranda, M. A. G. *J. Mater. Chem.* **2002,** 12, (4), 1142.
[62] Yabuuchi, N.; Yoshida, H.; Komaba, S. *Electrochemistry* **2012,** 80, (10), 716
[63] Rai, A. K.; Anh, L. T.; Gim, J.; Mathew, V.; Kim, J. *Ceram. Int.* **2014,** 40, (1), 2411.
[64] Didier, C.; Guignard, M.; Darriet, J.; Delmas, C. *Inorg Chem* **2012,** 51, (20), 11007.
[65] Matsumura, T.; Sonoyama, N.; Kanno, R. *Solid State Ionics* **2003,** 161, (1-2), 31.
[66] Yabuuchi, N.; Iwatate, J.; Kajiyama, M.; Yamamoto, Y.; Hitomi, S.; Okuyama, R.; Komaba, S. *220th ECS Meeting Abstract #649* **2011**.
[67] Wang, X.; Liu, G.; Iwao, T.; Okubo, M.; Yamada, A. *J. Phys. Chem. C* **2014,** 118, (6), 2970
[68] Vassilaras, P.; Toumar, A. J.; Ceder, G. *Electrochem. Comm.* **2014,** 38, 79.
[69] Yabuuchi, N.; Yano, M.; Yoshida, H.; Kuze, S.; Komaba, S. *J. Electrochem. Soc.* **2013,** 160, (5), A3131
[70] Xu, J.; Lee, D. H.; Clément, R. J.; Yu, X.; Leskes, M.; Pell, A. J.; Pintacuda, G.; Yang, X.-Q.; Grey, C. P.; Meng, Y. S. *Chem. Mater.* **2014,** 26, (2), 1260
[71] Kim, D.; Kang, S.-H.; Slater, M.; Rood, S.; Vaughey, J. T.; Karan, N.; Balasubramanian, M.; Johnson, C. *Adv. Energy Mater.* **2011,** 1, 333.
[72] Lu, Z.; Dahn, J. R. *J. Electrochem. Soc.* **2001,** 148, (11), A1225
[73] Shaju, K. M.; Subba Rao, G. V.; Chowdari, B. V. R. *Electrochem. Comm.* **2002,** 4, 633.
[74] Paulsen, J. M.; Dahn, J. R. *Solid State Ionics* **1999,** 126, 3.
[75] Lu, Z.; Dahn, J. R. *J. Electrochem. Soc.* **2001,** 148, (7), A710.
[76] Lee, D. H.; Xu, J.; Meng, Y. S. *Phys Chem Chem Phys* **2013,** 15, (9), 3304.
[77] Wang, H.; Yang, B.; Liao, X.-Z.; Xu, J.; Yang, D.; He, Y.-S.; Ma, Z.-F. *Electrochim. Acta* **2013,** 113, 200
[78] Komaba, S.; Yabuuchi, N.; Nakayama, T.; Ogata, A.; Ishikawa, T.; Nakai, I. *Inorg. Chem.* **2012,** 51, (11), 6211

[79] Carlier, D.; Cheng, J. H.; Berthelot, R.; Guignard, M.; Yoncheva, M.; Stoyanova, R.; Hwang, B. J.; Delmas, C. *Dalton. T.* **2011,** 40, (36), 9306
[80] Xia, X.; Dahn, J. R. *J. Electrochem. Soc.* **2012,** 159, (7), A1048
[81] Parant, J.-P. Sur quelques nouveaux oxydes ternaires du système manganèse - oxygène - sodium. Université de Bordeaux, 1970.
[82] Sharma, P. K.; Moore, G. J.; Zhang, F.; Zavalij, P.; Whittingham, M. S. *Electrochem. Solid. St.* **1999,** 2, (10), 494.
[83] Saadoune, I.; Maazaz, A.; Ménétrier, M.; Delmas, C. *J. Solid State Chem.* **1996,** 122, 111.
[84] Lu, Z.; Dahn, J. R. *Chem. Mater.* **2001,** 13, 1252
[85] Wang, Y.; Yu, X.; Xu, S.; Bai, J.; Xiao, R.; Hu, Y. S.; Li, H.; Yang, X. Q.; Chen, L.; Huang, X. *Nat Commun* **2013,** 4, 2365.
[86] Yuan, D.; Hu, X.; Qian, J.; Pei, F.; Wu, F.; Mao, R.; Ai, X.; Yang, H.; Cao, Y. *Electrochim. Acta* **2014,** 116, 300
[87] Bucher, N.; Hartung, S.; Gocheva, I.; Cheah, Y. L.; Srinivasan, M.; Hoster, H. E. *J. Solid State Electr.* **2013,** 17, (7), 1923.
[88] Wang, X.; Tamaru, M.; Okubo, M. i.; Yamada, A. *J. Phys. Chem. C* **2013,** 117, (30), 15545.
[89] Beck, F. R.; Cheng, Y. Q.; Bi, Z.; Feygenson, M.; Bridges, C. A.; Moorhead-Rosenberg, Z.; Manthiram, A.; Goodenough, J. B.; Paranthaman, M. P.; Manivannan, A. *J. Electrochem. Soc.* **2014,** 161, (6), A961.
[90] Yoshida, J.; Guerin, E.; Arnault, M.; Constantin, C.; Mortemard de Boisse, B.; Carlier, D.; Guignard, M.; Delmas, C. *J. Electrochem. Soc.* **2014,** 161, (14), A1987
[91] Buchholz, D.; Moretti, A.; Kloepsch, R.; Nowak, S.; Siozios, V.; Winter, M.; Passerini, S. *Chem. Mater.* **2013,** 25, (2), 142
[92] Chagas, L. G.; Buchholz, D.; Wu, L.; Vortmann, B.; Passerini, S. *J. Power Sources* **2014,** 247, 377
[93] Yuan, D.; He, W.; Pei, F.; Wu, F.; Wu, Y.; Qian, J.; Cao, Y.; Ai, X.; Yang, H. *J. Mater. Chem. A* **2013,** 1, (12), 3895
[94] Doubaji, S.; Valvo, M.; Saadoune, I.; Dahbi, M.; Edström, K. *J. Power Sources* **2014,** 266, 275
[95] Sathiya, M.; Hemalatha, K.; Ramesha, K.; Tarascon, J. M.; Prakash, A. S. *Chem. Mater.* **2012,** 24, (10), 1846
[96] Vidal-Abarca, C.; Lavela, P.; Tirado, J. L.; Chadwick, A. V.; Alfredsson, M.; Kelder, E. *J. Power Sources* **2012,** 197, 314.
[97] Ponrouch, A.; Marchante, E.; Courty, M.; Tarascon, J. M.; Palacín, M. R. *Energy and Environmental Science* **2012,** 5, (9), 8572.
[98] Aurbach, D.; Gamolsky, K.; Markovsky, B.; Gofer, Y.; Schmidt, M.; Heider, U. *Electrochim. Acta* **2002,** 47, (9), 1423.
[99] Komaba, S.; Ishikawa, T.; Yabuuchi, N.; Murata, W.; Ito, A.; Ohsawa, Y. *ACS Appl. Mater. Interfaces* **2011,** 3, (11), 4165
[100] Bhide, A.; Hofmann, J.; Durr, A. K.; Janek, J.; Adelhelm, P. *Phys Chem Chem Phys* **2014,** 16, (5), 1987.
[101] Petricek, V.; Dusek, M.; Palatinus, L. *Z. Kristallogr.* **2014,** 229, (5), 345
[102] Pitschke, W.; Hermann, H.; Mattern, N. *J. Appl. Crystallogr.* **1993,** 26, 132.
[103] Toby, B. H. *Powder Diffraction* **2006,** 21, 67.
[104] Leriche, J. B.; Hamelet, S.; Shu, J.; Morcrette, M.; Masquelier, C.; Ouvrard, G.; Zerrouki, M.; Soudan, P.; Belin, S.; Elkaïm, E.; Baudelet, F. *J. Electrochem. Soc.* **2010,** 157, (5), A606
[105] Mössbauer, R. L. *Z. Physik* **1958,** 151, 124.
[106] Mössbauer, R. L. *Naturwissenschaften* **1958,** 45, 538.
[107] Rougier, A. Relation entre la structure et le comportement électrochimique des phases $Li_xNi_{1-y}M_yO_2$ (M = Al, Fe, Co) : Matériaux d'électrodes positives pour batteries au lithium. Université de Bordeaux, 1995.
[108] Sayers, D. E.; Lytle, F. W.; Stern, E. A. **1969,** V 13, 248.
[109] Chick, L. A.; Pederson, L. R.; Maupin, G. D.; Bates, J. L.; Thomas, L. E.; Exarhos, G. J. *Materials Letters* **1990,** 10, (1–2), 6.
[110] Moore, J. J.; Feng, H. J. *Prog. Mater. Sci.* **1995,** 39, 243.
[111] Mauvy, F.; Bassat, J. M.; Boehm, E.; Dordor, P.; Loup, J. P. *Solid State Ionics* **2003,** 158, (3-4), 395.

[112] Djurdjevic, P. *Transition Met. Chem.* **1990,** 15, 345.
[113] Didier, C. Etude des oxydes lamellaires Na_xVO_2 : électrochimie, structure et propriétés physiques. Université de Bordeaux, 2013.
[114] Stoyanova, R.; Carlier, D.; Sendova-Vassileva, M.; Yoncheva, M.; Zhecheva, E.; Nihtianova, D.; Delmas, C. *J. Solid State Chem.* **2010,** 183, (6), 1372
[115] Bordet-Le Guenne, L.; Deniard, P.; Biensan, P.; Siret, C.; Breca, R. *J. Mater. Chem.* **2000,** 10, 2201
[116] Pouillerie, C.; Croguennec, L.; Delmas, C. *Solid State Ionics* **2000,** 132, (1), 15
[117] Seguin, L.; Amatucci, G.; Anne, M.; Chabre, Y.; Strobel, P.; Tarascon, J. M.; Vaughan, G. *J. Power Sources* **1999,** 81–82, (0), 604
[118] Stephens, P. W. *J. Appl. Crystallogr.* **1999,** 32, (2), 281
[119] Delmas, C.; Tessier, C. *J. Mater. Chem.* **1997,** 7, (8), 1439.
[120] Carlier, D.; Ménétrier, M.; Delmas, C. In *Lithium deintercalation in LiNi0.30Co0.70O2: Redox processes, electronic and ionic mobility as characterized by 7Li MAS NMR and electrical properties*, Materials Research Society Symposium - Proceedings, 2001; pp GG991.
[121] Prado, G.; Fournès, L.; Delmas, C. *J. Solid State Chem.* **2001,** 159, (1), 103
[122] Demourgues-Guerlou, L.; Fournès, L.; Delmas, C. *J. Solid State Chem.* **1995,** 114, (1), 6
[123] Guerlou-Demourgues, L.; Fournès, L.; Delmas, C. *J. Electrochem. Soc.* **1996,** 143, (10), 3083
[124] Baker, P. J.; Lancaster, T.; Blundell, S.; Brooks, M.; Hayes, W.; Prabhakaran, D.; Pratt, F. *Phys. Rev. B* **2005,** 72, (10).
[125] Baker, P. J.; Lancaster, T.; Blundell, S. J.; Brooks, M. L.; Hayes, W.; Prabhakaran, D.; Pratt, F. L. *Physica B: Condensed Matter* **2006,** 374-375, 47.
[126] Bongers, P. F.; ENZ, U. *Solid State Commun.* **1966,** 4, 153.
[127] Chappel, E.; Nùñez-Regueiro, M. D.; Dupont, F.; Chouteau, G.; Darie, C.; Sulpice, A. *E. P. J. B* **2000,** 17, 609.
[128] Darie, C.; Bordet, P.; de Brion, S.; Holzapfel, M.; Isnard, O.; Lecchi, A.; Lorenzo, J. E.; Suard, E. *E. P. J. B* **2005,** 43, (2), 159.
[129] de Brion, S.; Bonda, M.; Darie, C.; Bordet, P.; Sheikin, I. *J Phys Condens Matter* **2010,** 22, (12), 126001.
[130] de Brion, S.; Darie, C.; Holzapfel, M.; Talbayev, D.; Mihály, L.; Simon, F.; Jánossy, A.; Chouteau, G. *Phys. Rev. B* **2007,** 75, (9).
[131] Lewis, M.; Gaulin, B.; Filion, L.; Kallin, C.; Berlinsky, A.; Dabkowska, H.; Qiu, Y.; Copley, J. *Phys. Rev. B* **2005,** 72, (1).
[132] Sofin, M.; Jansen, M. *Z. Naturforsch* **2005,** 60b, 701.
[133] Molenda, J.; Stoklosa, A. *Solid State Ionics* **1990,** 38, 1.
[134] Han, M. H.; Gonzalo, E.; Casas-Cabanas, M.; Rojo, T. *J. Power Sources* **2014,** 258, 266.
[135] Tarascon, J. M.; Hull, G. W. *Solid State Ionics* **1986,** 22, 85